Proceedings of

ICADD–1

The First International Conference on Analysis of Discontinuous Deformation

Edited by

John C. Li

Chung-Yue Wang

Jopan Sheng

Proceedings of

The First International Conference on Analysis of Discontinuous Deformation

Chungli, Taiwan, R. O. C. December 21-23, 1995

Organized by
Department of Civil Engineering,
National Central University,
Chungli, Taiwan, R. O. C.

Sponsors

National Science Council, R. O. C.
Ministry of Education, R. O. C.
National Central University, Taiwan, R. O. C.
Sinotech Engineering Consultants Inc., Taipei, Taiwan, R. O. C.

Committee Chairman

John C. Li
Vice Chairman of Public Construction Commission, Taiwan, R. O. C.

Organizing Committee:

Ching-Lung Liao, National Taiwan Institute of Technology, R. O. C.
Ta-Peng Chang, National Taiwan Institute of Technology, R. O. C.
Jin-Ching Chern, Sinotech Engineering Consultants, Inc., Taipei, Taiwan, R. O. C.
T. H. Huang, National Taiwan University, R. O. C.
Fu-Shu Jeng, National Taiwan University, R. O. C.
A. B. Huang, National Chiao Tung University, R. O. C.
Y. J. Chiou, National Cheng-Kung University, R. O. C.
J. S. Tsai, National Cheng-Kung University, R. O. C.
T. C. Ke, Chung-Yuan University, R. O. C.
Lien-Kwei Chien, National Taiwan Ocean University, R. O. C.
Jopan Sheng, National Central University, R. O. C.
Chung-Yue Wang, National Central University, R. O. C.

PREFACE

This is the first International Conference on Analysis of Discontinuous Deformation. Due to anomalies including constituents, chemical reactions, voids and flaws, thermal treatments during manufacturing process or damage formed in service, there might be discontinuities existed inside the material or the physical field of engineering system. Complicated behaviors due to these discontinuities lead to difficulties of interpretation and analysis. In the past few years, a number of researchers and engineers have worked very hard on the topics containing discontinuities like the behaviors of jointed rocks, ice plates, granular materials, delamination of layered medium, blasting fragmentation and damage /fracture progression of material etc.. High quality and outstanding works have been produced. Those methods or algorithms have been developed offer powerful approaches to analyze complex engineering problems which can not be solved comprehensively by classical continuum analyses alone.

In order to gathering the most important development and improvement of the analysis of discontinuous deformation up to now and to provide an opportunity for interactions of researchers working on this important area, the first international conference on analysis of discontinuous deformation was planned and then be held in Taiwan, Republic of China.

These proceedings contain much of the recent research work performed in the field of discontinuous deformation, with contributions from many areas. A total of 25 papers from 5 different countries interweaves an interesting mix of sessions on rock mechanics, structural dynamics, fragmentation/ failure analysis, granular mechanics and some genetic theorems for the discontinuous deformation analysis. It is our hope that every attendant will gain some useful information to continue his further research on this new trend of engineering analysis

A conference of this topic would not be possible without the help of many institutes and individuals. The main sponsors of the conference are National Science Council, Ministry of Education, Sinotech Engineering Consultants Inc. and National Central University of R. O. C., their supports are deeply appreciated. We would also like to thank all, who have devoted their work to the conference and made it possible to present this volume.

John C. Li, Conference Chairman
Vice Chairman of Public Construction Commission
Taiwan, R. O. C.

Chung-Yue Wang and Jopan Sheng
Conference Secretaries
Department of Civil Engineering
National Central University
Taiwan, R. O. C.

TABLE OF CONTENTS

Simplex Integration for Manifold Method and Discontinuous Deformation Analysis

Gen-hua Shi

Geotechnical Lab, US Army Engineer Waterways Experiment Station, Vicksburg, MS 39180-6199

ABSTRACT: At least every engineer has to compute the volume of generally shaped blocks. Is there a formula where the volume is precisely represented by the coordinates of boundary vertices? If block movements are considered, center of gravity have to be computed. Is there a formula where the center of gravity is also represented by the coordinates of boundary vertices? The simplex integration developed for DDA computation can also solve these questions. The convergency and accuracy of DDA and manifold method algorithms depend upon mainly the analytical integrations on complex shapes. Simplex integrations are accurate solution on n-dimensional generally shaped domains. The integrand could be any n-dimensional polynomials. The computations of three rock and structure failure cases are presented.

1 SIMPLEX INTEGRATION ON A SIMPLEX

Simplex bas the most simple shape in $1, 2, 3, \ldots, n$ dimensional space. Different from the ordinary integration, simplex integration with only simplex as integral domain. Simplex also has positive or negative orientations. Positive or negative orientations define positive or negative volumes respectively.

One dimensional simplex P_0P_1 is a oriented segment, its volume is

$$J = \frac{1}{1!}\begin{vmatrix} 1 & x_0 \\ 1 & x_1 \end{vmatrix} = x_1 - x_0$$

The volume of simplex P_1P_0 is the negative volume of the simplex P_0P_1. Ordinary 1-d integrations are simplex integrations:

$$\int_{P_0P_1} f(x)D(x) = \int_{P_0}^{P_1} f(x)dx \qquad \int_{P_0}^{P_1} f(x)dx = -\int_{P_1}^{P_0} f(x)dx$$

Therefore, for any co-line point Q_0, with the order Q_0, P_0, P_1,

$$\overrightarrow{P_0Q_0} + \overrightarrow{Q_0P_1} = \overrightarrow{P_0Q_0} + \overrightarrow{Q_0P_0} + \overrightarrow{P_0P_1} = \overrightarrow{P_0P_1}$$

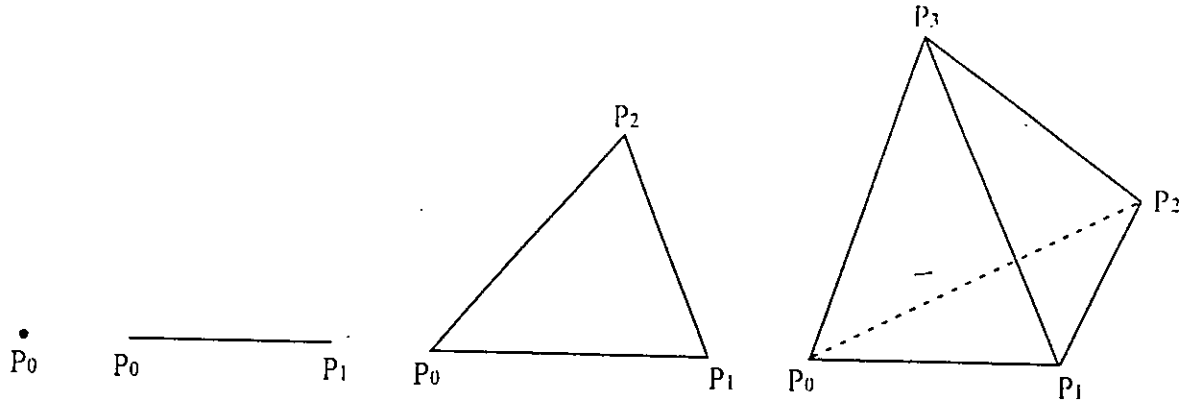

Figure 1. $0, 1, 2, 3$ dimensional simplex

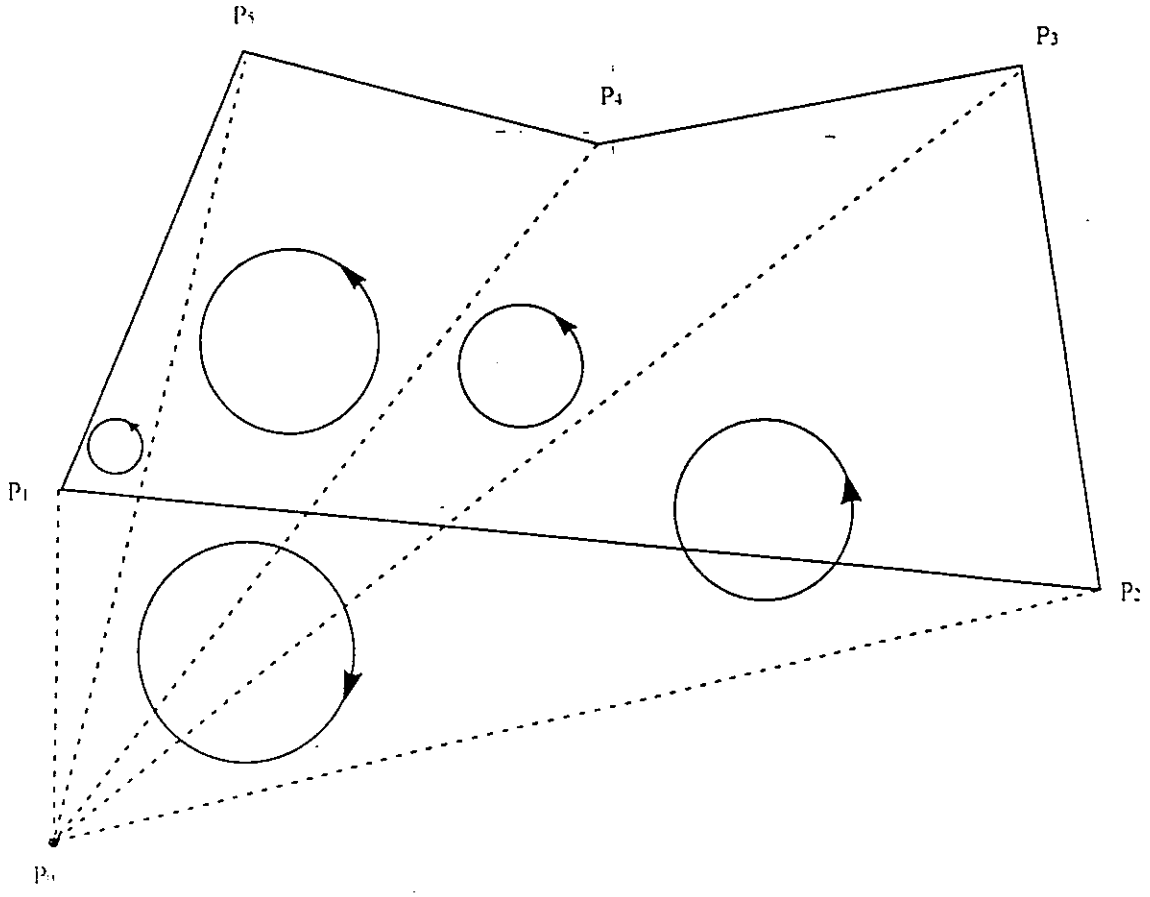

Figure 2. Addition of plus or minus area of simplex

$$\int_{P_0}^{Q_0} f(x)dx + \int_{Q_0}^{P_1} f(x)dx$$
$$= \int_{P_0}^{Q_0} f(x)dx + \int_{Q_0}^{P_0} f(x)dx + \int_{P_0}^{P_1} f(x)dx = \int_{P_0}^{P_1} f(x)dx$$
$$\int_{P_0Q_0} f(x)D(x) + \int_{Q_0P_1} f(x)D(x)$$
$$= \int_{P_0Q_0} f(x)D(x) + \int_{Q_0P_0} f(x)D(x) + \int_{P_0P_1} f(x)D(x) = \int_{P_0P_1} f(x)D(x)$$

The 1-d integration addition is the same as vector addition. The integrations on negative vectors and positive vectors can be nullified.

Unfortunately, two dimensional, three dimensional and higher dimensional ordinary integrations are volume integration, where the volume is always positive. For the 2 or higher dimensional ordinary integration, the integration domain has no orientation, therefore the integration has no algebraic addition of oriented domains. It is then necessary to introduce simplex integration on a simplex, which is a simple oriented domain.

Two dimensional simplex $P_0P_1P_2$ is a oriented triangle, its volume is

$$J = \frac{1}{2!}\begin{vmatrix} 1 & x_0 & y_0 \\ 1 & x_1 & y_1 \\ 1 & x_2 & y_2 \end{vmatrix}$$

The volume of simplex $P_1P_0P_2$ is the negative volume of simplex $P_0P_1P_2$.

$$P_1P_0P_2 = -P_0P_1P_2$$

The two dimensional simplex integration is defined by

$$\int_{P_0P_1P_2} f(x,y)D(x,y) = sign(J)\int\int_{P_0P_1P_2} f(x,y)dxdy$$

Giving a polygon $P_1P_2P_3P_4P_5P_6$ with $P_6 = P_1$, such that P_i rotate at the same direction as from ox to oy. For any point P_0, the algebraic addition of the 2-d simplex volume (area) $P_0P_1P_2$, $P_0P_2P_3$, $P_0P_3P_4$, $P_0P_4P_5$ and $P_0P_5P_1$ is the area A of the polygon.

In Figure 2, the area of simplex $P_0P_2P_3$, $P_0P_3P_4$, $P_0P_4P_5$ and $P_0P_5P_1$ are positive; the area of simplex $P_0P_1P_2$ is negative. The algebraic sum is exactly the area of polygon $P_1P_2P_3P_4P_5P_6$. The area A is then represented by the coordinates of boundary

vertices.

$$P_1P_2P_3P_4P_5P_6 = P_0P_1P_2 + P_0P_2P_3 + P_0P_3P_4 + P_0P_4P_5 + P_0P_5P_1$$

Let $P_0 = (0, 0)$,

$$A = \frac{1}{2}\sum_{i=1}^{5}\begin{vmatrix} 1 & 0 & 0 \\ 1 & x_i & y_i \\ 1 & x_{i+1} & y_{i+1} \end{vmatrix} = \frac{1}{2}\sum_{i=1}^{5}\begin{vmatrix} x_i & y_i \\ x_{i+1} & y_{i+1} \end{vmatrix}$$

For a general integrand $f(x, y)$, the normal integration on polygon $P_1P_2P_3P_4P_5P_6$ is the algebraic addition of the simplex integrations:

$$\int\int_{P_1P_2P_3P_4P_5P_6} f(x,y)dxdy = \sum_{i=1}^{5}\int_{P_0P_iP_{i+1}} f(x,y)D(x,y)$$

Three dimensional simplex $P_0P_1P_2P_3$ is a oriented tetrahedron, its volume is

$$J = \frac{1}{3!}\begin{vmatrix} 1 & x_0 & y_0 & z_0 \\ 1 & x_1 & y_1 & z_1 \\ 1 & x_2 & y_2 & z_2 \\ 1 & x_3 & y_3 & z_3 \end{vmatrix}$$

The volume of simplex $P_1P_0P_2P_3$ is the negative volume of simplex $P_0P_1P_2P_3$.

$$P_1P_0P_2P_3 = -P_0P_1P_2P_3$$

The three dimensional simplex integration is defined by

$$\int_{P_0P_1P_2P_3} f(x,y,z)D(x,y,z) = sign(J)\int\int\int_{P_0P_1P_2P_3} f(x,y,z)dxdydz$$

The simplex integration is not intended to do integrations on simplex only. Obviously a complex shape always can be subdivided into simplex, so simplex integration can be computed in each simplex, the summation of simplex integrations is the ordinary integration over the complex shape. However this is also not the way of using simplex integration.

In general, simplex integration can compute ordinary integrations without subdividing 2-d domains to triangles and 3-d volumes to tetrahedrons. FEM mesh is unnecessary for simplex integration. Using simplex integration, the integration of any n-dimensional polynomials can be represented by the coordinates of boundary vertices of generally shaped polyhedrons.

The definition of simplex integration can be extended to n dimensional space. The domains of simplex integrations can be extended from a n dimensional simplex to any n dimensional oriented domain. The n dimensional oriented domain (V) is a normal n dimensional polyhedron with a positive or negative orientation.

$$\begin{aligned}&\int_{(V)} f(x_1, x_2, x_3, \ldots, x_n) D(x_1, x_2, x_3, \ldots, x_n) \\ =&sign(J) \int\int\int \cdots \int_{(V)} f(x_1, x_2, x_3, \ldots, x_n)\, dx_1 dx_2 dx_3 \ldots dx_n \end{aligned} \tag{1}$$

The term $sign(J)$ is the sign of a determinant J representing the orientation of the oriented domain V. The simplex integrations over a general oriented domain V have the following two important properties.

(1) If as oriented domains, $V = V_1 + V_2$ then

$$\begin{aligned}&\int_{(V)} f(x_1, x_2, x_3, \ldots, x_n) D(x_1, x_2, x_3, \ldots, x_n) \\ =&\int_{(V_1)} f(x_1, x_2, x_3, \ldots, x_n) D(x_1, x_2, x_3, \ldots, x_n) \\ +&\int_{(V_2)} f(x_1, x_2, x_3, \ldots, x_n) D(x_1, x_2, x_3, \ldots, x_n) \end{aligned} \tag{2}$$

This is the generalization of the algebraic addition of the one dimensional normal integrations to multi-dimensional integrations.

(2) If $(x_1, x_2, x_3, \ldots, x_n)$ are functions of $(u_1, u_2, u_3, \ldots, u_n)$, and oriented domain V corresponds to oriented domain U then

$$\begin{aligned}&\int_{(V)} f(x_1, x_2, x_3, \ldots, x_n) D(x_1, x_2, x_3, \ldots, x_n) \\ =&\int_{(U)} f(x_1, x_2, x_3, \ldots, x_n) \frac{D(x_1, x_2, x_3, \ldots, x_n)}{D(u_1, u_2, u_3, \ldots, u_n)} D(u_1, u_2, u_3, \ldots, u_n) \end{aligned} \tag{3}$$

where

$$\frac{D(x_1, x_2, x_3, \ldots, x_n)}{D(u_1, u_2, u_3, \ldots, u_n)} = J$$

is a Jacobian, not a absolute value $|J|$. Simplex integration generalized the mean-

ing of "Leibniz" symbol "dx" of the normal one dimensional integration to multi-dimensional integrations.

2 TWO DIMENSIONAL SIMPLEX INTEGRATIONS

The two dimensional integrations here in this section are used for two dimensional DDA and manifold algorithm. A 2 dimensional simplex has 3 vertices P_0, P_1, P_2 and the 2 dimensional coordinate simplex has 3 vertices U_0, U_1, U_2.

$$\begin{array}{llll} P_0: & (x_0, & y_0) & \qquad U_0: \ (\ 0, \ 0) \\ P_1: & (x_1, & y_1) & \qquad U_1: \ (\ 1, \ 0) \\ P_2: & (x_2, & y_2) & \qquad U_2: \ (\ 0, \ 1) \end{array}$$

The following coordinate transformation $(u_1, u_2) \rightarrow (x, y)$ transfers coordinate simplex $U_0U_1U_2$ to normal simplex $P_0P_1P_2$

$$\begin{array}{rcllllll} x & = & x_0 & (1-\sum_1^2 u_i)+ & x_1 & u_1 & + \ x_2 & u_2 \\ y & = & y_0 & (1-\sum_1^2 u_i)+ & y_1 & u_1 & + \ y_2 & u_2 \end{array}$$

The Jacobi determinant is

$$J = \frac{D(x,\ y)}{D(u_1,\ u_2)} = \begin{vmatrix} \frac{\partial x}{\partial u_1} & \frac{\partial x}{\partial u_2} \\ \frac{\partial y}{\partial u_1} & \frac{\partial y}{\partial u_2} \end{vmatrix} = \begin{vmatrix} x_1 - x_0 & x_2 - x_0 \\ y_1 - y_0 & y_2 - y_0 \end{vmatrix} = \begin{vmatrix} 1 & x_0 & y_0 \\ 1 & x_1 & y_1 \\ 1 & x_2 & y_2 \end{vmatrix}$$

Since $P_0P_1P_2$ is a 2-dimensional simplex with non-zero volume, J is non-zero. Translation can be rewritten as $(u_0, u_1, u_2) \rightarrow (1, x, y)$

$$\begin{array}{rcllllllll} 1 & = & & u_0 & + & & u_1 & + & & u_2 \\ x & = & x_0 & u_0 & + & x_1 & u_1 & + & x_2 & u_2 \\ y & = & y_0 & u_0 & + & y_1 & u_1 & + & y_2 & u_2 \end{array}$$

Two dimensional simplex integration

$$\int_{P_0P_1P_2} x^{m_1} y^{m_2} D(x, y)$$

on a two dimensional simplex $P_0P_1P_2$ is defined as normal integration times the sign of determinant J.

$$\int_{P_0P_1P_2} x^{m_1} y^{m_2} D(x, y) = sign(J) \int\int_{P_0P_1P_2} x^{m_1} y^{m_2}\ dxdy$$

$$= sign(J) \int\int_{U_0U_1U_2} x^{m_1} y^{m_2} |J| du_1 du_2 = J \int\int_{U_0U_1U_2} x^{m_1} y^{m_2} du_1 du_2$$

Here $x_l^{m_l} = \left(\sum_{k=0}^{2} x_{lk} u_k\right)^{m_l}$, then the two dimensional simplex integration can be represented by the following basic forms of simplex integration:

$$S_1 = \int\int_{U_0U_1U_2} u_0^{i_0} u_1^{i_1} u_2^{i_2} du_1 du_2 = \int\int_{u_0,u_1,u_2 \geq 0}^{u_0+u_1+u_2=1} u_0^{i_0} u_1^{i_1} u_2^{i_2} du_1 du_2$$
$$= \int_0^1 \int_0^{1-u_2} u_2^{i_2} u_1^{i_1} u_0^{i_0} du_1 du_2 = \int_0^1 u_2^{i_2} \left(\int_0^{1-u_2} u_1^{i_1} (1-u_2-u_1)^{i_0} du_1 \right) du_2$$

After i_1 times of integration by parts, the inner integration can be computed.

$$\int_0^{1-u_2} u_1^{i_1} (1-u_2-u_1)^{i_0} du_1 = \int_0^{1-u_2} d(\frac{1}{i_1+1} u_1^{i_1+1})(1-u_2-u_1)^{i_0}$$
$$= \frac{1}{i_1+1} u_1^{i_1+1} (1-u_2-u_1)^{i_0} \Big|_0^{1-u_2} - \int_0^{1-u_2} \frac{1}{i_1+1} u_1^{i_1+1} d((1-u_2-u_1)^{i_0})$$
$$= -\int_0^{1-u_2} \frac{1}{i_1+1} u_1^{i_1+1} d((1-u_2-u_1)^{i_0}) = \int_0^{1-u_2} \frac{i_0}{i_1+1} u_1^{i_1+1} (1-u_2-u_1)^{i_0-1} du_1$$
$$= \int_0^{1-u_2} \frac{i_0(i_0-1)}{(i_1+1)(i_1+2)} u_1^{i_1+2} (1-u_2-u_1)^{i_0-2} du_1$$
$$= \int_0^{1-u_2} \frac{i_0(i_0-1)(i_0-2)}{(i_1+1)(i_1+2)(i_1+3)} u_1^{i_1+3} (1-u_2-u_1)^{i_0-3} du_1$$
$$= \int_0^{1-u_2} \frac{i_0(i_0-1)(i_0-2)\dots 2}{(i_1+1)(i_1+2)(i_1+3)\dots(i_1+i_0-1)} u_1^{i_1+i_0-1} (1-u_2-u_1)^1 du_1$$
$$= \int_0^{1-u_2} \frac{i_0(i_0-1)(i_0-2)\dots 1}{(i_1+1)(i_1+2)(i_1+3)\dots(i_1+i_0)} u_1^{i_1+i_0} du_1$$
$$= \int_0^{1-u_2} \frac{i_0! i_1!}{(i_1+i_0)!} u_1^{i_1+i_0} du_1 = \int_0^{1-u_2} \frac{i_0! i_1!}{(i_1+i_0+1)!} d(u_1^{i_1+i_0+1})$$
$$= \frac{i_0! i_1!}{(i_0+i_1+1)!} u_1^{i_0+i_1+1} \Big|_0^{1-u_2} = \frac{i_0! i_1!}{(i_1+i_0+1)!} (1-u_2)^{i_1+i_0+1}$$

$$S_1 = \int_0^1 u_2^{i_2} du_2 \int_0^{1-u_2} u_1^{i_1} (1-u_2-u_1)^{i_0} du_1$$
$$= \int_0^1 u_2^{i_2} (1-u_2)^{i_0+i_1+1} du_2 \frac{i_0! i_1!}{(i_0+i_1+1)!} = \frac{i_0! i_1! i_2!}{(i_0+i_1+i_2+2)!}$$

Based on the previous formula of S_1, the two dimensional integrations of polynomials of degree 0, 1, 2 can be computed.

$$\int_{P_0P_1P_2} 1 D(x,y) = sign(J) \int\int_{P_0P_1P_2} dxdy = J \int\int_{U_0U_1U_2} du_1 du_2 = J \frac{0!}{(0+2)!} = \frac{1}{2} J$$

$$\int_{P_0P_1P_2} xD(x,y) = sign(J)\int\int_{P_0P_1P_2} xdxdy$$
$$= J\int\int_{U_0U_1U_2}(x_0u_0+x_1u_1+x_2u_2)du_1du_2$$
$$= J\frac{1!}{(1+2)!}(x_0+x_1+x_2) = \frac{1}{6}J(x_0+x_1+x_2)$$
$$\int_{P_0P_1P_2} yD(x,y) = sign(J)\int\int_{P_0P_1P_2} ydxdy = \frac{1}{6}J(y_0+y_1+y_2)$$
$$\int_{P_0P_1P_2} x^2D(x,y) = sign(J)\int\int_{P_0P_1P_2} x^2dxdy$$
$$= J\int\int_{U_0U_1U_2}(x_0u_0+x_1u_1+x_2u_2)^2du_1du_2$$
$$= \frac{1}{24}J\begin{array}{lll}(2x_0x_0 & +x_0x_1 & +x_0x_2\\ +x_1x_0 & +2x_1x_1 & +x_1x_2\\ +x_2x_0 & +x_2x_1 & +2x_2x_2)\end{array}$$
$$\int_{P_0P_1P_2} y^2D(x,y) = sign(J)\int\int_{P_0P_1P_2} y^2dxdy$$
$$= \frac{1}{24}J\begin{array}{lll}(2y_0y_0 & +y_0y_1 & +y_0y_2\\ +y_1y_0 & +2y_1y_1 & +y_1y_2\\ +y_2y_0 & +y_2y_1 & +2y_2y_2)\end{array}$$
$$\int_{P_0P_1P_2} xyD(x,y) = sign(J)\int\int_{P_0P_1P_2} xydxdy$$
$$= J\int\int_{U_0U_1U_2}(x_0u_0+x_1u_1+x_2u_2)(y_0u_0+y_1u_1+y_2u_2)du_1du_2$$
$$= \frac{1}{24}J\begin{array}{lll}(2x_0y_0 & +x_0y_1 & +x_0y_2\\ +x_1y_0 & +2x_1y_1 & +x_1y_2\\ +x_2y_0 & +x_2y_1 & +2x_2y_2)\end{array}$$

3 TRANSFER A NORMAL N DIMENSIONAL SIMPLEX TO THE COORDINATE SIMPLEX

A n dimensional simplex has n+1 vertices $P_0, P_1, P_2, \ldots, P_n$. The n dimensional coordinate simplex has n+1 vertices $U_0, U_1, U_2, \ldots, U_n$.

$$\begin{array}{llllllll}
P_0: & (x_{10}, & x_{20}, & x_{30}, & \ldots, & x_{n0}) & U_0: & (\ 0,\ 0,\ 0,\ \ldots,\ 0\ )\\
P_1: & (x_{11}, & x_{21}, & x_{31}, & \ldots, & x_{n1}) & U_1: & (\ 1,\ 0,\ 0,\ \ldots,\ 0\ )\\
P_2: & (x_{12}, & x_{22}, & x_{32}, & \ldots, & x_{n2}) & U_2: & (\ 0,\ 1,\ 0,\ \ldots,\ 0\ )\\
\vdots & \vdots & \vdots & \vdots & \vdots & \vdots & \vdots & \vdots\ \vdots\ \vdots\ \vdots\ \vdots\ \vdots\\
P_n: & (x_{1n}, & x_{2n}, & x_{3n}, & \ldots, & x_{nn}) & U_n: & (\ 0,\ 0,\ 0,\ \ldots,\ 1\ )
\end{array}$$

The following coordinate transformation

$$(u_0, u_1, u_2, u_3, \ldots, u_n) \rightarrow (1, x_1, x_2, x_3, \ldots, x_n)$$

transfers coordinate simplex $U_0U_1U_2 \ldots U_n$ to normal simplex $P_0P_1P_2 \ldots P_n$.

$$\begin{pmatrix} 1 \\ x_1 \\ x_2 \\ x_3 \\ \vdots \\ x_n \end{pmatrix} = \begin{pmatrix} 1 & 1 & 1 & \ldots & 1 \\ x_{10} & x_{11} & x_{12} & \ldots & x_{1n} \\ x_{20} & x_{21} & x_{22} & \ldots & x_{2n} \\ x_{30} & x_{31} & x_{32} & \ldots & x_{3n} \\ \vdots & \vdots & \vdots & \vdots & \vdots \\ x_{n0} & x_{n1} & x_{n2} & \ldots & x_{nn} \end{pmatrix} \begin{pmatrix} u_0 \\ u_1 \\ u_2 \\ u_3 \\ \vdots \\ u_n \end{pmatrix} \tag{4}$$

The determinant is

$$J = \frac{D(x_1,\ x_2,\ x_3,\ \ldots,\ x_n)}{D(u_1,\ u_2,\ u_3,\ \ldots,\ u_n)} = \begin{vmatrix} \frac{\partial x_1}{\partial u_1} & \frac{\partial x_1}{\partial u_2} & \frac{\partial x_1}{\partial u_3} & \ldots & \frac{\partial x_1}{\partial u_n} \\ \frac{\partial x_2}{\partial u_1} & \frac{\partial x_2}{\partial u_2} & \frac{\partial x_2}{\partial u_3} & \ldots & \frac{\partial x_2}{\partial u_n} \\ \frac{\partial x_3}{\partial u_1} & \frac{\partial x_3}{\partial u_2} & \frac{\partial x_3}{\partial u_3} & \ldots & \frac{\partial x_3}{\partial u_n} \\ \vdots & \vdots & \vdots & \vdots & \vdots \\ \frac{\partial x_n}{\partial u_1} & \frac{\partial x_n}{\partial u_2} & \frac{\partial x_n}{\partial u_3} & \ldots & \frac{\partial x_n}{\partial u_n} \end{vmatrix}$$

$$= \begin{vmatrix} x_{11} - x_{10} & x_{12} - x_{10} & x_{13} - x_{10} & \ldots & x_{1n} - x_{10} \\ x_{21} - x_{20} & x_{22} - x_{20} & x_{23} - x_{20} & \ldots & x_{2n} - x_{20} \\ x_{31} - x_{30} & x_{32} - x_{30} & x_{33} - x_{30} & \ldots & x_{3n} - x_{30} \\ \vdots & \vdots & \vdots & \vdots & \vdots \\ x_{n1} - x_{n0} & x_{n2} - x_{n0} & x_{n3} - x_{n0} & \ldots & x_{nn} - x_{n0} \end{vmatrix}$$

$$= \begin{vmatrix} 1 & 1 & 1 & \ldots & 1 \\ x_{10} & x_{11} & x_{12} & \ldots & x_{1n} \\ x_{20} & x_{21} & x_{22} & \ldots & x_{2n} \\ x_{30} & x_{31} & x_{32} & \ldots & x_{3n} \\ \vdots & \vdots & \vdots & \vdots & \vdots \\ x_{n0} & x_{n1} & x_{n2} & \ldots & x_{nn} \end{vmatrix} = \begin{vmatrix} 1 & x_{10} & x_{20} & x_{30} & \ldots & x_{n0} \\ 1 & x_{11} & x_{21} & x_{31} & \ldots & x_{n1} \\ 1 & x_{12} & x_{22} & x_{32} & \ldots & x_{n2} \\ \vdots & \vdots & \vdots & \vdots & \vdots & \vdots \\ 1 & x_{1n} & x_{2n} & x_{3n} & \ldots & x_{nn} \end{vmatrix} \tag{5}$$

4 DEFINITION OF N DIMENSIONAL SIMPLEX INTEGRATION

Simplex integration on a n dimensional simplex $P_0P_1P_2 \ldots P_n$ is defined as normal integration times the sign of determinant J.

$$\int_{P_0P_1P_2 \ldots P_n} x_1^{m_1} x_2^{m_2} x_3^{m_3} \ldots x_n^{m_n} D(x_1, x_2, x_3, \ldots, x_n)$$

$$= sign(J) \int\int\int \cdots \int_{P_0P_1P_2\ldots P_n} x_1^{m_1} x_2^{m_2} x_3^{m_3} \cdots x_n^{m_n} \quad dx_1 dx_2 dx_3 \ldots dx_n$$

$$= sign(J) \int\int\int \cdots \int_{U_0U_1U_2\ldots U_n} x_1^{m_1} x_2^{m_2} x_3^{m_3} \cdots x_n^{m_n} |J| du_1 du_2 du_3 \ldots du_n$$

$$= \quad J \int\int\int \cdots \int_{U_0U_1U_2\ldots U_n} x_1^{m_1} x_2^{m_2} x_3^{m_3} \cdots x_n^{m_n} \quad du_1 du_2 du_3 \ldots du_n \qquad (6)$$

In order to compute the integration and the coefficients of invariants u_k^i in

$$x_l^{m_l} = (\sum_{k=0}^{n} x_{lk} u_k)^{m_l}$$

of formula (6), the following formula (7) is useful.

$$(\sum_{k=0}^{n} a_k)^m = \sum_{j_0,j_1,j_2,\ldots,j_n \geq 0}^{j_0+j_1+j_2+\ldots+j_n=m} \frac{(j_0+j_1+j_2+\ldots+j_n)!}{j_0!j_1!j_2!\ldots!j_n!} a_0^{j_0} a_1^{j_1} a_2^{j_2} \cdots a_n^{j_n} \qquad (7)$$

A brief derivation is given here for convenience. In case of $n = 0$ and $n = 1$, formula (7) is correct:

$$(\sum_{k=0}^{0} a_k)^m = \sum_{j_0 \geq 0}^{j_0=m} \frac{j_0!}{j_0!} a_0^{j_0} = a_0^m \qquad (\sum_{k=0}^{1} a_k)^m = \sum_{j_0,j_1 \geq 0}^{j_0+j_1=m} \frac{(j_0+j_1)!}{j_0!j_1!} a_0^{j_0} a_1^{j_1}$$

Assuming formula (7) is correct for n:

$$(\sum_{k=0}^{n} a_k)^m = \sum_{j_0,j_1,j_2,\ldots,j_n \geq 0}^{j_0+j_1+j_2+\ldots+j_n=m} \frac{(j_0+j_1+j_2+\ldots+j_n)!}{j_0!j_1!j_2!\ldots!j_n!} a_0^{j_0} a_1^{j_1} a_2^{j_2} \cdots a_n^{j_n}$$

then the following computation shows formula (7) is correct for n+1

$$(\sum_{k=0}^{n+1} a_k)^m = ((\sum_{k=0}^{n} a_k) + a_{n+1})^m = \sum_{i_n,j_{n+1} \geq 0}^{i_n+j_{n+1}=m} \frac{(i_n+j_{n+1})!}{i_n!j_{n+1}!} (\sum_{k=0}^{n} a_k)^{i_n} a_{n+1}^{j_{n+1}}$$

$$= \sum_{i_n,j_{n+1} \geq 0}^{i_n+j_{n+1}=m} \frac{(i_n+j_{n+1})!}{i_n!j_{n+1}!} \sum_{j_0,j_1,j_2,\ldots,j_n \geq 0}^{j_0+j_1+j_2+\ldots+j_n=i_n} \frac{(j_0+j_1+j_2+\ldots+j_n)!}{j_0!j_1!j_2!\ldots!j_n!} a_0^{j_0} a_1^{j_1} a_2^{j_2} \cdots a_n^{j_n} a_{n+1}^{j_{n+1}}$$

$$= \sum_{i_n,j_{n+1} \geq 0}^{i_n+j_{n+1}=m} \sum_{j_0,j_1,j_2,\ldots,j_n \geq 0}^{j_0+j_1+j_2+\ldots+j_n=i_n} \frac{(i_n+j_{n+1})!}{i_n!j_{n+1}!} \frac{(j_0+j_1+j_2+\ldots+j_n)!}{j_0!j_1!j_2!\ldots!j_n!} a_0^{j_0} a_1^{j_1} a_2^{j_2} \cdots a_n^{j_n} a_{n+1}^{j_{n+1}}$$

$$= \sum_{i_n+j_{n+1}=m}^{} \sum_{j_0+j_1+j_2+\ldots+j_n=i_n}^{} \frac{(i_n+j_{n+1})!}{j_0!j_1!j_2!\ldots!j_n!j_{n+1}!} a_0^{j_0} a_1^{j_1} a_2^{j_2} \cdots a_n^{j_n} a_{n+1}^{j_{n+1}}$$

$$= \sum_{j_0,j_1,j_2,\ldots,j_n,j_{n+1}\geq 0}^{j_0+j_1+j_2+\ldots+j_n+j_{n+1}=m} \frac{(j_0+j_1+j_2+\ldots+j_n+j_{n+1})!}{j_0!j_1!j_2!\ldots!j_n!j_{n+1}!} a_0^{j_0} a_1^{j_1} a_2^{j_2} \cdots a_n^{j_n} a_{n+1}^{j_{n+1}}$$

Denote $u_0 = 1 - \sum_1^n u_i$, from the previous algebraic formula,

$$x_l^{m_l} = \left(\sum_{k=0}^{n} u_k x_{lk}\right)^{m_l} = \sum_{i_{l0},i_{l1},i_{l2},\ldots,i_{ln}\geq 0}^{i_{l0}+i_{l1}+i_{l2}+\ldots+i_{ln}=m_l} \frac{(i_{l0}+i_{l1}+i_{l2}+\ldots+i_{ln})!}{i_{l0}!i_{l1}!i_{l2}!\ldots!i_{ln}!}$$
$$u_0^{i_{l0}} u_1^{i_{l1}} u_2^{i_{l2}} \cdots u_n^{i_{ln}} x_{l0}^{i_{l0}} x_{l1}^{i_{l1}} x_{l2}^{i_{l2}} \cdots x_{ln}^{i_{ln}} \tag{8}$$

Substituting (8) into (6), integral (9) is obtained.

$$\int_{P_0P_1P_2\ldots P_n} x_1^{m_1} x_2^{m_2} x_3^{m_3} \ldots x_n^{m_n} D(x_1,x_2,x_3,\ldots,x_n) =$$
$$J \int\int\int\cdots\int_{U_0U_1U_2\ldots U_n}$$
$$\left(\sum_{i_{10},i_{11},i_{12},\ldots,i_{1n}\geq 0}^{i_{10}+i_{11}+i_{12}+\ldots+i_{1n}=m_1} \frac{(i_{10}+i_{11}+i_{12}+\ldots+i_{1n})!}{i_{10}!i_{11}!i_{12}!\ldots!i_{1n}!} u_0^{i_{10}} u_1^{i_{11}} u_2^{i_{12}} \cdots u_n^{i_{1n}} \quad x_{10}^{i_{10}} x_{11}^{i_{11}} x_{12}^{i_{12}} \cdots x_{1n}^{i_{1n}}\right)$$
$$\left(\sum_{i_{20},i_{21},i_{22},\ldots,i_{2n}\geq 0}^{i_{20}+i_{21}+i_{22}+\ldots+i_{2n}=m_2} \frac{(i_{20}+i_{21}+i_{22}+\ldots+i_{2n})!}{i_{20}!i_{21}!i_{22}!\ldots!i_{2n}!} u_0^{i_{20}} u_1^{i_{21}} u_2^{i_{22}} \cdots u_n^{i_{2n}} \quad x_{20}^{i_{20}} x_{21}^{i_{21}} x_{22}^{i_{22}} \cdots x_{2n}^{i_{2n}}\right)$$
$$\left(\sum_{i_{30},i_{31},i_{32},\ldots,i_{3n}\geq 0}^{i_{30}+i_{31}+i_{32}+\ldots+i_{3n}=m_3} \frac{(i_{30}+i_{31}+i_{32}+\ldots+i_{3n})!}{i_{30}!i_{31}!i_{32}!\ldots!i_{3n}!} u_0^{i_{30}} u_1^{i_{31}} u_2^{i_{32}} \cdots u_n^{i_{3n}} \quad x_{30}^{i_{30}} x_{31}^{i_{31}} x_{32}^{i_{32}} \cdots x_{3n}^{i_{3n}}\right)$$
$$\ldots\ldots\ldots\ldots\ldots\ldots\ldots\ldots$$
$$\left(\sum_{i_{n0},i_{n1},i_{n2},\ldots,i_{nn}\geq 0}^{i_{n0}+i_{n1}+i_{n2}+\ldots+i_{nn}=m_n} \frac{(i_{n0}+i_{n1}+i_{n2}+\ldots+i_{nn})!}{i_{n0}!i_{n1}!i_{n2}!\ldots!i_{nn}!} u_0^{i_{n0}} u_1^{i_{n1}} u_2^{i_{n2}} \cdots u_n^{i_{nn}} \; x_{n0}^{i_{n0}} x_{n1}^{i_{n1}} x_{n2}^{i_{n2}} \cdots x_{nn}^{i_{nn}}\right)$$
$$du_1 du_2 du_3 \ldots du_n \tag{9}$$

$$\int_{P_0P_1P_2\ldots P_n} x_1^{m_1} x_2^{m_2} x_3^{m_3} \ldots x_n^{m_n} D(x_1,x_2,x_3,\ldots,x_n)$$
$$= J \sum_{i_{10},i_{11},i_{12},\ldots,i_{1n}\geq 0}^{i_{10}+i_{11}+i_{12}+\ldots+i_{1n}=m_1} \quad \sum_{i_{20},i_{21},i_{22},\ldots,i_{2n}\geq 0}^{i_{20}+i_{21}+i_{22}+\ldots+i_{2n}=m_2}$$
$$\sum_{i_{30},i_{31},i_{32},\ldots,i_{3n}\geq 0}^{i_{30}+i_{31}+i_{32}+\ldots+i_{3n}=m_3} \quad \cdots \quad \sum_{i_{n0},i_{n1},i_{n2},\ldots,i_{nn}\geq 0}^{i_{n0}+i_{n1}+i_{n2}+\ldots+i_{nn}=m_n}$$

$$\begin{array}{ccc} \frac{m_1!}{i_{10}!i_{11}!i_{12}!\ldots!i_{1n}!} & & \frac{m_2!}{i_{20}!i_{21}!i_{22}!\ldots!i_{2n}!} \\ \frac{m_3!}{i_{30}!i_{31}!i_{32}!\ldots!i_{3n}!} & \cdots & \frac{m_n!}{i_{n0}!i_{n1}!i_{n2}!\ldots!i_{nn}!} \\ x_{10}^{i_{10}}x_{11}^{i_{11}}x_{12}^{i_{12}}\cdots x_{1n}^{i_{1n}} & & x_{20}^{i_{20}}x_{21}^{i_{21}}x_{22}^{i_{22}}\cdots x_{2n}^{i_{2n}} \\ x_{30}^{i_{30}}x_{31}^{i_{31}}x_{32}^{i_{32}}\cdots x_{3n}^{i_{3n}} & \cdots & x_{n0}^{i_{n0}}x_{n1}^{i_{n1}}x_{n2}^{i_{n2}}\cdots x_{nn}^{i_{nn}} \end{array}$$

$$\int\int\int\cdots\int_{U_0U_1U_2\ldots U_n} u_0^{i_0}u_1^{i_1}u_2^{i_2}\cdots u_n^{i_n}du_1du_2du_3\ldots du_n \qquad (10)$$

where

$$i_l = i_{1l} + i_{2l} + i_{3l} + \cdots + i_{nl}, \qquad l = 0, 1, 2, \ldots, n.$$

5 FORMULA OF N DIMENSIONAL SIMPLEX INTEGRATIONS

The coordinate simplex integration in (10) is another form of well known Dirichlet integration in classical analysis. The direct computation of the integration is given below.

$$\begin{aligned} S_1 &= \int\int\int\cdots\int_{U_0U_1U_2\ldots U_n} u_0^{i_0}u_1^{i_1}u_2^{i_2}\cdots u_n^{i_n}du_1du_2du_3\ldots du_n \\ &= \int\int\int\cdots\int_{u_0,u_1,u_2,\ldots,u_n\geq 0}^{u_0+u_1+u_2+\ldots+u_n=1} u_0^{i_0}u_1^{i_1}u_2^{i_2}\cdots u_n^{i_n}du_1du_2du_3\ldots du_n \\ &= \int_0^1\int_0^{1-u_n}\int_0^{1-u_n-u_{n-1}}\cdots\int_0^{1-u_n-u_{n-1}-\cdots-u_2} \\ &\quad u_n^{i_n}u_{n-1}^{i_{n-1}}u_{n-2}^{i_{n-2}}\cdots u_1^{i_1}u_0^{i_0}du_1du_2du_3\ldots du_n \\ &= \int_0^1\int_0^{1-u_n}\int_0^{1-u_n-u_{n-1}}\cdots\int_0^{1-u_n-u_{n-1}-\cdots-u_3} u_n^{i_n}u_{n-1}^{i_{n-1}}u_{n-2}^{i_{n-2}}\cdots u_2^{i_2} \\ &\quad \left(\int_0^{1-u_n-u_{n-1}-\cdots-u_2} u_1^{i_1}\left(1-\sum_{k=1}^n u_k\right)^{i_0}du_1\right)du_2du_3\ldots du_n \end{aligned} \qquad (11)$$

After i_1 times of integration by parts, the inner integration of (11) can be computed.

$$\begin{aligned} &\int_0^{1-u_n-u_{n-1}-\cdots-u_2} u_1^{i_1}\left(1-\sum_{k=1}^n u_k\right)^{i_0}du_1 \\ =&\int_0^{1-u_n-u_{n-1}-\cdots-u_2} d\left(\frac{1}{i_1+1}u_1^{i_1+1}\right)\left(1-\sum_{k=1}^n u_k\right)^{i_0} \\ =&\frac{1}{i_1+1}u_1^{i_1+1}\left(1-\sum_{k=1}^n u_k\right)^{i_0}\Big|_0^{1-u_n-u_{n-1}-\cdots-u_2} \\ -&\int_0^{1-u_n-u_{n-1}-\cdots-u_2}\frac{1}{i_1+1}u_1^{i_1+1}d\left(\left(1-\sum_{k=1}^n u_k\right)^{i_0}\right) \end{aligned}$$

$$
\begin{aligned}
&= -\int_0^{1-u_n-u_{n-1}-\cdots-u_2} \frac{1}{i_1+1} u_1^{i_1+1} d\Big(\Big(1-\sum_{k=1}^n u_k\Big)^{i_0}\Big) \\
&= \int_0^{1-u_n-u_{n-1}-\cdots-u_2} \frac{i_0}{i_1+1} u_1^{i_1+1}\Big(1-\sum_{k=1}^n u_k\Big)^{i_0-1} du_1 \\
&= \int_0^{1-u_n-u_{n-1}-\cdots-u_2} \frac{i_0(i_0-1)}{(i_1+1)(i_1+2)} u_1^{i_1+2}\Big(1-\sum_{k=1}^n u_k\Big)^{i_0-2} du_1 \\
&= \int_0^{1-u_n-u_{n-1}-\cdots-u_2} \frac{i_0(i_0-1)(i_0-2)}{(i_1+1)(i_1+2)(i_1+3)} u_1^{i_1+3}\Big(1-\sum_{k=1}^n u_k\Big)^{i_0-3} du_1 \\
&= \int_0^{1-u_n-u_{n-1}-\cdots-u_2} \frac{i_0(i_0-1)(i_0-2)\ldots 2}{(i_1+1)(i_1+2)(i_1+3)\ldots(i_1+i_0-1)} u_1^{i_1+i_0-1} \\
&\quad \Big(1-\sum_{k=1}^n u_k\Big)^{1} du_1 \\
&= \int_0^{1-u_n-u_{n-1}-\cdots-u_2} \frac{i_0(i_0-1)(i_0-2)\ldots 1}{(i_1+1)(i_1+2)(i_1+3)\ldots(i_1+i_0)} u_1^{i_1+i_0} du_1 \\
&= \int_0^{1-u_n-u_{n-1}-\cdots-u_2} \frac{i_0!i_1!}{(i_1+i_0)!} u_1^{i_1+i_0} du_1 \\
&= \int_0^{1-u_n-u_{n-1}-\cdots-u_2} \frac{i_0!i_1!}{(i_1+i_0+1)!} d(u_1^{i_1+i_0+1}) \\
&= \frac{i_0!i_1!}{(i_0+i_1+1)!} u_1^{i_0+i_1+1} \Big|_0^{1-u_n-u_{n-1}-\cdots-u_2} \\
&= \frac{i_0!i_1!}{(i_1+i_0+1)!}\Big(1-\sum_{k=2}^n u_k\Big)^{i_1+i_0+1} \qquad (12)
\end{aligned}
$$

$$
\begin{aligned}
S_1 = &\int_0^1 \int_0^{1-u_n} \int_0^{1-u_n-u_{n-1}} \cdots \int_0^{1-u_n-u_{n-1}-\cdots-u_3} u_n^{i_n} u_{n-1}^{i_{n-1}} u_{n-2}^{i_{n-2}} \cdots u_2^{i_2} \\
&\int_0^{1-u_n-u_{n-1}-\cdots-u_2} u_1^{i_1}\Big(1-\sum_{k=1}^n u_k\Big)^{i_0} du_1 du_2 du_3 \ldots du_n \\
= &\int_0^1 \int_0^{1-u_n} \int_0^{1-u_n-u_{n-1}} \cdots \int_0^{1-u_n-u_{n-1}-\cdots-u_4} u_n^{i_n} u_{n-1}^{i_{n-1}} u_{n-2}^{i_{n-2}} \cdots u_3^{i_3} \\
&\int_0^{1-u_n-u_{n-1}-\cdots-u_3} u_2^{i_2}(1-\sum_{k=2}^n u_k)^{i_0+i_1+1} du_2 du_3 du_4 \ldots du_n \frac{i_0!i_1!}{(i_0+i_1+1)!} \\
= &\int_0^1 \int_0^{1-u_n} \int_0^{1-u_n-u_{n-1}} \cdots \int_0^{1-u_n-u_{n-1}-\cdots-u_4} u_n^{i_n} u_{n-1}^{i_{n-1}} u_{n-2}^{i_{n-2}} \cdots u_4^{i_4} u_3^{i_3} \\
&(1-\sum_{k=3}^n u_k)^{i_0+i_1+i_2+2} du_3 du_4 du_5 \ldots du_n \frac{i_0!i_1!i_2!}{(i_0+i_1+i_2+2)!} \\
= &\int_0^1 \int_0^{1-u_n} \int_0^{1-u_n-u_{n-1}} \cdots \int_0^{1-u_n-u_{n-1}-\cdots-u_5} u_n^{i_n} u_{n-1}^{i_{n-1}} u_{n-2}^{i_{n-2}} \cdots u_4^{i_4} \\
&\int_0^{1-u_n-u_{n-1}-\cdots-u_4} u_3^{i_3}(1-\sum_{k=3}^n u_k)^{i_0+i_1+i_2+2} \\
&du_3 du_4 du_5 \ldots du_n \frac{i_0!i_1!i_2!}{(i_0+i_1+i_2+2)!}
\end{aligned}
$$

$$
\begin{aligned}
&= \int_0^1 \int_0^{1-u_n} u_n^{i_n} u_{n-1}^{i_{n-1}} (1-u_{n-1}-u_n)^{i_0+i_1+i_2+\cdots+i_{n-2}+n-2} du_{n-1} du_n \\
&\quad \frac{i_0! i_1! i_2! \ldots! i_{n-2}!}{(i_0+i_1+i_2+\ldots+i_{n-2}+n-2)!} \\
&= \int_0^1 u_n^{i_n} (1-u_n)^{i_0+i_1+i_2+\cdots+i_{n-1}+n-1} du_n \frac{i_0! i_1! i_2! \ldots! i_{n-1}!}{(i_0+i_1+i_2+\ldots+i_{n-1}+n-1)!} \\
&= \frac{i_0! i_1! i_2! \ldots! i_n!}{(i_0+i_1+i_2+\ldots+i_n+n)!} \qquad (13)
\end{aligned}
$$

Substituting equation (13) into (11), the integrals of a n dimensional simplex is obtained.

$$
\begin{aligned}
&\int_{P_0P_1P_2\ldots P_n} x_1^{m_1} x_2^{m_2} x_3^{m_3} \ldots x_n^{m_n} D(x_1, x_2, x_3, \ldots, x_n) \\
&= J \sum_{i_{10},i_{11},i_{12},\ldots,i_{1n}\geq 0}^{i_{10}+i_{11}+i_{12}+\ldots+i_{1n}=m_1} \quad \sum_{i_{20},i_{21},i_{22},\ldots,i_{2n}\geq 0}^{i_{20}+i_{21}+i_{22}+\ldots+i_{2n}=m_2} \\
&\quad \sum_{i_{30},i_{31},i_{32},\ldots,i_{3n}\geq 0}^{i_{30}+i_{31}+i_{32}+\ldots+i_{3n}=m_3} \quad \cdots \quad \sum_{i_{n0},i_{n1},i_{n2},\ldots,i_{nn}\geq 0}^{i_{n0}+i_{n1}+i_{n2}+\ldots+i_{nn}=m_n} \\
&\quad \frac{m_1!}{i_{10}! i_{11}! i_{12}! \ldots! i_{1n}!} \qquad \frac{m_2!}{i_{20}! i_{21}! i_{22}! \ldots! i_{2n}!} \\
&\quad \frac{m_3!}{i_{30}! i_{31}! i_{32}! \ldots! i_{3n}!} \quad \cdots \quad \frac{m_n!}{i_{n0}! i_{n1}! i_{n2}! \ldots! i_{nn}!} \\
&\quad x_{10}^{i_{10}} x_{11}^{i_{11}} x_{12}^{i_{12}} \cdots x_{1n}^{i_{1n}} \qquad x_{20}^{i_{20}} x_{21}^{i_{21}} x_{22}^{i_{22}} \cdots x_{2n}^{i_{2n}} \\
&\quad x_{30}^{i_{30}} x_{31}^{i_{31}} x_{32}^{i_{32}} \cdots x_{3n}^{i_{3n}} \quad \cdots \quad x_{n0}^{i_{n0}} x_{n1}^{i_{n1}} x_{n2}^{i_{n2}} \cdots x_{nn}^{i_{nn}} \\
&\quad \frac{i_0! i_1! i_2! \ldots! i_n!}{(i_0+i_1+i_2+\ldots+i_n+n)!} \qquad (14)
\end{aligned}
$$

where

$$
i_l = i_{1l} + i_{2l} + i_{3l} + \cdots + i_{nl}, \qquad l = 0, 1, 2, \ldots, n.
$$

6 SIMPLEX INTEGRATIONS ON GENERAL TWO-DIMENSIONAL BLOCKS

Since simplex integrations always have the Jacobian J as factor and J is an oriented area, the integrations on positive area and negative area can be neutralized. Denote $P_1P_2P_3\cdots P_n \qquad P_{n+1} = P_1$ with $P_i = (x_i, y_i)$ as a polygon, the integrations (15)-(18) on $P_1P_2P_3\cdots P_n$ are computed by summations. (15)-(18) are the integrations of DDA method. Here P_0 can be any point, $P_0 = (0,0)$ are chosen in order to have simpler formulae.

$$
\int\int_{(A)} dxdy = \sum_{k=1}^{n} \int_{P_0P_kP_{k+1}} 1 D(x,y) = \frac{1}{2} \sum_{k=1}^{n} \begin{vmatrix} x_k & y_k \\ x_{k+1} & y_{k+1} \end{vmatrix} \qquad (15)
$$

Figure 3. equal-lateral of 2-dimensional polygons

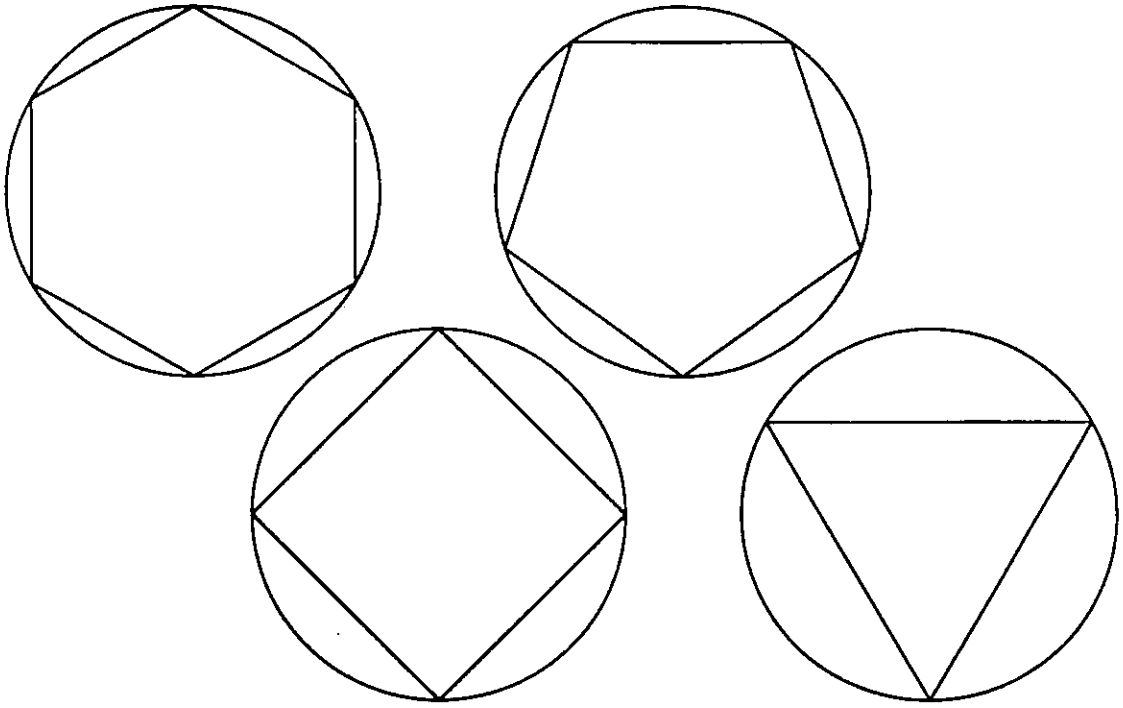

Figure 4. Oriented polygons of a 3-d block

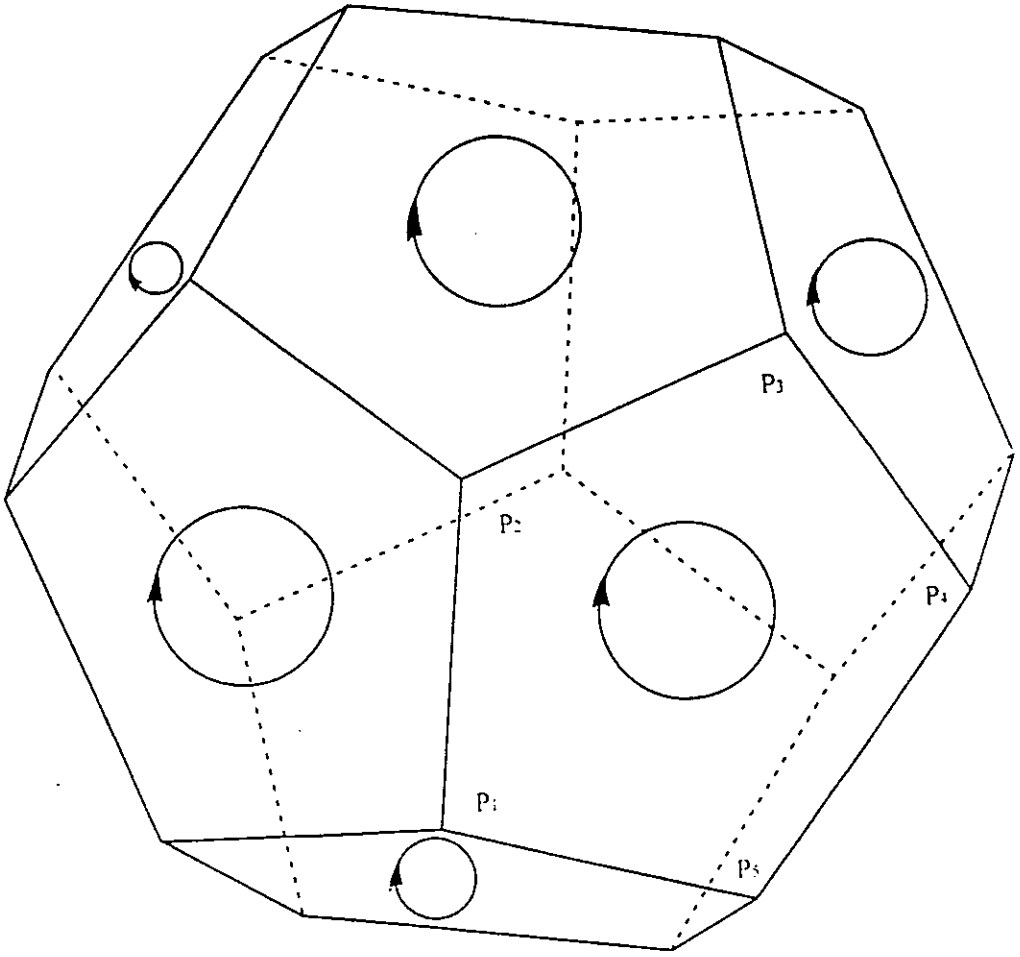

$$\int\int_{(A)} xdxdy = \sum_{k=1}^{n} \int_{P_0P_kP_{k+1}} xD(x,y) = \frac{1}{6}\sum_{k=1}^{n} \begin{vmatrix} x_k & y_k \\ x_{k+1} & y_{k+1} \end{vmatrix}$$
$$(x_k + x_{k+1}) \tag{16}$$

$$\int\int_{(A)} x^2dxdy = \sum_{k=1}^{n} \int_{P_0P_kP_{k+1}} x^2D(x,y) = \frac{1}{24}\sum_{k=1}^{n} \begin{vmatrix} x_k & y_k \\ x_{k+1} & y_{k+1} \end{vmatrix}$$
$$\begin{aligned}(&2x_kx_k \quad + x_kx_{k+1} \\ &+x_{k+1}x_k \quad + 2x_{k+1}x_{k+1})\end{aligned} \tag{17}$$

$$\int\int_{(A)} xydxdy = \sum_{k=1}^{n} \int_{P_0P_kP_{k+1}} xyD(x,y) = \frac{1}{24}\sum_{k=1}^{n} \begin{vmatrix} x_k & y_k \\ x_{k+1} & y_{k+1} \end{vmatrix}$$
$$\begin{aligned}(&2x_ky_k \quad + x_ky_{k+1} \\ &+x_{k+1}y_k \quad + 2x_{k+1}y_{k+1})\end{aligned} \tag{18}$$

Figure 3. shows equal-lateral polygons. The equal-lateral triangle, square, pentagon and hexagon are in the unit circle. The distance from each node to the circle center is 1. The edge length and area of each equal-lateral polygon are listed in the following table. The centers of gravity of the equal-lateral triangle, square, pentagon and hexagon are the center of the unit circle. Using the simplex integrations, the same area and center of gravity are obtained for each equal-lateral polygon.

polygon	edge length	area
equal-lateral triangle	$\sqrt{3}$	$\frac{1}{4}3\sqrt{3} = 1.299038$
equal-lateral square	$\sqrt{2}$	2.000000
equal-lateral pentagon	$\sqrt{\frac{1}{2}(5-\sqrt{5})}$	$\frac{5}{8}\sqrt{10+2\sqrt{5}} = 2.377641$
equal-lateral hexagon	1	$\frac{1}{2}3\sqrt{3} = 2.598076$

7 SIMPLEX INTEGRATIONS ON GENERAL THREE-DIMENSIONAL BLOCKS

Integrations (19)-(22) are the summations of simplex integrations on tetrahedrons. the volume or integrations of any 3-d block can be computed. Assume $P_1^{[i]}P_2^{[i]}P_3^{[i]}\cdots P_{n(i)}^{[i]}\ P_{n(i)+1}^{[i]} = P_1^{[i]} \quad i = 1,2,3,\ldots,s$ are all outward rotated polygons of a block (see Figure 4), $P_j^{[i]} = (x_j^{[i]}, y_j^{[i]}, z_j^{[i]})$ and $P_0 = (0,0,0)$. The volume of this block is given by (19). Computed by simplex integrations, integrals (19)-(22) are represented by the coordinates of the boundary vertices only.

$$\int\int\int_{(V)} dxdydz = \sum_{i=1}^{s}\sum_{k=1}^{n(i)} \int_{P_0P_1^{[i]}P_k^{[i]}P_{k+1}^{[i]}} 1D(x,y,z)$$

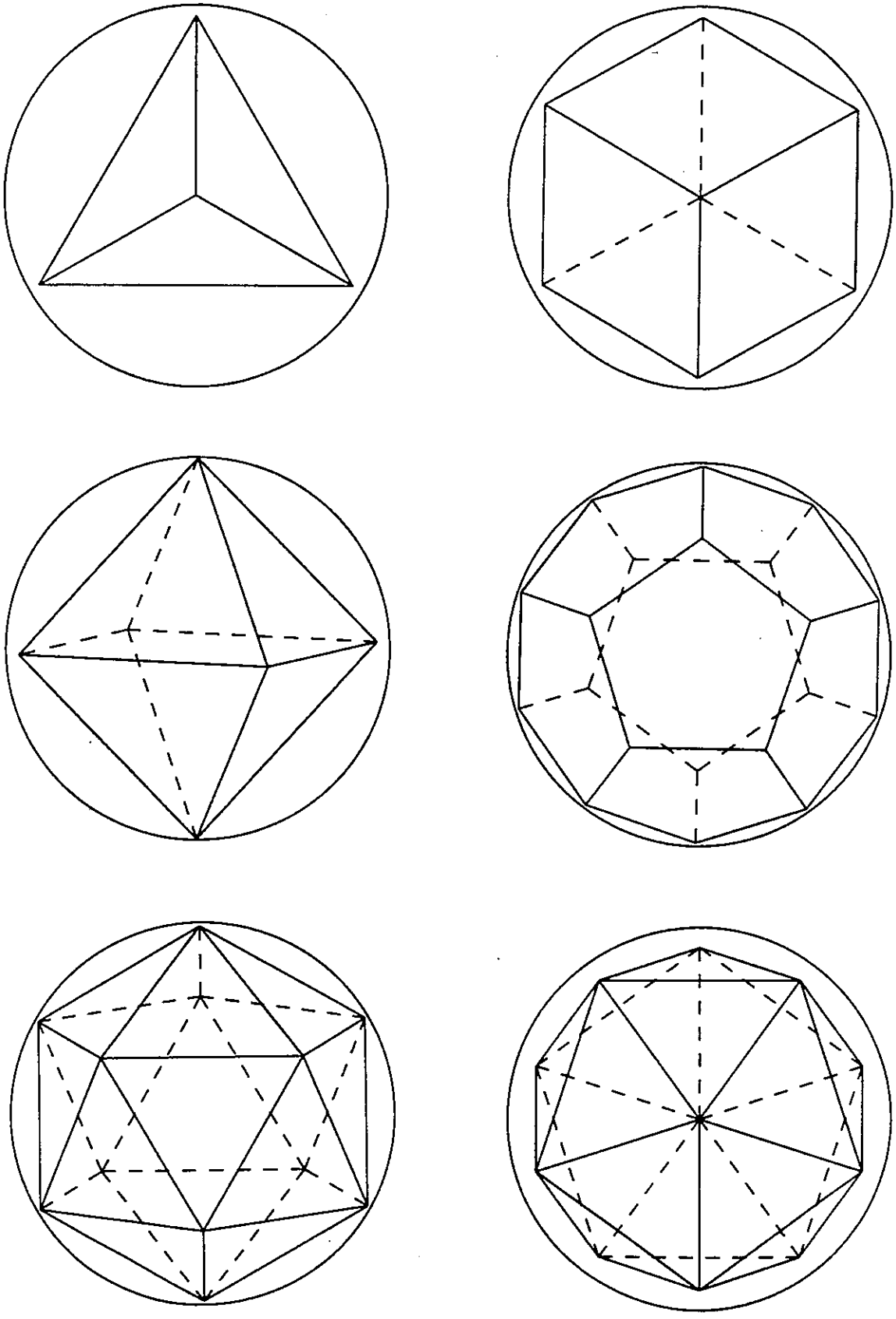

Figure 5. 3-dimensional blocks with equal-lateral boundary polygon

$$= \frac{1}{6}\sum_{i=1}^{s}\sum_{k=1}^{n(i)}\begin{vmatrix} x_1^{[i]} & y_1^{[i]} & z_1^{[i]} \\ x_k^{[i]} & y_k^{[i]} & z_k^{[i]} \\ x_{k+1}^{[i]} & y_{k+1}^{[i]} & z_{k+1}^{[i]} \end{vmatrix} \tag{19}$$

$$\int\int\int_{(V)} x\,dxdydz = \sum_{i=1}^{s}\sum_{k=1}^{n(i)}\int_{P_0P_1^{[i]}P_k^{[i]}P_{k+1}^{[i]}} xD(x,y,z)$$

$$= \frac{1}{24}\sum_{i=1}^{s}\sum_{k=1}^{n(i)}\begin{vmatrix} x_1^{[i]} & y_1^{[i]} & z_1^{[i]} \\ x_k^{[i]} & y_k^{[i]} & z_k^{[i]} \\ x_{k+1}^{[i]} & y_{k+1}^{[i]} & z_{k+1}^{[i]} \end{vmatrix}$$

$$(x_1 + x_k + x_{k+1}) \tag{20}$$

$$\int\int\int_{(V)} x^2\,dxdydz = \sum_{i=1}^{s}\sum_{k=1}^{n(i)}\int_{P_0P_1^{[i]}P_k^{[i]}P_{k+1}^{[i]}} x^2D(x,y,z)$$

$$= \frac{1}{120}\sum_{i=1}^{s}\sum_{k=1}^{n(i)}\begin{vmatrix} x_1^{[i]} & y_1^{[i]} & z_1^{[i]} \\ x_k^{[i]} & y_k^{[i]} & z_k^{[i]} \\ x_{k+1}^{[i]} & y_{k+1}^{[i]} & z_{k+1}^{[i]} \end{vmatrix}$$

$$\begin{aligned} &(2x_1x_1 \quad +x_1x_k \quad +x_1x_{k+1} \\ &+x_kx_1 \quad +2x_kx_k \quad +x_kx_{k+1} \\ &+x_{k+1}x_1 \quad +x_{k+1}x_k \quad +2x_{k+1}x_{k+1}) \end{aligned} \tag{21}$$

$$\int\int\int_{(V)} xy\,dxdydz = \sum_{i=1}^{s}\sum_{k=1}^{n(i)}\int_{P_0P_1^{[i]}P_k^{[i]}P_{k+1}^{[i]}} xyD(x,y,z)$$

$$= \frac{1}{120}\sum_{i=1}^{s}\sum_{k=1}^{n(i)}\begin{vmatrix} x_1^{[i]} & y_1^{[i]} & z_1^{[i]} \\ x_k^{[i]} & y_k^{[i]} & z_k^{[i]} \\ x_{k+1}^{[i]} & y_{k+1}^{[i]} & z_{k+1}^{[i]} \end{vmatrix}$$

$$\begin{aligned} &(2x_1y_1 \quad +x_1y_k \quad +x_1y_{k+1} \\ &+x_ky_1 \quad +2x_ky_k \quad +x_ky_{k+1} \\ &+x_{k+1}y_1 \quad +x_{k+1}y_k \quad +2x_{k+1}y_{k+1}) \end{aligned} \tag{22}$$

Figure 5. shows 5 different 3-d blocks. For each block, the nine geometric formulae are listed in the following tables. 1 boundary polygon number of the block, 2 edge number of each polygons, 3 angle of two adjacent polygon planes, 4 edge length of polygons, 5 distance from polygon to sphere center, 6 distance of node to its polygon center, 7 distance from block vertices to sphere center, 8 geometric formule of block volume, 9 computed volume by simplex integration.

1	4	6	8	12	20
2	3	4	3	5	3
3	$atan$	$\frac{\pi}{2}$	$2atan$	$\pi - atan(2)$	$acos(\sqrt{\frac{10+2\sqrt{5}}{15}} - \sqrt{\frac{5+2\sqrt{5}}{15}})$
3	$(2\sqrt{2})$		$(\sqrt{2})$		$+\pi - atan(3-\sqrt{5})$
4	$2\sqrt{\frac{2}{3}}$	$\frac{2}{\sqrt{3}}$	$\sqrt{2}$	$\frac{1}{\sqrt{3}}(\sqrt{5}-1)$	$\sqrt{2(1-\frac{1}{\sqrt{5}})}$

5	$\frac{1}{3}$	$\frac{1}{\sqrt{3}}$	$\frac{1}{\sqrt{3}}$	$\frac{1}{\sqrt{15}}\sqrt{5+2\sqrt{5}}$	$\sqrt{\frac{5+2\sqrt{5}}{15}}$
6	$\frac{2}{3}\sqrt{2}$	$\sqrt{\frac{2}{3}}$	$\frac{1}{\sqrt{6}}$	$\frac{1}{\sqrt{15}}\sqrt{2(5-\sqrt{5})}$	$\sqrt{\frac{2}{3}(1-\frac{1}{\sqrt{5}})}$
7	1	1	1	1	1
8	$\frac{8}{27}\sqrt{3}$	$\frac{8}{3\sqrt{3}}$	$\frac{4}{3}$	$\frac{2}{3\sqrt{3}}\sqrt{10(3+\sqrt{5})}$	$\frac{2}{3}\sqrt{(10+2\sqrt{5})}$
9	0.51320	1.53960	1.33333	2.78516	2.53615

In order to use the simplex integration, the node coordinates (x, y) in each boundary polygon have to be computed. Based on the angles of boundary planes and distances of these planes to the sphere center, the polygons, the edges and the vertices can be computed. The three dimensional simplex integrations give the same volume as computed directly from the geometric formulae listed in the table.

10 ROCK FAILURE EXAMPLES BY DDA

The equilibrium of the DDA method is reached by minimizing the total potential energy. As the energy is computed by integrations, most of the DDA formulae are formed by the polynomial integrations over the generally shaped blocks. The simplex integration is developed and applied to DDA formulation. Based on the simplex integration, DDA algorithms are simple, efficient yet accurate. Most important, the accurate integral solution of mass matrix ensured the convergence of "open-close" iterations.

Following a real time sequence, the DDA uses a step by step approach. The displacements of each time step are so small that normal linear equations for small displacements can be adopted. At the end of each time step, the equilibrium in both discontinuous interfaces and continuous zones are reached. As the step displacements are small, the kinematic relation and friction law are expressed as linear inequalities. Based on natural contact phenomena, an "entrance theory" was developed. The entrance lines are used to form linear inequality equations. The "open-close" iterations ensure that no tension and no penetration occur at all entrance positions. Coloumb's Law is also fulfilled at all entrance modes and all entrance positions.

There are 1500 to 2000 rock blocks in each example. The dimensions of computed regions are about 40 to 80 meters. The numbers of time steps are from 300 to 600. The total elapsed times are from 0.2 to 2.0 second. The maximum total displacements are more than ten times the average block diameter.

Figure 6 shows the penetration of a missile at a velocity of 300 meters per second into a blocky rock mass with two tunnels.

Figure 7 shows the damage state as a strong stress wave passing through three tunnels excavated in a blocky rock mass.

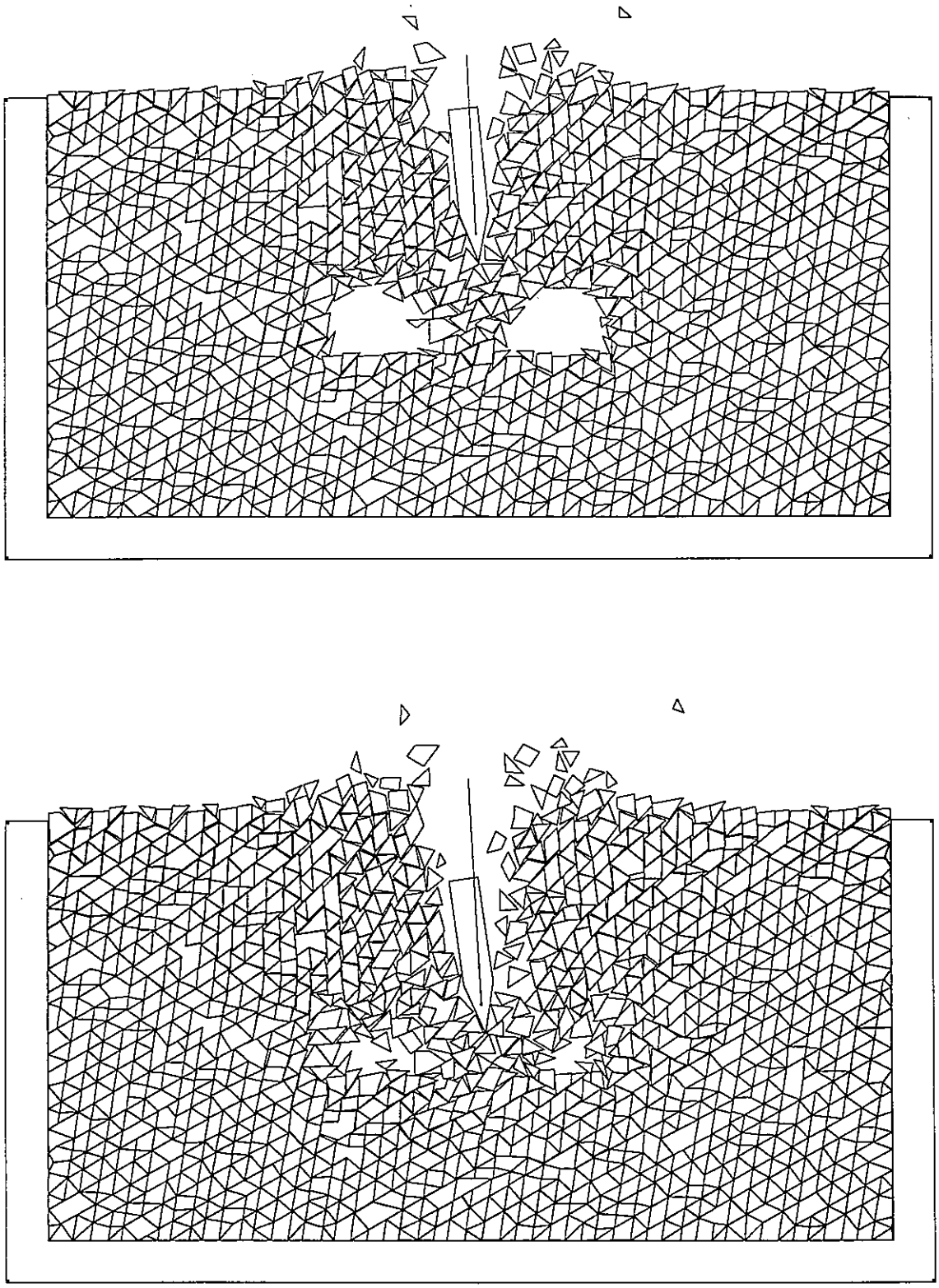

Figure 6. The penetration of a missile at a velocity of 300 meters per second into a blocky rock mass with two tunnels

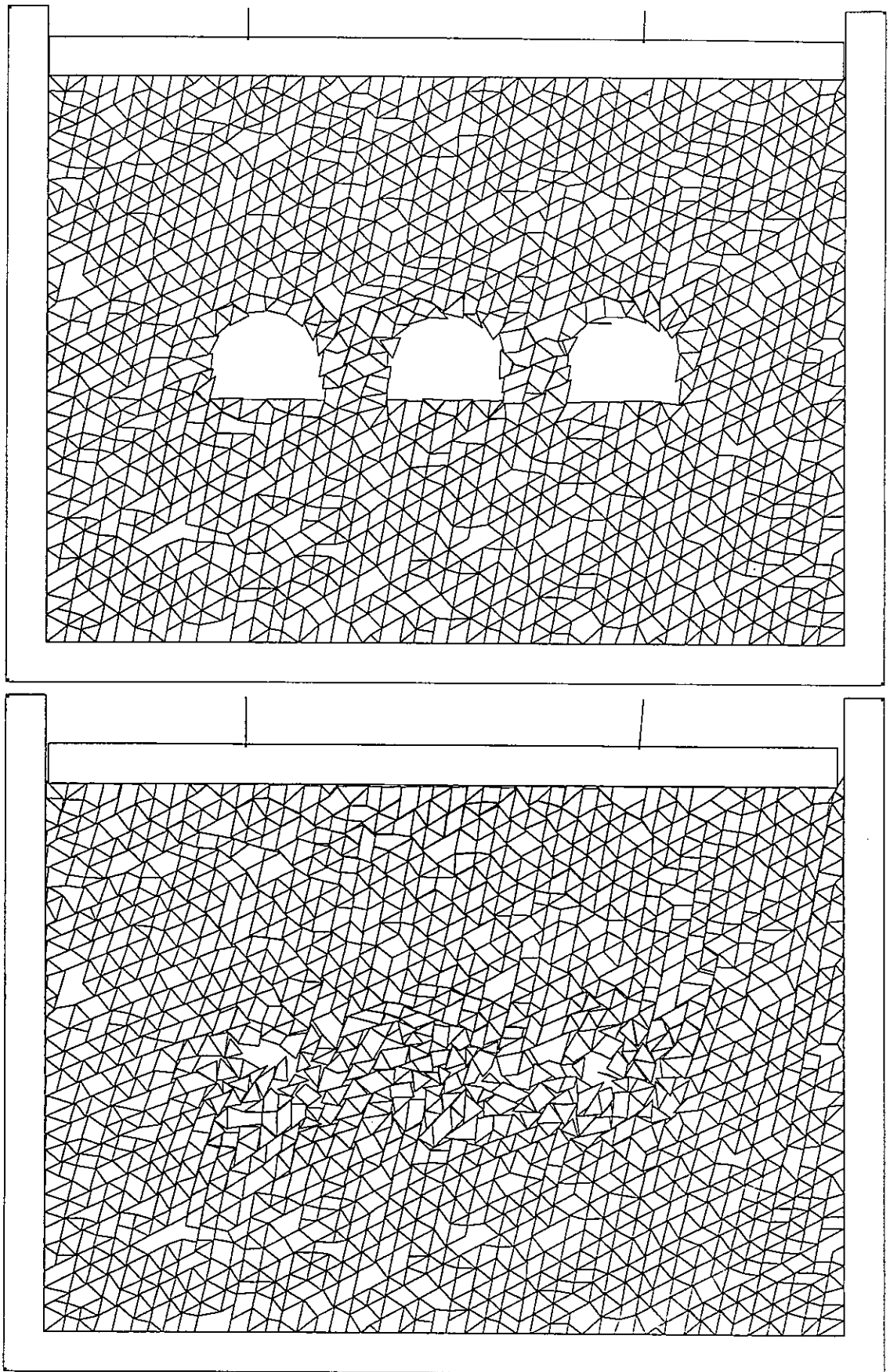

Figure 7. A strong stress wave passing through three tunnels excavated in a blocky rock mass

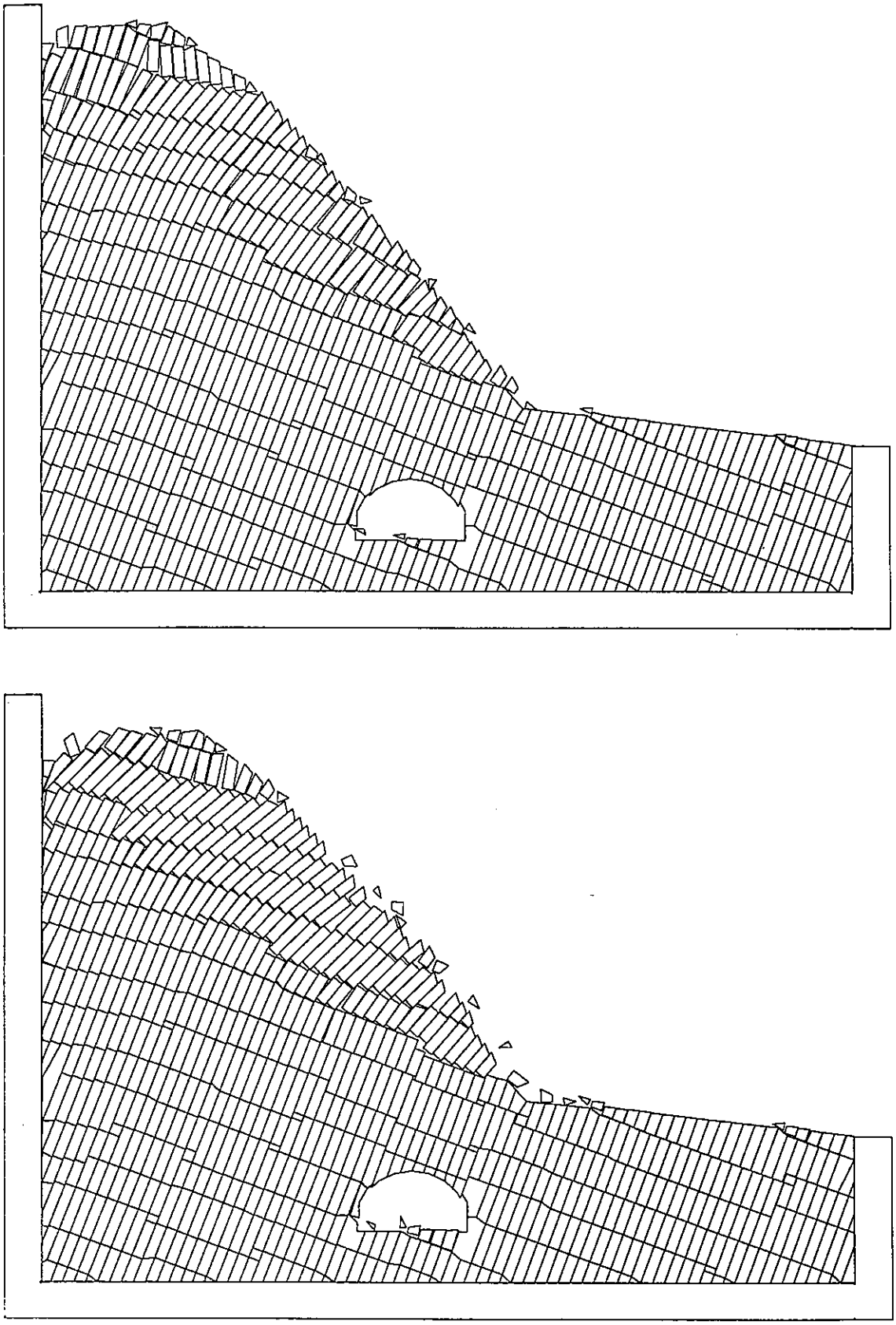

Figure 8. A rock toppling failure caused by slope excavation

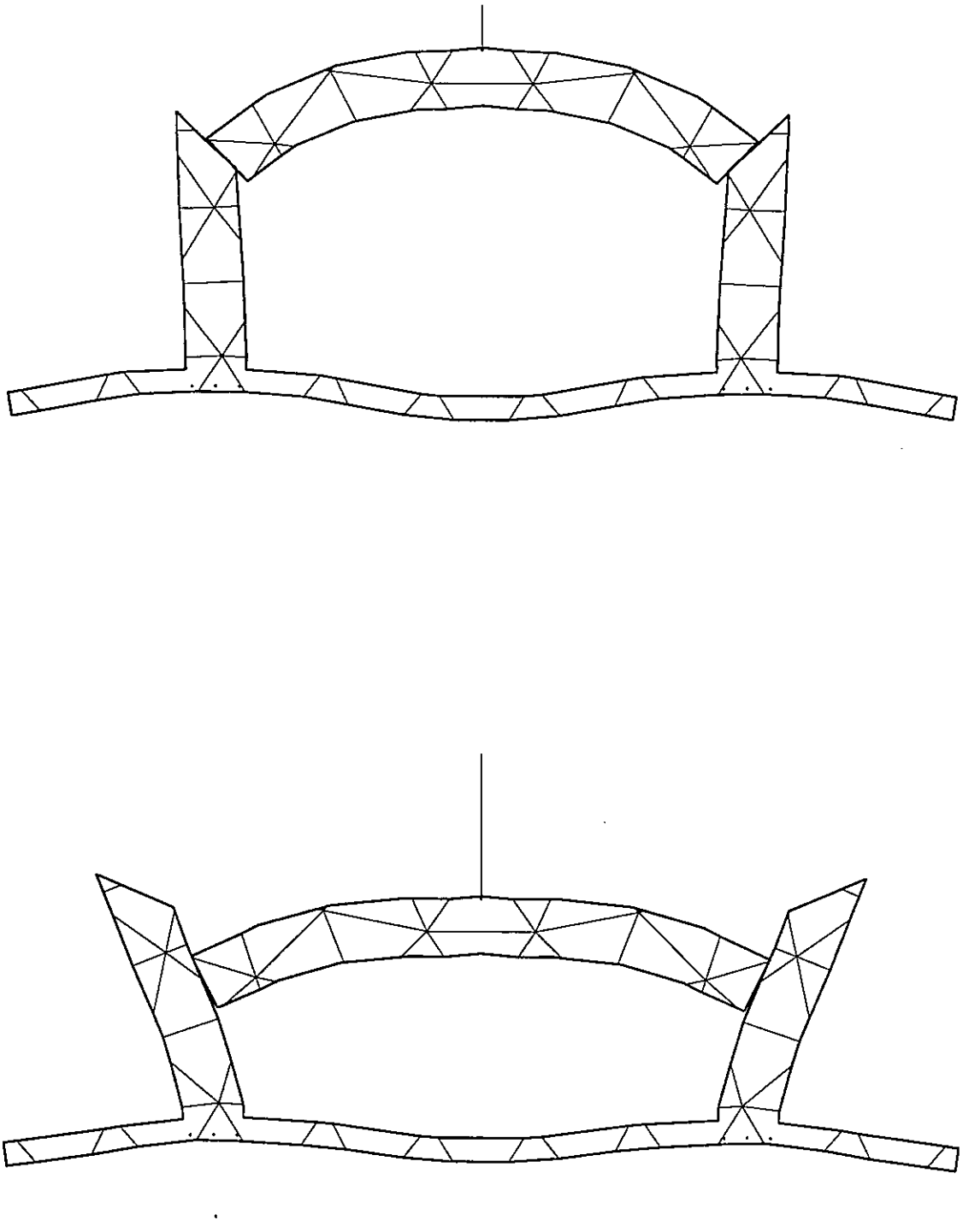

Figure 9. Two examples of manifold method

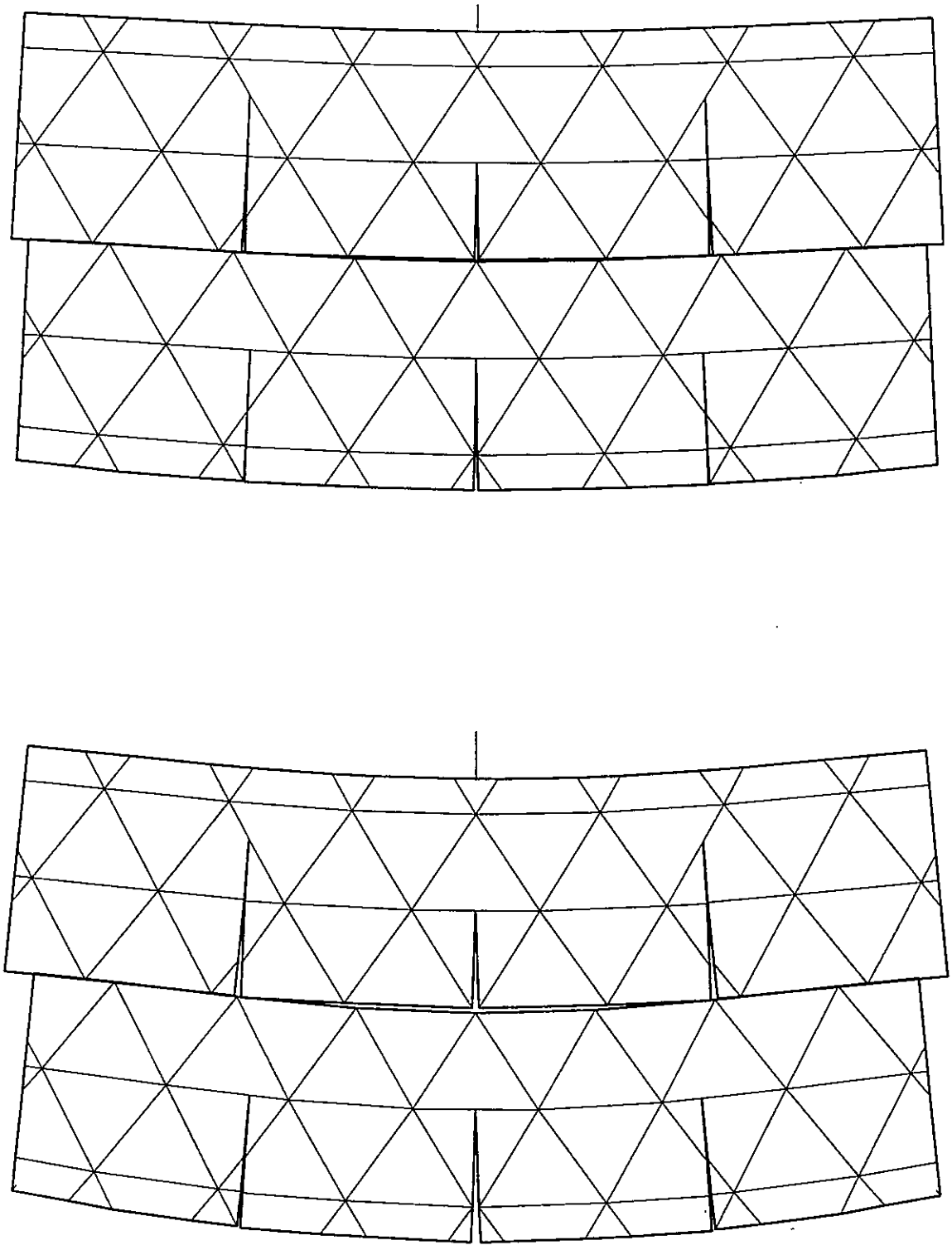

Figure 9. Two examples of manifold method

Figure 8 shows a rock toppling failure caused by slope excavation.

Figure 9 shows two examples of manifold method.

ACKNOWLEDGEMENT The development of the theory presented herein is the result of research for Work Unit No. 31700. Program sponsored by the US Army Corps of Engineers (USACE). The author would like to thank Mr. Jerry Huie and Dr. Don Banks for their helps.

REFERENCES

[1] Gen-hua Shi, 1993. "Block system modeling by discontinuous deformation analysis."

Southampton UK and Boston USA

[2] Gen-hua Shi, 1994. "Modeling Dynamic Rock Failure by Discontinuous Deformation Analysis with Simplex Integrations" *Proceedings of the 1st North American Rock Mechanics Symposium*, pp. 591-598 (Austin, Texas).

Recent Development of DDA in Rock Mechanics

Yuzo OHNISHI[1], Guangqi CHEN[2] and Shigeru MIKI[2]

[1]Kyoto University, Kyoto 606-01, Japan
[2]Kiso-Jiban Consultants Co., Ltd., Tokyo 102, Japan

Abstract

DDA developed by Goodman and Shi has attracted geotechnical engineers since it can handle static and dynamic behavior of assemblage of arbitrary shape blocks. However, when we consider to use DDA as an engineering tool, the original DDA has some shortcomings such as:

1) Elements for bolt, continuous concrete lining are not available.
2) It can not handle elasto-plastic behavior of a block.
3) A true circular (disk) block element is not yet formulated.
4) Erratic calculation of block area is encountered when a block is in fast rotation.
5) The high stiffness of penalty property at block interfaces often causes instability of calculation.
6) Complicated and non-friendly man-machine interface; difficulty in processing input and output data is not solved.

We have been working on developing a new code which can overcome the above mentioned shortcomings. The new concept of an interface, elasto-plastic block, circular element, nonlinear coordinate transformation to avoid erratic area calculation in rotation were developed and implemented in the code. A new user friendly man-machine graphic interface was introduced to ease heavy duty work to generate block meshes. Boundary condition input and mesh correction are done on the screen. Some example problems in relation to rock mechanics (e.g. rock slope, rock fall, tunnel excavation, rock foundation) were solved to check the new computer code. Some of them were compared with model test. The result of evaluation of the code was satisfactory.

1 Introduction

Discontinuous deformation analysis (DDA) was introduced by Shi and Goodman in 1985 and further developed by Shi. Discontinuous deformation analysis is used for analyzing force displacement interactions of block systems. For each block, displacements, deformations, and strains are permitted and for the entire block system, sliding, opening, and closing of block interfaces are also permitted.

DDA is a kind of hybrid displacement type model of the finite element method and is also very similar to Elastic Body Spring Method (EBSM) proposed by Kawai (1981). Shi (1984) succeeded to formulate the potential energy theory for the contact behavior of blocks by introducing a penalty function.

Discontinuous deformation analysis required the development of a complete kinematic theory that enables one to obtain large deformation solutions for numerous blocks under load or unload without penetration of one block by another. This kinematic theory recognizes the connections of joints around the perimeters of blocks so that correction-logic can be applied optimally.

The original DDA only considers the elastic deformation of blocks and at the contact

points blocks slide without any cohesive resistance. In order to apply this new tool to general rock mechanics problems, we need to modify and elaborate it up to the point which is comparable with FEM and DEM (Cundall 1971, 1981). We introduces a Drucker-Prager elasto-plastic constitutive law for solid blocks and a Mohr-Coulomb law for block interfaces. The main purpose to take into account the block yielding is to analyze soft rock mass behavior subjected to various loading conditions such as excavation and embankment.

The rockbolt element was introduced to represent the effect of confinement for rock masses. The bonding element which fuses two blocks was also invented to represent shotcrete and concrete lining in a tunnel structure. Additionally, damping coefficient was implemented to take into account the block collision.

The new DDA code was calibrated in comparison with laboratory model tests. Stability of rock slope and tunnel in a discontinuous rock mass is analyzed, and the effect of lining and rockbolts is discussed. Rockfall on a very steep slope was also calculated.

2 Verification of DDA

The DDA code has been compared with the results given by the theoretical analyses and a laboratory test to verify the ability of DDA. The toppling slope failure and the rock foundation were chosen for the evaluation. The simple biaxial test of a jointed rock was performed for comparison.

2.1 Limit Equilibrium Analysis of Toppling on a Stepped Base

Following the example shown in the text book written by Hoek and Bray (1977), the regular system of blocks shown in Fig. 1 was analyzed. The base is stepped upwards with an inclination. When a system of blocks commences to fail, it is generally possible to distinguish three separate groups according to their mode of behavior:

a) a group of sliding blocks in the toe region,
b) a group of stable blocks at the top,
c) an intermediate group section of toppling blocks.

Fig. 2 shows that the calculated result is very close to the theoretical prediction in which the bottom 4 blocks slide, whereas the computed result indicates that the bottom 2 blocks slide and other two blocks slide and topple.

2.2 Rock Foundation Analysis (Sasaki, et al, 1995)

In large scale rock foundations within the discontinuous planes existing in a rock mass, the behavior of deformation and stress distribution along structure foundations are strongly influenced by the pattern of the discontinuous planes. The behavior was examined by using Boussinesq analytical theory, and the experiment models of Maury (1971).

Table 1 gives the material properties of the experiments. The applied external load is $4.17 kgf/cm^2$ for the $12cm$ width at the center of the upper part of the rigid block made by irons as shown in Fig. 3. Fig. 4 – Fig. 7 show vertically and horizontally staggered models presented Maury (1971) through the use of $4cm \times 4cm$ duralumin square rods. Here, in order to express the roller conditions along boundaries, the dummy slender blocks are attached along the boundaries in DDA models shown in Fig. 3. This is to cut the friction between inner blocks and fixed blocks of the outer boundaries.

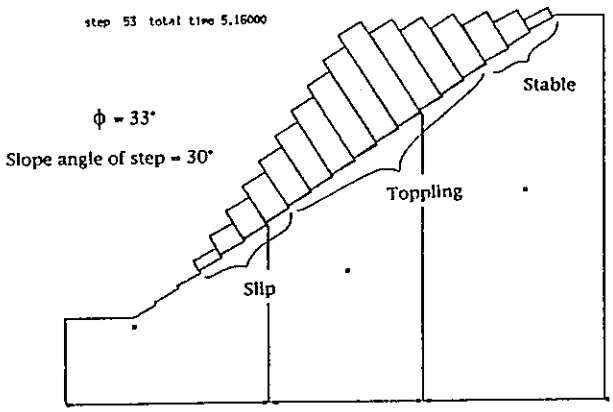

Fig.1. Analysis of toppling on a stepped base (Start to move).

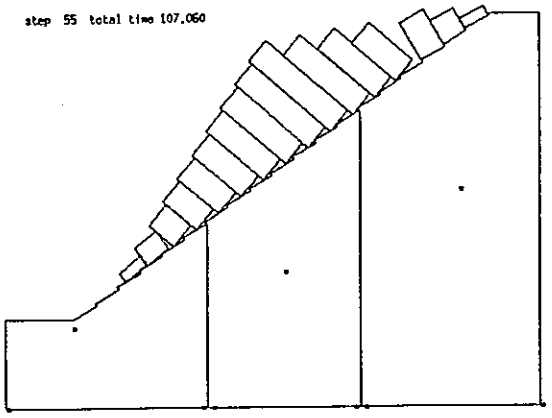

Fig.2. Analysis of toppling on a stepped base (Final stage).

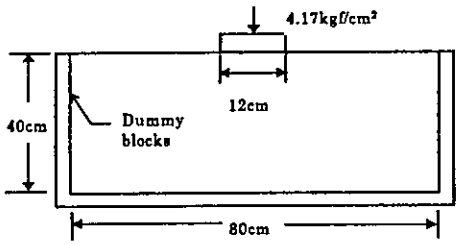

Fig.3. The boundary and loading conditions of DDA model.

Table1. Material properties of the block model test(Maury,1970).

Components	Properties
Young's modulus	7×10^5kgf/cm^2
Poisson's ratio	0.34
cohesion of surface	0 kgf/cm^2
friction angle	40°
cohesion of body	elastic
internal friction angle	elastic

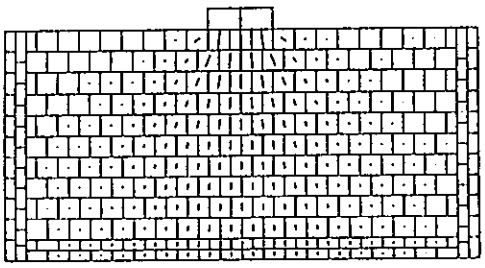

Fig.4. The vertically staggered model (Model-A, Continuum).

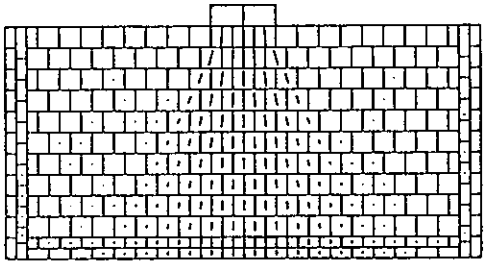

Fig.5. The horizontally staggered model (Model-A, Discrete).

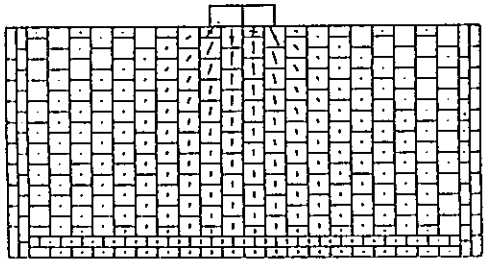

Fig.6. The vertically staggered model (Model-B, Continuum).

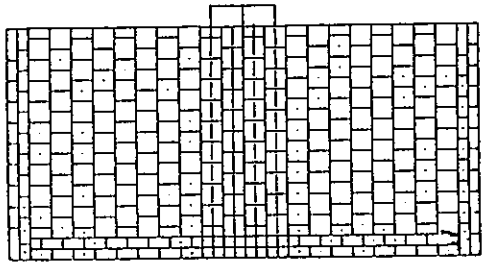

Fig.7. The horizontally staggered model (Model-B, Discrete).

Mohr-Coulomb friction criterion is employed for the block surface. A large penalty coefficient is applied for non-penetration conditions between blocks in the normal direction of the block surface. If shear stress of the block surface is greater than shear strength, the zero spring coefficient is employed for shear slip conditions.

Fig. 4 and Fig. 6 show the principal stress distribution of the continuum models in which the tensile strength is given for the friction conditions of a block surface. Fig. 5 and Fig. 7 show the principal stress distribution of discrete model of Model-A and Model-B.

Fig. 8 shows the vertical stress distribution along bottom boundary blocks of the vertically staggered model (Model-A, Discrete) and the result of Maury's experiment. Fig. 9 also shows the vertical stress distribution along bottom boundary blocks of the horizontally staggered model (Model-B, Discrete) and the result of Maury's experiment. The vertical stress concentration of Model-B is concentrated greater than of Model-A near the center of analytical region. The numerical results roughly agree with the experiments.

Fig. 10 shows comparison of the vertical stress distribution at the center of loading point for Model-A, Model-B and Boussinesq analytical theory. The stress concentration of the numerical solutions (DDA) is smaller than analytical theory at the center of loading point. Thus, the reason of different stress distribution seems due to the fundamental difference between the discontinuum and continuum models. In addition the analytical theory assumed the infinite boundary.

Fig. 11 and Fig. 12 show the principal stress distribution of the 45° inclined jointed model (Model-C) of the continuum model and the discrete model which simulate the model test result presented by Gaziev (1971) shown in Fig. 13. The maximum principal stress contours of Gaziev's experimental results and the numerical results obtained by DDA agreed with those experiments.

2.3 Biaxial Compression Test (Sasaki, *et al*, 1994)

A biaxial compression test of rock blocks was performed to compare with DDA calculation. A $40cm \times 80cm$ tuff specimen with some artificial discontinuities was tested as shown in Fig. 14. The confining stress at a constant $196kPa$ is applied by eight side jacks. The properties of the tested material, the jacks, and the loading plates are given in Table 2. The tephron sheets were used between the rock blocks and the loading plates of jacks. Observation points No.1–13 were dial gauges and No.14–21 were slip gauges. The observed test results are shown in Fig. 15. The maximum displacement of loading direction was 2 mm and reached the maximum load.

In the DDA analysis, the cylinder guides of the jack models are fixed and the loads are applied at the center of those cylinders as shown in Fig. 16. The friction angle between the blocks and loading plates is assumed to be 20°. The shear stiffness between the blocks is obtained by the experiments and was $1.47GN/m^3$. The analysis results are shown in Fig. 16. The main directions of the principal stresses of the rock blocks are shown along the lad convey direction between the external forces which form the upper part of the left side blocks to the down part of light side blocks (Block No.1, 3, 6, and 8 as shown in Fig. 15). It is clear that the deformation mode seen in the test is simulated very well in the analysis.

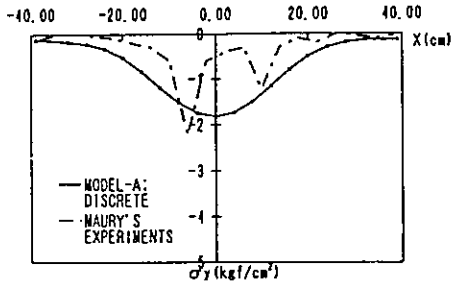

Fig.8. The vertical stress distribution along bottom boundary blocks (Model-A vs. Maury's experiments).

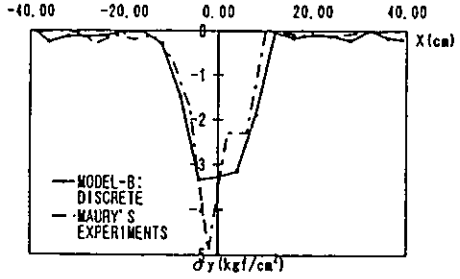

Fig.9. The vertical stress distribution along bottom boundary blocks (Model-B vs. Maury's experiments).

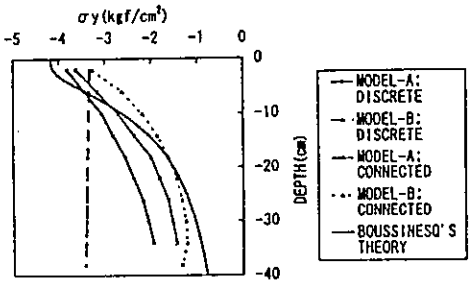

Fig.10. The vertical stress distribution along center reigon.

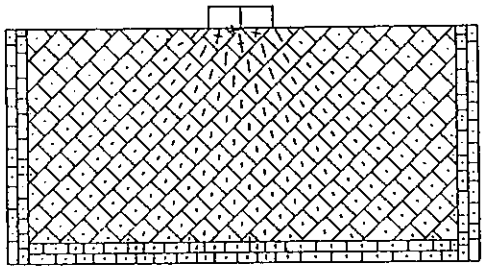

Fig.11. The 45deg. inclined model (Model-C, Continuum).

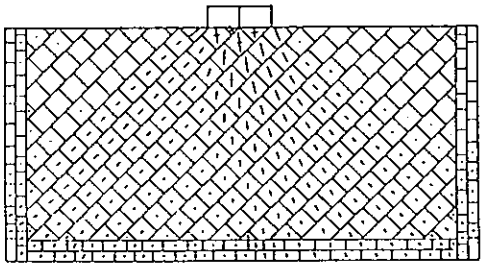

Fig.12. The 45deg. inclined model (Model-C, Discrete).

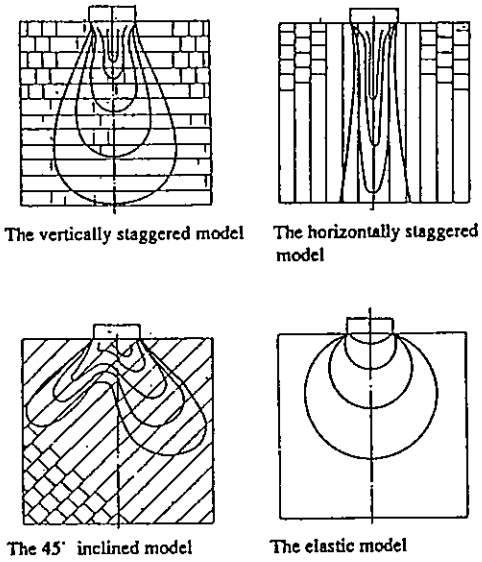

Fig.13. Maximum principal stress contours of Gaziev's experiment results(1971).

Table2. Material properties of the rock model test.

Components	rock blocks (tuff)	jucks and loading plates
Young's modulus	1412.1MPa	205.9GPa
Poisson's ratio	0.2	0.3
cohesion of surface	0 kPa	0 kPa
friction angle	40° (0.698rad)	0° (0rad)
unit weight	14.12kN/m^3	76.49kN/m^3

3 New Elements

3.1 Rock Bolt

We developed a rockbolt element (Sasaki *et al*, 1994). Fig. 17 shows that arbitrary two points (x_i, y_i) and (x_j, y_j) in blocks i and j are connected by a rockbolt. Let l the length, dl the deformation and s the stiffness of the rockbolt, the strain energy of the rockbolt is given by the following equation:

$$\Pi_b = \frac{s}{2l} dl^2. \tag{1}$$

Minimizing the potential energy of (1), the stiffness matrix of the rockbolt $[K_{\lambda R}]$ is given as follows.

$$[K_{rs}] = \frac{\partial^2 \Pi_b}{\partial d_{ri} \partial d_{si}} = \cdots = [K_{\lambda R}]. \tag{2}$$

3.2 Bonding Element

We developed a bonding element by introducing the penalty method, for the purpose of simulation the continuous region to analyze local stress and strain of blocks or bond of blocks like shotcrete as lining of tunnel (Sasaki *et al*, 1994). Fig. 18 shows the relationship between blocks i and j which are bonded to each other. Relative displacement of arbitrary points (x_i, y_i) and (x_j, y_j) in bonded blocks i and j is defined as a function of the coordinates and the displacements of the points, which must be zero at the bonding face. The spring force by the relative displacement is given by the product of the relative displacement and the stiffness of the bonding element. Then the strain energy of the element is

$$\Pi_f = -\frac{1}{2}(F_x dx + F_y dy) \tag{3}$$

where d_x and d_y are the relative displacements in x and y directions, respectively. Using displacements of the points (x_i, y_i) and (x_j, y_j), we can get the strain (potential) energy as the function of (x_i, y_i) and (x_j, y_j). Minimizing the potential energy, the stiffness matrix of bonding elements is given as follows. And we also get the external force vector.

$$[K_{rs}] = \frac{\partial^2 \Pi_f}{\partial d_{ri} \partial d_{si}} = \cdots = [K_{\lambda C}]. \tag{4}$$

3.3 Circular (Disc) Element

We developed a rigid circular element for the purpose of the analyzing mechanics and introduced a rigid circular element into the DDA code (Ohnishi and Miki, 1993). The displacements (u, v) in the rigid circular element i are expressed as functions of the coordinates (x, y) as follows:

$$\begin{pmatrix} u \\ v \end{pmatrix} = \begin{pmatrix} 1 & 0 & -(y - y_0) \\ 0 & 1 & (x - x_0) \end{pmatrix} \begin{pmatrix} u_0 \\ v_0 \\ r_0 \end{pmatrix} \tag{5}$$

where (u_0, v_0) are rigid translation, r_0 is rigid rotation.

A deformable element has six degree of freedom $(u_0, v_0, r_0, \varepsilon_x, \varepsilon_y, \gamma_{xy})$ while the rigid elements have only three degrees of freedom (u_0, v_0, r_0). The matrices depending on the

conditions of a rigid circluar element and the contacts between rigid circluar elements are derived by reducing the degree of freedom of the matrices in the deformable element. Fig. 19 shows an example of analysis for the granular system.

4 Constitutive Law for Block

4.1 Elasto-Plastic Element

The strength criterion for a block was introduced. The well known Drucker-Prager failure criterion with associated constitutive law as shown in Fig. 20 was implemented in the code to take into account the block failure of rock masses.

The authors adopted the Drucker-Prager associated constitutive law for a block:

$$F = \alpha J_1 + \sqrt{J_2} - \frac{\bar{\sigma}}{\sqrt{3}} = 0 \tag{6}$$

where

$$\alpha = \frac{1}{3}\sqrt{\frac{\sin^2\phi}{3+\sin^2\phi}} \tag{7}$$

and

$$\bar{\sigma} = 3C(1-12\alpha^2), \tag{8}$$

J_1 and J_2 are first and second invariants of deviator stress, C is a cohesion, ϕ is a friction angle of the block.

In case of large deformation, the coordinates of blocks should be updated at each time step. The stress increment with the rotation of the coordinate with block rotation at each time step is represented by Jaumann co-rotational differential, in order to fulfill the objectivity of the stress. Then the stresses before and after the rotation are superposed as following:

$$[\sigma_{ij}] = \frac{[\Delta\sigma_{ij}]}{\Delta t} + [\sigma_{ik}][\Delta W_{kj}] + [\sigma_{ik}][\Delta W_{ki}] \tag{9}$$

$$[\sigma_{ij}]^{t+\Delta t} = [\sigma_{ij}]^t + [\sigma_{ij}]\Delta t, \tag{10}$$

where $[\Delta W_{ki}]$ is a rotation increment matrix , $[\sigma_{ij}]$ is a stress rate tensor, $[\Delta\sigma_{ij}]$ is a stress increment tensor and Δt is a time step.

This manipulation is important for the case of large spin motion on toppling analysis of slope for instance and the elasto-plastic analysis in which a block has different principal axis of strain between each steps in particular.

4.2 Example - Stability Analysis of Rock Slope and Tunnel

A stability problem of slope and tunnel in a rock mass with some directions was analyzed for five cases. The model is shown in Fig. 21. The blocks outside are fixed. The friction forces of the blocks located at the first and the second layers from the outside are assumed to be zero, hence, the analysis imitates the roller supports used in FEM. A Drucker-Prager yield criterion and an associated plastic flow rule were adopted for blocks. And a Mohr-Coulomb friction criterion was adopted for block surfaces. An external loads of $588kN$ was applied on the crest of the slope and inertia forces in the vertical direction of the each

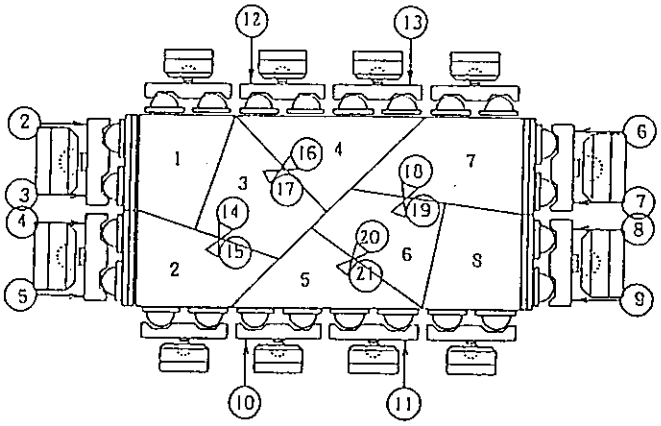

Fig.14. The rock specimens and observation points.

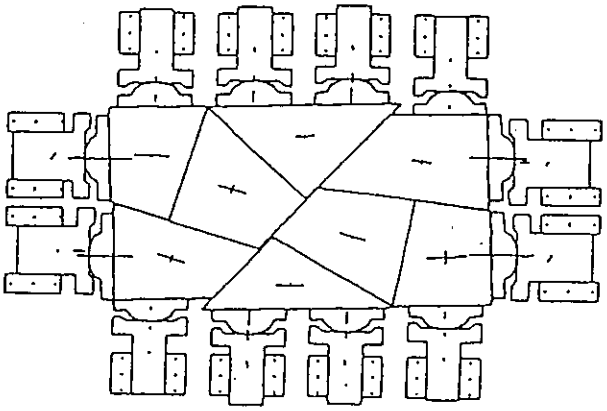

Fig.16. Numerical result of the rock block model test.

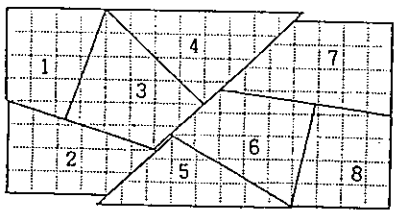

Fig.15. Result of the experiments by observation.

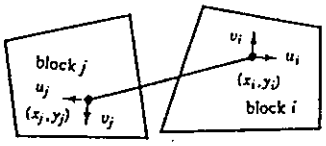

Fig.17. Modeling of Rockbolts.

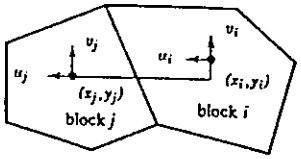

Fig.18. Bonded Blocks.

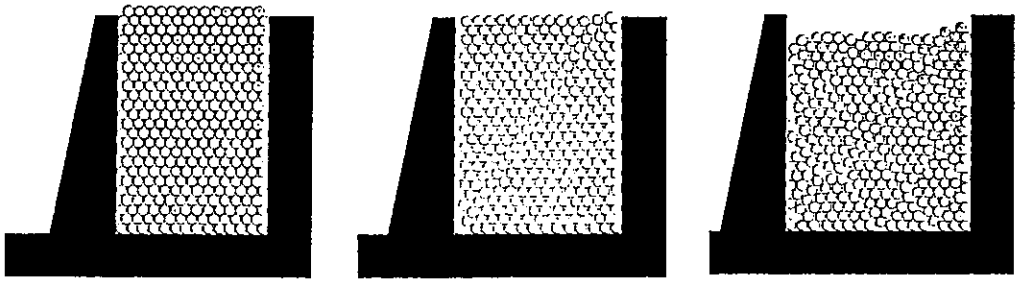

Fig.19. An example of analysis for the granular system.

block were also applied. The other analysis conditions are given in Table 3. In Cases-3.1 and 3.2, no reinforcement is installed around the tunnel.

In Cases-3.3 and 3.4, linings were installed. In Case-3.5, rockbolts and a lining were installed and the lining was bonded to the tunnel wall. The connecting elements used for the rockbolts and the lining were arranged as shown in Fig. 22.

The material property of the blocks is assumed to be elastic in Cases-3.1 and 3.3, and elasto-plastic following the Drucker-Prager associated constitutive law in Cases-3.2, 3.4, and 3.5. The results are shown in Figures 23 to 27. The principal stress distribution of the elastic analysis with no friction on block surfaces in Case-3.1 can be seen to agree approximately with the elastic solution for FEM in the instance shown Fig. 23. The plastic region and the displacement around the tunnel was very large in Case-3.2 without rockbolts and a lining as shown in Fig. 24. The large stress concentration is caused at the crest of the corner at the right hand side of the lining and the displacement is shown as very small in the elastic analysis of Case-3.3 as shown in Fig. 25. Fig. 26 shows the results of Case-3.4 with inner blocks of the tunnel and the plastic regions and the displacement is shown as smaller than Case-3.2 with no inner blocks of the tunnel. Fig. 27 shows the plastic regions and the displacement for Case-3.5 with rockboltings and the lining of the tunnel. The plastic regions are extremely reduced compared with those of Case-3.4. From the results, it is clear that DDA can show the difference between the five cases and represent the effect of tunnel supporting like shotcrete linings or rockbolts.

The results showed that this method can express the effects of the reinforcement to the tunnel. Since the method is applicable to the discontinuity between continuous models through its controlling of the friction criteria of block surfaces and using the rockbolt and concrete elements, the deformation of DDA depends strongly on the friction criterion of the block interface.

5 Improvement

5.1 Block Rotation

The problem related with block rotation in DDA was found in the research for the rock fall analysis. The purpose of the research was whether we can follow the actual rock fall in the high mountain by this new numerical technique DDA. A typical example was chosen from a site in Niigata Pref. in Japan.

The height of the slope is more or less $150m$ and slope angle is 45° to 50°. The volume of falling blocks are estimated to be $18m^3$ which is normally too big to protect with a usual concrete wall. The computation is underway to compare with conventional design criteria which usually does not handle such a large block.

Fig. 28 show the time series of falling blocks from the top of the slope. The estimated large block was cut into small pieces according to the joint pattern observed at the site. Fig. 29 also show the falling of idealized parallelepiped blocks when several barriers are set in the middle of the slope. Some blocks settles and some others are over-riding the barrier down to the bottom. The energy and velocity distribution of the blocks at each time steps are obtained and the results are now under examination.

In this research we found that the volume of falling blocks rapidly change according to the amount of rotation. Now, we discuss what is the reason and how to improve the problem.

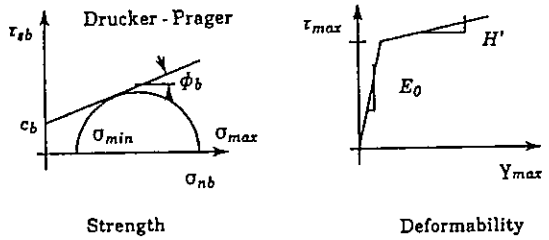

Fig.20. Strength and deformability of a block.

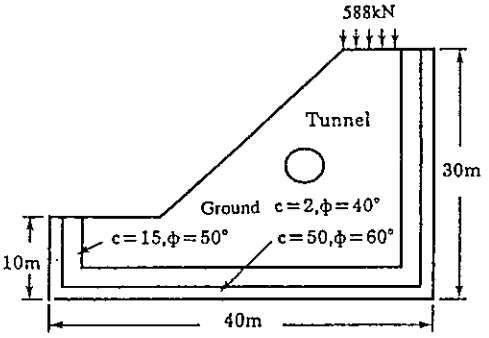

Fig.21. Analyzed model.

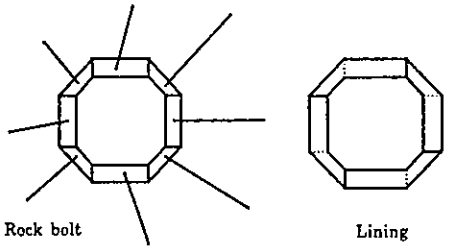

Fig.22. Arrengement of rockbolts and lining.

Table3. Material properties and analysis conditions.

Components	Properties and analysis conditions
number of time steps	20(Case-3.1-3.4) 40(Case-3.5)
time step interval	0.5s
penalty coefficient	1×10^8
maximum displacement ratio	0.01
inertia force (horizontal)	0 kN
inertia force (vertical)	-24.5 kN
initial stress	0 kPa
Young's modulus	98MPa
Poisson's ratio	0.24
cohesion of the body	49kPa
internal friction angle	40° (0.698rad)
unit weight	24.5kN/m^3

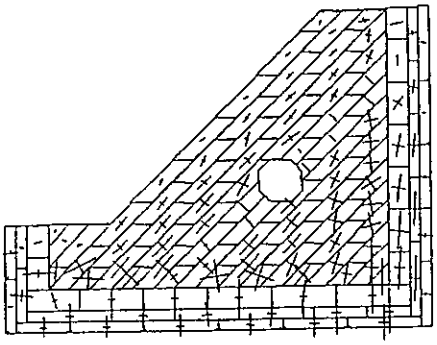

Fig.23. Result of tunnel stability analysis (Case-3.1 elastic,without lining, friction angle between blocks ϕ=0 degrees).

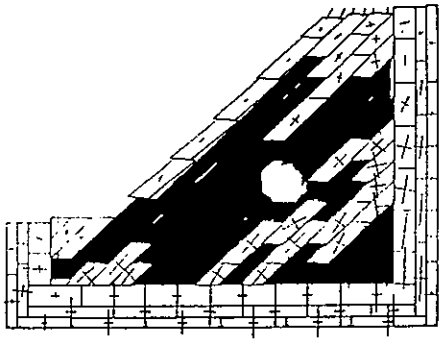

Fig.24. Result of tunnel stability analysis (Case-3.2 elasto-plastic,without lining, friction angle between blocks ϕ=40 degrees).

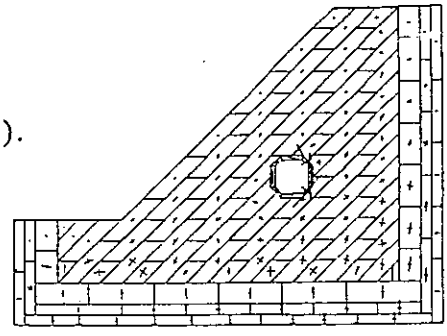

Fig.25. Result of tunnel stability analysis (Case-3.3 elastic,with lining, friction angle between blocks ϕ=40 degrees).

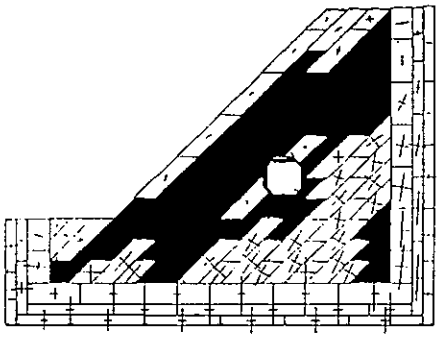

Fig.26. Result of tunnel stability analysis (Case-3.4 elasto-plastic,with lining, friction angle between blocks ϕ=40 degrees).

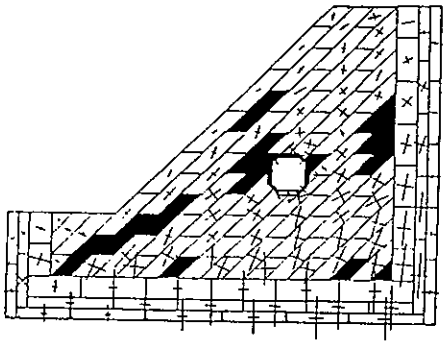

Fig.27. Result of tunnel stability analysis (Case-3.5 elasto-plastic,with lining bonded and rockbolts, friction angle between blocks ϕ=40 drgrees).

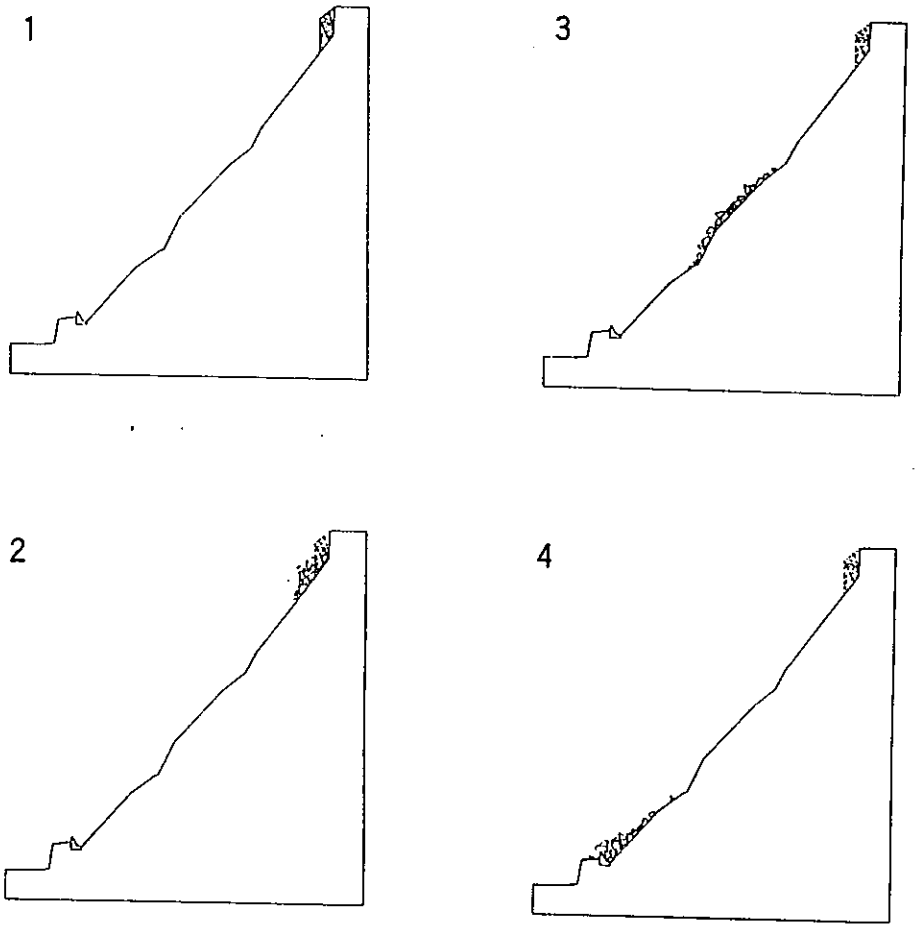

Fig.28. Modeling of rock fall.

The displacement (u, v) of any point (x, y) within a block is supposed to be the following in DDA:

$$\begin{pmatrix} u \\ v \end{pmatrix} = \begin{pmatrix} 1 & 0 & -(y-y_0) & (x-x_0) & 0 & (y-y_0)/2 \\ 0 & 1 & (x-x_0) & 0 & (y-y_0) & (y-y_0)/2 \end{pmatrix} \begin{pmatrix} u_0 \\ v_0 \\ r_0 \\ \varepsilon_x \\ \varepsilon_y \\ \gamma_{xy} \end{pmatrix} \tag{11}$$

where, (u_0, v_0) is the rigid displacement of the center point (x_0, y_0) within the block; r_0 is the angle of rigid rotation of the block around the point (x_0, y_0); ε_x, ε_y and γ_{xy} are the avearge elestic strains of the block.

It is known that (11) is only the first order approximation of displacement, and the rigid rotation r_0 is defined as

$$r_0 = \frac{1}{2}(\frac{\partial v}{\partial x} - \frac{\partial u}{\partial y}) \tag{12}$$

with $x = x_0$ and $y = y0$.

It is worth notice that (12) is defined as the rotation only under the presupposition of small deformation in elastic theroy. Obviously, it is not valid for large rotation, which can be shown as the follows.

Supposing that the displacement of a block only involves rigid rotation, then, (11) becomes

$$\begin{cases} u = -(y-y_0) \ r_0 \\ v = (x-x_0) \ r_0 \end{cases} \tag{13}$$

In this case, if a block as shown in Fig. 30(a) is rotated 60°, the vertices of the block will move to the new positions shown in Fig. 30(b) according to the displacemenets calculated from (13). Obviously, the area of the block increases by about two times.

In fact, the displacement of a point (x, y) from rigid rotation should be calculated by the following formula:

$$\begin{cases} u = (x-x_0)(\cos r_0 - 1) - (y-y_0)\sin r_0 \\ v = (y-y_0)(\cos r_0 - 1) + (x-x_0)\sin r_0 \end{cases} \tag{14}$$

Comparing (13) with (14), it can be seen that (13) is the first order approximation of (14).

However, when rotation angle r_0 is large enough, $(\cos r_0 - 1)$ is no longer approximate to 0 and $\sin r_0$ no longer to r_0. The larger the rotation angle r_0 is, the larger the differences between $(\cos r_0 - 1)$ and 0 as well as $\sin r_0$ and r_0 become.

Because of the nonlinearity of (14), it is difficult to be used directly in the displacement function of DDA. Therefore, there has not yet been a precise way to solve the problem up to now. Here we propose two measures to overcome the problem as far as possible:

1. The time increament for a step is taken as small as possible so that the rotation angle r_0 can be kept small.
2. Use (14) instead of (13) to calculate the displacements of block vertices in each step. This can avoid the areal increaments of blocks and reduce the accumulated errors from rotaions of each step.

The measure 2 has been involoved in the programs of DDA, and it has been shwon very effective by a lot of calculations.

5.2 Joint Behavior and Penalty Function

In DDA, the penalty function is used to avoid the physical intrusion of blocks and the theory is derived as follows.

Denote the stiffness of the spring as p and the inter-penetration distance as d, the strain energy of the contact spring is;

$$\Pi_k = \frac{p}{2}d^2. \tag{15}$$

The inter-penetration distance d of Fig. 31 can be expressed in terms of coordinate function $[e_i]$, $[g_j]$ and unknown variables $[D_i]$, $[D_j]$ of blocks i and j.

$$d = \frac{S_0}{l} + [e_i][D_i] + [g_j][D_j], \tag{16}$$

where p is a very large positive number and is the stiffness of the spring (penalty coefficient). And S_0 is the area of penetration as shown in Fig. 31. In DDA the penalty function is representing the contact spring between two blocks. However, if you look at the physical interface like a rock joint, the contact spring is much softer than the one used for the penalty function. Then the result of calculation by using the original method predicts less deformation than the actual one.

What we have done to modify the penalty function is as follows. Fig. 32 shows the concept of the criterion by Shi, in which he applied the penalty method to both normal and shear directions. In this criterion, if shear stress is smaller than the friction strength, no block stress conditions are caused due to the non-slip condition (locking) being applied to the block.

To relax this constraint, we introduced the shear stiffness K_s just for the shear component instead of penalty and the penalty method is applied only to the normal component.

5.3 Man-Machine Interface

In order to pursue the method to widely practical applications, a powerful system software for DDA is important and imperative since a vast of data are involved in both input and output of DDA calculation. In this section, we introduce our newly developed such a software called DDAWorkTool, which makes it very easy to apply DDA to any practical problems.

DDAWorkTool, based on window graphics and menu choices, contains three functional modules corresponding to the three procedures: model-making, calculation-executing and result-analyzing, which are controlled by a main menu panel (Fig. 33).

The model-making module is used to make DDA models and can be accessed from the main menu panel by pushing the menu button [`Make Model`]. Fig. 34 shows its work windows and menu buttons. It has the following major merits:

1. Grouped blocks are automatically made by filling the related parameters in panel tables. Joint blocks, tunnel blocks and the blocks from Voronoi Divisions are such kind of grouped blocks (Fig. 35).

2. Points and boundary lines of blocks can directly be drawn on the screen by use of mouse. Therefore, un-grouped blocks, fixed points, measured points and load points can be easily made (Fig. 34).

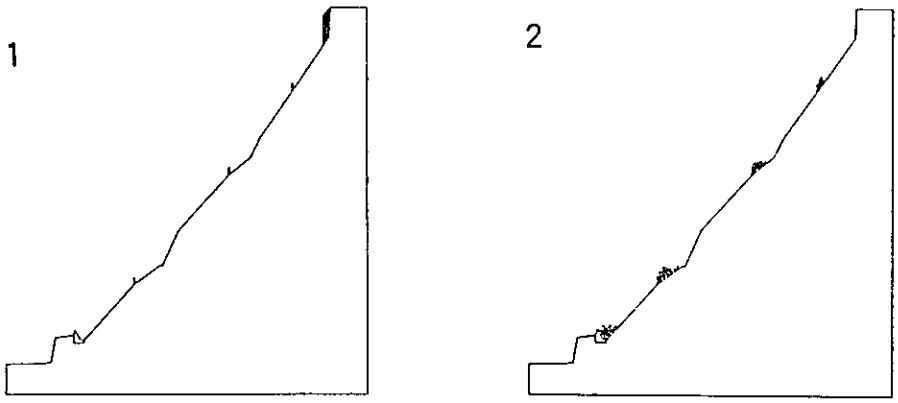

Fig.29. Modeling of rock fall by parallelepiped blocks.

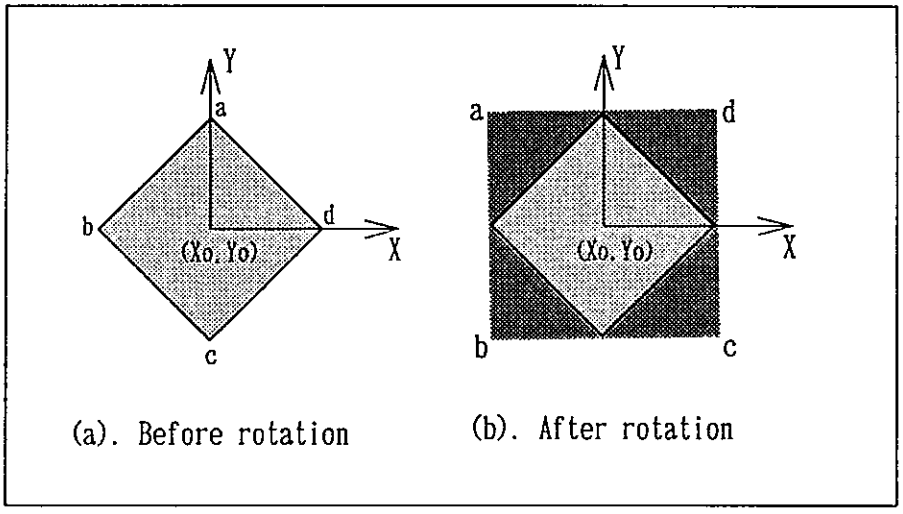

Fig.30. A block is rotated by 60 degrees counterclockwise.

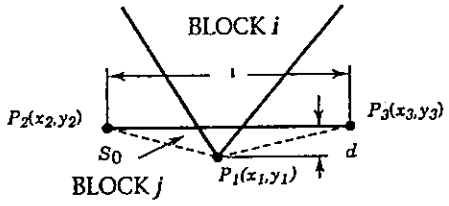

Fig.31. Inter-penetration of blocks.

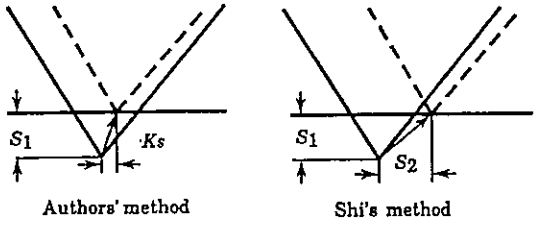

Fig.32. Criteria of penalty method.

3. All the parameters are directly inputed by filling the corresponding panel tables. Therefore, material parameters, boundary parameters and other controlling parameters can be easily added, deleted and corrected (Fig. 34).

4. The information and visual pictures of input data for a model are immediately shown on the windows for every operation. Therefore, it is easy to check the model while making.

The calculation of DDA can be executed from the main menu panel by pushing the menu button [`Calculation`]. The module is based on the codes made by G. Shi, 1994, but the following improvements have been made.

1. The name of the model to be calculated are directly chosen from the menu list which are collected automatically from the current directory.

2. Both ASCII and binary formats are available for the output of the calculation, the format and the number of output steps can be chosen by user.

3. The part of codes related to block rigid rotation are modified. Since the first approximation is taken in displacement functions of DDA, large errors will take place when large rigid rotations of blocks are involved in a step. By modification of the codes, the results have been improved considerably for this case.

The result-analyzing module can be accessed from the main menu panel by pushing the menu button [`Result Analysis`]. Fig. 36 shows its work windows and menu buttons. It provides various kinds of graphics and pictures based on the output data of DDA so that a user can analyze the calculated results easily. The following graphics and pictures are available:

1. The picture of the deformed whole block system can be shown for any step, forward and backward.

2. The animated drawing of the deformed whole block system can be automatically shown step by step.

3. The pictures of the deformed whole block system can be amplified so as to investigate the interesting part in detail.

4. The graphics of the stresses, strains, displacements and velocities from the first step to the last step for any block are immediately available when a block is pointed by mouse or a block number is assigned in the menu panel (Fig. 37).

The digital results of a specified block are also shown in the right window corresponding to each step.

DDAWorkTool has been coded with C language on Sun WorkStation, and it has been shown to be very efficient by a lot of practical uses. We expect that the useful DDA method will get more and more widely practical applications by using the tool.

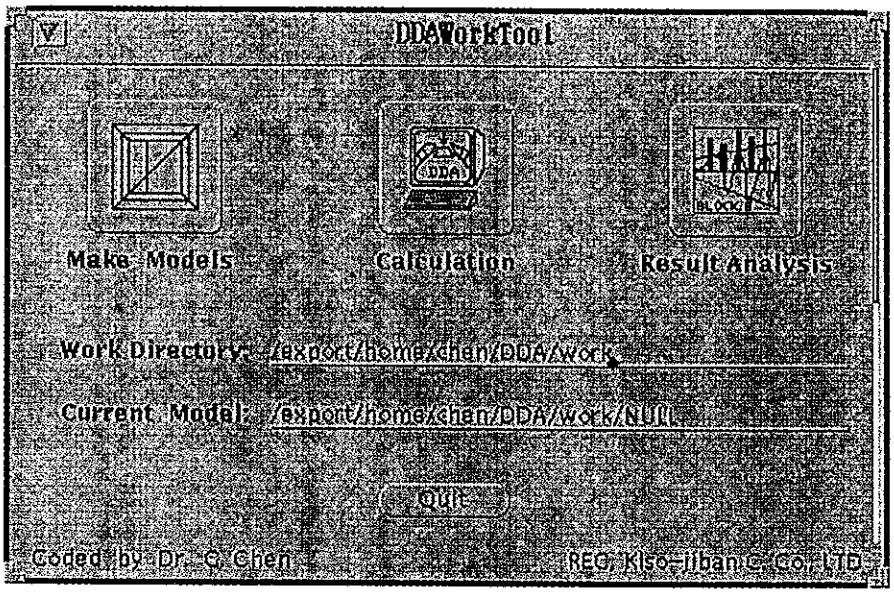

Fig. 33. The main menu panel of DDAWorkTool

5.4 Discussion

In the process of solving actual geotechnical engineering problems, we faced a lot of difficulties to use DDA method. Some of the difficulties have been solved, but there still exist problems to be discussed.

a) **cohesion c** In the Mohr-Coulomb failure criterion, we use cohesion c to add strength of the martial in geotechnical engineering. In any application of DDA nobody tried to include cohesion c term for the failure criterion. The problem comes from the nature of DDA block contact assumption in which the edge to edge contact is not considered. We should carefully examine how we can include c term in the DDA code which is often used in the engineering calculation.

b) **node (corner) to node (corner) contact** In DDA the fancy and amazing method was introduced to identify the block to block contact. Unfortunately in case of the node (corner) to node contact, the it takes so much time to identify the block contact and sometime computation time is intolerable. In order to avoid this problem, most of the example were calculated not using node to node contact when the block mesh was created.

However, if we use Volonoi tessellation for block mesh, the node to node contact is not avoidable. Then as a temporally solution we introduced the rounded corner for the special case.

c) **material damping for a block** In addition to the block rotation problem, we found the strange behavior of falling blocks when they collide each other. The energy

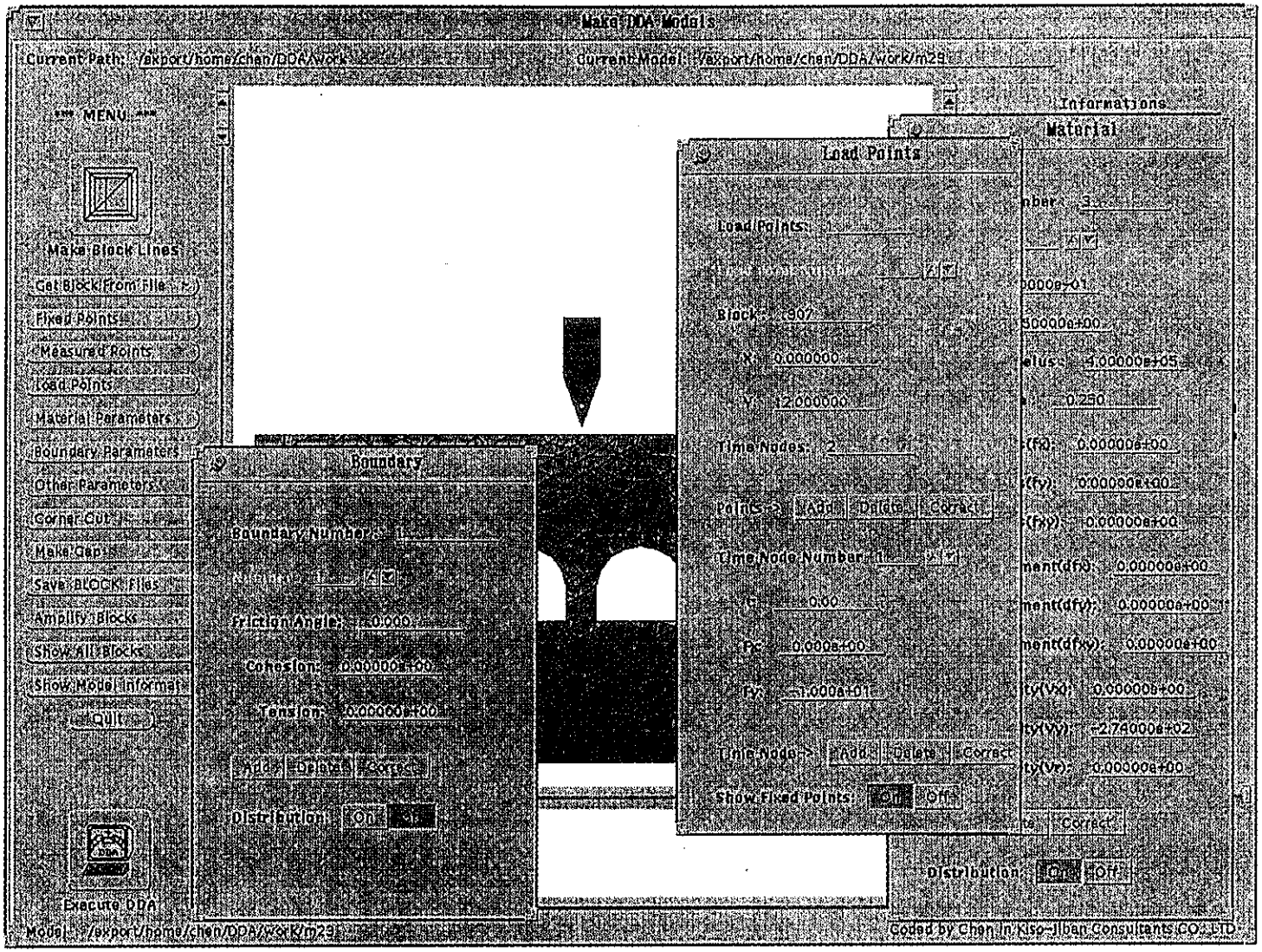

Fig. 34. Work windows, menu buttons and panel tables of the model-making module.

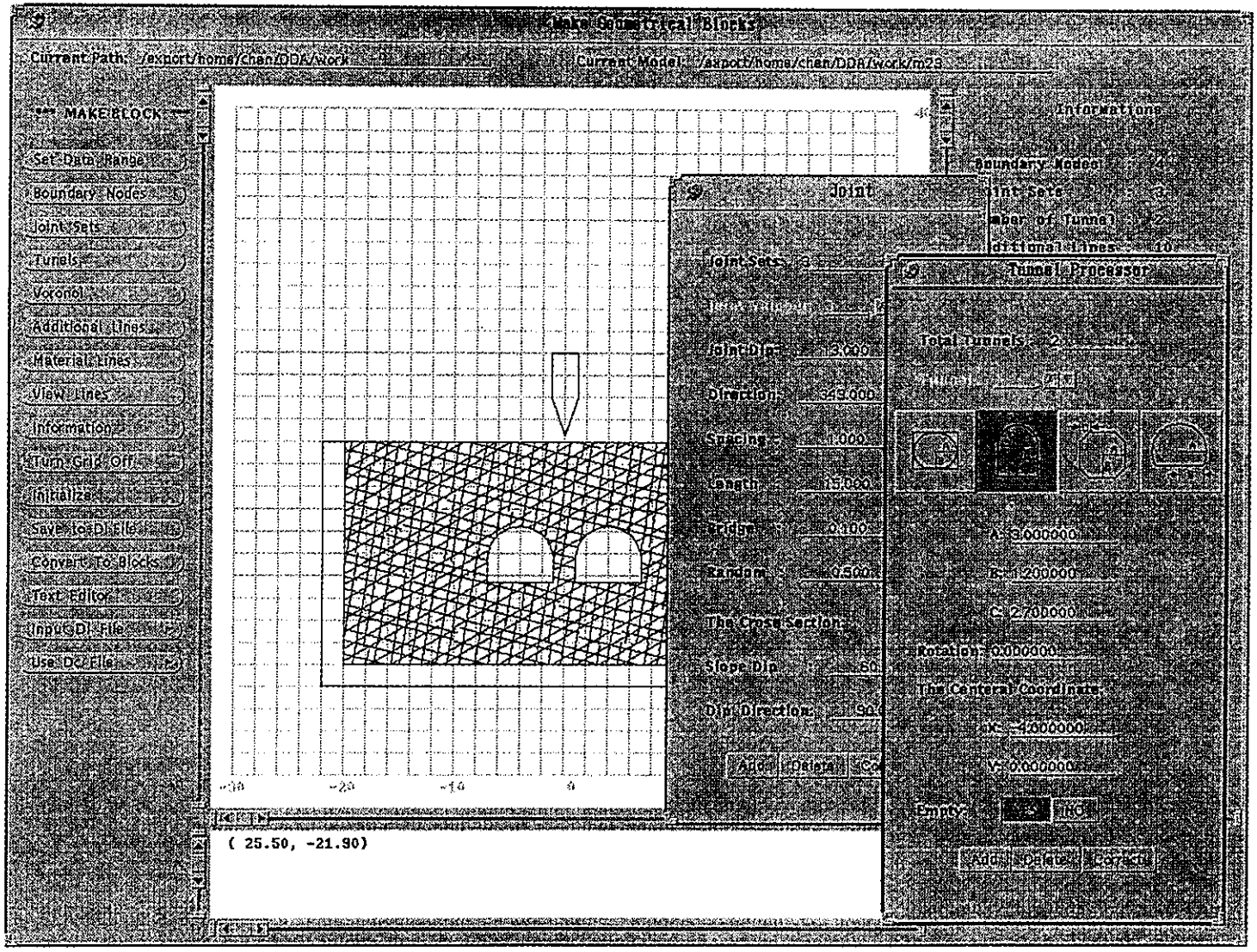

Fig. 35. Panel tables for assigning the related parameters of grouped blocks.

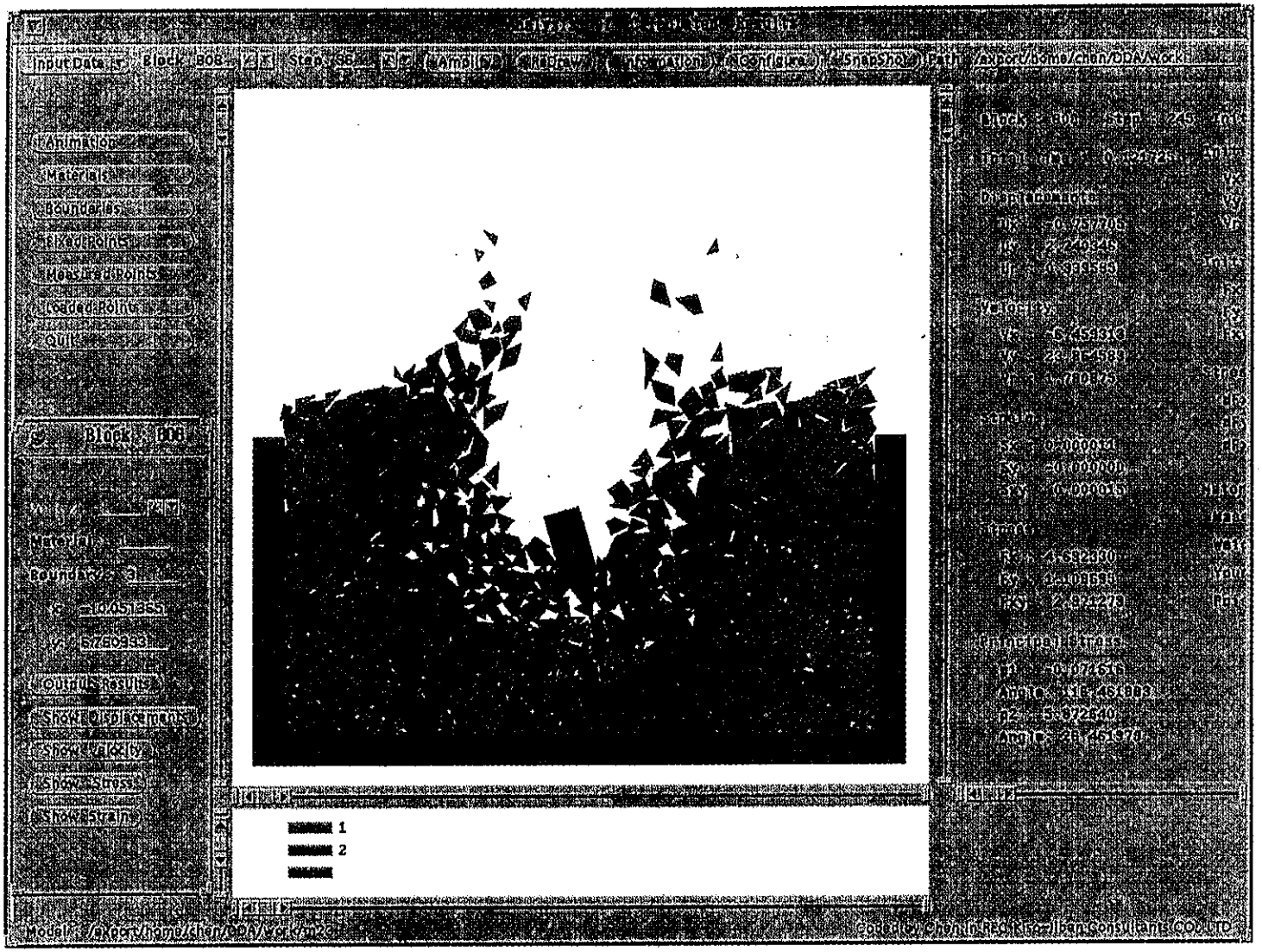

Fig. 36. Work windows, menu buttons of the result-analyzing module.

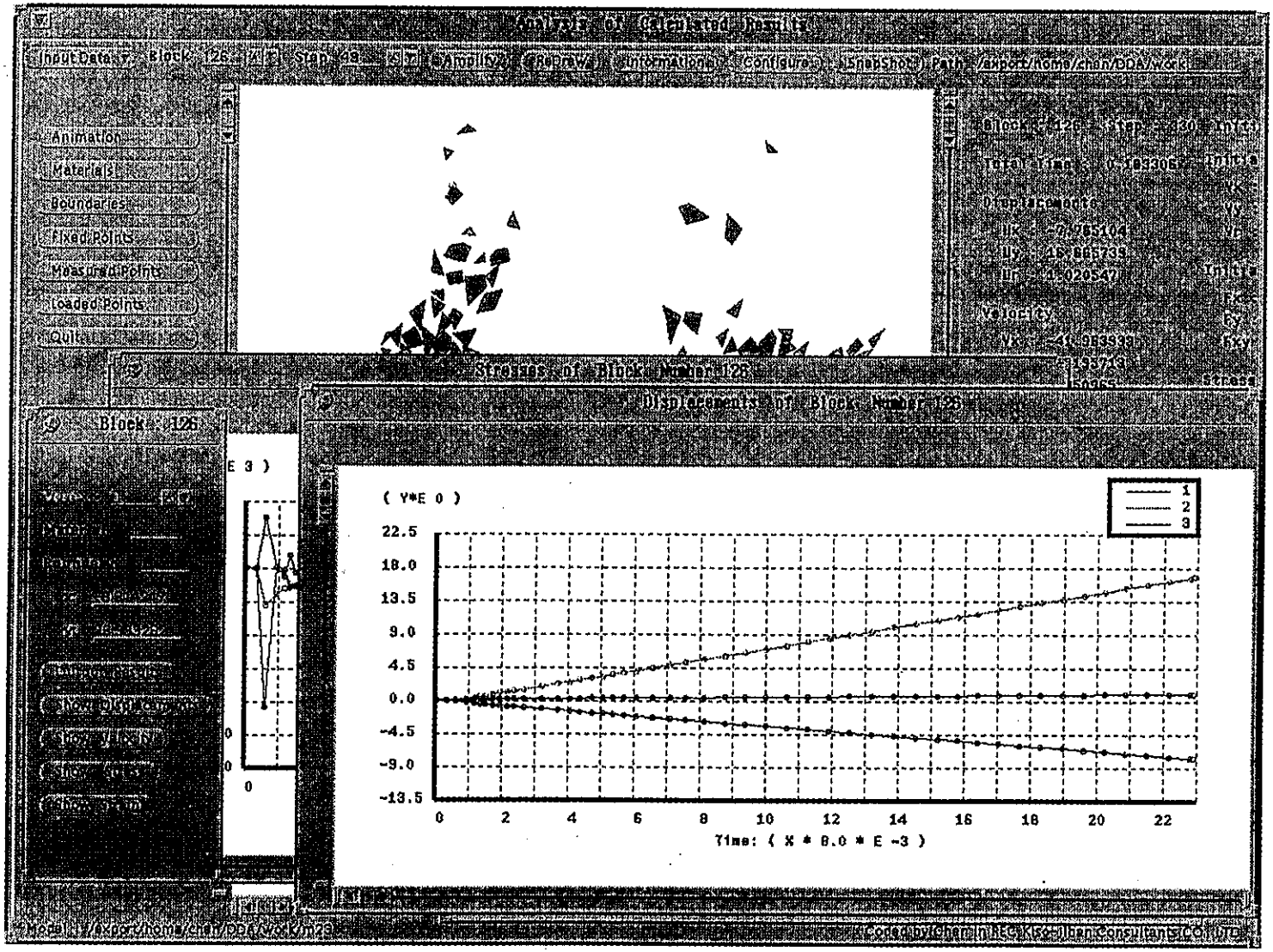

Fig. 37. The graphics of calculated results for any blocks.

balance between blocks has to be take into account. For the moment, the damping factor for the block was introduced, but the energy consumption at the collided interfaces has to be considered.

d) **uniform load (stress) boundary** There is no problem for the uniform displacement boundary in DDA because the stiff block behaves as the boundary. But, uniform stress boundary usually used in the laboratory test condition can not be created easy in the existing DDA code.

6 Conclusion

The potential use of a new tool, discontinuous deformation analysis technique, are investigated. The application of this method to the actual rock slope engineering has just started recently and we will try to develop more convenient and powerful technique for the future research.

The method of DDA with improvement has been proven to be very effective to analyze rock stability problems in discontinuous deformable rock masses, but we still have problems to be solved as discussed in the previous section.

Acknowledgment

Most of the work presented in this paper have been done in cooperation with the members of DDA Research and Development Committee in Japan Institute of Systems Research. We would like to express our gratitude to them for their support and advise.

References

Cundall P. (1971): A Computer Model for Simulating Progressive, Large Scale Movements in Blocky Rock Systems, Symposium of ISRM, Nancy, France, pp.11-18.

Cundall P. (1987): Distinct Element Methods of Rock and Soil Structure, Chapter 4 in Analytical and Computational Methods in Engineering Rock Mechanics, Brown, E.T. ed., pp.129-163.

Gaziev E. and S. Erlikhman (1971): Stresses and Strains in Anisotropic Rock Foundation (Model Studies), Symp. Soc. Int. Mec. des Roches, Nancy, II-1.

Hoek E. and J. Bray (1977): Rock Slope Engineering, Chapter 10, IMM, London.

Kawai T. , N. Takeuchi and T. Kumeta (1981): New Discrete Models and Their Application to Rock Mechanics, Int'l Symp. on Weak Rock, Tokyo, Vol.2, pp.725-730.

Maury V. (1970): Mechanique des milieux stratifies, experiences et calcuis, DUNDO, Paris.

Ohnishi Y. and S. Miki (1993): Analysis of Granular Mechanics by DDA, DDA Reserch and Development Committe 8th meeting, Japan Institute of Systems Reserch, pp35-38 (in Japanese).

Sasaki T. , Y. Ohnishi and R. Yoshinaka (1994): Discontinuous Deformation Analysis and its Application to Rock Mechanics Problems, Proc. JSCE. 493/III-27: 11-20 (in Japanese).

Sasaki T. , D. Ishii, Y. Ohnishi and R. Yoshinaka (1995): Stability Analysis of Jointed Rock Foundations by DDA, ISRM 8th Congress, Workshop; Rock Foundation, 337-342.

Shi G. and R. Goodman (1984): Discontinuous Deformation Analysis, Proc. 25th U. S. Symp. on Rock Mech. 269-277. Evanston: AIME.

Shi G. and R. Goodman (1985): Two dimensional discontinuous deformation analysis, Int'l J. Numerical Methods in Geomechanics, Vol.9, pp.541-556.

Shi G. and R. Goodman (1989): The Key Blocks of Unrolled Joint Traces in Developed Maps of Tunnel Walls. Int. J. Num. Anal. Meth. Geomech. 13, 131-158.

Shi G. (1989): Discontinuous Deformation Analysis – A New Numerical Model for the Statics and Dynamics of Deformable Block Structures, Proc. 1st US Conf. on Discrete Element Methods, Colorado. - Mustoe, et. al., Eds.

Discontinuous Modeling and Rock Mass Instablity Problems

Dezhang Lin

Rock Mechanics Institute, The University of Oklahoma, Norman, OK 73019, USA

1. INTRODUCTION

Due to its sheer size, the Three Gorges Project has been attracting world attention. The project is now underway and will take about seventeen years to complete. One of the largest engineering project in recent times, the Three Gorges Dam Project has the potential to provide unique field data and opportunities to advance rock mechanics and rock engineering.

Considering the geology and the engineering requirements of the project, rock mechanics tests and analyses have, so far, been focused on the following topics: 1) physical and mechanical properties of rocks and rock masses, with emphasis on weathering and discontinuities; 2) development of a general conceptual model for the behavior of the rock masses, i.e., engineering classification; 3) determination of the rock stress and groundwater fields in the vicinity of the dam site; 4) optimization of the dam foundation, i.e., feasibility of founding the dam on weathered rock; 5) stability of high and steep rock slopes; and, 6) stability analysis of landslide areas along the future reservoir, especially in the shiplock areas.

The Rock Mechanics Research Center (RMRC) at The University of Oklahoma conducts basic and applied research in rock mechanics and rock engineering. The RMRC and the Research Group of the Ship Loch High Slopes for the Three Gorges signed a teaming agreement on June 9, 1994 in order to start a mutually beneficial partnership.

2 GOALS

The Three Gorges Project is the largest water resources development scheme currently being constructed in China, and probably in the world. Local as well as foreign scientists and engineers have been approached to provide the technology required to complete this project in a more effective, safe, and environmentally acceptable fashion.

Design in rock engineering as well as the process of developing construction plans, should be based on sound principles of mechanics. The Three Gorges Project provides a number of unique facilities and sites to conduct scientific investigations on

these basic principles and their applications not only from a civil construction point of view, but also in economic exploration, resource extraction, and waste disposal.

3 OBJECTIVES

The objectives of the project are:

1) to conduct basic and applied research on rock mechanics related problems having a direct impact on the Three Gorges Project and provide the technology required to complete this project in a more cost effective , safe, and environmentally acceptable fashion.

2) to develop U.S.-China mutually-beneficial partnerships amongst scientists and engineers involved the rock mechanics research.

3) to help establish participation in international science and engineering activities that promise substantial benefits to research and education enterprises.

4) to enhance the international perspectives of the next generation of U.S. scientists and engineers in rock mechanics, including graduate students, post-doctoral fellows and visiting scholars through fellowships, summer programs, and research participation.

5) to access an unique research site (The Three Gorges site) and collaborate with outstanding Chinese researchers.

4 LITERATURE REVIEW

Significant research achievements over the past two decades by the U.S. rock mechanics community could easily be used to advance the technology required to optimize some of the aspects of the Three Gorges Project.

As Table 1 indicates, there have been numerous static analyses of the stability of a single block published in the rock mechanics literature over the past two decades. Most of these analyses have concentrated on the stability of a single block, with little or no consideration to the behavior of the system stability, and the possibility of a sequential instability of blocks affected by the motion of surrounding entities.

The behavior of a single simple block, such as a parallepiped or a tetrahedral wedge, adjacent to the excavation surface was the main focus of earlier studies (e.g, Londe (1965), Ashby (1971), Hoek et al. (1973), Goodman (1976), and Lucas (1980)), with results obtained either graphically by stereo graphic projection or analytically by vector techniques. Some recent stability analyses have attempted to consider more complex (polyhedral) block geometries. Two investigations, one developed by Warburton (1981), the other by Goodman and Shi (1985), are especially noteworthy. Both are implicit methods. The ingenious "Key Block Theory" by Goodman and Shi has become particularly well-known. In this procedure, all of the potentially unstable blocks (i.e. those for which displacement into the excavation or free surfaces of the rock structure is kinematically feasible) are identified. Each of these blocks is examined in turn to determine which of them are unstable, or "Key Blocks". Attention is then given to reinforcing or otherwise ensuring the stability of

these blocks. With these key blocks secured, it is argued that the entire fractured system is then stable, and it is not necessary to examine the stability of other blocks.

Two approaches, one developed by Warburton (1981), Goodman and Shi (1985), the other by Lin and Fairhurst (1988) are especially noteworthy.

Table 1. Modeling studies of the static stability of a single, two-dimensional or three-dimensional block

Investigator	Year	Dimension	Shape	Data Structure
Londe	1965	3	wedge	explicit
Benson et al	1971	2	polygon	"
Cording et al	1971	2	polygon	"
Ashby	1971	3	parallelepiped	"
Hoek et al	1973	3	wedge	"
Goodman	1976	3	wedge	implicit
Hoek and Bray	1977	3	wedge	explicit
Croney et al	1978	3	wedge	"
Bray	1979	2	polygon	"
Coric	1979	3	wedge	"
Hoek and Brown	1980	3	wedge	"
Priest	1980	3	wedge	implicit
Lucas	1980	3	wedge	"
Warburton	1981	3	polyhedron	"
Crawford	1982	2	wedge	explicit
Goodman and Shi	1981	3	polyhedron	implicit
Zhu and Xiao	1982	2	polygon	explicit
Crawford and Bray	1983	2	polygon	"
Elsworth	1983	2	polygon	"
Zhifa	1983	3	wedge	implicit
Goodman and Shi	1985	3	polyhedron	"
Lin and Fairhurst	1989	3	polyhedron	explicit

Footnote: In the context of the static analysis of blocky systems, there are two type of methods:

- Implicit methods are those where, in the problem formulation, the orientations of the joint sets are prescribed, but the spacing and spatial location are not defined. Implicit analyses set out to determine the 'worst- case', i.e that spacing and location of joints which will result in the most unstable combination for the particular excavation or structure under study.

- Explicit methods require that the joint (and hence block) system be completely specified, with given values for each joint orientation, joint spacing and location in space.

In the key block analysis, a complex block - formed by a number of discontinuities

- is regarded as a combination of geometrically simple convex blocks and classified according to the following conditions:

(1) finiteness: the block is finite, its boundary consists of either joint planes or excavated free surfaces;

(2) removability: there is at least one direction along which the block can move, without rotating, so as not to invade a neighboring block; and

(3) stability: the analysis of potential instability usually compares the joint strength with the external forces necessary to develop critical conditions for the block.

Owing to the absence of an explicit, well-formed data structure for the geometry of individual blocks and the block system, complexity and ambiguity are unavoidable with implicit methods. The sequential displacement of blocks and the progressive development of instabilities can not be determined. This limits the range of block instability problems to which implicit methods, including the key block theory, can be applied.

Several approaches, e.g, Elsworth (1986), Yow and Goodman (1987), Londe (1989) have been developed recently to evaluate the effects of such factors as initial stress, stiffness and dilatancy of the joint surface or block interface on the static stability of blocks. Most of these approaches are based on a static relaxation analysis of wedges in the roof of an underground opening, as presented by Bray [see Brady and Brown (1985, pp.227-236)]. Static relaxation takes into account joint stiffness and the effects of associated changes in joint force (due to a potentially destabilizing movement), prior to joint slip, on the equilibrium of a single block. Although these studies do consider the effect of block displacement to this limited degree, they do not examine the progressive deformational behavior of the blocky system.

While it is possible, in principle, to analyze how the stability of other blocks in a jointed mass are affected by instability (or 'removal') of the first block, relatively little attention has been paid to this problem in the static analyses described above. Stability of the jointed system, overall, is an important question both from the viewpoint of mining, where (controlled) instability of a blocky mass is often desired (e.g. in block caving operations) and in rock dam engineering, where a knowledge of the 'ultimate' behavior of a system is often essential to the safe design of structures.

A primary obstacle to undertaking a systematic study of the static stability of a blocky mass has been the absence of a well-designed computational procedure for identification of the geometrical and topological structure of a polyhedral blocky system.

As noted above, static analyses of block stability usually assume that the forces acting on a block are constant and independent of any block motion. In reality, of course, motion of one block relative to its neighbors must produce changes in the block-block forces. These changes will spread progressively through the block system until either the system reaches a new stable equilibrium, or it collapses - often after large inter-block displacements.

Dynamic analyses incorporate these changes in force and moment equilibria into studies of block motion. Thus, considerations of the behavior of the blocky system is inherent in a dynamic analysis.

Table 2 lists some of the main attempts to develop realistic descriptions of the dynamic deformation response of a jointed rock mass.

Table 2 Dynamic methods for modeling the stability of two- dimensional or three-dimensional blocky systems in rocks

Investigator	Year	Dimensions	Type of Constraint
Cundall	1971	2	explicit
Burman	1971	"	"
Chappel	1972	"	"
Cundall	1976	"	"
Hocking	1977	"	"
Kawai	1977	"	"
Kawai et al	1978	"	"
Lotstedt	1979	"	implicit
Cundall	1980	"	explicit
Kawai et al	1980	"	"
Dowding et al	1983	"	"
Belytshko	1984	"	"
Shi and Goodman	1988	2	(DDA) implicit
Hocking et al	1985	3	explicit
Williams et al	1987	"	"
Cundall et al	1988	"	"
Ghaboussi et al	1990	"	explicit
Lin	1990	3	explicit

As with static analyses, published results of dynamic stability studies may be classified into explicit and implicit methods. The explicit methods are based on 'reaction constraints', while implicit approaches are based on 'optimization constraints', as described below.

In explicit methods (reaction constraints), blocks are assumed to be related by a spring-damper-actuator element (a generalized spring). The attachment points are P_i and P_j. The spring constant is k. The damping coefficient is c, and the actuator force is F_a. With all parameters explicitly prescribed, the motion interaction between blocks is also explicitly specified.

In implicit methods (optimization constraint), constrained optimization procedure finds a minimum of a function f(x) on a specific subspace. During constrained optimization, the state vector x should be attracted to the subspace $g(x) = 0$, then slide along the subspace until it reaches the locally smallest value of the function f(x) on $g(x) = 0$.

Dynamic analyses consider the time history of position, velocity, and acceleration of the system of blocks under the changing distribution of forces and force interactions as the blocks deform and displace. Three types of block-block interactions may be considered: rigid blocks, 'simply deformable blocks'; 'fully deformable' blocks'.

Lotstedt (1979), and Shi and Goodman (1988) have used an implicit 'optimization constraint' approach. This method assumes that the system will seek a minimum energy condition and optimization is based on achieving such a condition.

Various techniques, such as the penalty method, augmented Lagrangian method, Lagrange multiplier or gradient descent method are used in the optimization constraint approach.

Review of the above-mentioned static and dynamic stability analyses has led to several conclusions:

- Dynamic analysis is physically more realistic and overcomes some intrinsic shortcomings of static analysis - but dynamic analysis can be computationally much more time- consuming.

- Key-block analysis is unsatisfying in that no consideration is given to the stability of the blocky system after removal of an unstable key block. Although, as note earlier, it is possible, in principle, to repeat the key block analysis technique successfully on the individual blocks after removal of a key block, the implicit nature of the analysis makes it difficult to examine the overall stability of a system of blocks. Users of key-block analysis contend that it is sufficient to identify the unstable block that intersects the open boundary of the block system. It is reasoned that, once this block is made stables by rock-bolting, all other blocks in the system will remain stable. (Note, however, that there are situations where individually stable blocks may become unstable when bolted so as to act as a single block - so it is necessary to examine the stability of such combined blocks.)

- Static analysis of blocky systems may help to define those block assemblages, orientations or regions (with respect to free surfaces, applied forces etc.) that may be intrinsically stable. Once these stable regions or situations are defined, it may be possible to restrict the dynamic analysis to those parts of the blocky system where stability is problematical. In other words, it may be possible to combine static and dynamic methods of analysis so as to provide a procedure that is physically realistic but less demanding computationally than a dynamic analyses of the entire system of blocks.

- The methods used to define blocks (i.e the 'data structure') in studies published to date have been different for the static and dynamic analyses. This makes it difficult to compare a static and dynamic analysis of the same system of blocks.

5 STUDY TASK DESCRIPTION

The Rock Mechanics Research Center is committed to carry out research to acquire a better understanding of the fundamental principles associated with rock engineering and to build this understanding into planning, design, and construction activities.

The five preferred topics of research, as outlined by U.S. and Chinese research partners, are the following:

Task 1: Micro- and Macro-failure Mechanism(s) Characterization

The inelastic behavior of fissured rock masses is due primarily to the presence of discontinuities and the frictional sliding on such surfaces. Consequently, this macroscopic inelastic response is inhibited by an increase in hydrostatic pressure and exhibits volume changes and strain softening.

The rate sensitivity on the location of the deformations in a visco-plastic rock mass will be examined under different stress conditions, especially at the base of the proposed shiplock. The microstatistical, rate-dependent, internal state variable approach is directly connected to microstructural variables; forming a link between microstructural failure and macro fracture (joint) deformation.

In dealing with strain localization damage and shear bands, it is necessary to introduce a material scale or internal dimension to allow for the discontinuous nature of the material. Cosserat's model, gradient theories, nonlocal concepts, special averaging schemes, and diffusion or relative motion through interfaces are among the possibilities for incorporating the effect of an internal dimension. Significant research will be needed in order to arrive at closed-form or experimentally determined formulae that would depend on factors such as interparticle properties and grain size.

Task 2: Fracture Network and Slope Stability Analyses

The natural rock mass consists of an interconnected network: main fracture channel, secondary fractures and pore matrix which are each characterized by their distinct porosities and permeabilities. Such a multi-level network approach is being developed at The University of Oklahoma.

In the context of the static analysis of blocky systems, there are two type of methods:

- Implicit methods are those where, in the problem formulation, the orientations of the joint sets are prescribed, but the spacing and spatial location are not defined. Implicit analyses set out to determine the 'worst- case', i.e that spacing and location of joints which will result in the most unstable combination for a particular excavation or structure under study.

- Explicit methods are those require that the joint system (and, hence, the block) to be completely specified, with given values for each joint orientation, joint spacing and location in three-dimensional space.

Owing to the absence of an explicit, well-formulated data structure for the rock mass geometry, complexity and ambiguity are unavoidable with implicit methods. The sequential displacement of blocks and the progressive development of instabilities can not be determined. This limits the range of block instability problems to which implicit methods, including the key block theory, can be applied.

Development of an efficient modeling procedure, based on geometry and topology, for definition of three-dimensional rock masses will allow the geological data input to be structured so as to simplify both the data structure; and the subsequent analysis

of the static or dynamic stability. A static (key block theory) and a dynamic (distinct element and DDA) stability analysis procedure for three-dimensional blocky systems will be compared and validated.

Task 3: Anchorage Optimization

It is reasoned that, once the key blocks are stabilized by bolting, all other blocks in the system will remain stable. (Note, however, that there are situations where individually stable blocks may become unstable when bolted so as to act as a single composite block - so it is necessary to examine the stability of such combined blocks.)

Static analyses of blocky systems (Warburton, 1981; Shi and Goodman, 1985 and Lin and Fairhurst, 1988) may help to define those block assemblages, orientations or regions (with respect to free surfaces, applied forces etc.) that may be intrinsically stable. Once these stable regions or situations are defined, it may be possible to restrict the dynamic analysis to those parts of the system where stability is problematical. In other words, it may be possible to combine static and dynamic methods of analysis so as to provide a procedure that is physically realistic but less demanding computationally than a dynamic analysis of the entire system of blocks.

Static relaxation takes into account joint stiffness and the effects of associated changes in joint forces (due to a potentially destabilizing movement), prior to joint slip, on the equilibrium of a single block. Although these studies do consider the effect of block displacement to a limited degree, they do not examine the progressive deformational behavior of the blocky system.

A topological structure has been developed to define three-dimensional fracture systems and blocky systems. This structure provides a unified framework for the static and dynamic analyses making it possible to compare such analysis.

Task 4: Excavation Effects

It is possible to estimate the stress concentrations, stress shadows and structure performance which occur in a complex excavation sequence; however, it is important to choose the correct analysis technique. Some guidelines will be given for the case of the Three Gorges project.

A series of experiments will be performed to define the fundamental behavior and validate the theoretical models. If the rock structure is considered important then the blocky approach seems to offer the best compromise between computational efficiency and realistic behavior. The success of the analysis interpretation will be directly proportional to the effort spent in back analysis, building up each particular rock engineering structure.

Task 5: Rock Classification

The different rock classifications developed in U.S. and China will be tested and validated using the Three Gorges' site data.

In view of the large area of the dam site and non-homogeneity of the rock mass, it will be necessary to divide the site into a number of sub-regions. In order to fit

the particular conditions of the Three Gorges project, a new method of rock mass quality classification, the "TG-YZP" (Three Gorges-Rock Mass Quality Evaluation) method, recently been developed by the Changjiang Water Resource Commission (CWRC) Investigation Service will be evaluated. This method is semi-qualitative, and is based on a comprehensive evaluation of five factors: 1) rock mass integrity; 2) rock strength; 3) character and status of the joint; 4) rock mass permeability; and, 5) rock mass deformability,

The rock mass rating (RMR), the mining rock mass rating (MRMR) and the design rock mass strength (DRMS), developed by western rock mechanics communities provide good guidelines for mine design purposes. However in the Three Gorges Project a more detailed investigation might be required; the difference between those classification systems will be examined at the dam site, including Barton's classification.

Task 6. Rock Mass Failure Database

An important step in decreasing failures is understanding the precursors, triggering mechanisms, failure initiation and propagation processes. The experience gained from rock failure data should facilitate the implementation of remedial measures by allowing modification of the support design, based on an improved understanding of failure mechanism of rock and support components.

The main database will be partitioned in several smaller databases. In addition, three further subdivisions or separate parts will be designed to contain information on support, destressing and rockbursts. The rock failure database program will be written for aiding data entry and information retrieval to locate specific records, create reports, calculate statistics, present graphics and conduct various database operations and text editing.

Rock failure data will be accumulated at the Three Gorges dam construction sites and shared with partners.

Task 7. Other Developments

The constitutive three-dimensional behavior of joints is a subject worthy of considerable experimental and theoretical research, to provide more realistic input to the static and, especially, the dynamic analyses of fractured rock masses.

There are important research opportunities to improve both current block modeling procedures and their applicability to slope stability problems such as the ones in the Three Gorges Project.

For example, extended models could include the coupled effects of: pressurized flow in rock joints and mechanical deformation behavior.

The following important concepts and approaches are also important when considering block motions:

1) topology to allow a better description of the internal relationship and deep structure of the geometrical entity; 2) Lie group to view the configuration manifold of a variational framework. 3) manifold to derive the Langrangian formulation of constraint systems as a coordinate-free generalization of Newton's equations (the

reaction force produced by the constraints are indeed orthogonal to the constraint manifold.) Through this approach a blocky body can be viewed as a vector bundle in the manifold.

6 PRELIMINARY WORK

Some preliminary work for the research has already been started as part of the efforts associated with the Rock Mechanics Research Center at The University of Oklahoma.

An efficient modeling procedure, based on geometry and topology, for definition of three-dimensional blocky systems for anchorage, has been developed to allow the geological data input to be structured so as to simplify both the topological data structure for blocky systems. A static (key block theory) and a dynamic (distinct element and DDA) stability analysis procedure for three-dimensional blocky systems have already been compared and validated.

A multi-level network method has also been developed recently. This technique differs fundamentally from most classic discrete models in that the subdivisions based on topological theory and the multiple families of flow paths, such as connectivity, are completely specified. The uninterrupted flow paths, which represents the "backbone" of the fracture system, is ultimately defined. This new discrete model represents a novel approach to characterize the transport phenomenon in fractured rock masses.

7 IMPACT OF THE PROPOSED RESEARCH

The study is expected to enhance understanding of the basic principles governing rock mass phenomena. Some of the associated problems are outlined below:

- Discontinuum Mechanics

  The two classical theories of rigid body mechanics and deformable body continuum mechanics have each followed separate paths of development and have reached levels that are quite sophisticated. It is only since the 70's that numerical simulation began to allow analyses of complex systems such as satellite ; cell motion and interaction in biology; robot motion in automation; and block motion in rock mechanics. However, resurgence of interest in the overall combination of the two classical theories needs to be considered.

- Imaging Technology

  Technology pioneered in medicine have been emulated in seismic tomography; together with three-dimensional imaging, this particular technology offers much enhanced opportunities for inventorying and characterizing rocks at engineering sites.

  Borehole scanners provide an extremely detailed optical survey, this digital information can be processed as part of a rock engineering analysis; for example, joint surveys including aperture distributions.

- Manifold Methods

  Continued contribution to the theory of material mechanics has created an analytical framework suitable for discontinuous rock. The current state of this field allows manifold concepts to be central in numerical modeling of problems in continuum and discontinuum.

- Stochastic Methods

  Applications of reliability analysis in fluid mechanics and environmental engineering areas, and other fields of application are presently under development. The use of the Monte Carlo method in multilple simulations (for example, fracture network) is a good example but more economical and direct methods should be sought where possible to establish risk, reliability, safety and probable outcomes.

ACKNOWLEDGEMENT

The author thanks Dr. Genhua Shi of WES, Department of the Army for helpful discussion. Funding was provided by The Rock Mechanics Institute, The University of Oklahoma and National Science Foundation China (NSFC).

REFERENCES

Abraham R, Marsden J.E. and Ratiu T (1987) " MANIFOLD, TENSOR ANALYSIS, AND APPLICATIONS", Addison-Wesley, Second Edition, Spring-Verlag, NY

Alexandroff P. (1961) "ELEMENTARY CONCEPTS OF TOPOLOGY", Dover Publications, INC. NY

Arnold V.I. (1978) "MATHEMATICAL METHODS OF CLASSICAL MECHANICS", Springer, NY

Ashby J.P. (1971) "Sliding and Toppling Modes of Failure in Models and Rock Slopes" M.Sc. Thesis. University of London, Imperial College

Bartlett M.S. (1975) "THE STATISTICAL ANALYSIS OF SPATIAL PATTERN", Chapman and Hall, London. 90pp.

Baumgart B. (1972) "Winged-edge Polyhedron Representation", Stanford Artificial Intelligence Report No. CS-320

Baecher G.B. "Statistical Analysis of Rock Mass Fracturing", Mathl Geol 15(2), pp 329-348

Belytschko T. M., Plesha M. and Dowding C.H. (1984) "A Computer Method for Stability Analysis of Cavern in Jointed Rock", Int. J. Numer. Analyt. Meth. Geomech., vol.8, pp 473- 492

Benson R.P, Conlon R.J, Joli-Coeur P, and Deere D.U. (1971) "Rock Mechanics at Churchill Falls", Proceedings of the ASCE Symposium on Underground Rock Chambers. Pheonix, AX. pp. 407- 486

Bottema O., and Roth B. (1979) "THEORETICAL KINEMATICS", North-Holland Press, New York. 550pp.

Brady B. H. and Brown E. T. (1985) ROCK MECHANICS FOR UNDERGROUND MINING George Allen and Unwin. London. 527pp.

Braid I. C., Hillyard R. C., and Stroud I. A. (1980) "Stepwise Construction of polyhedra in geometric Modeling", Mathematical Methods in Computer Graphics in CAD/CAM Systems edited by K. W. Brodlie, pp.123-141

Bray J. W. (1979) unpublished notes

Burman B. (1971) "A NUMERICAL APPROACH TO THE MECHANICS OF DISCONTINUA" Ph.D. Thesis, James Cook University of North Queensland, Townsville, Australia

Chappel B.A. (1972) "THE MECHANICS OF BLOCK MATERIAL" Ph.D. Thesis, Australian Natl. Univ., Canberra.

Croney P., Legge T.F. and Dhalla A. (1978) "Location of Block Release Mechanisms in Tunnels from Geologic Data and the Design of Associated Support" Proceedings of the Conference on Computer Methods in Tunnel Design. London. pp.97-119

Cording E.J, Hendron A.J, and Deere D.U. (1971) "Rock Engineering for Underground Caverns" Proceedings of the Symposium on Underground Rock Chambers. Phoenix, AZ. pp. 567- 600

Coric S. (1979) "Stability Analysis of Underground Cavities in Fissured Rock Masses," Proceedings of the 4th International Congress on Rock Mechanics. Montreux, Switzerland. Vol.3, pp.475-479

Crawford A.M. (1982) "Rock Wedge Stability," Proceedings of the 23rd U.S. Symposium on Rock Mechanics. Berkeley, CA. pp.1057-1064

Crawford A.M. and Bray J.W. (1983) "Influence of the in-situ Stress Field and Jointed Stiffness on Rock Wedge Stability in Underground Openings," Canadian Geotechnical Journal. Vol.20. pp.276-287

Cosserat E. and F. (1909) LA THEORIE DES CORPS DEFORMABLES. Paris: Herman et Fils

Cundall P.A. (1971) "A Computer Model for Simulating Progressive, Large-scale Movements in Blocky Rock System", Proceedings of Symposium in Rock Fracture. (ISRM) vol.1 Nancy

Cundall P.A. (1976) "Computer Interactive Graphics and the Distinct Element Method", Proceeding of Specialty Conference on Rock Engineering for Foundations and Slopes. Boulder, Colorado

Cundall P.A. and Marti J. (1979) " Some New Developments in Discrete Numerical Methods for Dynamic Modeling of Jointed Rock Masses", Proceedings of the Rapid Excavation and Tunnelling Conference.

Cundall P.A. (1980) "UDEC - A Generalized Distinct Element Program for Modeling Jointed Rock", Chapter PCAR-1-80, Peter Cundall Associates; Contract DAJA37-79-C-0548, European Research Office, U.S. Army

Cundall P.A. and Hart R. D. (1983) "Development of Generalized 2-D and 3-D distinct Element Programs for Modeling Jointed Rock", U.S. Army Engineers Waterway Exp. Stat. Tech. Rep.

Cundall P.A., Hart R., and Lemos J. (1988) "Formulation of a Three-dimensional Distinct Element Model. Pat I - A Scheme to Detect and Represent Contacts in a

System Composed of Many of Polyhedral Blocks. Part II - Mechanical Calculations for Motion and Interaction of A System Composed of Many Polyhedral Blocks", Int. J. Rock Mech. Min. Sci. vol.25, No.3., pp.117- 125

Dowding C. H., Ho C. and Belytschko T. B. (1983) "Earthquake Response of Caverns in Jointed Rock: Effects of Frequency and Jointing", in SEISMIC DESIGN OF EMBANKMENTS AND CAVERNS (Terry R. Howard, Ed.) pp.117-126

Edmonds J.A. (1960) "A Combinatorial Representation for Polyhedra Surfaces", Notices Amer. Math. Soc. 7, pp.646

Elsworth D. (1986) "Wedge Stability in the Roof of a Circular Tunnel: Plane Strain Condition", Int. J. Rock Mech. Min. Sci. and Geomech. Abstr. Vol. 23, No.2 pp.177-181

Funda J, Russell H. and Taylor H. "On Homogeneous Transforms, Quaternions, and Computational Efficiency", IEEE Transactions on Robotics and Automation, Vol. 6. No.3. pp.382- 388

Ghaboussi J. and Barbosa R. "Three-dimensional Discrete Element Method for Granular Materials", Int J. Numerical and Analytical Methods in Geomechanics Vol.14 No.7 1990. pp. 451-472

Goodman R.E (1976) "METHODS OF GEOLOGICAL ENGINEERING IN DISCONTINUOUS ROCK", West Publishing Company, St. Paul, MN

Goodman R.E. and Shi G. (1981) "Geology and Rock Slope Stability - Application of the Keyblock Concept for Rock Slopes", Proceedings of the 3rd International Conference on Stability in Surface Mining. Vancouver, Canada. pp.347-373

Goodman R.E. and Shi G. and Boyle W. (1982) "Calculation of Support for Hard, Jointed Rock Using the Keyblock Principle", Proceedings of the 23rd U.S. Symposium on Rock Mechanics Berkeley, CA. pp.883-898.

Goodman R.E. and Shi G. (1985) "BLOCK THEORY AND ITS APPLICATION TO ROCK ENGINEERING", Prentice Hall, Englewood Cliffs, NJ

Hoek E., Bray J. W. and Boyd J. M. (1973) "The Stability of a Rock Slope Containing a Wedge Resting on Two Intersecting Discontinuities", Quarterly J. Engineering Geology. Vol.6, No. 1

Hoek E. and Bray J. W. (1977) "ROCK SLOPE ENGINEERING", The Institution of Mining and Metallurgy, London, U.K. 402pp

Hoek E. and Brown E. T. (1980) "UNDERGROUND EXCAVATIONS IN ROCK", The Institution of Mining and Metallurgy, London, U.K

Hudson J.A. and Priest S.D. (1979) "Discontinuity and Rock Mass Geometry", Int. J. Rock Mech. Min.Sci and Geomech. Abstr, vol.16, pp.339-362

Hudson J.A. and Priest S.D. (1983) "Discontinuity Frequency in Rock Masses", Int. J. Rock Mech. Min.Sci and Geomech. Abstr, vol.20, pp.73-89

Hamilton W.R. (1969) "ELEMENTS OF QUATERNIONS", 3rd edition, Chelsea Publishing Co, NY

Harary F. "GRAPH THEORY", Addison-Wesley, Reading, Mass

Hocking G. (1977) "Development and Application of the Boundary Integral and Rigid Block Methods for Geotechnics", Ph.D. Thesis, Imperial College.

Hocking G. Mustoes G.G.W. and William J.R. (1985) "Influence of Artificial Island Side-shapes and Ice Ride-up and Pile-up", ARCTIC 85 Conference, ASCE

Hoek E. (1977) "Structurally Controlled Instability in Underground Excavations", Proceedings of Symposium on Underground Power Stations. New York, N.Y.

Hoek E and Brown E.T. (1980) "UNDERGROUND EXCAVATION IN ROCK", The Institution of Mining and Metallurgy, London, U.K.

Kahn D. W. (1975) "Topology: An Introduction to the Point- set and Algebraic Area", Baltimore: Williams and Wilkins

Kahn D. W. (1980) "Introduction to Global Analysis", Academic Press, New York

Kapur D. and Mundy J.L. (1989) "Geometric Reasoning", Elsevier Science Publisher B.V., Amsterdam, The Netherlands

Kawai T. (1977) "New Element Models in Discrete Structure Analysis", J.Soc. Naval Arch., Japan. vol.141, pp.174-180

Kawai T., Kawabata K. Y., Koudou I., and Kumagai K. (1978) "A New Discrete Model for Analysis of Solid Mechanics Problems", Proc. 1st Conf. Num. Meth. in Fracture Mech., Swansea, UK, PP.26-27.

Lin D., Fairhurst C. and Starfield A.M. (1987) "Geometrical Identification of Three-dimensional Rock Block Systems Using Topological Techniques", Int. J. Rock Mech. Min. Sci vol.24, No.6, pp.331-338

Lin D. and Fairhurst C. (1988) "Static Analysis of the Stability of Three-dimensional Blocky Systems Around Excavations in Rock", Int. J. Rock Mech. Min.Sci vol.25, No.3. pp.139-147

Londe P. (1965) "Une methode d'analyse a trois dimensions de la stabilite d'une rive rocheuse", Annales Ponts et Chaussess. pp.37-60

Lotstedt P. (1979) "On A Penalty Function Method For The Simulation Of Mechanical Systems Subject To Constraints", Royal Institute of Technology (Sweden), Report TRITA-NA-7919

Lostedt P. (1984) "Numerical Simulation of Time-dependent Contact and Friction Problems in Rigid Body Mechanics", SIAM J. Sci. Stat. Comput. vol.5, No.2., pp.370-393

Lozano-Perez T. (1983) "Spatial Planning: A Configuration Space Approach", IEEE Trans. Computers, C-32, No.2., pp.108- 120.

Lucas J.M. (1980) "A General Stereo graphic Method for Determining the Possible Mode of Failure of Any Tetrahedral Rock Wedge", Int. J. Rock Mech. Min. Sci. vol 17, pp. 57- 61

Luenberger D.G. (1969) "OPTIMIZATION BY VECTOR OR SPACE METHODS", Wiley NY

Mauder C.R.F (1970) "ALGEBRAIC TOPOLOGY", Van Nostrand Reinhold Co., London

Miles R. E. (1972) "The Random Division of Space", Adv. Appl. Probl., Suppl., pp.243-266

Muhlhaus H. B. and Vardoulakis I.G. (1987) "The Thickness of Shear Bands in Granular Materials", Geotechnique. vol.37, no. 3, pp.271-283

Muncaster R. G. (1984) "Invariant Manifolds in Mechanics II: Zero-dimensional Elastic Bodies with Directors", Arch. Rational Mech/ Anal. Vol.84, pp375-373

Munfres J.R. (1975) "TOPOLOGY: A FIRST COURSE", 413 pp. Prentice-Hall, Englewood Cliff, N.J.

Munfres J.R. (1984) "ELEMENTS OF ALGEBRAIC TOPOLOGY", Benjamin/Cummings. Menlo Park, Calif. 454pp

Nikravesh P.E., Wehave R.A. and Kwon O.K. "Euler Parameters in Computational Kinematics and Dynamics, Part 1", ASME J. Mech., and Auto. in Design. Vol.107, no.3, pp.358-365

Pinkerton T. (1966a) "An Algorithm for the Automatic Computation of Integral Homology Groups", Mathematical Algorithms 1(1) pp.27-44

Pinkerton T. (1966b) "An Algorithm for the Automatic Computation of Integral Homology Groups Part II–Description of the Program", Mathematical Algorithms 1(2) pp.33-39

Preparata F. and Shamos M. I. (1985) "COMPUTATIONAL GEOMETRY: AN INTRODUCTION", Springer-Verlag, New York 390pp

Priest S.D. (1980) "The Use of Inclined Hemisphere Projection Methods for the Determination of Kinematic Feasibility, Slide Direction and Volume of Rock Blocks", Int.J. Rock Mech. Min. Sci. Vol 17. pp.1-23

Requicha A.A.G. (1977) "Mathematical Models of Rigid Solid Objects", Technical Memo No.28, Production Automation Project, University of Rochester

Requicha A.A.G. (1980) "Representations of Rigid Solids - Theory, Methods, and Systems", ACM Computing Surveys, Vol. 12, No.4

Rockafeller R.T. (1970) "CONVEX ANALYSIS", Princeton, NJ: Princeton Univ. Press

Sahni S. (1981) "CONCEPTS IN DISCRETE MATHEMATICS", Camelo Publishing Company. Fridley, Minnesota

Salamin E. (1979) "Application of Quaternions to Computation With Rotations", Stanford AI Lab Internal Working Paper.

Sattinger D. H. and Weaver O. L. (1986). "LIE GROUPS AND ALGEBRAS WITH APPLICATIONS TO PHYSICS, GEOMETRIC, AND MECHANICS", New York: Springer-Verlage. pp.215

Schwartz J.T. and Sharir M (1983a) "On the Piano Movers Problem, Part 1: The Case of a Two-dimensional Rigid Polygonal Body Moving amidst Polygonal Barriers", Comm. Pure Appl. Math. Vol.36. pp.345-398

Schwartz J.T. and Sharir M (1983b) "On the Piano Movers Problem, Part 2: General Techniques for Computing Topological Properties of Real Manifolds", Adv. Appl. Math. Vol.4, pp.298-351

Schwartz J.T. and Sharir M (1983c) "On the Piano Movers Problem, Part 3: Coordinating the Motion of Several Independent Bodies: The Special Case of Circular Bodies Moving Amidst Polygonal Barrier", Rob, Res. Vol.2, No.3. pp. 46-75

Shi G. (1988) "DISCONTINUOUS DEFORMATION ANALYSIS A NEW NUMERICAL MODEL FOR THE STATICS AND DYNAMICS OF BLOCK SYSTEMS", PH.D Thesis, Berkeley, University of California. 212pp

Shi G. and Goodman R.E. (1988) "Discontinuous Deformation analysis – A New Method for Computing Stress, Stain and Sliding of Block Systems." in KEY QUESTIONS IN ROCK MECHANICS pp.381-393

Spivak M. (1979) "A COMPREHENSIVE INTRODUCTION TO DIFFERENTIAL GEOMETRY", Vols. 1-5, Publish or Perish, Inc., Berkeley

Tarski A. (1951) "A DECISION METHOD FOR ELEMENTARY ALGEBRA AND GEOMETRY", Univ. of Calif. Press, Berkeley.

Tiel J.V. (1984) "CONVEX ANALYSIS: AN INTRODUCTORY TEXT", John Willey and Sons. NY

Warburton P.M. (1981) "Vector Stability Analysis of Arbitrary Polyhedral Rock Block with Any Number of Free Faces", Int. J. Rock Mech. Min Sci. Vol. 18, pp.415-427

Whitney D.E. 1982 "Quasi-static Assembly of Compliantly Supported Rigid Part", J. Dyn. Sys Meas. Control Vol. 104, pp.65-77

Williams J.R. and Mustoe G.G.W. (1987) "Modal Methods for the Analysis of Discrete Systems", Computer and Geotechnics Vol.4, pp.1-19

Wittenburge J. (1977) "DYNAMICS OF SYSTEMS OF RIGID BODIES", Stullgart Teubner

Woo T.C. (1984) "A Combinatorial Analysis of Boundary Data Structure Schema", Department of Industrial and Operations Engineering, Tech. Report 84-12, University of Michigan .

Yao S.S. and Grabow P.C.A (1981) "A Model for Representing Programs Using Hierarchical Graphs", IEEE Trans. Software Engng SE-7(6). pp.556-573

Yow J.L.Jr and Goodman R.E. (1987) "A Ground Reaction Curve Based Upon Block Theory", Rock Mechanics and Rock Engineering, Vol.20, pp.167-190

Zhifa Y. (1983) "Application of the Method of Projection on Coordinates Planes to Designing an Underground Opening within Discontinuous Rock Mass", Proceedings of International Symposium on Engineering Geology and Underground Construction. Lisbon, Portugal. pp.I.15-I.24

Zhu J. and Xiao Z. (1982) "The Method of Evaluation for the Stability of Karst Caverns", in ROCK MECHANICS: CAVERNS AND PRESSURE SHAFTS Vol.1, pp.519-528

Development of Fracturing Algorithms for Jointed Rock Masses with the Discontinuous Deformation Analysis

C. T. Lin [1], B. Amadei [2], S. Ouyang [3], C. Huang[4]

[1] Researcher, Land and Mineral Resources Division, Energy and Resources Laboratories, Industrial Technology Research Institute, Hsinchu, Taiwan, R. O. C.

[2] Professor, Department of Civil Engineering, University of Colorado at Boulder, U. S. A.

[3] Manager, Land and Mineral Resources Division, Energy and Resources Laboratories, Industrial Technology Research Institute, Hsinchu, Taiwan, R. O. C.

[4] Director, Land and Mineral Resources Division, Energy and Resources, Laboratories, Industrial Technology Research Institute, Hsinchu, Taiwan, R. O. C.

Abstract

This paper presents a new development of fracturing algorithms for jointed rock masses with the Discontinuous Deformation Analysis (DDA) method over the past three years. Two types of block fracturing are included: (1) intact block fracturing, and (2) sub-block fracturing. In the first type, intact blocks can be broken into two blocks (with one tensile or one shear fracturing plane) or four blocks (with two shear fracturing planes) at one time of block failure. The fracture tips stop while the block boundary is met. In the second type, the fracture of sub-blocks embedded inside intact blocks is allowed to propagate within sub-blocks in Mode I, Mode II, or mixed Modes I and II. The capability of the newly developed block fracturing algorithms is to be examined by following examples: (1) rock-fall, (2) cliff failure, and (3) slope stability.

Introduction

The Discontinuous Deformation Analysis (DDA) method was first proposed by Shi and Goodman [1] in 1984 and published in Dr. Shi's PhD thesis [2] in 1988. Over the past three years, a number of extensions to the method were explored. The extensions are composed of (1) improving the contact algorithm, (2) adding sub-blocking , and (3) block fracturing capabilities. In the first extension, the penalty method first proposed by Dr. Shi in the DDA method to enforce the block contacts was replaced by the Augmented Lagrangian Method (ALM). The ALM enforces the block contacts more precisely and calculates block contact forces more accurately. The second extension introduced the sub-blocking capability in order to determine the stress variation within large blocks in which a number of sub-blocks is embedded. Along sub-block contacts, the continuity of displacements is preserved. The third extension, which is to be presented along with three illustrative examples later in this paper, provided several fracturing algorithms with the DDA method.

The details of the first two extensions can be seen in Lin's PhD thesis [3], entitled

"Extensions to the Discontinuous Deformation Analysis for jointed rock masses and other blocky systems".

Fracturing Criterion

The criterion selected in this research for block fracturing with the DDA method is a Mohr-Coulomb criterion with three parameters : s_o is the inherent shear strength of the block material, ϕ is its friction angle, and T_o represents its tensile strength. It is assumed that tensile normal stresses are positive, and the major and minor principal stresses are denoted as σ_1 and σ_3 (with $\sigma_1 \geq \sigma_3$), respectively. A critical value of the minor principal stress is defined as

$$\sigma_{3c} = -C_o + T_o \tan^2\left(\frac{\pi}{4}+\frac{\phi}{2}\right) \qquad (1)$$

where $C_o = 2s_o \tan(\pi/4 + \phi/2)$ is the unconfined compressive strength of the block material. According to the Mohr-Coulomb fracturing criterion, shear failure occurs when

$$\sigma_3 < \sigma_{3c} \quad \wedge \quad \sigma_3 \leq -C_o + \sigma_1 \tan^2\left(\frac{\pi}{4}+\frac{\phi}{2}\right) \qquad (2)$$

(where '$\wedge$'='and') and tensile failure occurs when

$$\sigma_3 \geq \sigma_{3c} \quad \wedge \quad \sigma_1 \geq T_o. \qquad (3)$$

The obvious advantage of using this criterion is that tensile or shear failure of blocks are well defined by the transitional normal stress σ_{3c}. Tensile failure often occurs in strong brittle rocks under tension. On the other hand, shear failure is more likely to occur in soil or in weak rocks.

Intact Block Fracture

The three-parameter Mohr-Coulomb criterion added to the DDA program is graphically shown in the theoretical and physical plots in Figures 1(a) and 1(b). For each block of the system, the major and minor in-plane principal stresses σ_1 and σ_3 determined at the block's centroid are compared to the third principal stress which is equal to 0 for a state of plane stress. The largest of the three principal stresses is taken as σ_1 and the smallest as σ_3. Before running the program, the user has to divide the blocks into two groups : those that are allowed to break (breakable blocks) and those that are not (intact blocks). Fracturing of the blocks in the first group is determined in the program by comparing σ_1 and σ_3 with the following expressions of the three-parameter Mohr-Coulomb criterion

$$\sigma_1 \geq T_0 \qquad if \quad \sigma_1 > \sigma_3 > 0 \tag{4a}$$

$$\sigma_1 \geq T_0 \qquad if \quad \sigma_1 > 0 > \sigma_3 > \sigma_{3c} \tag{4b}$$

$$\sigma_3 \leq -C_0 + \sigma_1 \tan^2\left(\frac{\pi}{4} + \frac{\phi}{2}\right) \qquad if \quad \sigma_1 > 0 > \sigma_{3c} > \sigma_3 \tag{4c}$$

$$\sigma_3 \leq -C_0 \qquad if \quad 0 > \sigma_1 > \sigma_3 \tag{4d}$$

If condition (4c) is satisfied within a breakable block, shear failure is assumed to occur with two failure planes passing through the block's centroid and inclined at $\pm (\pi/4 - \phi/2)$ with respect to σ_3, as shown in Figure 1(b). Then, the block is divided into four blocks and the analysis is resumed with a new block configuration. If, on the other hand, either condition (4a) or (4b) is satisfied within a breakable block, tensile failure occurs with a failure plane passing through the block's centroid and oriented at right angles to σ_1 as shown in Figure 1(a). In this case, the block is divided into two blocks and the analysis is resumed. This process is repeated for all breakable blocks in the system. In this formulation, no energy dissipation is assumed to occur during shear or tensile failure. Upon breaking, the new blocks are assumed to have the same velocities as the original block. Also, the new fractures have Coulomb friction and cohesion. Note that condition (4d) is not considered in this paper since, in that case, shear failure occurs on two planes in a direction parallel to σ_1.

Sub-block Fracture

Consider a large block divided into several sub-blocks, as shown in Figure 2. The sub-block contacts satisfy the displacement compatibility conditions along block-to-block contacts. A crack has been initiated. Fracturing takes place at the crack tip (point A in Figure 2) and the direction of crack propagation depends on the state of stress in the sub-block in direct contact with the crack tip (shaded sub-block in Figure 2). Mode I (tensile), Mode II (shear), or mixed Mode I and Mode II fracture propagation is allowed as specified by the user. In each case, propagation results in the sub-block in contact with the crack tip to be divided into two new sub-blocks and the process is repeated at the next time step. In contrast to the independent fracturing of whole blocks, sub-block fracturing allows continuous crack propagation. All new crack surfaces have Coulomb friction and cohesion.

Mode I Fracture (Tensile Failure)

With this type of fracture mode, the crack will propagate through the sub-block just ahead of the crack tip if the principal stresses σ_1 and σ_3 in that sub-block satisfy condition (3). The direction of crack propagation will be perpendicular to σ_1.

A typical example of this type of fracture is shown in Figure 3. The crack is initiated at point 1. Point O is the centroid of the sub-block. When the state of stress of the sub-block (or at point O) satisfies condition (3), the crack propagates from point 1 to point 2 in a direction perpendicular to σ_1.

Mode II Fracture (Shear Failure)

The crack will propagate through the sub-block just ahead of the crack tip if the principal stresses σ_1 and σ_3 in that sub-block satisfies (2). Now, the direction of propagation is inclined at $+(\pi/4-\phi/2)$ or $-(\pi/4-\phi/2)$ with respect to σ_3. One of those two directions is specified by the user.

A typical example of this type of fracture is shown in Figures 4(a) and 4(b). In Figure 4(a), the crack is initiated at point 1. Point O is the centroid of the sub-block. When the state of stress in the sub-block ahead of the crack front satisfies (2), the crack propagates from point 1 to 2 in a direction inclined at $+(\pi/4 - \phi/2)$ with respect to σ_3. Similarly, Figure 4(b) shows another possible shear cracking plane, with the direction of propagation from point 1 to 2 inclined at $-(\pi/4 - \phi/2)$ with respect to σ_3.

Mixed Mode Fracture

Here, the crack will propagate through the sub-block ahead of the crack front if the principal stresses σ_1 and σ_3 in the sub-block satisfy either Equation (2) or (3). The direction of propagation is perpendicular to σ_1 if σ_1 and σ_3 satisfy condition (3). On the other hand, the direction of propagation is inclined at $+(\pi/4-\phi/2)$ or $-(\pi/4-\phi/2)$ with respect to σ_3 if σ_1 and σ_3 satisfy condition (2). In the latter case, one of the shear fracturing directions must be specified by the user.

The advantage of the mixed mode option is that either tensile or shear fracture is determined by the state of stress in the sub-block ahead of the crack front at the time of fracture.

Energy Balance during Fracturing

Although classical fracture mechanics stipulates that some strain energy is released during fracture [4], the current research does not include an energy loss criterion. Therefore, an alternative kinematic condition has to be satisfied and enforced in the model.

Consider a block (or sub-block) i that is to be fractured at a certain time step when the state of stress in the block satisfies the fracturing criterion. A fracture plane is introduced and two new blocks are formed. One is denoted as block i1 and the other as block i2. At the end of the time step, the new block velocities $\partial D_{i1}(t)/\partial t$ and $\partial D_{i2}(t)/\partial t$ are assumed to satisfy the following equation

$$\frac{\partial D_i(t)}{\partial t} = \frac{\partial D_{i1}(t)}{\partial t} = \frac{\partial D_{i2}(t)}{\partial t} \tag{5}$$

where $\partial D_i(t)/\partial t$ is the velocity of the original block. Since velocities are conserved, there is no energy loss associated with fracturing.

Numerical Examples

The purpose of this section is to examine the capability of the newly developed DDA program for the following applications: (1) rock-fall, (2) cliff failure, and (3) slope stability. All the illustrative examples presented in this section employ the Augmented Lagrangian Method to enforce block contacts and the dynamic analysis to model block kinematics.

rock-fall

Rock-fall analysis has been the subject of many engineering research programs in recent years because rock-fall hazard is a major threat to human safety both on highways and on construction sites. Therefore, several methods for rock-fall analysis have been carried out to capture the different modes of motion of falling rocks such as free falling, bouncing, rolling and sliding.

Consider a hexagonal intact rock with a diameter of 120 ft (36.6 m) resting at the top of a 300 ft (90 m) high slope, as shown Figure 5. Note that the ground structure is composed of five intact blocks while the fence is represented by one intact block. No external load is applied. The material of the falling rock has a shear strength s_0=90 ksf (4.3 MPa), a tensile strength T_0=60 ksf (2.8 MPa), and a 39.1° friction angle. All interfaces have a friction angle of 30° and zero cohesion.

In this case, the falling block is represented by one DDA element. As the intact rock fracturing algorithm is applied, the intact block is allowed to break a maximum of three times. Either shear or tensile fracturing of the block is allowed in this example, depending on the values of the major and minor principal stresses, as described in the previous section. When shear fracturing occurs, two fracturing planes pass through the centroid of the block and are inclined at $-(\pi/4-\phi/2)$ and $+(\pi/4-\phi/2)$ with respect to the minimum principal stress σ_3, respectively. When tensile fracturing occurs, the fracturing plane passes through the centroid of the block and is perpendicular to the major principal stress σ_1.

Figure 6(a) shows that the falling block starts rolling down and becomes loose after 130 time steps. Figures 6(b)-(f) show that the intact block breaks into smaller blocks upon impact with the ground and show the trajectory of the resulting block fragments after 230, 300, 340, 400 and 600 time steps. Following breaking, the block fragments continue to roll and bounce until they are stopped by the fence.

cliff failure

In mountainous area like Taiwan, it is usual to find roads being constructed beside high mountains with fractured rock masses. The rock masses with no fracture were stable. However, if the rock masses were fractured due to disturbance of construction, change of temperature, or intrusion of water into the rock joints, the rocky mountain would become unstable. The example presented below is designed to show how the new DDA program can capture the failure of a sloped mountain.

Consider a 10 ft (3 m) high mountain with a slope inclined at 60.3 degrees to the horizontal existing an initial crack with a depth of 1 ft (0.3 m), as shown in Figure 7(a). The initial crack is located at 2.5 ft (0.76 m) from the right top edge of the mountain. No external load is applied. The material in the mountain is assumed to be homogeneous with a Young's Modulus $E=1 \times 10^8$ psf (4,800 MPa), a Poisson's ratio $\nu=0.25$, a unit weight $\gamma=130$ pcf (2×10^{-2} MN/m^3), an inherent shear strength (cohesion) $s_0=400$ psf (1.92×10^{-2} MPa), a tensile strength $T_0=400$ psf (1.92×10^{-2} MPa), and a 30° friction angle. All interfaces have a friction angle of 30° and zero cohesion. In the DDA sub-blocking analysis, the mountain was represented by one block divided into 71 sub-blocks; 19 of which were fixed in the horizontal and vertical directions (Figure 7(b)).

In this case, either shear or tensile fracturing of the block is allowed in this example, depending on the values of the major and minor principal stresses, as described in the previous section. When shear fracturing occurs, one specified fracturing plane passes through the centroid of the block and is inclined at $-(\pi/4-\phi/2)$ with respect to the minimum principal stress σ_3. When tensile fracturing occurs, the fracturing plane passes through the centroid of the block and is perpendicular to the major principal stress σ_1.

Figures 8(a)-(f) show the trajectory of crack propagation and the fractured mountain after 4, 7, 100, 200, 400 and 500 time steps, respectively. Gravity loading toward the slope results in the crack propagate along a almost vertical direction. After 7 time steps, the mountain starts fracturing at the initial crack tip and the crack propagates towards the slope. The mountain is then divided into two distinct sections. The right hand side section continues to move downward. Large displacements can be noticed. The results clearly demonstrate that the new DDA method may be a useful tool in the analysis of a range of slope problems in the mountainous area.

slope stability

Gravity can cause instability in natural slopes, in slopes formed by excavation and in slopes of earth dams and embankments. Slope failure can be of three major types : rotational (circular or noncircular) slip, translational slip and compound slip. In classical soil mechanics, slope stability analysis is usually conducted using limiting equilibrium methods. Various techniques are available such as the Fellenius method, the Bishop method, the Morgenstern method, etc. [5]. The example presented below is used to show how the enhanced DDA method can predict rotational slip in slopes with homogeneous properties. It is also used to demonstrate the sub-blocking capability.

Consider a footing resting at the crest of a 10.5 ft (3.2 m) high slope with an angle of 45 degrees (Figure 9(a)). A 1.5 ft (0.46 m) deep initial tension crack is located along the right side

of the footing. Two vertical loads of 11 kips (4.9×10^{-2} MN) each are applied on the footing. The material in the slope is assumed to be homogeneous with a Young's Modulus $E=1 \times 10^{8}$ psf (4,800 MPa), a Poisson's ratio $\nu=0.3$, a unit weight $\gamma=130$ pcf (2×10^{-2} MN/m^3), an inherent shear strength (cohesion) $s_0=1000$ psf (4.8×10^{-2} MPa), a very high tensile strength, and a friction angle of 26°. In selecting a high tensile strength, only shear failure was allowed to occur. When shear fracturing occurs, the fracturing plane passes through the cracking front and is inclined at $+(\pi/4-\phi/2)$ with respect to the minimum principal stress σ_3. The footing was assumed to have the same elastic properties at the slope material. In the DDA analysis, the footing was represented by one non-breakable block. The slope was represented by one block divided into 103 sub-blocks; 24 of which were fixed in the horizontal and vertical directions (Figure 9(b)). The contact between the footing and the slope, the initial crack and all subsequent cracks were given a friction angle of 30 degrees and zero cohesion.

Figures 10(a)-(f) show the trajectory of crack propagation and the fractured and deformed slope after 5, 11, 150, 250, 300 and 500 time steps, respectively. Loading of the footing results in having the crack propagate in a rotational manner. After 11 time steps, the foundation starts fracturing at the initial crack tip and the crack propagates towards the slope. The slope is then divided into two distinct sections. The upper section continues to slide downward along the newly created crack surface. Large displacements along the footing-slope contact and the rotational slip surface can be noticed. The results clearly demonstrate that the assumption of a rotational failure surface is valid in this case. This validation also provides further confidence in the capability of the enhanced DDA model and the sub-blocking feature. Again, it suggests that the new DDA method may be a useful tool in the analysis of a range of slope stability problems.

Conclusions

Those examples demonstrated in the previous section have shown that the newly developed DDA method is more widely applicable to a greater range of rock engineering problems than the original DDA method. In the rock-fall analysis, the DDA method is capable of capturing quite well block trajectories with free falling, rolling, sliding, bouncing and even the compact with rock barriers, which definitely can not be simulated by the Finite Element Method (FEM). In modeling cliff failure, which is a very common problem in the mountainous area, the DDA sub-block analysis along with sub-block fracturing capability is capable of modeling cliff failure with capturing fracture propagation within sub-blocks. In modeling slope stability, the DDA sub-block analysis clearly demonstrates that not only the assumption of a rotational failure surface, which has been made by many researchers before, is valid, but also that large displacements along the footing-slope contact and the rotational slip surface can be captured.

Since the DDA method assumes discontinuity of element joints, the newly created discontinuous element joints resulting from block fracturing can be naturally handled by the method. Coulomb friction and cohesion are also given along the block joints. The addition of the block fracturing algorithms in the DDA method makes the method a powerful tool for modeling fracture propagation in already fractured rock masses or other blocky systems.

References

[1] Shi, G-H, and Goodman, R. E. (1984) "Discontinuous Deformation Analysis." *Proceedings of the 25th U.S. Symposium on Rock Mechanics*, pp. 269-277.

[2] Shi, G-H (1988) "Discontinuous Deformation Analysis : a new numerical model for the statics and dynamics of block systems." PhD thesis, University of California, Berkeley.

[3] Lin, C. T. (1995) "Extensions to the Discontinuous Deformation Analysis for jointed rock Masses and other blocky systems." PhD thesis, University of Colorado, Boulder.

[4] Kanninen, M. F., and Popelar, C. H. (1985) "Advanced fracture mechanics." Oxford University Press, New York.

[5] Lambe, T. W., and Whitman, R. V. (1979) "Soil Mechanics, SI version." Wiley, New York.

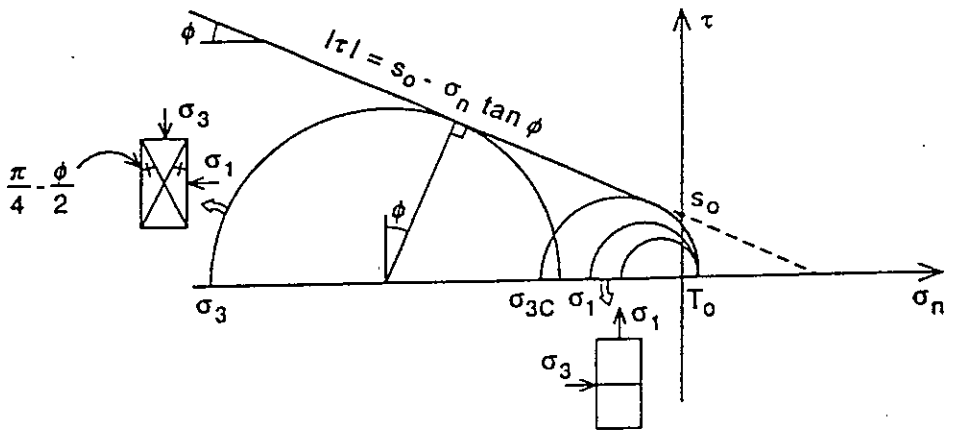

(a)

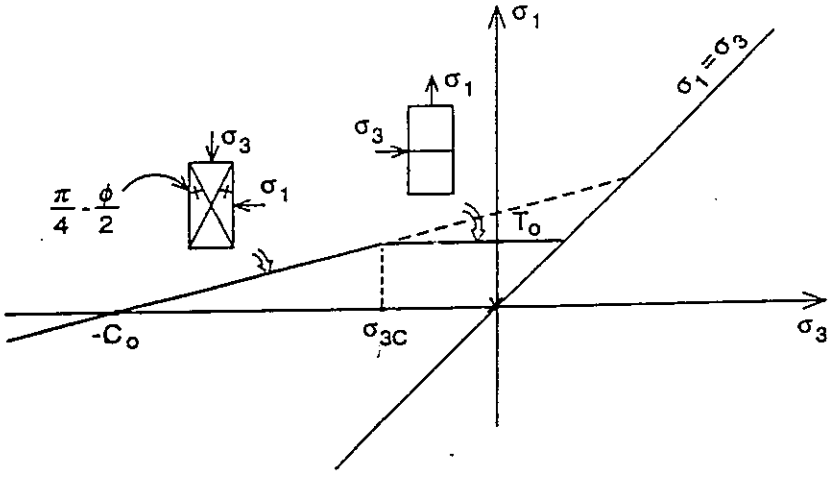

(b)

Fig 1 : The Mohr-Coulomb criterion with three parameters.

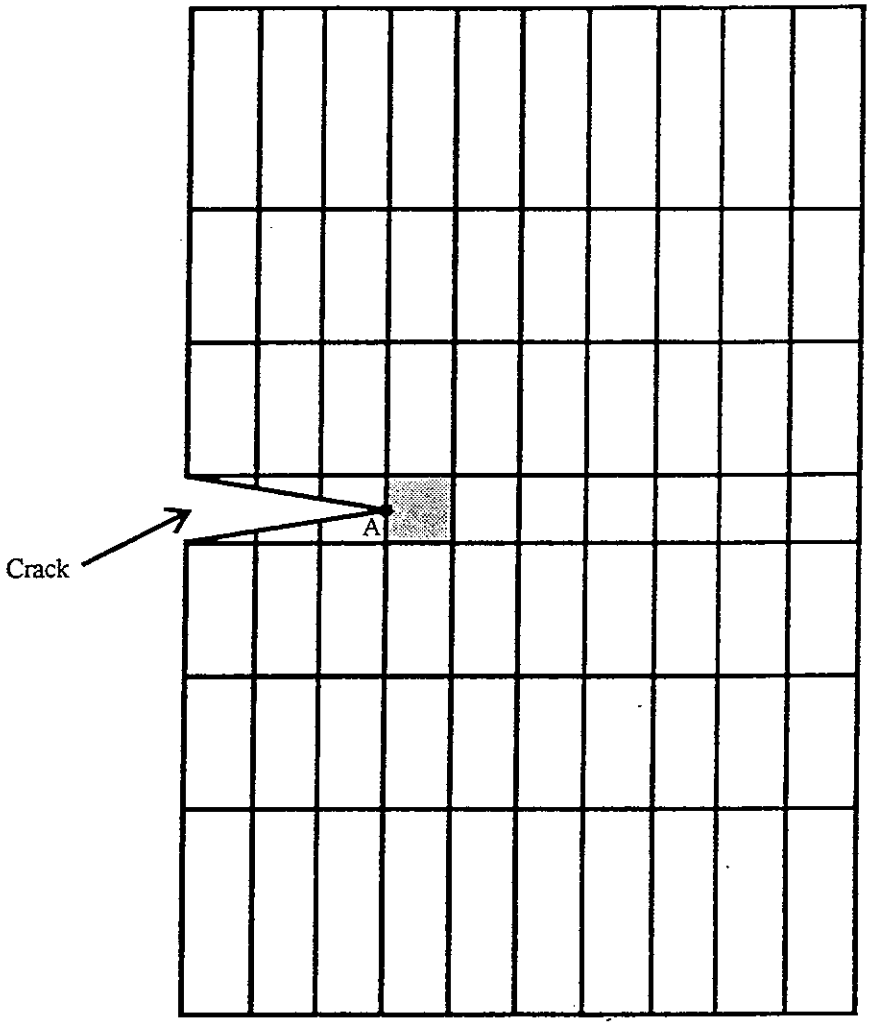

Fig 2 : A large block consists of several sub-blocks and a initial crack with crack tip at point A. The sub-block in contact with the crack tip is shaded.

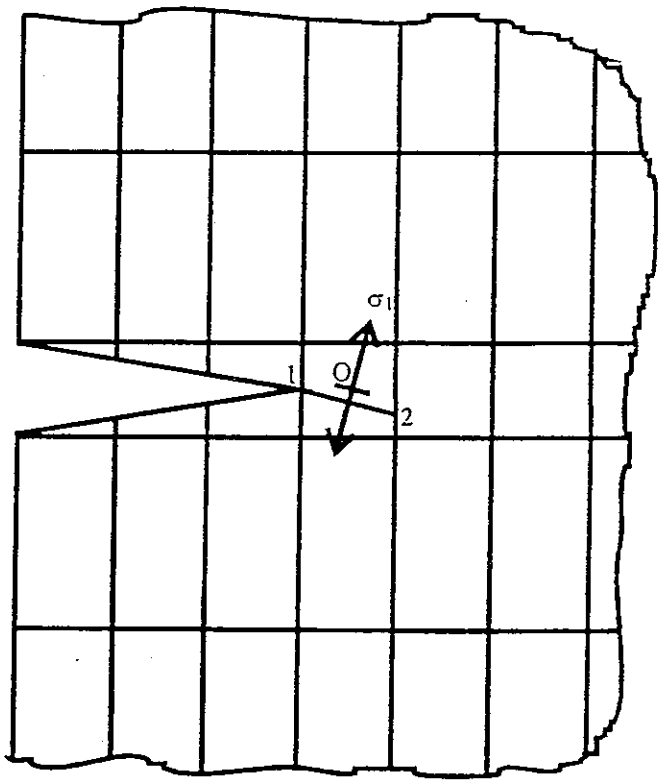

* O : represents centroid of the sub-block.
** 1-2 : represents the Mode I cracking plane.
*** σ_1 : represents the major principal stress.

Fig 3 : Mode I sub-block fracturing.

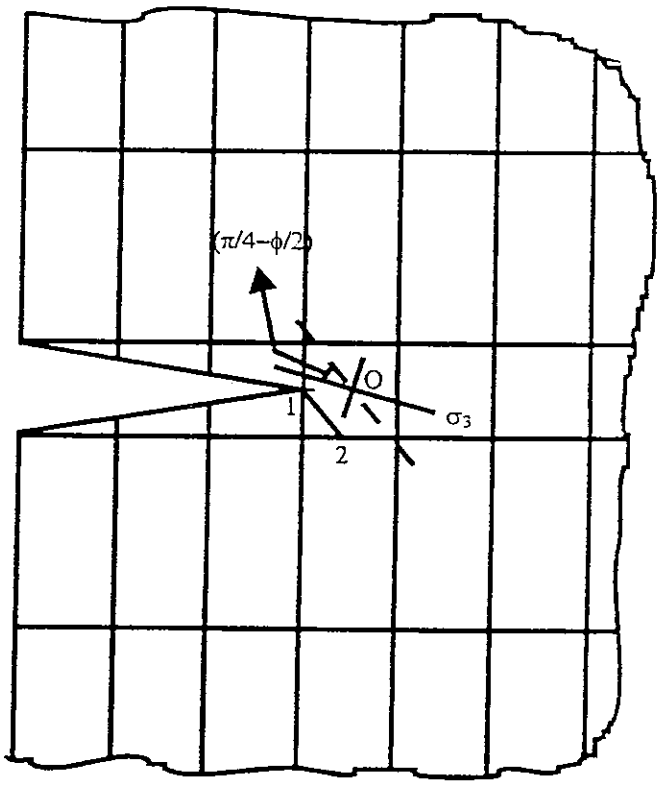

* O : represents centroid of the sub-block.
** 1-2 : represents the Mode II cracking plane.
*** σ_3 : represents the minor principal stress.

(a)

Fig 4 : (a) Mode II sub-block fracturing.

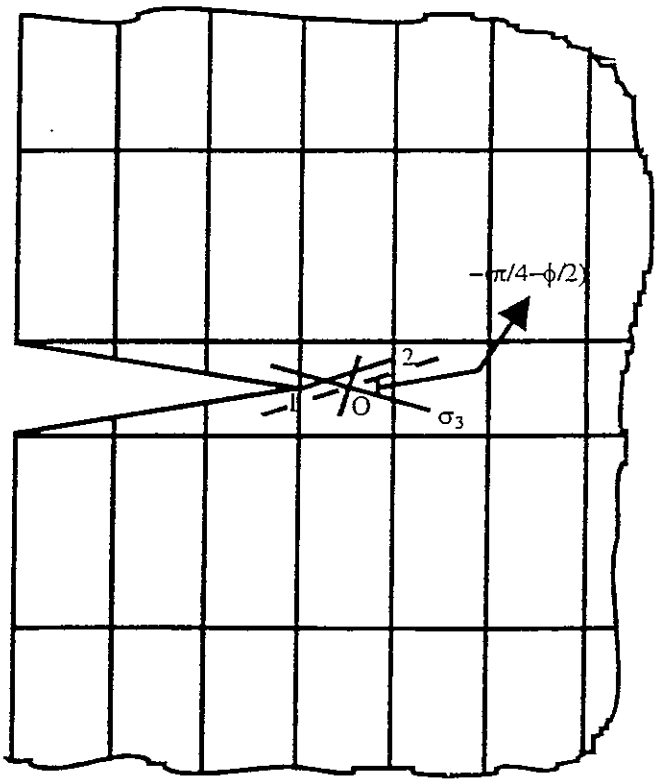

* O : represents centroid of the sub-block.
** 1-2 : represents the Mode II cracking plane.
*** σ_3 : represents the minor principal stress.

(b)

Fig 4 : (b) Mode II sub-block fracturing.

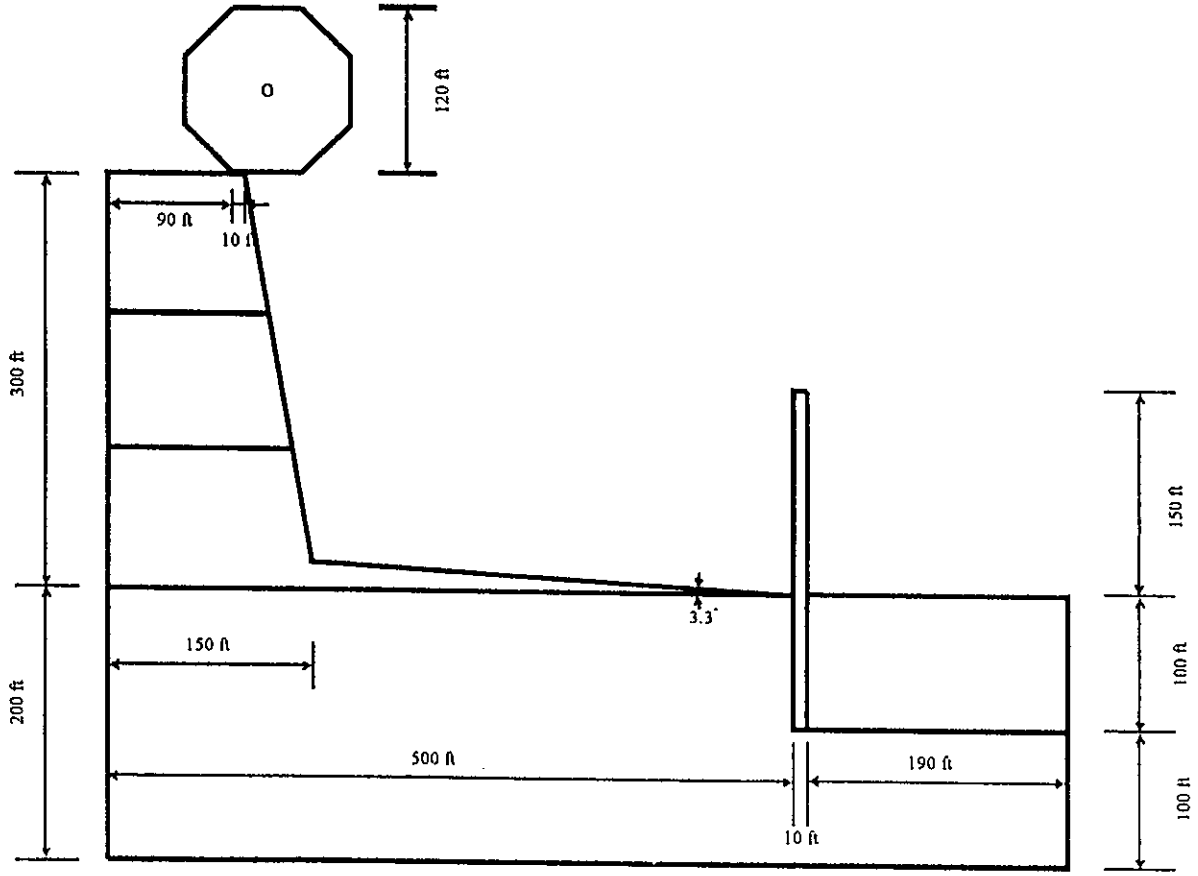

Fig 5 : Initial configuration of a hexagonal intact rock resting at the top of a 300 ft (90m) high slope.

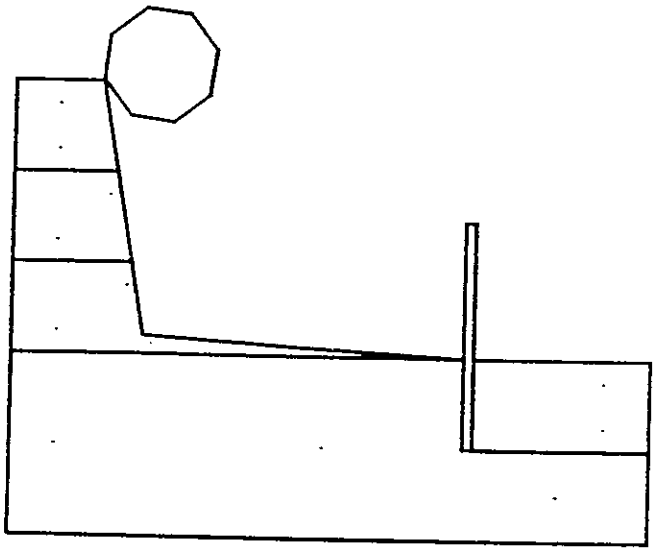

(a)

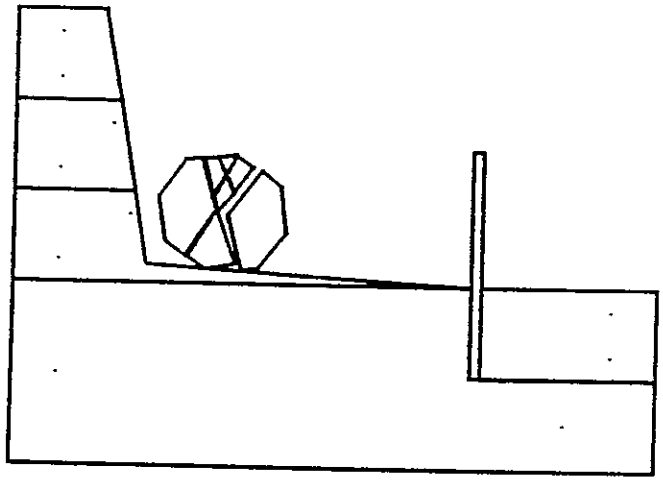

(b)

Fig 6 : Rock-fall example 2. Block trajectories after 130 and 230 time steps of 0.03 seconds in (a) and (b), respectively.

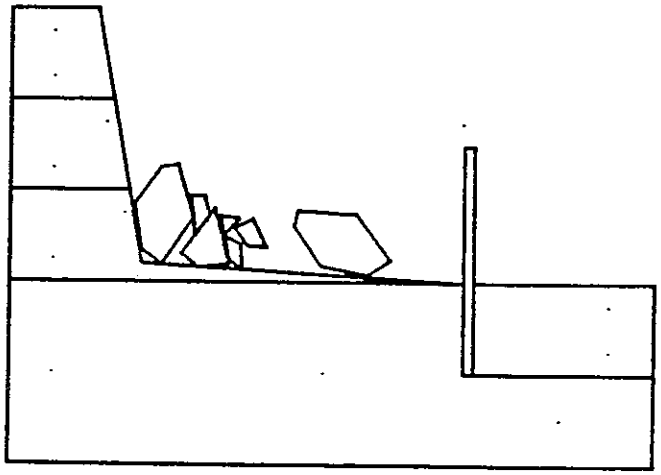

(c)

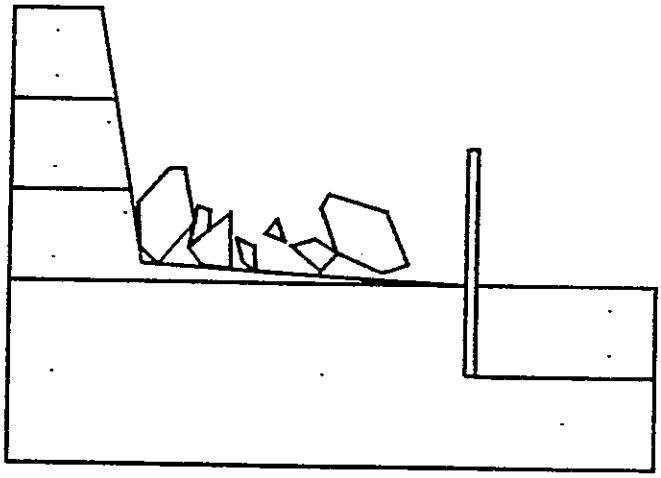

(d)

Fig 6 : Rock-fall example 2. Block trajectories after 300 and 340 time steps of 0.03 seconds in (c) and (d), respectively.

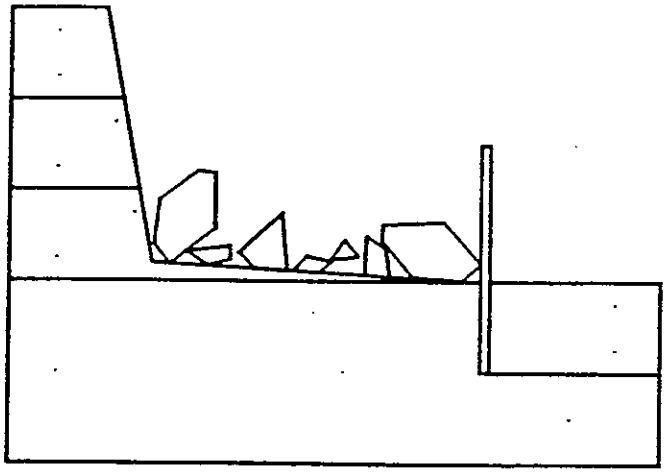

(e)

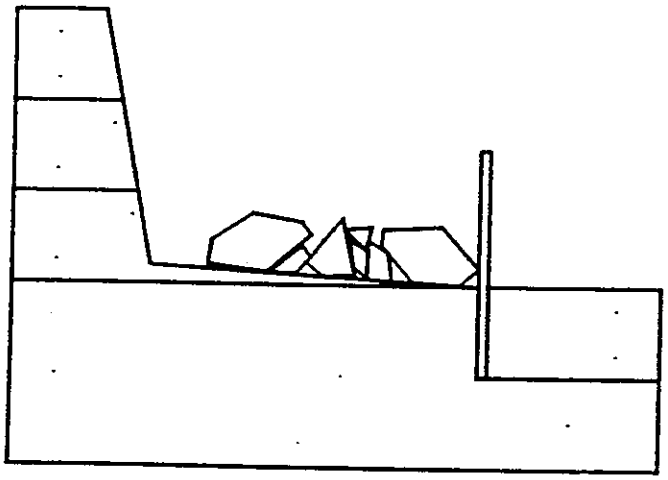

(f)

Fig 6 : Rock-fall example 2. Block trajectories after 400 and 600 time steps of 0.03 seconds in (e) and (f), respectively.

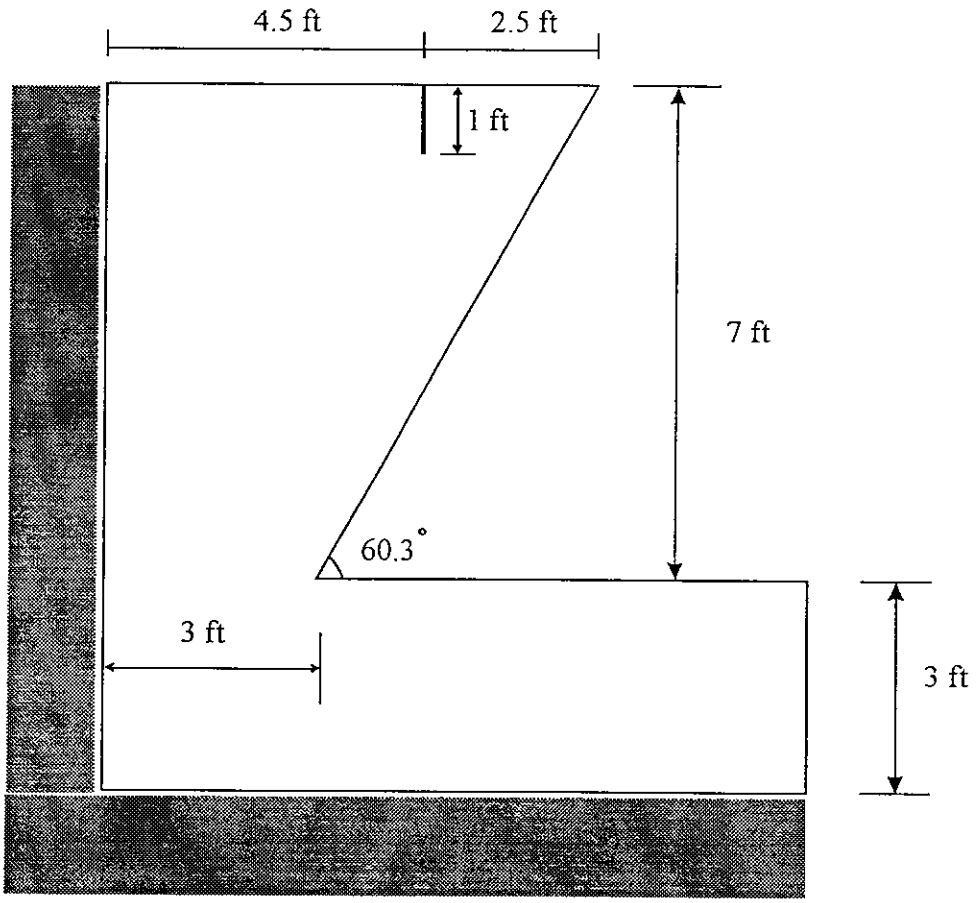

(a)

Fig 7 : (a) Problem geometry. Mountain with a 1 ft (0.3 m) deep tension initial crack on top.

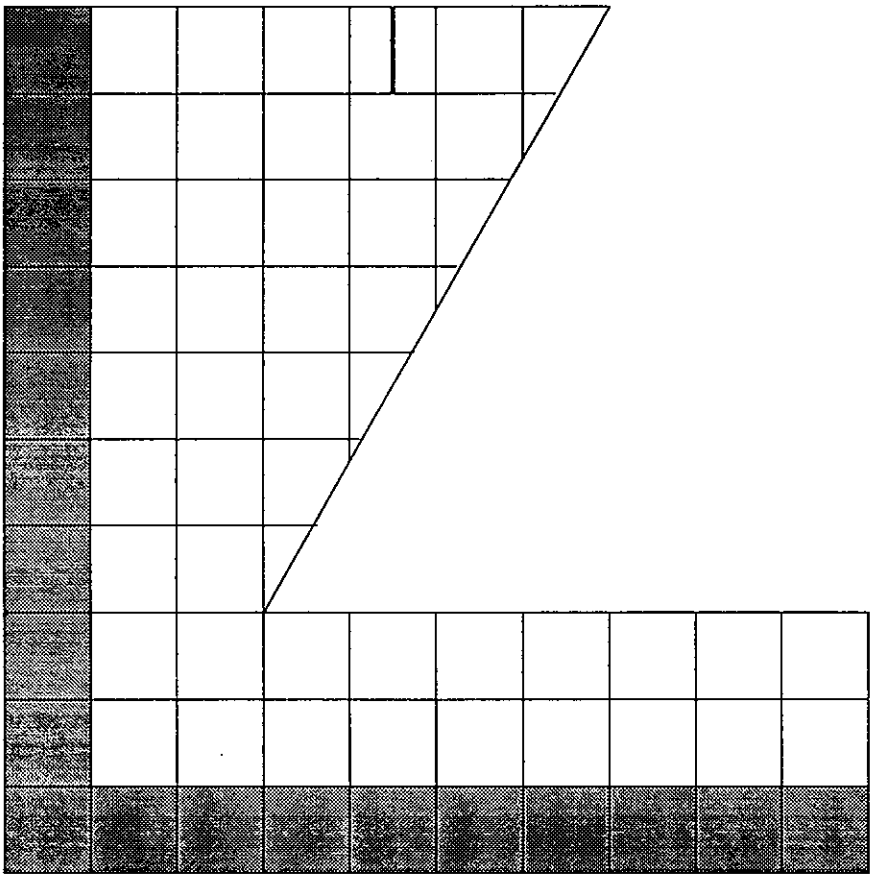

(b)

Fig 7 : (b) Mesh and initial configuration.
The blocks in the shaded area are fixed.

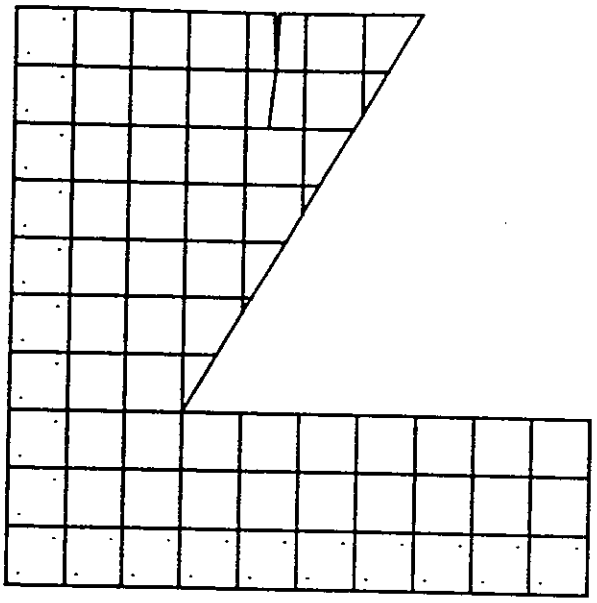

(a)

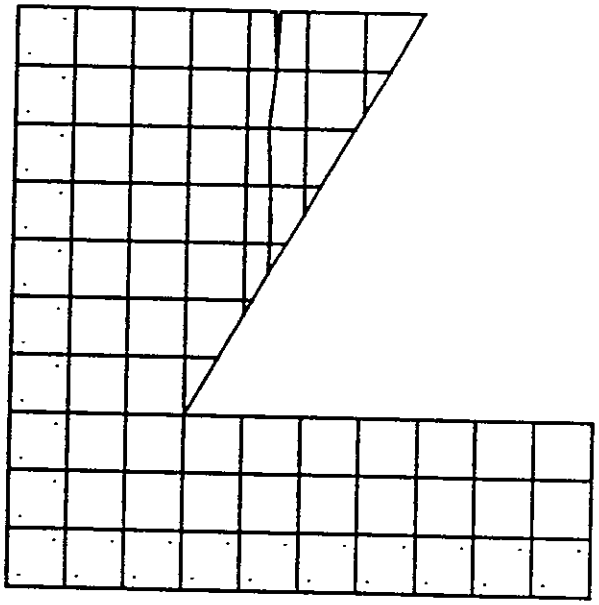

(b)

Fig 8 : Fractured slope after 4 and 7 time steps of 1 x 10^{-3} seconds in (a) and (b), respectively.

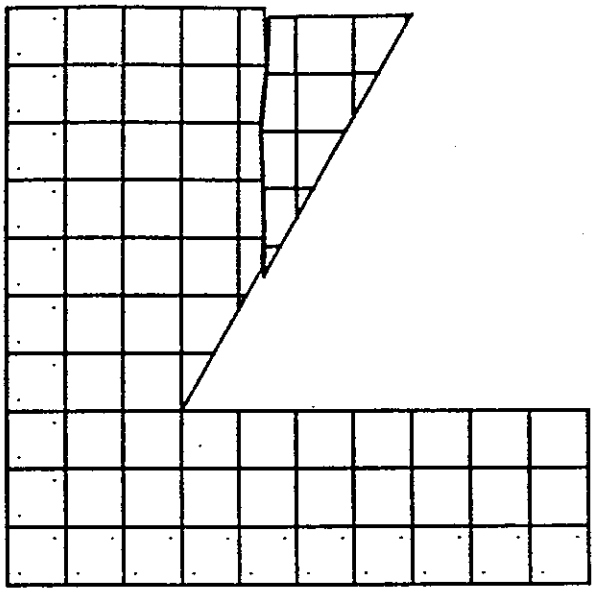

(c)

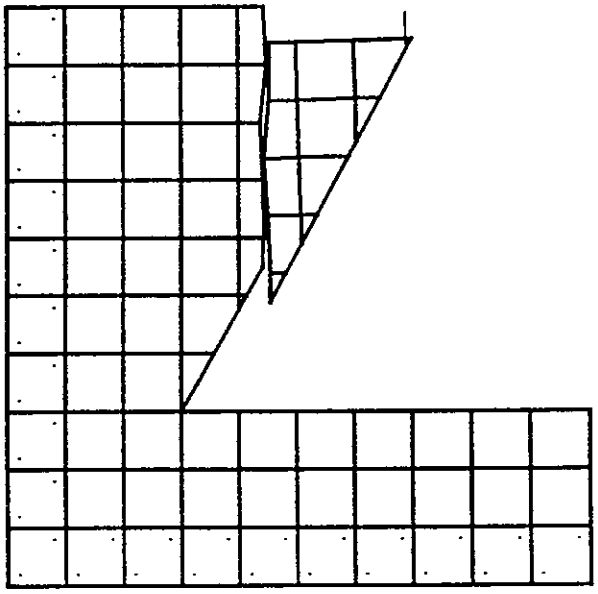

(d)

Fig 8 : Fractured slope after 100 and 200 time steps of 1 x 10^{-3} seconds in (c) and (d), respectively.

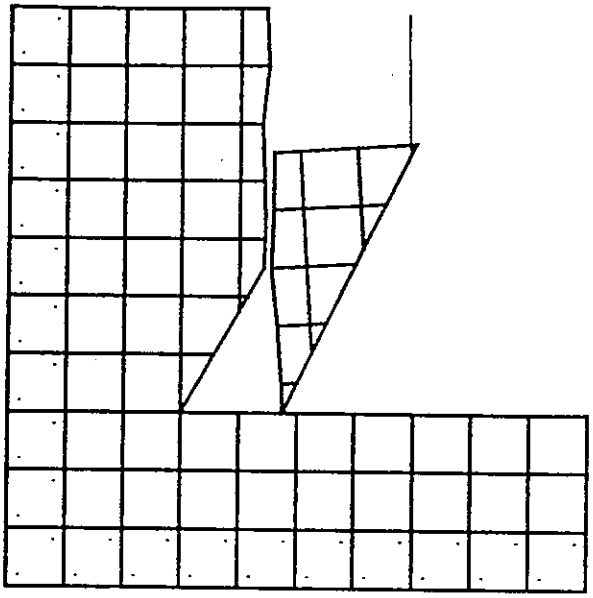

(e)

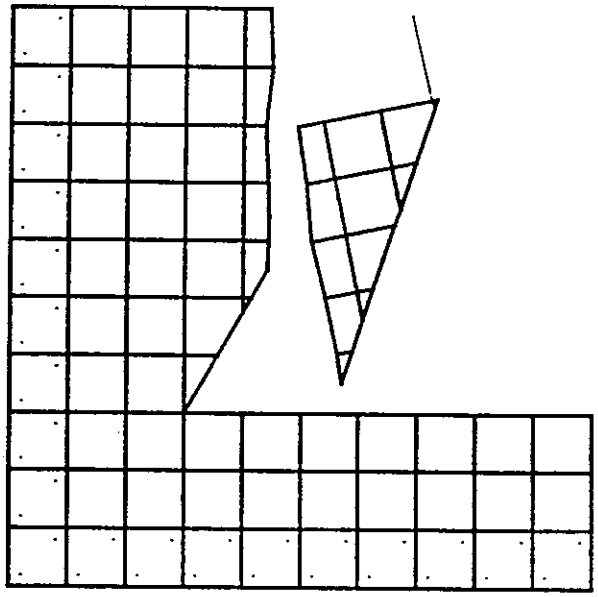

(f)

Fig 8 : Fractured slope after 400 and 500 time steps of 1 x 10^{-3} seconds in (e) and (f), respectively.

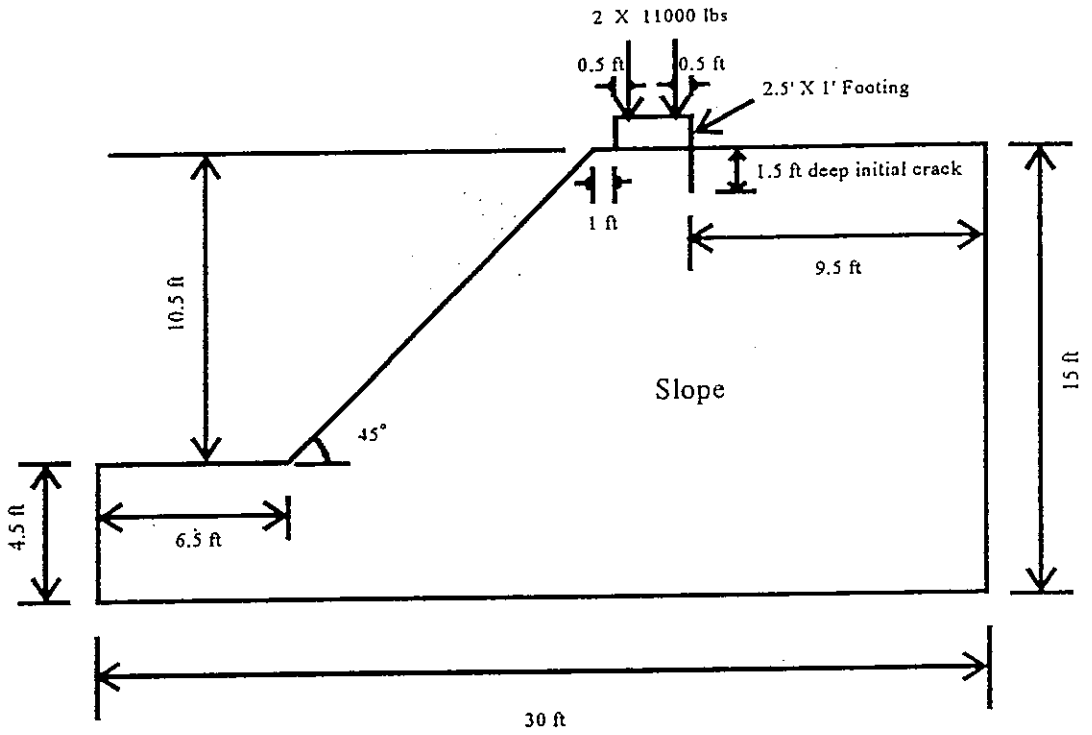

(a)

Fig 9 : (a) Problem geometry. Slope with a 1.5 ft (0.46 m) deep tension initial crack and a footing. The footing, loaded by two vertical loads 11,000 lbs (48.9 kN) each, rests at the corner of the slope.

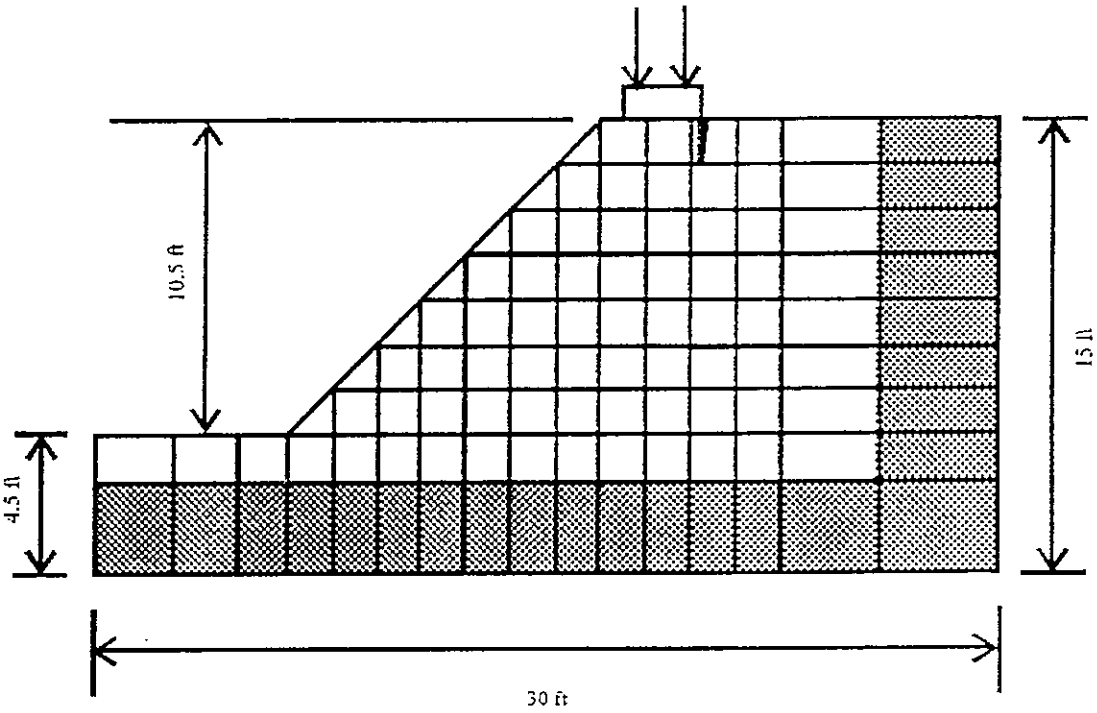

(b)

Fig 9 : (b) Mesh and initial configuration. The blocks in the shaded area are fixed.

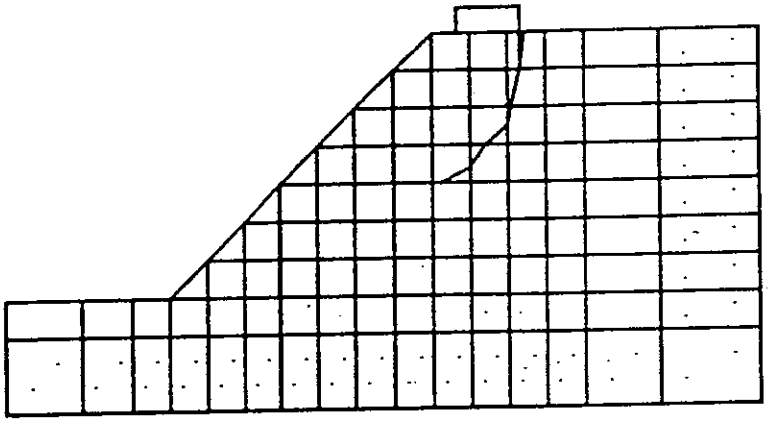

(a)

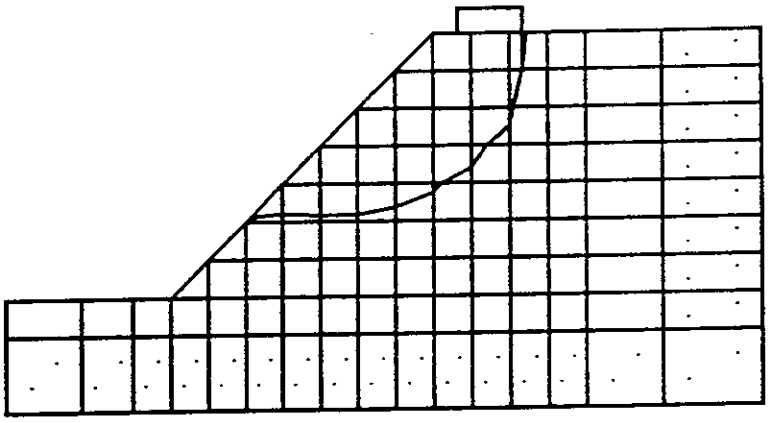

(b)

Fig 10 : Fractured slope after 5 and 11 time steps of 6×10^{-4} seconds in (a) and (b), respectively.

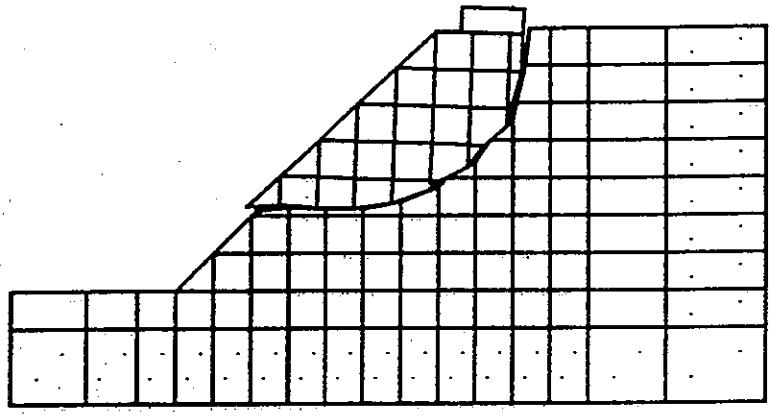

(c)

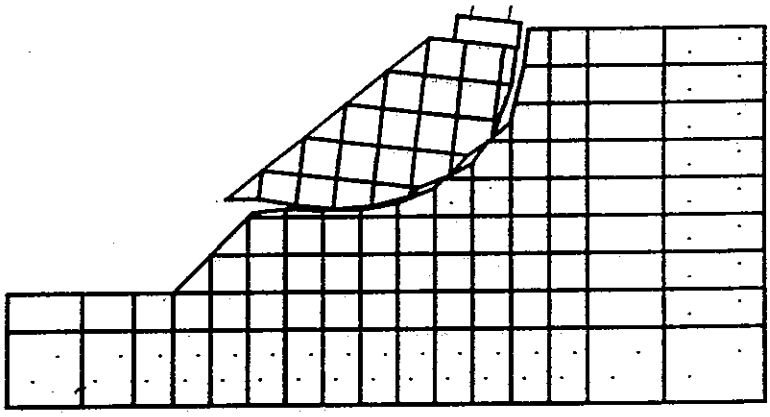

(d)

Fig 10 : Fractured slope after 150 and 250 time steps of 6 x 10^{-4} seconds in (c) and (d), respectively.

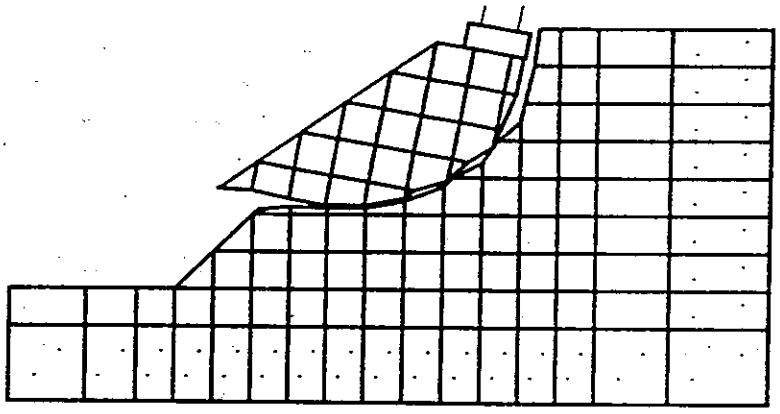

(e)

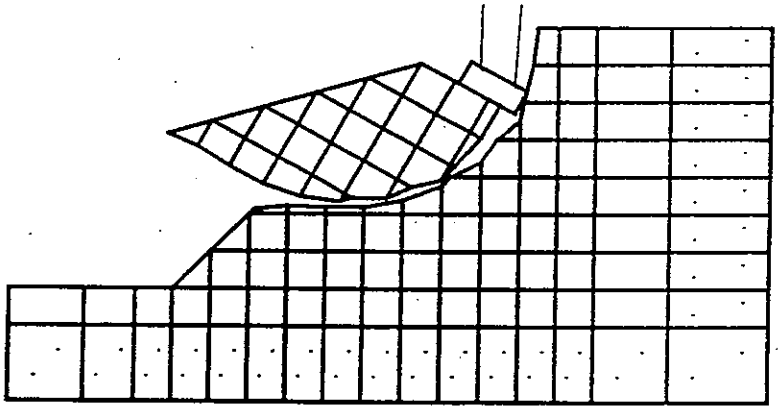

(f)

Fig 10 : Fractured slope after 300 and 500 time steps of 6×10^{-4} seconds in (e) and (f), respectively.

Development of Second Order Displacement Function for DDA

C.Y. Koo, J.C. Chern and S. Chen

Geotechnical Research Center, Sinotech Engineering Consultants, Inc., Taipei, R.O.C.

1. INTRODUCTION

DDA is a new displacement method developed by Shi in late 1980's by minimizing the total potential energy for analyzing the statics and dynamics of discontinuous block system. Original DDA adopted the first order displacement function and did not allow penetration and tension between blocks. In 1993, a new version of DDA was released by Shi in which considerable modification was made. In this new version of DDA, friction angle, cohesion and tensile strength in contacts can be taken into account. In addition, time step, displacement ratio and contact spring are adjusted automatically.

Results of the previous researches (Chen, 1993; Chern, Chen and Koo, 1995) revealed that DDA was well suited to simulate the discontinuous block system. However, it still has limitations, such as constant strain and stress in blocks. To overcome these limitations, several methods may be used, such as the concept of artificial joints. In order to model the mechanical behavior more accurately, the fine-drawn block system are always needed in using the artificial joints concept (Ke, 1993). Therefore, the adoption of high order displacement function may be a better alternative in which less artificial joints are required.

From these points of view, the formulation for the second order displacement function were derived and a new code, Second Order DDA, was developed. Several verification examples of continuum which used the concept of artificial joints are carried out. In addition, the high order simplex integrations needed in the formulation were also derived.

2. THE FORMULATION OF DDA WITH SECOND ORDER DISPLACEMENT FUNCTION

2.1 Displacement and Deformation of Block

Current version of DDA considers the first order displacement function. Thus, the stress and strain are constant over the entire block. The unknowns of individual block can be represented by selecting the six displacement variables ($u_0, v_0, r_0, \varepsilon_x, \varepsilon_y, r_{xy}$), in which u_0, v_0 are rigid body translation of a specific point (x_0, y_0) within the block; r_0 is the rigid body rotation of the block with rotation center at (x_0, y_0); ε_x , ε_y and r_{xy} are

the normal and shear strains of block. When the displacement and strain are small, movement (u,v) at any point (x,y) within a block can be written in terms of first order approximation as:

$$u = a_1 + a_2 x + a_3 y$$
$$v = b_1 + b_2 x + b_3 y \qquad (2\text{-}1)$$

If second order displacement approximation were used, these equations are expanded as the following forms:

$$u = a_1 + a_2 x + a_3 y + a_4 x^2 + a_5 xy + a_6 y^2$$
$$v = b_1 + b_2 x + b_3 y + b_4 x^2 + b_5 xy + b_6 y^2 \qquad (2\text{-}2)$$

For the 6 more variables $(a_4, a_5, a_6, b_4, b_5, b_6)$ being included, equivalent number of unknowns are added to $[D]$ matrix, and block deformation matrix $[T]$ is also modified concurrently to determine the total displacement [u, v] of point (x, y) in block. Then, the new $[D]^T$ becomes :

$$\begin{bmatrix} u_0 & v_0 & r_0 & \varepsilon_x^c & \varepsilon_y^c & r_{xy}^c & \varepsilon_{x,x} & \varepsilon_{x,y} & \varepsilon_{y,x} & \varepsilon_{y,y} & r_{xy,x} & r_{xy,y} \end{bmatrix} \qquad (2\text{-}3)$$

And $[T]$ is expressed as : $\begin{bmatrix} T_1 & T_2 & T_3 \end{bmatrix}$ (2-4)

where,

$$T_1 = \begin{bmatrix} 1 & 0 & -(y-y_0) & (x-x_0) & 0 & \frac{1}{2}(y-y_0) \\ 0 & 1 & (x-x_0) & 0 & (y-y_0) & \frac{1}{2}(x-x_0) \end{bmatrix}$$

$$T_2 = \begin{bmatrix} \frac{1}{2}(x^2-x_0^2) & (xy-x_0y_0) & -\frac{1}{2}(y^2-y_0^2) \\ 0 & -\frac{1}{2}(x^2-x_0^2) & (xy-x_0y_0) \end{bmatrix}$$

$$T_3 = \begin{bmatrix} 0 & 0 & \frac{1}{2}(y^2-y_0^2) \\ \frac{1}{2}(y^2-y_0^2) & \frac{1}{2}(x^2-x_0^2) & 0 \end{bmatrix}$$

Consequently, the total displacement (u,v) is obtained by the following equation:

$$\begin{bmatrix} u \\ v \end{bmatrix}_{2x1} = [T]_{2x12}[D]_{12x1} \qquad (2\text{-}5)$$

For a block system with N blocks, the simultaneous equations may be derived by minimizing the total potential energy. And the simultaneous equations can be expressed in matrix form as follows:

$$[K_g][D_g] = [F_g] \qquad (2\text{-}6)$$

where $[K_g]$ is the global stiffness matrix which is formed by the stiffness sub-matrices $[K]_{12x12}$ of each block.

$$[K_g]=\begin{bmatrix} K_{11} & K_{12} & K_{13} & \cdots & K_{1N} \\ K_{21} & K_{22} & K_{23} & \cdots & K_{2N} \\ K_{31} & K_{32} & K_{33} & \cdots & K_{3N} \\ \vdots & \vdots & \vdots & \ddots & \vdots \\ K_{N1} & K_{N2} & K_{N3} & \cdots & K_{NN} \end{bmatrix}_{(12\times N)\times(12\times N)} \qquad (2\text{-}7)$$

$[F_g]$ is the global force matrix which is formed by the force sub-matrices $[F]_{12x1}$, and $[D_g]$ is the global unknown matrix which is formed by $[D]_{12x1}$.

$$[D_g]=\begin{bmatrix} D_1 \\ D_2 \\ D_3 \\ \vdots \\ D_N \end{bmatrix}_{(12\times N)\times 1}, \quad [F_g]=\begin{bmatrix} F_1 \\ F_2 \\ F_3 \\ \vdots \\ F_N \end{bmatrix}_{(12\times N)\times 1} \qquad (2\text{-}8)$$

To form the individual sub-matrices of stiffness and force by second order displacement function, the total potential energy done by all concerned forces and stresses must be computed, then the derivatives with respect to the corresponding deformation variables for individual potential energy can be derived. The sub-matrices for each loading and stress are depicted as follows.

2.2 Elastic Stiffness Matrix

For linear elastic material, the elastic strain energy Π_e produced by the stresses in the block is:

$$\begin{aligned} \Pi_e &= \iint \frac{1}{2}\left(\sigma_x\varepsilon_x+\sigma_y\varepsilon_y+\tau_{xy}r_{xy}\right)dxdy \\ &= \iint \frac{1}{2}[\varepsilon][\sigma]dxdy \end{aligned} \qquad (2\text{-}9)$$

For plane stress condition, the stress-strain relationship is given by:

$$\begin{bmatrix} \sigma_x \\ \sigma_y \\ \tau_{xy} \end{bmatrix} = \frac{E}{1-\nu^2}\begin{bmatrix} 1 & \nu & 0 \\ \nu & 1 & 0 \\ 0 & 0 & \frac{1-\nu}{2} \end{bmatrix}\begin{bmatrix} \varepsilon_x \\ \varepsilon_y \\ r_{xy} \end{bmatrix} = [E_i]\begin{bmatrix} \varepsilon_x \\ \varepsilon_y \\ r_{xy} \end{bmatrix} \qquad (2\text{-}10)$$

where E and ν are Young's modulus and Poisson's ratio. The strains can be approximated by

$$\begin{aligned} \varepsilon_x &= \varepsilon_x^c+\varepsilon_{x,x}x+\varepsilon_{x,y}y \\ \varepsilon_y &= \varepsilon_y^c+\varepsilon_{y,x}x+\varepsilon_{y,y}y \\ r_{xy} &= r_{xy}^c+r_{xy,x}x+r_{xy,y}y \end{aligned} \qquad (2\text{-}11)$$

and can be written in matrix form as follows:

$$\begin{bmatrix}\varepsilon_x & \varepsilon_y & r_{xy}\end{bmatrix} = [D]^T \begin{bmatrix} 0 & 0 & 0 \\ 0 & 0 & 0 \\ 0 & 0 & 0 \\ 1 & 0 & 0 \\ 0 & 1 & 0 \\ 0 & 0 & 1 \\ x & 0 & 0 \\ y & 0 & 0 \\ 0 & x & 0 \\ 0 & y & 0 \\ 0 & 0 & x \\ 0 & 0 & y \end{bmatrix} = [D]^T [N]^T \qquad (2\text{-}12)$$

Therefore, the elastic strain energy of the i-th block can be written in matrix form as:

$$\Pi_e = \frac{1}{2}\iint [D_i]^T_{1x12} [N_i]^T_{12x3} [E_i]_{3x3} [N_i]_{3x12} [D_i]_{12x1} dxdy \qquad (2\text{-}13)$$

By minimizing the strain energy, it leads to the stiffness matrix:

$$K_{rs} = \frac{\partial^2 \Pi_e}{\partial d_{ri} \partial d_{si}} = \iint [N_i]^T_{12x3} [E_i]_{3x3} [N_i]_{3x12} dxdy \qquad (2\text{-}14)$$

where the integration $\iint [N_i]^T_{12x3} [E_i]_{3x3} [N_i]_{3x12} dxdy$ can be expressed as the following form:

$$\frac{E}{1-\nu^2} \begin{bmatrix} 0 & 0 & 0 & 0 & 0 & 0 & 0 & 0 & 0 & 0 & 0 & 0 \\ & 0 & 0 & 0 & 0 & 0 & 0 & 0 & 0 & 0 & 0 & 0 \\ & & 0 & 0 & 0 & 0 & 0 & 0 & 0 & 0 & 0 & 0 \\ & & & S & S\nu & 0 & S_x & S_y & S_x\nu & S_y\nu & 0 & 0 \\ & & & & S & 0 & S_x\nu & S_y\nu & S_x & S_y & 0 & 0 \\ & & & & & \frac{(1-\nu)}{2}S & 0 & 0 & 0 & 0 & S_x\frac{(1-\nu)}{2} & S_y\frac{(1-\nu)}{2} \\ & & & & & & S_{xx} & S_{xy} & S_{xx}\nu & S_{xy}\nu & 0 & 0 \\ & & & & & & & S_{yy} & S_{xy}\nu & S_{yy}\nu & 0 & 0 \\ & & & & & & & & S_{xx} & S_{xy} & 0 & 0 \\ & & & & & & & & & S_{yy} & 0 & 0 \\ & & & & & \textit{Symmetric} & & & & & S_{xx}\frac{(1-\nu)}{2} & S_{xy}\frac{(1-\nu)}{2} \\ & & & & & & & & & & & S_{yy}\frac{(1-\nu)}{2} \end{bmatrix}$$

in which S , S_x , S_y , S_{xx} , S_{xy} *and* S_{yy} are the two dimensional Simplex integrations as defined by Shi(1989).

2.3 Initial Stress Matrix

For the i-th block, the potential energy of the initial stresses $\left(\sigma_x^0, \sigma_y^0, \tau_{xy}^0\right)$ is:

$$\Pi_{\sigma^0} = -\iint \left(\varepsilon_x \sigma_x^0 + \varepsilon_y \sigma_y^0 + r_{xy} \tau_{xy}^0\right) dxdy = -\iint [\varepsilon]^T [\sigma^0] \, dxdy$$

$$= -\iint [D_i]^T [N_i]^T [E_i] \begin{bmatrix} \varepsilon_x^0 \\ \varepsilon_y^0 \\ r_{xy}^0 \end{bmatrix} dxdy \qquad (2\text{-}15)$$

in which

$$\varepsilon_x^0 = \varepsilon_x^{c0} + \varepsilon_{x,x}^0 x + \varepsilon_{x,y}^0 y$$
$$\varepsilon_y^0 = \varepsilon_y^{c0} + \varepsilon_{y,x}^0 x + \varepsilon_{y,y}^0 y$$
$$r_{xy}^0 = r_{xy}^{c0} + r_{xy,x}^0 x + r_{xy,y}^0 y$$

Therefore,

$$\Pi_{\sigma^0} = -\iint [D_i]^T [N_i]^T [E_i][N_i][D_i^0] \, dxdy \qquad (2\text{-}16)$$

By minimizing the potential energy, it leads to the force matrix of the initial stress of the i-th block as follows:

$$f_r = -\frac{\partial \Pi_{\sigma^0}}{\partial d_{ri}} = \iint [N_i]^T [E_i][N_i] \, dxdy \cdot [D_i^0]$$

$$= [\mathrm{NN_i}]_{12x12} \cdot [D_i^0]_{12x1} \quad , \quad r = 1, \ldots, 12 \qquad (2\text{-}17)$$

where

$$[NN_i] = \iint [N_i]_{12x3}^T [E_i]_{3x3} [N_i]_{3x12} \, dxdy$$

and

$$[D_i^0]_{1x12}^T = \begin{bmatrix} u_0^0 & v_0^0 & r_0^0 & \varepsilon_x^{c0} & \varepsilon_y^{c0} & r_{xy}^{c0} & \varepsilon_{x,x}^0 & \varepsilon_{x,y}^0 & \varepsilon_{y,x}^0 & \varepsilon_{y,y}^0 & r_{xy,x}^0 & r_{xy,y}^0 \end{bmatrix}$$

2.4 Point Load Force Matrix

The potential energy of the i-th block due to point loads $\left(F_x, F_y\right)$ is:

$$\Pi_p = -\left(F_x u + F_y v\right) = -\begin{bmatrix} u & v \end{bmatrix} \begin{bmatrix} F_x \\ F_y \end{bmatrix}$$

$$= -[D_i]^T [T_i]^T \begin{bmatrix} F_x \\ F_y \end{bmatrix} \qquad (2\text{-}18)$$

By minimizing the potential energy, the force matrix due to point load is obtained as:

$$f_r = \frac{\partial \Pi_P}{\partial d_{ri}} = [T_i]^T \begin{bmatrix} F_x \\ F_y \end{bmatrix} \quad , \quad r = 1, \ldots, 12 \qquad (2\text{-}19)$$

2.5 Body Force Matrix

Assuming that $\left(f_x, f_y\right)$ are the constant body force of the i-th block, the potential energy due to the body force is:

$$\Pi_B = -\iint \left(f_x u + f_y v\right) dxdy$$

$$= -\iint \begin{bmatrix} u & v \end{bmatrix} \begin{bmatrix} f_x \\ f_y \end{bmatrix} dxdy = -[D_i]^T \iint [T_i]^T dxdy \begin{bmatrix} f_x \\ f_y \end{bmatrix} \qquad (2\text{-}20)$$

The integration can be written as:

$$\iint [T_i]^T dxdy = \begin{bmatrix} S & 0 \\ 0 & S \\ 0 & 0 \\ 0 & 0 \\ 0 & 0 \\ 0 & 0 \\ \frac{1}{2}\left(S_{xx} - \frac{S_x^2}{S}\right) & 0 \\ S_{xy} - \frac{S_x S_y}{S} & -\frac{1}{2}\left(S_{xx} - \frac{S_x^2}{S}\right) \\ -\frac{1}{2}\left(S_{yy} - \frac{S_y^2}{S}\right) & \left(S_{xy} - \frac{S_x S_y}{S}\right) \\ 0 & \frac{1}{2}\left(S_{yy} - \frac{S_y^2}{S}\right) \\ 0 & \frac{1}{2}\left(S_{xx} - \frac{S_x^2}{S}\right) \\ \frac{1}{2}\left(S_{yy} - \frac{S_y^2}{S}\right) & 0 \end{bmatrix}$$

where S , S_x , S_y , S_{xx} , S_{xy} *and* S_{yy} are the Simplex integrations.
By minimizing the potential energy, the body force matrix is

$$f_r = \frac{\partial \Pi_B}{\partial d_{ri}} = -\iint [T_i]^T dxdy \begin{bmatrix} f_x \\ f_y \end{bmatrix} \quad , \quad r = 1, \ldots, 12$$

which will be added into the global force matrix.

2.6 Inertia Force Matrix

The potential energy for the i-th block due to inertia forces $\left(F_x, F_y\right)$ of unit area is:

$$\Pi_I = -\iint \begin{bmatrix} u & v \end{bmatrix} \begin{bmatrix} F_x \\ F_y \end{bmatrix} dxdy \qquad (2\text{-}21)$$

The initial forces per unit area are

$$\begin{bmatrix} F_x \\ F_y \end{bmatrix} = -M \begin{bmatrix} \frac{\partial^2 u(t)}{\partial t^2} \\ \frac{\partial^2 v(t)}{\partial t^2} \end{bmatrix} \qquad (2\text{-}22)$$

according to Newton's Second Law of Motion. M is the mass per unit area. From equations (2-9) and (2-22), the potential energy can be expressed as:

$$\Pi_I = \iint M[u \quad v]\begin{bmatrix}\frac{\partial^2 u(t)}{\partial t^2}\\ \frac{\partial^2 v(t)}{\partial t^2}\end{bmatrix} dxdy$$

$$= \iint M[D_i]^T[T_i]^T[T_i]\frac{\partial^2 D_i(t)}{\partial t^2}\,dxdy \qquad (2\text{-}23)$$

Neglecting the higher order term of Taylor's series expansion,

$$\frac{\partial^2 D_i(t)}{\partial t^2} = \frac{2}{\Delta^2}[D_i] - \frac{2}{\Delta}\frac{\partial D_i(t)}{\partial t}$$

where Δ is the time increment, therefore, the potential energy due to inertia force is

$$\Pi_I = [D_i]^T \iint [T_i]^T[T_i]\,dxdy\left(\frac{2M}{\Delta^2}[D_i] - \frac{2M}{\Delta}[V_0]\right)$$

Minimizing the potential energy, we obtained

$$K_{rs} = \frac{2M}{\Delta^2}\iint [T_i]^T_{12x2}[T_i]_{2x12}\,dxdy \quad , \quad r,s = 1,\ldots,12 \qquad (2\text{-}24)$$

which will be added into stiffness matrix, and another term

$$f_r = \frac{2M}{\Delta}\iint [T_i]^T_{12x2}[T_i]_{2x12}\,dxdy\,[V_0] \quad , r = 1,\ldots,12 \qquad (2\text{-}25)$$

will be added into the force matrix. The integration $\iint [T_i]^T[T_i]\,dxdy$ is a 12x12 matrix and is in the following form:

$$\begin{bmatrix}
S & 0 & 0 & 0 & 0 & 0 & \frac{1}{2}S_1 & S_3 & -\frac{1}{2}S_2 & 0 & 0 & \frac{1}{2}S_2 \\
 & S & 0 & 0 & 0 & 0 & 0 & -\frac{1}{2}S_1 & S_3 & \frac{1}{2}S_2 & \frac{1}{2}S_1 & 0 \\
 & & S_1+S_2 & -S_3 & S_3 & \frac{1}{2}S_1-\frac{1}{2}S_2 & -\frac{1}{2}S_7 & -S_{12}-\frac{1}{2}S_8 & \frac{1}{2}S_9+S_{11} & \frac{1}{2}S_{10} & \frac{1}{2}S_8 & -\frac{1}{2}S_9 \\
 & & & S_1 & 0 & \frac{1}{2}S_3 & \frac{1}{2}S_8 & S_{11} & -\frac{1}{2}S_{10} & 0 & 0 & \frac{1}{2}S_{10} \\
 & & & & S_2 & \frac{1}{2}S_3 & 0 & -\frac{1}{2}S_7 & S_{12} & \frac{1}{2}S_9 & \frac{1}{2}S_7 & 0 \\
 & & & & & \frac{1}{4}S_1+\frac{1}{4}S_2 & \frac{1}{4}S_7 & \frac{1}{2}S_{12}-\frac{1}{4}S_8 & -\frac{1}{4}S_9+\frac{1}{2}S_{11} & \frac{1}{4}S_{10} & \frac{1}{4}S_8 & \frac{1}{4}S_9 \\
 & & & & & & \frac{1}{4}S_{13} & \frac{1}{2}S_{16} & -\frac{1}{4}S_{15} & 0 & 0 & \frac{1}{4}S_{15} \\
 & & & & & & & S_{18}+\frac{1}{4}S_{13} & -\frac{1}{2}S_{17}-\frac{1}{2}S_{16} & -\frac{1}{4}S_{15} & -\frac{1}{4}S_{13} & \frac{1}{2}S_{17} \\
 & & & & & & & & \frac{1}{4}S_{14}+S_{18} & \frac{1}{2}S_{17} & \frac{1}{2}S_{16} & -\frac{1}{4}S_{14} \\
 & & & & & \textit{Symmetric} & & & & \frac{1}{4}S_{14} & \frac{1}{4}S_{15} & 0 \\
 & & & & & & & & & & \frac{1}{4}S_{13} & 0 \\
 & & & & & & & & & & & \frac{1}{4}S_{14}
\end{bmatrix}$$

in which $S, S_1, \ldots, S_{18}$ are functions of Simplex integration.

2.7 Fixed Point Matrix

The constraint at the fixed point on the block boundary may be simulated by using two stiff springs acting on the fixed points. The potential energy due to the springs at the i-th block is equal to :

$$\Pi_f = -\frac{1}{2}\begin{bmatrix} u & v \end{bmatrix}\begin{bmatrix} f_x \\ f_y \end{bmatrix}$$

$$= -\frac{1}{2}\begin{bmatrix} u & v \end{bmatrix}\begin{bmatrix} -pu \\ -pv \end{bmatrix}$$

$$= \frac{p}{2}[D_i]^T[T_i]^T[T_i][D_i] \qquad (2\text{-}26)$$

where p is the spring constant at the fixed point. The stiffness matrix due to fixed point can be obtained as follows:

$$K_{rs} = \frac{\partial^2 \Pi_f}{\partial d_{ri} \partial d_{si}} = p[T_i]^T_{12x2}[T_i]_{2x12} \quad , \quad r,s = 1,\ldots,12 \qquad (2\text{-}27)$$

2.8 Line Load Force Matrix

The potential energy of the i-th block due to line loads (F_x, F_y) are:

$$\Pi_L = -\int_0^1 \left(F_x u + F_y v\right) l dt = -\int_0^1 \begin{bmatrix} u & v \end{bmatrix}\begin{bmatrix} F_x \\ F_y \end{bmatrix} l dt$$

$$= -[D_i]^T[T_i]^T\begin{bmatrix} F_x \\ F_y \end{bmatrix} \qquad (2\text{-}28)$$

By minimizing the potential energy, the force matrix due to line load is obtained as:

$$f_r = \frac{\partial \Pi_L}{\partial d_{ri}} = \int_0^1 [T_i]^T\begin{bmatrix} F_x \\ F_y \end{bmatrix} l dt \quad , \quad r = 1,\ldots,12 \qquad (2\text{-}29)$$

which are added to $[F_i]$. In that, l is the length of loading line, F_x, F_y are loading at x and y directions.

2.9 Rock Bolt Force Matrix

The potential energy of the i-th block due to rock bolt force f is:

$$\Pi_B = -\frac{1}{2} f dl$$

where $f = -s\frac{dl}{l}$; s is the stiffness of rock bolt; l is the length of rock bolt. The potential energy can be expressed as follows.

$$\Pi_B = \frac{s}{2l} dl^2$$

$$= \frac{s}{2l}\left([D_i]^T [T_i]^T \begin{bmatrix} l_x \\ l_y \end{bmatrix} - [D_j]^T [T_j]^T \begin{bmatrix} l_x \\ l_y \end{bmatrix} \right)^2$$

$$= \frac{s}{2l}[D_i]^T [E_i][E_i]^T [D_i] - \frac{s}{l}[D_i]^T [E_i][G_j]^T [D_j]$$

$$+ \frac{s}{2l}[D_i]^T [G_j][G_j]^T [D_i]$$

where

$$[E_i]_{12x1} = [T_i]^T_{12x2} \begin{bmatrix} l_x \\ l_y \end{bmatrix}_{2x1} \quad ; \quad [G_j]_{12x1} = [T_j]^T_{12x2} \begin{bmatrix} l_x \\ l_y \end{bmatrix}_{2x1}$$

By minimizing the potential energy, the stiffness matrices due to rock bolt force are obtained as:

$$\frac{s}{l}[E_i]_{12x1}[E_i]^T_{1x12} ; -\frac{s}{l}[E_i]_{12x1}[G_j]^T_{1x12} ; -\frac{s}{l}[G_j]_{12x1}[E_i]^T_{1x12} ; \frac{s}{l}[G_j]_{12x1}[G_j]^T_{1x12}$$

which are added to the stiffness matrix $[K_{ii}]$, $[K_{ij}]$, $[K_{ji}]$, $[K_{jj}]$

2.10 Normal and Shear Contact Matrices

The formulations for normal and shear contact matrices are exactly the same as those given by Shi(1989) with the exception of using extended $[T]$ *and* $[D]$ matrices. The sub-matrices due to the interaction between blocks are mainly induced by the contact forces which are determined by the quantity of penetration, relative movement between blocks and stiffness of contact spring. They are :

$$p[e_i]_{12x1}[e_i]^T_{1x12} \; , \; p[e_i]_{12x1}[g_j]^T_{1x12} \; , \; p[g_j]_{12x1}[e_i]^T_{1x12} \; , \; p[g_j]_{12x1}[g_j]^T_{1x12}$$

which are added to the stiffness matrix $[K_{ii}]$, $[K_{ij}]$, $[K_{ji}]$, $[K_{jj}]$; and

$$-\frac{pS_0}{l}[e_i]_{12x1} \; , \; -\frac{pS_0}{l}[g_j]_{12x1}$$

are added to the force matrix$[F_i]$;$[F_j]$.

In these sub-matrices, p is the stiffness of contact spring, l is the length of contact edge, and $[e_i]$, $[g_j]$ have the following forms:

$$[e_i]_{12x1} = \frac{1}{l}[T_i(x_1, y_1)]^T \begin{bmatrix} y_2 - y_3 \\ x_3 - x_2 \end{bmatrix}$$

$$[g_j]_{12x1} = [T_j(x_2, y_2)]^T \begin{bmatrix} y_3 - y_1 \\ x_1 - x_3 \end{bmatrix} + [T_j(x_3, y_3)]^T \begin{bmatrix} y_1 - y_2 \\ x_2 - x_1 \end{bmatrix}$$

and

$$S_0 = \begin{vmatrix} 1 & x_1 & y_1 \\ 1 & x_2 & y_2 \\ 1 & x_3 & y_3 \end{vmatrix}$$

The stiffness and force matrices at the individual block derived above are assembled into global stiffness and force matrices for the block system. Simultaneous equations were formed for solving the unknowns $[D]$ for all blocks.

3. HIGH ORDER SIMPLEX INTEGRATIONS

Because blocks in DDA can be in any shape, it is difficult to calculate the integrations by using the Gauss integration method. To solve this problem, Simplex integration method was developed by Shi. In this study, the high order expansions of simplex integration are required in the formulation of Second Order DDA.

In this method, the integration of a function over an arbitrary polygonal block can be divided into a sum of many triangles, and the integration in each triangle is calculated analytically. The vertex of block can be expressed as $P_1, P_2, P_3, \ldots, P_M, P_1$, and the vertex of each triangle may be defined as P_0, P_i, P_{i+1}, where P_0 can be any point in the calculation domain. In this study, let (0,0) be the coordinates of P_0 in order to write the high order simplex integrations more clearly. Therefore, the high order simplex integrations can be written in the following form.

$$S_{xxx} = \iint x^3 dxdy = \sum_{i=1}^{M} \frac{1}{20}(x_i^3 + x_i^2 x_{i+1} + x_i x_{i+1}^2 + x_{i+1}^3) J_0$$

$$S_{yyy} = \iint y^3 dxdy = \sum_{i=1}^{M} \frac{1}{30}(y_i^3 + y_i^2 y_{i+1} + y_i y_{i+1}^2 + y_{i+1}^3) J_0$$

$$S_{xxxx} = \iint x^4 dxdy = \sum_{i=1}^{M} \frac{1}{30}(x_i^4 + x_i^3 x_{i+1} + x_i^2 x_{i+1}^2 + x_i x_{i+1}^3 + x_{i+1}^4) J_0$$

$$S_{yyyy} = \iint y^4 dxdy = \sum_{i=1}^{M} \frac{1}{30}(y_i^4 + y_i^3 y_{i+1} + y_i^2 y_{i+1}^2 + y_i y_{i+1}^3 + y_{i+1}^4) J_0$$

$$S_{xxy} = \iint x^2 ydxdy = \sum_{i=1}^{M} \frac{1}{60}(3x_i^2 y_i + 2x_i x_{i+1} y_i + x_{i+1}^2 y_i + x_i^2 y_{i+1} + 2x_i x_{i+1} y_{i+1} + 3x_{i+1}^2 y_{i+1}) J_0$$

$$S_{xyy} = \iint xy^2 dxdy = \sum_{i=1}^{M} \frac{1}{60}(3y_i^2 x_i + 2y_i y_{i+1} x_i + y_{i+1}^2 x_i + y_i^2 x_{i+1} + 2y_i y_{i+1} x_{i+1} + 3y_{i+1}^2 x_{i+1}) J_0$$

$$S_{xxxy} = \iint x^3 ydxdy = \sum_{i=1}^{M} \frac{1}{120}(4x_i^3 y_i + 3x_i^2 x_{i+1} y_i + 2x_i x_{i+1}^2 y_i + x_{i+1}^3 y_i + x_i^3 y_{i+1} + 2x_i^2 x_{i+1} y_{i+1} + 3x_i x_{i+1}^2 y_{i+1} + 4x_{i+1}^3 y_{i+1}) J_0$$

$$S_{xyyy} = \iint xy^3 dxdy = \sum_{i=1}^{M} \frac{1}{120}(4y_i^3 x_i + 3y_i^2 y_{i+1} x_i + 2y_i y_{i+1}^2 x_i + y_{i+1}^3 x_i + y_i^3 x_{i+1} + 2y_i^2 y_{i+1} x_{i+1} + 3y_i y_{i+1}^2 x_{i+1} + 4y_{i+1}^3 x_{i+1}) J_0$$

$$S_{xxyy} = \iint x^2 y^2 dxdy = \sum_{i=1}^{M} \frac{1}{180}(6x_i^2 y_i^2 + 3x_i^2 y_i y_{i+1} + x_i^2 y_{i+1}^2 + 3x_i x_{i+1} y_i^2 + 4x_i x_{i+1} y_i y_{i+1} + 3x_i x_{i+1} y_{i+1}^2 + x_{i+1}^2 y_i^2 + 3x_{i+1}^2 y_i y_{i+1} + 6x_{i+1}^2 y_{i+1}^2) J_0$$

where M is the vertex number of each block. It is different from the Gauss integration method that Simplex integration need not to convert the element(or block) shape into local regular element to get the approximate solution. Therefore, exact analytical solutions of integrations in Second Order DDA can be obtained by using the high order simplex integrations. In addition, the calculation of integration in other numerical methods such as finite element and manifold method may also be done by the same method.

4. VERIFICATION OF Second Order DDA

4.1 Modification of DDA Code

DDA code version(1993) developed by Dr. Gen-hua Shi was used as the basic program for modification. The main features of the modified version of DDA program include :

(1) incorporate the second order displacement function;
(2) add line loading and rock bolt functions;
(3) revise the variable contact spring constant to fixed value;
(4) change the convergence criteria from iteration number of 200 or relative criterion of 10^{-8} to an absolute criterion of 10^{-8}.

By the concept of artificial joints(Ke ,1993), Second Order DDA can simulate not only the discontinuous problems but also continuous problems. For this reason, several examples of continuum with analytical solutions were used for validation to check the correctness of formulation and coding. The results are presented in the following section.

4.2 Example 1

The first example is the case of cantilever beam shown in Figure 1. An 8 m long x 1 m deep cantilever beam with unit thickness subjected to 1 ton concentrated load at the end of the beam was used for validation. The material properties of the beam were assumed to be E=$10^5 T/m^2$ and ν=0.2. The problem was solved by dividing the beam into 1, 4, 8, 16, 32 and 64 blocks. The results for the deformation along the beam axis are shown in Figure 2. And stress component σ_x at the centroid of each block for the case of 64 blocks are shown in Figure 3. It may be seen that 64 blocks can obtain good approximation as compared with analytical solution. This example also illustrates that the Second Order DDA can release the restriction of block shape requirement for certain types of problem, such as beams. It also requires a smaller number of blocks to achieve the same degree of accuracy as the first order code.

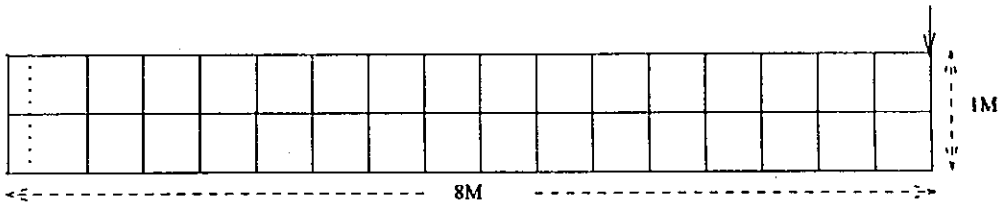

Figure 1 The 32 rectangular sub-blocks for example 1.

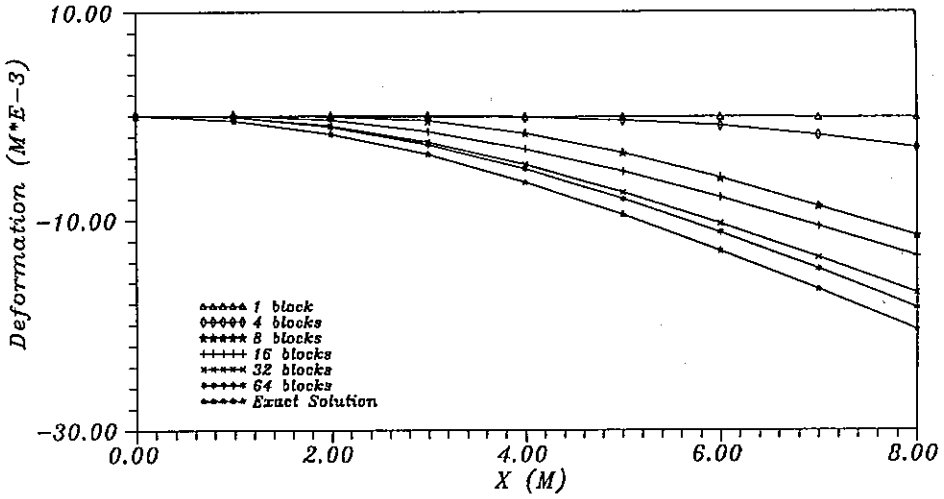

Figure 2 Results for the deformation of cantilever beam.

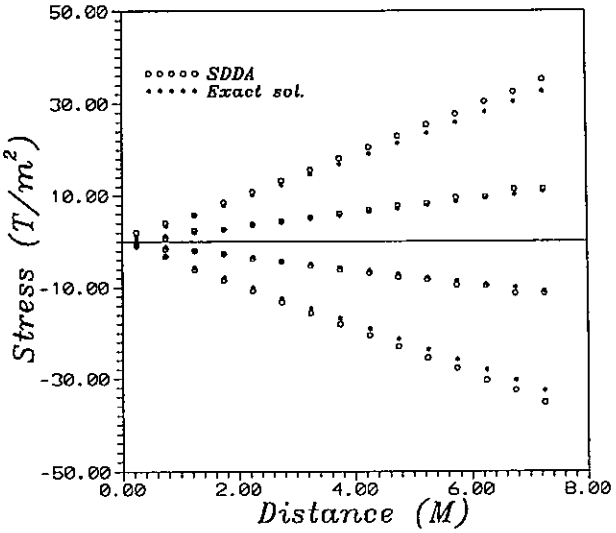

Figure 3 Results for the distribution of σ_x at the centroid of blocks.

4.3 Example 2

A beam with both ends fixed and subjected to concentrated load P at the center was used for validation. The dimensions and material parameters are the same as example 1. For this analysis, the beam was divided into 32 sub-blocks as shown in Figure 4. The results computed from Second Order DDA are summarized and plotted in Figure 5.

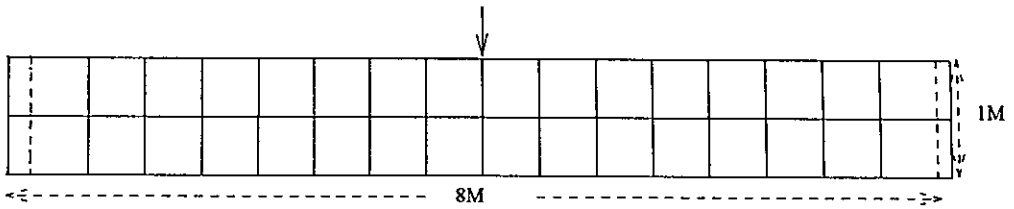

Figure 4 The 32 rectangular sub-blocks for example 2.

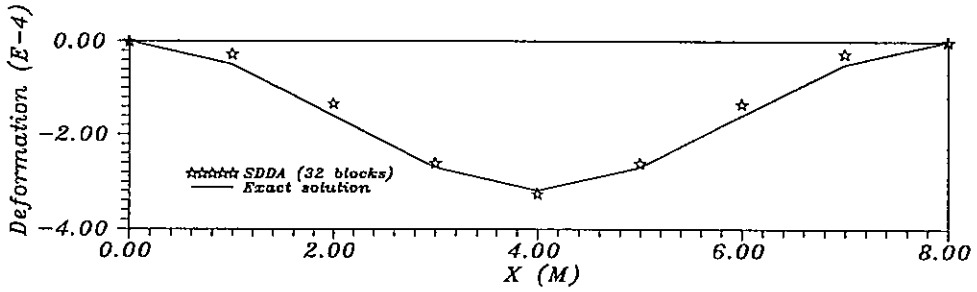

Figure 5 Results for the deformation of fixed beam.

4.4 Example 3

The third example used a uniformly loaded linear elastic plate with a central circular opening to study the effect of stress concentration. To simplify the calculation, a slice of the plate as shown in Figure 6 was used. The problem was analyzed by using 8 blocks together with 2 rigid blocks to provide the frictionless lateral boundaries which simulate the condition of zero circumferential displacement. The results of stress concentration factors for radial stress, circumferential stress and shear stress at the block centroid together with the analytical solutions are shown in Figure 7. Very good agreement in results may be seen even for the very crude blocks adopted.

5. DISCUSSION OF RESULTS

In 1993, a new version of DDA was released in which tensile strength between blocks can be assumed. Hence, the simulation of continuum becomes possible. Second Order DDA follows the same approaches used in 1993's DDA so that it is able to simulate the problems of continuum. But modifications are needed and described as follows.

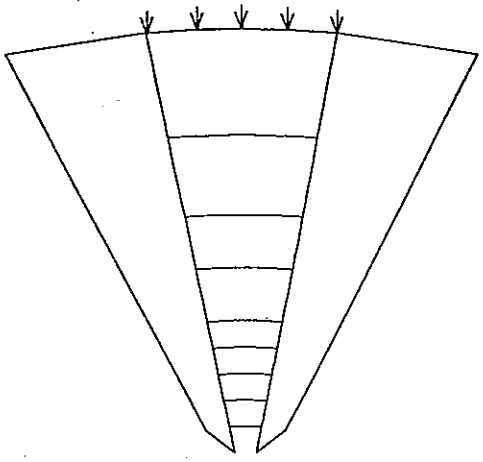

Figure 6 Block system for simulating the Kirsch solution.

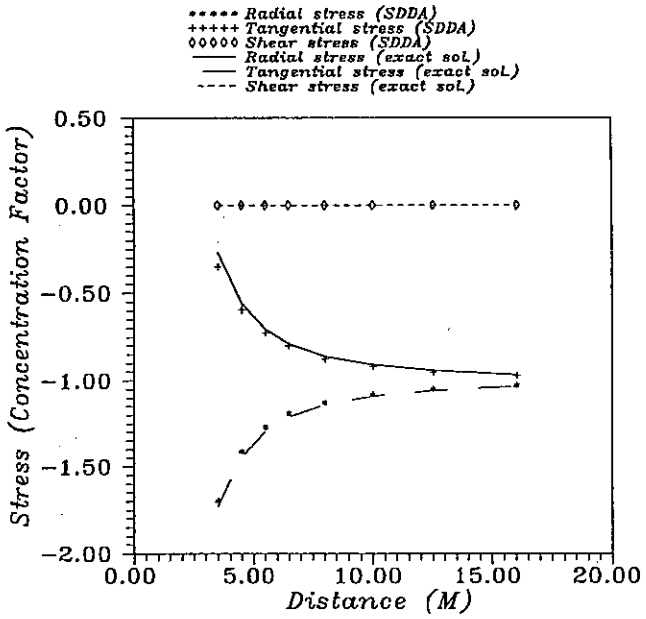

Figure 7 The Results Calculated by Second Order DDA.

5.1 Multiple Co-line Vertex Edge

In DDA, the deformation of each block can be efficiently drawn by two-vertices e lge under the assumption of linear strain and stress inside element. However, it is not suitable for Second Order DDA because the deformation of each block is non-linearly distributed. For improvement, multiple co-line vertices are introduced to the block edge in Second Order DDA so that the image of large deformation may be caught. In other words, the picture of large deformation of block is simulated by piece-wise linear sections along block edge. In order to implement this approach, the original DC program has to be modified and the existence of co-line vertices in each block edge may be allowed. Figure 9 and 11 show the numerical results computed from modified

DC and Second Order DDA programs and they may be compared with the results computed form original DC and DDA programs as shown in Figure 8 and 10. From these Figures, it can be seen that the large deformation along the block edge can be depicted reasonably by modified DC and Second Order DDA programs even if the whole cantilever beam is considered as one block.

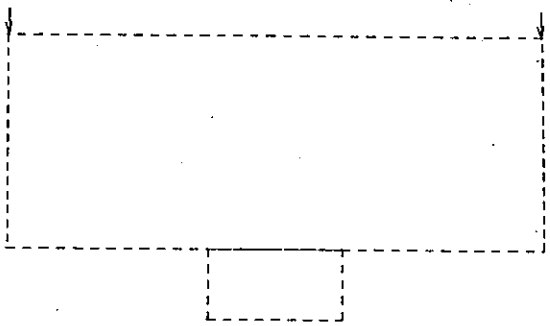

Figure 8 Block system and results for large deformation test by using First Order DDA.

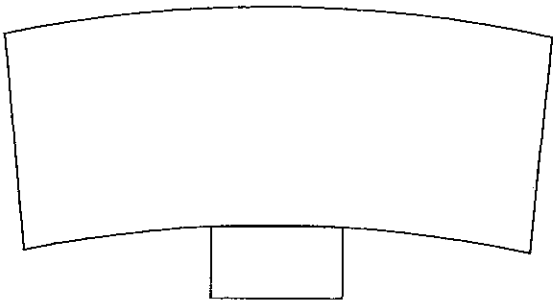

Figure 9 Results for large deformation test by using Second Order DDA.

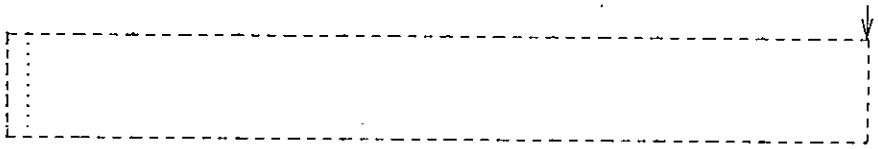

Figure 10 Cantilever beam and results for large deformation test by using First Order DDA.

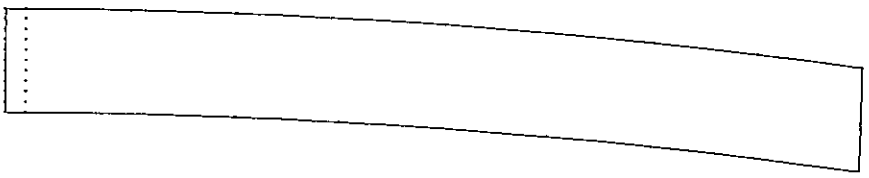

Figure 11 Results of cantilever beam deformation by using Second Order DDA.

5.2 Influence of Varying k_n

In the current version of DDA, the stiffness of contact spring, k_n, will be adjusted at every time step so that the number of iterations to reach the state of convergence may be reduced. But in solving the problem of cantilever beam which is a continuum problem, the change in spring constant may result in significant error.

To investigate the influence of k_n on the results, a cantilever beam the same as Example 1 with the stiffness of constant spring ranging from 6.5, 100, 1000 and 5000 times of the block modulus was used, and these values were fixed throughout the computation. The results are summarized in Figure 12. It was found that small contact spring would result in excessive deformation as indicated by the solid line in Figure 12. As the spring constant is over 1000, the results converge to a value very close to the exact solution. This means that by changing the contact spring constant during calculation may affect the final solution. From limited experience gained, the contact spring should not only be fixed but also be greater than 1000 times of the Young's modulus of block material in solving continuum problems.

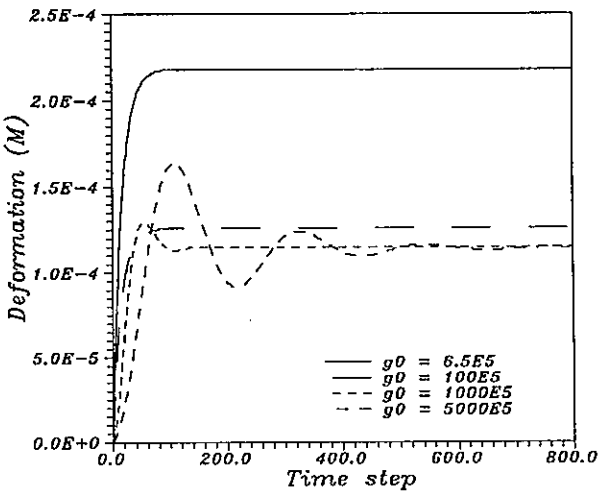

Figure 12 Results for contact spring stiffness test.

5.3 Block Shape Effects

From the results of previous research(Ke, 1993), it was found that the first order DDA can only describe uniform extension in two directions or simple shearing when square sub-blocks are used. Therefore, it can not simulate the problem, such as cantilever beam, appropriately. However, this can be overcome by using the Second Order DDA as shown by the previous examples. It means that the limitations in block shape of the first order DDA may be released. To further illustrate this point, the cantilever beam problem with three different meshes were used. They are 32 rectangular sub-blocks(Figure 1), 64 rectangular sub-blocks(Figure 13) and 34 triangular sub-blocks(Figure 14), respectively. From the results summarized in Figure 15, it appears that the block shape makes no significant difference in results. Unlike DDA by first order displacement function, the results can be very large.

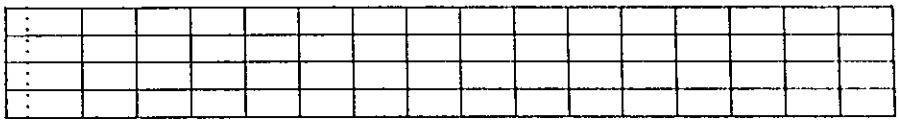

Figure 13 64 rectangular sub-blocks.

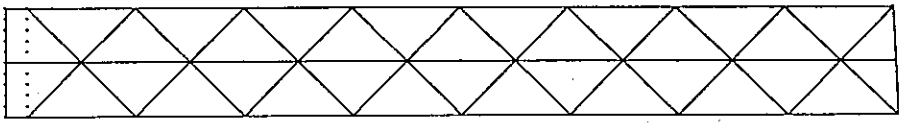

Figure 14 34 triangular sub-blocks.

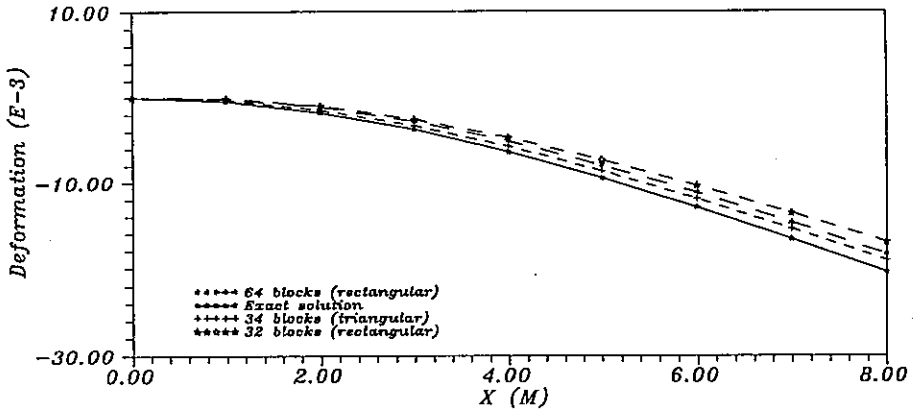

Figure 15 Results for the tests of block shape test.

6. CONCLUSIONS

In this study, the formulation and computer code for the Second Order DDA were developed. Validations have been performed by comparing the results obtained with analytical solutions. From these results, several aspects are observed as follows :

1. From the results of several validated examples, it is obvious that the Second Order DDA is more suitable for simulating continuum problems of large deformation than the first order DDA.
2. Based on the results of analyzing continuum problems obtained in this study, the stiffness of contact spring k_n can affect the results significantly. It appears that reasonable results can be obtained when k_n value is fixed and is greater than 1000 times of block modulus.
3. The adoption of second order displacement function in DDA can reduce the block number required. However, fixing the contact spring stiffness would increase the number of iteration to reach the convergence criterion. Enormous amount of CPU time and memory capacity are the main constraints in applying it to the practical

engineering problem currently. Hence, it is very important to improve the calculation efficiency of Second Order DDA.

4. During the development of Second Order DDA, high order simplex integrations were also derived. This method of integration can also be adopted in other numerical methods, such as finite element and manifold method.

ACKNOWLEDGMENT

The authors are deeply indebted to the original developer of DDA, Dr. Gen-hua Shi, for his continued guidance, assistance and encouragement during the course of these studies. Thanks are also due to Dr. Jeen-shang Lin of University of Pittsburgh for his valuable suggestions and comments in the development of second order DDA formulation. Acknowledgment is also extended to Sinotech Engineering Consultants, Inc. for funding this research project.

REFERENCES

1. Chen, S. (1993), "Slope Stability Assessment Based Upon Discontinuous Deformation Analysis" Ph.D. Dissertation, Dept. of Civil Engineering, University of Pittsburgh
2. Chern, J.C., Chen, S. and Koo, C. Y.,(1995) "Application of DDA in Stability Assessment of Tunnel near Slope", Invited paper for International Journal for Numerical & Analytical Methods in Geomechanics. (in press)
3. Ke, Te-chih (1993), "Simulated Testing of Two Dimensional Heterogeneous and Discontinuous Rock Masses Using Discontinuous Deformation Analysis," Ph.D. Dissertation, Dept. of Civil Engineering, University of California, Berkeley.
4. Lin, J.S. and Chen, S.,(1994)"Determination of Safety of Factor for slope stability analysis by using DDA" Rock Engineering Symposium in Taiwan, pp.269~277.
5. Shi, G.H. (1988), "Discontinuous Deformation Analysis: A New Numerical Model for the Static and Dynamics of Block Systems," Ph.D. Dissertation, Dept. of Civil Engineering, University of California, Berkeley.
6. Shi, G.H. (1994) ,"Discontinuous Deformation Analysis with Simplex Integrations", Geotechnical Lab., U.S. Army Engineer Waterways Experiment Station, Vicksburg.
7. Shi, G.H. (1994) ,"Manifold Method of Material Analysis", Geotechnical Lab., U.S. Army Engineer Waterways Experiment Station, Vicksburg.
8. Shyu, K. K. (1993), "Nodal-based Discontinuous Deformation Analysis" Ph.D. Dissertation, Dept. of Civil Engineering, University of California, Berkeley.
9. "The Application of Discontinuous Deformation Analysis in Rock Mechanics" Report to the Research Foundation of Sinotech Engineering Consultants, Inc., Taipei. Taiwan. (in press , in Chinese) ◦
10. William, H.P., Saul, A.T., William T.V. and Brian, P.F.,(1992) "Numerical Recipes", Cambridge University Press, New York.

Study on the Performance of Tunnel near Slope by DDA

S. Chen, J.C Chern and C.Y. Koo

Geotechnical Research Center, Sinotech Engineering. Consultants, Inc., Taipei, R.O.C

1. INTRODUCTION

Tunnels are often constructed near the slope of mountain ridge to meet the alignment requirement and/or to minimize its length. Results of analytical study[1,2] and case histories have demonstrated that they often lead to unstable conditions as indicated by large tunnel closure and cracking on the slope surface. In the extreme case, it could cause instability in slope and/or tunnel rendered the remedial measures very expensive and difficult.

A section of highway project was planned to pass through the periphery of mountain ridge. Due to the alignment requirement, a 3-lane roadway would have to be constructed using tunneling method and the other line by open cut in the original design. The slope is about 100m high, and the overall slope angle is around 30°. Excavation for the top half section of tunnel and the slope with 8 benches were carried out simultaneously. Reinforcement for the slope were installed right after the excavation of each bench. When half of the tunnel excavation was completed and two more benches of slope excavation remained to be done, monitoring data showed excessive slope movements and tunnel closures occurred with accompanying cracks in shotcrete slope protection and in shotcrete tunnel lining. The total monitored ground settlement and horizontal movements at berm 5 range from 10 to 30 cm and 20 to 35 cm respectively. The crown settlements in the tunnel are around 25 to 35 cm.

Numerical analyses have been conducted through the computing code named FLAC to study the stability of tunnel-slope by using elasto-plastic continuum model. Extensive yield zone around the tunnel and tension zone in the upper part of the slope were obtained from these studies. However, due to the special geological structure presented at the site and the evidence of shear plane development from inclinometer data, the results from continuum model may not be very useful in explaining the failure mechanism and in the choosing of effective remedial measures.

Discontinuous Deformation Analysis, DDA, was first developed by Gen-hua Shi[3] in late 1980's. It is a rigorous solution with a complete scheme of block kinematics in dealing with complicated interaction between discrete blocks under ensured equilibrium conditions at any time by minimizing the total potential energy of the system. It is capable of simulating the discontinuous as well as continuous masses as demonstrated by Shi[3], Yeung[4], Chen[5], Ke[6], Chen, Koo and Chern[7], and Koo, Chern and Chen[8]. Therefore, DDA was adopted to analyze the performance of the tunnel-slope by

considering the geological conditions at the site and the construction procedures used in the field. It intends to understand whether the mechanism of developing unstable situation is due to the toppling of slope or sliding of surficial layer due to slope and tunnel excavation. Comparison studies[9] on the effect of the tunnel excavation on the stability of the tunnel/slope were also conducted. It also intends to evaluate the suitability of DDA in solving engineering problem.

2. GEOLOGICAL CONDITIONS AND ROCK CHARACTERISTICS

2.1 Geological Structure

The rock strata encountered at the site belong to Nan-kang formation of Miocene sedimentary rocks. It consists mainly of massive sandstone and a zone of sandstone/shale interbeds near the toe of the slope as shown in Fig. 1. The uniaxial compressive strength of rock core are in the range of 1500 to 3000 t/m^2 for fresh sandstone and 400 to 900 t/m^2 for weathered sandstone. The strength of sandstone/shale interbeds is very low and the uniaxial compressive strength of rock core is generally less than 500 t/m^2.

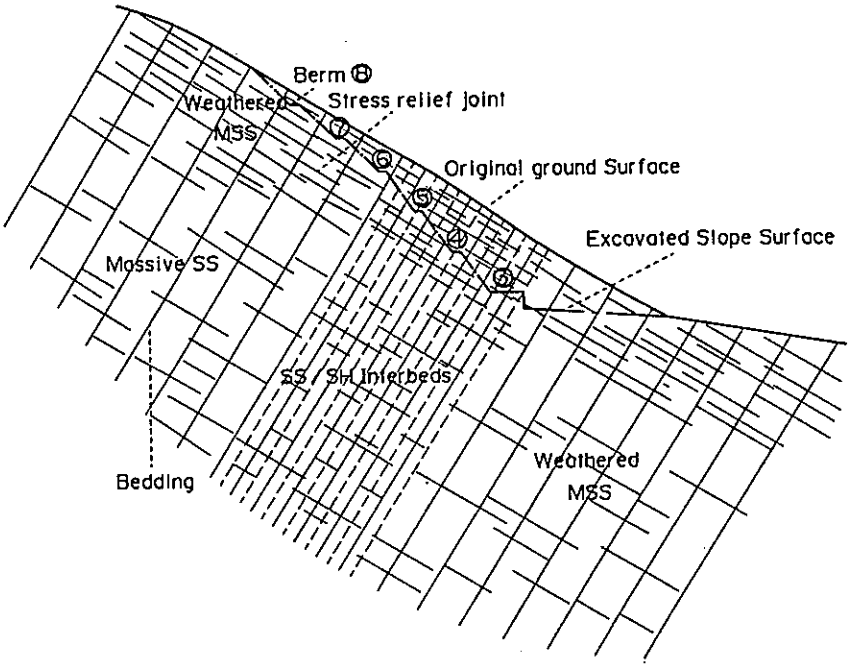

Fig. 1. Geological conditions.

The rock strata strike more or less paralleled to the slope and dip 55° to 65° into the slope. The major weak planes controlling the slope stability appear to be the beddings and stress relief joints. Bedding seams are well-developed with spacing ranging from several centimeters in the sandstone/shale interbeds to tens of centimeter to several meters in massive sandstone. Clay seams and slickensides are prevalent in these planes.

The stress relief joints, which run more or less parallel to the slope surface, are well-developed in the surficial layers as revealed by the drilling cores. The joint spacing is in the range of 10 to 80 cm. At depth, however, they are sparsely developed. These joints are generally stained and filled. The joint development assumed in this study are given in the following table.

Weak planes	Joint Spacing	Joint Length	Bridge	Degrees of Randomness
Bd in MSS	5.0m	100m	0	0.1
Bd in SS/SH	2.0m	100m	0	0.1
Jt in surf. layer	2.0m	15~30m	1.0m	0.1
Jt at depth	4.5~7.5m	20~45m	2.2m	0.8

2.2 Rock Properties

For simulation purpose, the rock masses are divided into 4 distinct zones with similar rock properties and joint development. They are: (1) well-jointed, weathered massive sandstone on the slope surface, (2) fresh massive sandstone, (3) sandstone/shale interbeds and (4) weathered massive sandstone near the toe of the slope. Their properties including elastic moduli of rock masses, Mohr-Coulomb strength parameters for weak planes are assumed as follows:

Zone	Rock Blocks	Weak Planes	
	Elastic Moduli (t/m^2)	$c(t/m^2)$	ϕ (degree)
(1) Jointed, W. MSS	40,000	0	20°
(2) Fresh MSS	200,000	20	36°
(3) SS/SH	40,000	2	20°
(4) W. MSS	40,000	2	20°

3. NUMERICAL MODELING

3.1 Modification of DDA Code

The DDA code of 1993 Version developed by G. H. Shi was used as basic code in this study. In order to deal with practical engineering problem, several modifications of the code have been made to simulate the complicated geological conditions, in-situ stresses, staged excavation and rock reinforcement. The modification included the following aspects.

(1) ' Line Producing Program (DL)

In the original DL program, the joints are produced by using statistical information of spacing, length, bridge and degree of randomness for each joint set. However, the same pattern of joint development is produced in the entire analytical domain. In this study, the code was revised to contain several zones in the domain. Different joint patterns can be generated in each zone according to its statistical joint information.

(2) In-situ stress generation and restart function

In engineering problem, the in-situ stress conditions are the resultant of gravitational force and tectonic stress. The distribution of the stresses is further influenced by topographical and geological conditions. It is generally very complicated and can not be predetermined easily and precisely in a block system. In this study, the in-situ stresses existed in the slope before construction were produced by a consolidation stage and a restart function was added into the program for carrying out further stage of analysis. The excavation was simulated by taking off the blocks in the excavation area. By implementing these functions, a better simulation to the in-situ stress conditions and excavation procedures in the field can be made.

(3) Cable Element

In the original code, cable reinforcement was not included although the formulation was provided in the manual. In the current version, simple, linear elastic cable elements were incorporated for considering the rock reinforcement installed to stabilize the rock masses.

3.2 Problem Modeling

From the geological model and joint development assumed, the block system for analysis is shown in Fig. 2. The in-situ stress conditions at the site are considered mainly due to gravitational force and are influenced by the topography. The in-situ stresses were generated by consolidating the rock blocks under gravity with horizontally fixed lateral roller boundaries. This process was terminated when the settlement reaches a stable condition.

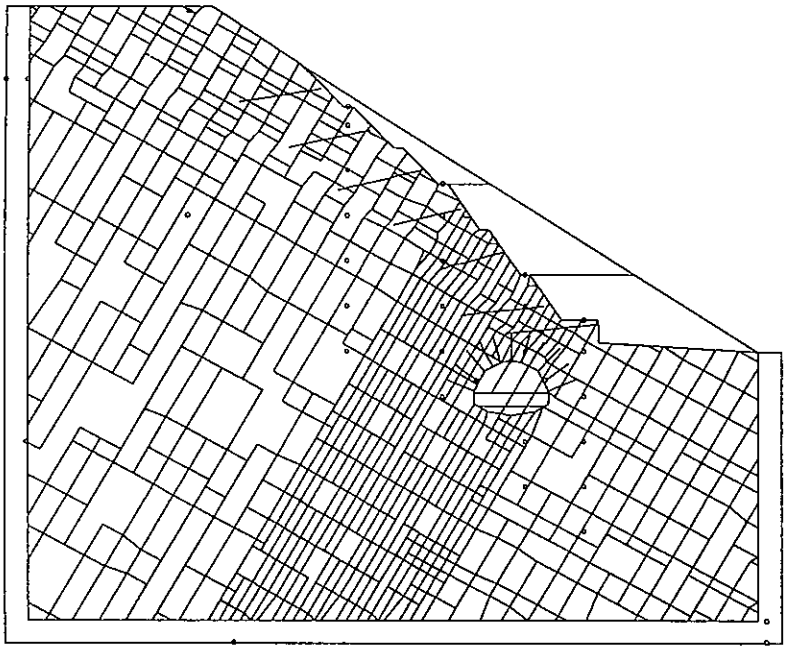

Fig. 2. Generated block system for analysis.

After consolidation, the slope excavation was simulated by taking off the preset blocks in one step. 15 to 20 m long, 60 t capacity prestressed cable anchors spaced at 3m were also activated during slope excavation. When the effects of slope excavation reaches a stable condition, the top half of the tunnel was excavated and 6 m long, 15 t capacity rock bolts spaced at 1.5 m activated. For comparing the influence of tunnel location on the slope and tunnel stability, a case by moving the tunnel away from the strata of weak sandstone/shale interbeds was also analyzed. Another case is also analyzed for studying the behavior of tunnel deformation which is induced by the further excavation on the lower part of tunnel.

29 measuring points were prescribed in the analytical model to monitor the rock movements during the processes of consolidation, slope excavation and tunnel excavation. The locations of measuring points are shown in Fig. 2.

4. DISCUSSION OF RESULTS

The initial stresses before excavation and the stress conditions at the ends of slope and tunnel excavation are illustrated in Fig. 3, 4 and 5, respectively. The deformed configurations of the whole block system at various construction stages are also shown in the figures. The displacements occurred at the points monitoring the movement of slope of the model are summarized in Fig. 6 for comparison purpose. The configuration and deformation of blocks near tunnel at various excavation stages are displayed in Fig.7 and 8. The settlement at tunnel's crown and the convergence of tunnel during different excavation stages are summarized in Fig.9 and 10. For comparison, the monitoring data of the crown settlement and the convergence of tunnel at field during different excavation stages are also summarized in Fig.11. From the results obtained, the following points may be observed.

(1) The movements of the slope are predominantly settlement at the top, lateral bulge near the toe and the combination of lateral and downward settlements at the mid-height of the slope. Macroscopically, no apparent discontinuity in the deformation pattern can be observed.

(2) The predominant shearing of weak plane occurs along the bedding plane. This cause slight toppling of rock strata in the surficial layers around berms 4 to 6. This is consistent with the crack development observed in the field.

(3) The calculated slope movements and field monitoring data are shown in the following table.

	Slope Movement (cm)		Tunnel Settlement (cm)
	mid-height	top	at crown
Numerical analysis	30(H), 12(V)	28(V)	17.5(V)
Field data*	10~28(H), 20~35(V)	13(V)	25~35(V)

* Field data not including the movements induced by two heavy storm events.

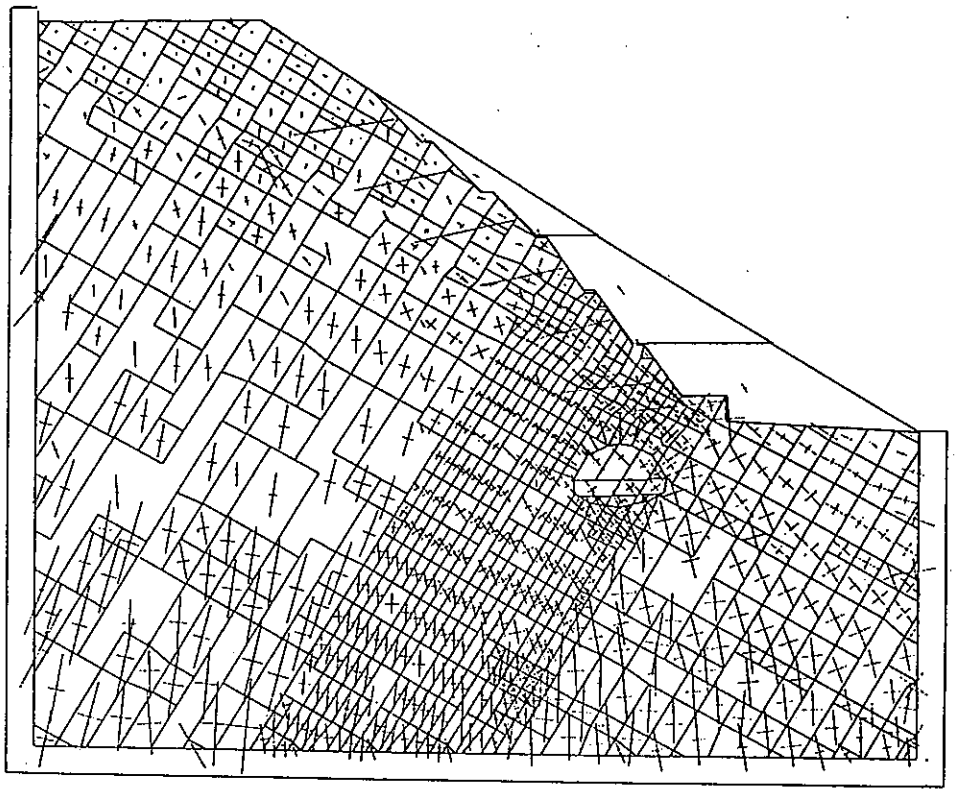

Fig. 3. Configuration and initial stresses before slope excavation.

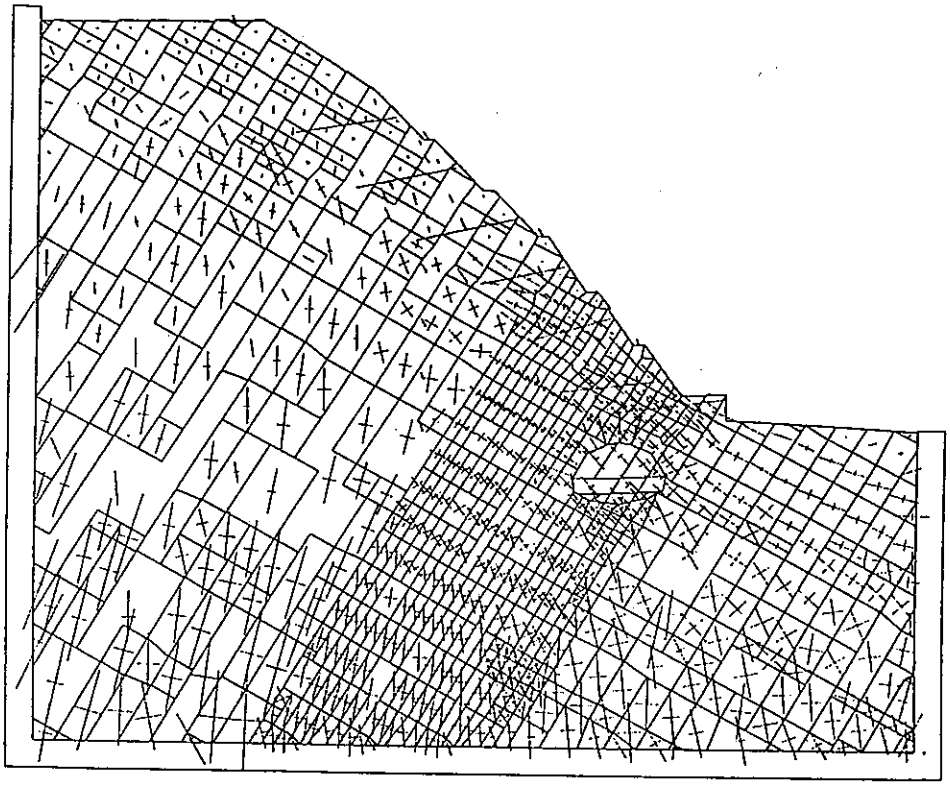

Fig. 4. Configuration and stresses at the end of slope excavation.

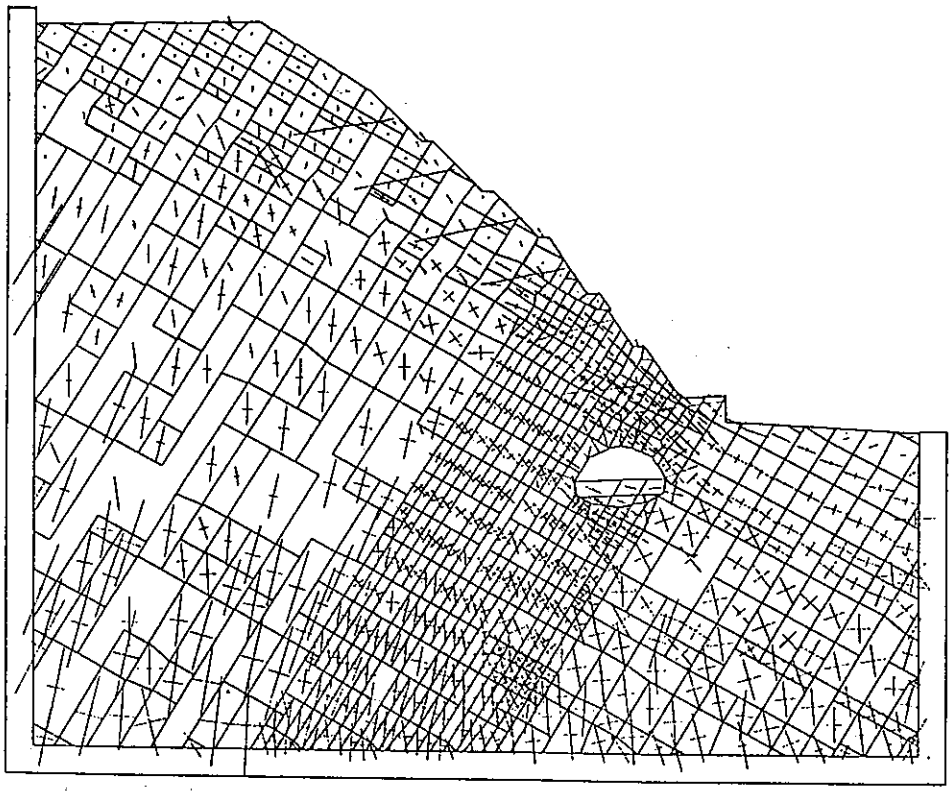

Fig. 5. Configuration and stresses after the excavation of upper part of tunnel.

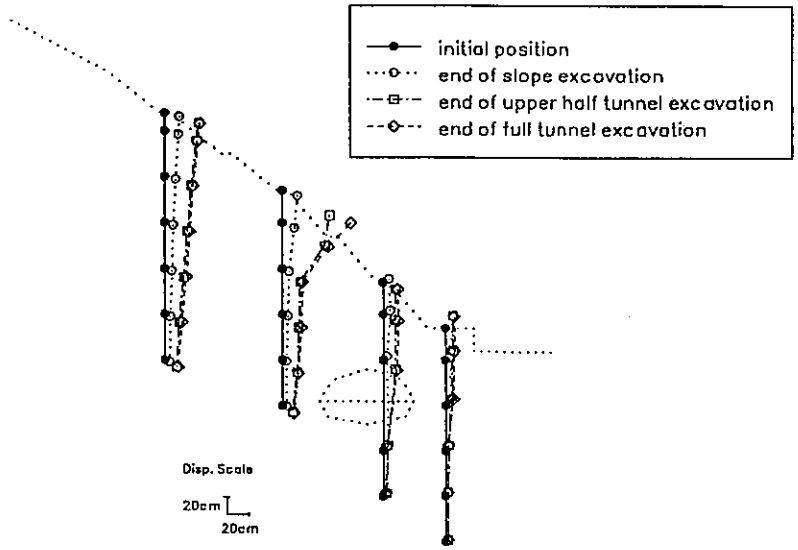

Fig. 6. Displacement induced by excavation.

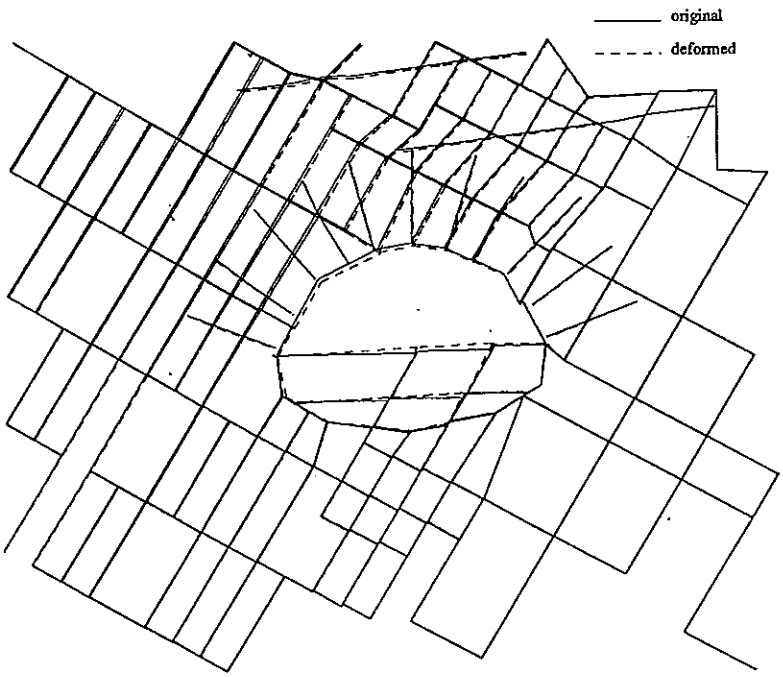

Fig. 7 Deformation of blocks around tunnel after the upper part excavation.

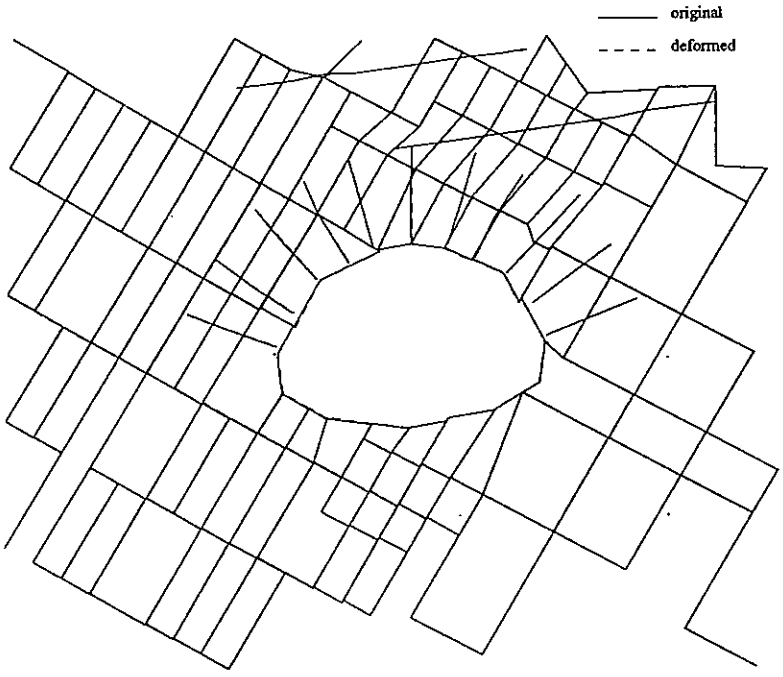

Fig. 8 Additional deformation of blocks around tunnel after the completion of tunnel excavation.

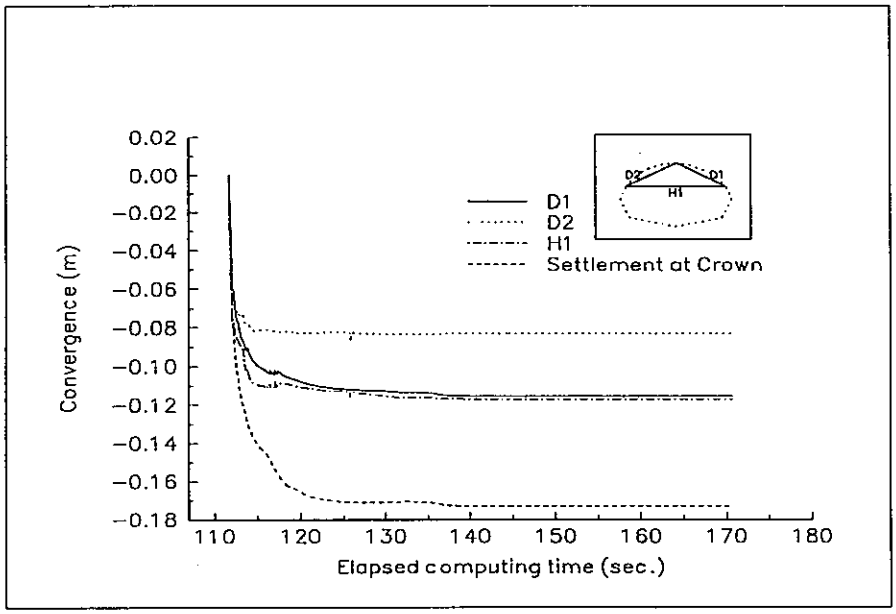

Fig. 9 Tunnel Convergence due to the excavation of upper part of tunnel.

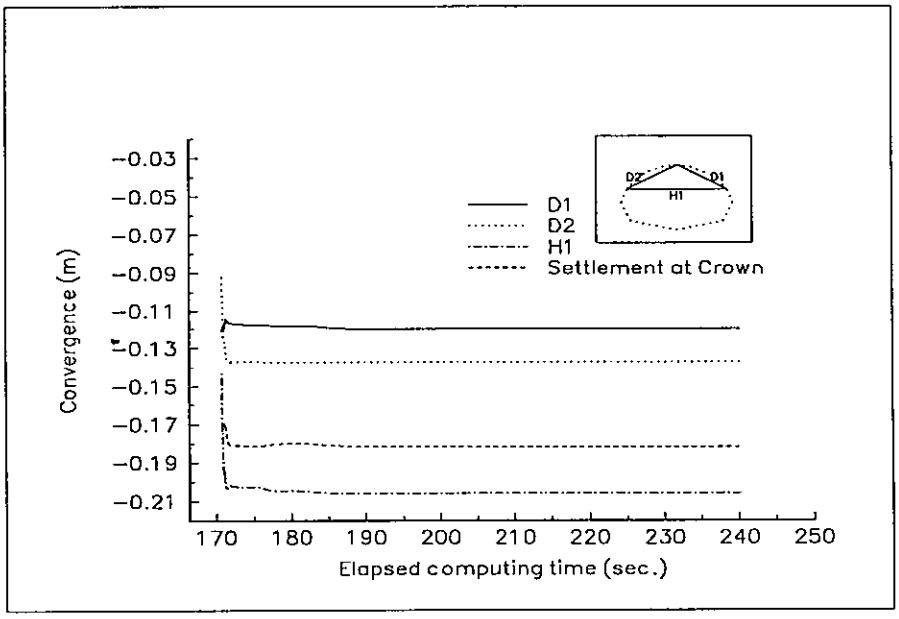

Fig. 10 Tunnel Convergence due to benching and invert excavation.

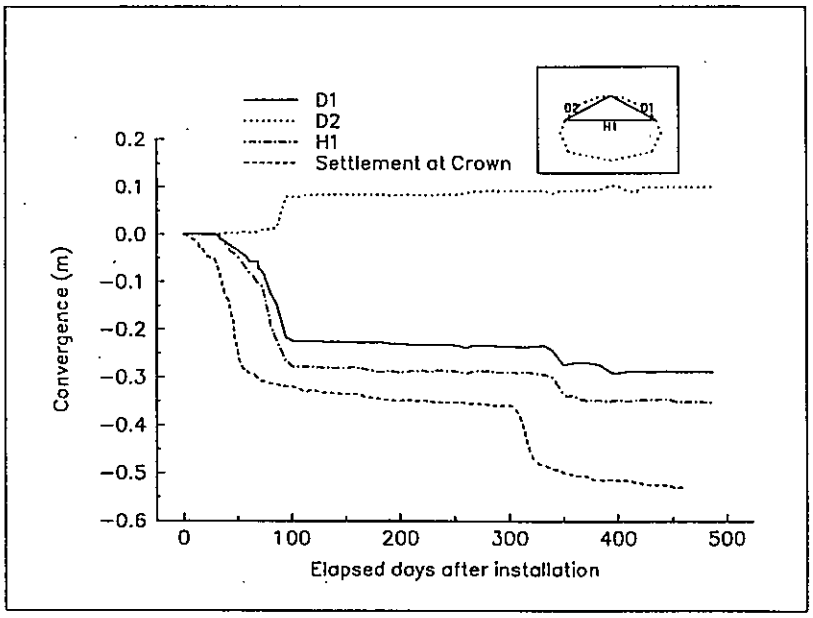

Fig. 11 Tunnel Convergence from monitoring.

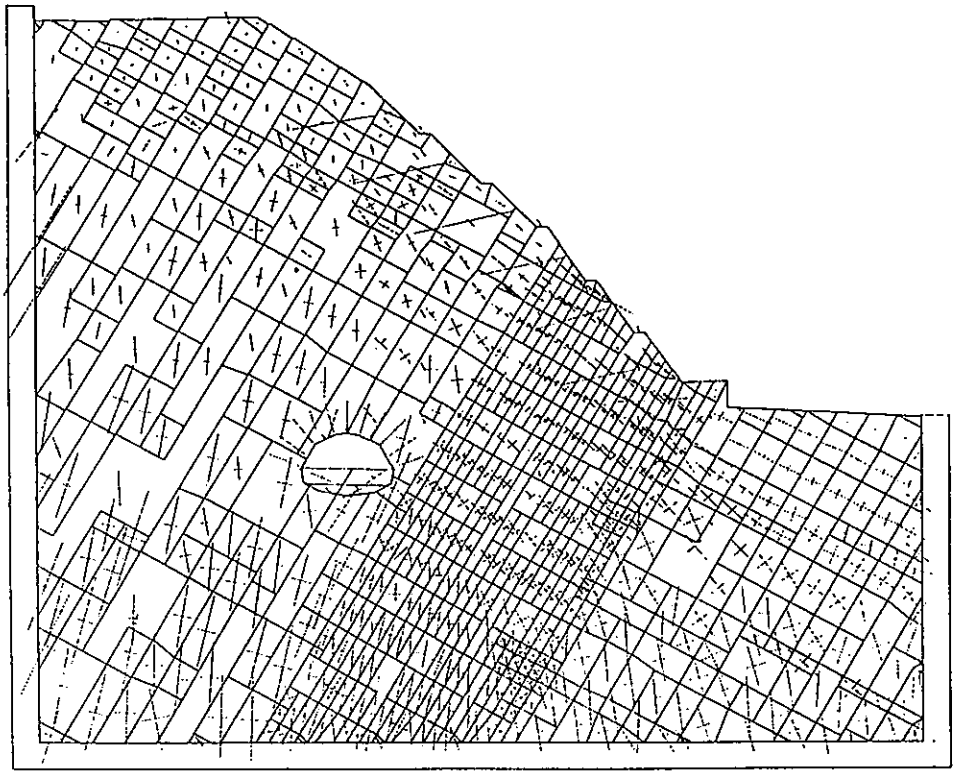

Fig. 12. Configuration and stresses after the excavation of upper part of tunnel for alternative tunnel position.

It may be seen that the numerical analysis results are in the same order of magnitude as those measured in the field if the effect of two storm events were not included. It slightly over-estimates the settlement at the top of the slope and under-estimates the settlement at the crown of the tunnel.

(4) Aside from the effect of storm events which was simulated in the current analysis, the major discrepancy is in the trend of diagonal convergence measurement D2. In the field, a small relative extension at the two measuring points were obtained as shown in Fig.11. However, net convergence in D2 was obtained in the analysis as indicated in Fig.9.

(5) With the aid of Fig.7, it is observed that the convergence of tunnel from the hill side and the heave of the temporary tunnel invert are mainly induced by the stress release from the left upper part above tunnel. That also indicates that the excavation of tunnel will have a negative effect on the stability of slope.

(6) Further benching and invert excavation of tunnel was analyzed and the results are summarized in Figs.6, 8 and 10. From Fig.6, the movement along slope in this stage is not obvious except some local area near surface. Figs.8 and 10 show that the movements of blocks around tunnel are minor and mainly occur on the left side and bottom of tunnel. This phenomenon may be explained by the fact that the stresses in the invert area are released during the excavation of the upper portion of tunnel as indicated by Fig.5.

Based on the observations described above, it appears that there is no imminent danger of slope instability. However, two heavy storm events, which is not considered in this study, triggered slips of the slope. Considerable amount of additional slope and tunnel movements were observed. As indicated by inclinometer data, continuous slip plane might have been formed. This analysis may not be able to predict such a behavior due to much wider joint spacing adopted as compared with the 10 to 80 cm spacing observed in the field. Also the elastic, constant strain block model used would constrain the development of large sliding rock mass by a key block, unless much smaller block sizes are used or block fracturing are incorporated. Therefore, the development of continuous slip plane maybe the reason for different trend of left diagonal measurement (D2) in tunnel convergence obtained from numerical simulation and field measurement.

It may be seen that considerable slope movement occurred during slope excavation. An additional movement around 10~30 cm in the surficial layer occurred during tunnel excavation. This is the result of weakening in toe support by the tunnel excavation. An alternative tunnel excavation scheme by moving the tunnel into a deeper position to avoid the weak SS/SH strata near the toe of the slope was analyzed. The final results are shown in Fig. 12, the pattern of slope movement in Fig. 13, deformation of blocks near tunnel and tunnel convergence during tunnel excavation in Fig.14~17. Much smaller downward slope movement may be observed, and the toppling of surficial layer is less severe. The deformation and convergence of tunnel are also insignificant. Therefore, this tunnel excavation scheme would be more favorable for the stability of slope and tunnel. This is consistent with the results obtained from numerical analysis and field experiences.

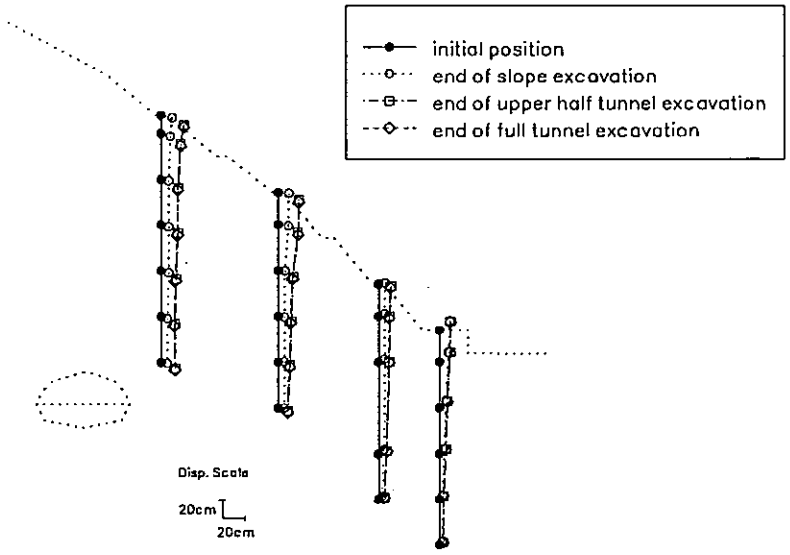

Fig. 13. The displacement induced by excavation for alternative tunnel position.

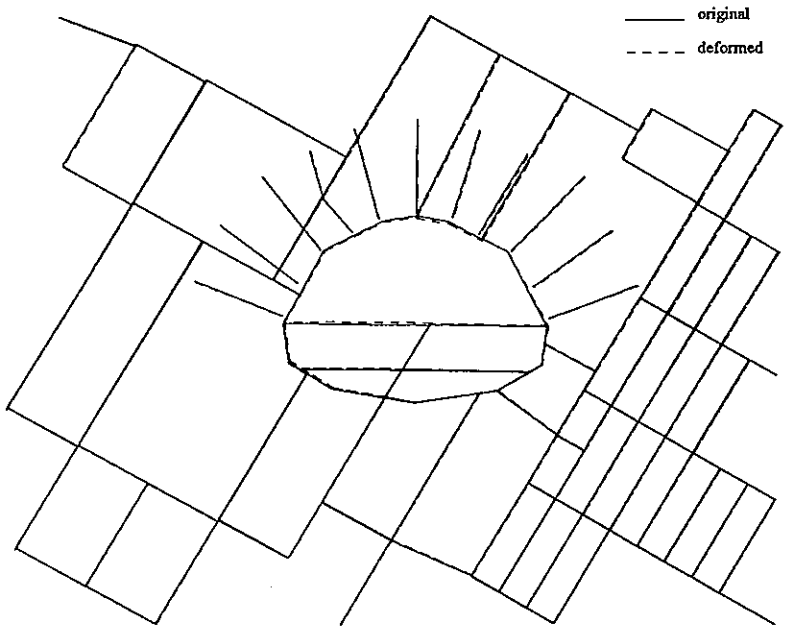

Fig. 14 Deformation of blocks around tunnel after the upper part excavation for alternative tunnel position.

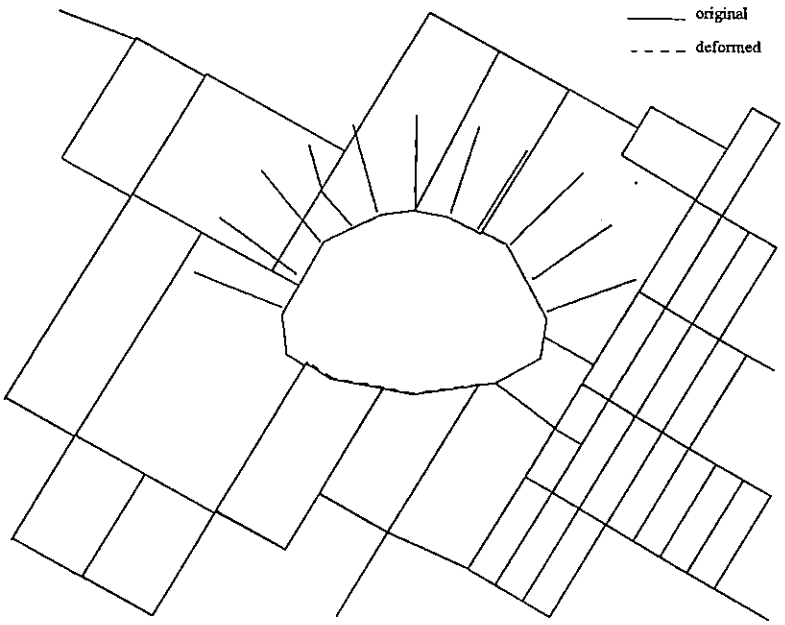

Fig. 15 Additional deformation of blocks around tunnel after the completion of tunnel excavation for alternative tunnel position.

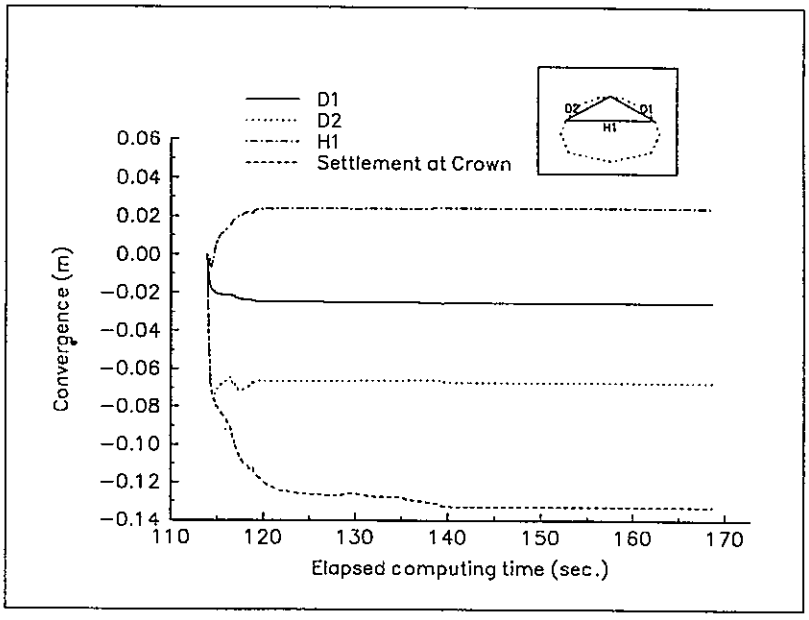

Fig. 16 Tunnel Convergence due to the excavation of upper part of tunnel for alternative tunnel position.

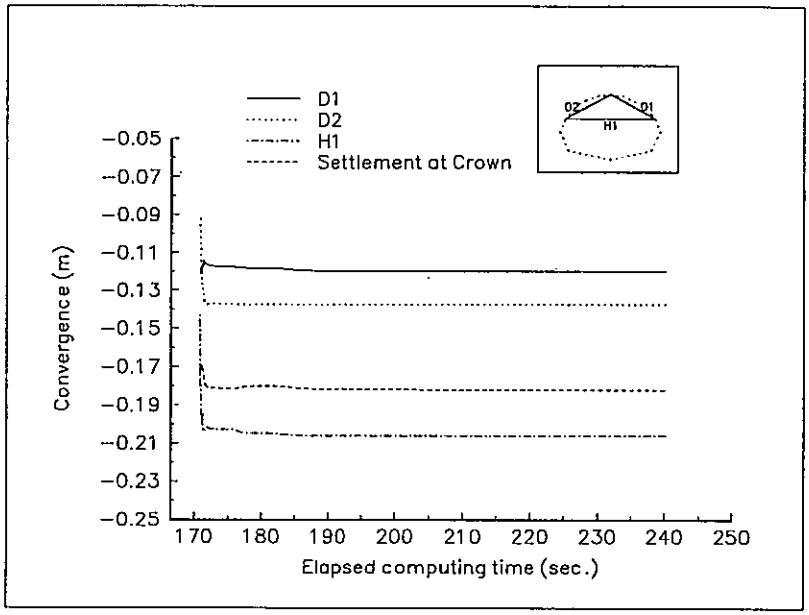

Fig. 17 Tunnel Convergence due to benching and invert excavation for alternative tunnel position.

5. CONCLUSIONS

This paper describes a preliminary attempt in using the DDA method for analyzing a complicated engineering problem. Following conclusions may be drawn from these studies.

(1) From the comparison of numerical results with the field performance, it appears that DDA method can model the slope/tunnel behavior qualitatively prior to the influence of two storm events.

(2) Current DDA version lacks the function of developing block fracture and internal uplift pressure. Therefore, it can not model the development of sliding plane or the effect of rising ground water table.

(3) To model the behavior of an engineering problem more accurately, it requires a closer simulation of block system in the field. However, the main limitations lies in the memory capacity of computing facility and the computing time required.

ACKNOWLEDGMENTS

The authors are deeply indebted to the original developer of DDA, Dr. Gen-hua Shi, for providing the newest version of DDA source code as well as continued guidance, assistance and encouragement during the course of these studies. Thanks are also due

to Dr. Tze-ping Lin and Dr. Te-Chi Ke for their valuable comments. In addition, the field information and well-prepared monitoring data provided by Mr. Kuan-lin Lin and Mr. Fu-yuan Shaw are also appreciated. Acknowledgment is also extended to Sinotech Engineering Consultants, Inc. for funding this research project.

REFERENCES

1. Hoek, E., "Lessons from Case Histories in Rock Engineering, " Course notes, Department of Civil Engineering, Univ. of Toronto (1991).
2. Wang, M.T., Lin, K.L. and Chern, J.C., " Stability of Tunnels Excavated near Sloped Surfaces," *Proc., Int. Symp. on Application of Computer Methods in Rock Mechanics and Engineering*, Xian, China (1993).
3. Shi G. H., "Discontinuous Deformation Analysis: A New Numerical Model for the Static and Dynamics of Block Systems," Ph.D. Dissertation, Dept. of Civil Engineering, University of California, Berkeley (1988).
4. Yeung, M. R. and Goodman, R. E., "Use of Shi's Discontinuous Deformation Analysis on Rock Slope Problems." *Stability and Performance of Slopes and Embankments II, Geotechnical Special Publication No. 31, ASCE,* 461-478 (1992).
5. Chen, S., "Slope Stability Assessment Based Upon Discontinuous Deformation Analysis" Ph.D. Dissertation, Dept. of Civil Engineering, University of Pittsburgh (1993).
6. Ke, Te-chih, "Simulated Testing of Two Dimensional Heterogeneous and Discontinuous Rock Masses Using Discontinuous Deformation Analysis," Ph.D. Dissertation, Dept. of Civil Engineering, University of California, Berkeley (1993).
7. Chen, S., Koo, C.Y. and Chern, J.C., "The Study on Simulating the Behavior during Excavation in Gravel Deposit by Discontinuous Deformation Analysis," *Proc. International Symposium on Underground Construction in Gravel Formations,* Taipei, Taiwan, 1995, Part 1, 31-40 (1995). (in Chinese)
8. Koo, C.Y., Chern, J.C. and Chen, S., "The Development of the Second Order Displacement Function for Discontinuous Deformation Analysis," *Proc. The 6th Conference on Current Researches in Geotechnical Engineering in Taiwan,* 1995, 665-674 (1995). (in Chinese).
9. Chen, S., Chern, J.C. and Koo, C.Y., "Preliminary Study on Application of DDA in the Stability Assessment of Tunnel Near Slope," *Proc. The 6th Conference on Current Researches in Geotechnical Engineering in Taiwan,* 1995, 943-952 (1995). (in Chinese).

DDA Combined with the Artificial Joint Concept

Te-Chih Ke[1]

[1]Chung Yuan University, Chungli, Taiwan, R.O.C.

ABSTRACT: This paper presents new capabilities of Shi's discontinuous deformation analysis (DDA) when combined with "the artificial joint concept". These capabilities refine the determination of the stress field within selected blocks of any shape, and permit simulating fracture propagation in intact blocks. Implementation of this concept does not sacrifice the simplicity and beauty of the original DDA formulation and code. When compared with the other improvement schemes for DDA, this conceptual scheme seems to be more flexible and practical.
KEYWORDS: discontinuous deformation analysis, artificial joint concept, refined stress field, fracture propagation.

1. INTRODUCTION

Discontinuous deformation analysis (DDA) was introduced in 1988 by Dr. Shi [1], with constant stress within each block of a discrete block system. Since then, accumulated efforts have been attempted to explore its full potential. Table 1 provides a partial list of the current and future developments of DDA, according to the personal opinion of the author (some of which are extracted from the reference [2]). This paper describes an innovation for DDA modelling - "the artificial joint concept" that computes variable stress states within blocks, thereby allowing modelling of problems with complex block domains containing holes, interior blocks, or cracks. The latter capability permits analysis of problems of fracture propagation across previously intact blocks. The scheme involves the addition of *artificial joints* which subdivide blocks. The artificial joints are assumed to be infinitely strong if the intra-block stress field is simply to be detailed within a block, but not perturbed. Assignment of finite strengths to the artificial joints allows perturbation of the block stresses as new fractures form and propagate.

Table 1 Partial list of current and future developments of DDA

Group	Sub-group	Contributors
DDA Blocks	Refined stress field	Shyu [3], Ke [4], Chang [5], Koo etc. [6], Ma [7], Shi [8]
	Non-linearity	Chang [5], Ohnishi etc. [9]
	Fragmentation	Lee [10], Lin etc. [11]
	Fracture propagation	Ke [4], Lin etc. [11]
	3D DDA blocks	Shi [12]
	Circular blocks	Lin [13], Ke [14]
	Coupled flows	-
Block contacts/ Joints	Strength properties	Shi [15], Ke [4]
	Joint dilation	Thapa [16]
	Non-linear laws	-
	Lagrange multiplier	Hilbert etc. [17], Lin etc. [11]
Various constraints	Displacement const.	Ke [4], Ohnishi etc. [9]
	Force constraints	Ke [4]
Insight studies	Time integration	Ke [4]
	Rigid-body rotation	Yeung [18], Ke [4]
	Simplex integration	Shi [19]
Applications	Rock slopes	Yeung [18], Ke [20], Chen & Lin [21]
	Underground works	Ke [4], Chang [5], Yeung etc. [22]
	Rock foundations	Yeung [18]
	Particulate media	Lin [13], Ke [13]
	Composite materials	Shyu [3], Ke [23]
	Fracturing	Ke [4], Lin etc. [11]
	Impact	-
	Joint flows	-
	Reliability-coupling	-

2. DISCONTINUOUS DEFORMATION ANALYSIS

A system of simultaneous equations in DDA is formulated by minimizing the total potential energy of a block system. The total potential energy includes that belonging to individual blocks and that due to contact interactions. Inertia terms are implicitly included; the global stiffness matrix is positive definite and diagonally dominant. If a 'static' mode is chosen, the velocities of all the blocks are set to zero at the start of every time step and DDA resembles a pseudo-static analysis. If a 'dynamic' mode is specified, DDA yields a real-time response of a block system. DDA incorporates complete block kinematics to fulfill constraints of no inter-penetration of blocks and no

tension between blocks[1]. The interactions between blocks are simulated by linear contact springs.

Shi's original DDA code can handle a system of linearly elastic blocks subjected to large displacements, rotations and deformations, and fairly general loading conditions. However, it does not analyze fracture propagation because the modelled blocks are not allowed to degrade during the process of deformation. Further, since DDA uses a first-order displacement function, each block is modelled by a single constant stress state, no matter how complicated its geometry. Figure 1a shows a complex block domain with a notch at the left, one isolated crack below and another with a branching crack above the notch, and two interior boundaries at the right. (The spaces within the interior boundaries may be holes or other blocks.) Obviously it is unrealistic to assume this complex region has a single constant stress state. Under a certain loading condition, fracture may initiate from near or at the crack tips or the notch (Figure 1a).

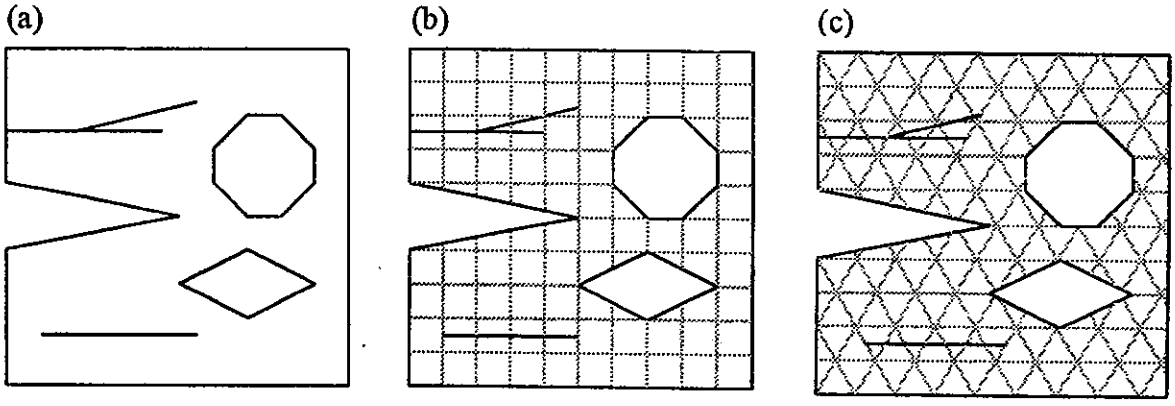

Figure 1 (a) A block with complex geometry and interior features; and refined geometry by: (b) Type A artificial joints; (c) Type C artificial joints

3. THE ARTIFICIAL JOINT CONCEPT

The artificial joint concept includes two parts: *cutting* and *patching*. Cutting is a process of *dividing* a DDA block into sub-blocks by a certain pattern of artificial joints so that the block becomes an assemblage of sub-blocks created by imaginary boundaries. (Of course, the selection of artificial joint patterns affects the simulation results of DDA, and this subject will be discussed in the latter section.) Patching is a process of assigning strengths to the artificial joints to *glue* sub-blocks together.

If the artificial joints are infinitely strong, the contacts between sub-blocks never fail, leading to continuous connection of two adjacent sub-blocks by contact springs. As the stiffness of contact springs increases, the contact sides of two adjacent sub-blocks will displace similarly. As a result, the assemblage of sub-blocks behaves as a continuous

[1] the 'no-tension' constraint can be relaxed for incipient joints which are assigned a tensile strength.

body like the original block but with refined stress distribution since DDA computes a constant stress state for each sub-block.

If the artificial joints are assigned finite strengths, they provide potential cracking paths wherever contact forces exceed limiting values. The energy loss due to cracking is represented by the strain energy release of failed contact springs. Accordingly, fracture propagation of an intact block along a predestined path can be simulated. The failure criterion for (τ,σ) along the contacts between sub-blocks follows the Mohr-Coulomb's law with a tensile strength *cut-off*. Ke [4] added to the DDA code the procedures to deal with joints having cohesion and tensile strength, in which contact pairs, each composed of two contact points, need to be sought first.

Artificial joints intersecting the cracks, or boundaries of holes and interior blocks, allow these complex features to be modelled. In this case, after artificial joints have been added and a block system generated, DDA analyzes the contact behavior along real joints as well along artificial joints. Figures 1b and 1c show the resultant sub-block systems of the block domain in Figure 1a by adding regular artificial joint meshes. Note that any portions of the added artificial joints outside the refined domain have been automatically deleted by the joint mesh generator. Type A artificial joint mesh (Figure 1b) contains two orthogonal joint sets and generates rectangular sub-blocks; Type C artificial joint mesh (Figure 1c) contains three joint sets to produce equilateral triangular sub-blocks. However, it can be seen in these figures that the sub-blocks formed near the outer or interior boundaries of the block are not regular at all. There are another three artificial joint mesh types available to refine a homogeneous and/or isotropic block domain, as follows.

Type	Number of joint sets	Sub-blocks formed
B	4	Right-angle triangular
D	2	Diamond-shaped
E	3	Hexagon-shaped

4. NUMERICAL EXAMPLES

The applicability of DDA combined with the artificial joint concept is illustrated by the following five examples. The 'static' analysis of DDA is used in the first three examples; while the 'dynamics' analysis of DDA is used in the last two where a progressive failure is involved.

4.1 Cantilever Beam

This example examines the performance of Types A and C artificial joint meshes for stress analysis in a cantilever beam. The beam, 8m long and 1m high, is fixed at its left end and is loaded at its right tip. The Young's modulus and Poisson's ratio of the beam are 100 MPa and 0.2, respectively; the tip load is 100 kN. Type A artificial joints divide the beam into 128 sub-blocks; while Type C artificial joints cut the beam into 228 sub-blocks. The added artificial joints have infinite strength.

Figure 2a shows the deformed geometry and principal stress field[2] of the Type A refined beam. The results are unsatisfactory; all sub-blocks have the same tensile principal stress at -45° and the same compressive stress at 45°. The whole beam responded in simple shear rather than bending, because the deformed shape of the rectangular sub-blocks generated by Type A artificial joint mesh is restrained by, the first-order displacement function used in DDA, to deform only into parallelograms[3].

Figure 2b depicts the deformed geometry and principal stress field of the beam refined by Type C artificial joints. In contrast to Figure 2a, Type C mesh allows the beam to deflect, developing a neutral axis with tensile fiber stress in its upper part and compressive fiber stress in its lower part. This example shows the adequacy of Type C artificial joints to detail beam structures. Ke [4] examined other cases with smaller deflection, in which Type C artificial joint mesh yielded results agreeing with those calculated using classical simple beam theory.

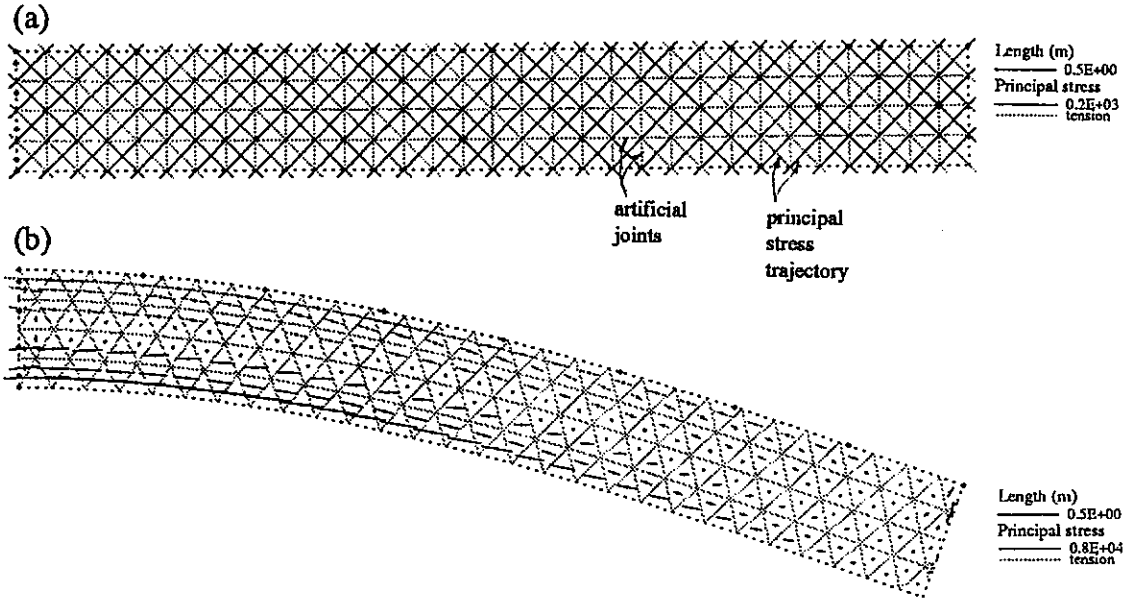

Figure 2 Principal stress field of: (a) Type A refined beam; (b) Type C refined beam

4.2 Stress Concentration Near a Crack Tip

Analytical solutions to two-dimensional crack problems for various loading conditions show that the stresses at a small distance r from the crack tip always vary as $r^{1/2}$ [24]. Two behavioral modes of a crack, Mode I (in-plane opening) and Mode II (in-plane shearing), are investigated here. Figures 3a or b show a block, 1m high and 1m wide,

---

[2] the principal stress field described in this paper means the DDA graphic output showing the principal stresses of each block at its centroid; compressive stresses are indicated by solid lines and tensile stresses by dotted lines.

[3] this is no longer true when using a higher-order displacement function.

with a horizontal crack extending six tenths of the way across its width; the block is fixed at its two bottom corners. In Figure 3a, a vertical load P pulls the upper-left corner of the block upward, causing crack opening (Mode I); in Figure 3b, a horizontal load H at the left end of the top crack wall causes sliding (Mode II crack shearing). The block has the same Young's modulus and Poisson's ratio as in the cantilever beam example and the crack is assigned zero friction to signify the sliding behavior in Mode II. The cracked block was refined into 252 sub-blocks by Type C artificial joints with infinite strength.

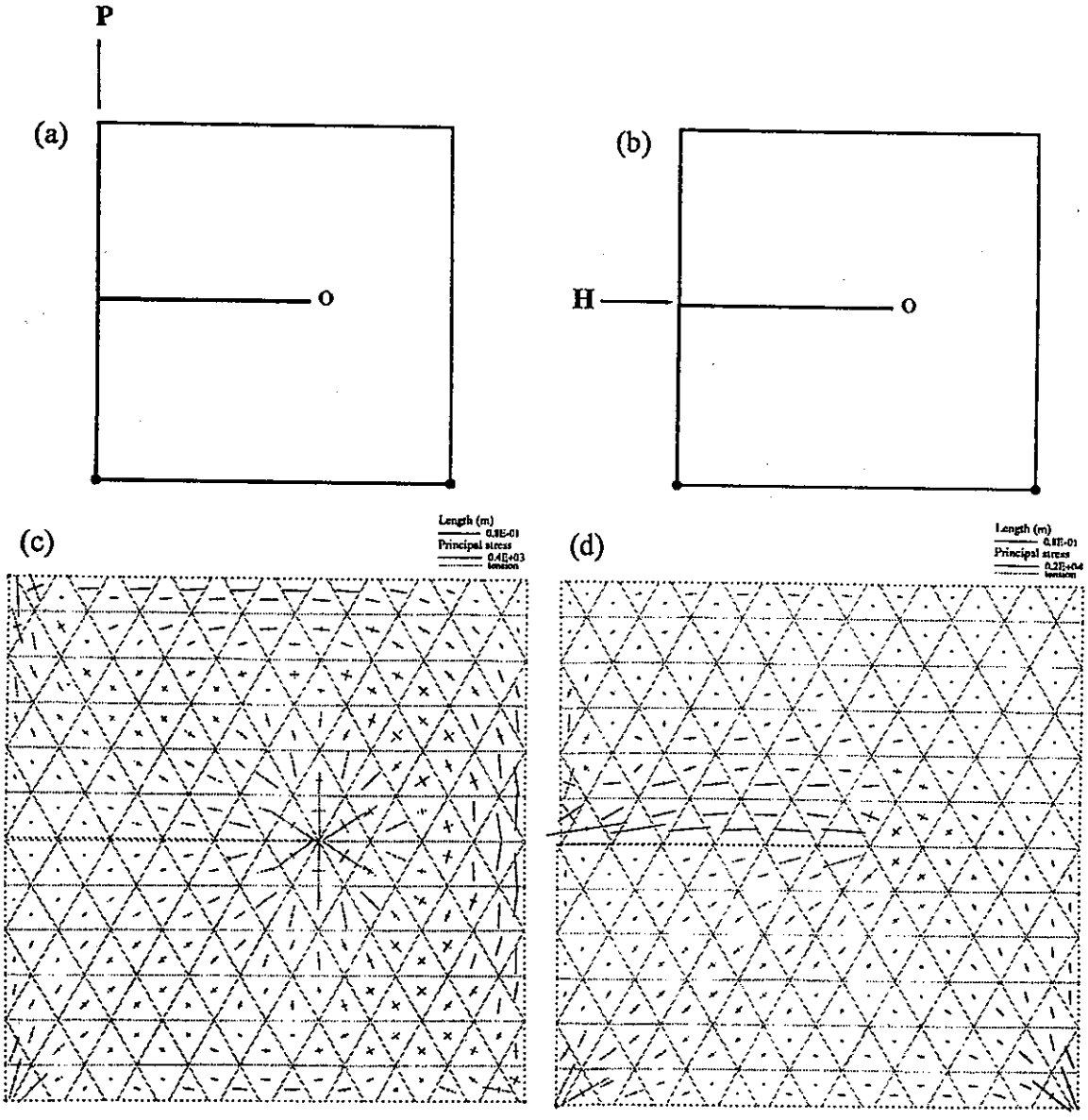

Figure 3 A block with a crack: (a) vertical load P (Mode I); (b) horizontal load H (Mode II); (c) principal stress field (Mode I); (d) principal stress field (Mode II)

Figure 3c shows the deformed geometry and principal stress field of the cracked block subjected to $P=10$ kN. In this figure, the crack is open, and higher values of tensile principal stresses are present near the crack tip in the radial direction. If more sub-blocks are used, the stress concentration near the crack tip in Mode I will be more precisely described.

Figure 3d depicts the deformed geometry and principal stress field of the cracked block subjected to $H=100$ kN. The adjacent crack walls are in contact at the tip and on the left end, but open between these two points. Higher compressive principal stresses run from the loading point, along the top crack wall, around the tip, then attenuate finally to merge toward the lower-right fixed corner; tensile stress is distributed below the crack wall and concentrated near the lower-left fixed corner.

4.3 Block-in-Matrix Materials

A block-in-matrix material contains isolated (interior) blocks which are embedded within a matrix. The properties of the matrix and interior blocks may not be the same; the interfaces between the matrix and interior blocks are inherent discontinuities. The matrix domain represents a complex space which contains interior boundaries and is thus not simply-connected. The global behavior of a block-in-matrix material is a function of the proportion, orientation, arrangement, and size of interior blocks and, especially, the interface strengths [23].

Figure 4 shows two specimens from a particular case of block-in-matrix materials, *melange*, found in the subduction zones paralleling present and ancient convergent plate margins. Melange is distinguished by its oriented lenticular interior blocks. The specimen in Figure 4a contains 19 horizontally oriented blocks (shaded areas) which occupy 40% of the total "volume"; that of Figure 4b has 27 vertically oriented blocks covering 58% of the "volume".

Young's moduli of the matrix and interior blocks are 250 and 420 MPa, respectively; both materials have the same Poisson's ratio of 0.4. The interfaces are assumed to be frictionless. A *numerical* uniaxial compression test was conducted on both specimens (Figure 4) by adding stiff loading plates on the top and bottom of the *specimen*. The bottom plate is fixed; a vertical load, P, is applied to the top of the upper plate. The displacements of selected points around the specimens were used to compute their overall secant moduli and Poisson's ratios[4]. The matrix domain was refined by Type C artificial joints with infinite strength.

Table 2 lists the DDA results of two specimens, in which moduli are expressed in units of MPa. Both specimens behave non-linearly, indicated weakly by the computed secant moduli and more convincingly by Poisson's ratios[3]. The non-linear behavior derives from the large number of frictionless interfaces that undergo sliding in several directions, leading to continuous reduction in stiffness with increasing load. Some of the interfaces intersect the outer boundaries, especially on the free side walls of the specimens (Figure 4), further degrading the overall stiffness. Table 2 also shows that although the block proportion of Specimen 2 is higher than that of Specimen 1 by 18%, the increase in modulus is not proportionally large. This is probably because Specimen

[4] ratios of average horizontal to vertical displacements revealed by the output.

2 loses some stiffness due to increased chance for sliding along its longer frictionless interfaces.

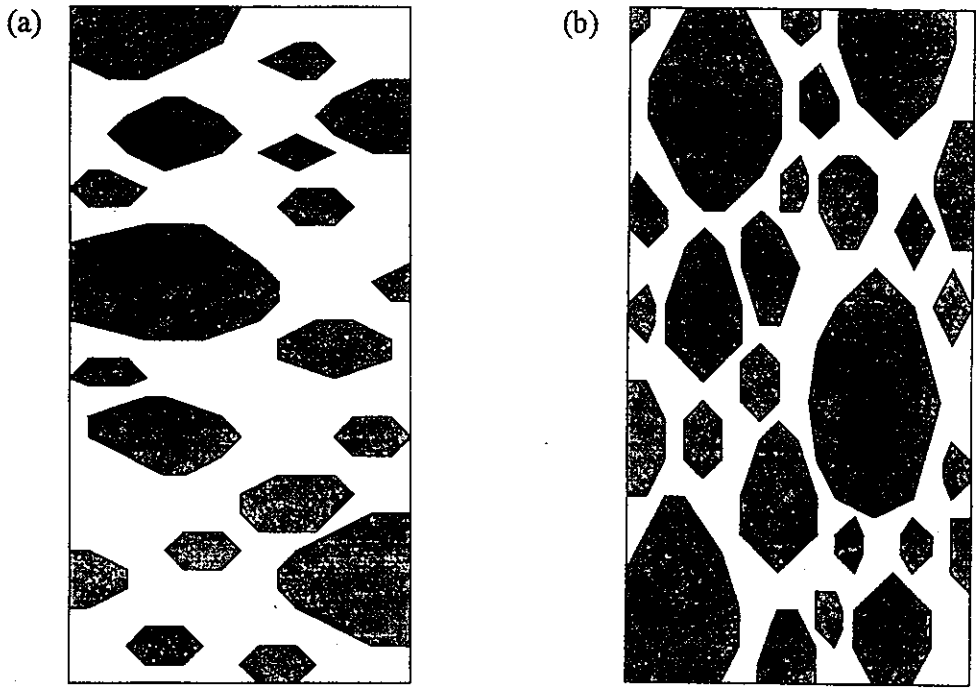

Figure 4 Melange specimens: (a) specimen 1 with 19 horizontally oriented blocks; (b) specimen 2 with 27 vertically oriented blocks

Table 2 Computed secant moduli and Poisson's Ratios in Example 3

	P=1(kN)	P=2(kN)	P=5(kN)	P=10(kN)
Secant moduli: Specimen 1	298.5	298.0	297.9	297.9
Secant moduli: Specimen 2	312.2	310.3	309.9	309.9
Poisson's ratios: Specimen 1	0.4819	0.5165	0.5262	0.5205
Poisson's ratios: Specimen 2	0.5986	0.6595	0.8422	0.8755

4.4 An Arch Dam Subjected to Impact

As an example of showing the fracture propagation capability of this refined scheme, cracking and destruction of an arch dam subjected to enormous impact is simulated here. Figure 5a gives a plan view of an arch dam abutting on jointed rock and a huge block at t=0 approaching the dam in the indicated direction. Points 1 to 11 are fixed. Because an arch dam is always made of rectangular concrete blocks, Type A artificial joints were used to refine the dam into 36 concrete sub-blocks, as depicted in Figure

5a. Each concrete sub-block was not further refined at the stage of this study.

Young's modulus and Poisson's ratio of the dam are 1000 MPa and 0.2, respectively, and those of the abutments are 200 MPa and 0.2, respectively. All joints in the abutments are cohesionless and have a friction angle of 15°; the interfaces between the dam and abutments have a friction angle of 30° and a cohesion of 0.1 MPa. The added artificial joints (interfaces between concrete blocks in the dam) have a limited strength: a friction angle of 30°, a cohesion of 0.1 MPa and a tensile strength of 0.03 MPa. The velocity of the approaching rock is 141.1 m/sec.

Figure 5b shows the deformed geometry of the dam at t=0.002sec when the rock just hit the dam. Many interfaces near the collision point fail (indicated by solid lines), and lose their initial cohesion and tensile strength. Two gaps form in the interfaces of concrete blocks below the impact point. At t=0.003sec, cracking of interfaces is propagating into the two wings of the dam, as revealed in Figure 5c. Figure 5d depicts the significantly deformed geometry of the dam at t=0.01sec. In this figure, no interface survives at this time, and remarkable gaps arise between the concrete blocks below the hitting point. At this stage, imagine that water at a reservoir pressure enters these gap, leading to the total collapse of the dam.

4.5 A Flying Object Hitting a Shelter Roof

This imaginary example provides a second illustration of fracture propagation within a solid structure. As depicted in Figure 6a, the structure subjected to impact resembles a military shelter for tanks or aircraft, which is composed of 80 concrete blocks (this was also done using Type A artificial joints). A warhead-like object is approaching the middle point of the shelter at a downward velocity of 100 m/sec. The foundation block are fixed at its three corners.

Young's modulus and Poisson's ratio of the shelter and foundation are 1000 MPa and 0.2, respectively. The interfaces between the shelter and foundation have a friction angle of 30° and a cohesion of 0.1 MPa. The added artificial joints (interfaces between concrete blocks in the shelter) have a finite strength: a friction angle of 40°, a cohesion of 0.05 MPa and a tensile strength of 0.01 MPa.

Figure 6b shows the deformed geometry of the cracking shelter at t=0.0015sec when the object started to penetrate the shelter roof. Many interfaces near the collision point fail (indicated by solid lines), and lose their initial cohesion and tensile strength. At t=0.01sec, cracking is propagating into the two wings of the shelter, as revealed in Figure 6c. Figure 6d depicts the total collapse of the initially intact shelter at t=0.05sec. In this figure, the intruding object has already dug into the shelter and the protected object(s) inside will be destroyed shortly.

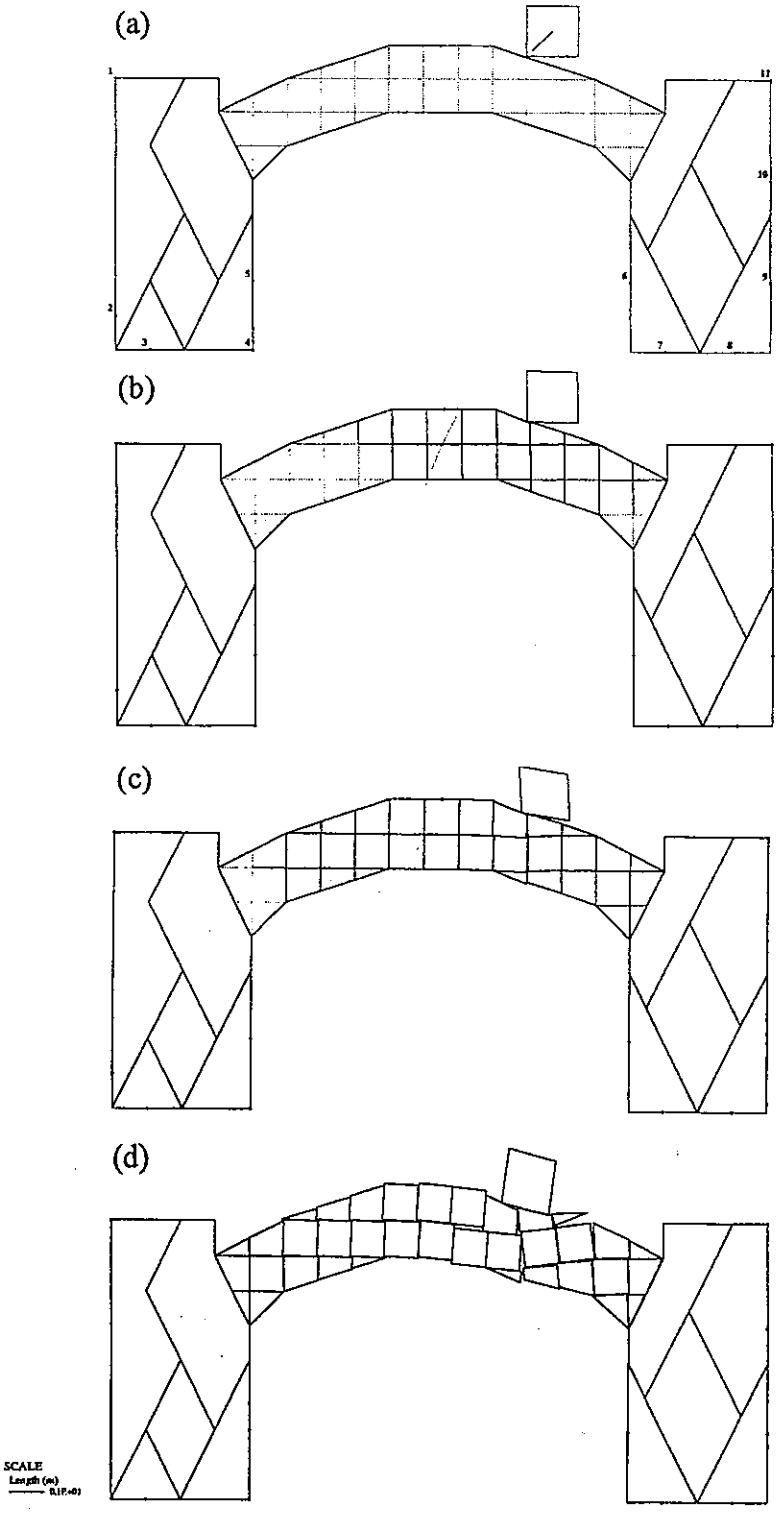

Figure 5 Cracking of an arch dam at t=: (a) 0; (b) 0.002; (c) 0.003; (d) 0.01sec

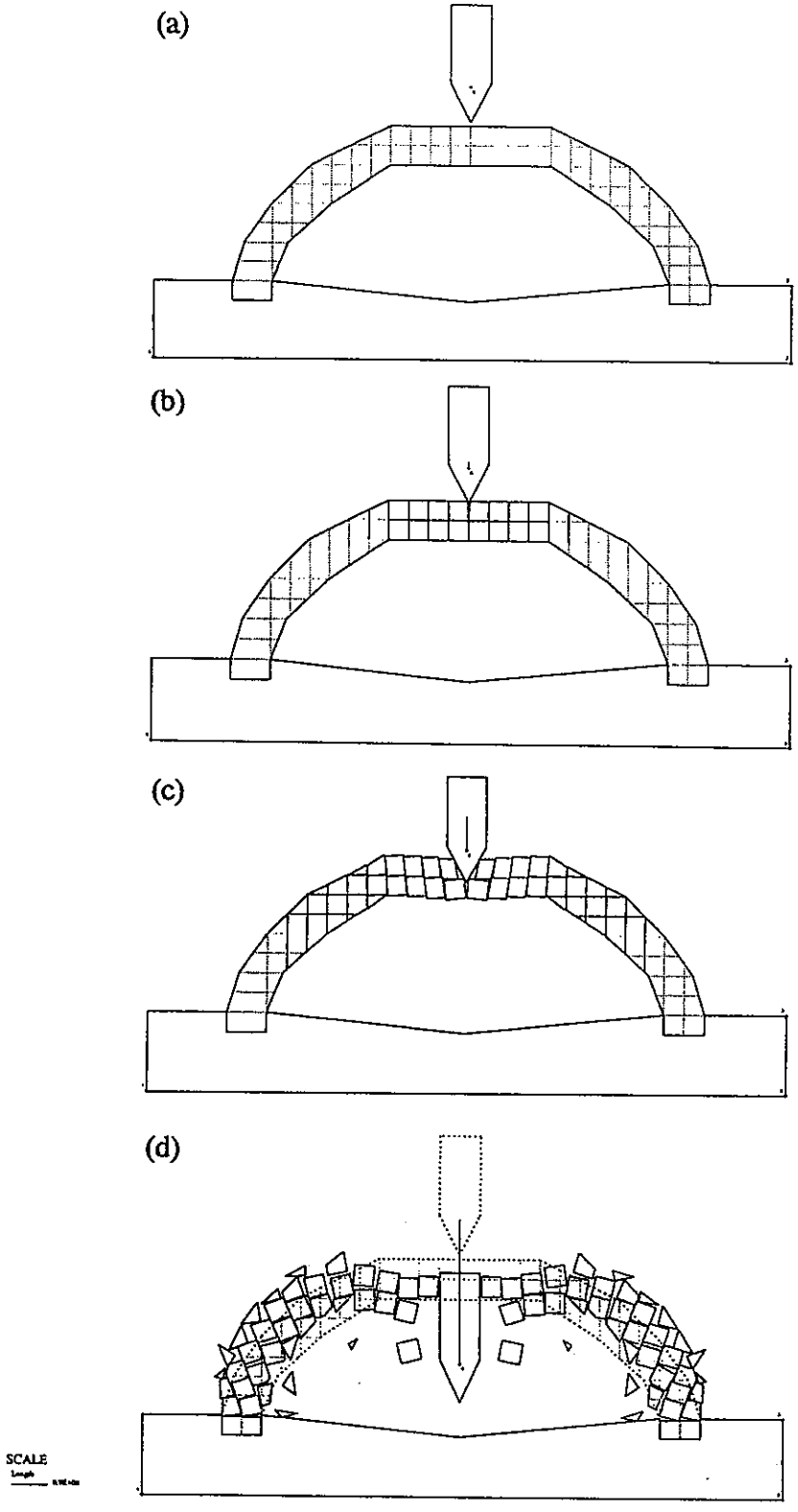

Figure 6 Cracking of an shelter at t=: (a) 0; (b) 0.0015; (c) 0.01; (d) 0.05sec

5. DISCUSSIONS

5.1 Comparison of Various Improvement Schemes

In addition to the artificial joint concept, there are at least three schemes which enable DDA to handle variable stress and fracture propagation within a DDA block. They include using a higher-order displacement function, finite element coupling [3,5], and the manifold method [8]. Tables 3 and 4 compare these schemes with respect to refined stress distribution and fracture propagation capabilities.

Table 2 Comparison of Various Schemes for Variable Stress Capability

Scheme	Computation Need	Complex Block Shape	Inclusions[1]
Higher-order displacement function[2]	-[3]	-[3]	Impossible
FE coupling	O.K.	Need good mesh generator	Need good mesh generator
Manifold method	O.K.	O.K.	O.K.
Artificial joint concept	Higher	O.K.	O.K.

[1] such as non-crossing cracks and interior blocks.
[2] additional nodes needed along initial straight block sides.
[3] depending on the order of displacement function.

Table 3 Comparison of Various Schemes for Fracture Propagation Capability

Scheme	Capability	Energy Loss	Cracking Direction
Higher-order displacement function	Fragmentation only	Damping/$\Delta\sigma$	Any
FE coupling	Possible	Damping/$\Delta\sigma$	Along element boundaries
Manifold method	O.K.	Damping/$\Delta\sigma$	Any
Artificial joint concept	O.K.	Strain energy release of failed contact springs	Along artificial joints[1]

[1] relaxed by allowing the breakage of sub-blocks.

Adopting a higher-order displacement function in DDA is the most straight-forward to attain a varied stress field and to indicate a point where stress concentration occurs and cracking initiates. In this case, since straight block sides become curved after deformation, additional nodes must be added along those long straight block sides for better detection of contacts. The computation time and complexity of block integration involved increase with the order of the displacement function used. However, this scheme alone can not resolve a DDA domain having extremely irregular shape and containing non-crossing cracks or interior blocks. Also because it does not identify and allow non-crossing cracks within a block, it can only simulate the fragmentation of blocks, i.e. a block breaks into two or four pieces instantly.

Since a DDA block/domain is a continuous region, refining it by traditional finite elements is not surprising. The original block unknowns are now replaced by finite element nodal displacements. To refine a complex DDA domain containing non-crossing cracks, a versatile mesh generator is required. It is possible for this scheme to simulate fracture propagation if the element boundaries are allowed to break down. The energy loss due to cracking can be modelled by damping or reduction in stress, which may require input from physical tests.

The manifold method invented by Dr. Shi [8] represents a new approach to analyze the interactions of different material domains based on the concept of separation of mathematical and physical meshes. In its early form, the mathematical mesh used for the blocks is the three-noded finite elements, and a versatile finite element mesh generator is included to refine a block domain even containing swirling non-crossing cracks. Block interactions are modelled according the block kinematics in DDA. With adopting the adequate failure criteria, the fracture propagation within a solid can be readily simulated. However, the energy loss due to cracking must be represented by the same way as used in the above scheme.

When attaining a refined stress distribution under the same order of solution precision, the total number of degree of freedom required by the artificial joint concept scheme are about 40% larger than the other schemes, leading to longer computation time. However, this does not remain true when modelling fracture propagation, in which an intact solid is gradually fractured and finally broken into pieces. In this scheme, the energy-loss associated with cracking is naturally modelled by the strain energy release of failed contact springs, with no need of inputting other measured or artificial quantities. The cracking direction is constrained by the artificial joint network selected, but this problem can be overcome by allowing the breakage of sub-blocks according to a certain failure criterion.

5.2 Selection of Adequate Artificial Joint Meshes

Solid materials are usually composed of crystals or grains in the micro scale, as schematically shown in Figure 7. Figure 7a depicts the interpretive drawing of a thin section of gabbro, in which the main minerals are pyroxene (pyx), plagiclase (plag), iron oxide (Fe), and Figure 7b shows an assemblage of uniform sand grains. The crystal/grain boundaries are essentially softer and weaker than the solid parts of crystal/grains. Therefore, these boundaries are more deformable and represent potential cracking routes. If an artificial joint mesh could match exactly these boundaries or mostly their macro-pattern which would be mappable, then the DDA simulation results

with an adequate displacement function should be much more compatible to the actual behavior of the solid domain, in terms of deformation and strength.

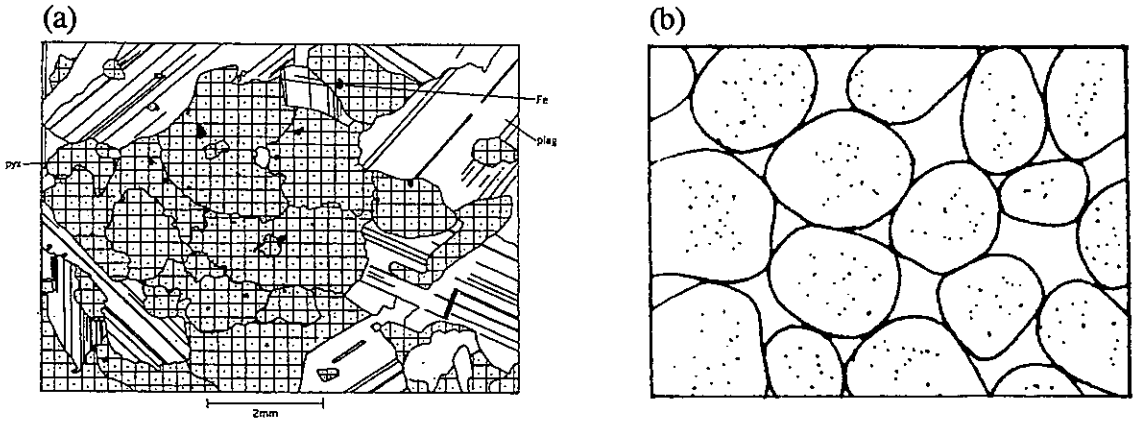

Figure 7 Sketch map of a solid composed of: (a) crystals; (b) grains

For a homogeneous and/or isotropic solid with unknown crystal/grain boundary pattern, a regular artificial joint mesh should be used, like those as described in the Section of The Artificial Joint Concept. If a first-order displacement function is used in DDA, only those generating triangular sub-blocks (such as Types B and C) should be used. In the case of a higher-order displacement function used, all joint mesh types can be adopted. When a transversely isotropic material is encountered, Type A joint mesh may be applied, with one closely-spaced joint set being parallel to the geological structure like foliation.

6. CONCLUSIONS

DDA is a powerful numerical tool to analyze the mechanical response of discrete block systems. Without losing the simplicity and beauty of Shi's original formulation, "the artificial joint concept" was introduced to enhance its capabilities. The new capabilities include determining refined stress distributions even in blocks with complex geometry and interior features, and simulating the fracture propagation of intact blocks. When compared with other improvement schemes, this conceptual scheme seems to be more flexible and practical. Selection of an adequate artificial joint mesh depends upon the understanding of the solid material under investigation.

7. ACKNOWLEDGEMENTS

The author deeply appreciates Professor R. E. Goodman and Dr. G.-H. Shi for endless encouragement and guidance during his graduate study at Berkeley. The former brought him to the practical world of rock mechanics and engineering geology, and the latter to the fascinating paradise of mathematics and computation, especially his wonder, DDA.

8. REFERENCES

1. Shi, G.-H, *Discontinuous Deformation Analysis - A New Numerical Model for the Statics and Dynamics of Block Systems*, Ph.D Dissertation, Department of Civil Engineering, University of California at Berkeley (1988).
2. Goodman, R. E. and Ke, T.-C, Keynote Lecture - Advances in computation of jointed rock, *Proc. 8th Intl. Conf. Computer Methods and Advances in Geomech.*, Morgantown, W. Virginia, vol:4, 14p (1994).
3. Shyu, K.-K., *Nodal-based Discontinuous Deformation Analysis*, Ph.D Dissertation, Department of Civil Engineering, University of California at Berkeley (1993).
4. Ke, T.-C, *Simulated Testing of Two-Dimensional Heterogeneous and Discontinuous Rock Masses Using Discontinuous Deformation Analysis*, Ph.D Dissertation, Department of Civil Engineering, University of California at Berkeley (1993).
5. Chang, T.-C., *Nonlinear Dynamic Discontinuous Deformation Analysis with Finite Element Meshed Block Systems*, Ph.D Dissertation, Department of Civil Engineering, University of California at Berkeley (1994).
6. Koo, C.-Y., Chern, J.-C. and Chen, S., The development of the second-order displacement function for discontinuous deformation analysis, *Proc. 6th conf. Geotechnical Engrg. in Taiwan*, 665-674 (1995)
7. Ma, M., Single field manifold method using Fourier function in wave propagation, *Proc. Working Forum on the Manifold Method of Material Analysis*, Jenner, CA, 39-60 (1995).
8. Shi, G.-H., Modelling rock joints and blocks by manifold method, *Proc. 32rd U.S. Rock Mechanics Symp.*, Santa Fe, New Mexico, 639-648 (1992).
9. Ohnishi, Y., Tanaka, M. and Sasaki, T., Modification of the DDA for elasto-plastic analysis with illustrative generic problems, *Proc. 35th U.S. Symp. on Rock Mechanics*, Lake Tahoe, CA, 45-50 (1995).
10. Lee, J., Unpublished DDA program to simulate the cracking of intact blocks according to a prescribed maximum tensile strain rate, University of California at Berkeley (1990).
11. Lin, C.-T., Amadei, B. and Sture, S. and Jung, J., Using an augmented Lagrangian method and block fracturing in the DDA method, Proc. *8th Intl. Conf. Computer Methods and Advances in Geomech.*, Morgantown, W. Virginia, vol:1, 837-842 (1994).
12. Shi, G.-H., *Personal communication* (1995).
13. Lin, H.-C., *Discontinuous Deformation Analyses of Block and Granule Systems*, Master Thesis, Department of Civil Engineering, National Central University, Chungli, Taiwan (1993).
14. Ke, T.-C. and Bray, J., Modelling of particulate media by DDA, accepted for publication in *J. Engrg. Mechanics, ASCE* (late 1995).
15. Shi, G.-H., *User Manual of DDA* ('94 Version).
16. Thapa, B. B., Joint shear displacement-dilation analysis using in-situ opposing profiles, *Proc. 35th U.S. Symp. on Rock Mechanics*, Lake Tahoe, CA, 51-56 (1995).
17. Hilbert, L. B., Yi, W., Cook, N. G. W., Cai, Y. and Liang, G.-P., A new

discontinuous finite element method for interaction of many deformable bodies in geomechanics, *Proc. 8th Intl. Conf. Computer Methods and Advances in Geomech.*, Morgantown, W. Virginia, vol:1, 831-836 (1994).
18. Yeung, M., Application of Shi's Discontinuous Deformation Analysis to Rock Slope, Ph.D Dissertation, Department of Civil Engineering, University of California at Berkeley (1991).
19. Shi, G.-H., Modelling dynamic rock failure by discontinuous deformation analysis with simplex integration, *Proc. 1st North American Rock Mechanics Symp.*, Austin, TX, 591-598 (1994).
20. Ke, T.-C., Thapa, B. and Goodman, R. E., Stability analysis of a penstock slope, *Proc. 1st North American Rock Mechanics Symp.*, Austin, TX, 1109-1116 (1994).
21. Chen, S. and Lin, J.-S., Application of DDA to evaluation and solution of slope stability, *Proc. '94 Rock Engrg. Symp. in Taiwan*, 269-277 (1994).
22. Yeung, M., Klein, S. J. and Ma, M., Application of the discontinuous deformation analysis to the evaluation of rock reinforcement for tunnel stabilization, *Proc. 1st North American Rock Mechanics Symp.*, Austin, TX, 607-614 (1994).
23. Ke, T.-C., Application of DDA to block-in-matrix materials, *Proc. 35th U.S. Symp. on Rock Mechanics*, Lake Tahoe, CA, 33-38 (1995).
24. Rice, J. R., Mathematical analysis in the mechanics of fracture, *Fracture, and Advanced Treatise* (2), 191-311 (1968).

Algorithm for the Transition from Continuous to Discontinuous and Free Bodies in Finite Element Failure Analysis

Edward C. Ting[1], Yeon-Kang Wang[1] and Austin Pan[2]

[1] School of Civil Engineering, Purdue University, West Lafayette, IN 47906 USA

[2] Department of Civil Engineering, University of Hong Kong, Hong Kong

Summary:

There are two groups of numerical approaches in structural analysis. One group may be termed as numerical analysis, which includes methods such as the finite element, finite difference, and boundary element. By modeling the structure as a continuum, the analysis obtains quantitative predictions of the pre-failure responses in the form of stresses, deformations, and velocities. In these analyses, treating discontinuity and large geometrical change commonly associated with failure is usually difficult. The second group may be termed as numerical simulation. By modeling the structure as an assemblage of discontinuous media, the motion histories of the structural components are recreated qualitatively. Often, each discontinuous medium is treated as a rigid body. In these analyses, quantitative predictions of the stress and deformation due to applied loading condition are often not available or less accurate. Examples of this group are methods such as distinct elements and block theories for rock masses.

Attempts to integrate the stress analysis of continua and the motion simulation of discontinuous media to form a comprehensive procedure for the study of complete failure process have been reported in recent years. One of the key issues in the development of such an algorithm is to find an accurate, simple, flexible, and numerically stable procedure to handle the transition from a single continuous deformable body to multiple distinct deformable bodies subjected to free rigid body motions. Such a transition may occur during the fragmentation of a structure after fracture.

In this paper, we first discuss the numerical and analytical difficulties in treating the transition behavior. Then, we summarize our recent attempt in the study of structure fragmentation which involves a similar transition period. Briefly, our work is based on a vector formulation of finite element and an explicit integration procedure for transient loadings. This allows the simultaneous treatment of multiple bodies and rigid body

motions in finite element analysis. A concept of updated material frame is introduced to handle the large deformation and the high rate of motion at the instant of transition.

Sample numerical solutions are given for the fragmentation of frame structures and for a rigid projectile penetrating through a plain concrete medium.

Introduction:

The advancement of structural design has historically been influenced by the availability of analytical technics and the development of computational facilities. In a century ago, the concept of differential calculus established the foundation for the breakthrough concepts of stress and strain distributions, which led to the important theories of beams and columns. These analytical tools facilitated the design and construction of long span bridges, arches, and structural foundations. However, the lack of efficient computational facilities limited the capability of analysis and design, engineers relied primarily on hand calculations and graphical methods. The availability of desk calculators and new slide rules at the turn of this century led to another breakthrough. The facilities made the concept of numerical iterations and direct computational methods viable for practical applications. These analytical tools led to the design and construction of highly redundant structures. Tall buildings with complex frame components, efficient bridge designs and integrated naval and airplane structures become possible. Using these computing facilities, linear mathematics such as series, transformations and differential equations were developed as engineering tools to study a variety of problems, including the inelastic material theories and multi-axial stress behaviors. As a result, two dimensional structures including plates, shells, pavements and mate foundations became standard components of structural design.

With the advent of efficient personal computer and algorithms, structural engineers have the opportunity to enter another new era. Due to the limited capacity and restrictions on accessibility, earlier impact of computer has been in the broadening engineer's capability to manage a large number of structural components and to handle complex structural geometries. Direct stiffness method, finite difference and finite element methods were developed by following essentially the traditional concepts such as variational approaches. We are yet to realize the potentially revolutionary changes in engineering practice.

With the advancement in personalized computing power during the last decade, structural engineers are now given the tool to approach design and analysis far beyond the traditional confinements. One of the possible developments which may have such far-reaching impact in engineering practice is an efficient and flexible design procedure based on a realistic assessment of structural service condition. Such a procedure requires an accurate evaluation of the component reliability and a new approach to predict the progressive failure of a structural component under the service load and the service environment.

Failure-Based Structural Design:

Finite element techniques combined with the developments in material modeling have provided a solid basis to study the stress and strain distributions in a structural component before it begins to fail. Because of the high redundancy built in a structure, the initial failure of the structure often occurs at merely a small fraction of the ultimate structural capacity. To assess the true load carrying capacity, one needs to consider the continuous changes in material property, for example the yielding and hardening of metals and microcracking of brittle and inhomogeneous materials. Part of the structure may fracture and separate into multiple pieces. Due to the overall ductility, a structure may be subjected to very large geometrical changes before collapse. Thus, one of the primary concerns is finding new concepts and techniques to treat large displacements and fracture.

Traditional approaches to define fracture and to incorporate fractures into the design procedure can be categorized into two groups. Empirical approaches use extensively the test data to develop relationships between the input and output parameters. Such approaches have successfully included failure modes into the design practice. Member and connection designs for reinforced concrete structures and the fatigue design for metal structures are typical examples. However, the resulting formulas are often not correlated to the intrinsic phenomena of the structural material and geometry. They can not be extrapolated to predict cases which are beyond the test environment. Hence, the application is confined to simple structural geometry and simple loading conditions.

Mathematical formulation of the physical phenomenon, such as the classical fracture mechanics, provides a rational basis for more general studies of failure. Simplifications are often required to reduce the equations and the ensuing analysis to manageable sizes. Singularities for example, are introduced to represent the cracked region as a point or as a line. Other simplifications including plastic hinges, slip zones, jump conditions, yield and fracture surfaces have been successfully used by structural engineers to handle different forms of failure in the practice. Similar to the empirical approaches, the analytical approaches are limited in their scope and range of application. They offer valuable understanding of the initial failure of a structural component, but do not provide an efficient tool for the prediction of the progressive failure and the ultimate collapse of a structural system. Infact, the extensive use of singularities may prove to be efficient in the mathematical formulations; they become troublesome obstacles in the implementation for numerical evaluations.

Direct numerical approaches which do not follow the traditional empirical or analytical concepts seem to show the greatest promise in the development of a viable technique to simulate structural failure. Most of the advancements have been reported within the last decade. Although a satisfactory algorithm is yet to be available, significant progresses have been made in various areas. In general, such an algorithm should have the capability to handle some of the basic behaviors common to most fracture processes.

a. Stress Analysis of the Continuum:
Formulation of the mechanical properties of materials is based on the assumption of a continuous body. Numerical analysis should be convenient to handle the study of stress and strain prior to failure in the context of continuum mechanics.

b. Irreversible and Inelastic Materials and Failure Criteria.:
Permanent deformation and irreversible stress-strain relationships are critical behaviors to a quantitative prediction of ultimate loading capacity. The algorithm should be able to handle these properties without the need for extensive computational efforts. Implementing failure criteria should be easy. They define changes in material properties and identify the nature of failure. For example, the algorithm should be easy to include yielding, plastic flow, and rate-dependant plasticity without the need for multiple iterations.

c. Post-fracture Material Properties:
Material models should be implemented to describe the degenerated material properties according to the nature of failure and how fractures occur. For example, concrete may exhibit behaviors similar to anisotropic elastic or plastic models with a degenerated stiffness parameters when concrete members are subjected to tension cracks. Concrete may also behave similar to granular materials when it is crushed due to hydrostatic compressions.

d. Mixture of Stiff and Soft Media:
Due to local failures in a continuous body, some structural members may become significantly weaker in stiffness compared to other members. For example, part of a continuous concrete body may be crushed or cracked and yet trapped within the medium due to constraints. Continuity is still maintained due to aggregate interlock. This forms a mixture of hard and soft components which behaves as a continuous body. Current finite element and stiffness methods have difficult handling such diversities in stiffness.

Classical continuum analysis often assumes homogeneity in material properties. This assumption has excluded many physical conditions. For example, soil media often include large boulders. Rock masses include soft soil layers. The algorithm should be able to handle these diverse properties.

e. Large Deformations and Very Large Geometrical Changes:
Before fractures to start, the local deformations near the fracture zone can be extremely large for ductile materials. Slender and thin-walled structures may be subjected to very large geometrical changes before fracture. Layered structures may subjected to very large inter-layer slides. Large deformation may occur in the soft layers, while the motions of stiff layers are essentially in rigid-body motions. Large geometrical changes usually lead to complicated interaction effects. In classical mechanics, these interactions are often treated as isolated cases. For example, beam-column and buckling are usually taken

separately in the analysis of frame structures. To predict structural fracture, these interactions should be integrated into the algorithm as natural conclusions of the geometrical changes.

f. Impact and Dynamic Responses:
Critical loading environments often involve forces applied within a very short period known as impacts and shocks. Even for a gradually applied loading condition, the inertia effect and the wave phenomenon can become important when a structural component is subjected to a sudden fragmentation. Sudden changes of the constraint and loading conditions of a fragmented member may induce rapid redistributions of the stresses and strains in a manner similar to impacts and shocks. Very high rate of deformation may occur near the fragmented zone which could lead to additional fracture and propagation of the fracture zone.

g. Rigid Body Motions:
In the classical stress analysis , the considerations of rigid body motions and deformable body motions are separated. By solving simultaneous equations, traditional finite element and finite difference methods generally assume static equilibrium and ignore the rigid body motions. To study fracture and to consider more realistic modeling of structures, rigid body motions due to inter-layer sliding or due to fragmented components separated from the original body should be integrated into the stress analysis procedure.

h. Multiple Deformable Bodies and Free Bodies:
To handle phenomena such as the break-off of structural components, sliding of layered medium and the penetration of a projectile into a structure, the algorithm should have the capability of computing stresses and motions of several interacting continuous bodies. Multiple deformable bodies are generally not permitted in the classical continuum concepts and the analytical methods associated with these concepts. They should thus be modified to incorporate these conditions. For example, the breaking a fixed-fixed beam changes the problem into two cantilevered beams. The algorithm should be able to trace this transition and handle the sudden change in natural frequency of each component beam without incurring the numerical problem of instability. For some loadings, parts of the beam may also be fragmented and separated from the original structure. To trace the trajectories of separated fragments, unconstrained free bodies may be treated either as rigid bodies with translations and rotations, or as deformable bodies subjected to oscillations as well as the large rigid body motions.

Recent Developments:

Numerical methods for structural analysis are generally intended to study the pre-failure responses of a single continuum. They provide quantitative predictions of the stress, strain and displacement values with satisfactory accuracy. Using for example, the finite difference to handle time variables and the finite element for the displacement

distributions over the continuum, responses due to impact and shock can readily be predicted.

Considerable advancements have been reported in the area of modeling permanent deformation, irreversible behaviors and other inelastic responses. Most of the developments have generally followed the traditional theories of plasticity, creep and viscoplasticity. Accurate predictions can be obtained for the stress and strain responses due to complicated loading conditions. However, modeling of the post-fracture responses and the progression of failure zones through the media are not as accurate..

Extensions of the linear finite element formulations for small strains to study large deflections of thin structures have been reported. For example, a large rotation and small strain approximation known as the co-rotational approach has yielded accurate results for moderately large deflections of frames, plates and shells. The method is computationally efficient and requires a small computer code. For structures subjected to very large deformations, lengthy iterations are often required for most of the algorithms reported in the literature. Convergence of the iteration process remains to be uncertain.

To simulate the fracture process which involves many different discrete bodies and very large rigid body motions, discrete element methods have been developed and applied to engineering practice with considerable success. This group of simulation methods has been utilized mainly in modeling discontinuous media to qualitatively recreate the behaviors of granular or jointed materials. By analyzing the contact forces acting on the discrete bodies and the changing contact points, motion histories of the discrete elements can be obtained.

To accurately predict the failure process, it seems necessary to combine the stress analysis methods and the motion simulation techniques to form a comprehensive procedure. The resulting algorithm should have the capability of calculating the stress, strain and displacement prior to failure. Based on a set of failure criteria, the algorithm should predict where and how failures occur in a given structural system. The analysis is then phased into the study of post-failure behaviors. The structural system is transformed from a continuous body to a system of multiple discrete bodies. Large geometrical changes may change the structural configuration of each discrete body due to large deflections or large deformations. As the fracture process continues to progress, some portions of the structure become free bodies or separated deformable bodies.

An Algorithm for the Structure Transition:

As an initial attempt in the direction of developing a comprehensive procedure for failure prediction, an algorithm is proposed which seems to have the capability of handling stable transitions of a continuous medium into multiple deformable bodies and free bodies. The algorithm has been implemented to study frame structures and two dimensional solid media. We briefly summarize the essential ingredients of the algorithm.

a. A Vector Formulation of Finite Elements:
In the traditional finite element analysis, the stiffness and force matrices are calculated based on structural discretization. These matrices are assembled to form a system of simultaneous linear equations for the solution of nodal displacements. For dynamic problems, a similar procedure to find the mass matrix and a system of differential equations are obtained.

Instead of using the matrix formulation, we propose to adopt a transient formulation developed earlier by Key, Belytschko and Hallquist. In the formulation, the continuous medium is approximated by discrete mass particles. Using the standard finite element analysis, energy equivalent internal and external forces are found. They are the forces applied on the mass particles. Newton's law of motion and time integrations complete the formulation to determine the acceleration, velocity and the displacement of each particle for a particular time increment.

Since the discretization considers only the lumped mass particles and forces acting on the particles, the formulation is written in vector form. One of the distinct advantages of a vector formulation is that the code development is considerably simpler than a matrix analysis.

Note that the equations of motion for each mass particle are essentially solved independently. Mass particles are related to one another only through the internal forces. This property of a mass-force system offers considerable advantages in the study of structural failure.

* The motion of each particle is calculated independently. The equations of motion yield total absolute motion of the particle, including both the rigid body motion and deformable motion.
* The system is an assemblage of independent particles, regardless whether these particles form a unit body or multiple bodies. The only difference is in the calculation of internal forces. Hence, the algorithm automatically permits multiple bodies and body separations.
* Since material properties are included in the computation of internal forces, inelastic and discontinuous material properties are easy to handle.
* Adding or subtracting a set of nodes do not affect the original discretization. Hence, creating new surfaces or eliminating portions of the medium due to failure presents no numerical problem.
* Numbering of the nodes has no effect on the computation. Again this is convenient for creating or eliminating surfaces and bodies.
* Since the interactions between two components are through the internal forces, the co-existence of soft and stiff components do not present numerical problems. The extreme case is that some components have zero stiffness as a result of failure.
* It is easy to handle different types of structural component without the need for complicated assemblage process.

* Coding for the algorithm is simple. The resulting program is short and compact.
* it is easy to handle inelastic and discontinuous material properties.

Since Newton's law of motion forms the basis, the algorithm is a transient procedure by nature. Static solutions can be obtained by attenuating the motion through the use of dynamic relaxation and apply external loads incrementally.

Figure 1 shows a schematic diagram of the lumped mass-force model for the discretization. Figure 2 shows a typical static solution obtained by introducing an artificial damping to attenuate the motion.

b. Explicit Time Integration:
To avoid the complexity of iterations, a simple explicit time integration formulation is suggested to find velocity and displacement for each time increment. This simplifies the implementation for complicated material models, changing constraint conditions and loading conditions. Fracture, particle collision, and penetration conditions become much simpler to incorporate. However, small time and force increments are required for numerical stability. This leads to longer computational times in general.

c. An Updated Material Frame Formulation for Large Deformation:
During the fragmental process, it is required that the large rigid body motion and the large displacement should be tracked accurately. Approximated techniques such as co-rotational formulation do not provide enough accuracy for these large geometrical changes. Errors can accumulate rapidly and even cause numerical instability. Figure 3 shows a typical example of the error induced by the use of a co-rotational approach to handle large displacement of a frame member after the member is fragmented.

To develop a more accurate approach to handle very large deformation and yet simple in computation, an updated material frame formulation of the deformation is proposed. Instead of using the undeformed geometry as the material reference frame to calculate the deformation gradients and Lagrangian strains, we propose to use the current configuration as the material frame and adopt an incremental procedure for the deformation process. For each time or force increment, the geometry of the structural element is updated. A new material frame is defined based on the current geometry. A set of geometry shape functions can be defined to described element geometry in terms of nodal geometry parameters such as positions and slopes. At a given time increment, a structural element is subjected equilibrated stresses. And the stresses are also in equilibrium with the applied external loads.

This process may be formulated as a modification of the traditional co-rotational approach. If the load increments are small, linear stress and strain relationships can be used to describe the material properties.

If isoparametric elements are used for the analysis of solid medium, the geometry updates can be introduced by continuously updating the nodal positions and the element stress values for each load increment.

d. Mixture of Rigid and Deformable Motions:
A master node-slave node approach is proposed to monitor the motion of each rigid body imbedded in a continuous medium. The rigid bodies may be subjected to very large motions and at the same time the continuous body undergoes large deformations. A slip and frictional behavior can be introduced to represent the interface medium between different bodies. Then the algorithm permits sliding between two surfaces.

e. Fragmentation Algorithms:
Several basic algorithms are needed for the purpose of monitoring the recreation of new surfaces or new bodies. Most of them can be choices of the programmer according to how the computer codes are developed. We list a few essential choices in our programming process.
* Surface Creation or Adding Bodies:
When the element stresses or the nodal displacement values satisfy a failure criterion, new nodes are added and new free surfaces are formed. The algorithm is required to check whether a new surface is permitted to exist at that location and to determine the types of constraint conditions which should be imposed on the new nodes. For the new nodes, dynamic allocations and parameter storages should be adjusted accordingly.
* Internal Force Calculations:
After an element is found to be fractured, all the internal forces should be recalculated to examine whether more fracture should occur in the elements, including those already fractured.
* Time Increment Adjustment:
To ensure numerical stability, the size of time and load increment should be re-examined according to the change of effective structural dimensions and the stiffness of the new structure.
* Inter-element Collision:
Fragmented components are allowed to move freely according to the force conditions. Thus, fragments may penetrate through other elements numerically. An algorithm should be adopted to control the motions of fragmented bodies.
A simple algorithm may define each fragment as a circle. Its center position is compared to the positions of other components. If the circular zones are found to be coincided, a set of equal and opposite collision forces are applied on the coinciding components. The total collision forces are distributed to the nodes and treated as external forces. Using the explicit approach, these new nodal forces are imposed in the calculations for the subsequent time increment.
* Contact and Sliding Surfaces:
The master node-slave node approach can be used to handle contact and sliding surfaces commonly encountered in the study of projectile penetrations. For example, the nodes on the projectile can be designated as master nodes, and the target nodes are slave nodes. At

each time increment, the positions of the slave nodes are examined to determine if the slave nodes have penetrated into the master node boundaries. If they have done so, the positions of the slave nodes and moved back to the master boundary, and the resulting changes in momentum are transferred to the master nodes.

* Penetration of Projectiles:

Discretized models and material properties of the projectiles can be treated as separated inputs. Their motions can be calculated in the program as part of the multiple bodies. Motions of the bodies can be evaluated simultaneously, or computed in series. When they are calculated in series, motions of one body can be used as the constraint conditions for the next body. This simplification provides considerable flexibility in programming and should be sufficiently accurate for practical applications if small time and load increments are chosen.

Numerical Samples:

Without giving the details, we show samples of a variety of numerical examples. Figure 4 shows the motion histories of an unrestrained frame structure subjected to an impact force acting at its left end. Without any support, the structure is deformed and undergoes a large rigid body motion. The applied force is a triangular force which lasts 0.2 seconds.

Figure 5 demonstrates the updated material frame approach for large deformation. A square frame is supported at the lower mid-point. An impact force of triangular shape is applied at the center of the upper cord. Figure 5 plots the deformed phase as well as the rebound phase of large deflection. The plotted deflections are in proportion to the frame size. At the center, the deflection is about 30% of the span length.

Figures 6(a) to (e) plot three fragmental conditions of a fixed-fixed beam subjected to a set of concentrated forces on the middle three nodes. Assume that the forces are sufficiently large to satisfy a failure criterion. The middle three nodes fractured. Subsequently, the two neighboring nodes also fractured due to the high rate of deformation induced by the fragmentation. Figure 6(a) shows the geometry, loading condition, and a schematic diagram of the fragments. Figure 6(b) shows the traces of the five nodes of the fragments. The fragments are subjected to translations as well as rotations. Figure 6(c) shows the trajectories of the four fragmented elements. If gravity forces are considered in the transverse or y direction, additional elements will fracture in a later time. Figure 6(d) shows the traces of all eleven fractured nodes. It is interesting to note that the outside elements which fractured at a later time are essentially in free fall without spinning motion. Figure 6(e) considers the same beam with gravity force applied in the -x or axial direction. Thus it is a column subjected to horizontal impact forces.

Figure 7 plots the results of a rigid projectile penetrating through a plain concrete medium. The concrete medium is modeled by axi-symmetrical isoparametric elements.

An elastic-plastic model with a four-parameter failure criterion is implemented to describe the pre-failure and post-failure concrete properties. For a deep concrete medium subjected to a hypervelocity projectile, it is expected that the projectile will create a tunnel of crushed concrete and penetrate through without extensive cracking. The fractured pattern shown in Figure 7 seems to agree with the observation.

References:

1. T. Belytschko and B. J. Hsieh, " Nonlinear transient finite element analysis with convected coordinates," Int. J. Num. Meth. Eng.. vol. 7, p. 255, 1973.

2. J. O. Hallquist, Theoretical manual for DYNA3D, Lawrence Livermore Laboratory Report No. UCID-19401, University of California, 1982.

3. R. D. Krieg and S. W. Key, "Transient shell response by numerical time integration," Int. J. Num. Meth. Eng., vol. 7, p. 273, 1973.

4. D. L. Rice and E. C. Ting, " large displacement transient analysis of flexible structures," Int. J. Num. Meth. Eng., vol. 36, p. 1541, 1993.

5. D. L. Rice and E. C. Ting, " Fragmentation algorithm for finite element failure simulation and analysis," Int. J. Num. Meth, Eng., vol. 36, p. 3859, 1994.

6. D. L. Rice and E. C. Ting, "Finite element analysis of ballistic impact and projectile penetration of concrete targets," Structural Engineering Report CE-STR-95-6, School of Civil Engineering, Purdue University, 1995.

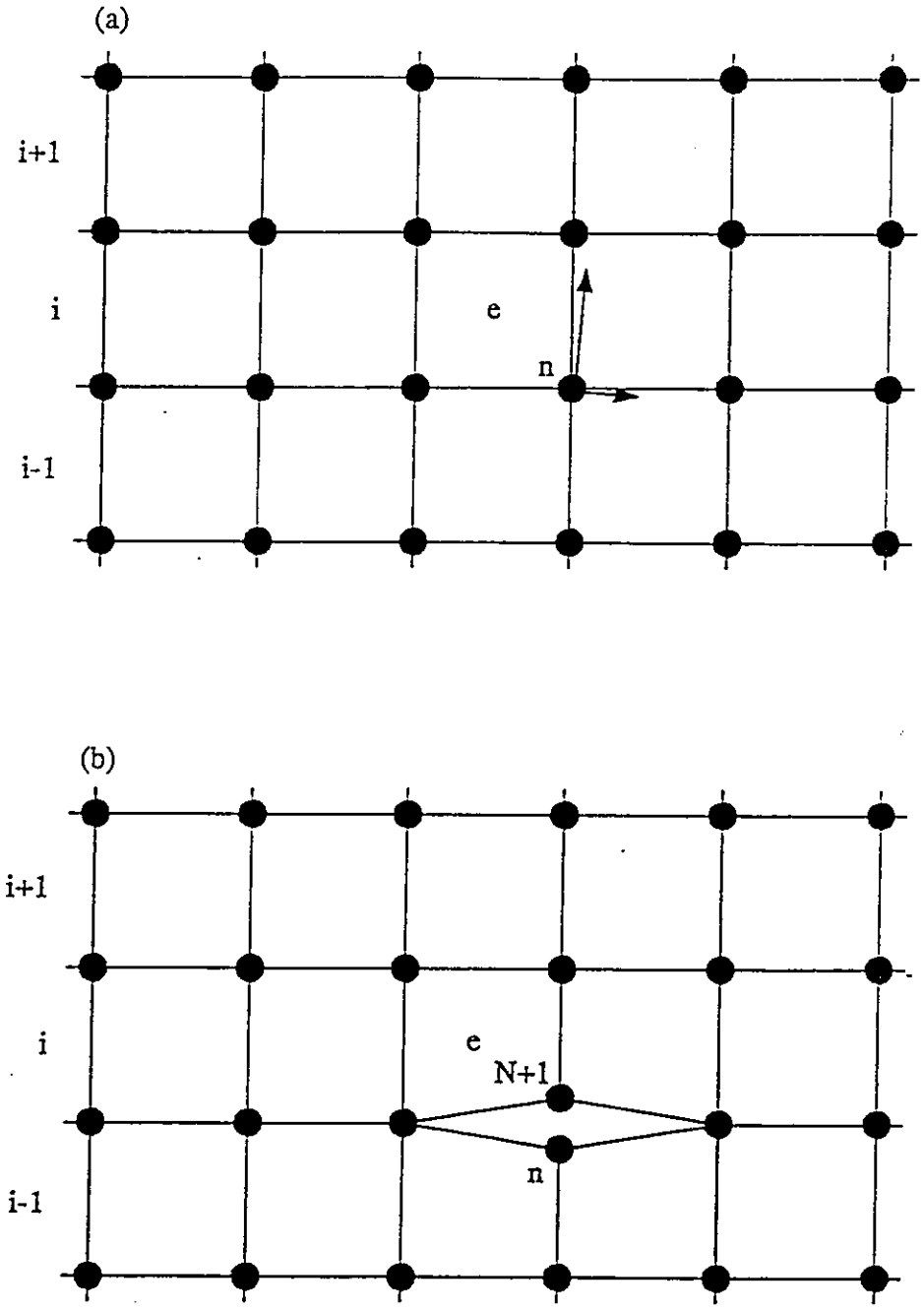

Figure 1. A schematic diagram of the lumped mass-force model of a continuum

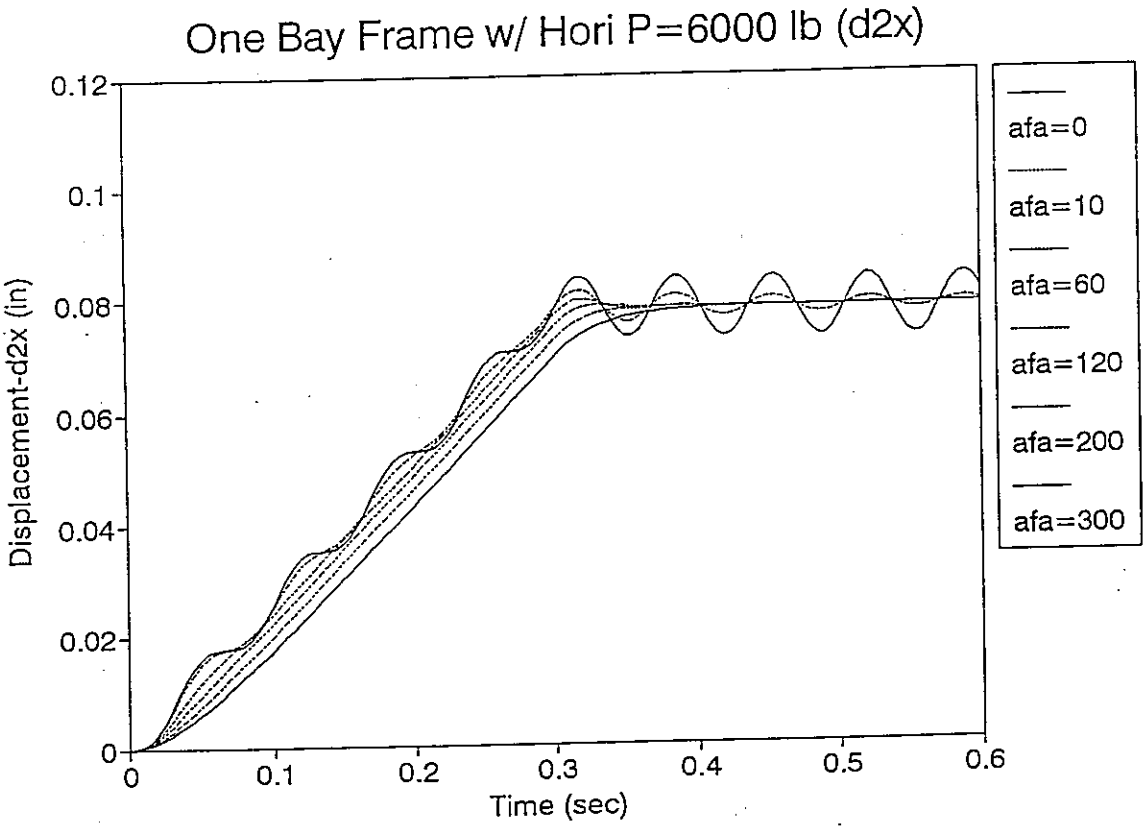

Figure 2. Typical solutions obtained by a dynamic relaxation procedure
(a) A one-bay frame subjected to a horizontal force of ramp type

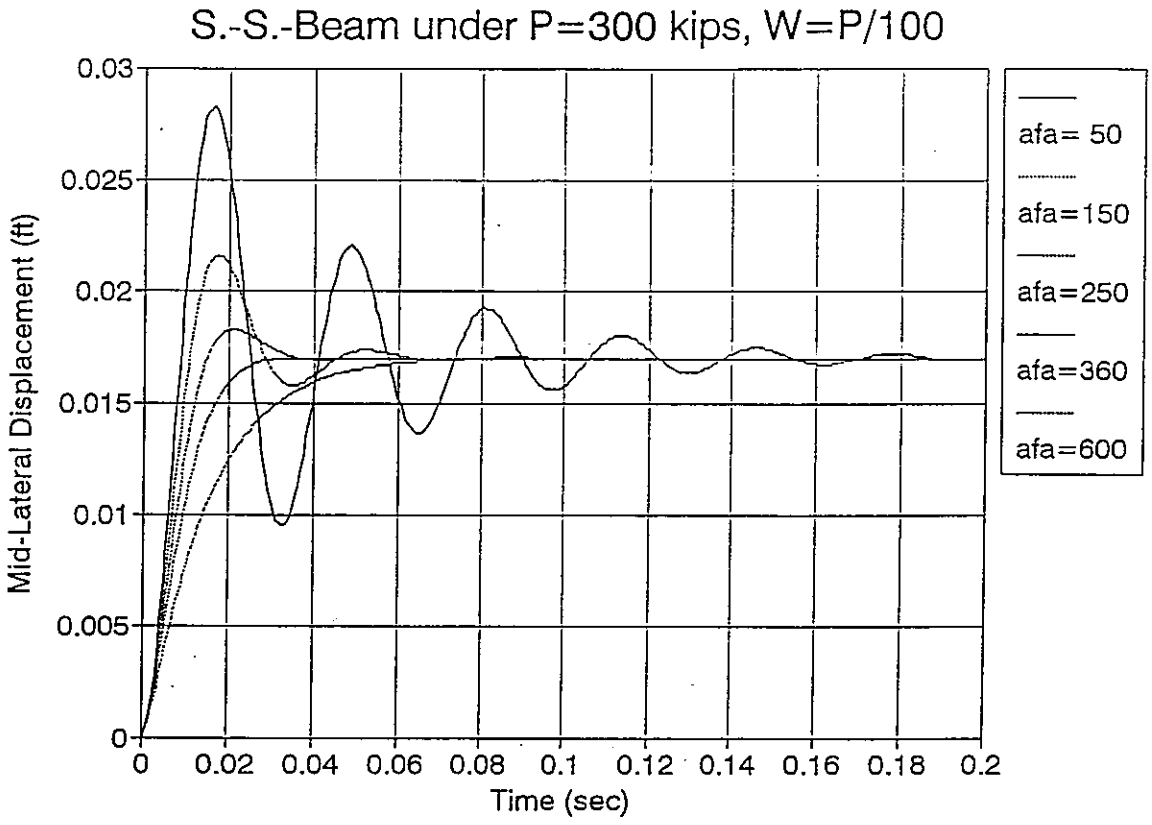

Figure 2(b). A simply-supported beam subjected to an axial force, a beam-column problem. Buckling load is obtained by introducing artificial damping.

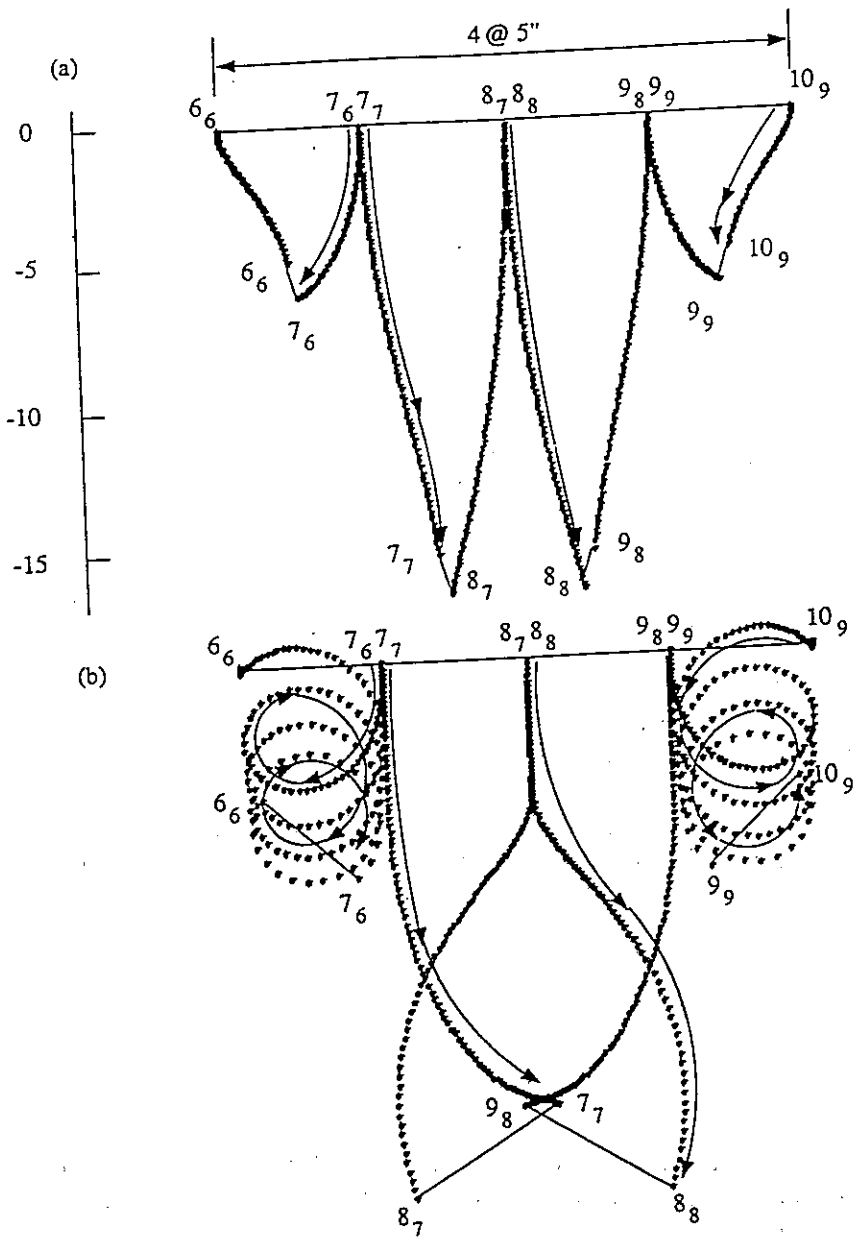

Figure 3. An example of the errors in fragmentation due to co-rotational approximation of large displacement
(a) Fragment pattern obtained by co-rotational approach
(b) Fragment pattern obtained by updated material frame approach

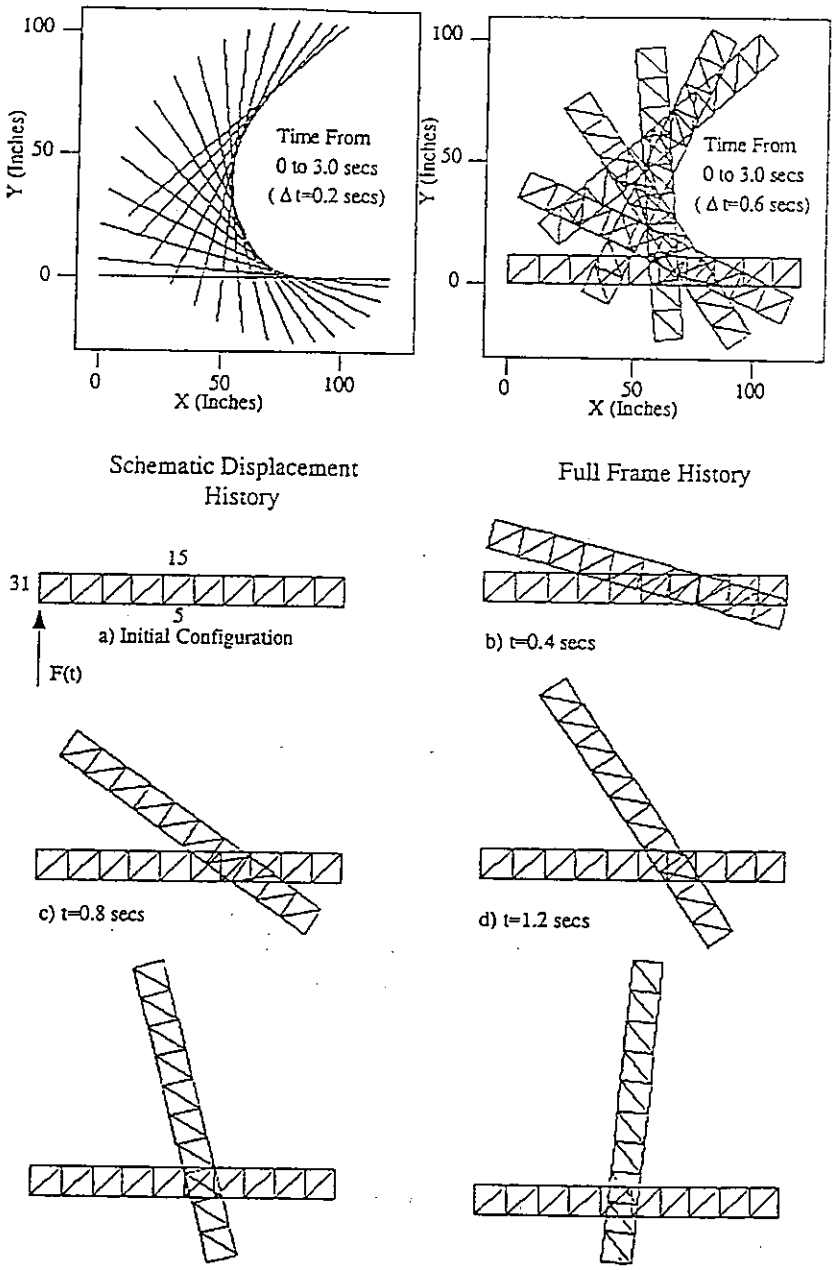

Figure 4. An unrestrained frame subjected to a force at its left end.

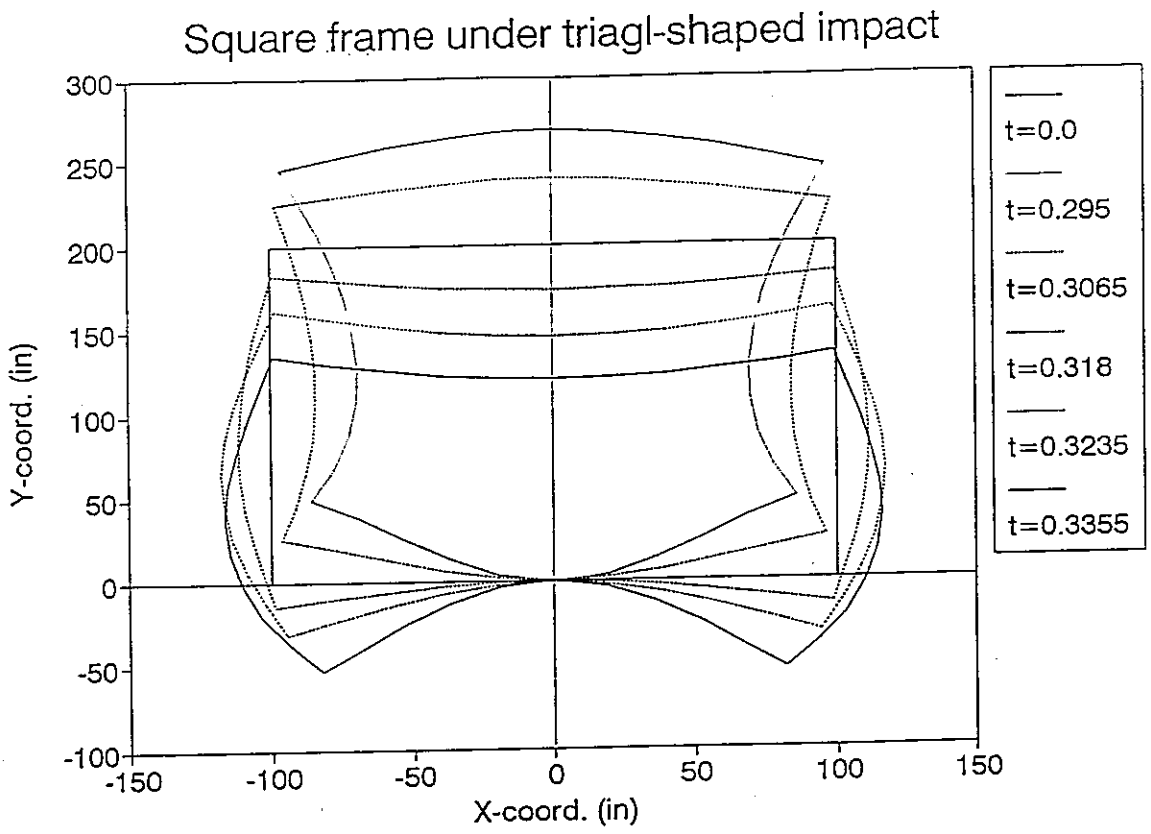

Figure 5. Transient large displacement of a square frame subjected to a triangular impact force

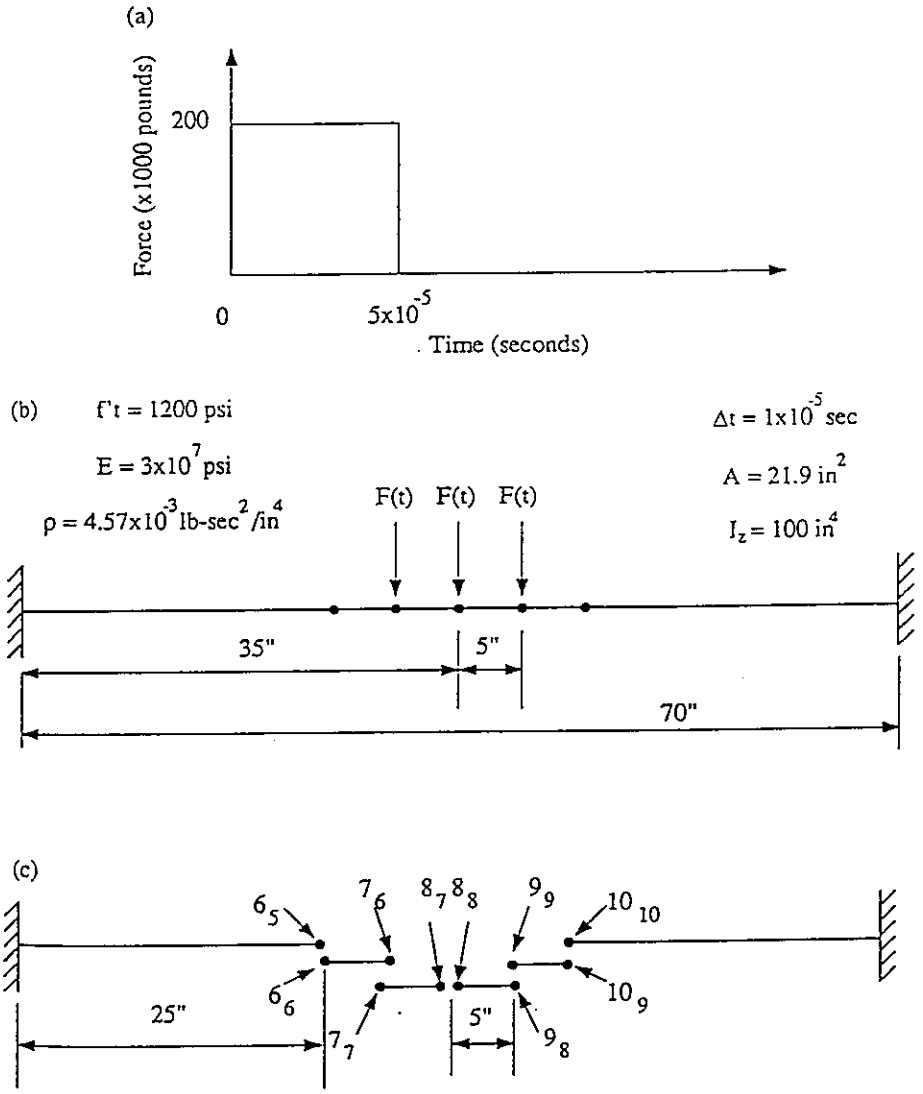

Figure 6. A fixed-fixed beam subjected to central impact force
(a) Geometry, material, and force input

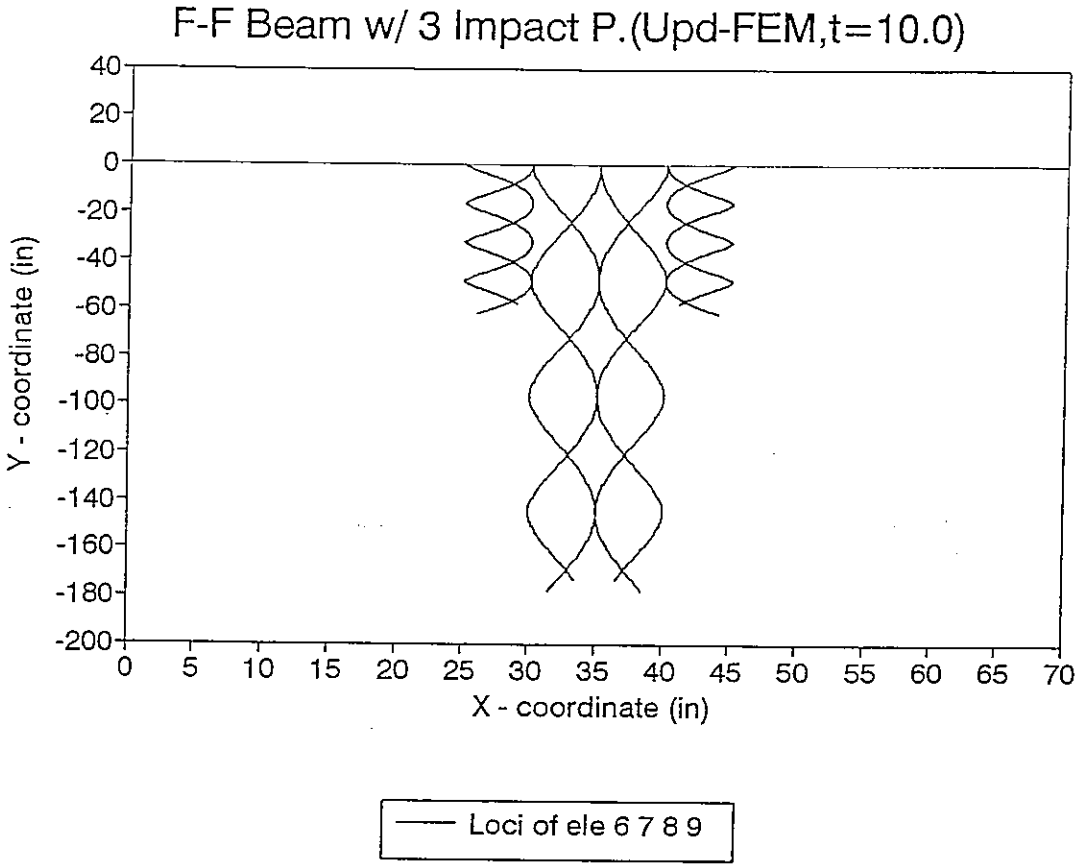

Figure 6(b). Displacement histories of four fragments, loci of nodes 6,7,8, 9 and 10. No gravity.

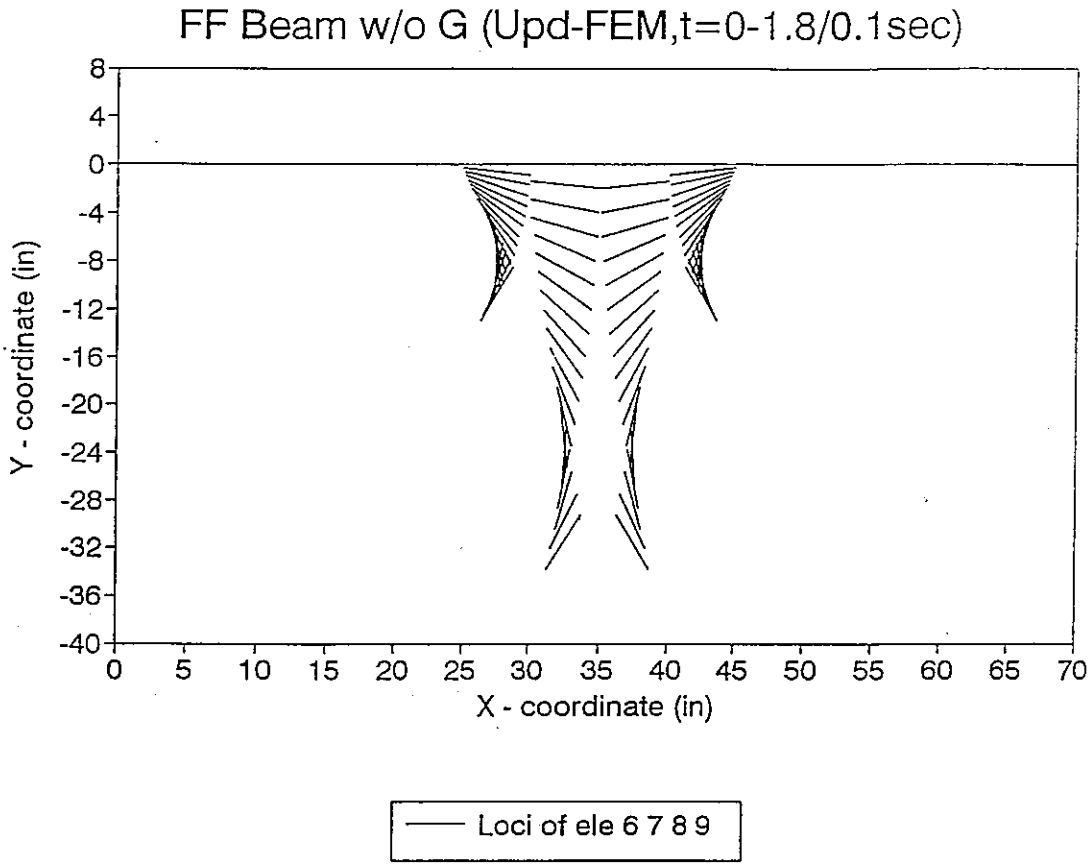

Figure 6(c). Fragment motions, four central elements. No gravity

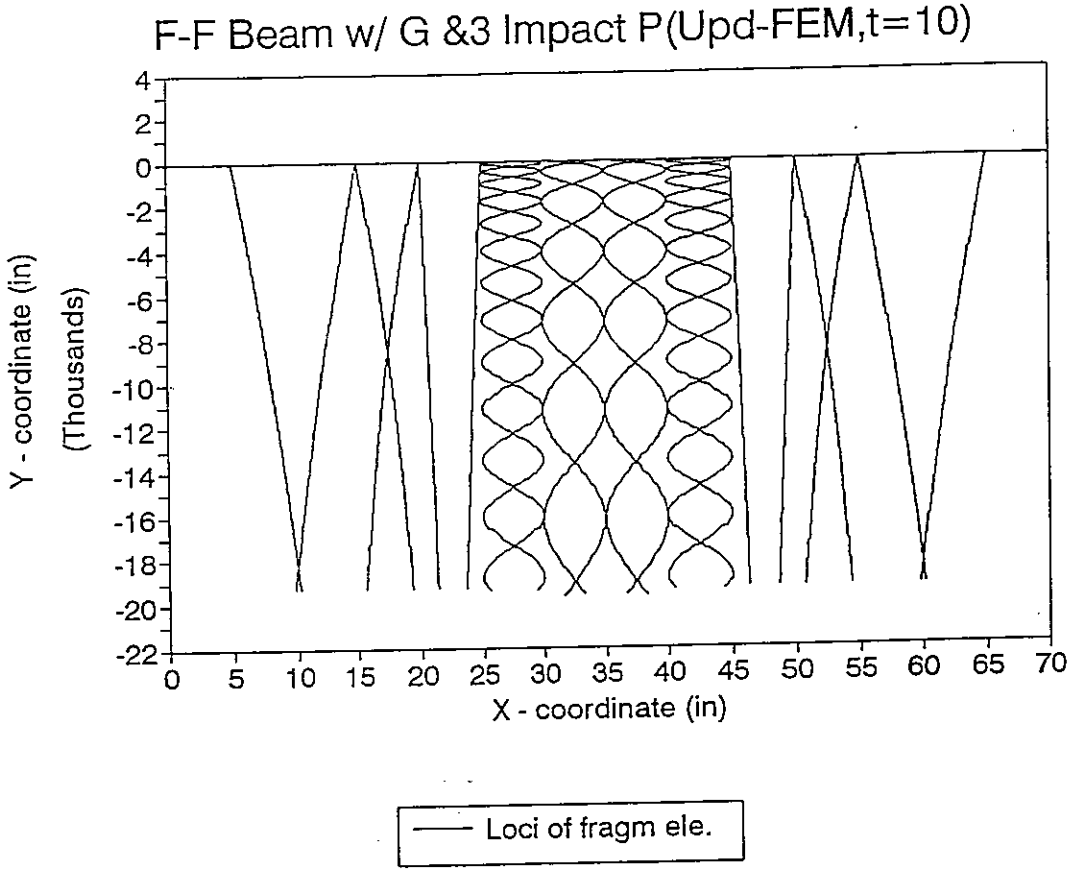

Figure 6 (d). Fragment motions with gravity in y direction. 10 fragments.

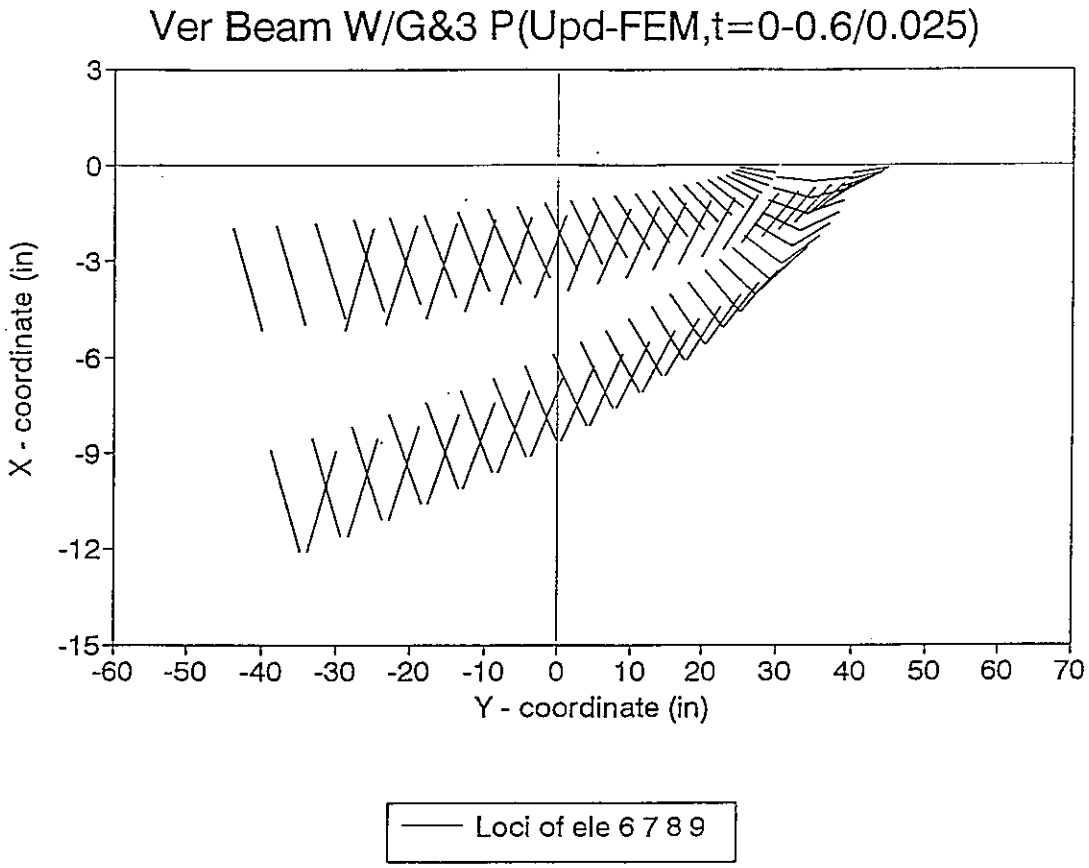

Figure 6 (e). Fragment motions with gravity in -x direction.

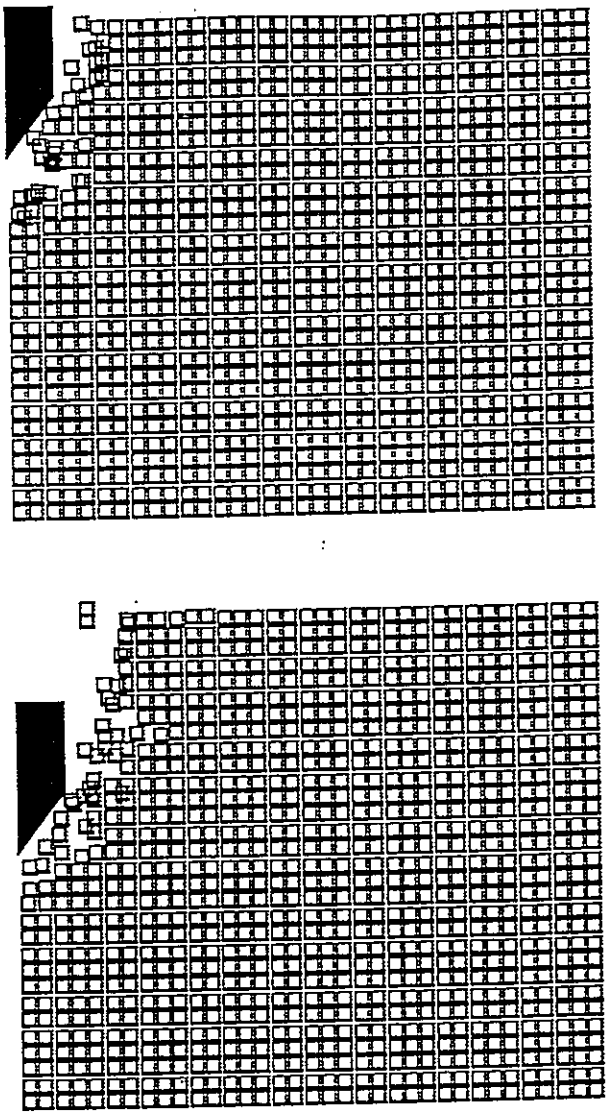

Figure 7. Penetration of a rigid projectile in an axi-symmetrical plain concrete solid.

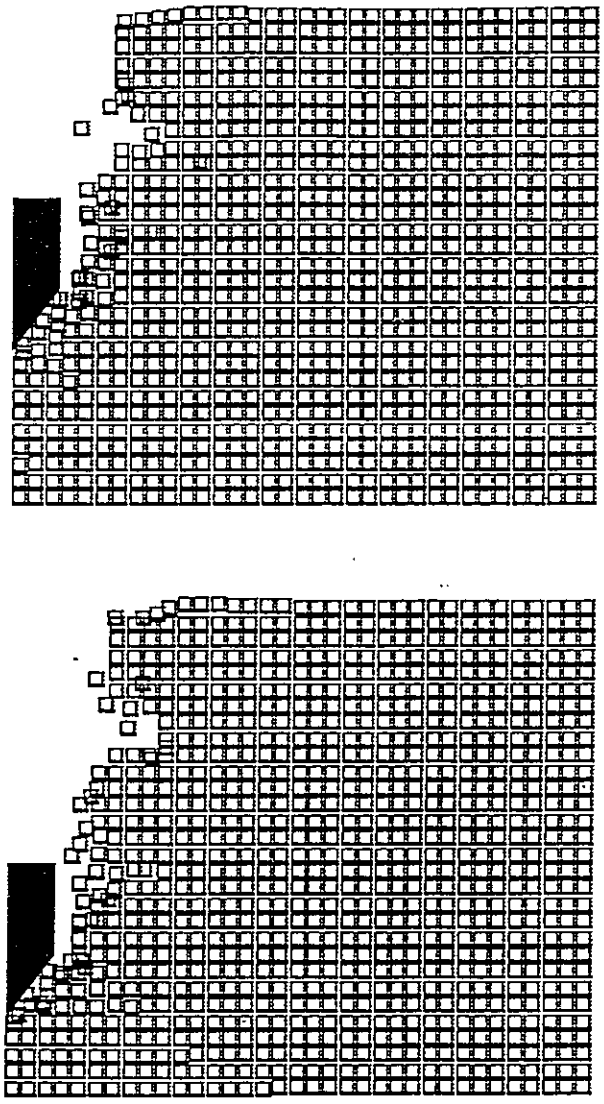

Figure 7 continued.

Modelling Aspects of Discrete/Finite Element Technology in Continuum and Fracture

A. Munjiza, D. R. J. Owen, G. J. Huang

Department of Civil Engineering, University of Wales, Swansea, U. K.

SUMMARY:

Advances over recent years in the deformable discrete/finite element method combined with parallel advances in the numerical treatment of non-linear continuum problems have allowed discrete and finite element techniques to be merged to provide solution capabilities for progressively fracturing solids. Early applications concentrated mostly on brittle (mainly strain softening) materials. The models included crack propagation and fracture algorithms based on assumption of localisation zone being orthogonal to the maximum plastic strain. This assumption is limited to applications of the methodology to problems with mode I dominated fracture patterns.

On going developments within a wider framework of the so called DEFT (discrete/finite element technology) have introduced elasto-plastic/viscoplastic deformation under finite strain conditions including problems of condensed matter physics with thermal and phase change phenomena. More robust fracturing algorithms are employed enabling a greater choice of both yield and fracture/rupture criteria. In this paper some algorithmic issues concerning continuum based DEFT applications with fracture for both 2D and 3D problems are discussed and relevant numerical examples are presented.

The outline of the paper is as follow:

- *A short review of the state of the art of DEFT. Special attention is paid to the limitations of early formulations and a need for more robust formulations; especially of fracture propagation algorithms is established. This includes extension to 3D problems with accent on energy and momentum preserving contact algorithms at finite penetrations.*
- *Application to ductile materials is reviewed. This includes detection of strain localisation zones, fracture propagation and adaptivity. Related numerical results (micromechanical friction behaviour and metal cutting) are presented.*

1. INTRODUCTION

1.1. Finite Element Method

Many properties of engineering materials and systems coincide very closely with predictions based on the assumption of continuity. The general formulation of a continuum problem involves constitutive equations and conservation law. The most widely used solution strategy is finite element method.

Since its advent some four decades ago, the finite element method has proved an effective technique in industrial analysis and design. Finite element methods are well established in many branches of engineering and are now routinely used in the solution of large scale industrial problems.

As the mainstream numerical technique, the finite element method has been applied to almost all conceivable disciplines of industries and has become an important module in the integrated computer-aided engineering environment. This situation has been brought about by the increased maturity of numerical analysis methods in general, and in particular for nonlinear problems, combined with dramatic developements in computer performances.

1.1. Discrete Element Method

The general statement of problems involving several particles or bodies must specify the interaction law between any pair of particles and a conservation law. The most widely employed solution strategy in this context is the discrete element method. The overall algorithmic framework for discrete element methods is straight forward and has remained more or less the same since the method was first introduced. The simplest computational sequence for discrete elements typically proceeds by solving the equations of motion using an explicit time marching scheme, while updating force histories as a consequence of contacts between particles or bodies (using a penalty format) and/or resulting from contacts with model boundaries at a given time. An increased complexity of different discrete element models is achieved by incorporating the deformability of the solid material and/or by more complex interaction laws, and particularly by the introduction of any failure or fracturing criteria controlling the solid material behaviour. From the computational point of view, complexities arise from the need to detect and continuously keep on updating pairs of bodies in contact in an efficient manner, where a number of sophisticated searching algorithms and data representation techniques are employed.

The origins of the discrete element method can be traced to the late sixties. A model by Goodman, Taylor and Brekke [1], for example, was aimed at the simulation of jointed rock and was accomplished by introducing discontinuities into an existing continuum. In the early seventies, models based on the a priori assumption of discontinous behaviour were introduced, with continuum behaviour being treated as a special case (Cundall [2]). The methodology was initially applied to jointed rock systems, with later application being made to industrial processes

such as granular media [6] and shear flow [7]. The set of methods developed was generally termed *the distinct element method.*

Further developement took place in the eighties with the incorporation of deformable behaviour for the more precise modelling of individual elements and the term discrete element methods became widely accepted. The continuum representation of individual elements was dealt with through polynomial approximation of the strain field (Williams [3], Goodman [4]) or by incorporation of central difference procedures (Cundall [5]). Fracture models were either based on rigid fracture energy release rate concepts or on the breakage of cohesive links between discrete elements.

Recent developements [6, 7] have centered on improved physical models and associated computational algorithms. Improved formulation for nonlinear physical models and associated computational issues for discrete element method are closely related to advances in continuum based computational plasticity. In this context more robust fracturing algorithms have also being developed in contrast to more traditional element interface based rigid fracture modes. Notable advances also include improved contact detection and interaction algorithms and the introduction of advanced computational concepts (parallel and distributed computing, object oriented programming and in core data bases). The first approaches for coupling discrete element methods with fluid flow methods have also appeared [10], as well as combined finite element/discrete element simulations.

1.3. Combined Finite/Discrete Element Method

Apart from more traditional continua and/or multibody based methods, engineering practice requires computational technology for problems that involve transition from continua to discontinua (demolition, blasting, etc). The most appropriate solution strategy in this context is a so called combined finite/discrete element method.

Early attempts to combine finite and discrete elements were made by Ghabousy [9]. However, a systematic development of a so called combined finite/discrete element method which involves fracturing, fragmentation, coupled problems, viscoplasticity, finite strains, strain localisation and adaptivity can be found in [11]. First successful applications of the methodology to relevant practical engineering problems can also be found in [11,12].

It may be argued that the only tangible difference between a traditional explicit transient finite element analysis and combined finite/discrete element formulations lies in the automatic creation of new discrete elements and the detection of new contacts. However, both the algorithmic issues and applications are much more complex then that.

The discussions to follow consider the issues involved in the development of a combined finite/discrete element method from a fundamental theoretical viewpoint and, in addition, some related algorithmic considerations essential for the efficient

numerical solution of a large scale problems are elaborated upon. In considering fracturing media, starting from a continuum representation by finite elements of the solid domain of interest, progressive fracturing is allowed to take place according to some fracturing criterion, thereby forming discontinuities, leading eventually to discrete elements which may be composed of several deformable finite elements. Subsequent motion of these elements and further fracturing of both the remaining continuum domain and previously created discrete elements is then modelled and monitored.

2. DEFORMABILITY OF DISCRETE ELEMENTS

The deformability of individual discrete elements was initially dealt with by subdividing discrete elements into constant strain zones [13]. An alternative was suggested by Williams and Mustoe [3], introducing several discrete body deformation shapes superimposed on top of the body centroid motion and a similar deformability model was proposed by Shi [8], where so called discontinuous deformation analysis (DDA) employs polynomial approximation of the strain field superimposed to the centroid movement for each discrete element.

More robust solution for deformability of individual discrete elements is achieved by discretisation of each discrete element into finite elements followed by a subsequent generally nonlinear finite element analysis.

This approach is computationally efficient and very suitable for computer parallelization. The nature of deformation demands a finite strain elasto-plastic model be implemented.

Nowadays, *hyperelastic* models based on stored energy potentials are widely accepted as the correct approach in implicit models. The extensions for plasticity require multiplicative decomposition of the deformation gradient:

$$\mathbf{F} = \frac{\delta \mathbf{x}}{\delta \mathbf{X}} = \mathbf{F_e F_p} \tag{1}$$

However, for explicit integration with small time increments and small elastic stretches, the error arising from a *hypoelastic* approach is practically negligible, while element database requirements and computational speed benefits occure. The stress integration scheme is based on the objective stress rate, while the plasticity is modelled via a standard elastic predictor-plastic corrector procedure. If the additive strain rate composition

$$\mathbf{d} = \mathbf{d_e} + \mathbf{d_p} \tag{2}$$

is assumed in the mid-time step configuration, this procedure takes the classical small strain format. For the plane stress case, a consistent algorithmic treatment

has been derived in [14]. It should be noted that local iterations on the element level are not omitted in the present work, as is usually done in other explicit schemes.

3. MECHANICAL CONTACT

3.1. Contact Interaction

One of the key issues in the developement of combined finite/discrete element technology for a large class of industrially relevant problems is the treatment of general 2D and 3D contact impact, i.e. enforcement of the constraint that no point in the space is occupied by more then one body at the same time.

The surfaces of solids are wavy and rough, Figure 1. As a consequence of the surface irregularities, the contact between two surfaces is always discrete. In mechanical contact pressure is actually transferred through a set of points in which surfaces touch. With increasing normal pressure elastic and/or plastic deformation of individual asperities occurs, resulting in an increase in the real contact area. At some point, undulations over which asperities are distributed begin to influence significantly the shape and size of the real contact area, through change of the shape of the contour area.

Figure 1. Typical rough surface profile

Experimantal tests and theoretical investigations relate normal stress in the contact interface to the approach between the two contact surfaces

$$\sigma_n = \hat{\sigma}_n(a_n, \mathbf{s}) \tag{3}$$

where a_n is the approach and $\mathbf{s}$ is a vector of state variables depending on the magnitude and nature of normal forces, degree of fracture of surface asperities, work hardening of surface asperities, wear, plowing phenomena, phase changes, thermal effects, etc.

The most simple contact law expresses normal pressure as a function of the approach only

$$\sigma_n = \hat{\sigma}_n(a_n) \tag{4}$$

in which case $\hat{\sigma}_n$ is in general a nonlinear function, although in computational literature for the sake of simplicity a linear relationship is often adopted.

Over the last decade a considerable body of literature has also been devoted to tangential resistance in contact. Among theoretical approaches to friction phenomena are local and nonlocal theories of friction [16,17] based on detailed analysis of interaction among asperities, adhesion, microcutting, etc.

In practical applications concerning computational mechanics, the analogy which exists between plastic and frictional phenomena [18,19,20] have been usually exploited. In static problems for small tangential force it is assumed that the tangential displacement increases with increase in the tangential force.

$$\tau = \hat{\tau}_n(\mathbf{a_T}) \tag{5}$$

Considerable sliding occurs only after the tangential resistance is reached. The tangential resistance to motion is in general a function of normal pressure and in the most simple form a law similar to the classical theory of plasticity can be derived

$$F_n(\sigma_n, \tau, \kappa_n) = 0 \tag{6}$$

$$F_T(\sigma_n, \tau, \kappa_T) = 0 \tag{7}$$

$$\dot{a}_n = \dot{a_n}^{el} + \dot{a_n}^{in} \tag{8}$$

$$\dot{\mathbf{a}}_T = \dot{\mathbf{a}}_T^{el} + \dot{\mathbf{a}}_T^{in} \tag{9}$$

$$\dot{a_n}^{in} = \begin{cases} 0, & \text{if } F_n < 0; \\ \lambda \frac{\delta F_n}{\delta \sigma_n}, & \text{otherwise.} \end{cases} \tag{10}$$

$$\dot{a_T}^{in} = \begin{cases} 0, & \text{if } F_T < 0; \\ \lambda \frac{\delta F_T}{\delta \tau}, & \text{otherwise.} \end{cases} \tag{11}$$

where separate yield/slip surfaces for normal stress and tangential resistance are assumed. There are two reasons for this assumption. Firstly the physical nature of tangential and normal resistance is different. Secondly, an associated flow rule can be applied at least formally for normal and tangential components in turn. In fact the above formulation is a logical extension of the formulation employed in metal plasticity [20] and in a similar way leads to a nonsymmetric tangent operator.

3.1. Contact Kinematics

Numerical methods employed for implementing contact constraints [21] are based either on Lagrange multiplier methods or penalty function methods, although for some applications special approaches have been introduced, e.g. for high-velocity impact problems or dynamics of loosely packed particles in which transfer of momentum is the dominant effect of the contact interaction, a method based on momentum conservation has been employed [15].

In static problems a consistent linearisation of the field equations in the Newton iterative scheme is needed to ensure quadratic convergence in the region close to the solution [22]. Recent applications of non-associated flow rules have opened the way to a consistent linearisation, and thus quadratic convergence, although sometimes at the expense of complicated expressions for handling changing contact kinematics.

Within an implicit transient dynamics context the Lagrange multiplier method is implemented in a rigorous manner, whilst in explicit transient dynamics the term Lagrange multiplier method implies that the impenetrability conditions are satisfied approximately [24] (often through iterative solution of a coupled system of equations, e.g. Gauss iterative solver, and sufficiently small time steps taken to impose energy and momentum balance). The penalty method is either used to impose the impenetrability condition in an iterative manner or to ensure the correct response of the physical system despite violating impenetrability conditions. In explicit transient dynamics the penalty formulation is well suited for contact modelling, however, the presence of nonlinear contact kinematics may induce instability of the numerical integration scheme [11,12].

In large systems [11,12] it may not always be possible to keep the penetration "small", in which case a finite penetration may occur but a correct overall behaviour of the system may still be achieved. However, with most algorithms in use, the finite penetration produces imbalance of energy and/or momentum and in cases with pronounced local confinement can lead to a solution failure due to the instability induced by repeated contact/release.

The kinematics of contact is often treated by slideline algorithms [25]. Traditionally one surface is designated as the master (target) surface while the other surface is designated as the slave (contactor) surface [26]. The common feature of all algorithms that handle contact kinematics in this way are the concentrated contact forces that arise although there have been some attempts at applying a distributed approach through calculation of overlapping volumes between bodies in contact [27].

Both distributed and concentrated approaches may involve many branches of code and can be difficult to vectorise or parallelise [28], in which case contact processing can be the critical issue in deciding the efficiency of a algorithm. To deal with the problem, a so called pinball algorithm has been proposed [29]. The pinball algorithm is among the simplest slideline algorithms. Its core idea is to

embed pinballs in surface elements and to enforce the impenetrability condition only on pinballs. Difficulties can arise from the large number of pinballs needed to discretise the surface and/or unrealistic contact force distribution due to the discrete nature of the pinballs.

More realistic contact force distribution is achieved by a so called defence node algorithm [30]. The normal force is proportional to the gap between the contact node and the target face. The major difficulty with this model is a need for additional logic if more complex 3D situations are to be handled, which makes the model extremely difficult for tuning to preserve energy balance.

The solution to this problem was considered in the context of computer graphics and discrete element methods. However initial considerations of the model based on intersection volumes were abolished because of the computational costs involved. One of the interesting algorithms from this class is the algorithm based on fuzzy boundaries [27]. However the model employed trades off efficiency against reliability.

Energy balance at both small and finite penetrations is exactly preserved with a contact model based on the concept of contact elements [11,12]. The model employed for contact kinematics was originally developed to handle 2D problems. The major drawback of the algorithm is difficulty in implementing it for 3D problems, where for instance a surface normal may not be defined at all surface points.

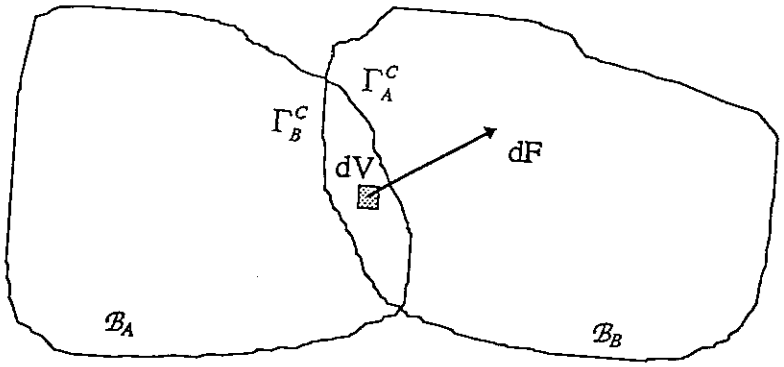

Figure 2. Potential contact force

In this work a potential contact force approach, figure 2, is applied. The contact algorithm developed has to date been applied to 2D and 3D explicit transient dynamics problems. The most important feature of the algorithm is the preservation of momentum and energy balance irrespective of the permitted overlaps (penetrations).

3.2. Contact Detection

In the discrete element methods, each element is considered as a separate, distinct body that interacts with neighbouring elements. In this context both representation of individual bodies and contact detection algorithms are very important both from practical and algorithmic point of view. The geometry of individual bodies is traditionally represented through discretisation or through mathematical objects, such as superquadrics and hyperquadrics [31], which are specially suitable for systems comprising small particles where deformability is not of greater importance. The effective solution of large scale discrete element problems relies upon a robust and computationally efficient contact detection algorithms. Consequently considerable research has been focused on this topic.

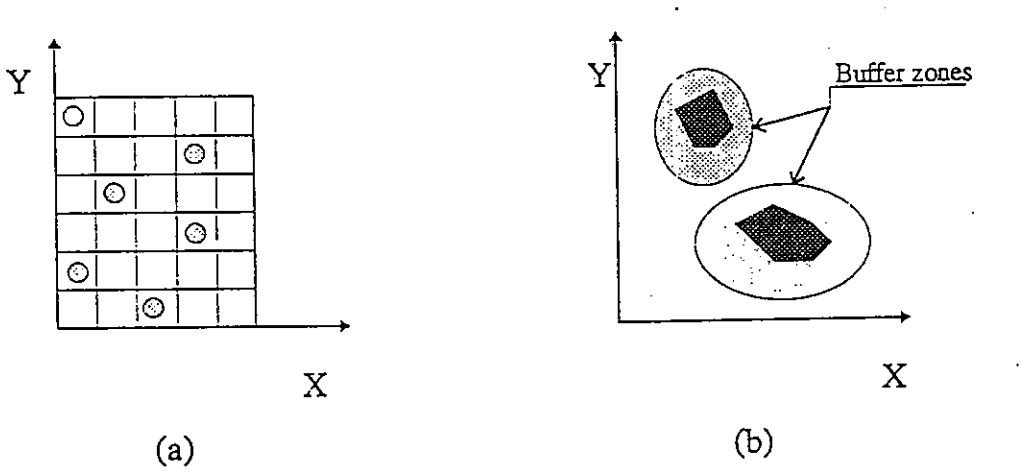

Figure 3. (a)space subdivision and (b) buffer zones

In general the optimal contact detection algorithm is dependent upon the problem to be solved. For instance, the master and slave surface algorithm better suits two-surface contact situations and the single surface algorithm is preferred in problems with highly distorted contact surfaces with self-contact situations. On the other hand, for quasi-static problems, relative motion of individual bodies is restricted, relative arrangements of individual bodies remain constant and well established contact detection concepts from finite element based applications can be considered. However, transient dynamics problems allow significant relative motion of individual bodies, thus more robust contact detection algorithms for either dense or loose packing are required. In the last decade a number of contact detection algorithms has been reported in the literature, most of them having $Nln(N)$ proportional contact detection time. The majority of these algorithms can be classified as body based search or space based search, figure 3.

The master and slave surface interface concept usually starts with global search for the closest master node to each slave node [28]. After this rather costly initial search, only the closest neighbourhood of each master and slave node combination

is checked in succeding time steps. The algorithm is likely to fail if contact surfaces become too distorted or if single surface contact situations should occur.

The direct checking (brute force search) method is computationally most simple and usually most expensive and for this reason in most cases not affordable.

A so called linear complexity contact detection algorithm [33] is especially suited for detailed analysis of object to object intersection. The representation makes use of mapping of boundary coordinates into a single valued function. The algorithm benefits from the simple data structure employed to present geometry.

A concept of contact hierarchies is exploited by the algorithm proposed by Zhong [30]. The search procedure is based on definitions of contact territories of cubic shape. When the common territory is detected, the elements at the same levels of the hierarchy which are enclosed or intersected by common territory are tested.

A so called single surface contact algorithm [32] assigns to each node a segment of space (bucket). The list of nodes in each bucket is used to find all segments that are candidate contact segments for each contact node, figure 4.

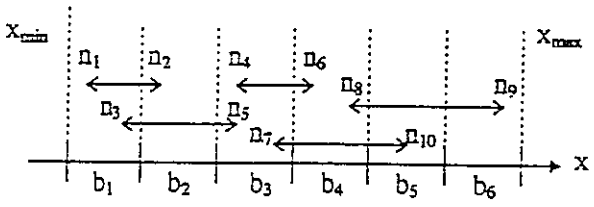

Figure 4. Set of buckets in one dimension

The so called position codes algorithm [32] is based on similar concepts - the problem of sorting and searching in three dimensions is transformed to a one dimensional sorting and searching with contact detection time being proportiopnal to $NlnN$.

Alternating digital tree algorithm [23] was originally developed for mesh generation purposes. However with minor modifications it can also be successfully employed for discrete elements. A quad tree and binary tree based algorithm [11,12] based on a so called coordinate based space decomposition also achieves logarithmic efficiency.

In this work BSD contact detection algorithm [11,12] is employed. As the name implies, B stands for binary, S for space cell decomposition and D for direct evidence. The core of the algorithm is a binary tree search, figure 5. The particular advantage of the algorithm is its ability to handle both loose and dense packing

and systems comprising of mixture of small particles and very large self contacting general shape bodies.

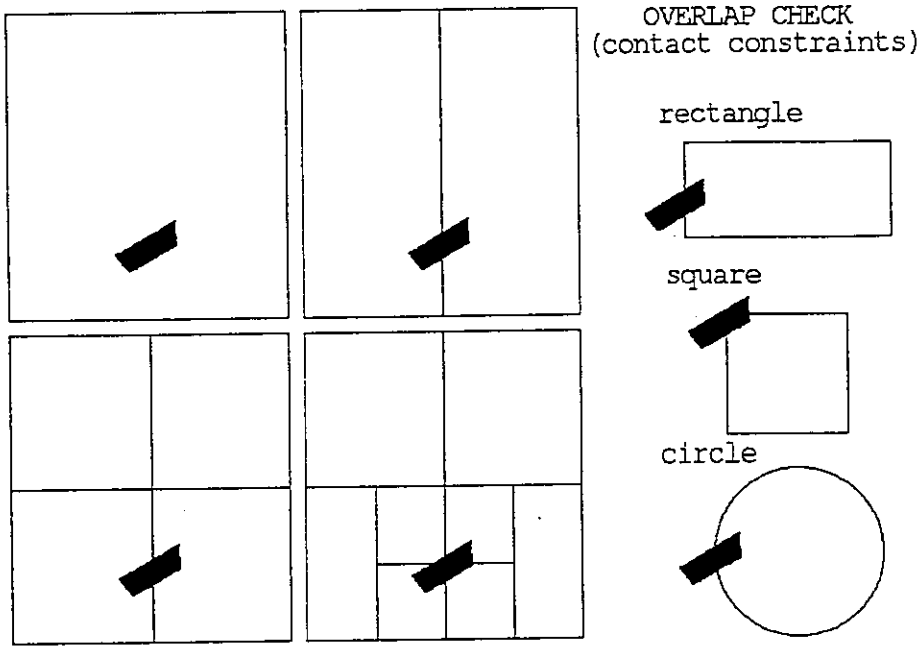

Figure 5. The binary tree search

3. TRANSITION FROM CONTINUA TO DISCONTINUA - FRACTURING

3.1. Brittle Fracture

The main tasks in describing fracturing are: (1) to predict crack initiation (2) to predict propagation (3) to perform the necessary remeshing (4) to transfer variables from the old to new mesh and (5) to replace released internal forces with equivalent contact forces.

Fracture mechanics concepts could be applied in this context. A more robust approach is however achieved through modelling of conditions for gradual fracturing (strain localisation prior to separation by cracking or shear slip).

Nonlinear continuum based material models for fracturing media are usually generalisations of elasto-plasticity laws using different failure (or fracture) surface descriptions, and no discontinuities are admitted in the displacement field as the geometry of a problem remains unchanged. Some models attempt also to simulate post fracturing behaviour, again via continuum formulations. Models adopted for prefragmentation, i.e. continuum, stage are usually based on concepts of damage mechanics, strain softening plasticity formulations (utilising fracture mechanics concepts of energy release required to open a crack or induce a shear slip) or have been formulated using some higher order continuum theory. The numerical

modelling of pressure dependent civil engineering materials (e.g. rocks, concrete) is far more complex than modelling of metals, and it frequently requires more complex constitutive modelling (non local theories, vectorial damage description, localisation modelling, Cosserat continuum) to be adopted as a basis for analysis.

Pressure dependant quasi brittle materials are often treated as softening materials, i.e. materials which show a reduction of the load-carrying capacity accompanied by incresaing (localised) deformations after reaching the maximum load-carrying capacity. Beyond the failure load i.e. when the material gradually disintegrates, two types of failure mechanisms are observed, namely decohesion and frictional slip. In the first type of failure fracture zones are observed (cracks), while in the latter failure zones propagate along shear bands (faults).

Standard continuum mechanics formulation incorporating softening fails for such a case of localised failure, as its use is beyond the limit of its applicability and the underlying mathematical problem becomes ill-posed. Physically, this is because standard, rate independent coninuum models do not recognise or include a length scale and therefore no characteristic dimensions or spatial interaction in any potential localisation zone can be present. As a result, numerical solutions in the limit predict a vanishing energy dissipation upon spatial discretisation refinement and scale effects such as spacing of cracks or faults cannot be captured.

A mathematically well-posed problem can be obtained by using an enriched or higher-order continuum formulation for the softening solid. Failure behaviour of softening materials can be rigorously described through various ways - a non-local or gradient model where the higher order gradients of the deformation field are included in the formulation, or a rate-dependent model, with the higher order time derivatives included. The inclusion of a first-order time derivative term in the constitutive equations (rate dependent crack model, viscoplasticity model) of the softening solid is not only natural from a physical point of view (high loading rates) but also from a mathematical point of view. Finally, a Micro-polar (Cosserat) model can be adopted, based on the idea that a macro- structure consists of micro-elements with a finite length.

Although the well posed problem can be rigorously formulated by using the above enriched or higher-order continuum formulation for the softening solid, a relatively straight forward alternative utilising a fracture energy based softening plasticity framework has been successfully adopted, where a mesh size dependent softening modulus ensures objective energy dissipation and remedies this spurious behaviour to a large extent.

In the authors' experience, the use of a fracture energy based softening plasticity model to control the evolution of the failure surface in most cases suffices to overcome any mesh dependance problems. This is because the influence of mesh alignment in small discrete elements may not have a large inflence on the overall response. If this is not true and if the discrete elements remain large, i.e.consist of a large number of finite elements, the influence of the orientation of the mesh lines

cannot be neglected and enriched or higher-order continuum models may also have to be considered for the discrete elements.

3.2. Ductile Fracture

A common feature of recent attempts is to move beyond the classical failure criteria (Rankine) and employ more robust descriptions of initial and residual failure surfaces. In this context a computationally convinient analogy with Classical Theory of Plasticity can be derived with Fracture criterion being equivalent to yield criterion, crack propagation rule being equivalent to flow rule and fracture hardening-softening rule being equivalent to classical hardening-softening rule.

The crack propagation rule defines the direction of crack growth from a crack tip. It is known from fracture mechanics that for two dimensinal cases there are two possible independent movements of the crack boundaries. They are referred to as Mode I (opening) and Mode II (shearing) fracture modes, depicted in figure 6.

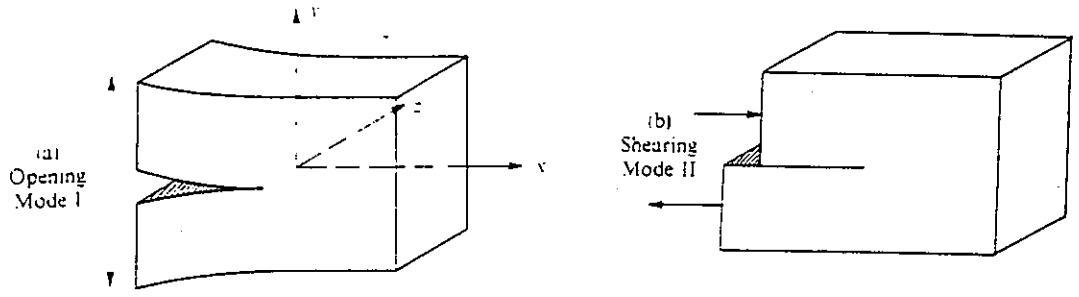

Figure 6. Fundamental modes of fracture

In the present work, two crack propagation rules have been formulated which approximate these two modes. However, they are based on the direction of principal plastic strains, which are more fundamental physical factors then stresses.

For Mode I, the crack direction is assumed perpendicular to the direction of maximal tensile plastic strain and can be referred to as *tensile fracture mode.* Computationally, the plastic strain tensor is updated incrementally according to the hypoelastic rotation measure.

While this rule is straightforward and unambigous, for Mode II a failure along the direction maximal shear plastic strain, or *shear fracture mode* is assumed, which obviously gives two possible solutions. The following procedure based on integration of a *fail factor* has been formulated which provides the choice between the two shear options: Starting from the crack tip, the following average integral is calculated in each semidirection, providing four scalar values:

$$I_F = \int_0^r F_F \, dr \tag{12}$$

Here, F_F indicates the fail factor which is linearly interpolated between element edges, while r is equal to a predefined value r_I (radius of influence), or less then r_I if a discrete element boundary is encountered on the integral path.

Generally, a fracture criterion can take either the classical form where a scalar function of the material point state parameters (stress, strain, internal variables,...) is defined, or it can be expressed directly by means of an elasto-plastic damage model [34]. Although the latter approach is more general in terms of variety of stress and strain histories, the former is easier for a numerical implementation, yet accurate enough if the parameters are obtained from experiments calibrated to match the problems to be simulated.

A comprehensive review of ductile fracture criteria are summarized in reference [34], where original references can also be found. Other criteria have been advocated for brittle fracture, with the most widely used being the Rankine model.

In the present research, the simpler criteria have been considered [34], namely Freudenthal (total plastic work), Cockroft-Latham (tensile plastic work) and Oyane. Numerical investigations have shown that the Oyane criterion represents a good compromise between simplicity and accuracy.

3.3. Discretisation

As it has already been said, a new algorithmic problem arises upon separation, as the "book keeping" of neighbours and updating of the discrete element list is needed whenever a new partial or complete failure occurs. In addition, there is also a need to transfer state variables (plastic strains, equivalent plastic strain, dissipated energy, damage variables) from the original deformable discrete element to the newly created deformable discrete elements.

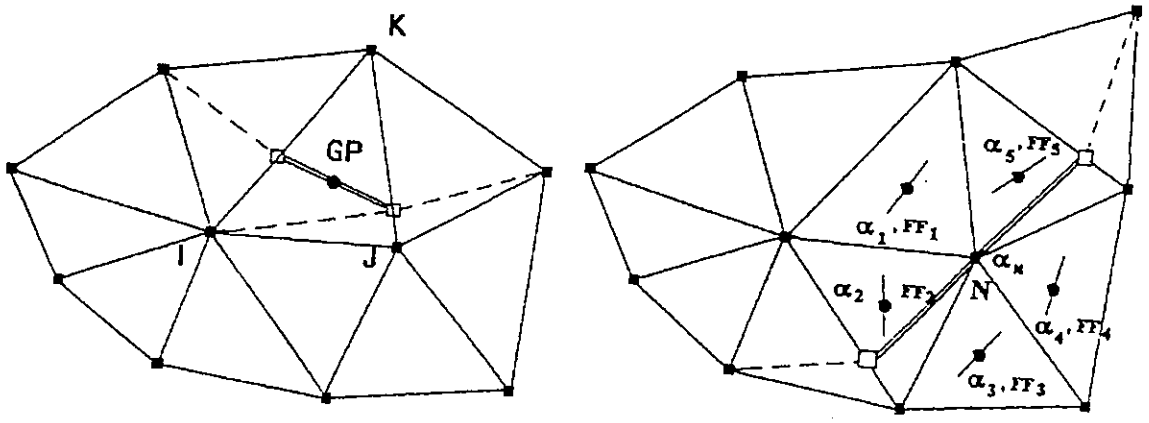

Figure 7. Local remeshing

In modelling the fragmentation, the required minimum number of finite elements needed in the localisation zone to describe the sharp peak in the deformations can be prohibitively high if the direction of crack or fault propagation is not known in advance. When the load-carrying capacity in the crack or the shear band reduces to zero the continuum has been split up. A network of fully developed localisation zones leads to the appearance of discrete elements, consisting of one or more finite elements, requiring some form of remeshing, figure 7. When parts of the fractured continuum become fully separated, the problem topology changes with the creation of new discrete bodies. The separate bodies are again considered deformable.

The total number of finite elements can be kept within reasonable limits when the mesh is adapted dependent on the localisation process. If mesh adaptivity techniques are used, a finer division of elements can be applied in the localisation zone, while keeping the discretisation of the remainder of the body relatively coarse.

The automated adaptive finite element simulation comprises discretisation, finite element analysis and accuracy assessment. The discretisation procedure discretises each discrete element into finite elements. The finite element model goes through the analysis procedure to perform finite/discrete element analysis. The finite element solution, yielded by the combined finite/discrete element analysis, as an approximative solution goes through an error estimating procedure and if the pre-set accuracy is not reached, or the model is evolved beyond the tolerance limit, this procedure will pass the required data and switch the control to the mesh prediction module within the accuracy assessment procedure. Based on the (discretisation) error data, the module is capable of designing a better mesh, figure 8. In this process finite element solutions from the old mesh are mapped to the newly adapted mesh.

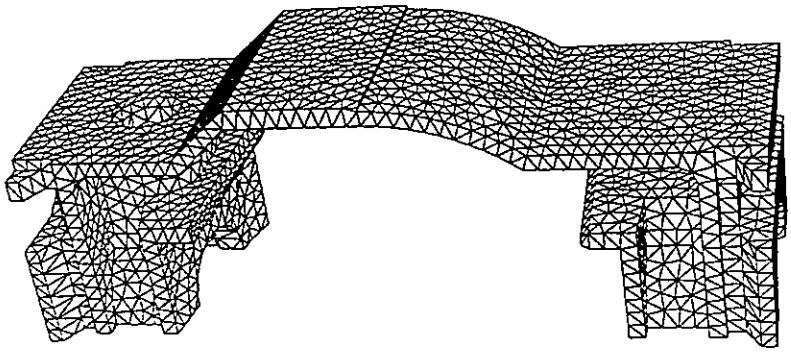

Figure 8. A 3D mesh

3.4. Infinite Domains

An important discretisation problem is also related to the treatment of model boundaries. If fracturing of a continuum is considered, problems with treatment of artificial boundaries extending into infinite domains remains the same as for the

transient dynamic finite element analysis, i.e. the issue of nonreflecting boundaries need to be taken into account. In the context of particle mechanics, the imposition of rigid or the so called periodic (repeated) boundaries may restrict discontinuities or localisation patterns that would potentially develop at model boundaries.

3.5. Temporal Discretisation

Apart from spatial discretisation, temporal discretisation requires attention in situations where repeated contact-release situations are common (confined systems). Problems with spurious energy generation arise when applying the central difference explicit time integration scheme. Local contact energy dissipation is often necessary to avoid energy imbalance or unstable solution. Such modified temporal operators [11] do not affect the critical time step. However other types of nonlinearity such as softening may impose additional limits on the time step. Furthermore, if a higher order continuum formulation is adopted, the time integrator should be modified to increase accuracy as the use of such a framework leads to dispersion of waves, i.e. the waves with different wave numbers propagate with different velocities in the localisation zone. A dispersion analysis results in even more severe limits for element size and time step.

4. NUMERICAL EXAMPLES

Recent developments concerning ductile fracture are illustrated by means of numerical examples. Three examples are shown. The first example is concerned with determination of macroscopic friction laws based on micromechanical numerical simulations. Frictional contact of rigid obstacle asperities with two different configuration of deformable body asperities has been simulated by means of the obstacle prescribed displacement Δx and Δy. Local Coulomb friction $\mu = 0.2$ and isotropic hardening of the bulk material are assumed. Deformed configurations for both meshes, including the resulting global forces and global friction coefficient diagrams are shown in figure 9.

The fracturing of a deformable asperity in contact with a series of rigid counterparts is modelled in the second example. Similar material parameters as in the first example have been employed. The Cockroft-Latham fracture criterion is used with a tensile fracture crack propagation rule. Global and zoomed meshes at various stages of wear particle creation are depicted in figure 10.

Finally, the generality of the numerical model developed in this work has been tested in the macroscopic simulation of a cold metal cutting operation. Oyane's criterion and a shear fracture crack propagation rule have been found to represent closely the metal behaviour in this industrial forming process. The results are shown in figure 11.

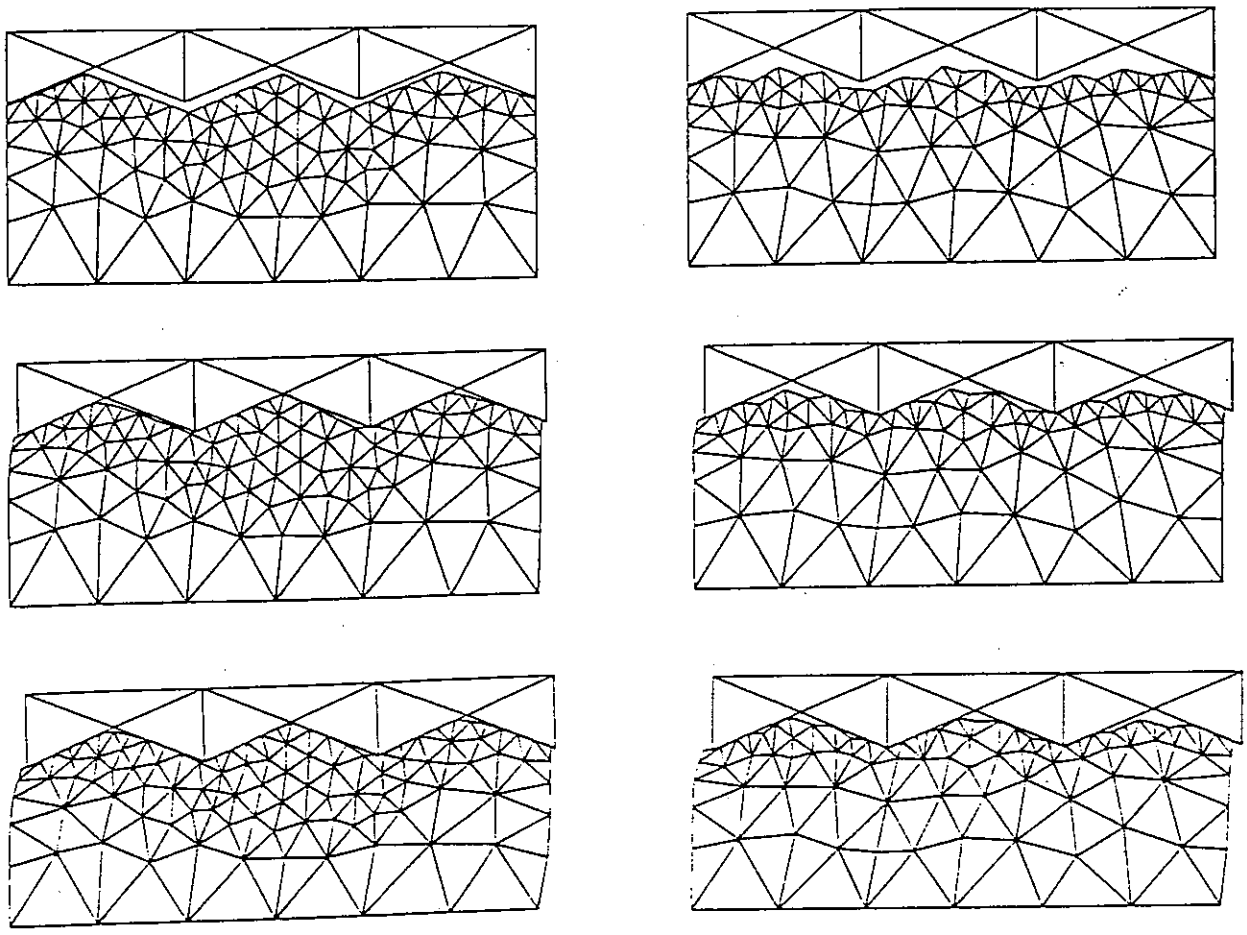

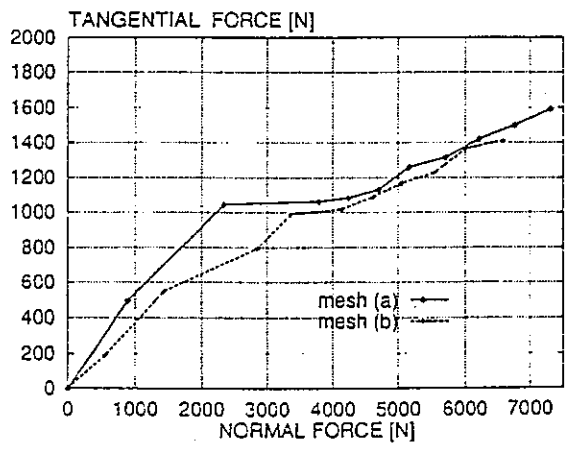

(a) Normal-tangential force diagram

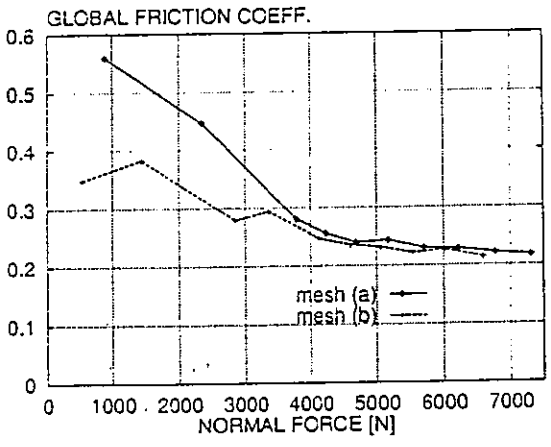

(b) Normal force-global friction coefficient diagram

Figure 9. Rigid-deformable asperities contact

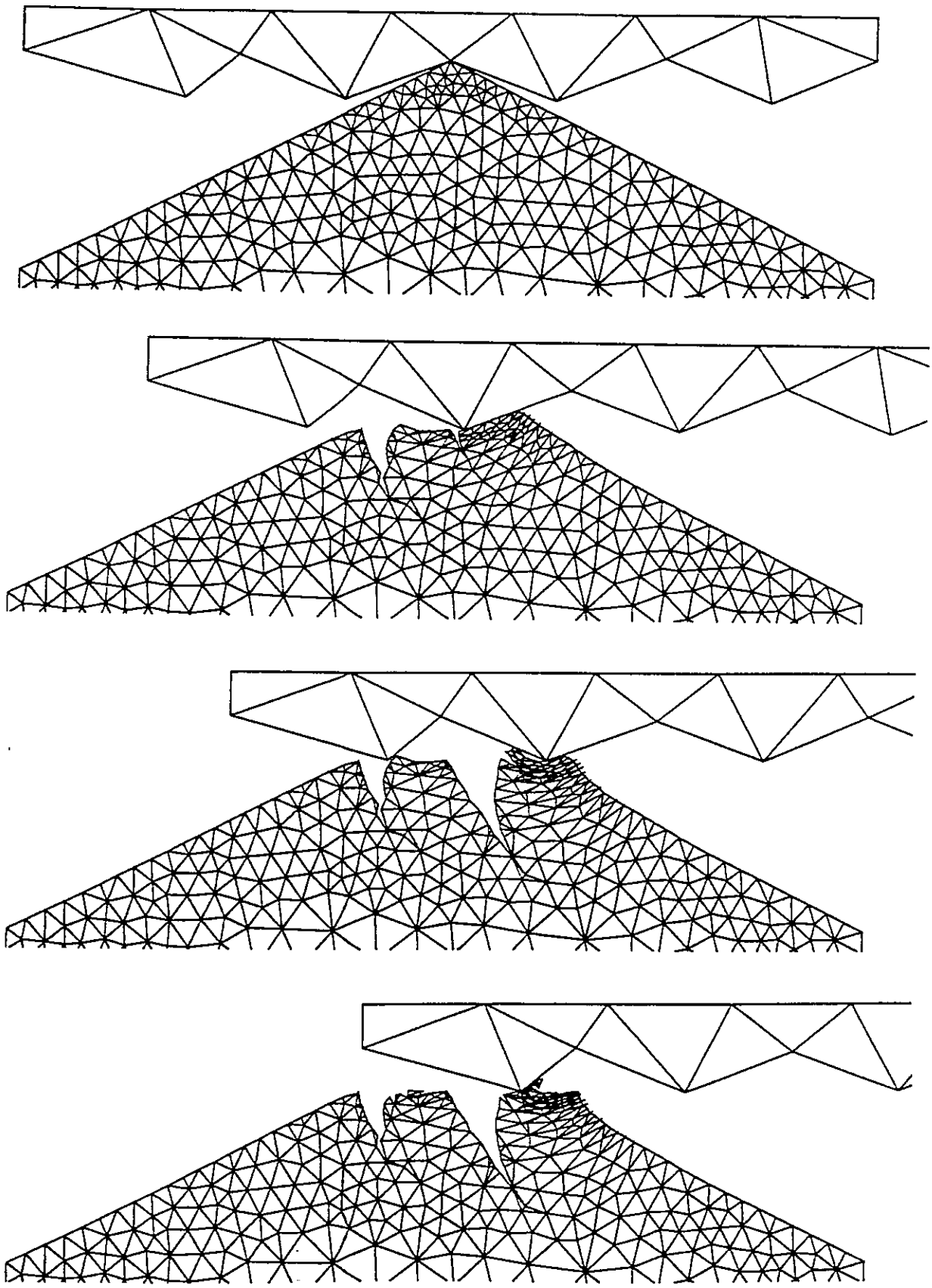

Figure 10. Rigid-deformable asperities wear simulation

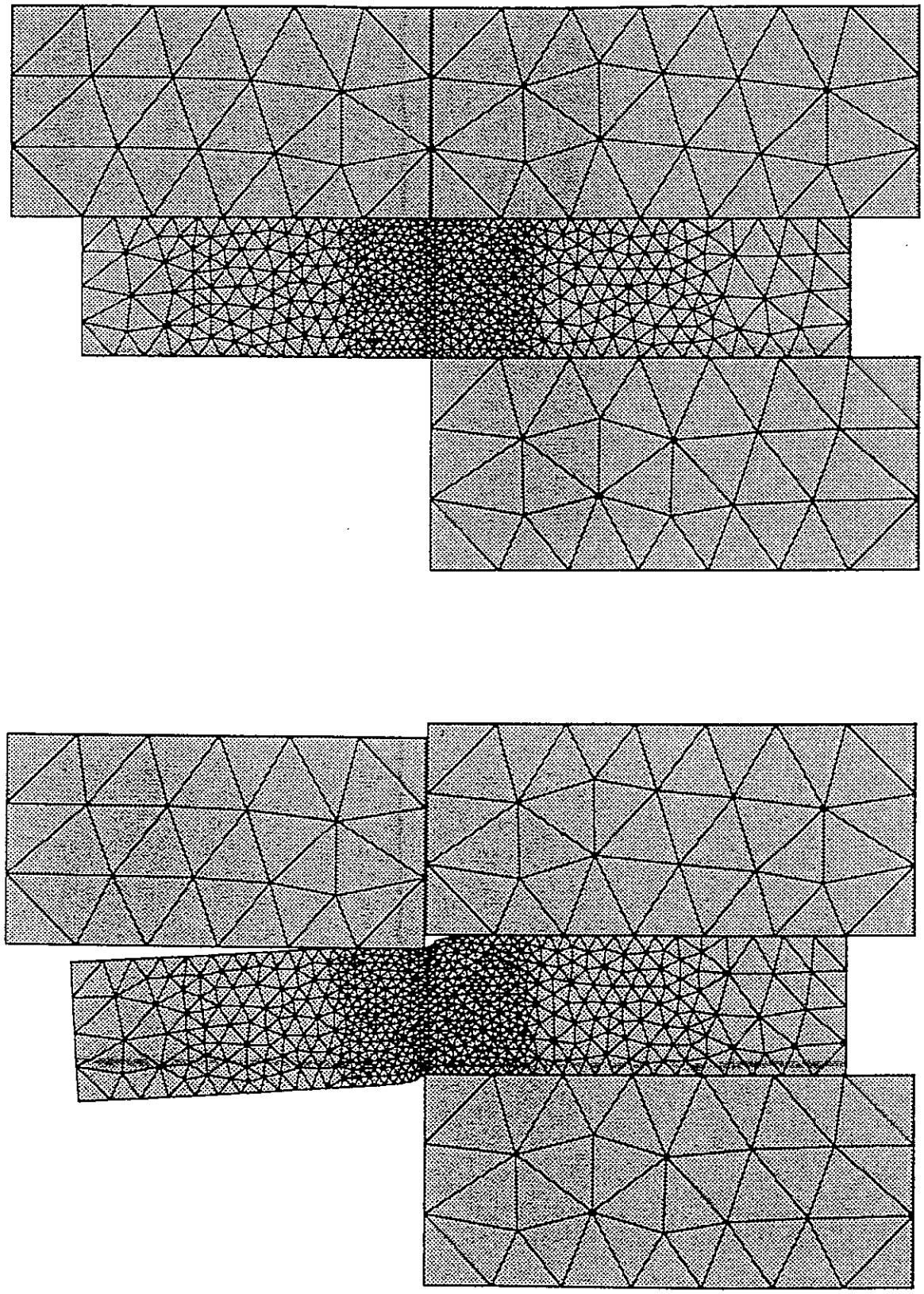

Figure 11a. Metal cutting simulation

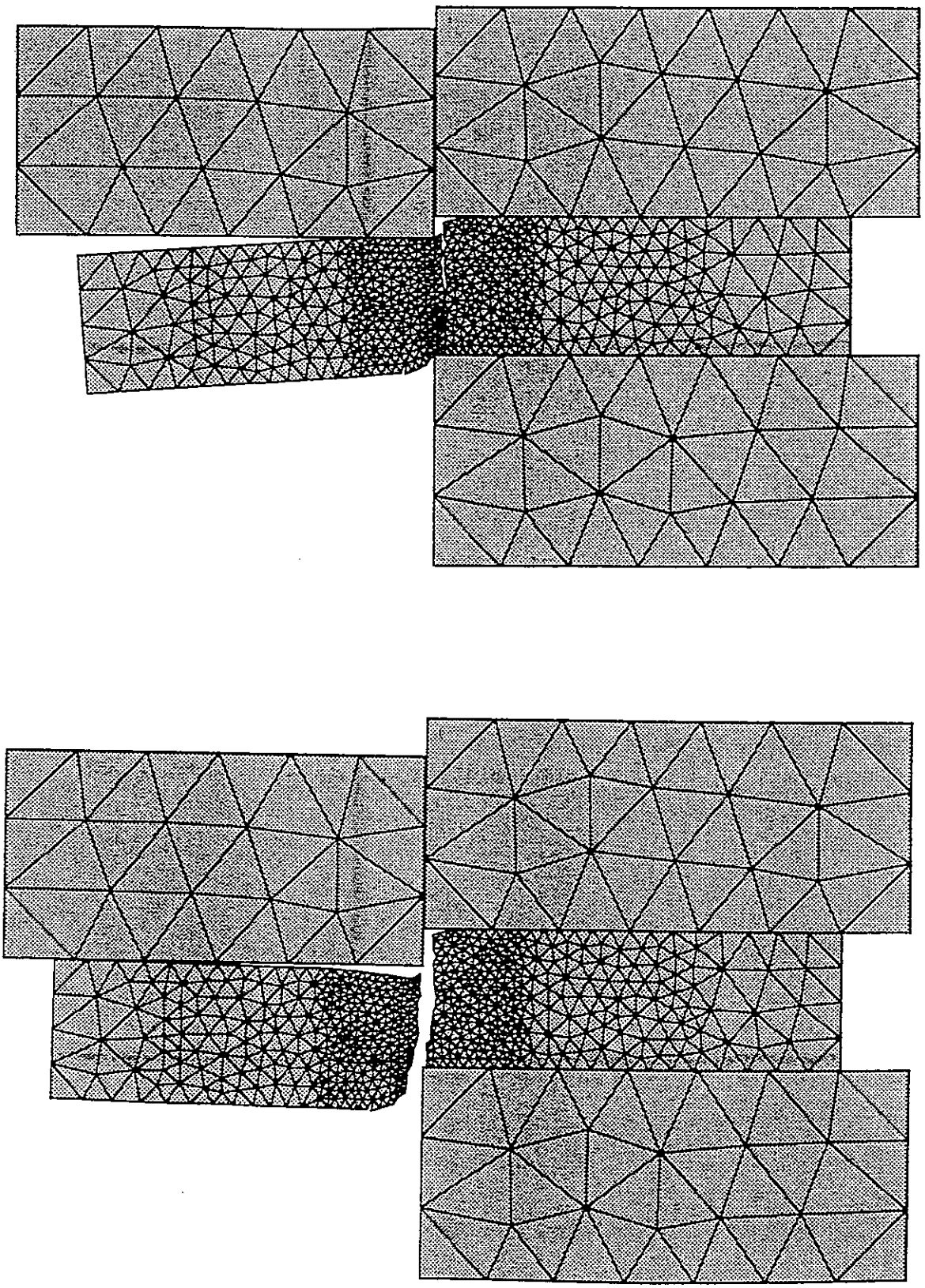

Figure 11b. Metal cutting simulation

5. CONCLUSIONS AND RESEARCH RECOMMENDATIONS

A combined finite/discrete element approach to the simulation of progressively fracturing continua has been presented. The need for efficient algorithms for modelling the separate phenomena that arise has been emphasised.

Basic elements of a comprehensive, general and upgradable numerical model for a wide range of engineering applications have been described. Although the results shown here and elsewhere can be considered as initial attempts in the field, realistic simulations have already yielded useful and practically aplicable results.

The future research and enhancement of the model should be directed in three principal directions: (1) development of efficient element technology for plane strain/axisymmetric and possibly 3-D explicit finite element models; (2) remeshing techniques with approprite mapping algorithms; (3) experimental verification of the proposed models and/or combined numerical-experimental inverse identification of fracture and contact law parameters

In view of the large scale nature of practical industrial problems, the use of parallel processing strategies in computational solution is particularly attractive. The explicit nature of the methodology makes it particularly suitable for parallelisation. The situation may be complicated by fracturing and contact conditions that take place throughout the transient process.

REFERENCES

1. R.E.Goodman, R.L.Taylor and T.Brekke, 'A model for mechanics of jointed rock', *J. Soil Mechanics & Foundation Div.*, ASCE 94, SM3, (1968).
2. P.A.Cundall, 'A computer model for simulating progressive large-scale movements in blocky rock systems', *Proc. Int. Symp. on Rock Fracture*, Nancy, France, II-8, (1971).
3. J.R.Williams, G.G.W.Mustoe, 'Modal methods for the analysis of discrete systems', *Computers and Geotechnics* 4, 1-19, (1987).
4. S.Gen-Hua, R.E. Goodman, 'Discontinuous deformation analysis - a new method for computing stress, strain and sliding of block systems', in P.A. Cundall *et al* (Eds.) *Key Questions in Mechanics*, Balkema, Rotterdam, 381-393, (1988).
5. J.Lemos, R.D.Hart, P.A.Cundall, 'A generalized distinct element program for modelling jointed rock mass', in Stephansson, O (Ed.) *Fundamentals of rock joints*, Centek Publishers, Lulea, 335-343, (1985).
6. G.Mustoe, J.R.Williams, *Proc. 1st U.S. Conf. on Discrete Element Methods*, Golden, Colorado, Oct. (1989).
7. J.R.Williams, G.Mustoe, *Proc. 12nd U.S. Conf. on Discrete Element Methods*, MIT, MA, (1993).
8. G.H.Shi, *Discontinuous deformation analysis - a new numerical method for the statics and dynamics of block system*, PhD thesis, Dept. Civil Engng., University of California, Berkeley, (1988).

9. J.Ghaboussi, 'Fully deformable discrete element analysis using a finite element approach', *Intl. Journal of Computers in Geotechnics*, 5, 175-195, (1988).
10. K.Oda, T.Shigematsu, N.Onishi, 'A new numerical method for liquid-solid flows - its application to analysing behaviour of solid particles dumped into water', *Proc. 2nd Intl Conf on DEM*, Williams and Mustoe, (Eds), IESL Publications, Boston, 165-177, (1993).
11. A.Munjiza, *Discrete elements in transient dynamics of fractured media*, Ph/D. thesis, Department of Civil Engineering, University College of Swansea, (1992).
12. A.Munjiza, D.R.J.Owen, N.Bićanić, 'A Combined finite-discrete element method in transient dynamics of fracturing solids', *Int. J. Engineering Computat ions*, 12, 145-174, (1995).
13. P.Cundall, *UDEC - A generalised distinct element program for modelling jointed rock*, US Army European Research Office, NTIS Order No. AD-A087-610/2, (1987).
14. J.C.Simo, R.L.Taylor, 'A return mapping algorithm for plane stress plasticity', *Int. J. Num. Meth. Eng.*, 22, 649-670, (1986).
15. T.B.Belytschko and J.I.Lin, 'A three-dimensional impact-penetration algorithm with erosion' *Comp. Struct.*, 25, 95-104 (1987).
16. J.T.Oden and J.A.C.Martins, 'Models and computational methods for dynamic friction phenomena' *Comp. Methods Appl. Mech. Eng.*, 52, 527-634 (1985).
17. J.T.Oden and E.B.Pires, 'Nonlocal and nonlinear friction laws and variational principles for contact problems in elasticity', *J. of Appl. Mech., ASME,*, 50, 67-76 (1983).
18. A.Curnier, 'Atheory of friction' *Int. J. Solids Struct.*, 20, 637-647 (1984).
19. R.Michalowski and Z.Mroz, 'Associated and non-associated sliding rules in contact friction problems' *Arch. Mech.*, 30, 259-276 (1978).
20. P.Wriggers, T.V.Van and E.Stein, 'Finite element formulation of large deformation impact-contact problems with friction' *Comp. Struct.*,37, 319-331, (1990).
21. J.Bohm, 'A comparison of different contact algorithms with applications', *Comp. Struct.*, 26, 207-221 (1987).
22. H.Parisch, 'A consistent tangent stiffness matrix for three-dimensional non linear contact analysis', *Int. J. Num. Methods. Eng.*, 28, 1803-1812 (1989).
23. J.Bonet, J.Peraire, 'An alternating digital tree (ADT) algorithm for 3D geometric searching and intersection problems', *Int. J. Numer. Methods. Eng.*, 31, 1-17, (1991).
24. N.J.Carpenter, R.L.Taylor and M.G.Katona, 'Lagrange constraints for transient finite element surface contact' *Int. J. Num. Methods Eng.*, 32, 129-147 (1991).
25. J.T.Oden and J.A.C.Martins, 'Models and computational methods for dynamic friction phenomena' *Comp. Methods Appl. Mech. Eng.*, 52, 527-634 (1985).
26. T.J.R.Hughes, R.L.Taylor, J.L.Sackman, A.Curnier and W.Kanoknukulchai, 'A finite element method for a class of contact impact problems' *Comp. Methods Appl. Mech. Eng.*, 8, 249-276 (1976).

27. J.R.Williams, 'Contact analysis of large numbers of interacting bodies using discrete modal methods for simulating material failure on the microscopic scale' *Eng.Comput.*, 5, 198-209, (1988).
28. J.G.Malone, N.L.Johnson'A parallel finite element contact/impact algorithm for non-linear explicit transient analysis: part I-the search algorithm and contact mechanics' *Int. J. Num. Methods. Eng.*, 37, 559-590 (1994).
29. T.Belytschko and M.O.Neal, 'Contact-impact by the pinball algorithm with penalty and Lagrangian methods' *Int. J. Num. Methods Eng.*, 31, 547-572, (1991).
30. Z.H.Zhong and L.Nilsson, 'A contact search algorithm for general 3-D contact-impact problems' *Comp. Struct.*, 34, 327-335 (1990).
31. J.R.Williams, A.P.Pentland, 'Superquadrics and modal dynamics of discrete elements in concurrent design, *1st US Conference on Discrete Element Methods*, (1988).
32. M.Oldenberg, L.Nilsson, 'A position code algorithm for contact searching', *Int. j. numer. methods. eng.*, 37, 359-386 (1994).
33. R.O'Connor, M.J.Gill, J.R.Williams, 'A linear complexity contact detection algorithm for multy-body simulation', *Proceedings of the 2nd International Conference on Discrete Element Methods*, MIT, (1993).
34. S.Cescotto, Y.Y.Zhu, TITLE *Proceedings of the Fourth International Conference on Computational Plasticity - COMPLAS IV, Barcelona, Spain*, 987-998, (1995).

Numerical Manifold Method

Gen-hua Shi

Geotechnical Lab, US Army Engineer Waterways Experiment Station, Vicksburg, MS 39180-6199

Abstract. Aiming global analysis, the well known mathematical manifold is perhaps the most important subject of modern mathematics. Based upon mathematical manifold, this numerical manifold method is a newly developed general numerical method. This method computes the movements and deformations of structures or materials. The meshes of the numerical manifold method are finite covers. The finite covers overlapped each other and covered the entire material volume. On each cover, a independent cover displacement function is defined. The cover displacement functions on individual covers are connect together to form a global displacement function on the entire material volume. The global displacement function are the weighted averages of the independent cover functions on the common part of several covers.

Using the finite cover systems, continuous, jointed or blocky materials can be computed in a mathematically consistent manner. The mathematical covers and physical mesh are independent. As mathematical covers can be moved, split removed and added, the large deformations can be computed by steps. Dividing a cover to two or more covers, jointed and blocky materials can be modeled. Both the finite element method (FEM) for continua and the discontinuous deformation analysis (DDA) for block systems are special cases of this numerical manifold method. In the current development stage of numerical manifold method, the extended finite element method can compute more flexible deformations and movements of joints and blocks.

1 Finite Covers Formed by Mathematical Mesh and Physical Mesh

Physically, material objects often have different shapes. When the material volumes have fractures or blocks the shapes and boundaries become more complex. Manifolds connect many individual folded covers together to study the entire material volume. The new method has separated mathematical covers and physical mesh: the mathematical covers define only the fine or rough approximations; as the real material boundary, the physical mesh defines the integration fields. The mathematical covers are chosen by user; the physical mesh includes the material boundaries, joints, blocks and the interfaces of different material zones. The physical mesh can not be chosen artificially. If the joints or block boundaries divide a mathematical cover to two or more completely disconnected domains, Those domains are defined as physical covers.

In Figure 1.1 and 1.2, two circles and one rectangle (indicated by thin lines) delimit three mathematical covers V_1, V_2, V_3. The thick lines indicate the material boundary and inner curved joints. In Figure 1.1, V_1 is divided by the physical mesh into two physical covers 1_1, 1_2, V_2 has two physical covers 2_1, 2_2 and V_3 has two physical covers 3_1, 3_2.

Figure 1.2 shows more joints. Mathematical cover V_2 contains two curved lines, but only two totally disconnected physical covers 2_1, 2_2 are formed. The upper curve (inside cover 2_1) can not cut through rectangle V_2 to form more physical covers, therefore cover 2_1 is a single physical cover. Similarly mathematical cover V_3 contains two physical covers 3_1, 3_2. In both Figure 1.1 and 1.2, the common part of two or more physical covers are defined as "elements" and marked by its cover numbers.

Figure 2.1 shows a simple but often useful chain cover system. This cover system is specially convenient for long and narrow material shapes. Figure 2.2 shows a DDA block system, here each block is a mathematical cover and a physical cover. There are no overlaps between any two covers in DDA case.

The finite element meshes can be used to define finite covers for manifold method. Considering any node, all elements having this node form a mathematical cover (called

"star" in algebraic topology). In Figure 3, there are 10 nodes, each node has a mathematical cover. Cover U_1 of node 1 has two elements $(1,2,5)$ and $(1,5,4)$. Cover U_5 of node 5 has 6 elements $(1,5,4)$, $(1,2,5)$, $(2,6,5)$, $(5,6,9)$, $(5,9,8)$, $(4,5,8)$. Any original finite element is the common area of the mathematical cover of its nodes. The element $(1,5,4)$ is the common area of covers U_1, U_5, U_4.

The physical mesh of Figure 3 is the thick lines, which are the boundaries and the joints of the material volume. In Figure 3 mathematical cover U_1 splits to two physical covers: $1_1, 1_2$; mathematical cover U_5 splits to three physical covers: $5_1, 5_2, 5_3$. The original element $(2,5,6)$ splits to three new elements $(2_1, 6_1, 5_1)$, $(2_2, 6_2, 5_2)$ and $(2_1, 6_3, 5_1)$.

Now, each physical cover is a new "node". Each "element" is a common part of exactly three physical covers. The element $(1_1, 5_1, 4_1)$ is the common part of three physical covers 1_1,5_1 and 4_1. Using the new nodes and elements, the joints can open and slide, the blocks can move away and the continuous area can still be connected. Two new elements $(1_1, 2_1, 5_1)$ and $(1_2, 2_2, 5_2)$ have no common new nodes and can be separated after the loads applied. Therefore the joint dividing the two elements can open or slide. The new elements $(1_2, 2_2, 5_2)$ and $(2_2, 6_2, 5_2)$ are divided by a edge $2, 5$ which is not a joint. Then the two elements have common edge $2_2, 5_2$

Before the deformation, some nodes share the same position. It can be understood as many layers divided by discontinuities on the original simple finite element mesh. Using the manifold definition of nodes and elements, the following important conclusions can be seen directly from Figure 3:

[1] the elements are irregularly shaped;

[2] each element has three physical cover numbers or "nodes";

[3] these three covers have one element as their common area;

[4] the adjacent elements have the same nodes along the common edge;

[5] two elements divided by joints have different nodes.

2 Cover Functions and Weight Functions on Finite Covers

The one dimensional cover functions $u_i(x)$ defined on physical cover U_i $u_i(x)$ $x \in U_i$ can be constant, linear, high order polynomials or locally defined series. These cover functions are connected together by the weight functions $w_i(x)$

$$w_i(x) \geq 0 \quad x \in U_i, \qquad w_i(x) = 0 \quad x \notin U_i, \qquad \sum_{x \in U_j} w_j(x) = 1$$

The weight functions $w_i(x)$ are the weighted average, which is to take a percentage from each cover function $u_i(x)$ for all physical covers U_i containing x. Using the weight functions $w_i(x)$, a global function $F(x)$ on the whole physical cover system is defined

$$F(x) = \sum_{i=1}^{n} w_i(x) u_i(x).$$

Figure 4.1 is a one dimensional example of three physical covers

$u_1(x) =$	A_3A_4	$U_1 = A_1A_2$	$w_1(x)u_1(x) = A_3A_5A_2$	$x \in U_1$
$u_2(x) =$	B_3B_4	$U_2 = B_1B_2$	$w_2(x)u_2(x) = B_1B_5B_6B_2$	$x \in U_2$
$u_3(x) =$	C_3C_4	$U_3 = C_1C_2$	$w_3(x)u_3(x) = C_2C_5C_4$	$x \in U_3$

The global function $F(x)$ is

$$F(x) = \sum_{i=1}^{n} w_i(x) u_i(x) = A_3A_5B_5B_6C_5C_4.$$

Figure 4.2 shows seven one dimensional physical covers $U_1 = x_0x_1$, $U_2 = x_0x_2$, $U_3 = x_1x_3$, $U_4 = x_2x_3$, $U_5 = y_3x_4$, $U_6 = y_3x_5$, $U_7 = x_4x_5$ Since the function has a jump at the point $x_3 = y_3$, the mathematical cover x_2x_4 was split to two physical covers $U_4 = x_2x_3$ and $U_5 = y_3x_4$.

$w_1(x)u_1(x)$	$w_2(x)u_2(x)$	$w_3(x)u_3(x)$	$w_4(x)u_4(x)$	$w_5(x)u_5(x)$	$w_6(x)u_6(x)$	$w_7(x)u_7(x)$
A_0x_1	$x_0A_1x_2$	$x_1A_2x_3$	x_2A_3	B_3x_4	$y_3A_4x_5$	x_4A_5
$x \in U_1$	$x \in U_2$	$x \in U_3$	$x \in U_4$	$x \in U_5$	$x \in U_6$	$x \in U_7$

The global function $F(x) = \sum_{i=1}^{7} w_i(x)u_i(x) = A_0A_1A_2A_3B_3A_4A_5$ is very close to the original natural curve.

For two dimensional manifold computation, the cover displacement functions $u_i(x,y)$ and $v_i(x,y)$ are defined on cover U_i. The global displacement functions $u(x,y)$ and $v(x,y)$ on the whole material body are two global functions:

$$\begin{Bmatrix} u_i(x,y) \\ v_i(x,y) \end{Bmatrix} = \sum_{j=1}^{m} \begin{pmatrix} f_{ij}(x,y) & 0 \\ 0 & f_{ij}(x,y) \end{pmatrix} \begin{Bmatrix} d_{i\ 2j-1} \\ d_{i\ 2j} \end{Bmatrix} \quad (x,y) \in U_i \tag{1}$$

The cover displacement functions are connected together by the weight functions $w_i(x,y)$

$$w_i(x,y) \geq 0 \quad (x,y) \in U_i, \qquad w_i(x,y) = 0 \quad (x,y) \notin U_i \tag{2}$$

with $\sum_{(x,y)\in U_j} w_j(x,y) = 1$ The global displacement function $u(x,y)$ and $v(x,y)$ on the whole physical cover system is

$$\begin{Bmatrix} u(x,y) \\ v(x,y) \end{Bmatrix} = \begin{Bmatrix} \sum_{i=1}^{n} w_i(x,y)u_i(x,y) \\ \sum_{i=1}^{n} w_i(x,y)v_i(x,y) \end{Bmatrix} = \sum_{i=1}^{n}\sum_{j=1}^{m} [T_{ij}(x,y)]\{D_{ij}\} \tag{3}$$

$$[T_{ij}(x,y)] = \begin{pmatrix} w_i(x,y)f_{ij}(x,y) & 0 \\ 0 & w_i(x,y)f_{ij}(x,y) \end{pmatrix} \quad \{D_{ij}\} = \begin{Bmatrix} d_{i\ 2j-1} \\ d_{i\ 2j} \end{Bmatrix}$$

For finite element, the cover functions are are the simplest function namely constant $m = 1$, $f_{ij}(x,y) = 1$, $d_{i1} = u_i$ and $d_{i2} = v_i$ in (3). Therefore,

$$\begin{Bmatrix} u(x,y) \\ v(x,y) \end{Bmatrix} = \sum_{i=1}^{n} [T_i(x,y)]\{D_i\}$$

$$[T_i(x,y)] = \begin{pmatrix} w_i(x,y) & 0 \\ 0 & w_i(x,y) \end{pmatrix} \quad \{D_i\} = \begin{Bmatrix} u_i \\ v_i \end{Bmatrix} \tag{4}$$

Denote the nodes of a triangle element e as $e(1), e(2), e(3)$, then e is the common region of three covers of its three nodes $e = U_{e(1)} \cap U_{e(2)} \cap U_{e(3)}$. On all points of this element, the only non-zero weight functions are $w_{e(1)}, w_{e(2)}, w_{e(3)}$. Denote (x_i, y_i) as the coordinates of node i, the weight functions of element e are computed.

$$\begin{aligned} &(\, w_{e(1)}(x,y) \quad w_{e(2)}(x,y) \quad w_{e(3)}(x,y)\,) \\ &= (\,1 \quad x \quad y\,) \begin{pmatrix} 1 & x_{e(1)} & y_{e(1)} \\ 1 & x_{e(2)} & y_{e(2)} \\ 1 & x_{e(3)} & y_{e(3)} \end{pmatrix}^{-1} = (\,1 \quad x \quad y\,) \begin{pmatrix} f_{11} & f_{12} & f_{13} \\ f_{21} & f_{22} & f_{23} \\ f_{31} & f_{32} & f_{33} \end{pmatrix} \end{aligned} \tag{5}$$

For each element, the summation of three weight function of three nodes are 1.

$$(\, w_{e(1)}(x,y) \quad w_{e(2)}(x,y) \quad w_{e(3)}(x,y)\,) \begin{pmatrix} 1 & x_{e(1)} & y_{e(1)} \\ 1 & x_{e(2)} & y_{e(2)} \\ 1 & x_{e(3)} & y_{e(3)} \end{pmatrix} = (\,1 \quad x \quad y\,)$$

$$w_{e(1)}(x,y) + w_{e(2)}(x,y) + w_{e(3)}(x,y) = 1$$

For element e and $(x,y) \in e$, (4) will reduce to normal element displacement function,

$$\begin{Bmatrix} u(x,y) \\ v(x,y) \end{Bmatrix} = \sum_{r=1}^{3} [T_{e(r)}][D_{e(r)}] = (\, T_{e(1)} \quad T_{e(2)} \quad T_{e(3)}\,) \begin{Bmatrix} D_{e(1)} \\ D_{e(2)} \\ D_{e(3)} \end{Bmatrix}$$

$$[T_{e(r)}(x,y)] = \begin{pmatrix} f_{1r} + f_{2r}x + f_{3r}y & 0 \\ 0 & f_{1r} + f_{2r}x + f_{3r}y \end{pmatrix} \tag{6}$$

3 Coefficient Matrix of Equilibrium Equations

Assume the number of physical covers is n, and there are $2m$ unknowns in each physical cover, the total potential energy has the form

$$\Pi = \frac{1}{2}\begin{pmatrix} D_1^T & D_2^T & D_3^T & \dots & D_n^T \end{pmatrix} \tag{7}$$
$$\begin{pmatrix} K_{11} & K_{12} & K_{13} & \dots & K_{1n} \\ K_{21} & K_{22} & K_{23} & \dots & K_{2n} \\ K_{31} & K_{32} & K_{33} & \dots & K_{3n} \\ \vdots & \vdots & \vdots & \ddots & \vdots \\ K_{n1} & K_{n2} & K_{n3} & \dots & K_{nn} \end{pmatrix} \begin{Bmatrix} D_1 \\ D_2 \\ D_3 \\ \vdots \\ D_n \end{Bmatrix} + \begin{pmatrix} D_1^T & D_2^T & D_3^T & \dots & D_n^T \end{pmatrix} \begin{Bmatrix} F_1 \\ F_2 \\ F_3 \\ \vdots \\ F_n \end{Bmatrix} + C$$

Submatrices $[K_{ij}]$ are $2m \times 2m$ matrices. $[D_i]$ and $[F_i]$ are $2m \times 1$ submatrices, where $[D_i]$ represents the displacement variables $(d_{i1}\ d_{i2}\ d_{i3}\ d_{i4}\ \dots\ d_{i2m})^T$ of physical cover i. From the formulation of Π, the formula (7) can be written as a symmetric representation, $[K_{ij}] = [K_{ji}]^T$.

The equilibrium equations are derived by minimizing the total potential energy Π. The i-th row of following equation (8) consists of $2m$ linear equations

$$\frac{\partial \Pi}{\partial d_{ir}} = 0, \quad r = 1, 2, 3, 4, \dots, 2m,$$

The matrix of obtained simultaneous equilibrium equations is same as the matrix of quadratic form (7):

$$\begin{pmatrix} K_{11} & K_{12} & K_{13} & \dots & K_{1n} \\ K_{21} & K_{22} & K_{23} & \dots & K_{2n} \\ K_{31} & K_{32} & K_{33} & \dots & K_{3n} \\ \vdots & \vdots & \vdots & \ddots & \vdots \\ K_{n1} & K_{n2} & K_{n3} & \dots & K_{nn} \end{pmatrix} \begin{Bmatrix} D_1 \\ D_2 \\ D_3 \\ \vdots \\ D_n \end{Bmatrix} = \begin{Bmatrix} F_1 \\ F_2 \\ F_3 \\ \vdots \\ F_n \end{Bmatrix} \tag{8}$$

For material analysis, $[F_i]$ is the loading on cover i distributed to the $2m$ displacement variables. Submatrices $[K_{ii}]$ depend on the material properties of cover i and $[K_{ij}]$, where $i \neq j$ is defined by the overlapping of cover i and cover j.

For the two dimensional triangle elements, $m = 1$. The unknown $[D_i]$ and the force term $[F_i]$ of cover i are 2×1 submatrices. The coefficient submatrices $[K_{ij}]$ are 2×2.

4 Stiffness Matrix

For FEM, the integration domains of the stiffness matrices are whole elements with standard boundaries. For manifold method, the integration domains of the stiffness matrices are the manifold elements, which can be part of the elements.

Same as FEM method, the relationship between stress and strain, is given by

$$\begin{Bmatrix} \sigma_x \\ \sigma_y \\ \tau_{xy} \end{Bmatrix} = [E] \begin{Bmatrix} \epsilon_x \\ \epsilon_y \\ \gamma_{xy} \end{Bmatrix}, \qquad [E] = \frac{E}{1-\nu^2} \begin{pmatrix} 1 & \nu & 0 \\ \nu & 1 & 0 \\ 0 & 0 & \frac{1-\nu}{2} \end{pmatrix} \tag{9}$$

E, ν are the Young's modulus and Poisson's ratio respectively. From (5), element strain can be computed

$$\begin{Bmatrix} \epsilon_x \\ \epsilon_y \\ \gamma_{xy} \end{Bmatrix} = \begin{Bmatrix} \frac{\partial u(x,y)}{\partial x} \\ \frac{\partial v(x,y)}{\partial y} \\ \frac{\partial u(x,y)}{\partial y} + \frac{\partial v(x,y)}{\partial x} \end{Bmatrix} = \begin{pmatrix} [B_{e(1)}] & [B_{e(2)}] & [B_{e(3)}] \end{pmatrix} \begin{Bmatrix} D_{e(1)} \\ D_{e(2)} \\ D_{e(3)} \end{Bmatrix}$$

$$[B_{e(r)}] = \begin{pmatrix} \frac{\partial w_{e(r)}}{\partial x} & 0 \\ 0 & \frac{\partial w_{e(r)}}{\partial y} \\ \frac{\partial w_{e(r)}}{\partial y} & \frac{\partial w_{e(r)}}{\partial x} \end{pmatrix} = \begin{pmatrix} f_{2r} & 0 \\ 0 & f_{3r} \\ f_{3r} & f_{2r} \end{pmatrix} \quad r = 1, 2, 3 \tag{10}$$

The strain energy Π_e done by the elastic stresses of element e is the integration over the entire material area $\mathcal{S}$ in that element. Then

$$\Pi_e = \iint_{\mathcal{S}} \frac{1}{2} \begin{pmatrix} \epsilon_x & \epsilon_y & \gamma_{xy} \end{pmatrix} \begin{Bmatrix} \sigma_x \\ \sigma_y \\ \tau_{xy} \end{Bmatrix} dx\, dy$$

$$= \frac{1}{2}\mathcal{S}\begin{pmatrix} D_{e(1)}^T & D_{e(2)}^T & D_{e(3)}^T \end{pmatrix}\begin{pmatrix} B_{e(1)}^T \\ B_{e(2)}^T \\ B_{e(3)}^T \end{pmatrix}[E]\begin{pmatrix} B_{e(1)} & B_{e(2)} & B_{e(3)} \end{pmatrix}\begin{Bmatrix} D_{e(1)} \\ D_{e(2)} \\ D_{e(3)} \end{Bmatrix} \quad (11)$$

Then

$$\mathcal{S}[B_{e(r)}]^T[E][B_{e(s)}] \quad \rightarrow \quad [K_{e(r)e(s)}], \quad r, s = 1, 2, 3,$$

5 Initial Stress Matrix

Following the time sequence, the manifold method computes step by step. The computed stresses of previous time step will be the initial stresses of the next time step. Therefore the initial stresses are essential for manifold computation.

For the element e, the potential energy of the initial constant stresses $\{\sigma^0\} = \begin{pmatrix} \sigma_x^0 & \sigma_y^0 & \tau_{xy}^0 \end{pmatrix}^T$ is

$$\begin{aligned} \Pi_\sigma &= \iint_{\mathcal{S}} \begin{pmatrix} \epsilon_x & \epsilon_y & \gamma_{xy} \end{pmatrix}\begin{Bmatrix} \sigma_x^0 \\ \sigma_y^0 \\ \tau_{xy}^0 \end{Bmatrix} dx\, dy \\ &= \mathcal{S}\begin{pmatrix} D_{e(1)}^T & D_{e(2)}^T & D_{e(3)}^T \end{pmatrix}\begin{pmatrix} B_{e(1)}^T \\ B_{e(2)}^T \\ B_{e(3)}^T \end{pmatrix}\begin{Bmatrix} \sigma_x^0 \\ \sigma_y^0 \\ \tau_{xy}^0 \end{Bmatrix} \end{aligned} \quad (12)$$

where $\mathcal{S}$ is the area of that element.

$$-\mathcal{S}[B_{e(r)}]^T\begin{Bmatrix} \sigma_x^0 \\ \sigma_y^0 \\ \tau_{xy}^0 \end{Bmatrix} \quad \rightarrow \quad \{F_{e(r)}\}, \quad r = 1, 2, 3.$$

6 Point Loading Matrix

Different from ordinary FEM method, a load point can be any point in its element. The point loading force $(F_x \quad F_y)^T$ acts on point (x_0, y_0) of element e. The potential energy due to the point loading is

$$\begin{aligned}\Pi_p &= -(u(x_0,y_0) \quad v(x_0,y_0)) \begin{Bmatrix} F_x \\ F_y \end{Bmatrix} \\ &= -(D^T_{e(1)} \quad D^T_{e(2)} \quad D^T_{e(3)}) \begin{pmatrix} T_{e(1)}(x_0,y_0)^T \\ T_{e(2)}(x_0,y_0)^T \\ T_{e(3)}(x_0,y_0)^T \end{pmatrix} \begin{Bmatrix} F_x \\ F_y \end{Bmatrix} \end{aligned} \tag{13}$$

Then

$$[T_{e(r)}(x_0,y_0)]^T \begin{Bmatrix} F_x \\ F_y \end{Bmatrix} \quad \rightarrow \quad \{F_{e(r)}\}, \qquad r = 1,2,3,$$

7 Body Loading Matrix

Assuming that $(f_x \quad f_y)^T$ is the constant body force acting on the material area of element e. The potential energy due to the body loading is

$$\begin{aligned}\Pi_w &= -\int\int_S (u(x,y) \quad v(x,y)) \begin{Bmatrix} f_x \\ f_y \end{Bmatrix} dx\,dy \\ &= -(D^T_{e(1)} \quad D^T_{e(2)} \quad D^T_{e(3)}) \int\int_S \begin{pmatrix} T_{e(1)}(x,y)^T \\ T_{e(2)}(x,y)^T \\ T_{e(3)}(x,y)^T \end{pmatrix} dx\,dy \begin{Bmatrix} f_x \\ f_y \end{Bmatrix} \\ &= -(D^T_{e(1)} \quad D^T_{e(2)} \quad D^T_{e(3)}) \begin{pmatrix} C_1 \\ C_2 \\ C_3 \end{pmatrix} \begin{Bmatrix} f_x \\ f_y \end{Bmatrix} dxdy \end{aligned} \tag{14}$$

$$[C_r] = \int\int_S T_{e(r)}(x,y)^T dxdy = \int\int_S \begin{pmatrix} S_r & 0 \\ 0 & S_r \end{pmatrix}$$

$$S_r = f_{1r}S + f_{2r}\int\int_S x dxdy + f_{3r}\int\int_S y dxdy$$

S_r can be computed by formulae (5) and (20). Then

$$\begin{pmatrix} S_r & 0 \\ 0 & S_r \end{pmatrix} \begin{Bmatrix} f_x \\ f_y \end{Bmatrix} \quad \rightarrow \quad \{F_{e(r)}\}, \qquad r = 1, 2, 3.$$

8 Inertia Force Matrix

The inertia force matrix is equivalent to the mass matrix of FEM. This matrix is the most important matrix of manifold method. The inertia force matrix will control the movements of all points of the whole material volume. Choosing small time steps, the discontinuous contact computation will be stable. From the beginning of the current time step, denote $(u(t) \quad v(t))^T$ as the time dependent displacements of any point (x, y) of element e and $\mathcal{M}$ as the mass per unit area. The force of inertia per unit area is

$$\begin{Bmatrix} f_x(x,y) \\ f_y(x,y) \end{Bmatrix} = -\mathcal{M}\frac{\partial^2}{\partial t^2}\begin{Bmatrix} u(t) \\ v(t) \end{Bmatrix} = -\mathcal{M}\,(T_{e(1)} \quad T_{e(2)} \quad T_{e(3)})\,\frac{\partial^2}{\partial t^2}\begin{Bmatrix} D_{e(1)}(t) \\ D_{e(2)}(t) \\ D_{e(3)}(t) \end{Bmatrix}$$

At the beginning of the time step, the node displacement $\{D_{e(i)}(0)\} = \{0\}$. At the end of the time step, the node displacement $\{D_{e(i)}(\Delta)\} = \{D_{e(i)}\}$, Δ is the time interval of this time step. Then

$$\begin{aligned} \{D_{e(r)}(\Delta)\} &= \{D_{e(r)}(0)\} + \Delta\frac{\partial\{D_{e(r)}(0)\}}{\partial t} + \frac{\Delta^2}{2}\frac{\partial^2\{D_{e(r)}(0)\}}{\partial t^2} \\ &= \Delta\frac{\partial\{D_{e(r)}(0)\}}{\partial t} + \frac{\Delta^2}{2}\frac{\partial^2\{D_{e(r)}(0)\}}{\partial t^2}, \end{aligned} \tag{15}$$

$$\frac{\partial^2\{D_{e(r)}(0)\}}{\partial t^2} = \frac{2}{\Delta^2}\{D_{e(r)}(\Delta)\} - \frac{2}{\Delta}\frac{\partial\{D_{e(r)}(0)\}}{\partial t} = \frac{2}{\Delta^2}\{D_{e(r)}\} - \frac{2}{\Delta}\{V_{e(r)}(0)\},$$

$$\{V_{e(r)}(0)\} = \frac{\partial\{D_{e(r)}(0)\}}{\partial t}, \qquad \{D_{e(r)}\} = \{D_{e(r)}(\Delta)\} \tag{16}$$

$\{V_{e(r)}(0)\}$ is the velocity at the beginning of the time step. Then the potential energy becomes

$$\Pi_i = -\int\int_S (u(x,y) \quad v(x,y)) \begin{Bmatrix} f_x(x,y) \\ f_y(x,y) \end{Bmatrix} dxdy$$

$$= \int\int_S \mathcal{M} \begin{pmatrix} u(x,y) & v(x,y) \end{pmatrix} \begin{pmatrix} T_{e(1)} & T_{e(2)} & T_{e(3)} \end{pmatrix} dxdy \frac{\partial^2}{\partial t^2} \begin{Bmatrix} D_{e(1)}(t) \\ D_{e(2)}(t) \\ D_{e(3)}(t) \end{Bmatrix}$$

$$= \mathcal{M}\frac{2}{\Delta^2} \begin{pmatrix} D^T_{e(1)} & D^T_{e(2)} & D^T_{e(3)} \end{pmatrix}$$

$$\int\int_S \begin{pmatrix} T_{e(1)}(x,y)^T \\ T_{e(2)}(x,y)^T \\ T_{e(3)}(x,y)^T \end{pmatrix} \begin{pmatrix} T_{e(1)} & T_{e(2)} & T_{e(3)} \end{pmatrix} dxdy \begin{Bmatrix} D_{e(1)} - V_{e(1)}(0) \\ D_{e(2)} - V_{e(2)}(0) \\ D_{e(3)} - V_{e(3)}(0) \end{Bmatrix} \quad (17)$$

$$\int\int_S [T_{e(r)}]^T [T_{e(s)}] dxdy = \begin{pmatrix} t_{e(r)e(s)} & 0 \\ 0 & t_{e(r)e(s)} \end{pmatrix} \quad (18)$$

$$t_{e(r)e(s)} = \int\int_S w_{e(r)} w_{e(s)} dxdy$$

$$= \int\int_S (f_{1r} + f_{2r}x + f_{3r}y)(f_{1s} + f_{2s}x + f_{3s}y) dxdy$$

Number $t_{e(r)e(s)}$ can be computed by formulae (5) and (20). Then the final formula is

$$\frac{2\mathcal{M}}{\Delta^2} \begin{pmatrix} t_{e(r)e(s)} & 0 \\ 0 & t_{e(r)e(s)} \end{pmatrix} \quad \rightarrow \quad [K_{e(r)e(s)}], \qquad r,s = 1,2,3,$$

$$\frac{2\mathcal{M}}{\Delta} \begin{pmatrix} t_{e(r)e(s)} & 0 \\ 0 & t_{e(r)e(s)} \end{pmatrix} \{V_s(0)\} \quad \rightarrow \quad \{F_{e(r)}\}, \qquad r,s = 1,2,3,$$

9 Fixed Point Matrix

Assume the fixed point is (x,y) at element e. There are two springs which are along the x and y directions respectively. The stiffness of the springs is p. The spring forces are

$$\begin{Bmatrix} f_x \\ f_y \end{Bmatrix} = -p \begin{Bmatrix} u(x,y) \\ v(x,y) \end{Bmatrix}$$

The strain energy of the springs is

$$\Pi_f = \frac{p}{2} \begin{pmatrix} u(x,y) & v(x,y) \end{pmatrix} \begin{Bmatrix} u(x,y) \\ v(x,y) \end{Bmatrix}$$

$$= \frac{p}{2} \left(D^T_{e(1)} \quad D^T_{e(2)} \quad D^T_{e(3)} \right) \begin{pmatrix} T^T_{e(1)} \\ T^T_{e(2)} \\ T^T_{e(3)} \end{pmatrix} \left(T_{e(1)} \quad T_{e(2)} \quad T_{e(3)} \right) \begin{Bmatrix} D_{e(1)} \\ D_{e(2)} \\ D_{e(3)} \end{Bmatrix}$$

$$p[T_{e(r)}][T_{e(s)}] \quad \rightarrow \quad [K_{e(r)e(s)}], \quad r, s = 1, 2, 3. \tag{19}$$

10 Simplex Integration

As a element of the manifold method is a generally shaped polygon, $P_1\ P_2\ \ldots\ P_{m-1}\ P_m\ P_1, \quad P_1 = P_{m+1}, \quad P_i = (x_i, y_i)$ are its ordered vertices rotating from axis x to axis y. As a arbitrary chosen point, $P_0 = (0, 0)$. The following integrations are analytical solutions

$$\begin{aligned}
S &= \frac{1}{2} \sum_{i=1}^{m} \begin{vmatrix} x_i & y_i \\ x_{i+1} & y_{i+1} \end{vmatrix}, \\
S_x &= \frac{S}{3} \sum_{i=1}^{m} (x_i + x_{i+1}), \\
S_y &= \frac{S}{3} \sum_{i=1}^{m} (y_i + y_{i+1}), \\
S_{xx} &= \frac{S}{6} \sum_{i=1}^{m} (x_i^2 + x_{i+1}^2 + x_i x_{i+1}), \\
S_{yy} &= \frac{S}{6} \sum_{i=1}^{m} (y_i^2 + y_{i+1}^2 + y_i y_{i+1}), \\
S_{xy} &= \frac{S}{12} \sum_{i=1}^{m} (2x_i y_i + 2x_{i+1} y_{i+1} + x_i y_{i+1} + x_{i+1} y_i).
\end{aligned} \tag{20}$$

11 Definition of Entrances

Thus far, only individual covers and elements were considered. For the movements of discontinuous boundaries, no tension and no penetration must be satisfied between two contact sides. The entrances are defined in the beginning of each time step.

[1] A entrance is formed with two sides, their minimum distance is less than 2ρ, here ρ is the maximum step displacement.

[2] When one entrance side translates to the other side without rotation, the maximum overlapping angle is less than 2δ, here $\delta = 1.5$ is used in the computer program.

Figure 5.2 shows two complex blocks, under this contact criteria, there are only two contacts even if the distance limit 2ρ is lager than the block diameters.

The kinematics can be imposed on the global equations by adding stiff springs in the entrance positions.

[1] For the angle to angle entrance, if both angles are less than 180°, the two entrance lines are defined as the two thick lines shown by Figure 6.1 and 6.2. according to the following table:

		two entrance lines	
$\alpha \leq 180°$	$\beta \leq 180°$	OE_3	OE_2
$\alpha \leq 180°$	$\beta > 180°$	OE_3	OE_4
$\alpha > 180°$	$\beta \leq 180°$	OE_1	OE_2
$\alpha > 180°$	$\beta > 180°$	OE_1	OE_4

Penetration will occur if the two entrance lines are passed by the vertices of the other angles. A normal stiff spring is attached between the vertex and its entrance line where the entrance occurs first.

[2] For an angle to angle entrance, if a angle is larger than 180°, the two entrance lines are the two edges of the angle greater than 180°. If a entrance line has been passed by the vertex of another angle, a normal stiff springs is applied to the vertex and its entrance line. If two entrance lines have been passed, two springs are applied to the two entrance lines.

[3] For the angle to edge contact, the only entrance line is the edge, as showing by Figure 7. If the vertex passes its entrance line, a normal stiff spring is applied

to the entrance line.

the definition of entrance line is still correct even if edges of two sides of the entrance are parallel or slightly penetrated.

12 Entrance Distances

Assume P_1 is a point before deformation which moves to point P_1' after deformation; P_2P_3 is the entrance line and (x_i, y_i) and (u_i, v_i) are the coordinates and displacement increments of $P_i, i = 1, 2, 3$ respectively. If points P_1, P_2 and P_3 rotate in the same sense as the rotation of ox to oy (see Figure 7.1 and 7.2), then P_1' has passed line P_2P_3 and is stated by the inequality:

$$\Delta = \begin{vmatrix} 1 & x_1 + u_1 & y_1 + v_1 \\ 1 & x_2 + u_2 & y_2 + v_2 \\ 1 & x_3 + u_3 & y_3 + v_3 \end{vmatrix} < 0, \tag{21}$$

This simple formula is still correct even when these three points move simultaneously.

Since Δ is small, distance formula can be simplified

$$\begin{aligned} d &= \frac{\Delta}{\sqrt{(x_2 + u_2 - x_3 - u_3)^2 + (y_2 + v_2 - y_3 - v_3)^2}} \\ &= \frac{\Delta}{\sqrt{(x_2 - x_3)^2 + (y_2 - y_3)^2}} \end{aligned} \tag{22}$$

The friction law or Coloumb's law is also inequalities. $\mathcal{F} \leq \mathcal{N} \tan(\phi) + \mathcal{C}$.

If a entrance is open in the beginning of a time step and is closed in the end of the same time step, the entrance time and position in this time step can be computed. Assume $t = 0$ in the beginning of the time step, and $t = 1$ in the end of the time step, and

$$\Delta(t) = \begin{vmatrix} 1 & x_1 + tu_1 & y_1 + tv_1 \\ 1 & x_2 + tu_2 & y_2 + tv_2 \\ 1 & x_3 + tu_3 & y_3 + tv_3 \end{vmatrix} \tag{23}$$

then $\Delta(0) > 0 \quad \Delta(1) < 0$. The entrance time t_0 satisfies equation $\Delta(t_0) = 0$. Neglecting the second order infinite small, the entrance time t_0 and the entrance

position (x_0, y_0) can be computed by simpler formula:

$$t_0 = -\begin{vmatrix} 1 & x_1 & y_1 \\ 1 & x_2 & y_2 \\ 1 & x_3 & y_3 \end{vmatrix} \left(\begin{vmatrix} 1 & u_1 & y_1 \\ 1 & u_2 & y_2 \\ 1 & u_3 & y_3 \end{vmatrix} + \begin{vmatrix} 1 & x_1 & v_1 \\ 1 & x_2 & v_2 \\ 1 & x_3 & v_3 \end{vmatrix} \right)^{-1}, \quad \begin{Bmatrix} x_0 \\ y_0 \end{Bmatrix} = \begin{Bmatrix} x_1 + u_1 t_0 \\ y_1 + v_1 t_0 \end{Bmatrix} \tag{24}$$

These formulae are still correct even when the three points move simultaneously.

13 Normal Springs

From equation (22), the distance d from P_1 of element i to the entrance line P_2P_3 of element j is $d = \frac{\Delta}{\sqrt{(x_2-x_3)^2+(y_2-y_3)^2}}$, d should be *zero* if P_1 passed edge P_2 P_3. Let

$$S_0 = \begin{vmatrix} 1 & x_1 & y_1 \\ 1 & x_2 & y_2 \\ 1 & x_3 & y_3 \end{vmatrix}, \qquad l = \sqrt{(x_2 - x_3)^2 + (y_2 - y_3)^2}$$

Neglecting the second order infinite small, the distance d can be a linear function of $\{D_i\}$:

$$\begin{aligned} d &= \frac{1}{l} S_0 + \frac{1}{l} \begin{vmatrix} 1 & u_1 & y_1 \\ 1 & u_2 & y_2 \\ 1 & u_3 & y_3 \end{vmatrix} + \frac{1}{l} \begin{vmatrix} 1 & x_1 & v_1 \\ 1 & x_2 & v_2 \\ 1 & x_3 & v_3 \end{vmatrix} \\ &= \frac{1}{l} S_0 + \frac{1}{l} \begin{pmatrix} y_2 - y_3 & x_3 - x_2 \end{pmatrix} \begin{Bmatrix} u_1 \\ v_1 \end{Bmatrix} \\ &+ \frac{1}{l} \begin{pmatrix} y_3 - y_1 & x_1 - x_3 \end{pmatrix} \begin{Bmatrix} u_2 \\ v_2 \end{Bmatrix} + \frac{1}{l} \begin{pmatrix} y_1 - y_2 & x_2 - x_1 \end{pmatrix} \begin{Bmatrix} u_3 \\ v_3 \end{Bmatrix} \\ &= \frac{S_0}{l} + \begin{pmatrix} H_1^T & H_2^T & H_3^T \end{pmatrix} \begin{Bmatrix} D_{i(1)} \\ D_{i(2)} \\ D_{i(3)} \end{Bmatrix} + \begin{pmatrix} G_1^T & G_2^T & G_3^T \end{pmatrix} \begin{Bmatrix} D_{j(1)} \\ D_{j(2)} \\ D_{j(3)} \end{Bmatrix} \end{aligned} \tag{25}$$

where

$$\{H_r\} = \frac{1}{l}[T_{i(r)}(x_1, y_1)]^T \begin{Bmatrix} y_2 - y_3 \\ x_3 - x_2 \end{Bmatrix}, \qquad r = 1, 2, 3,$$

$$\{G_s\} = \frac{1}{l}[T_{j(s)}(x_2, y_2)]^T \begin{Bmatrix} y_3 - y_1 \\ x_1 - x_3 \end{Bmatrix} + \frac{1}{l}[T_{j(s)}(x_3, y_3)]^T \begin{Bmatrix} y_1 - y_2 \\ x_2 - x_1 \end{Bmatrix}, \qquad s = 1, 2, 3, \tag{26}$$

The potential energy of the normal spring is

$$\begin{aligned} \Pi_s = \frac{p}{2}d^2 = \frac{p}{2}\begin{pmatrix} D_{i(1)}^T & D_{i(2)}^T & D_{i(3)}^T \end{pmatrix} \begin{Bmatrix} H_1 \\ H_2 \\ H_3 \end{Bmatrix} \begin{pmatrix} H_1^T & H_2^T & H_3^T \end{pmatrix} \begin{Bmatrix} D_{i(1)} \\ D_{i(2)} \\ D_{i(3)} \end{Bmatrix} \\ + \frac{p}{2}\begin{pmatrix} D_{j(1)}^T & D_{j(2)}^T & D_{j(3)}^T \end{pmatrix} \begin{Bmatrix} G_1 \\ G_2 \\ G_3 \end{Bmatrix} \begin{pmatrix} G_1^T & G_2^T & G_3^T \end{pmatrix} \begin{Bmatrix} D_{j(1)} \\ D_{j(2)} \\ D_{j(3)} \end{Bmatrix} \\ + p\begin{pmatrix} D_{i(1)}^T & D_{i(2)}^T & D_{i(3)}^T \end{pmatrix} \begin{Bmatrix} H_1 \\ H_2 \\ H_3 \end{Bmatrix} \begin{pmatrix} G_1^T & G_2^T & G_3^T \end{pmatrix} \begin{Bmatrix} D_{j(1)} \\ D_{j(2)} \\ D_{j(3)} \end{Bmatrix} \\ + p\frac{S_0}{l}\begin{pmatrix} D_{i(1)}^T & D_{i(2)}^T & D_{i(3)}^T \end{pmatrix} \begin{Bmatrix} H_1 \\ H_2 \\ H_3 \end{Bmatrix} \\ + p\frac{S_0}{l}\begin{pmatrix} D_{j(1)}^T & D_{j(2)}^T & D_{j(3)}^T \end{pmatrix} \begin{Bmatrix} G_1 \\ G_2 \\ G_3 \end{Bmatrix} + \frac{p}{2}\left(\frac{S_0}{l}\right)^2 \end{aligned} \tag{27}$$

Then

$$\begin{aligned} p\{H_r\}\{H_s\}^T &\rightarrow [K_{i(r)i(s)}], \qquad r, s = 1, 2, 3, \\ p\{H_r\}\{G_s\}^T &\rightarrow [K_{i(r)j(s)}], \qquad r, s = 1, 2, 3, \\ p\{G_r\}\{H_s\}^T &\rightarrow [K_{j(r)i(s)}], \qquad r, s = 1, 2, 3, \\ p\{G_r\}\{G_s\}^T &\rightarrow [K_{j(r)j(s)}], \qquad r, s = 1, 2, 3, \end{aligned}$$

$$
\begin{aligned}
-p\left(\frac{S_0}{l}\right)\{H_r\} \quad &\rightarrow \quad \{F_{i(r)}\}, \qquad r=1,2,3, \\
-p\left(\frac{S_0}{l}\right)\{G_r\} \quad &\rightarrow \quad \{F_{j(r)}\}, \qquad r=1,2,3,
\end{aligned} \tag{28}
$$

14 Shear Springs

In Figure 8, (x_0, y_0) is on the edge P_2P_3 and is the assumed contact point of vertex P_1. The shear spring is on the direction P_2P_3, and connects vertices P_1 and P_0. Denote

$$
S_0 = (\, x_1 - x_0 \quad y_1 - y_0 \,) \begin{Bmatrix} x_3 - x_2 \\ y_3 - y_2 \end{Bmatrix}, \tag{29}
$$

Since P_0P_1 is small, the shear displacement of P_0 and P_1 along line P_2P_3 is

$$
\begin{aligned}
d &= \frac{1}{l}\overrightarrow{P_0P_1} \cdot \overrightarrow{P_2P_3} \qquad (30) \\
&= \frac{1}{l}(\, x_1 + u_1 - x_0 - u_0 \quad y_1 + v_1 - y_0 - v_0 \,) \begin{Bmatrix} x_3 + u_3 - x_2 - u_2 \\ y_3 + v_3 - y_2 - v_2 \end{Bmatrix} \\
&= \frac{S_0}{l} + \frac{1}{l}(\, x_3 - x_2 \quad y_3 - y_2 \,) \begin{Bmatrix} u_1 \\ v_1 \end{Bmatrix} + \frac{1}{l}(\, x_2 - x_3 \quad y_2 - y_3 \,) \begin{Bmatrix} u_0 \\ v_0 \end{Bmatrix} \qquad (31) \\
&= \frac{S_0}{l} + (\, H_1^T \quad H_2^T \quad H_3^T \,) \begin{Bmatrix} D_{i(1)} \\ D_{i(2)} \\ D_{i(3)} \end{Bmatrix} + (\, G_1^T \quad G_2^T \quad G_3^T \,) \begin{Bmatrix} D_{j(1)} \\ D_{j(2)} \\ D_{j(3)} \end{Bmatrix}
\end{aligned}
$$

$$
\begin{aligned}
\{H_r\} &= \frac{1}{l}[T_{i(r)}(x_1, y_1)]^T \begin{Bmatrix} x_3 - x_2 \\ y_3 - y_2 \end{Bmatrix}, \qquad r=1,2,3, \\
\{G_s\} &= \frac{1}{l}[T_{j(s)}(x_0, y_0)]^T \begin{Bmatrix} x_2 - x_3 \\ y_2 - y_3 \end{Bmatrix}, \qquad s=1,2,3,
\end{aligned} \tag{32}
$$

The formula of the potential energy of the shear spring is same as (27); the submatrices contributing to simultaneous equations are same as (28) accept that the definition of H_r, G_s, S_0 are different.

15 Friction Force Matrix

When the Coulomb's law allows sliding between two sides of the entrances, there exist the couple of friction forces on the two sliding sides. The friction force is calculated from the normal compressive force, $\mathcal{F} = pd\tan(\phi)$, where d is the normal penetration distance, $\tan(\phi)$ is the friction coefficient. The directions of the friction force couple are against the movement of P_1 relative to P_0 in the direction $\pm\overrightarrow{P_2P_3}$.

Then the potential energy of friction force pair is

$$\begin{aligned}\Pi_f &= \frac{\mathcal{F}}{l}\begin{pmatrix} u_1 & v_1 \end{pmatrix}\begin{Bmatrix} x_3 - x_2 \\ y_3 - y_2 \end{Bmatrix} - \frac{\mathcal{F}}{l}\begin{pmatrix} u_0 & v_0 \end{pmatrix}\begin{Bmatrix} x_3 - x_2 \\ y_3 - y_2 \end{Bmatrix} \\ &= \mathcal{F}\begin{pmatrix} D^T_{i(1)} & D^T_{i(2)} & D^T_{i(3)} \end{pmatrix}\begin{Bmatrix} H_1 \\ H_2 \\ H_3 \end{Bmatrix} - \mathcal{F}\begin{pmatrix} D^T_{j(1)} & D^T_{j(2)} & D^T_{j(3)} \end{pmatrix}\begin{Bmatrix} G_1 \\ G_2 \\ G_3 \end{Bmatrix} \quad (33)\end{aligned}$$

where

$$\begin{aligned}\{H_r\} &= \frac{1}{l}[T_{i(r)}(x_1, y_1)]^T \begin{Bmatrix} x_3 - x_2 \\ y_3 - y_2 \end{Bmatrix}, \qquad r = 1, 2, 3, \\ \{G_s\} &= \frac{1}{l}[T_{j(s)}(x_0, y_0)]^T \begin{Bmatrix} x_3 - x_2 \\ y_3 - y_2 \end{Bmatrix}, \qquad s = 1, 2, 3, \end{aligned} \quad (34)$$

the loading matrix of the coupled friction forces are

$$-\mathcal{F}\{H_r\} \quad \rightarrow \quad \{F_{i(r)}\}, \qquad r = 1, 2, 3,$$

$$+\mathcal{F}\{G_r\} \quad \rightarrow \quad \{F_{j(r)}\}, \qquad r = 1, 2, 3,$$

16 Equation Solver and Open-Close Iterations

The manifold method computations follow the time steps. The following items are to be transferred from the end of the previous time step to the beginning of the next time step: stresses, strains and velocities of each element, current geometry, contact positions, contact forces and contact states.

The current version of the manifold code is a simple version. In the beginning of a time step, the dynamic computations inherit the velocity of the end of the last step. For static computation, the initial velocity of each time step is zero.

Within each time step, the global equations have to be solved repeatedly while adding and removing stiff springs. This open-close iterations to ensue no-penetrations in the open contacts, no-tensions in the contacts with normal springs. If the two conditions are not fulfilled for all entrances after five times of open-close iterations, the time step will be reduced to one third, and the open-close iteration continues.

The principles of choosing time steps Δ are: Δ is small enough, so that the second order displacements are neglected; Δ is small enough, so that the SOR iteration will converge in less than 30 iterations; Δ is small enough, so that the open-close iterations will converge in less than 5 iterations, Δ is large enough, so that the computation will represent larger time span and the displacements are stabilized if possible.

17 Applications of Numerical Manifold Method

Figure 9.1 shows the deformation of the joints and the continuous materials of double simply supported beams. Figure 9.2 shows the failure of a tunnel lining under the point load on the arch top. Figure 9.3 shows the ground movements under horizontal force. Figure 9.4 shows the failure of rocks with horizontal bedding planes. Figure 9.5 shows the deformations of a domain with a spiral joint.

Acknowledgement The development of the theory presented herein is the result of research for Work Unit No. 31700. Program sponsored by the US Army Corps of Engineers (USACE). The author would like to thank Mr. Jerry Huie, Dr. Don Banks and IBM Corporation for their helps.

References

[1] Gen-hua Shi, 1992. "Manifold Method," *Fractured and Jointed Rock Masses* (Lake Tahoe, California).

[2] Gen-hua Shi, 1992. "Modeling Rock Joints and Blocks by Manifold Method," *Rock Mechanics Proceedings of the 33rd U. S. Symposium*, pp. 639-648 (Santa Fe, New Mexico).

[3] Gen-hua Shi, 1992. " Manifold Method of Material Analysis," *Transactions of the Ninth Army Conference on Applied Mathematics and Computing*, pp. 51-76 (Minneapolis, Minnesoda).

[4] Shi, Gen-hua 1993. Block system modeling by discontinuous deformation analysis. Southampton UK and Boston USA

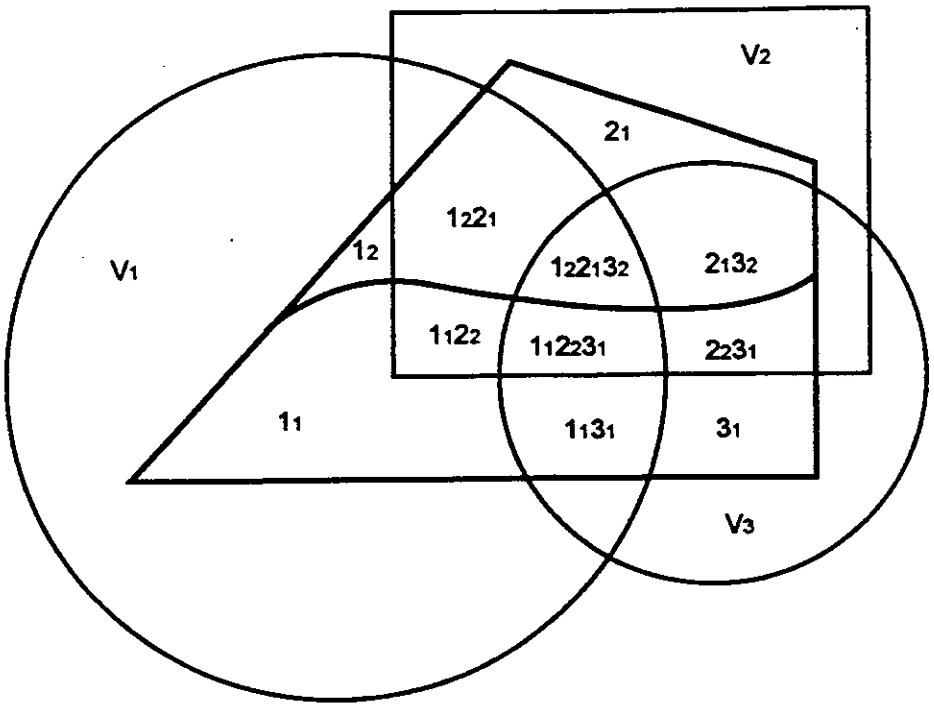

Figure 1.1 Finite covers on the materials of two blocks

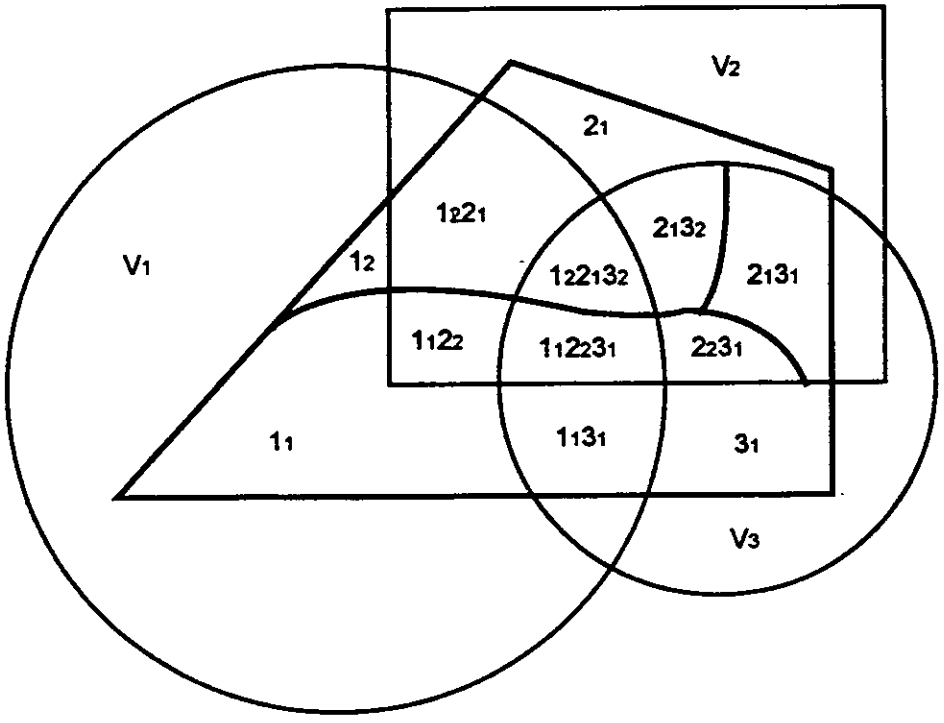

Figure 1.2 Finite covers on the materials with joints

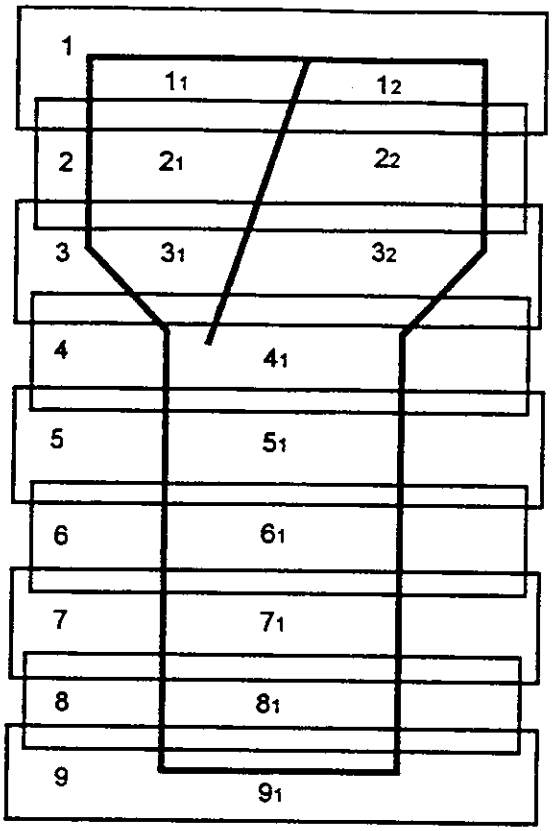

Figure 2.1 Chain cover system for narrow material shapes

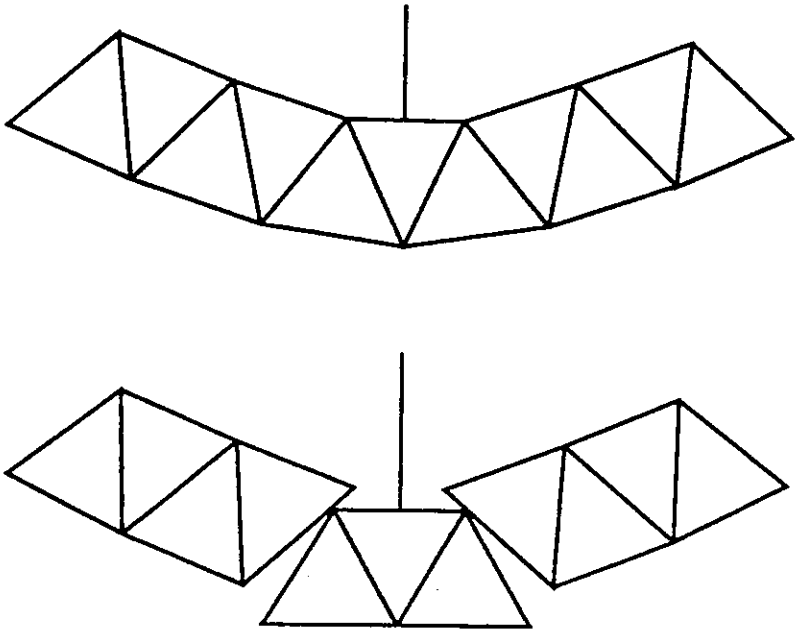

Figure 2.2 Finite covers formed by individual blocks

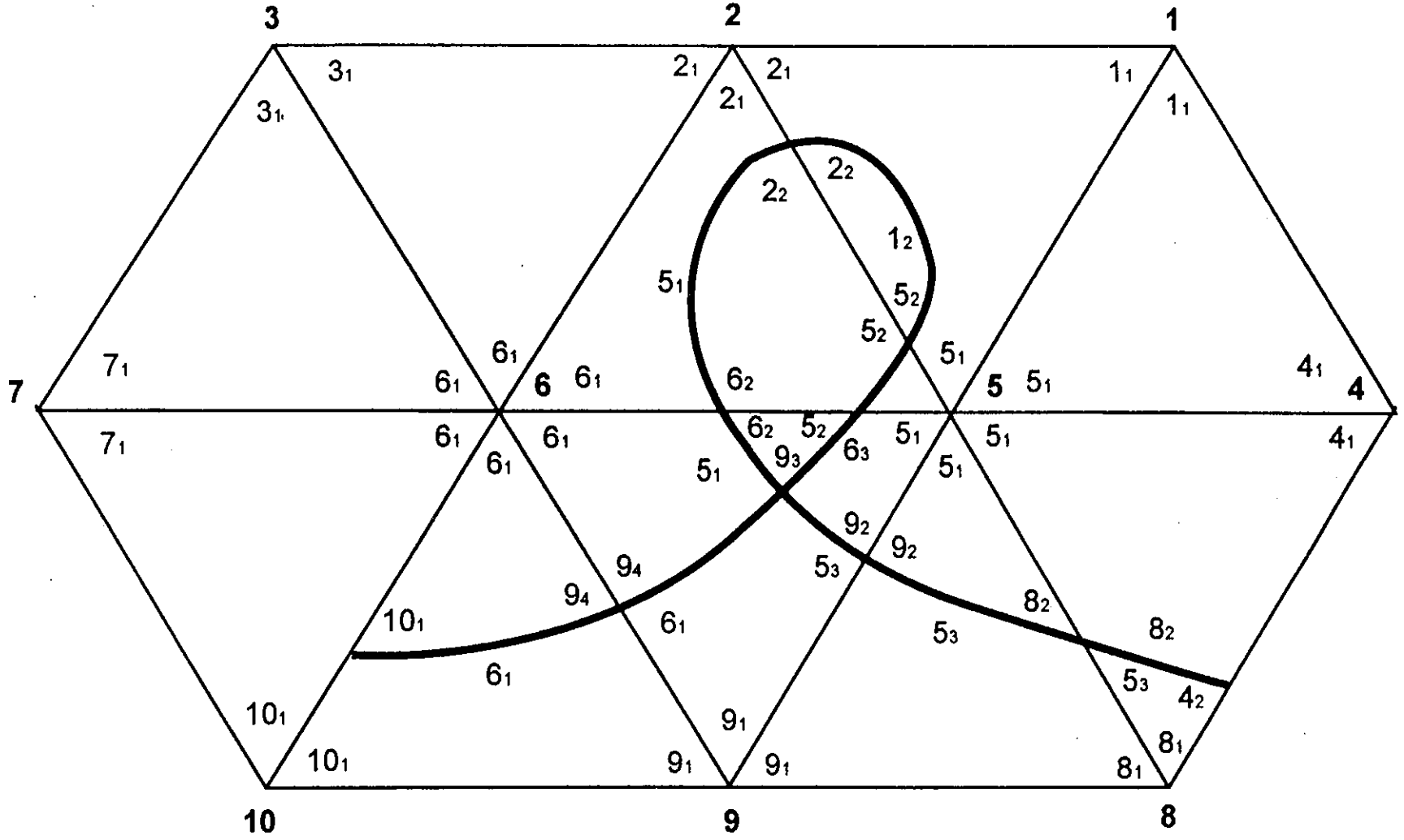

Figure 3 Finite covers formed by finite elements

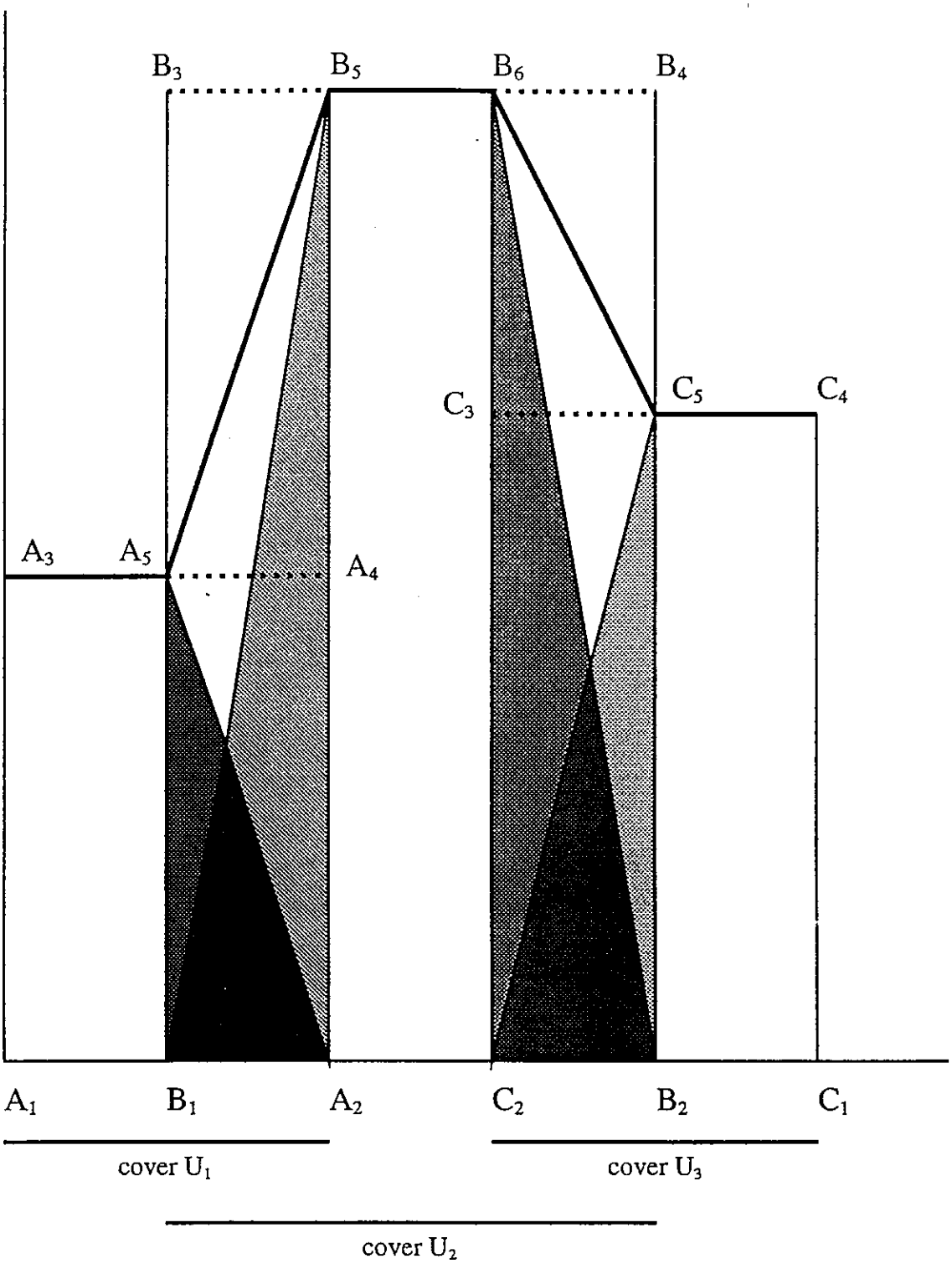

Figure 4.1 One dimensional cover functions

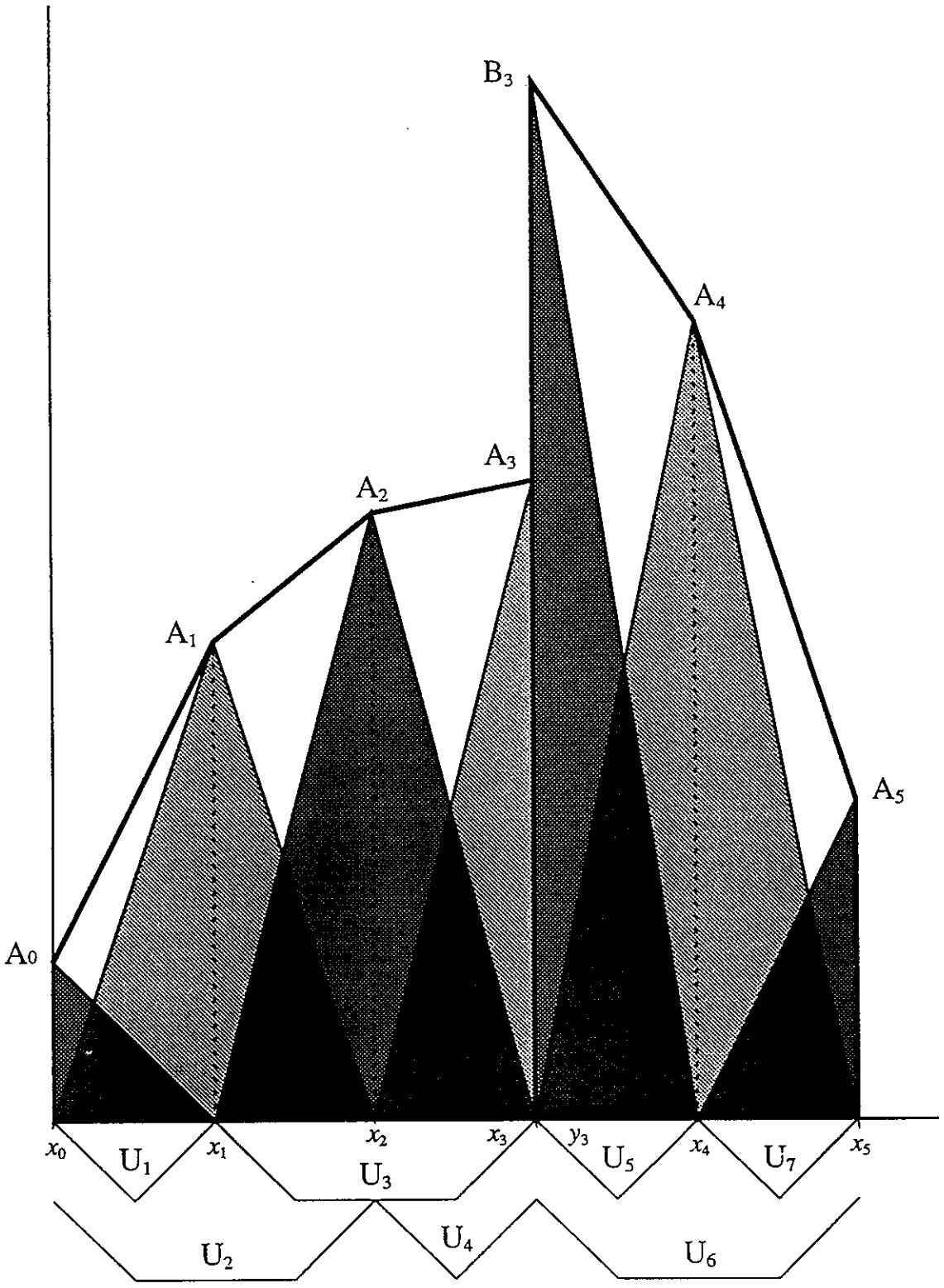

Figure 4.2 One dimensional discontinuous global function

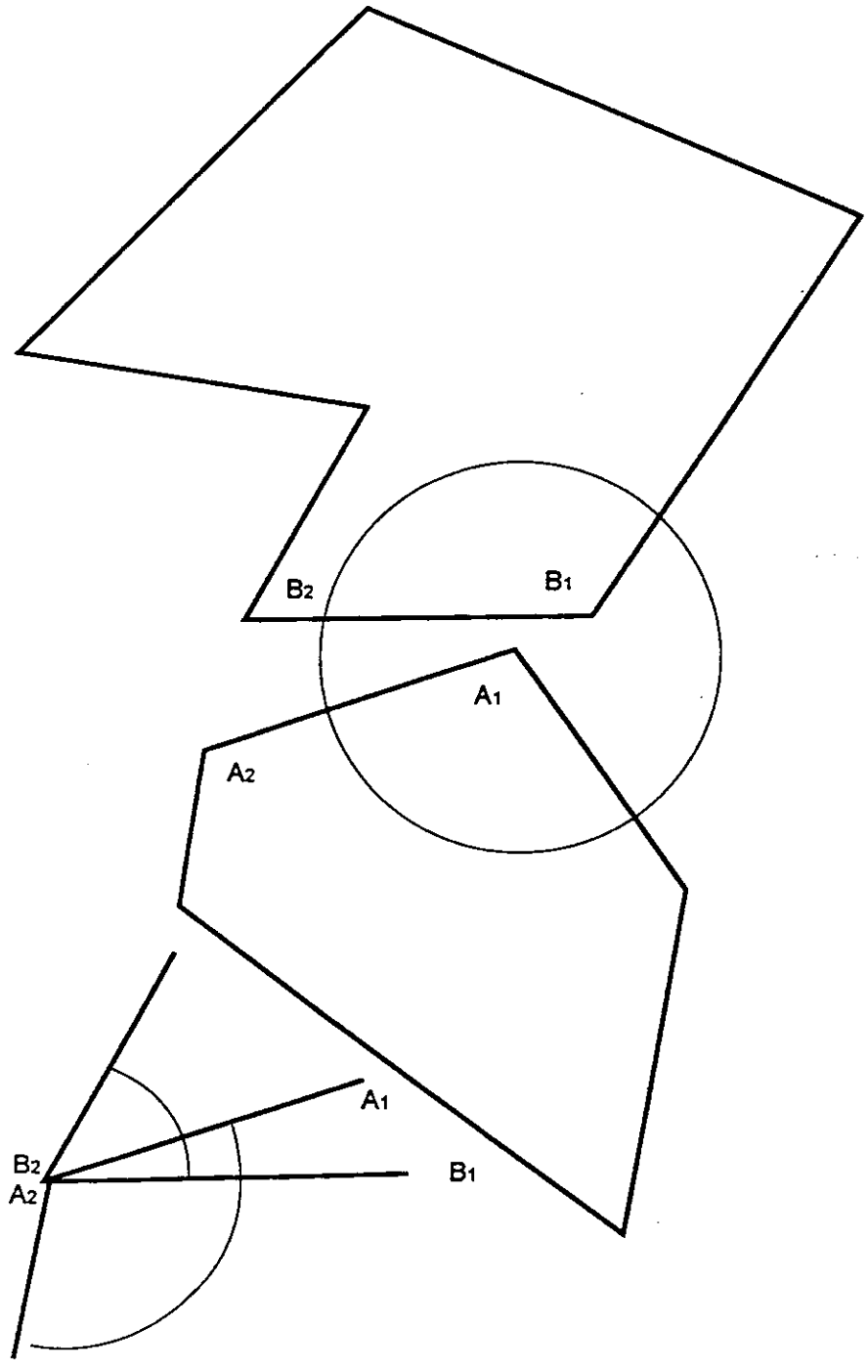

Figure 5 Entrance positions between two blocks

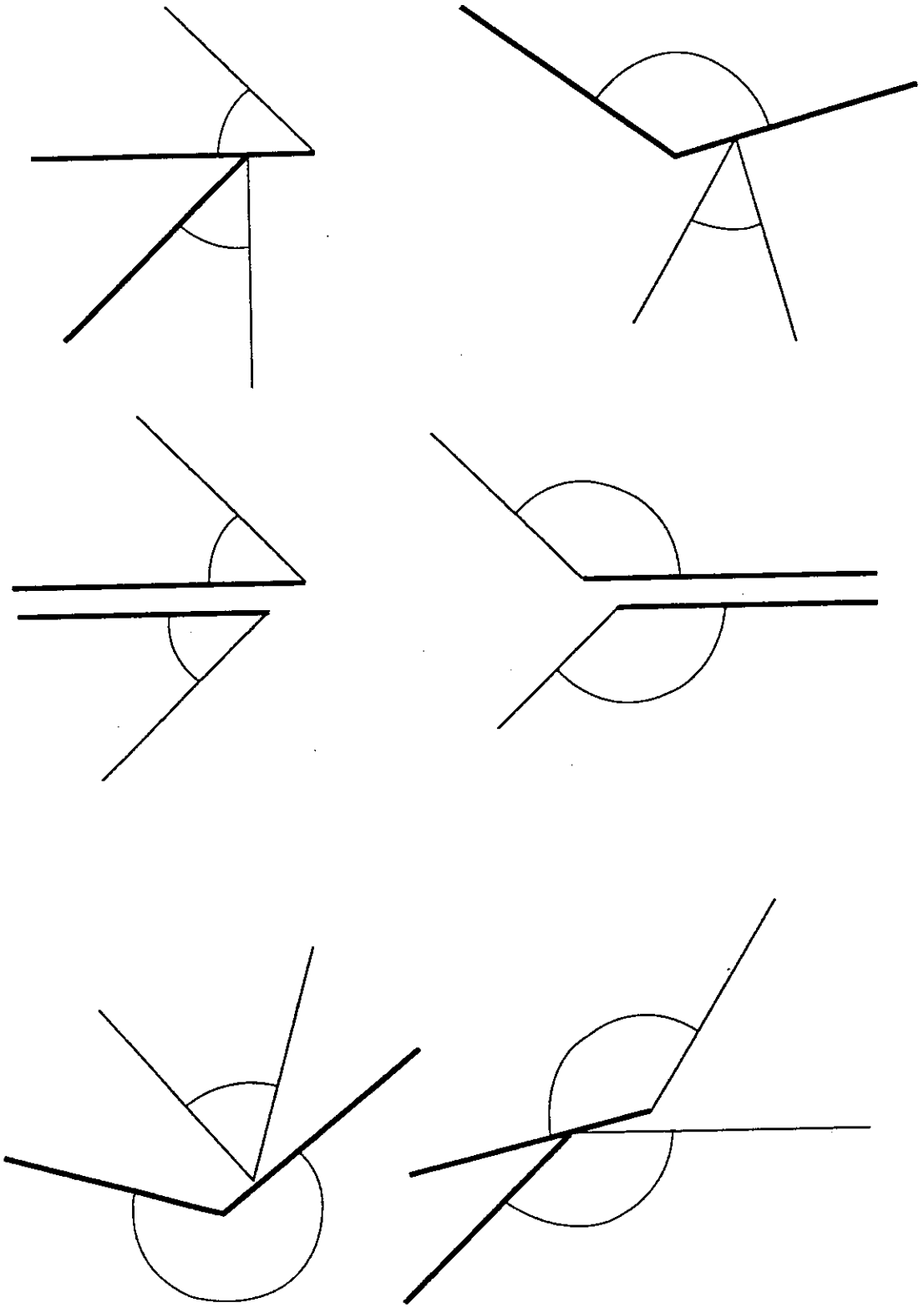

Figure 6.1 Entrance lines between two angles

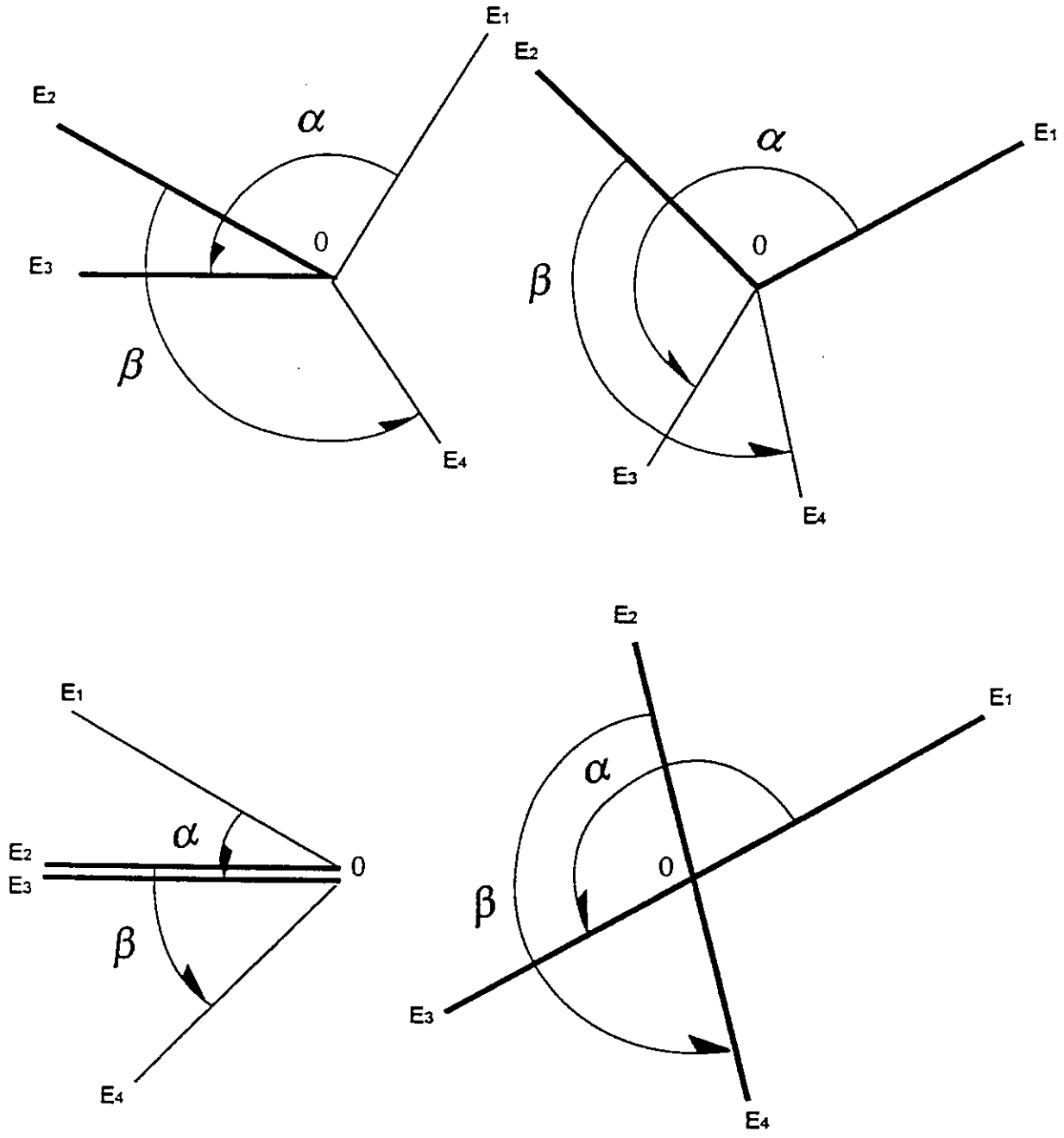

Figure 6.2 Criteria of entrance lines

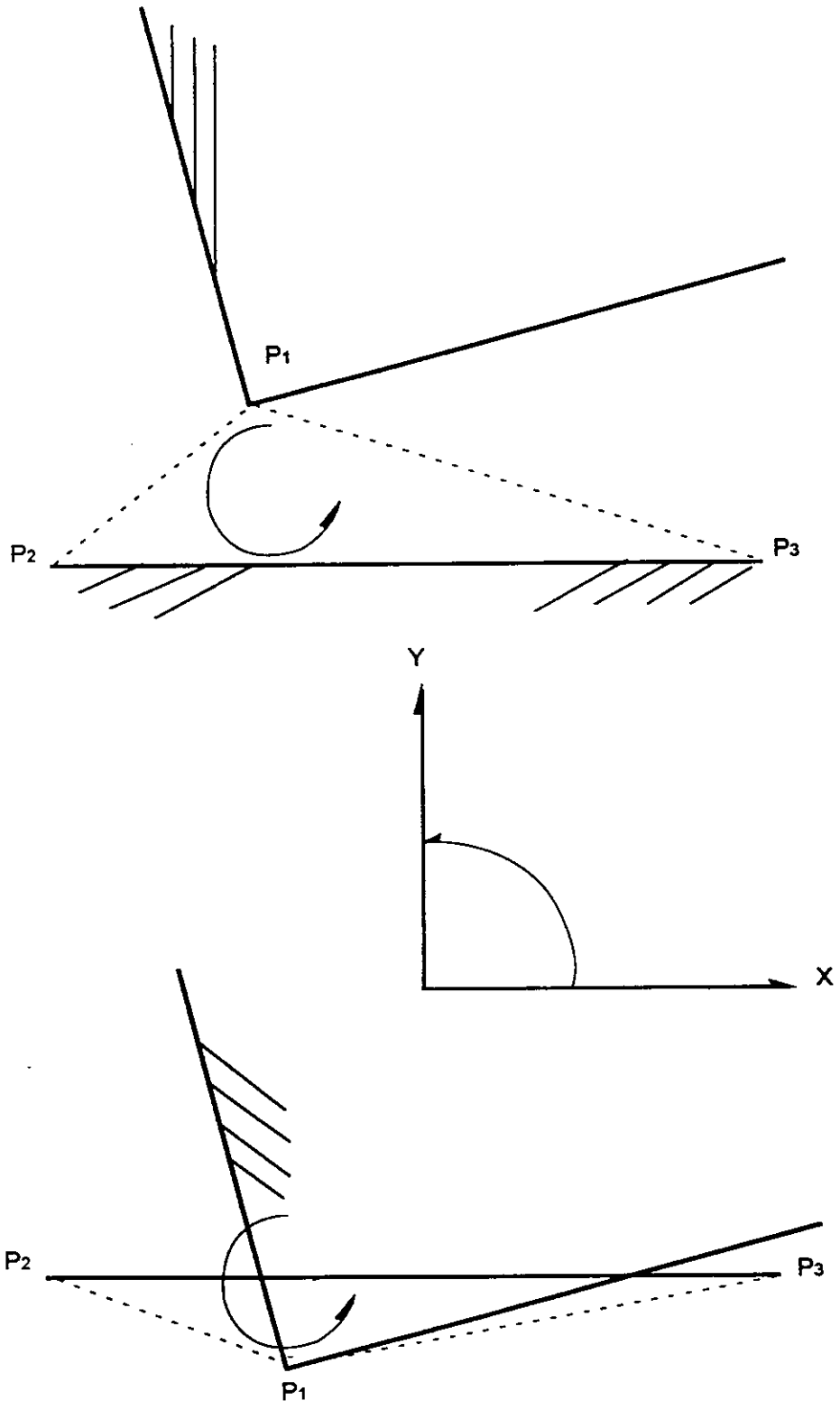

Figure 7 Penetration judgement

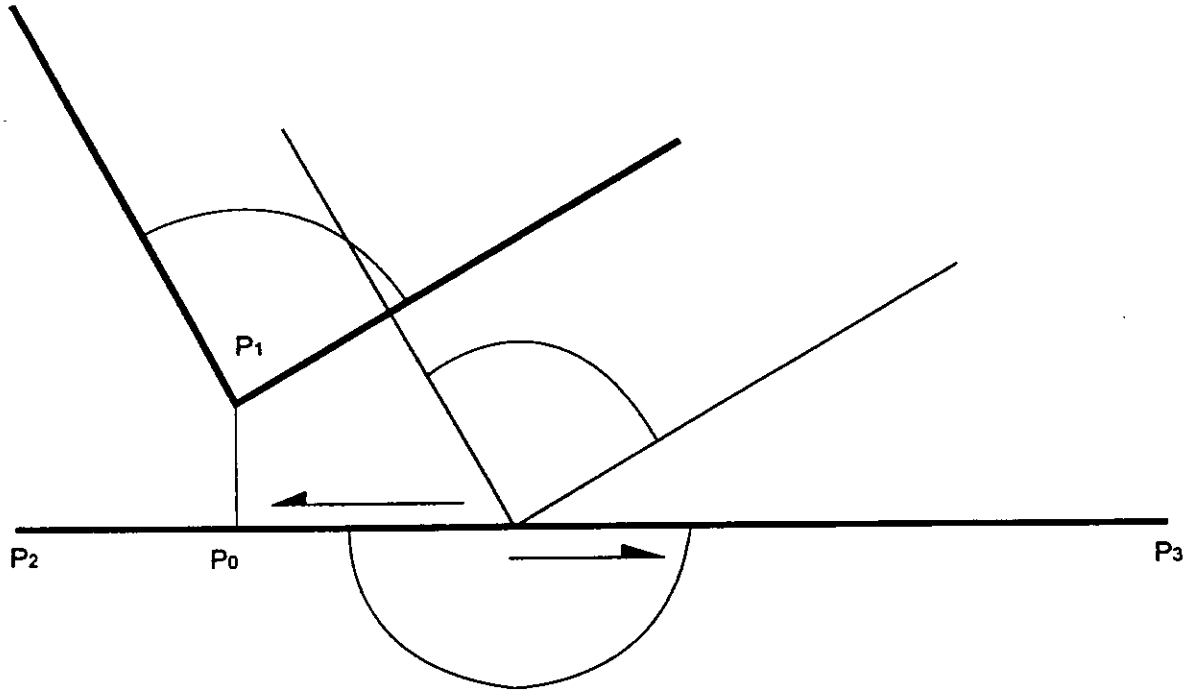

Figure 8 Position of shear spring

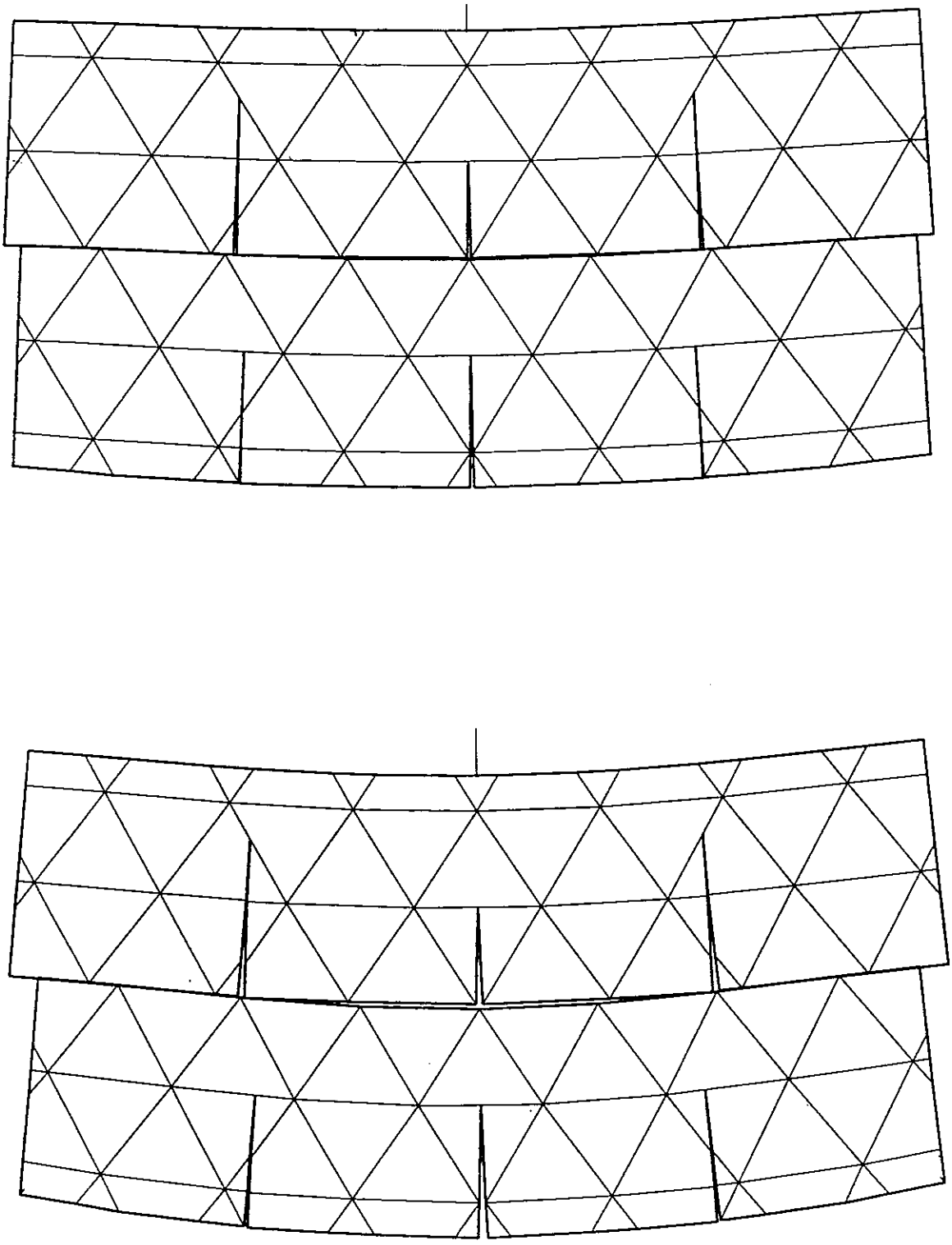

Figure 9.1 Deformation of double simply supported beams

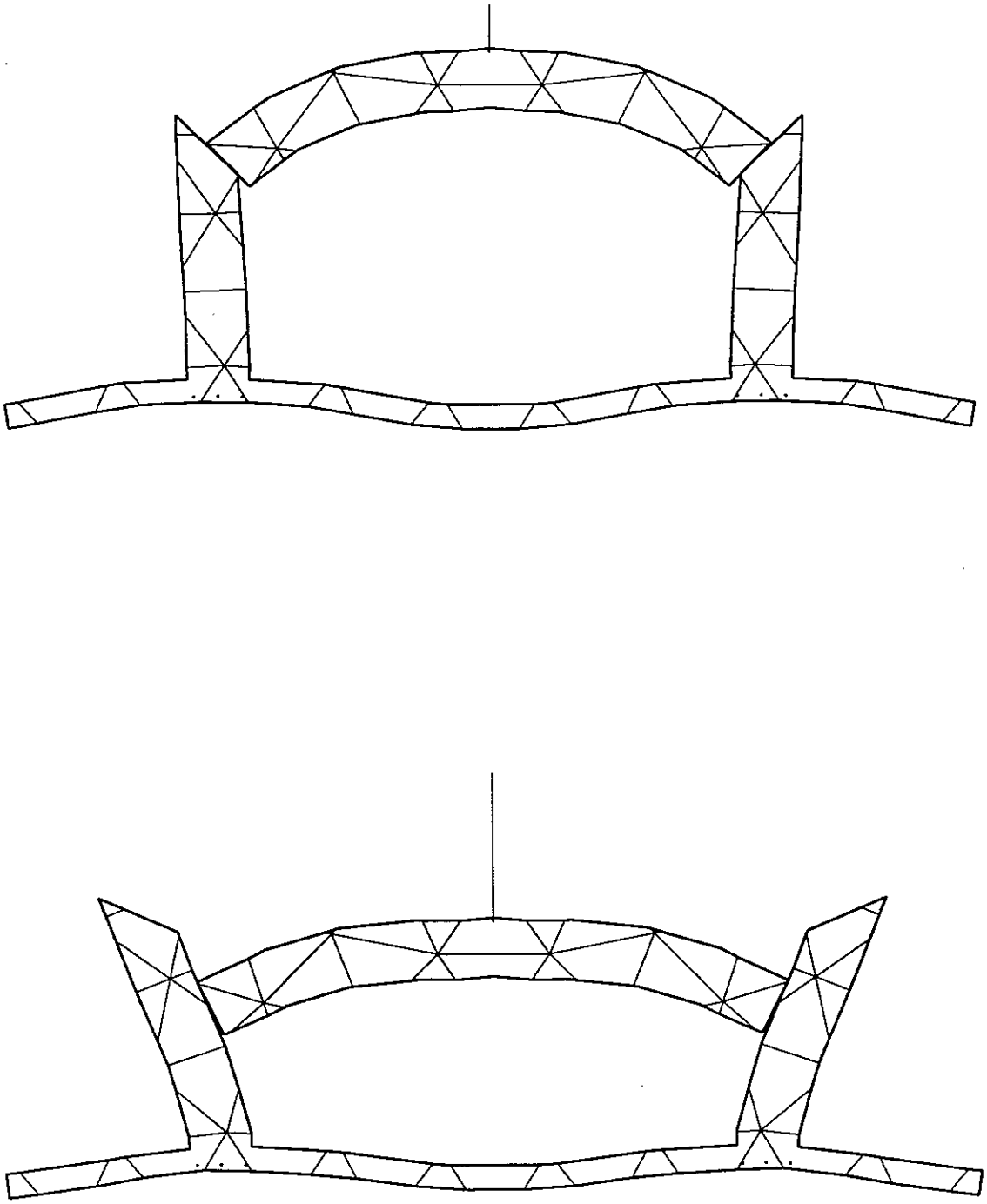

Figure 9.2 Failure of a tunnel lining under point loads

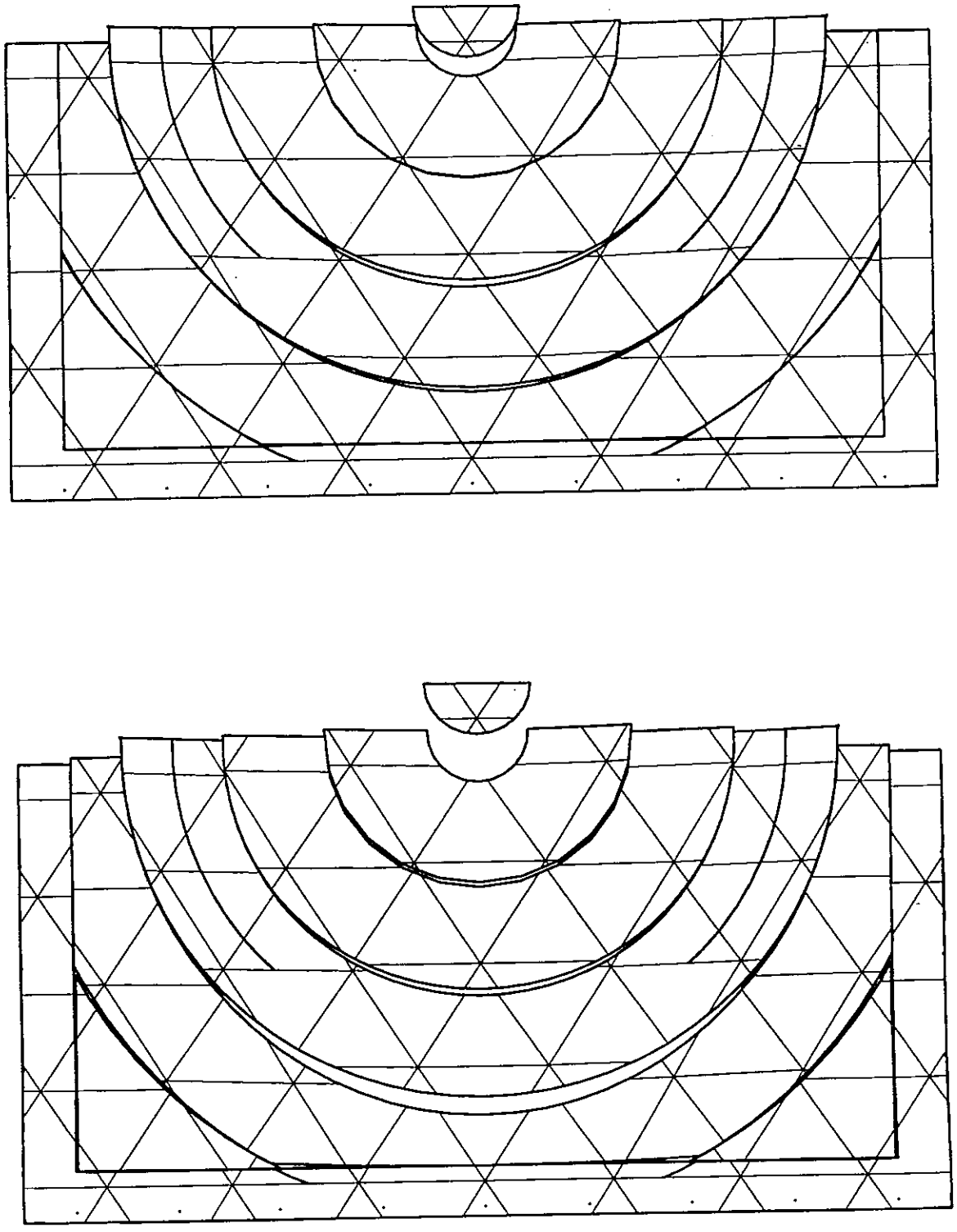

Figure 9.3 Ground movements under horizontal force

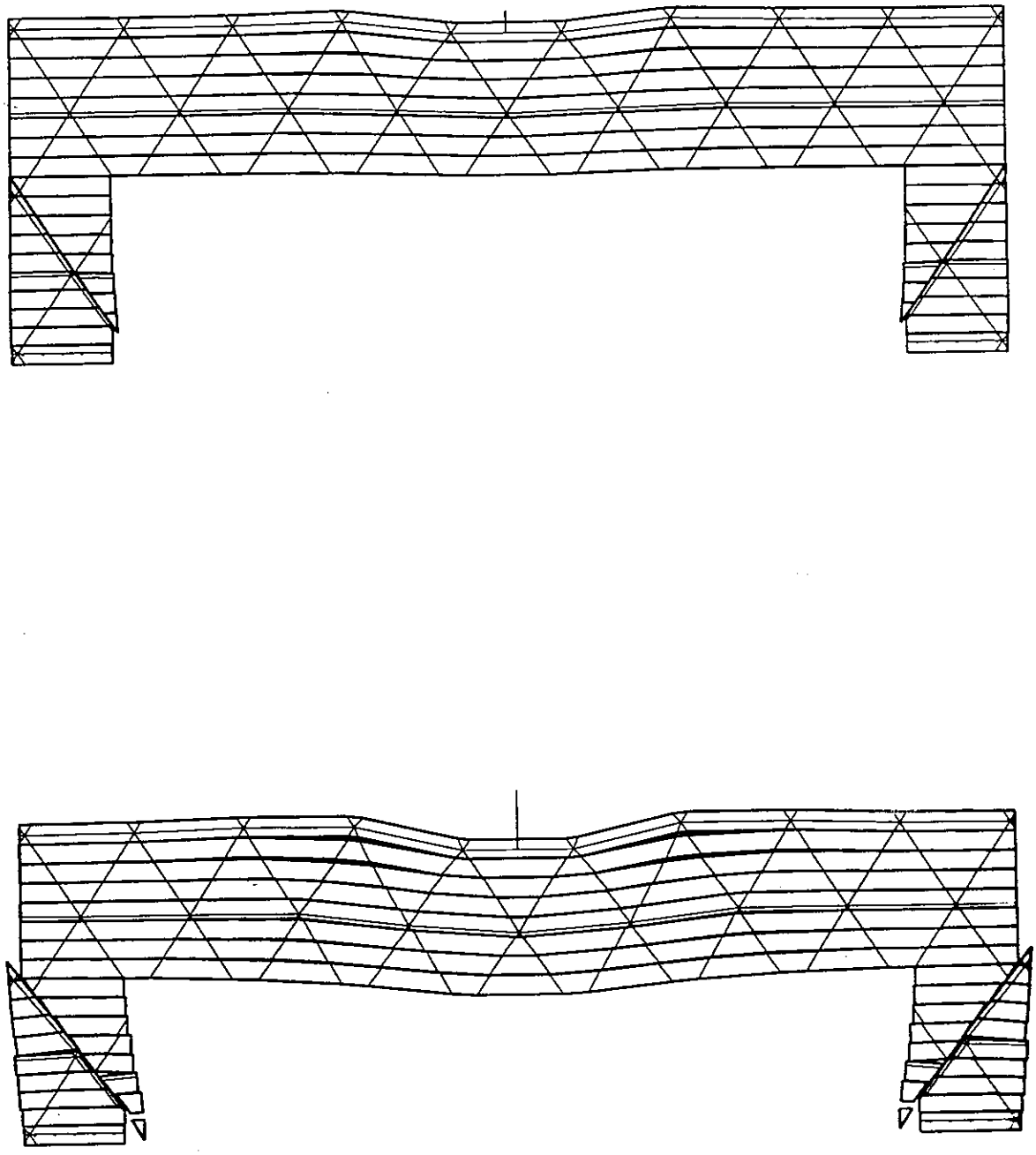

Figure 9.4 Failure of rocks with horizontal bedding planes

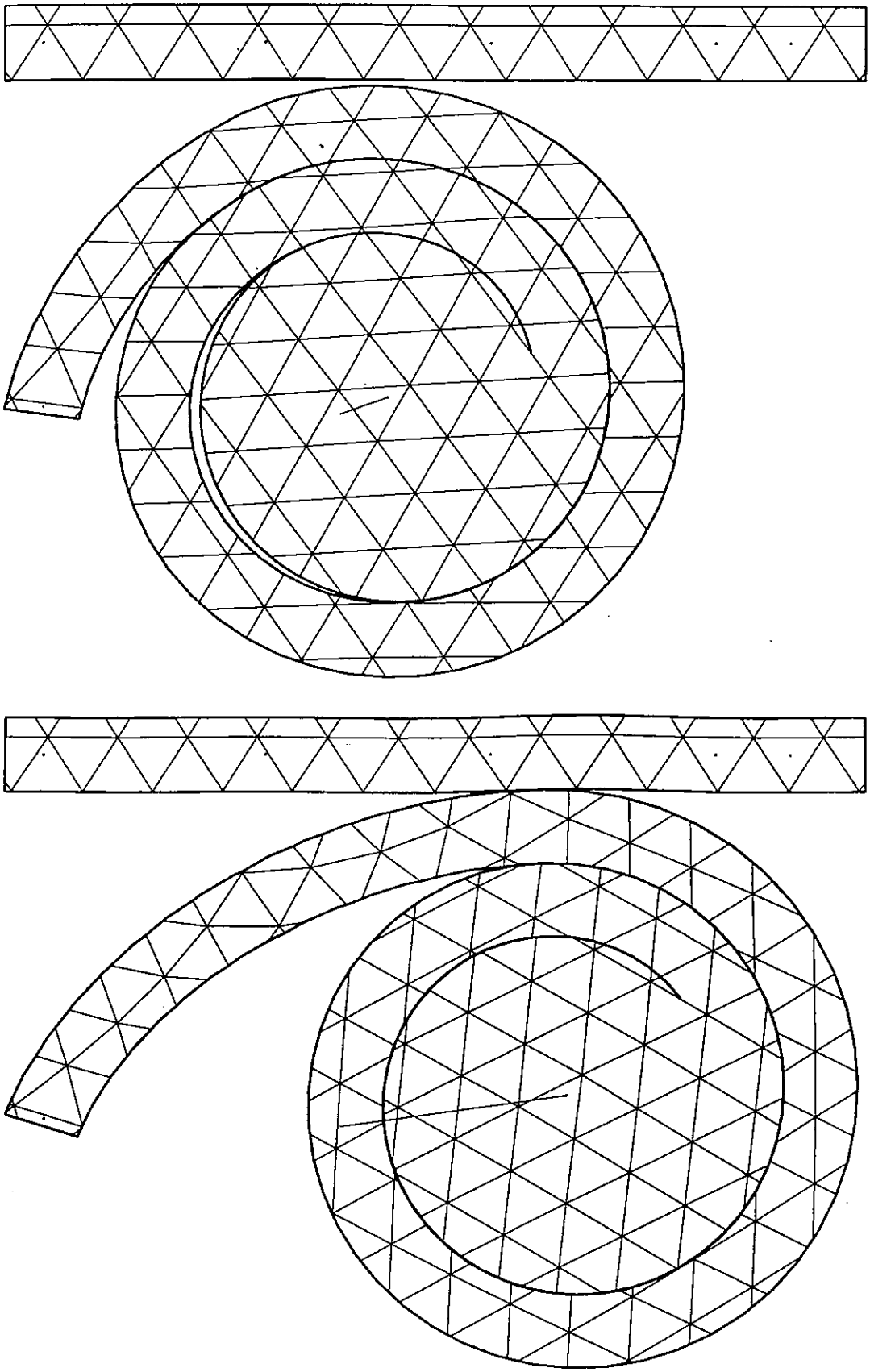

Figure 9.5 Computation of a spiral joint

Continuous and Discontinuous Analysis Using the Manifold Method

Jeen-Shang Lin

Department of Civil and Environmental Engineering, University of Pittsburgh, USA

1. INTRODUCTION

Materials often are characterized very differently depending upon the nature of a problem, the scale or dimension of interest, or even the focus of an investigation. Under some circumstances a material may be modeled as a continuous medium, while under others as a discontinuous medium. Then there are occasions to characterize it as a mixture of both. For the purposes of analysis, the available methods of analysis frequently dictate how a material is to be modeled. Time and again, we find ourselves forced to neglect some important features of a problem in order to attain a solution. This, in turn, casts doubts on the validity of the analysis results.

The manifold method is a novel concept that when implemented gives us a better grip on the modeling. The method was conceptualized by Shi [1, 2]. In the manifold method, the independent response variables, such as displacements, can be continuous or discontinuous throughout a problem domain. This paper provides an overview of the method and presents a computational procedure. Some results from a on-going study are also given.

The term "manifold" originates from topology. Topology is a branch of geometry which studies the properties of geometric figures under continuous transformation [3]. The manifolds is one of the most important geometric figures it studies. Briefly stated, a manifold is simply a collection of objects, such as points, that satisfies certain homogeneity and continuity requirements. For instance, a two-dimensional manifold, or 2-manifold, is a geometric figure in that every point has a neighborhood equivalent to the interior of a disk. Therefore,surfaces of a sphere and torus are both 2-manifold. In a broad view, engineering analysis also falls into the general areas studied by topology. This is because a problem domain of an engineering analysis is, mathematically speaking, a manifold, and its response such as deformation is simply a transformation of the manifold. It is therefore not surprising that the methods of topology also have important bearings. For example, when a manifold is subjected to a complicated transformation, it is frequently decomposed into simpler shapes such as triangles or polygons through a process called triangulation. These simpler shapes are then covered by other figures that are easier to analyze. By so doing, a complicated problem is converted into smaller and simpler problems on these covering figures. For problems of engineering interests, often the number of the covering figures is finite.

The concept of finite covers is the basis of the manifold method. In the case of two-dimensional plane strain problems, the tangent plane coincides with the problem domain, the compatibility among the covers are automatically satisfied insofar as the coordinate patches are concerned.

Because the concepts involved may be abstract and , at times, difficult to engineers, this paper also presents an explanation as to how different parts of the manifold method are formulated and put together. Whenever possible this study employs the finite element analogy to facilitate the explanation. The essential issues addressed include how to cover a manifold, what constitute the generalized elements and the generalized nodes, how to derive the stiffness matrix and the force vector, and how to obtain a solution.

2. A TWO-LAYER DESCRIPTION OF A PROBLEM

Shi's proposal of using a two-layer description for a problem is perhaps one of the most innovative features of the manifold method. The first layer of the description is called a physical mesh. A physical mesh is a unique portrait of the physical domain of a problem that should include all the discontinuities. It defines the manifold whose response is being sought. The second layer of description is called a mathematical mesh. A mathematical mesh can be a mesh of some regular pattern, or a combinations of some of arbitrary figures. The mesh or shape size may be chosen according to the problem geometry, solution accuracy requirements, and the physical property zoning. The mathematical mesh is used for building covers and has to be large enough to cover every point of the physical mesh.

This two-layer description concept is illustrated here with a retaining wall example. The soil behind the retaining wall above the potential sliding plane is modeled as consists of several thin slices to facilitate the occurrence of a particular mode. These decisions define a physical mesh for the problem which is depicted in Fig. 1(b). A triangular mesh, as shown in Fig. 1(a), is arbitrarily selected as the mathematical mesh. A superposition of these two meshes, shown as Fig. 1(c), gives a covered manifold of the problem. It is important to note that the manifold method does not require a mathematical mesh to conform to the physical boundary of a problem. This greatly simplifies an input preparation.

In the narrow scope of this study the manifold method can be viewed as a combination of the finite element and the discrete element methods. Thus many features of the finite elements and the discrete elements, particularly those of the Discontinuous Deformation Analysis, DDA [4] are incorporated into the current manifold method formulation.

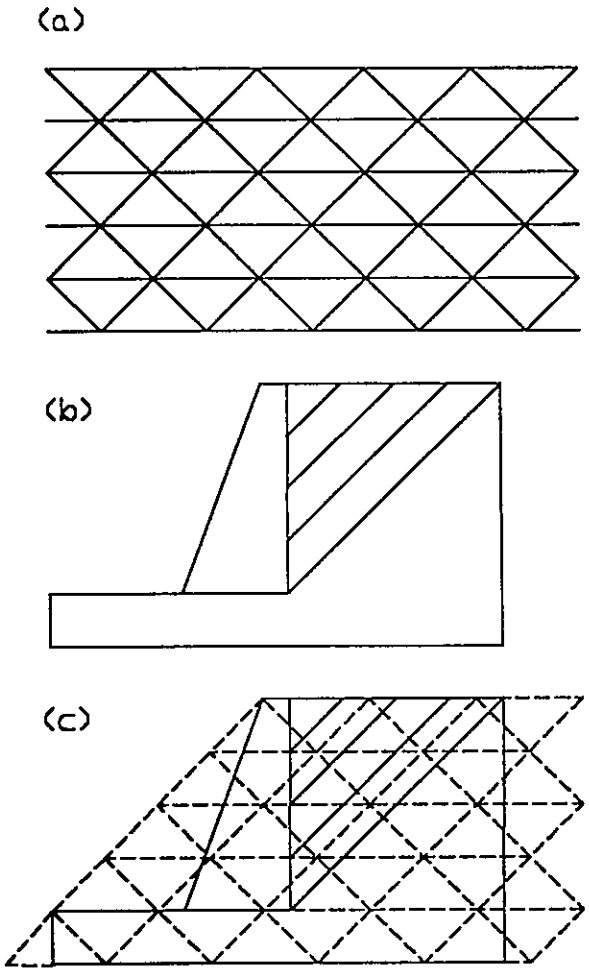

FIGURE 1 A manifold example (a) an arbitrary triangular mathematical mesh (b) a physical description of a retaining wall problem (c) a covered manifold

3. GENERALIZED NODES AND ELEMENTS

The key to the manifold method as an analysis tool lies in the generalization of the node and element concepts. The manifold method, by not requiring a mathematical mesh to coincide with the physical boundary of a problem, departs significantly from the finite element, or the discrete element methods for that matter. Two generalizations in the manifold method make it possible for a rather arbitrary selection of the mathematical mesh. First, it constructs the interpolation on the basis of the mathematical mesh. Second, it uses weighting functions to track the physical boundary of a problem.

Without losing generality, the following discussion considers displacements as the only independent variables. In other words, the so-called assumed displacement method [5] is adopted here. Other considerations include the use of a triangular mesh as the mathematical mesh and the use of a linear displacement field within a basic triangle. To avoid confusion, an intersection point on a physical mesh is denoted as a vertex, while one on a mathematical mesh is denoted as a node. Also, a basic triangle refers to a triangle formed by three neighboring nodes.

Within a basic triangle bounded by three nodes, say 0,1, and 2, the assumption of a linear displacement field leads to the following linear equations,

$$\begin{aligned} u(x,y) &= a_0 + a_1 x + a_2 y \\ v(x,y) &= b_0 + b_1 x + b_2 y \end{aligned} \tag{1}$$

where, u(x,y) and v(x,y) are the x- and y- displacements, respectively, at a point (x,y). Evaluation of u(x,y) at all three nodes gives

$$\begin{bmatrix} u_0 \\ u_1 \\ u_2 \end{bmatrix} = \begin{bmatrix} 1 & x_0 & y_0 \\ 1 & x_1 & y_1 \\ 1 & x_2 & y_2 \end{bmatrix} \begin{bmatrix} a_0 \\ a_1 \\ a_2 \end{bmatrix} = [X][a_i] \tag{2}$$

The coefficients $[a_i]$ can be expressed as a function of nodal displacement $[u_i]$ as

$$[a_i] = [A][u_i] \tag{3}$$

where, [A] is the inverse of the nodal coordinate matrix [X]. A similar relationship can also be written for the coefficients $[b_i]$:

$$[b_i] = [A][v_i] \tag{4}$$

Substituting (4) and (3) to (1), the internal displacement within a basic triangle can be written in terms of nodal values by

$$\begin{bmatrix} u(x,y) \\ v(x,y) \end{bmatrix} = \begin{bmatrix} N_0(x,y) & 0 & N_1(x,y) & 0 & N_2(x,y) & 0 \\ 0 & N_0(x,y) & 0 & N_1(x,y) & 0 & N_2(x,y) \end{bmatrix} \begin{bmatrix} u_0 \\ v_0 \\ u_1 \\ v_1 \\ u_2 \\ v_2 \end{bmatrix} \tag{5}$$

where, $N_i(x,y)$ is the so-called interpolation function or shape function of a node i, which has a peak value of 1 at i, and 0 at the rest of the nodes. $N_i(x,y)$ can be found as,

$$N_i(x,y) = \frac{1}{\det|X|}(n_{i0} + n_{i1}x + n_{i2}y) \tag{6}$$

and using the arithmetic of mod 3, one can write,

$$\begin{aligned} n_{i0} &= x_{i+1}y_{i+2} - x_{i+2}y_{i+1} \\ n_{i1} &= y_{i+1} - y_{i+2} \\ n_{i2} &= x_{i+2} - x_{i+1} \end{aligned} \tag{7}$$

Fig. 2 shows a plot of the interpolation function $N_i(x,y)$ and the domain area it affects. This area affected by a node i is the combined area of all triangles with a common node i. In topology, such an area is called a star, or a neighborhood star. A nodal response, such as u_i or v_i, is but a scaling factor for the interpolation function that resides on a star. Adopting this geometric view, the manifold method considers stars as the generalized nodes. The benefits of such a viewpoint become apparent when a discontinuity is encountered.

Another generalization can be realized from a different interpretation of (5). What (5) implies is: "Within a basic triangle bounded by three nodes, the internal displacement is determined once the nodal displacements are known." If the statement is recasted in terms of stars, a generalization emerges. (5) may be interpreted as– "Any physical area that is covered by three stars has its displacement field defined." This is significant: Within any such an area, the strain, stress, strain energy can all be computed from the defined displacement field, and it is, therefore, possible to apply to it mechanical theories such as the minimum energy principle. Using the finite element

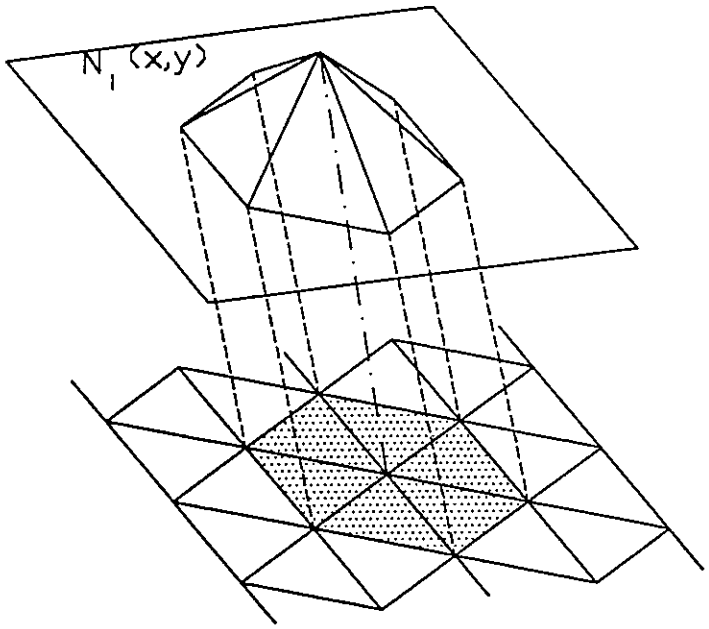

FIGURE 2 A geometric view of an interpolation function and the star it covers.

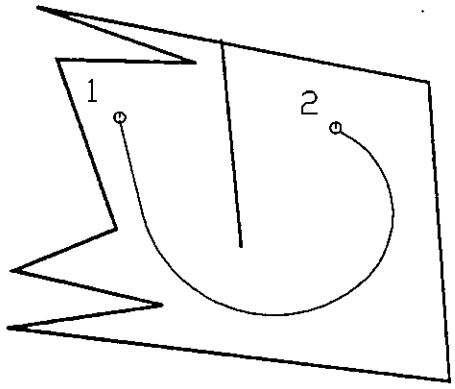

FIGURE 3 A path-connected domain.

analogy, such a physical area constitutes an element. In the manifold method, a generalized element is hence defined as "any physical area that is covered simultaneously by a certain number of stars". This number of covering stars required depends upon the type of interpolation functions used. Using a triangular mesh with a linear interpolation function, a generalized element is an area covered by three stars. If, however, a rectangular mesh is used together with a four-term bilinear interpolation function, a generalized element becomes a physical area covered by four stars. On the other hands, a rigid object is a star by itself.

Thus from this very simple generalization, a new way of generating elements is established. Considering the basically infinite ways of defining response functions--which may be different physical entities, the possibility of coming up new elements are therefore without limit.

4. DISCONTINUITIES AND WEIGHTING FUNCTIONS

In order to conduct a continuous-discontinuous analysis, the issue of continuity and discontinuity has to be clarified first. This study finds the issue can easily be resolved using the concept of "connectedness" from topology which is central to question such as if a figure is of one piece [5]. Among the various types of connectedness, the concept of path-connectedness is found particularly useful. A domain is called path-connected if any pair of its points can be connected by a path in it. For example, the domain as depicted in Fig. 3 is path-connected because any pair of points, such as 1 and 2, can be connected by a path. It can readily be shown that a path-connected domain has a continuous response. On the other hand, a discontinuity is a figure, or a curve in a 2-dimensional case, that makes it impossible for a domain to stay path-connected. Thus a discontinuity always divides a domain into components each of which is path-connected, and no points from different components can be connected without crossing the discontinuity.

Discontinuities may enter an analysis because they are present physically. Or, they may be introduced by a mathematical mesh. This study is concerned mainly with the star discontinuity. Because whenever a star is divided, its components may response independently, and the interpolation function resides on the divided star becomes discontinuous.

Fig. 4 shows a physical domain a-b-c-d which contains a physical discontinuity e-f that divides it into two components a-e-f-d and e-b-c-f. A partial mathematical mesh is also depict on it. The star associated with the node 5, shown in hatch, covers the polygon of 1-2-6-9-8-4, is divided by e-f into two components. This reflects the fact that a physical discontinuity always causes a discontinuity in the star it crosses. On the other hand, the curves g-h and mn are not physical discontinuities since the components they are in remain path-connected. But g-h nonetheless introduces a discontinuity in the star associated with the node 6 that covers the polygon 2-3-7-10-9-5, while m-n does not introduce and discontinuity in the stars that cover it. This clearly illustrates that the selection of a mathematical mesh reflects our view of the scale

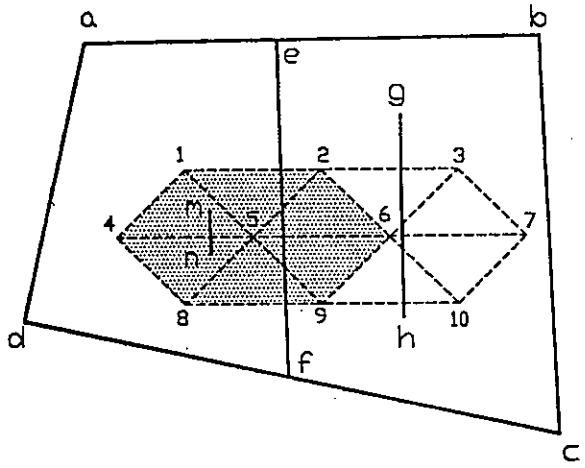

Figure 4 Physical discontinuities and star discontinuities.

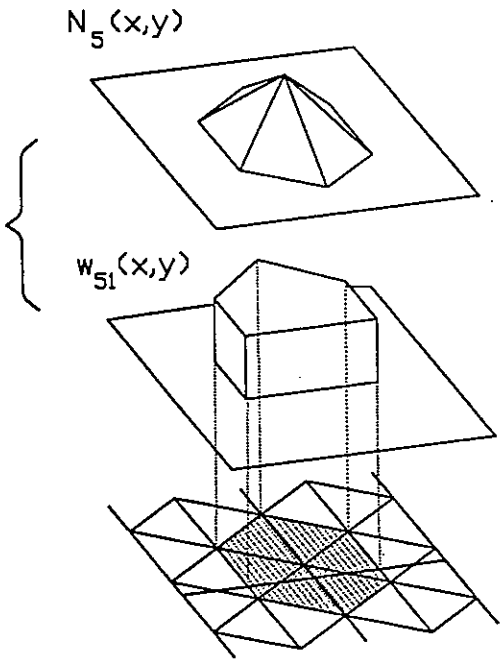

FIGURE 5 Construction of the interpolation function for the star 5_1.

effects. We would choose a mathematical mesh with a size compatible to the scale of discontinuity of concern to us.

The manifold method uses an elegant approach to model a discontinuous interpolation over a divided star. Whenever a star is divided a new star is added for each additional component. Following Shi's notation, this study denotes a star with a node number and a subscript that starts from 1 onward to distinguishes all its components. In the case of the node 5 of the above example, two independent stars are needed since two components are formed. Two stars are independent only if they are scaled by two independent nodal values. To accomplish this, two sets of nodal values are stored at node 5. For the two stars at 5, let 5_1 represent the component to the left of e-f and 5_2 to its right. For each one of them, its interpolation function is constructed in two steps. First, the same interpolation function, $N_5(x,y)$, as defined by (2) are used for both 5_1 and 5_2. Second, different weighting functions, $w_{5_1}(x,y)$ and $w_{5_2}(x,y)$, are then introduced. Each weighting function has the value of 1 over its corresponding component area, and 0 elsewhere. For example, the weighting function, $w_{5_1}(x,y)$, for 5_1 is depicted in Fig. 5. The actual interpolation function used in an analysis is obtained by multiplying the interpolation function with the weighting function. That is, the actual displacement field, say u(x,y), due to 5_1 is

$$u(x,y)=w_{5_1}(x,y)N_5(x,y)u_{5_1} \tag{8}$$

where u_{5_1} is nodal value assigned for scaling the star 5_1. Similar equation can be written for 5_2. The displacement over the combined 5_1 and 5_2 area, i.e., the polygon 1-2-6-9-8-4 due to these two 5 stars becomes

$$u(x,y)=w_{5_1}(x,y)N_5(x,y)u_{5_1}+ w_{5_2}(x,y)N_5(x,y)u_{5_2} \tag{9}$$

which is continuous within 5_1 or 5_2, but becomes discontinuous when crossing e-f. In general, the displacement u(x,y) within an element can be written as,

$$u(x,y)=\sum_i \sum_j w_{i_j}(x,y)N_i(x,y)u_{i_j} \tag{10}$$

where i is a sum over all the covering stars on an element, j is a sum over all the component within an i star.

Fig. 6 further illustrates how to integrate the concepts of stars and discontinuities into identifying the generalized elements. Just to illustrate the liberty we have in selecting the mathematical mesh, a rectangular mesh is adopted here for this example. The underlying response is assumed to be bi-linear within each star. Here except for the node 2, each node is associated with one star only. A 2 star covers the quadrilateral

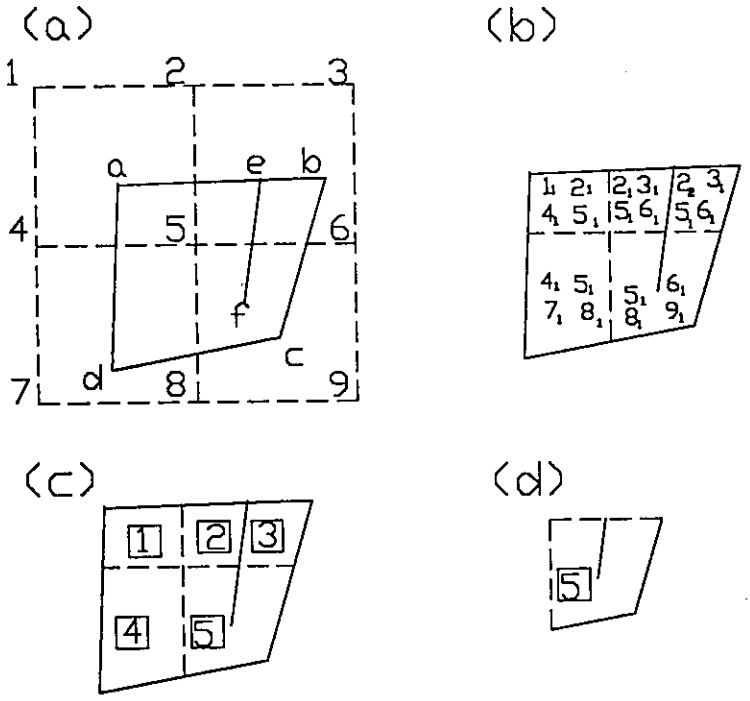

FIGURE 6 Identification of stars and elements

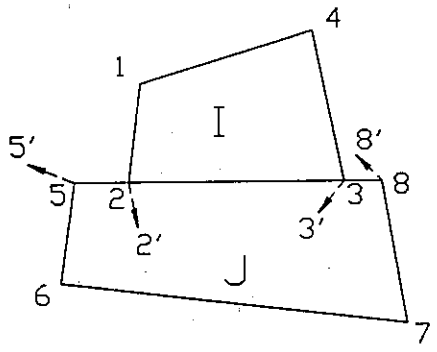

FIGURE 7 Modeling the constraints between element boundaries.

area 1-4-6-3 which is divided into two components by e-f. Here, the star 2_1 is designate as the cover over the domain left of e-f, while star 2_2 to its right. There are therefore 10 stars in this problem: 1_1 , 2_1 , 2_2 , 3_1 , 4_1 , 5_1 , 6_1 , 7_1 , 8_1 , and 9_1 . Each generalized element in this example is an area covered by four stars. There are, therefore, five elements for this problem. Element 1 is covered by 1_1, 2_1 ,4_1 and 5_1 ; element 2 by 2_1 , 3_1, 5_1 and 6_1; element 3 by 2_2, 3_1 , 5_1 and 6_1; element 4 by 4_1, 5_1 , 7_1 and 8_1; and element 5 by 5_1 , 6_1 , 8_1 and 9_1 . It is important to note that each element can take a rather arbitrary physical shape.

5. BASIC FORMULATIONS ON ELEMENTS

Since most engineers are familiar with the finite element method, the following discussions use the finite element terminology. Stiffness matrix of an element due to the strain energy is derived here to illustrate the basic formulations. Here, the strain energy over a basic triangle is derived first, which is then modified by a weighting function to give the real strain energy over its physical domain.

In a plane strain small deformation problem, the strain-displacement relationship can be expressed as follows,

$$[\varepsilon]=\begin{bmatrix}\varepsilon_{xx}\\ \varepsilon_{yy}\\ \gamma_{xy}\end{bmatrix}=\begin{bmatrix}\dfrac{\partial u}{\partial x}\\ \dfrac{\partial v}{\partial y}\\ \dfrac{1}{2}\left(\dfrac{\partial u}{\partial y}+\dfrac{\partial v}{\partial x}\right)\end{bmatrix} \tag{11}$$

Rewriting (5) as

$$[u(x,y)]= [N(x,y)]\ [u_i] \tag{12}$$

the element strain can be related to the nodal displacement with

$$[\varepsilon]=[B(x,y)][u_i] \tag{13}$$

where, [B(x,y)] is a linear derivative of [N(x,y)]. Furthermore, let the constitutive relationship be

$$[\sigma]=[C][\varepsilon] \tag{14}$$

then the strain energy density, $u_o(x,y)$, may be written as

$$u_o(x,y)=\frac{1}{2}[\varepsilon]^T[\sigma]=\frac{1}{2}[u_i]^T[B(x,y)]^T[C][B(x,y)][u_i] \quad (15)$$

and the total strain energy of an element can be obtained through integration. To account for the physical area of a generalized element, again, the weighting function is introduced. The true total strain energy of an element is obtained as follows,

$$U=\int_A w(x,y)u_o(x,y)dA \quad (16)$$

Employing the minimum potential energy principle, the stiffness matrix associate with the straining of the element can be found as follows,

$$[K]=\int_A w(x,y)[B(x,y)]^T[C][B(x,y)]dA \quad (17)$$

In a similar fashion, other components of the stiffness matrix and the force vectors can be derived. Among the factors that are considered for a general applications are initial strains, initial stresses, body forces, inertia forces, interactions through contacts, boundary loadings, and other structures components such as earth anchors or rock bolts.

6. FORMULATIONS ACROSS DISCONTINUITIES

Discontinuities pose two sets of constraints. First, objects should not penetrate each other across the discontinuities that separate them. Second, the motion of one object against another along a discontinuity is affected by the surface strength characteristics. In the manifold method, the first constraint is modeled via the use of a penalty formulation, namely, a very stiff normal spring is inserted at the point of contact. Any tendency to penetrate is restrained by the spring's high stiffness. The second constraint is modeled by inserting a shear spring which yields if its strength governed by Mohr-Coulomb's law is reached. The strain energy in the contact springs is modeled as part of the overall potential energy of the system. This results in the coupling of the stiffness matrices of the elements that are in contact. It is important that the stiffness matrices are coupled because it allows the motion constraints be imposed as soon as interactions take place.

A simple example is depicted in Fig.7 to illustrate how a discontinuity is modeled. Here only the physical boundaries of elements are shown. Initially, edge 2-3 of an element I is in contact with edge 5-8 of an element J. As the loading is applied, both elements may move. Before a constraint across the discontinuity is imposed, the edge 2-3 may move, say to 2'-3', while the edge 5-8 to 5'-8'. In the manifold method, just

like in DDA, edge contacts are modeled via vertex-edge contacts. For this example, the two edge contacts are modeled as two contacts, one between vertex 2' and edge 5'-8', and the other between vertex 3' and edge 5'-8'. Here only the formulation for the first one is detailed. If the vertex 2' penetrates the edge 5'-8', the movement from 2 to 2' is first decomposed into a normal and a shear components against the edge 5'-8' and they are denoted as **d** and **s** respectively. From a geometric consideration using vector cross product, **d** can be written as [4],

$$d=\frac{\Delta}{l_{58}}=\frac{1}{l_{58}}\begin{vmatrix}1 & x_2+u_2 & y_2+v_2\\ 1 & x_5+u_5 & y_5+v_5\\ 1 & x_8+u_8 & y_8+v_8\end{vmatrix} \tag{18}$$

where, l_{58} is the length of 5-8, u_i and v_i are unknown vertex displacements, x_i and y_i are known vertex coordinates and Δ can be expressed as

$$\Delta=d_o+[(y_5-y_8)\ (x_8-x_5)]\begin{bmatrix}u_2\\ v_2\end{bmatrix}+[(y_8-y_2)\ (x_2-x_8)]\begin{bmatrix}u_5\\ v_5\end{bmatrix}+[(y_2-y_5)\ (x_5-x_2)]\begin{bmatrix}u_8\\ v_8\end{bmatrix} \tag{19}$$

In this expression, d_0 is a function of known vertex coordinates and is a constant; while the displacements at vertices 2, 5 and 8 are functions of the unknown nodal displacements. For instance, u_2 and v_2 can be expressed in terms of the nodal displacements of the element I by substituting the (x_2,y_2) coordinates into the interpolation relationship of element I as follows,

$$\begin{bmatrix}u_2\\ v_2\end{bmatrix}=[N(x_2,y_2)]_I\ [u_i]_I \tag{20}$$

Similarly, u_4,v_4 and u_5, v_5 can be expressed in terms of those of the element J. Thus **d** can be expressed as a linear functions of unknown nodal displacements of elements I and J in the following form,

$$d=d_o+[a][u_i]_I+[b][u_i]_J \tag{21}$$

where, [a] and [b] are constant row vectors. Since 2' is not to penetrate 5'-8', a correct solution should make this normal penetration **d** zero. As stated, this is carried out by inserting a very stiff spring in the penalty formulation. The potential energy, Π, of a contact spring is

$$\Pi=\frac{k_n d^2}{2} \tag{22}$$

A solution obtained from a minimum potential energy of the complete system generally gives negligible penetration. It is important to note that in a penalty formulation, which is an approximation to the Lagrange multiplier [7], a constraint is only approximately satisfied. A small penetration always takes place. If the penetration is deemed too large, improvements can be made by increasing the spring stiffness or by reducing the time step size. The penalty method has the advantage, however, that the spring constant does have physical meaning and can be selected to match laboratory test results be they linear or nonlinear.

The shear deformation, s, of point 2' along 5'-8' causes shear stresses which is modeled by a shear spring, k_s. Expressing s in terms of nodal displacements, the potential energy of the spring is also formulated. The corresponding stiffness and forcing terms can be similarly determined. Again, the stiffness matrices due to shear movements are coupled in this approach. Iteration is required if the shear spring yields.

Elements may form new contacts or may disengage from existing contacts. Because of the coupling in the stiffness matrix, how large a memory area should be reserved for an analysis becomes an important issue as the number of elements increases.

7. CONSTRUCTION OF PHYSICAL BOUNDARIES OF ELEMENTS

To show that the computational geometry also plays an important role in the manifold method, the construction of the physical boundaries of elements from a covered manifold is described here.

1) First of all, the physical mesh is obtained which includes the boundary of blocks and discontinuities with them. A computational algorithm devised by Shi for DDA can be adopted for this purpose. The algorithm uses tree-cutting analogy and the "coherent orientation" scheme in topology [8].

2) One may choose to work on all blocks simultaneously, or one block a time. The latter approach is described here. For instance, Fig. 8 (a) depicts a rather general block. One may easily determine a rectangular box that covers the block. Let the lower left corner be (x_min,y_min) and the upper right corner be (x_max,y_max).

3) According to the size of the mathematical mesh selected, the mathematical mesh may be generated starting from (x_min,y_min), until the mesh covers (x_max,y_max).

4) For each point on the mesh, determines if the point or its immediate neighbors fall on the boundary or within the interior of the block. If so, the point is retained for constructing stars. In Fig. 8(b), it shows 12 points are retained. This means that at least

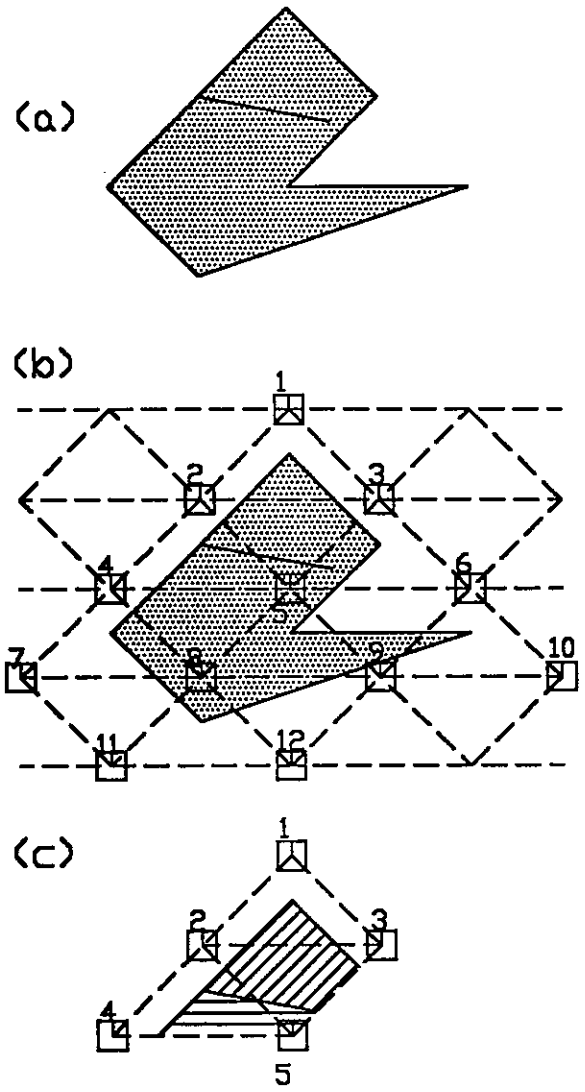

FIGURE 8 Construction of physical boundaries of elements (a)A typical object (b) after identifying the relevant nodes (c) construction of stars.

12 stars are need to cover the block.

5) For each point retained, the corresponding star or stars are constructed. If a star falls completely within the block, no thing needs to be done. If it intersects with the block, the intersected region is the real star area. This step can be achieved with some polygon intersection algorithm. If a star is divided by discontinuities, the number of components are determined. For instance, there are two 2-stars as depicted in Fig. 8 (c).

6) Obtain the total number of elements and their physical boundaries. This is equivalent to obtain the area overlapped by three stars associated with the triangles of the underlying mesh. .

8. EXAMPLE APPLICATIONS

Two problems are solved here for illustration. For the purpose of illustration, these examples are much simplified: large size mathematical meshes are used together with linear interpolation functions. All the elastic objects have a Poisson ratio of 0.3, a mass density of 1.8 Mg/m^3, a unit weight of 18 kN/m^3, and elastic moduli ranging from 1500 to 4000 kN/m^2. All the rigid bodies are marked by hatch dots in the following drawings.

The first problem tackles an elastic medium with rigid inclusions. In this problem the elastic medium has both exterior and interior boundaries. Here, two rigid plates are pressed against an elastic medium with two rigid inclusions placed unsymmetrically. Initially, there are perfect contacts between the elastic medium and the rigid inclusions, as well as between the elastic medium and the rigid plates. The covered manifold is depicted in Fig. 9 (a). All contacts are modeled as frictional with a friction angle of 5°. The deformed configuration after experiencing a 14.7% vertical strain is shown in Fig. 9(b). Because of the way inclusions are placed, the elastic medium deformed unsymmetrically. Part of the contacts between the inclusions and the medium are separated. The contacts between the rigid plates and the elastic medium also shift.

The second problem, as shown in Fig. 10(a), studies an elastic object, which contains a set of well-defined fissures, and is being pressed from the sides. Surfaces of the fissures are characterized by a friction angle of 5°. This problem is presented here to illustrate the capability of the manifold method in modeling discontinuities. For this purpose, tips of the fissures are not allowed to propagate. Even with this simplification, this is still a rather difficult problem. Pressing the sample from sides, the fissures show a complicated movement pattern. The side rigid blocks in this example are assumed smooth frictionless surfaces. The deformed configuration at a horizontal strain of 20.8 % is summarized in Fig. 10(b). In order to show the deformed configuration clearly, the mathematical mesh is not shown in this plot. Because of the rough mesh used, this result is only a crude approximation. Although much simplified, the example shows the manifold method may have a potential use in

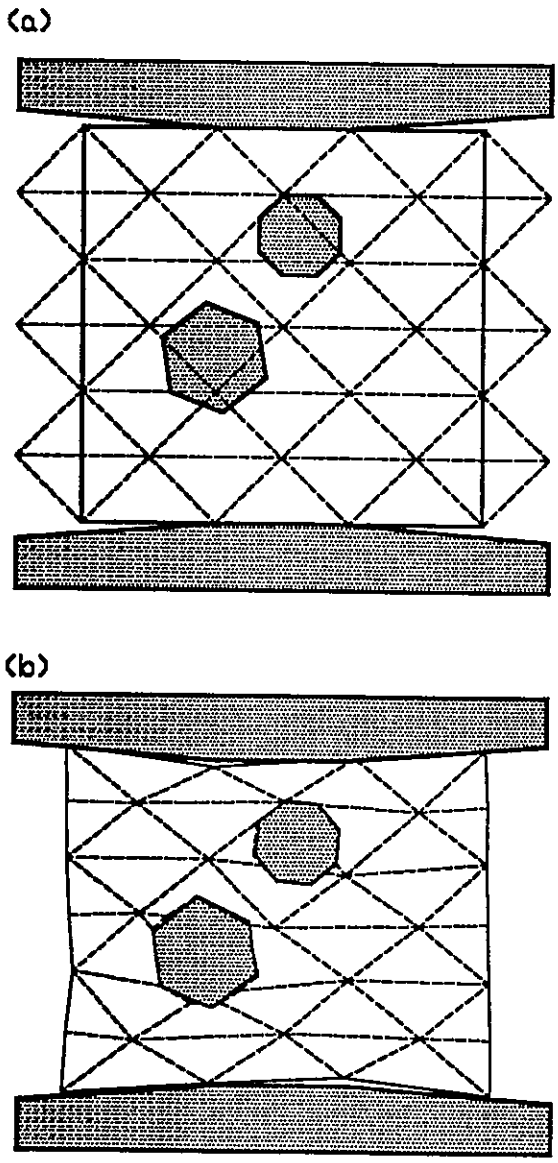

FIGURE 9 An elastic medium with rigid inclusion problem (a) a covered manifold (b) its deformed configuration.

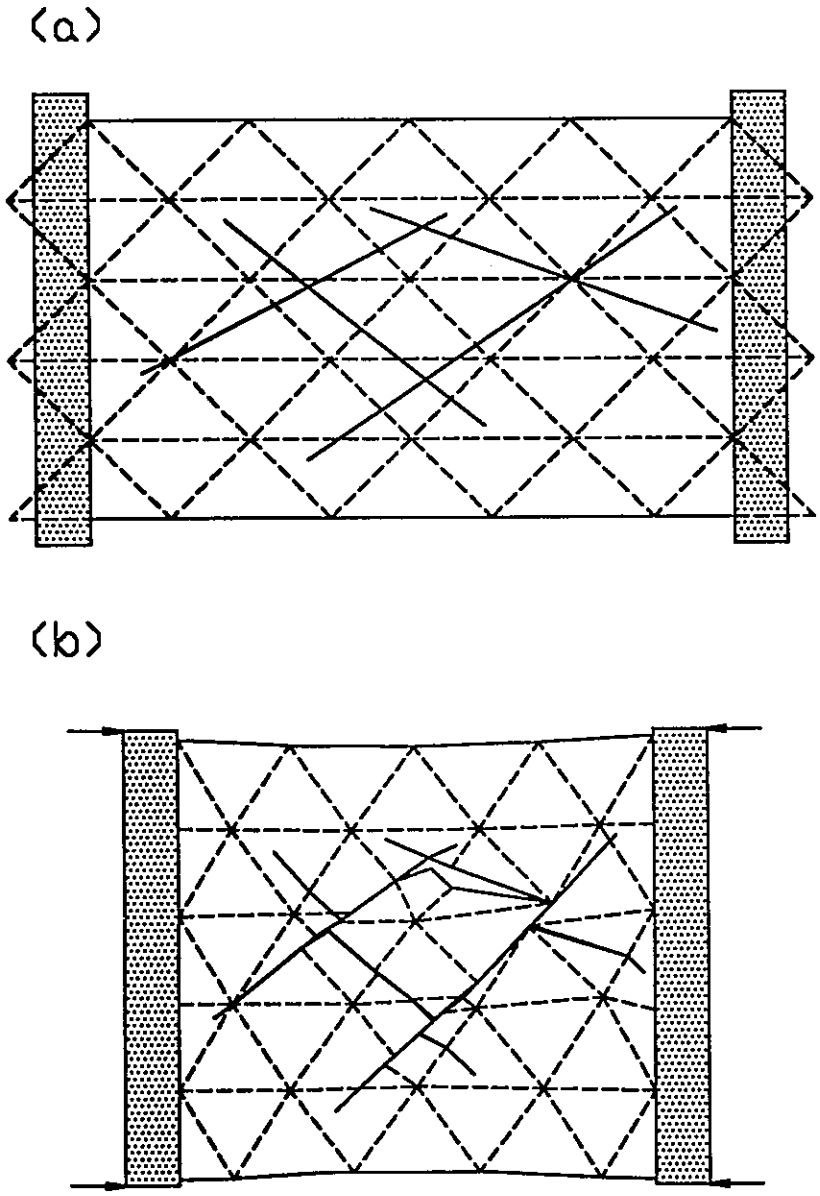

FIGURE 10 An elastic medium with non-propagating fissures (a) a covered manifold (b) its deformed configuration.

solving problems involving clusters of discontinuities in various arrangements.

9. CONCLUSIONS

This paper explains the fundamentals of the manifold method using concepts with which engineers are familiar, and shows how different parts are put together for an engineering analysis. The illustrative examples may also shed lights on what problems may be benefited from its use.

The manifold method has several distinctive features that are important from engineering analysis point of view. First and foremost, by using a covered manifold it opens up a new way for the continuous and the discontinuous methods of analysis. Second, it satisfies the minimum energy principle globally, namely both within elements and across elements. Except for the discretization simplifications, the procedure is rigorous both analytically and numerically. Third, the unifying underlying formulations allows extensions be introduced, such as the inclusion of rigid bodies, in a consistent manner.

ACKNOWLEDGEMENTS

The author would like to acknowledge the support of a grant, 1434-94-G2434, from National Earthquake Hazard Reduction Program for the present work. This program has been administered by United States Geological Survey. The author would also like to thank Dr. Gen-Hua Shi of the Waterways Experiment Station, USAE, for his comments and suggestions. The computer program developed for this research also benefits from adapting some code from a DDA program written by Dr. Shi.

REFERENCES

1. Shi, G. W., "Manifold Method of Material Analysis," Proceeding, Ninth Army Conference on Applied Mathematics and Computing.
2. Shi, G. W., "Modeling Rock Joints and Blocks by Manifold Method," Proceeding of the 33rd U.S. Symposium on Rock Mechanics, SanTa Fe, New Mexico, pp. 639-648, 1992.
3. Stillwell, J., Classical Topology and Combinatorial Group Theory, 2nd Ed., Spriner-Verlag, New York, 1991.
4. Shi, G. W., Block System Modeling by Discontinuous Deformation Analysis, Computational Mechanics Publication, Southampton, UK, 1993.
5. Macneal, R. H., Finite Elements: Their Design and Performance, Marcel Derkkere Inc. New York, 1994.
6. Mendelson, B., Introduction to Topology, 2nd Edition, Dover, 1990.
7. Hughes, T.J.R., The Finite Element Method, Linear Static and Dynamic Finite Element Analysis, Prentice-Hall, Inc., Englewood Cliffs, 1987.
8. Giblin, P.J., Graphics, Surfaces and Homology, Chapman and Hall, London, 1977.

Formulation and Solution Scheme of the Nonlinear Contact Problem in the DDA Method

Frank C. Tsai

Woodward Clyde Federal Services, Las Vegas, USA

Abstract

To elucidate the Discontinuous Deformation Analysis (DDA) method for other researchers, the exploration of the concepts, theories, and approximations used to formulate this method are presented. The mechanical response of bodies in a discontinuous system is a nonlinear problem since there is energy dissipation involved in the process of frictional sliding. Two main issues about how to formulate a nonlinear contact problem in the DDA method are addressed in this paper: (1) how to post mathematically the *nonlinear* contact problem using *linear* equations; and (2) how to select the correct solution.

1. INTRODUCTION

The Discontinuous Deformation Analysis (DDA) method[1] is a numerical method for simulating the dynamic mechanical response of a discontinuous system. A discontinuous system is a system of multiple continuous bodies which are in motion under external loads and interact with each other through contacts. In a discontinuous system, any pair of bodies in a small neighborhood may either be detached or in contact. If two bodies are detached, they are in free body motion independent from each other. If two bodies are in contact, the Coulomb's frictional law can be used to govern the relative motion from one to another. If the shear component of the contact force is less than the shear strength, these two bodies are locked together by the frictional constraint. Otherwise, they are sliding on each other. There is always energy dissipation involved in the process of frictional sliding even when bodies in contact deform elastically. The shear strength is defined as the product of the frictional coefficient between the contact surfaces and the normal component of the contact force. The contact interaction is generated by the bodies' motion which is the result of external loads and boundary constraints. Simultaneously, there are reactional contact forces generated by the contact interaction. Considering a body in the system as a free body, its motion is induced simultaneously by the external loads and the contact forces. The motion of a body includes not only the rigid body motion according to Newton's law of motion but also the deformation of the body according to the continuum mechanics.

The above described mechanical response of bodies in a discontinuous system must be presented as a nonlinear problem. The solution is always unique in linear problems, but this is no longer the case in many nonlinear situations. Thus, if a solution is achieved it may not

necessarily be the solution sought. To obtaining a solution using a numerical method, presenting the nonlinear problem in a series of linear equations is essential. Physical insight into the nature of the problem in the solution process is essential to obtaining physically significant answers. The questions "how the nonlinear contact problem is posted mathematically using linear equations" and "how the correct solution of the nonlinear contact problem is selected" have always been interesting subjects. To provide answers to these two questions and to expedite the understanding of the DDA method for other researchers, the physical insight of the solution process formulated in the method is presented in this paper.

In order to present a nonlinear contact problem using a series of sets of linear equations, the DDA method implements the following aspects: the approximation of a dynamic phenomenon as a recurrence relation over discrete time intervals, the decomposition of displacement into a linear combination of translation, rotation, and deformation, the constant acceleration within a discrete time interval, the elastic behavior for all bodies, Newton's law for rigid body motions, the minimum total potential energy theory with conserved boundary constraints of forces and displacements, the contact analogy using stiff springs and/or substituted external forces, the conserved contact positions within a time interval, and the selection of contact positions iteratively by trial-and-error. The solution at the end of a time-step for the nonlinear contact problem is determined to be correct if Coulomb's frictional law is satisfied at each contact, each final contact position converges to its trial position, and the equilibrium condition is satisfied at each contact and at all particles of each body.

In this paper, the development background of the DDA method is first introduced to illustrate its major improvement as a material analysis method for the discontinuous system. Second, the basic concepts and analogies used to formulate the nonlinear contact problem in a linear form are discussed. Then, the physical theories and numerical approximations adopted in the method are organized in three sections: the displacement decomposition, the time discretization, and the minimum total potential energy.

2. NUMERICAL METHOD DEVELOPMENT BACKGROUND

To model the mechanical behavior of a discontinuous system, Cundall [2, 3] created the distinct element method in early 70's. Since then, this method has been continuously developed and widely accepted in the mining and civil engineering industries for simulations of the behavior of jointed rock masses. The distinct element method uses an explicit iterative solution procedure to solve the nonlinear problem. Using the body position and the contact forces produced in the previous iteration, the main calculation sequence in the current iteration can be stated as follows:

1. Block centroid forces are accumulated from the contact forces, internal nodal forces, and external boundary forces;
2. The block centroid forces determine the block centroid accelerations based on the law of motion;
3. Block velocities and displacements are then determined by the integration of

accelerations over the time increment, and thus, new block positions are obtained;

4. For each contact, the relative velocities/displacements of a contact corner of a block and of an edge of a neighboring block determine the new contact force based on the contact constitutive model;
5. The strain rates (increment strains) and the rotation rates (increment rotations) can be computed based on the grid point velocities of blocks; and
6. The strain rates determine the incremental stresses based on the block constitutive model, and the incremental internal nodal point forces can be integrated from the incremental stresses.

Following this procedure, three sets of governing equations for the law of motion, the contact constitutive model, and the block constitutive model are formulated and solved sequentially using fictitious forces as unknowns of governing equations. The iterative solution process is repeated until all bodies are at equilibrium state or until such time as the system undergoes unstable motion, i.e., the solution diverges.

The above described formulation method adopted in the distinct element method is fundamentally different from the one adopted in the finite element method. Hence, the future development of this method for the application in many other engineering fields is limited. To analyze the mechanical behavior of a material system, the finite element method has been proved to be the most powerful tool ever developed. It has been adopted widely by many disciplines of engineering and science. The finite element method represented a revolution in developing numerical methods for the material analysis. In the last four decades, a vast amount of research and development effort has been devoted into the improvement of the finite element method. To create a new numerical method, one may take the advantage of such an existing effort.

The finite element method was first introduced using an analogy between real discrete elements and finite portions of a continuum. A real discrete system is formed using a finite number of well-defined members (elements) and connections. The well-defined members and the connections require that only certain special types of forces and deformations may occur in the elements and at the connections. A standard matrix method may be used for the analysis of problems of a real discrete system[4]. As an analogy of the real discrete elements, the behavior of elements in the finite element method is specified by a finite number of parameters, and the solution of the complete system is obtained from a direct assemblage, in the form of the standard matrix method, of its elements. It converted the differentiation problem into the problem of integration which is much easier solved using computers. As a result, the finite element method provides a unified computational procedure for the approximation of the discrete analogy[5].

In the displacement-based finite element method, the force-displacement relationships for each element is first calculated. Then it proceeds to assemble a set of simultaneous equations by following a well-defined procedure for establishing the local equilibrium conditions at each connecting point (node) of the structure. This original finite element concept established using the local equilibrium at nodes was abandoned in later development. The advanced concept considers a displacement function that is defined as a continuous function over the whole continuum, and the global equilibrium of the entire structure is based on the virtual work theory, the minimum potential energy theory, or

variational principle[5]. After the displacement function for the whole structure is defined, the problem of establishing governing equations for the system equilibrium becomes one of how to obtain the total work or the total potential energy for the entire structure. The definite integral of the physical term in the global equilibrium equations require that the total is the sum of its parts: $\int_V (A)\,dV = \sum \int_{V^e} (A^e)\,dV$, where V^e is the element volume and A^e is the physical term in the corresponding element volume.

This approximation of the finite element method for the behavior of a discretized system lies simply in the requirement of writing the approximation in integral form. The assembly rule as well as the whole derivation has been achieved without involving the concept of "inter-element forces". The properties of the discretized system are recovered if the approximating equation is written in an integral form. The adopted thermodynamic theory ensures satisfaction of equilibrium conditions within the limits prescribed by the assumed displacement pattern. If the number of parameters that describe the displacement increases, an ever closer approximation to the equilibrium conditions can be ensured.

In a discontinuous system, stiff springs are inserted between continuous bodies to model the contact interactions. Since there is only one degree of freedom assigned to the motion of a spring, the displacement of the entire discontinuous system can not be described using a single continuous function. Hence, the global equilibrium established using energy theories for setting up the governing of the entire system can not directly applied. However, it can be applied separately to formulate the particle motion in each continuous body in the system. Since a discontinuous system is a real discrete system, the local equilibrium concept can be adopted to formulate the equilibrium condition at all contact points for the relative motion among bodies. While contacts are modeled using stiff springs inserted between bodies at the contact points (if the contact points are known), the displacements of end points of springs are identical to the displacements of the connecting particles in the bodies. With respect to a single body, a contact interaction can then be considered as a prescribed displacement boundary constraint which is determined by the behavior of contact springs. Hence, in a displacement-based numerical method, the motion of all particles in a body can be formulated into the standard matrices using the direct summation of the energy computed from each discretized displacement parameter. Since the local equilibrium between bodies is expressed in terms of the displacement of end points of springs, the matrices representing the particle motion of each body can again be formulated into global matrices representing the motion of the entire discontinuous system using the direct summation based on the local equilibrium at contact points.

As an improvement comparing to the distinct element method, the DDA method was developed based on the computation procedure established in the finite element method. Using the global equilibrium (with respect to each body) and the local equilibrium (with respect to each contact point) developed in the finite element method, the particle motion within each continuous body and the relative motion among bodies can be simultaneously formulated into one set of equations using the minimum total potential energy theory. Hence, an implicit solution scheme can be established for the nonlinear contact problem. Most of all, the future development of the DDA method can be in parallel with the development of the finite element method. In fact, to discretize the displacement function over each continuous body, the finite element discretization, i.e., each continuous body can be discretized into a number of elements, can be directly applied in the DDA method[6].

3. BASIC CONCEPTS AND ANALOGIES

In a discrete time system[7], the dynamic response of the system is described by a series of instantaneous responses at discrete instants of time. The time interval between two consecutive instants is referred to as a time-step. The recurrence relation is the identical mathematical description in functional form to describe the mapping from the initial state to the final state for every time-step. In any given time-step, the mapping is expressed as a function of the initial state and the history of external condition. System equations are developed to express such a function of the recurrence relation. Solving the system equations with the initial state and the boundary constraints, the final state at the final instant of the time-step is obtained. Then, the final state of the current time-step is inherited as the initial state at the beginning instant of the next time-step. The DDA method is such a numerical model which describes the dynamic response of multiple bodies in a given domain using the discrete time system and the recurrence relation.

In the DDA method, a contact is always referred by the interaction between a vertex of a body and an edge of another body. An edge-to-edge contact is simply treated as two vertex-to-edge contacts. Let us define the term "open contact" as the state of two bodies which are detached with the condition that a vertex of one body is in the small neighborhood of an edge of another body. Hence, the status of a contact at any instant may be open, locked, or sliding. Within a time-step, an open contact may become a locked frictional contact or a sliding contact and a locked or sliding contact may become open. In the meantime, a locked contact may change to a sliding one or vice versus. Due to the possible sliding between bodies occurred within a time-step, the positions of all contacts in a dynamic process are a part of the system configuration. However, it is almost impossible to include the contact positions as a part of unknowns in the system equations. To overcome this problem, the system equations are formulated by pre-determining the contact positions and by keeping the contact positions conserved within the entire time-step. Hence, the system equations derived using the minimum total potential energy theory can be formulated in a simple mathematical form due to the conserved external condition within the entire time-step.

Using the conserved contact positions, together with a linear strain-displacement approximation and a linear stress-strain material behavior in each continuous body, the mechanical behavior of a discontinuous system occurring within a time-step can be formulated as a "linear" problem. Traditionally, engineers use physical intuitions as the analogy to establish the simple mathematical description of a complicated process. The trial-and-error concept and a simple physical analogy are adopted to solve the nonlinear contact problem. A trial set of contact positions based on the geometric relationships among bodies are first selected for all contacts in the system. The trial contact positions are the estimated final contact positions at the final instant of the current time-step. Then, each contact is modeled with stiff spring(s) and/or sliding forces inserted between bodies at the trial contact position. Hence, a set of linear equations can be established for the motion of each continuous body and each spring. These linear equations are established based on the minimum total potential energy theory to represent the equilibrium of particles in the body. Applying the local equilibrium at each contact point, all sets of linear equations for all

bodies are directly summed together to form a large set of linear equations. The final set of linear equations represents simultaneously the equilibrium of particles in each body and the contact equilibrium between bodies at the final instant of the time-step.

At the first iteration of the current time-step, the trial position and the status of each contact are inherited from the result of the previous time-step. In addition, all sets of vertex -to -edge reference which may possibly become a contact at the end of the current time-step are defined as open contacts. Each locked contact is modeled using a pair of stiff springs inserted at the trial contact position in the directions normal and parallel to the reference edge of the contact. Each sliding contact is modeled by a stiff spring normal to the reference edge and a substituted external force couple acting on two bodies in the direction parallel to the reference edge at the trial contact position. The magnitude of the substituted sliding forces are determined by the on site of the frictional law. Then, the system equations of the system of multiple bodies with trial contacts are formulated and solved.

The result of each iteration is checked according to three contact status adjustment rules: first, comparing the contact forces at all locked contacts with the sliding criterion , second, comparing the sliding direction against the direction of the substituted sliding force for each sliding contact, and third, evaluating the vertex-to-edge penetration for each open contact. If the normal contact force is compressive and the shear force of each locked contact is less than the shear strength, the contact remains to be locked and its trial contact position remains the same in the next iteration. If the normal contact force is compressive and the shear force is equal to or greater than the shear strength, the locked contact becomes a sliding one and its trial contact position remains the same for the next iteration computations. If the normal contact force of a locked contact is tensile, it becomes an open contact in the next iteration.

If the shear movement of a sliding contact is in the reverse direction of the substituted sliding force, it remains to be a sliding contact in the next iteration. The displaced contact position is considered as the trial contact position in the next iteration. If the shear movement is in the same direction of the substituted sliding force, a sliding contact becomes a locked one and its trial contact position remains the same in the next iteration. If the vertex-to-edge penetration of an open contact is positive, it remains to be an open one for the next iteration. If the vertex-to-penetration is negative, an open contact becomes a locked one in the next iteration. Its trial contact position in the next iteration is the projection of the vertex on the reference edge.

Since the contact position of a sliding contact may change within an iteration, its trial contact position is not conserved, i.e., the points of application of the substituted external force couple (the shear contact forces) acting on bodies is not conserved. Therefore, the motion of continuous body formulated using the minimum potential energy does not corresponding to the equilibrium condition at the final instant of a time-step. The iteration process should continue not until only there is no more change of the contact status for all contacts but also the relative position between the vertex and the reference edge of each sliding contact converges to the condition that the final contact position is the same as the initial one. In such a case, the trial contact position for all contacts represents the final positions. Upon the convergence of the contact status of all contacts and the contact position of all sliding contacts, the set of trial contact positions is correct and the solution correctly represents the instantaneous motion of all bodies.

The above described solution analogy brings to light an important point. The formulation of system equations with stiff spring(s) and/or substituted external contact forces at the trial contact position assumes that the contact positions are fixed during the entire time-step. In other words, the trial contact positions are a part of the conserved system configuration. This approach adopts not only the concept of trial-and-error but also the concept of creating a perturbation of the system configuration before the beginning instant of a time-step and after the final instant of the previous time-step. Generally, in other numerical models, the initial configuration/state of a system at the current time-step is inherited entirely from the final one at the previous time-step. This configuration perturbation between two consecutive time-steps is one of the unique features introduced in the DDA Method.

While the position of a contact changes, the point of application of the contact force is displaced. Hence, the work, which equals the contact force times the distance between the original and the change points of application, is done and the energy has been dissipated. However, the formulation of the system equations does not include the change of positions for sliding contacts because fixed contact positions during the entire time-step are assumed. In other words, the energy dissipation due to the frictional sliding between two bodies is not computed in the system equations that represent the response of the system within a time-step. It is implicitly included at the instant before the current time-step and after the previous time-step. The formulation of system equations for each iteration computation is obtained on the condition that the system energy is conservative within a time-step (if the constitutive behavior of the material of all bodies is reversible). The amount of energy dissipated within a time-step is implicitly represented by the change of the contact positions between the selected trial positions and the final positions obtained in the previous time-step. It is assumed that the correct amount of energy dissipation occurring within a time-step is reflected in the model if all bodies in the system are in equilibrium, each final contact position converge to its trial position, and the Coulombs frictional law is satisfied in each contact at the final instant of the time-step.

In the process of developing the DDA method, Shi[8] created the simplex integration which is an analytical integration of any n-dimensional polynomial function on any n-dimensional generally shaped domain. The simplex integration can significantly improve the numerical method for the material analysis. Since the finite element method converts a problem represented by differential equations into an integration problem, the success of a numerical approximation method lies simply in the requirement of writing the approximation in integral form. Before the simplex integration is established, numerical integrations, such as Gauss integration, are usually used. This is the reason that a domain to be analyzed must be discretized into some regular shaped subdivisions and the mapping of the subdomain of the function to be integrated into even more restricted regular shaped subdomain must be implemented in the finite element method.

In order to integrate the potential energy as a function of displacement over a material domain, an arbitrary continuous displacement function of coordinates over the entire domain is approximated by a piecewise linear function of nodal displacements in the four-nodes isoparametric finite element method. Hence, nodes are used not only to specify the nodal displacements as the unknown parameters of system equations and the nodal force as the known parameters, but also used to specify the subdomain of the integration. These

constraints make the discretization of the finite element very difficult. Often, they cause unnecessary increase in the degree of freedom of the approximation due to the complex shape of the material domain rather than the desire of a more accurate approximation.

Using the simplex integration and the global equilibrium, a high order polynomial function (rather than the piecewise linear function) can be assigned to the continuous material domain to describe the displacement field. Thus, the discretization of the domain may not be necessary. The higher order of polynomial is chosen, the higher degrees of freedom of the approximation is made. In the analysis of a discontinuous system, the interactions between bodies are the main subject to be analyzed. Hence, we may chose the least order polynomial displacement function for each continuous body so that we can study the motion of a system of many bodies within a limited computer resource. The DDA method adopted the linear displacement function (zero order approximation of strain field) which is the least order of approximation of the deformable continuous body of an arbitrary complex shape for any numerical method. This can only achieved by using the simplex integration and the formulation of the global equilibrium with respect to a single body. The use of a second order displacement function in each body for the higher degrees of freedom approximation in a discontinuous system has been illustrated by Chern, Koo, and Chen[9]. If a much higher order of polynomial function is adopted, physical meaning can no longer be designated on the unknown parameters in the governing equations. Nevertheless, the solution of this pure mathematical process for the approximation of mechanical behavior of a continuous body remains to be physically valid.

4. LINEAR DECOMPOSED DISPLACEMENT FUNCTION

This section discusses the motion of particles in a continuous body of a discontinuous system. The domain of a discontinuous system is a Euclidean space. A continuous body is composed of particles. When some physical action is imposed, the body as a whole moves in a Euclidean space and particles in the body move relative to each other. A description of the instantaneous locations of all particles must include both the movement of the body as a whole and the relative movement between particles. The movement of the body as a whole is referred to as the rigid body motion which consists of translation and rotation. The relative movement between particles is defined as the body deformation.

Rigid body translation is characterized by the constant displacements and velocities for all particles in the body at any given instant of time. The motion of rotation is the self spinning motion without considering any relative motion between particles. Although there is no stretching (change of length) between any pair of particles in the course of rigid body rotation, the rigid body rotation displacement of each particle measured with respect to a given rotation axis is a function of its position vector. Consequently, the rotation displacements of particles are coordinate dependent. The body deformation is the change of body configuration which is characterized by the change of the length between any pair of particles in the body. Measured with respect to a given reference point, each particle has a unique deformation displacement which is a function of the particle position in relationship to the reference point. Hence, the deformation displacement of particles in a body is also coordinate dependent.

Based on the motions defined above, the displacement vector u_i, where i refers the axes of the reference frame, of all particles used to characterize the motion of a body is composed of the displacement of rigid body translation, u_i^t, the displacement of rigid body rotation, u_i^r, and the displacement of body deformation, u_i^d. To obtain the most simple displacement function, we like to express the displacement of a particle as a simple superposition of its components:

$$u_i = u_i^t + u_i^r + u_i^d \tag{1}$$

For any admissible displacement function u_i, an admissible function must be sought for each of the displacement components, u_i^t, u_i^r, and u_i^d. Furthermore, the displacement components must be defined independent from each other if they will be used as unknown variables of a set of system equations for describing a dynamic process. The main object of this section is to define the composed displacement function shown in Equation 1 that displacement components, u_i^t, u_i^r, and u_i^d are admissible and independent.

Let $u_i(\bar{P})$ be the displacement of a point $\bar{P}$ in the time interval from instant t_0 to t. Consider a neighboring point P in the body. Let the coordinates of $\bar{P}$ and P be x_i and $x_i + dx_i$, respectively. The displacement u_i of particle P at the instant of time t can be obtained by a line integral along a continuous curve joining P and $\bar{P}$ as

$$u_i = u_i(\bar{P}) + \int_{\bar{P}}^{P} du_i \tag{2}$$

By the ordinary rule of differentiation, the relative displacement of P with respect to $\bar{P}$ is

$$du_i = \frac{\partial u_i}{\partial x_j} dx_j \tag{3}$$

This can be rewritten as

$$du_i = \frac{1}{2}\left(\frac{\partial u_i}{\partial x_j} + \frac{\partial u_j}{\partial x_i}\right) dx_j + \frac{1}{2}\left(\frac{\partial u_i}{\partial x_j} - \frac{\partial u_j}{\partial x_i}\right) dx_j \tag{4}$$

Due to the algebraic operation, two terms on the right-hand side of the above equation are always independent from each other. These two terms are identical to the Cauchy's infinitesimal strain tensor ϵ_{ij} and the infinitesimal rotation tensor ω_{ij} that

$$\epsilon_{ij} = \frac{1}{2}\left(\frac{\partial u_i}{\partial x_j} + \frac{\partial u_j}{\partial x_i}\right) \tag{5}$$

and

$$\omega_{ij} = -\frac{1}{2}\left(\frac{\partial u_i}{\partial x_j} - \frac{\partial u_j}{\partial x_i}\right) \tag{6}$$

From this antisymmetric rotation tensor we can always build a dual rotation vector ω_k as $\omega_k = \frac{1}{2}e_{kij}\omega_{ij}$, where e_{ijk} is the permutation tensor. Using the delta identity operation, $e_{ijk}e_{ist} = \delta_{js}\delta_{kt} - \delta_{jt}\delta_{ks}$ (δ is the Kronocker Delta), the rotation vector can be written as $e_{ijk}\omega_k = \frac{1}{2}(\omega_{ij} - \omega_{ji})$. Since ω_{ij} is antisymmetric, $\omega_{ij} = e_{ijk}\omega_k$. Therefore, the relative displacement of point P with respect to point $\bar{P}$ shown in Equation 4 can be rewritten as

$$du_i = \epsilon_{ij}dx_j - e_{ijk}\omega_k dx_j \tag{7}$$

Inserting Equation 7 into Equation 2, yields

$$u_i = u_i(\bar{P}) - \int_{\bar{P}}^{P} e_{ijk}\omega_k dx_j + \int_{\bar{P}}^{P} \epsilon_{ij}dx_j \tag{8}$$

Because $u_i(\bar{P})$ is the given displacement of an arbitrary specified point $\bar{P}$, it is a coordinate independent prior. As indicated by Equation 5, each element of the strain tensor of any particle is a single-valued function of the particle position so that $\epsilon_{ij} = \epsilon_{ij}(x_1, x_2, x_3)$. Equation 6 shows that each element of the dual rotation vector ω_k is single-valued and the vector itself is coordinate independent. Hence, the integrations of ϵ_{ij} and ω_k from $\bar{P}$ to P are admissible for any arbitrary particle $P(x_1, x_2, x_3)$ in the domain of a continuum.

The first term $u_i(\bar{P})$ in Equation 8 is the absolute displacement of the specified particle $\bar{P}$ with respect to the system frame of reference. It may includes all displacement components defined in Equation 1. The displacement of body deformation of a single particle vanishes due to the basic concept of the theorem of continuum that a physical particle is approximated by a mathematical point. Therefore, the absolute displacement $u_i(\bar{P})$ of particle $\bar{P}$ with respect to the system frame of reference can be decomposed into a component of translation $u_i^t(\bar{P})$ and a component of rotation $u_i^r(\bar{P})$ that

$$u_i = u_i^t(\bar{P}) + u_i^r(\bar{P}) - \int_{\bar{P}}^{P} e_{ijk}\omega_k\, dx_j + \int_{\bar{P}}^{P} \epsilon_{ij}\, dx_j \tag{9}$$

The third term on the right-hand side of Equation 9 is only a portion of the rotation component of the absolute displacement of the particle P with respect to the system frame of reference. Another part of the rotation component is represented by the rotation component of the absolute displacement of the reference particle $u_i^r(\bar{P})$.

To simplify Equation 9, we select the centroid, O, of the body as the reference particle.

Since all rotation axes of a free body pass through the centroid, the rotation displacement of centroid O always vanishes. Hence, $u_i^r(\bar{p})$ in the right-hand side of Equation 9 is omitted and $-\int_o^P e_{ijk}\omega_k dx_j$ is the only term representing the rotation displacement of any particle in the body. The translation displacement component of any particle P in the body is identical to the translation displacement of the centroid u_i^o. Expressing all independent variables of coordinates and time, we can rewrite the displacement decomposition shown in Equation 9 in a simple form as

$$u_i(x_1, x_2, x_3, t) = u_i^o(t) - \int_o^P e_{ijk}\omega_k(t)\, dx_j + \int_o^P \epsilon_{ij}(x_1, x_2, x_3, t)\, dx_j \tag{10}$$

Relating Equation 10 to Equation 1, the translation, rotation, and deformation displacement components are defined as

$$u_i^t(x_1, x_2, x_3, t) = u_i^o(t) \tag{11}$$

$$u_i^r(x_1, x_2, x_3, t) = -\int_o^P e_{ijk}\omega_k^o(t)\, dx_j \tag{12}$$

and

$$u_i^d(x_1, x_2, x_3, t) = \int_o^P \epsilon_{ij}(x_1, x_2, x_3, t)\, dx_j \tag{13}$$

While using the displacement method for the formulation of the system equations, the independent parameters used to express the displacement functions are adopted as the unknown variables. In the Discontinuous Deformation Analysis method, ϵ_{ij} in the entire continuum domain is assumed to be constant. Hence, the independent parameters u_i^t, ω_k^o, and ϵ_{ij} can be used as the unknown variables. If the small rotation approximation shown in Equation 6 is adopted and the line integration of the strain field (the deformation displacement field) can be approximated using a linear function of a number of independent parameters, the set of system equations established to describe the motion of a continuous body can be linear. In the finite element method, the deformation displacement field can be approximated by a piecewise linear function of nodal displacements. Hence, each body in a discontinuous system can be discretized using the finite element method to increase the degrees of freedom of the approximation within each body.

The velocity field of a body is the material derivation of the displacement field. Since the translation displacement u_i^t is coordinate independent, and the rotation displacement u_i^r and the deformation displacement u_i^d are the integration of infinitesimal terms, the distinction between the Lagrangian and Eulerian strain tensor disappears. It is immaterial whether a derivative of the displacement is executed using the initial particle position or the current

particle position as the independent variables. Therefore, the velocity is just a partial derivative of the displacement with respect to the time. Similarly, the acceleration is just a partial derivative of the velocity with respect to the time. Following the same method used for the displacement decomposition, the velocity and acceleration can be decomposed into functions of some independent variables.

5. THE TIME DISCRETIZATION

in a dynamic analysis, independent variables may be coordinates and time. In the finite element method, the displacement approximation is a partial discretization that the displacement is only discretized with respect to independent variables of coordinates. Let a_i, where $i = 1, 2, \ldots, n$ and n is the total number of independent parameters, represents u_i^t, ω_k^o, and the adopted deformation displacement parameters for describing the strain field. After this spatial discretization, the derivatives of a_i with respect to time will remain in the final expression of the governing equations which are a set of ordinary differential equations. Time t is the independent variable of these equations. Approximating the differential equations into a set of algebraic equations with unknown parameters a_i using the weighted residuals method or the variational principle, the general form of such equations for a linear problem can be expressed as

$$p\ddot{a}_i + q\dot{a}_i + ra_i + f_i' = 0 \tag{14}$$

where $\dot{a}_i = \frac{da_i}{dt}$ and $\ddot{a}_i = \frac{d\dot{a}_i}{dt}$.

If coefficients p, q, and r in the above differential equation are independent from time t, the solution of the system can frequently be carried out efficiently by standard analytical methods. Systems of ordinary, linear, differential equations can always be solved analytically, in principle, as an eigenvalue problem, without introducing additional approximations. However, the solution of the eigenvalue problem provides the behavior patterns of the dynamic motion of a body rather than the transient dynamic phenomena. The transient dynamic process can be simulated using the recurrence relation in the discrete time domain.

The recurrence relation of a transient dynamic problem[7] within a small time increment $[t_0, t)$ relates the initial conditions at t_0 to those at time t. The algorithm of the recurrence relation in a small time increment $[t_0, t)$ can be obtained by introducing additional approximations for velocities and accelerations. Displacements $u_i(t_0)$ at the initial instant of the time increment are updated to a null vector. Final velocities $\dot{u}_i(t)$ of the previous time-step computations are considered as initial velocities $\dot{u}_i(t_0)$ of the current time-step. Initial accelerations $\ddot{u}_i(t_0)$ correspond to the loading and boundary conditions at the initial instant of time t_0. Because it is a nonanticipatory deterministic system, initial accelerations $\ddot{u}_i(t_0)$ remain unknown. If the loading and boundary conditions remain conserved during the

entire time increment, the acceleration of each particle is constant with respect to time and can be represented as unknown $\ddot{u}_i$. Since t_0 and $u_i(t_0)$ are prescribed, time independent unknown $\ddot{u}_i$ can be expressed in terms of unknown displacement field $u_i(t)$. Using unknown parameters a_i to express displacement u_i,

$$\ddot{a}_i = \frac{2}{(\Delta t)^2} a_i(t) - \frac{2}{(\Delta t)} \dot{a}_i(t_0) \tag{15}$$

and

$$\dot{a}_i(t) = \frac{2}{(\Delta t)} a_i(t) - \dot{a}_i(t_0) \tag{16}$$

where $\Delta t = t - t_0$.

Inserting Equations 15 and 16 into Equation 14, the general form of the governing differential equation of a linear transient dynamic problem approximated using the discrete-time system can then be expressed as

$$\frac{2p}{(\Delta t)^2} a_i + \frac{2q}{(\Delta t)} a_i + r a_i + f_i' - \frac{2p}{(\Delta t)} \dot{a}_i(t_0) - q \dot{a}_i(t_0) = 0. \tag{17}$$

This equation is rewritten as

$$K a_i + f_i = 0 \tag{18}$$

where

$$K = \frac{2p}{(\Delta t)^2} + \frac{2q}{(\Delta t)} + r \tag{19}$$

and

$$f_i = f_i' - \frac{2p}{(\Delta t)} \dot{a}_i(t_0) - q \dot{a}_i(t_0) \tag{20}$$

The mathematical form of the general governing equation of the transient dynamic process in a small time increment shown by Equation 18 is identical to the one for the general governing equation for a time independent linear continuum problem.

6. MINIMUM TOTAL POTENTIAL ENERGY THEOREM

In the DDA method, the transient state (equilibrium under D'Alembert's principle) of a discontinuous system at an instant of time is found by seeking the minimum of the total potential energy of the system at the end of a time-step. The application of the minimum potential energy theory in a discontinuous system is similar to its application in the structural analysis of a truss where continuous truss components are connected with structural connectors. Since there are simplified degrees of freedom assigned to the connectors, the global displacement function assigned to the entire discontinuous domain or the truss system can not be a continuous one. In general, the analytic mathematical expression of the minimum potential energy theory in classic mechanics is only valid within the domain of a continuum. However, the physical meaning of the theory extends far beyond its mathematical representation. In the level of treatment for the entire system, the potential of a discontinuous system can be expressed as $\int_V (A)dV = \Sigma \int_{V^e} (A^e)dV$, where V^e is the volume of a continuous body, A^e is the potential energy in the body, and the summation represents all continuous bodies of the system. Then, the minimum of the total potential energy of the entire system at an instant of time can be computed. This concept of integrated potential energy can also be applied in the level of treatment for each continuum or connector in the system.

In the DDA method, the potential energy of a block is not only contributed by all external loads, boundary constraints, initial stresses, initial velocities, and strain energy, but also is contributed by the contact interactions between bodies. Using the contact spring(s) and/or the substituted shear contact forces for simulating the contact interactions, the potential energy of the contact springs and bodies can be computed using the displacements of the contact points of two bodies in contact. However, to obtain an analytic mathematical expression of the minimum total potential energy theorem, the trial contact positions must be a part of the conserved system configuration within a time-step.

In order to adopt some thermodynamic energy theories expressed in a simple mathematical form for modeling the response of a system, the requirement for a constant external condition within a time-step is necessary. Furthermore, if a lower order approximation for the displacement function is used for simplifying the system equations, the small time-step is also required to ensure that only small strains and rotations are generated in each time-step. The small time-step is defined as the time interval corresponding to a small change of the system state and the external condition. Hence, the external restraints imposed on the system must be presented with a step function that only a small change of the functional value may occur at the instant between two consecutive small time-steps.

In the continuum mechanics[10], the principle of virtual work based on Eulerian equation of motion can be expressed as

$$\int_\Gamma b_i \delta u_i \, d\Gamma + \int_\Omega g_i \delta u_i \, d\Omega - \int_\Omega \rho \ddot{u}_i \delta u_i \, d\Omega - \int_\Omega \sigma_{ij} \delta \epsilon_{ij} \, d\Omega = 0 \qquad (21)$$

where ρ is the density of the homogeneous material, g_i is the body force, b_i is the surface

traction, σ_{ij} is the differentiable stress field, Γ is the surface of the continuum, and Ω is the volume. Applying the principle of virtual work to a dynamic process which changes the initial state at the instant of time t_0 to the state at the instant of time t, all terms in Equation 21 should be evaluated at the instant of time t, particularly δu_i means $\delta u_i(t)$. Time independent acceleration $\ddot{u}_i$ may be approximated as shown in Equation 15. Replacing stress σ_{ij} with $D_{ijkl}\epsilon_{kl}$, where D_{ijkl} is the material constants for the elastic continuum body, the principle of virtual work becomes

$$\int_\Gamma b_i \delta u_i d\Gamma + \int_\Omega g_i \delta u_i d\Omega - \int_\Omega \epsilon_{ij} D_{ijkl} \delta \epsilon_{kl} d\Omega - \frac{2}{(\Delta t)^2}\int_\Omega \rho u_i \delta u_i d\Omega - \frac{2}{\Delta t}\int_\Omega \rho \dot{u}_i(t_0)\delta u_i d\Omega = 0 \qquad (22)$$

where Δt is a scalar representing a time increment of a discrete time interval. Since the conserved applied forces over the small time increment and the infinitesimal strain and rotation theories are adopted, all forces acting on the body are time independent. The expression of the principle of virtual work can then be simplified as

$$\delta\int_\Gamma b_i u_i d\Gamma + \delta\int_\Omega g_i u_i d\Omega - \delta\frac{1}{2}\int_\Omega \epsilon_{ij} D_{ijkl}\epsilon_{kl} d\Omega - \delta\frac{1}{(\Delta t)^2}\int_\Omega \rho u_i u_i d\Omega - \delta\frac{2}{\Delta t}\int_\Omega \rho \dot{u}_i(t_0)u_i d\Omega = 0 \qquad (23)$$

where u_i and ϵ_{ij}, at the instant of time t, are the unknown displacement and deformation occurring within the time increment $[t_0, t)$, and $\dot{u}_i(t_0)$ is the known initial velocity at the instant of time t_0. This may be written as

$$\delta \Pi = 0 \qquad (24)$$

The function Π is called the total potential energy of the system so that

$$\Pi = \int_\Gamma b_i u_i d\Gamma + \int_\Omega g_i u_i d\Omega - \frac{1}{2}\int_\Omega \epsilon_{ij} D_{ijkl}\epsilon_{kl} d\Omega - \frac{1}{(\Delta t)^2}\int_\Omega \rho u_i u_i d\Omega - \frac{2}{\Delta t}\int_\Omega \rho \dot{u}_i(t_0)u_i d\Omega \qquad (25)$$

Equation 24 is the mathematical statement of the principle of minimum total potential energy. It states that all displacements $u_i(t)$ satisfying the given boundary conditions that satisfy the equation of motion are distinguished by a stationary (extreme) value of the total potential energy at the instant of time t. The above function Π is driven by a given set of traction, body forces, strain energies, and kinetic energies. It may also include other types of potential energy which can be defined (measured) independently at a given state of the system, such as heat input or mechanically dissipated energy[11]. The strains at any point in the continuum can be determined in terms of the displacement field as shown in Equation 5. Since all displacement terms in Equation 25 can be decomposed into translation, rotation, and deformation displacements, the potential energy can be decomposed into potential energy of translation, rotation, and deformation.

Let the displacement field is approximated by a linear function of independent parameters a_i, where $i = 1, 2, \ldots, n$ and n is the total number of parameters. The variational principle can be expressed as the variation of the potential energy Π in the differential form:

$$\delta \Pi = \frac{\partial \Pi}{\partial a_i} \delta a_i = 0 \tag{26}$$

This being true for any variation, δa_i yields a set of equations

$$\frac{\partial \Pi}{\partial a_i} = 0 \tag{27}$$

These equations are of an integral form necessary for the discretization approximation where the original specification of Π was given in terms of a volume and surface integral.

If the functional Π is quadratic, i.e., if the displacement function u_i and its derivatives occur in powers not exceeding 2, then Equation 27 reduces to a standard linear form:

$$\frac{\partial \Pi}{\partial a_i} = K_{ij} a_j + f_i = 0 \tag{28}$$

where K_{ij} and f_i are scalar coefficients. Differentiating these equations again yields

$$K_{ij} = \frac{\partial \Pi}{\partial a_i \partial a_j} \tag{29}$$

This equation shows that $K_{ij} = K_{ji}$, i.e., K_{ij} is symmetric. f_i represents the free terms of differentiation in Equation 28 so that

$$f_i = \frac{\partial \Pi(0)}{\partial a_i} \tag{30}$$

7. SUMMARY

Due to the energy dissipation associated with a frictional sliding process, the contact problem is nonlinear. The DDA method adopts the displacement method to solve the contact problem without reformulation of the discretization process, i.e., without rewriting the basic variational statements. The unified computational procedure, i.e., the direction summation of the function values integrated within each discretized sub-domain into a matrix form, developed in the finite element is adopted. A solution to the "linear" problem is reached by a trial and error process in which the contact positions at the final instant of a time-step are so adjusted that the Coulomb's frictional law and the equilibrium are satisfied

everywhere in the system.

Solving the contact problem using the trial-and-error iteration scheme, the correct result of the mechanical response of a discontinuous system at the final instant of a time-step is formulated and solved in the last iteration. All other iterations are just a part of the trial process. The change of contact positions obtained in the previous time-step to the trial positions selected for the last iteration of the current time-step is a perturbation of the system configuration since the contact positions can not be included as unknowns in the system equations. After the trial set of contact positions have been selected, computations in each iteration are fairly independent from others. The only substitution process required from one iteration to another is the shear contact force couple applied on each sliding contact. The shear force of a sliding contact substituted in the current iteration, which is treated as an external applied force, is updated using the normal contact force computed in the previous iteration.

As demonstrated in this paper, the DDA method implements the following aspects to post the nonlinear contact problem mathematically using linear equations:

1. The recurrence relation in a discrete time system,
2. Decomposed displacements including translation, rotation, and deformation,
3. The small time discretization with constant acceleration,
4. The elastic behavior of continuous bodies,
5. Newton's law for the rigid body motion,
6. The minimum total potential energy with the conserved external constraints,
7. Conserved contact positions selected iteratively by trial-and-error scheme, and
8. Contact interactions modeled by stiff spring(s) and/or substituted shear forces.

REFERENCES

1. Shi, G., Block System Modeling by Discontinuous Deformation Analysis, Computational Mechanics Publication, Southhampton, United Kingdom (1993).

2. Cundall, P. A., A Computer Model for Simulating Progressive Large Scale Movements, in Blocky Rock Systems, in Proceedings of the Symposium of the International Society of Rock Mechanics Vol. 1, Paper No. II-8, Nancy, France (1971).

3. Cundall, P. A., Adaptive Density-Scaling for Time-Explicit Calculations, in Proceedings of the 4th International Conference on Numerical Methods in Geomechanics, Edmonton, Alberta, pp. 23-26, (1982).

4. Livesley, R. K., Matrix Methods in Structural Analysis, 2nd Edition, Pergamon Press (1975).

5. Zienkiewicz, O. C., and Taylor, R. L., The Finite Element Method, Fourth Edition, McGraw-Hill Book Company, London, United Kingdom (1989).

6. Tsai, F., Dynamic Interaction of Discrete Continua - The Theory of Non-Overlapping Continua, Ph.D. Dissertation, Department of Engineering-Material Science and Mineral Engineering, University of California at Berkeley, Berkeley, California (1993).

7. Freeman, H., Discrete-Time Systems, An Introduction to the Theory, Robert E. Krieger Publishing Company, Huntington, New York (1980).

8. Shi, G., Modeling Dynamic Rock Failure by Discontinuous Deformation Analysis with Simplex Integrations, Proceedings of the 1st North American Rock Mechanics Symposium, The University of Texas at Austin, Austin TX (1994).

9. Chern, J. C., C. Y. Koo, and S. Chen, Development of Second Order Displacement Function for DDA and Manifold Method, The Forum of Manifold Method of Material Analysis, Waterways Experiment Station, Corps of Engineering, Vicksburg, Mississippi (1995).

10. Fung, Y. C., Foundations of Solid Mechanics, Prentice-Hall, Inc. Englewood Cliffs, New Jersey (1965).

11. Tsai, F., Drift Scale Thermomechanical Analysis for the Retrievability Systems Study, The Workshop on Rock Mechanics Issues in Repository Design and Performance Assessment, Center for Nuclear Waste Regulatory Analyses, San Antonio, TX (1994).

Modification of DDA with respect to Rigid-body Rotation

Te-Chih Ke[1]

[1]Chung Yuan University, Chungli, Taiwan, R. O. C.

ABSTRACT: In the original form of DDA, the separation of rigid-body rotation term from the other deformation variables is a breakthrough idea. However, without precaution to update physical terms after each step computation, severe distortions associated with non-zero rigid-body rotation may be encountered. They include insufficient rotation updating, free expansion, disturbed stress and velocity fields. More importantly, these distortions are accumulative, regardless of rotation direction. This paper presents the concise procedures to correct up these rotation-related distortions. The same laws described can be easily applied to the traditional DDA formulation with a higher-order displacement function. Several numerical examples are included to examine the sensitivity of physical terms to rigid-body rotation.
KEYWORDS: discontinuous deformation analysis, rigid-body rotation, free expansion

1. INTRODUCTION

Since Shi [1] pioneered to introduce the forward model of two-dimensional discontinuous deformation analysis (abbreviated as DDA) in 1988, DDA has received increasing attention from international researchers in both academic and industrial societies. Through years' verifications, DDA has shown its excellent ability to deal with complex interactions between discrete deformable blocks. Great efforts have also been made to continuously improve the capabilities of DDA in dealing with various problems in rock mechanics, material science and structural engineering. Based on the increasing cooperation of researchers in the related fields, it is expected that the potential of DDA would be fully explored upon the advent of the 21th century, making it be extensively used in the real world of engineering design. Table 1 provides a partial list of the current and future developments of DDA, according to the personal opinion of the author (some of which are extracted from the reference [2]). This paper addresses the study of DDA on the subject of rigid-body rotation and the corresponding treatments.

Table 1 Partial list of current and future developments of DDA

Group	Sub-group	Contributors
DDA Blocks	Refined stress field	Shyu [3], Ke [4], Chang [5], Koo etc. [6], Ma [7], Shi [8]
	Non-linearity	Chang [5], Ohnishi etc. [9]
	Fragmentation	Lee [10], Lin etc. [11]
	Fracture propagation	Ke [4], Lin etc. [11]
	3D DDA blocks	Shi [12]
	Circular blocks	Lin [13], Ke [14]
	Coupled flows	-
Block contacts/ Joints	Strength properties	Shi [15], Ke [4]
	Joint dilation	Thapa [16]
	Non-linear laws	-
	Lagrange multiplier	Hilbert etc. [17], Lin etc. [11]
Various constraints	Displacement const.	Ke [4], Ohnishi etc. [9]
	Force constraints	Ke [4]
Insight studies	Time integration	Ke [4]
	Rigid-body rotation	Yeung [18], Ke [4]
	Simplex integration	Shi [19]
Applications	Rock slopes	Yeung [18], Ke [20], Chen & Lin [21]
	Underground works	Ke [4], Chang [5], Yeung etc. [22]
	Rock foundations	Yeung [18]
	Particulate media	Lin [13], Ke [13]
	Composite materials	Shyu [3], Ke [23]
	Fracturing	Ke [4], Lin etc. [11]
	Impact	-
	Joint flows	-
	Reliability-coupling	-

In the original formulation of DDA, a complete first-order displacement function is used. That is, the displacement increments (u,v) of a point (x,y) within Block i can be expressed by

$$\begin{pmatrix} u \\ v \end{pmatrix}^i_{(x,y)} = [T^i]_{(x,y)} \quad [D^i] = \begin{pmatrix} \Sigma_{j=1}^{M} t_{1j}\, d_j \\ \Sigma_{j=1}^{M} t_{2j}\, d_j \end{pmatrix}^i \tag{1}$$

in which the number of block unknowns M is six in this case, $[T^i]$ is the first-order displacement function given by

$$[T^i]_{(x,y)} = \begin{pmatrix} t_{11} & t_{12} & t_{13} & t_{14} & t_{15} & t_{16} \\ t_{21} & t_{22} & t_{23} & t_{24} & t_{25} & t_{26} \end{pmatrix}^i = \begin{pmatrix} 1 & 0 & -(y-y_0) & (x-x_0) & 0 & (y-y_0)/2 \\ 0 & 1 & (x-x_0) & 0 & (y-y_0) & (x-x_0)/2 \end{pmatrix}^i \quad (2)$$

where (x_0,y_0) are the centroid coordinates of Block i, and $[D^i]$ is the corresponding displacement vector of Block i, including two rigid-body translations, one rigid-body rotation, and three 2D strain components defined by

$$[D^i] = \begin{pmatrix} d_1 \\ d_2 \\ d_3 \\ d_4 \\ d_5 \\ d_6 \end{pmatrix}^i = \begin{pmatrix} u_0 \\ v_0 \\ \gamma_0 \\ \epsilon_x \\ \epsilon_y \\ \gamma_{xy} \end{pmatrix}^i \quad (3)$$

Among several advantages of adopting Eqn(1-3)s, the separation of the rigid-body rotation term γ_0 from the other deformation variables is a breakthrough, since this term can not be easily and simply computed using the traditional finite element or boundary element methods. Following the basic format of Eqn(3), the displacement vector $[D^i]_{2nd}$ corresponding to the complete second-order displacement function with M=12 is given by

$$[D^i]^T_{2nd} = (u_0 \; v_0 \; \gamma_0^c \; \epsilon_x^c \; \epsilon_y^c \; \gamma_{xy} \; \epsilon_{x,x} \; \epsilon_{y,x} \; \gamma_{xy,x} \; \epsilon_{x,y} \; \epsilon_{y,y} \; \gamma_{xy,y}) \quad (4)$$

where the six first-derivatives of strain components are added, and which still contains the rigid-body rotation term γ_0^c (but now associated with the block centroid). For a much higher-order DDA, $[D^i]$ will contain other higher-order derivatives of strain components. The following lists the relationship between the order of DDA displacement function and the number of block unknowns M.

Order	0	1	2	3	...	n
M	3	6	12	20	...	(n+1)(n+2)

After each step computation, DDA updates block vertex coordinates, initial stresses and block velocity vectors according to the solution of $[D^i]$s. However, without precaution to update these tensor terms, the above advantage may be totally impaired by the severe distortions associated with the rigid-body rotation γ_0 (especially when it is large). This problem includes two types of distortions. Type I relates to the linearization error of rigid-body rotation in the DDA formulation, leading to insufficient rotation updating and free expansion. Type II corresponds to the rotation of local reference frames, resulting in distortion of stress and velocity fields, which are subsequently regarded as external forces for the next step calculation. The following

two sections will describe these detailed phenomena and provide the strategies to correct them up. A toppling block system will then be presented to examine the effect of rigid-body rotation before and after the proposed correction.

2. INSUFFICIENT ROTATION AND FREE EXPANSION

The free expansion phenomenon of a DDA block can be easily observed if it has a rotation-dominant motion mode. This problem was first addressed by Yeung [18]. Even when a small maximum displacement ratio, say 0.001, is used, the increase in the area of a rotating DDA block is considerable and it remains as long as the block rotates. This weird phenomenon can be clarified by investigating the linearization procedure used in the original DDA formulation for a rigid-body rotation. The initial discussions on this subject can be found in Appendix A of the reference [4].

Figure 1 depicts a rigid square block[1] subjected to a known rigid-body rotation increment γ_0, with respect to the block centroid, $\mathbf{O}(x_0,y_0)$. A local Polar coordinate system is set with its origin centered at Point **O**. Given a γ_0, Point $\mathbf{P}(x,y)$ moves to $\mathbf{P}^E(x^E,y^E)$. The exact displacement increments of $\mathbf{P}(x,y)$ due to γ_0 are given by

$$\begin{aligned}\begin{pmatrix} u \\ v \end{pmatrix}_{P(x,y)} &= L \begin{pmatrix} \cos(\theta+\gamma_0) - \cos(\theta) \\ \sin(\theta+\gamma_0) - \sin(\theta) \end{pmatrix} \\ &= L \begin{pmatrix} \cos(\theta)\cos(\gamma_0) - \sin(\theta)\sin(\gamma_0) - \cos(\theta) \\ \sin(\theta)\cos(\gamma_0) + \cos(\theta)\sin(\gamma_0) - \sin(\theta) \end{pmatrix}\end{aligned} \tag{5}$$

where L = the square root of $(x-x_0)^2+(y-y_0)^2$ and $\theta = \tan^{-1}((y-y_0)/(x-x_0))$; or

$$\begin{pmatrix} u \\ v \end{pmatrix}_{P(x,y)} = \begin{pmatrix} (x-x_0)(\cos\gamma_0-1) - (y-y_0)\sin\gamma_0 \\ (x-x_0)\sin\gamma_0 + (y-y_0)(\cos\gamma_0-1) \end{pmatrix} \tag{6}$$

Obviously, Eqn(5-6)s are non-linear with respect to γ_0 (because of involving trigonometric functions of γ_0). In order to manipulate a system of linear equilibrium equations in DDA, *linearization* must be employed. By assuming a very small γ_0, Eqn(5) is approximated as

$$\begin{aligned}\begin{pmatrix} u \\ v \end{pmatrix}_{P(x,y)} &\simeq \begin{pmatrix} -L\cdot\sin(\theta) \\ L\cdot\cos(\theta) \end{pmatrix} \cdot \gamma_0 \\ &\simeq \begin{pmatrix} -(y-y_0) \\ (x-x_0) \end{pmatrix} \cdot \gamma_0\end{aligned} \tag{7}$$

Eqn(7) is exactly the form given in the first-order displacement function of DDA (see Eqn(1-3)s). According to Eqn(7), $\mathbf{P}(x,y)$ moves to $\mathbf{P}^L(x^L,y^L)$, instead of $\mathbf{P}^E(x^E,y^E)$ as shown in Figure 1.

---

[1] It is also good for blocks of other shape.

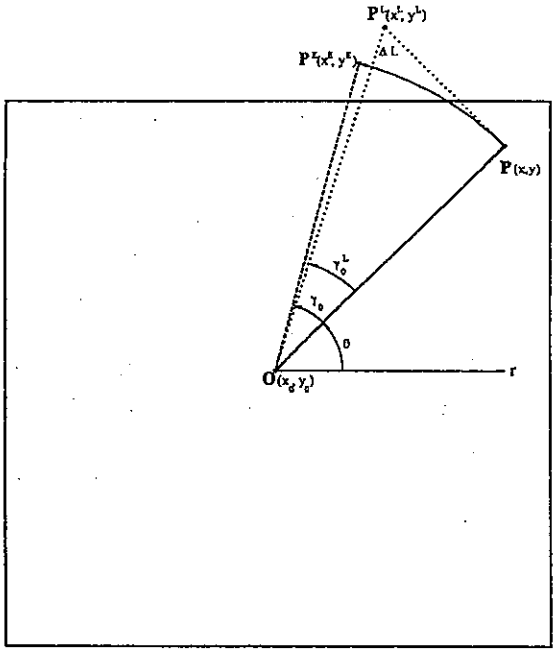

Figure 1 Linearized Error Induced by Rigid-body Rotation

2.2 Insufficient Rotation Updating

Denote $\angle \mathbf{P^L OP}$ in Figure 1 as γ_0^L, which is the actual rotation defined by Eqn(7). From Eqn(7), the length of line $\mathbf{P^L P}$ equals to $\gamma_0 L$ and $\angle \mathbf{OPP^L}$ is a right angle. As a result, γ_0^L is equal to $\tan^{-1}(\gamma_0)$. As a trigonometric rule, it can be easily shown that γ_0^L is always smaller than γ_0. In other words, an insufficient rotation error is introduced according to Eqn(7). However, this error becomes negligible if $\gamma_0 < 0.1$ radian.

2.2 Free Expansion

A free expansion ΔL along the direction of $\mathbf{OP^L}$, is observed in Figure 1. The amount of free expansion is given by

$$\Delta L = \sqrt{\gamma_0^2 L^2 + L^2} - L = (\sqrt{\gamma_0^2 + 1} - 1) \cdot L \qquad (8)$$

and the corresponding area expansion ΔA equals to

$$\Delta A = A\ (\gamma_0^2 + 1 - 1) = A\ \gamma_0^2 \qquad (9)$$

where A is the block area of the previous step. The normalized free expansions in terms of length and area can be expressed by

$$\frac{\Delta L}{L} = \sqrt{\gamma_0^2 + 1} - 1$$
$$\frac{\Delta A}{A} = \gamma_0^2 \qquad (10)$$

both of which are always positive, regardless of the sign of γ_0. If the block experiences N steps of identical rigid body rotation γ_0, then the accumulated normalized free expansions in terms of length and area are

$$\frac{\Sigma_1^N(\Delta L)}{L_0} = (\gamma_0^2 + 1)^{\frac{N}{2}} - 1$$
$$\frac{\Sigma_1^N(\Delta A)}{A_0} = (\gamma_0^2 + 1)^N - 1 \qquad (11)$$

where L_0 is the initial length of line **OP**, and A_0 the initial block area.

2.3 Remedy

Here, the concept of post-adjustment is used. For each step, the system of linear equilibrium equations is formulated based on the linearized form of Eqn(1-3)s and the $[D^i]$s are solved. But the γ_0-induced displacement increments of the relevant points (x,y), including block vertices, are calculated using Eqn(6). Accordingly, Eqn(1) becomes the sum of γ_0-induced and γ_0-unrelated contributions, expressed by

$$\begin{pmatrix} u \\ v \end{pmatrix}_{(x,y)} = \begin{pmatrix} (x-x_0)(\cos\gamma_0 - 1) - (y-y_0)\sin\gamma_0 \\ (x-x_0)\sin\gamma_0 + (y-y_0)(\cos\gamma_0 - 1) \end{pmatrix} + \begin{pmatrix} \Sigma_{j=1}^M t_{1j} d_j \\ \Sigma_{j=1}^M t_{2j} d_j \end{pmatrix}_{j \neq 3} \qquad (12)$$

Using Eqn(12) can overcome both the distortions mentioned in this section. However, since the penetrations of normal contact springs and the shear movements along the reference lines are still computed based on Eqn(1-3)s, a maximum rotation limit per step G_r, say 0.1 radian, should be set up to reduce the errors in computing contact forces. That is, once the maximum step block rotation computed exceeds this limit, Δt will be reduced and the step computation is re-started.

2.4 Example I

Figure 2a shows the initial position of a square block at t=0, which is assigned a constant angular velocity of 1 radian/sec with respect to its centroid O. No other external load is present. Δt used in the DDA run is 0.1sec, and the DDA is run until t=0.5sec. Table 1 compares the results of the normalized free expansions in area, in which the values of the second column are computed by Eqn(11), the third column by the DDA without correction and the 4th column by the DDA with Eqn(12)'s correction. It is found that Eqn(11) and the DDA without correction yield the same free expansion values, and the DDA with Eqn(12)'s correction gives zero free expansion. Besides, an insufficient rotation phenomenon is observed for the DDA without correction because its computed value of $\Sigma\gamma_0$ is always less than that of the DDA with correction. Figures 2b,c display the final block geometries of the DDA

without and with correction at t=0.5sec (solid lines).

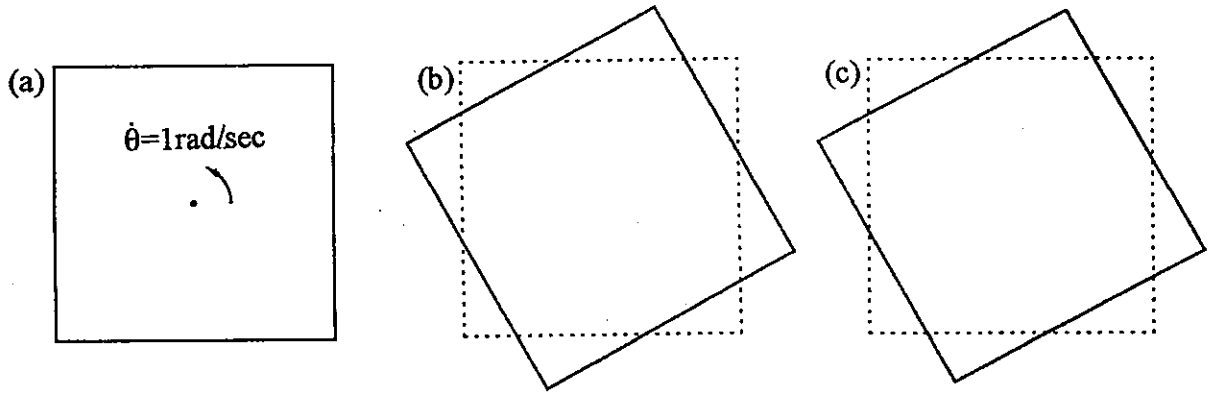

Figure 2 Example I: a) initial geometry; b) final geometry at t=0.5s (DDA without correction); c) final geometry at t=0.5s (DDA with correction)

Table 1 Comparison of Results for Example I

Time (sec)	$\Delta A/A_0$[1] (%)	$\Delta A/A_0$[2] (%)	$\Delta A/A_0$[3] (%)	$\Sigma\gamma_0$[2] (radian)	$\Sigma\gamma_0$[3] (radian)
0.1	1.0	1.0	0.0	0.0997	0.1
0.2	2.01	2.01	0.0	0.1993	0.2
0.3	3.0301	3.0301	0.0	0.2990	0.3
0.4	4.0604	4.0604	0.0	0.3987	0.4
0.5	5.1010	5.1010	0.0	0.4983	0.5

[1] defined by Eqn(11); [2] computed by DDA without correction; [3] by DDA with Eqn(12)'s correction.

2.5 Example II

Figure 3a shows the initial position of a square block at t=0, which is fixed at its lower-right corner. Gravity as the only external load turns on at t=0 and the block is assumed to be rigid. Δt used in the DDA run is 0.1sec, and the DDA is run until t=0.5sec. Table 2 compares the results of normalized free expansion in area, in which the values of the second column are computed by the DDA without correction, and the third column by the DDA with Eqn(12)'s correction. It is seen that the DDA with Eqn(12)'s correction gives negligible free expansion but the DDA without correction does not. Also, an insufficient rotation phenomenon is observed for the DDA without correction, when comparing the values of $\Sigma\gamma_0$ computed by the DDA with and without correction. Figures 3b,c depict the final block geometries of the DDA without and with correction at t=0.5sec (solid lines).

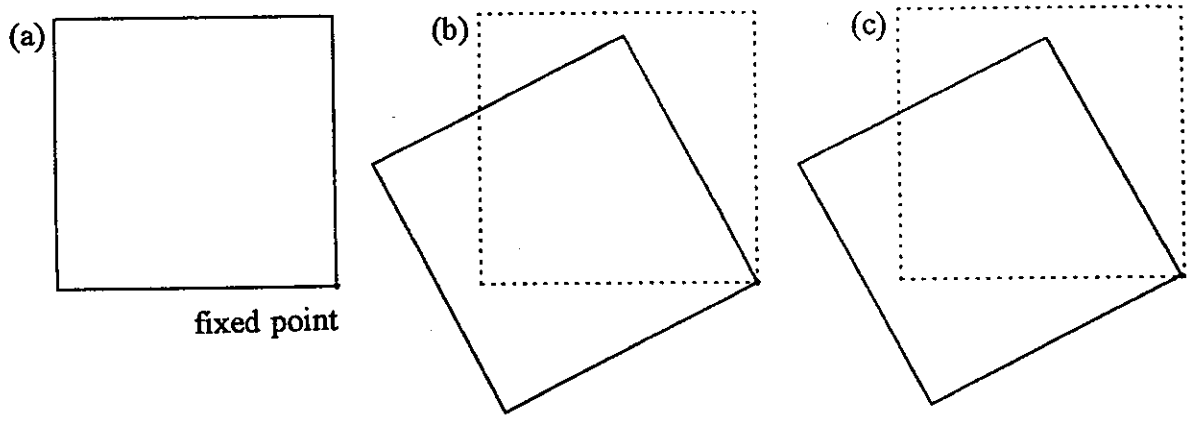

Figure 3 Example II: a) initial geometry; b) final geometry at t=0.5s (DDA without correction); c) final geometry at t=0.5s (DDA with correction)

Table 2 Comparison of Results for Example II

Time (sec)	$\Delta A/A_0^1$ (%)	$\Delta A/A_0^2$ (%)	$\Sigma\gamma_0^1$ (radian)	$\Sigma\gamma_0^2$ (radian)
0.1	0.0338	~0.0	0.0184	0.0184
0.2	0.3420	~0.0	0.0738	0.0739
0.3	1.2236	~0.0	0.1673	0.1678
0.4	3.0820	~0.0	0.3004	0.3024
0.5	6.2322	~0.0	0.4747	0.4812

[1] computed by DDA without correction; [2] by DDA with Eqn(12)'s correction.

3. DISTORTION OF STRESS AND VELOCITY FIELDS

At the end of each step computation, initial stresses, block velocity vectors as well as the block vertex coordinates are updated according to the solved $[D^i]$s. However, once the block vertex coordinates are updated, all updated components of initial stresses and block velocity vectors must be referred to the new local axes of each block. No adjustment of these tensor terms with respect to the rotation of the local reference frames will cause the accumulated distortion of stress and velocity fields.

Figure 4a shows that the local x,y axes and the global X,Y axes for Block i are parallel in the beginning of Step j. If the $[D^i]$ solved for Step j contains a non-zero γ_0, then Block i will rotates around its centroid by this amount at the end of Step j (after updating the coordinates of block vertices), i.e., at the start of Step j+1, the local x,y axes inclines with the global X,Y axes by γ_0, as shown in Figure 4b.

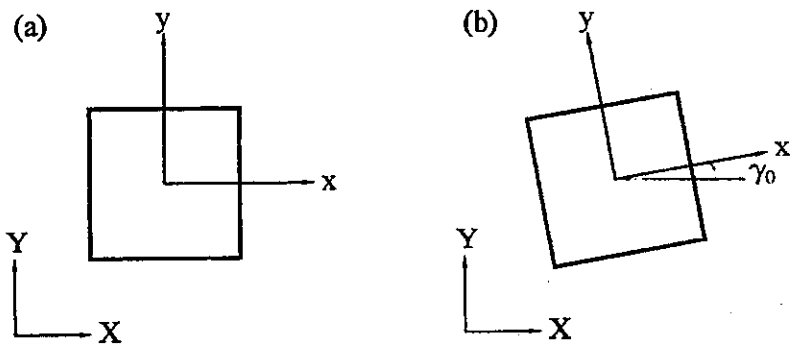

Figure 4 Rotation of Reference Frames between Step Computations: a) at the start of Step j; b) at the start of Step j+1

3.1 Initial Stress Distortion

In the DDA formulation, initial stresses $[\sigma_0]$ are converted into *force* terms. At the end of Step j, the initial stresses of Block i $[\sigma_0]^{j+1}$ for the next step can be computed by

$$[\sigma_0]^{j+1} = [\sigma_0]^j + \Delta[\sigma] \tag{13}$$

where $\Delta[\sigma]$, the stress increments is equal to the product of the elastic matrix and the strain increments $\Delta[\epsilon]$ in $[D^i]$ of Eqn(3). After updating the coordinates of block vertices, the initial stresses defined by Eqn(13) are associated with the local axes, i.e. $[\sigma_0]^{j+1}{}_{xy}=[\sigma_0]^{j+1}$. However, all of the DDA computations are performed on the basis of the global axes, so that using $[\sigma_0]^{j+1}{}_{xy}$ in place of $[\sigma_0]^{j+1}{}_{XY}$ to compute the force terms will cause the stress distortion for Step j+1.

3.2 Velocity Vector Distortion

Velocity vector $[H_0]$ at the start of each step will be converted into one part of *inertia force*. At the end of Step j, $[H_0]^{j+1}$ for the next step can be computed by

$$[H_0]^{j+1} = \frac{2[D^j]}{\Delta t} - [H_0]^j \tag{14}$$

Similarly, after updating the coordinates of block vertices at the end of Step j, the components of velocity defined by Eqn(14) are also associated with the local axes, i.e. $[H_0]^{j+1}{}_{xy}=[H_0]^{j+1}$. Using $[H_0]^{j+1}{}_{xy}$ in place of $[H_0]^{j+1}{}_{XY}$ to compute the inertia force will also result in the distortion of velocity field for Step j+1.

3.3 Remedy

To overcome the stress distortion corresponding to rotation, the components of $[\sigma_0]^{j+1}$ with respect to the global axes have to be computed, which can be given by

$$[\sigma_0]_{XY}^{j+1} = [T]^T [\sigma_0]_{xy}^{j+1} [T] \tag{15}$$

where [T] is the transformation matrix

$$[T] = \begin{pmatrix} \cos\gamma_0 & \sin\gamma_0 \\ -\sin\gamma_0 & \cos\gamma_0 \end{pmatrix} \tag{16}$$

By denoting $s=\sin\gamma_0$ and $c=\cos\gamma_0$, Eqn(15) becomes explicitly

$$[\sigma_0]_{XY}^{j+1} = \begin{pmatrix} c^2\sigma_{xx}-2cs\sigma_{xy}+s^2\sigma_{yy} & cs(\sigma_{xx}-\sigma_{yy})+(c^2-s^2)\sigma_{xy} \\ cs(\sigma_{xx}-\sigma_{yy})+(c^2-s^2)\sigma_{xy} & s^2\sigma_{xx}+2cs\sigma_{xy}+c^2\sigma_{yy} \end{pmatrix}^{j+1} \tag{17}$$

If γ_0 is small, Eqn(14) can be approximated as

$$[\sigma_0]_{XY}^{j+1} \simeq \begin{pmatrix} \sigma_{xx}-2\gamma_0\sigma_{xy} & \sigma_{xy} \\ \sigma_{xy} & 2\gamma_0\sigma_{xy}+\sigma_{yy} \end{pmatrix}^{j+1} \tag{18}$$

Since $[H_0]^{j+1}$ in DDA contains the velocity components as well as 2D strain rate components, the corrections must be conducted separately as follows. For the three velocity components,

$$\begin{pmatrix} \dot{u}_0 \\ \dot{v}_0 \\ \dot{\gamma}_0 \end{pmatrix}_{XY}^{j+1} = \begin{pmatrix} c & -s & 0 \\ s & c & 0 \\ 0 & 0 & 1 \end{pmatrix} \begin{pmatrix} \dot{u}_0 \\ \dot{v}_0 \\ \dot{\gamma}_0 \end{pmatrix}_{xy}^{j+1} \tag{19}$$

For the three strain rate components,

$$\begin{pmatrix} \dot{\epsilon}_x \\ \dot{\epsilon}_y \\ \dot{\gamma}_{xy} \end{pmatrix}_{XY}^{j+1} = \begin{pmatrix} c^2\dot{\epsilon}_x-2cs\dot{\gamma}_{xy}+s^2\dot{\epsilon}_y \\ cs(\dot{\epsilon}_x-\dot{\epsilon}_y)+(c^2-s^2)\dot{\gamma}_{xy} \\ s^2\dot{\epsilon}_x+2cs\dot{\gamma}_{xy}+c^2\dot{\epsilon}_y \end{pmatrix}^{j+1} \tag{20}$$

If γ_0 is small, Eqn(20) can be approximated as

$$\begin{pmatrix} \dot{\epsilon}_x \\ \dot{\epsilon}_y \\ \dot{\gamma}_{xy} \end{pmatrix}_{XY}^{j+1} \simeq \begin{pmatrix} \dot{\epsilon}_x-2\gamma_0\dot{\gamma}_{xy} \\ \dot{\gamma}_{xy} \\ 2\gamma_0\dot{\gamma}_{xy}+\dot{\epsilon}_y \end{pmatrix}^{j+1} \tag{21}$$

For the displacement vector $[D^i]$ corresponding to a higher-order displacement function, the velocity vector will contain the higher-order derivatives of strain rates. Computing the components with respect to the global axes needs the tensor operation.

3.4 Example III

Figure 5 shows the initial position of a square block at t=0, which has initial stresses $(\sigma_X,\sigma_Y,\tau_{XY})_0=(-1,0,0)$MPa and the two side walls are always subjected to a normal compression of 1MPa (a follower loading). The block is rotating at a constant angular

velocity of 1 radian/sec, and it has a Young's modulus of 100MPa and a Poisson's ratio of 0.2. Δt used in the DDA run is 0.1sec, and the DDA is run until the block rotates by 90°. Table 3 compares the initial stresses $(\sigma_X, \sigma_Y, \tau_{xy})$ with respect to the global axes versus time, in which the values of the second column are the theoretical solutions[2] using the Mohr's circle, the third column computed by the DDA without correction, and the 4th column by the DDA with Eqn(12,17,19,20)s' correction. It is found that DDA with the correction yields the same $(\sigma_X, \sigma_Y, \tau_{XY})$ as the theoretical solution, whiles DDA without correction yields a seriously disturbed stress state.

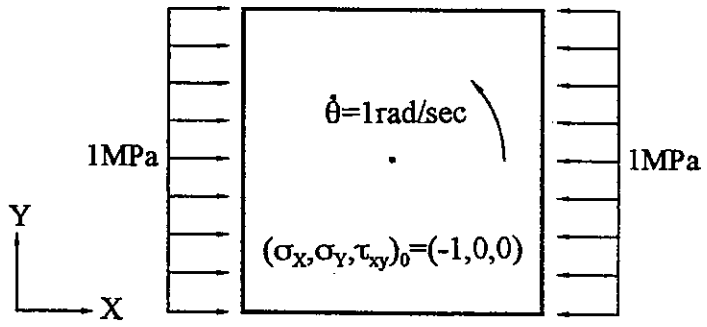

Figure 5 Example III: initial geometry and loading

Table 3 Comparison of Results for Example III

Time (s)	$\Sigma\gamma_0$[3]	$(\sigma_x,\sigma_y,\tau_{xy})$[1] (MPa)	$(\sigma_x,\sigma_y,\tau_{xy})$[2] (MPa)	$(\sigma_x,\sigma_y,\tau_{xy})$[3] (MPa)
0.0	0.0	(-1,0,0)	(-1,0,0)	(-1,0,0)
0.5	0.5	(-.770,-.230,-.421)	(-.855,-.123,-.387)	(-.770,-.230,-.421)
1.0	1.0	(-.292,-.708,-.455)	(-.370,-.585,-.468)	(-.292,-.708,-.455)
1.5708	1.5708	(0,-1,0)	(0.009,-.935,-.096)	(~0.0,-1.0,~0.0)

[1] theoretical solution; [2] computed by DDA with no correction; [3] by DDA with Eqn(12,17,19,20)'s correction.

4. ILLUSTRATIVE EXAMPLE

This section provides an example of multiple blocks involving rotation mode, in order to evaluate the error magnitude associated with the original DDA formation and computer program. Figure 6 depicts a system of 14 discrete blocks sitting on a slope. Gravity is the only external force, and the block has a Young's modulus of 1000MPa and a Poisson's ratio of 0.2. The friction angle along all block sides is selected as 26°

[2] $(\sigma_x,\sigma_y,\tau_{xy})=(-½-½\cos 2\Sigma\gamma_0, -½+½\cos 2\Sigma\gamma_0, -½\sin 2\Sigma\gamma_0)$MPa

such that the blocks near the middle (specially Block 9) are under toppling. The following lists the horizontal displacement of the toe and the stresses of Block 9 at t=1sec, computed by the DDA without and with correction. The difference is not significant but still recognizable.

	DDA without correction	DDA with correction
Toe horizontal displacement	0.1639m	0.1657m
$(\sigma_x,\sigma_y,\tau_{xy})$[1] of Block 9	(-19.74,-.369.82,-40.76)	(-16.13,-383.67,-45.49)

[1] in units of MPa

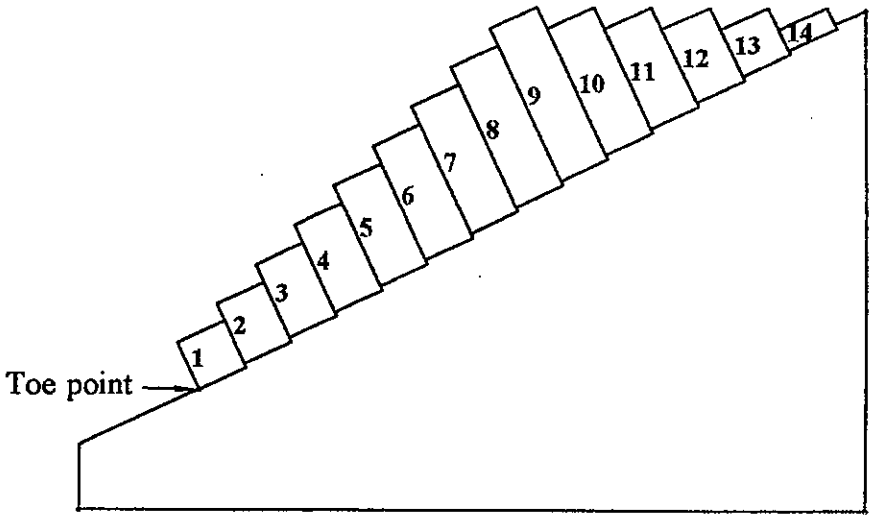

Figure 6 Illustrative example: initial geometry

5. CONCLUSIONS

This paper discussed the distortions associated with rigid-body rotation in DDA when updating physical terms without precaution. Table 4 summarizes the strategies to correct up these distortions. The same laws can also be applied to the traditional DDA formulation with a higher-order displacement function. For the corrections of the higher-order derivatives of strain rate components, tensor operation may be used.

6. ACKNOWLEDGEMENTS

The author wishes to thank Dr. Gen-Hua Shi of U.S. Army Corps for bringing him to the fascinating paradise of mathematics and computation, especially his wonder, DDA, as well as for continued encouragement for many years.

Table 4 Summary of Correction Strategies to Rotation-induced Distortions

Distortion Type	Remedy
Linearization Error	
Insufficient rotation	Using Eqn(12) to compute (u,v)
Free expansion	Setting up G_r=0.1 radian
Rotation of Reference Frames	
Stress distortion	Using Eqn(17) to adjust $[\sigma_0]$
Velocity distortion	Using Eqn(19) for adjustment
Strain rate distortion	Using Eqn(20) for adjustment[1]

[1] for higher-order displacement functions, tensor operation is needed.

7. REFERENCES

1. Shi, G.-H, *Discontinuous Deformation Analysis - A New Numerical Model for the Statics and Dynamics of Block Systems*, Ph.D Dissertation, Department of Civil Engineering, University of California at Berkeley (1988).
2. Goodman, R. E. and Ke, T.-C, Keynote Lecture - Advances in computation of jointed rock, *Proc. 8th Intl. Conf. Computer Methods and Advances in Geomech.*, Morgantown, W. Virginia, vol:4, 14p (1994).
3. Shyu, K.-K., *Nodal-based Discontinuous Deformation Analysis*, Ph.D Dissertation, Department of Civil Engineering, University of California at Berkeley (1993).
4. Ke, T.-C, *Simulated Testing of Two-Dimensional Heterogeneous and Discontinuous Rock Masses Using Discontinuous Deformation Analysis*, Ph.D Dissertation, Department of Civil Engineering, University of California at Berkeley (1993).
5. Chang, T.-C., *Nonlinear Dynamic Discontinuous Deformation Analysis with Finite Element Meshed Block Systems*, Ph.D Dissertation, Department of Civil Engineering, University of California at Berkeley (1994).
6. Koo, C.-Y., Chern, J.-C. and Chen, S., The development of the second-order displacement function for discontinuous deformation analysis, *Proc. 6th conf. Geotechnical Engrg. in Taiwan*, 665-674 (1995)
7. Ma, M., Single field manifold method using Fourier function in wave propagation, *Proc. Working Forum on the Manifold Method of Material Analysis*, Jenner, CA, 39-60 (1995).
8. Shi, G.-H., Modelling rock joints and blocks by manifold method, *Proc. 32rd U.S. Rock Mechanics Symp.*, Santa Fe, New Mexico, 639-648 (1992).
9. Ohnishi, Y., Tanaka, M. and Sasaki, T., Modification of the DDA for elasto-plastic analysis with illustrative generic problems, *Proc. 35th U.S. Symp. on Rock Mechanics*, Lake Tahoe, CA, 45-50 (1995).
10. Lee, J., Unpublished DDA program to simulate the cracking of intact blocks according to a prescribed maximum tensile strain rate, University of California at

Berkeley (1990).
11. Lin, C.-T., Amadei, B. and Sture, S. and Jung, J., Using an augmented Lagrangian method and block fracturing in the DDA method, Proc. *8th Intl. Conf. Computer Methods and Advances in Geomech.*, Morgantown, W. Virginia, vol:1, 837-842 (1994).
12. Shi, G.-H., *Personal communication* (1995).
13. Lin, H.-C., *Discontinuous Deformation Analyses of Block and Granule Systems*, Master Thesis, Department of Civil Engineering, National Central University, Chungli, Taiwan (1993).
14. Ke, T.-C. and Bray, J., Modelling of particulate media by DDA, accepted for publication in *J. Engrg. Mechanics, ASCE* (late 1995).
15. Shi, G.-H., *User Manual of DDA* ('94 Version).
16. Thapa, B. B., Joint shear displacement-dilation analysis using in-situ opposing profiles, *Proc. 35th U.S. Symp. on Rock Mechanics*, Lake Tahoe, CA, 51-56 (1995).
17. Hilbert, L. B., Yi, W., Cook, N. G. W., Cai, Y. and Liang, G.-P., A new discontinuous finite element method for interaction of many deformable bodies in geomechanics, *Proc. 8th Intl. Conf. Computer Methods and Advances in Geomech.*, Morgantown, W. Virginia, vol:1, 831-836 (1994).
18. Yeung, M., Application of Shi's Discontinuous Deformation Analysis to Rock Slope, Ph.D Dissertation, Department of Civil Engineering, University of California at Berkeley (1991).
19. Shi, G.-H., Modelling dynamic rock failure by discontinuous deformation analysis with simplex integration, *Proc. 1st North American Rock Mechanics Symp.*, Austin, TX, 591-598 (1994).
20. Ke, T.-C., Thapa, B. and Goodman, R. E., Stability analysis of a penstock slope, *Proc. 1st North American Rock Mechanics Symp.*, Austin, TX, 1109-1116 (1994).
21. Chen, S. and Lin, J.-S., Application of DDA to evaluation and solution of slope stability, *Proc. '94 Rock Engrg. Symp. in Taiwan*, 269-277 (1994).
22. Yeung, M., Klein, S. J. and Ma, M., Application of the discontinuous deformation analysis to the evaluation of rock reinforcement for tunnel stabilization, *Proc. 1st North American Rock Mechanics Symp.*, Austin, TX, 607-614 (1994).
23. Ke, T.-C., Application of DDA to block-in-matrix materials, *Proc. 35th U.S. Symp. on Rock Mechanics*, Lake Tahoe, CA, 33-38 (1995).

The Discontinuous Deformation Analysis of "H" Block Retaining Wall

Huang Tien-Kuen

National Chung-Hsing University, Taichung, Taiwan, R. O. C.

1. INTRODUCTION

Retaining walls are used to prevent excessive movement of retained soils. Typical retaining walls, such as gravity, reinforced concrete, reinforced earth, tieback and other walls, have been widely used. However, from practical viewpoint, there are still drawbacks among these often constructed retaining walls.

While rigid gravity and reinforced concrete walls are less susceptible to differential settlements, their drainage pipes are often blocked with age, which allows high water pressure and excessive saturation of the base soils to develop. The inherent flexibility of reinforced earth walls allow them to function despite differential settlements. However, more space than for other walls is necessary to accommodate the reinforced earth wall and corrosion of reinforcing materials may become a problem. Tieback walls are also flexible, but the tensile metal and anchor parts are highly susceptible to corrosions. High costs can be expected to overcome corrosion as well as to ensure adequate anchorage.

Other type of retaining walls, such as mortared blocks and gabionade, etc. are used very often in the slopes of country road. However, the height of mortared blocks is limited to about 3 meters due to stability consideration and they are weakened with large settlements. The gabionade can sustain large settlement and provide a good drainage, but corrosion of the network will lead to the final failure.

A new type of retaining wall constructed with H-type concrete blocks is proposed. This type of retaining wall incorporates two H-type of concrete blocks interconnected to build up a flexible retaining wall system. Shearing or compressive resistance in the concrete blocks is developed in the stress transfer between blocks. Proper space between concrete blocks provide a non-blocked drainage path and a good front view can be obtained by adjusting the interconnection of concrete blocks in a specific way.

This paper introduces the proposed retaining walls and describes briefly the principles of discontinuous deformation analysis(DDA) method employed to calculate the wall performance. The DDA method, another numerical procedure in the family of discrete element method(DEM) is well suited for studying the mechanical behavior of the distinct concrete block system. The method fully considers the kinematic behaviors and frictional properties among the distinct blocks. Then, models of "H" block walls were presented to study their behavior. To verify the adequacy of DDA method on the analysis of "H" block wall, a field test was conducted and compar-

isons were also made between the analytical and monitoring results.

2. PROPOSED RETAINING WALLS

Two types of "H" concrete blocks shown in Fig.1 are proposed to construct the retaining walls. A typical wall is illustrated in Fig.2, in which each layer of the proposed retaining wall is composed of concrete blocks of type I or type II. For the type II layers, two-way interconnection as shown in Fig.3, is developed in the adjacent concrete blocks, while the type I layers only connect adjacent concrete blocks in the direction of the wall section. Additional space between type I concrete blocks in any layers can be obtained to increase drainage of a large quantity of water.

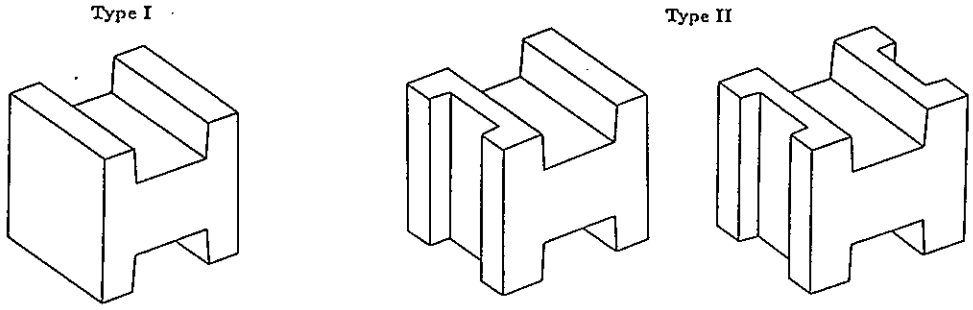

FIG. 1 "H" Concrete Blocks

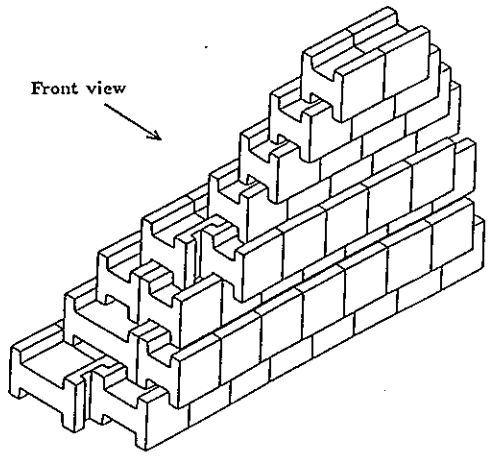

FIG. 2 Typical "H" Block Wall

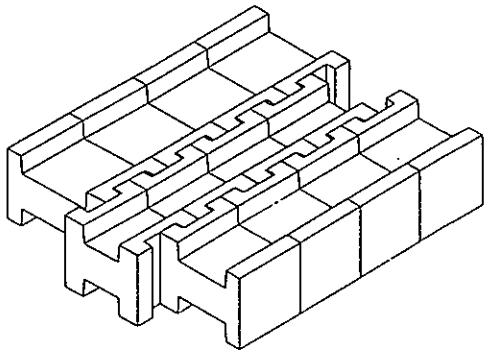

FIG. 3 Interconnection between Type II Blocks

The proposed retaining structure shown in Fig.2, is flexible and allows large displacements and differential settlements. Stresses are transferred between concrete blocks through compression and shear. Since no tensile stress is induced in the concrete blocks, no reinforcing steel is needed. Appearance can be improved at the front indented portion of concrete by planting.

Concrete blocks basically one meter in length in all three directions are considered in the model analysis. The overall size along the horizontal direction of the wall section can vary to fit the retaining wall requirements. Detailed dimensions of the

concrete blocks are schematically shown in Figs.4 and 5. For general engineering projects, the size of the concrete blocks can be proportionally changed to meet the practical requirements.

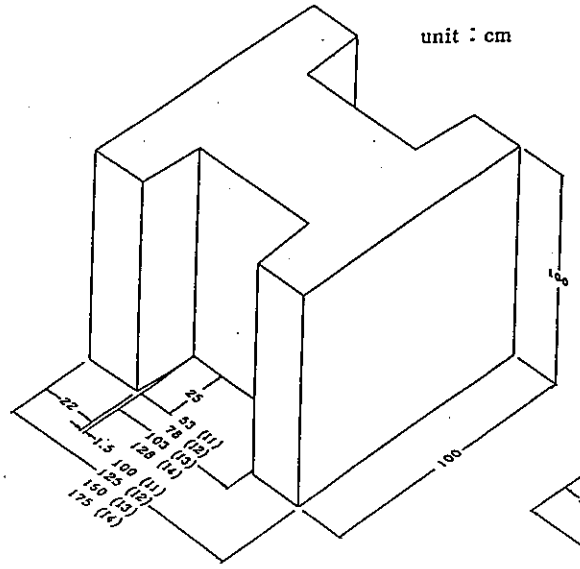

FIG. 4 Detailed Dimensions of Type I Blocks(I1 - I4)

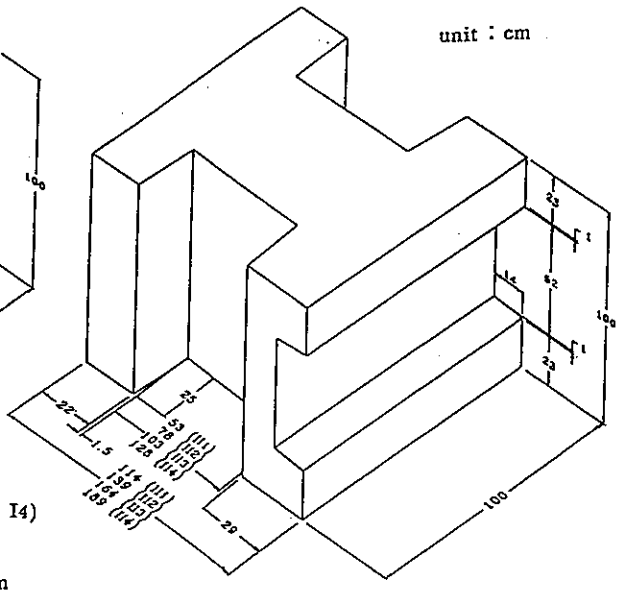

FIG. 5 Detailed Dimensions of Type II Blocks(II1 - II4)

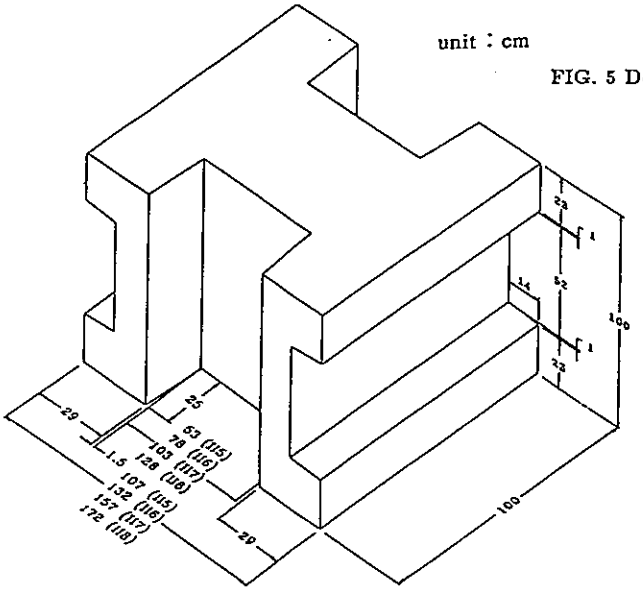

FIG. 5 (Continued) (II5 - II8)

3. THE DISCRETE ELEMENT METHOD

Since Cundall[1] first introduced discrete element method(DEM) to simulate progressive movements in blocky rock system, DEM has been developed rapidly. The early version of DEM only handled a system of discrete rigid blocks. After later extension and development[2] [3] [4], the capability of current DEM allows the mod-

elling of 3D geometry, large deformations and displacements, heterogenous rocks, nonlinear rocks and joints, rock fracturing and coupled joint flows.

DEM employs an explicit central difference time-marching scheme to generalize the equations of motion directly[5]. At every step, contacts are detacted from the current penetration between blocks. Given the elastic contact stiffness, the amount of penetration at each contact determines the contact forces between blocks, which are regarded as additional external forces in the system. Then, unbalanced forces drive the solution process, and a mathematical damping is used to dissipate the extra kinetic energy. The current block kinematics in DEM can not handle complex contact situations, and the explicit scheme used in DEM may result in a questionable equilibrium of the system at any step. Nevertheless, the method has made great contributions to many aspects of rock mechanics problems.

The discontinious deformation analysis(DDA) method employed in this paper was originally developed by Shi and Goodman[6] for analyzing the discontinuous behavior of block systems. Since then, DDA has become another numerical procedure in the family of discrete element method[5]. Although both DEM and DDA can simulate the complex behavior of block system, they are different theroetically. DDA method is a displacement and an implicit method, in which the unknowns in the equilibrium equations are displacement-based variables. Shi[7] addressed five unique features of DDA including: (1) complete block kinematics and its realization; (2) perfect first-order displacement approximation; (3) strict postulate of equation; (4) correct energy consumption; and (5) high computing efficiency.

In the DDA method, a practical problem is modelled as an assemblage of blocks. It allows individual blocks to separate or slide away from each other, satisfying the conditions of no tension and no penetration between blocks. The interactions between blocks are simulated by contact springs. A system of equilibrium equations for the block assemblage is derived through the minimization of the total potential energy. These equations are then solved iteratively within each step to achieve the convergence of opening-closing contraints between blocks. The equation solver used in DDA is based on graph theory, which is highly efficient because it stores and operates on non-zero elements in the triangular decomposition of the coefficient matrix. The Coulomb's friction law is applied on the contact surfaces to model friction. A complete kinematic theory in DDA method is developed to deal with complex contact situations between blocks.

The DDA method can handle large deformation and large displacement using the deformed block shape in the generation of equilibrium equation and solution for the updated block geometry. Practical applications of the DDA method can be used to perform the stability analyses and support designs for tunnels, slopes, retaining walls, dam abutments and foundations, etc. In the following, the principles of the DDA method are briefly summarized. More detailed descriptions about the DDA method can be referred to the Shi's thesis or book[7] [8].

3.1 Block Deformation

Assuming each block has constant stresses throughout, the displacement (u, v) of any point (x, y) of block i for two-dimensional case can be represented as :

$$\left\{ \begin{array}{c} u \\ v \end{array} \right\} = \mathrm{T_i D_i} \tag{1}$$

where

$$\mathrm{T_i} = \left| \begin{array}{cccccc} 1 & 0 & -(y-\mathrm{y_0}) & (x-\mathrm{x_0}) & 0 & 1/2(y-\mathrm{y_0}) \\ 0 & 1 & (x-\mathrm{x_0}) & 0 & (y-\mathrm{y_0}) & 1/2(x-\mathrm{x_0}) \end{array} \right|_i \tag{2}$$

$$\mathbf{D}_i^T = \left\{ \begin{array}{cccccc} u_0 & v_0 & r_0 & \varepsilon_x & \varepsilon_y & \gamma_{xy} \end{array} \right\}_i \tag{3}$$

(u_0, v_0) is the rigid body translation of the centroid (x_0, y_0) within the block ; r_0 is the rotation angle with center at (x_0, y_0) ; $\varepsilon_x, \varepsilon_y, \gamma_{xy}$ are the normal and shear strains of this block. The strains used in the matrix of deformation variables D_i incorporating with the corresponding elements in matrix T_i will result in displacement componenets. In the establishment of a system of equilibrium equations, the global force matrix and displacement matrix can be related through the introduction of global stiffness matrix.

3.2 Generation of Block System

In the DDA method, the block system is generated from discontinuous joints. Using the sectioning method, the block system is produced and represented by the ordered vertices. The procedures for generating the block system can be summarized as follows:

(1). Input the coordinates of end points for each joint.

(2). Compute the intersections of all joints.

(3). Delete the irrelevant intersection and remove the dead ends of some joints.

(4). Trace the block system.

An example to illustrate the procedure for generating the block system from joints is shown in Fig.6.

3.3 Simultaneous Equations

The movements and deformations of a block are defined by the given displacement functions (see Eq.(1)). The total potential energy can be computed based on the stresses, external load, body force, inertia force, contact spring deformation, and displacement constraint, etc. within a single block. The derivatives with respect

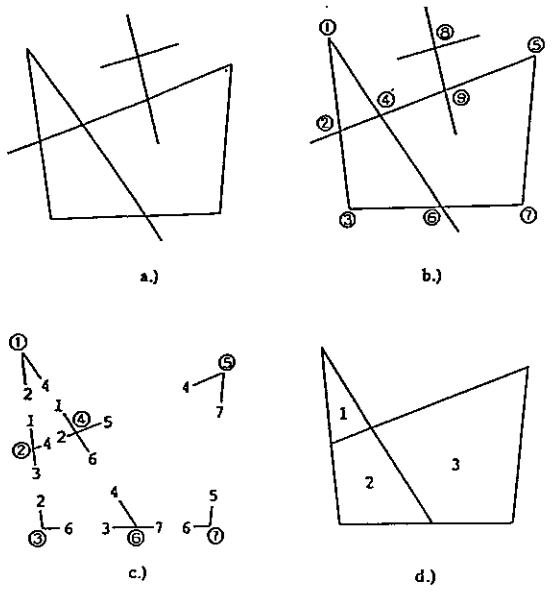

FIG. 6 Example Procedure for Generating Block System

to the deformation variables $\mathbf{D}_i$(in Eq.(1)) of individual potential energy for block i are calculated and the corresponding submatrices are formed separately. The global simultaneous equations are established by assembling the individual submatrices to the matrices of the global equations. The global simultaneous equilibrium equations have the form:

$$\begin{vmatrix} \mathbf{K}_{11} & \mathbf{K}_{12} & \cdots & \mathbf{K}_{1n} \\ \mathbf{K}_{21} & \mathbf{K}_{22} & \cdots & \mathbf{K}_{2n} \\ \vdots & \vdots & \ddots & \vdots \\ \mathbf{K}_{n1} & \mathbf{K}_{n2} & \cdots & \mathbf{K}_{nn} \end{vmatrix} \begin{Bmatrix} \mathbf{D}_1 \\ \mathbf{D}_2 \\ \vdots \\ \mathbf{D}_n \end{Bmatrix} = \begin{Bmatrix} \mathbf{F}_1 \\ \mathbf{F}_2 \\ \vdots \\ \mathbf{F}_n \end{Bmatrix} \tag{4}$$

where $\mathbf{K}_{ij}$ is the stiffness submatrix influenced by blocks i and j ; $\mathbf{D}_i$ represents the deformation variables (u_0 v_0 r_0 ε_x ε_y γ_{xy}) of block i ; $\mathbf{F}_i$ is the loading on block i distributed to the six deformation variables.

3.4 Block System Kinematics

In the DDA method, no tension and no penetration are allowed between blocks for block movement. When the block system moves or deforms, the blocks are in contact along the boundary and non-penetration inequalities can be transformed in the equilibrium equations by adding springs or penalties to regulate the contact movement. If two blocks have a tensile contact force between them, the non-tension inequalities can be added to reduce the locking. The global equilibrium equations have to be solved with opening-closing iterations within each step under the constraints of no interpenetration and no tension.

The solution procedure of DDA method is shown in Fig.7.

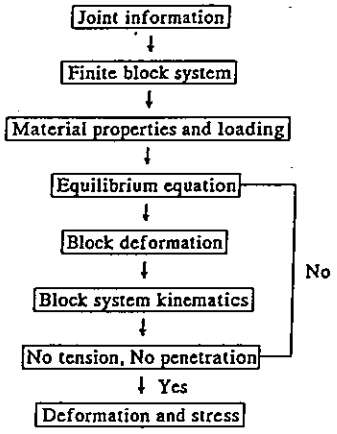

FIG. 7 Flow Chart of DDA Method

4. NUMERICAL STUDIES

For the understanding of the mechanical behavior of "H" type retaining walls, three typical models 4, 6.25 and 9.25 meters respectively in height are studied. The material properties used in the three models are summarized as:

For concrete blocks

unit weight 23 KN/m^3

Young's modulus 2.1 x 10^7 KN/m^2

Poisson's ratio 0.15

Compressive strength 210 kg/cm^2

For soils

unit weight $18KN/m^3$

Young's modulus 2.1 x 10^4 KN/m^2

Poisson's ratio 0.25

frictional angle 30^0

cohesion 0

The frictional angles developed between concrete blocks, soil and block walls are taken as 20^0. The values of spring stiffness in the contact are one hundred times the block stiffness. The proposed retaining wall is composed of two types (I and

II) of "H" concrete blocks. In the upper layers, small quantities of concrete blocks (usually type I) are placed in the wall cross section. While in the lower part, more quantities of concrete blocks (type I or II) are needed to provide enough resistance for the large lateral earth pressure in the bottom area. As for the placement of concrete blocks, they are arranged in such a way to develop more effectively the shear resistance between block connections.

The generation of block system in the "H" block retaining wall can be divided into two parts. The concrete block system is obtained by directly introducing the vertex coordinates of each block. While the block system in the backsoil is generated by assuming logspiral-sandwich failure mechanism[9] and sectioning the sliding mass along the base of failure mechanism. More detailed descriptions for generating the critical logspiral-sandwich failure surface in the backsoil of retaining wall can be found in the book by Chen[9].

Figures 8-10 show the cross sections of three "H" block walls 4.0, 6.25 and 9.25 meters in height, respectively. The placements of concrete blocks are also included in the figures. The block systems of soils for three "H" block walls are sectioned along the assumed failure mechanisms and discretized as shown in Figs.11-13 for further analyses. Some corners of the soil blocks, especially close to the "H" block walls are reduced in the block system. The reason is that extra energy is required to lift and rotate blocks for excessively stiff and locking in block contacts, resulting in high resistance[10].

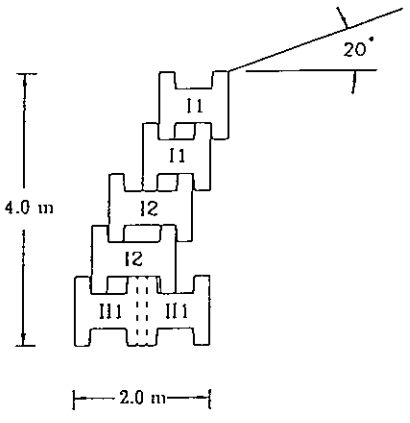

FIG. 8 4-m-High "H" Block Wall

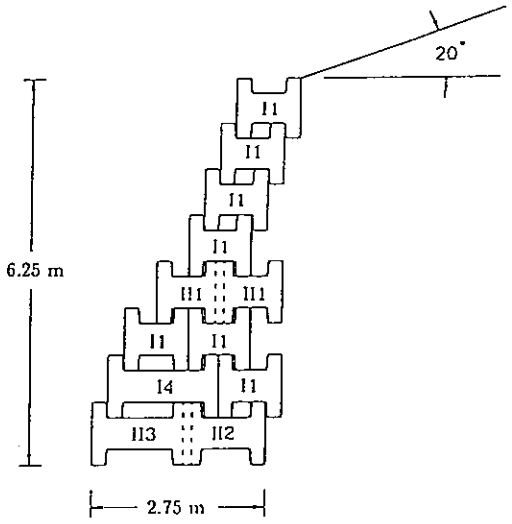

FIG. 9 6.25-m-High "H" Block Wall

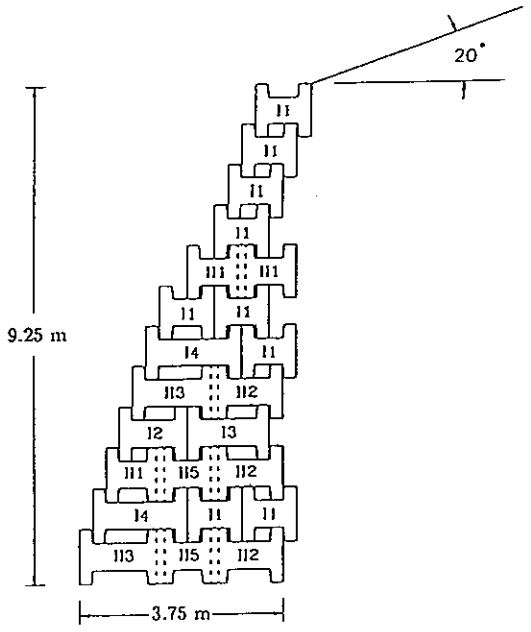

FIG. 10 9.25-m-High "H" Block Wall

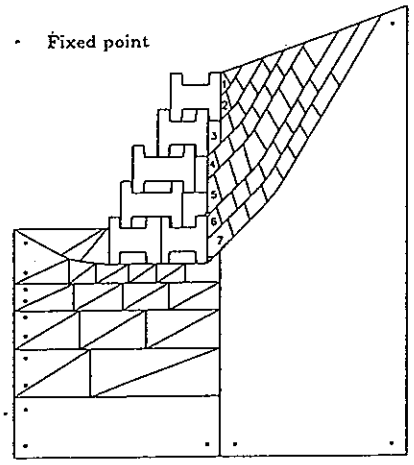

FIG. 11 Block System of 4-m-High "H" Block Wall

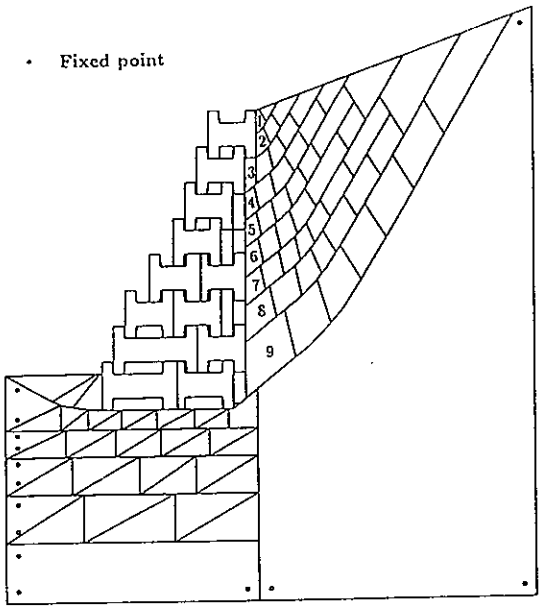

FIG. 12 Block System of 6.25-m-High "H" Block Wall

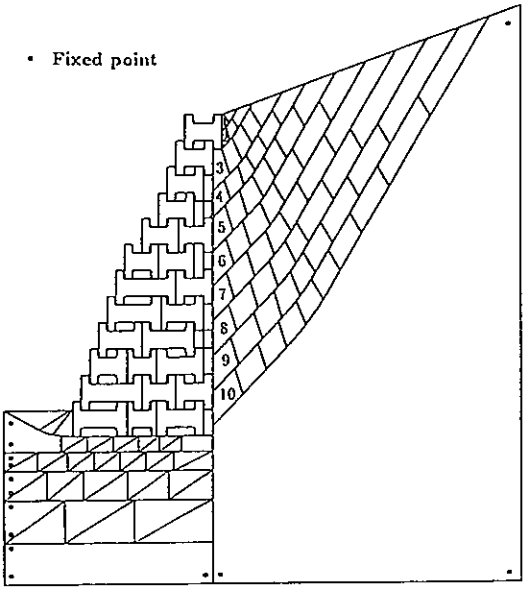

FIG. 13 Block System of 9.25-m-High "H" Block Wall

Imposing the constraints on the soil boundary and assuming a plane-strain condition, the mechanical behaviors for three "H" block or rigid retaining walls under gravity load of concrete and soil can be evaluated. All the analyses are performed in the workstation of HP 9000-720 computer series and are proceeded in more time steps for producing enough movement to mobilize the wall friction.

The relationships of the lateral earth pressure of the backsoil developed versus displacement at the toe of the wall for three "H" block walls were shown in Figs.14-16, respectively. The corresponding block number in the backsoil of three "H" block walls can be referred to Figs.11-13. More movements of the backsoil in the lower area are needed to reach the active stage. From Figs.14-16, the active states of three "H" block walls can be estimated for further study and discussion.

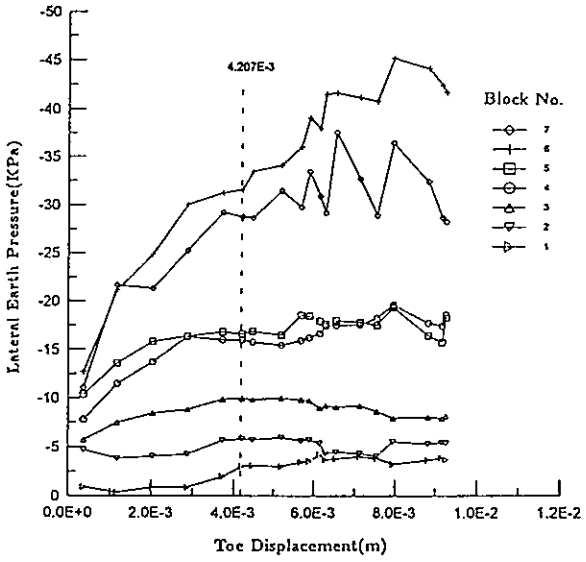

FIG. 14 Lateral Earth Pressure vs. Toe Displacement for 4-m-High "H" Block Wall

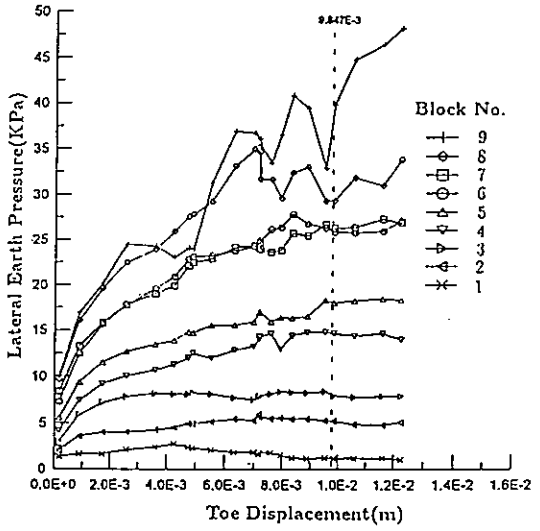

FIG. 15 Lateral Earth Pressure vs. Toe Displacement for 6.25-m-High "H" Block Wall

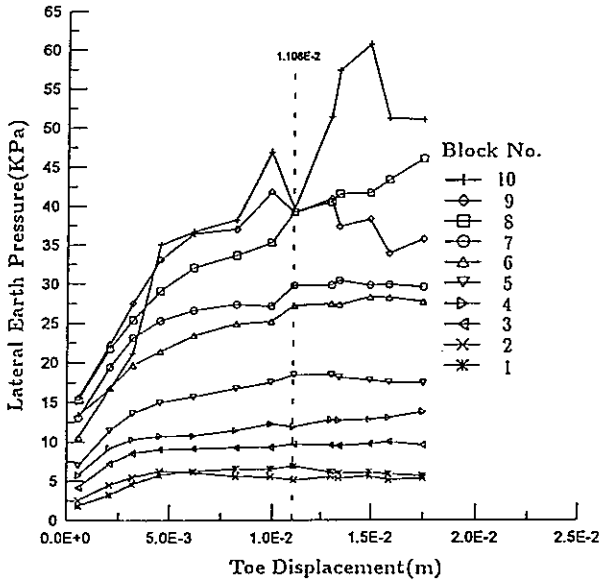

FIG. 16 Lateral Earth Pressure vs. Toe Displacement for 9.25-m-High "H" Block Wall

The analyzed results of the active earth pressure distributions for three"H" block walls were shown in Figs.17-19, respectively. The K_a and K_0 earth pressure distributions from Coulomb theory are also included in the related figures. The resultant forces and their locations for three "H" block walls were calculated and summarized in Table 1. The resultant forces of rigid and massive walls replaced for the "H" block walls were evaluated by the limit analysis method. Those results were included in the last column of Table 1. As for the stress states in the concrete blocks, the calculated average maximum values of compression, tension and shear in all blocks of the three "H" block walls are shown in Table 2 and design values of concrete are also included. Discussions on various results are summarized as follows:

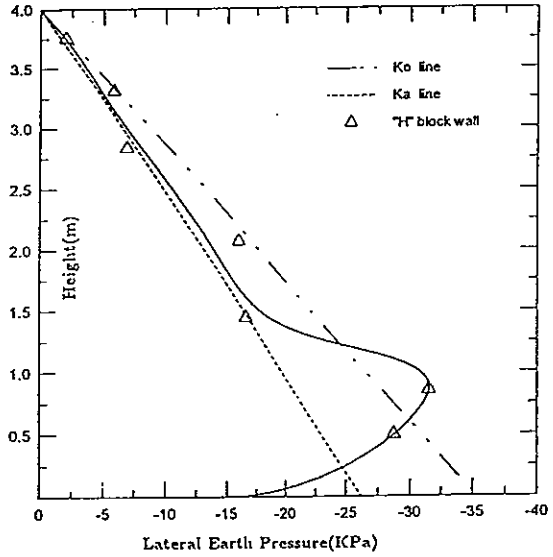

FIG. 17 Lateral Earth Pressure Distribution of 4-m-High Retaining Wall

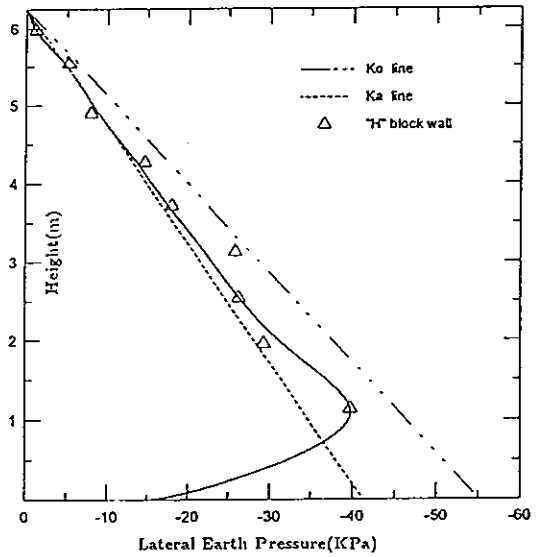

FIG. 18 Lateral Earth Pressure Distribution of 6.25-m-High Retaining Wall

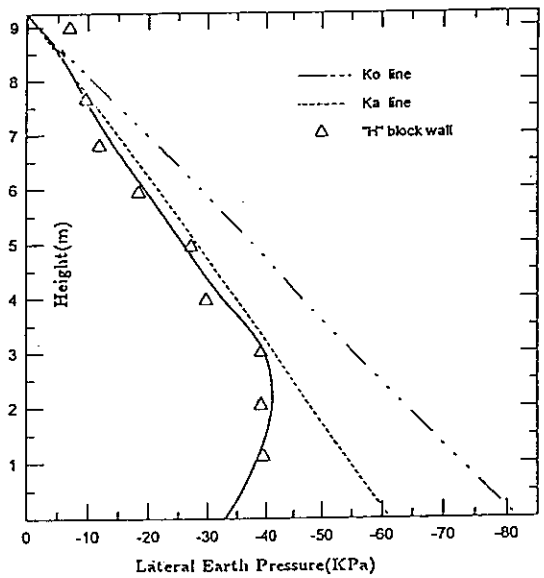

FIG. 19 Lateral Earth Pressure Distribution of 9.25-m-High Retaining Wall

Table 1. Summary of Resultant Forces and Locations

	Locations (from the bottom)	Resultant forces (KN/m)	
		"H" block wall	Massive wall
4-m-High	0.35H	60	53
6.25-m-High	0.36H	129	129
9.25-m-High	0.33H	237	283

H : Height of the wall

Table 2. Summary of Maximum Values in Concrete Blocks

	Compression	Tension	Shear
4-m-High	47.7	0	25.4
6.25-m-High	117.3	0	47.3
9.25-m-High	132.2	0	52.5
Design value	9270.5	927.1	412.3

unit : KPa

(1). The active earth pressure distributions of "H" block walls follow the K_a line in the upper part of the wall and reduce in the lower area. The reduction is relatively apparent for higher "H" block walls.

(2). When compared with the rigid wall system, the resultant force is of sigificant reduction for higher "H" block walls. There is no apparent difference for the medium-height "H" block walls.

(3). As for the locations of resultant forces, they are about 0.35H above the bottom of the wall. The design height of the rigid wall is commonly on the order of 0.4 to 0.5H[11]. This will effectively improve the overturning stability for "H" block walls.

(4). The average maximum values of compression, tension and shear in concrete blocks of "H" block walls are much less than the design values.

5. FIELD TEST

To confirm the adequacy of DDA method on the analysis of "H" block wall, a full-scale field test was carried out. Figure 20 shows the cross section of the test wall, in which four soil pressure cells were installed. The material properties used in the test wall are obtained by in-situ sampling and laboratory testing. The block system after sectioning is shown in Fig. 21 and the analyzed results of active earth

pressure distributions on the wall and base are obtained as in Figs. 22-23, in which the monitoring values are also included. On the whole, the DDA method performs suitably in the analysis of discretized "H" block wall system. Lower lateral earth pressure was measured at the bottom area of the wall may be due to the incomplete action. It is hard in practice to develop full action on the wall for soils near the bottom area of the wall.

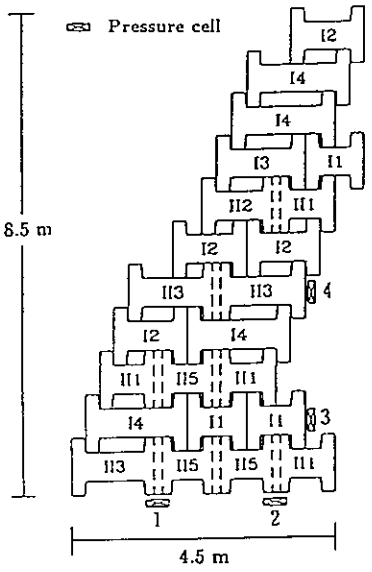

FIG. 20 "H" Block Wall in Field Test

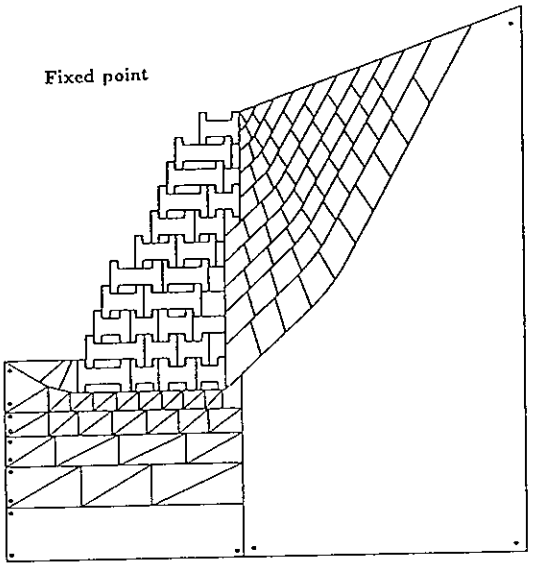

FIG. 21 Block System of Field Test Wall

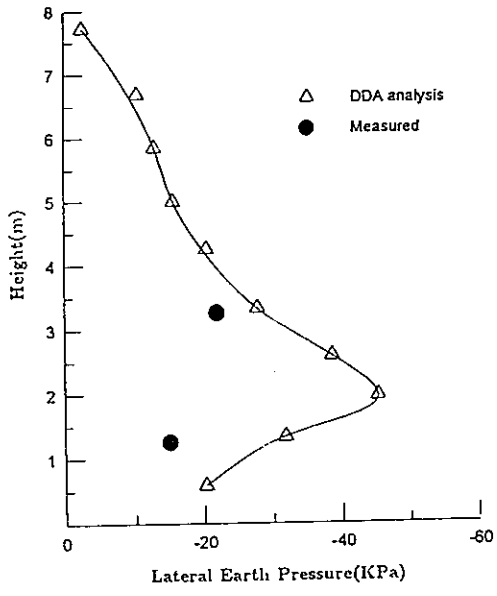

FIG. 22 Lateral Earth Pressure Distribution of Field Test Wall

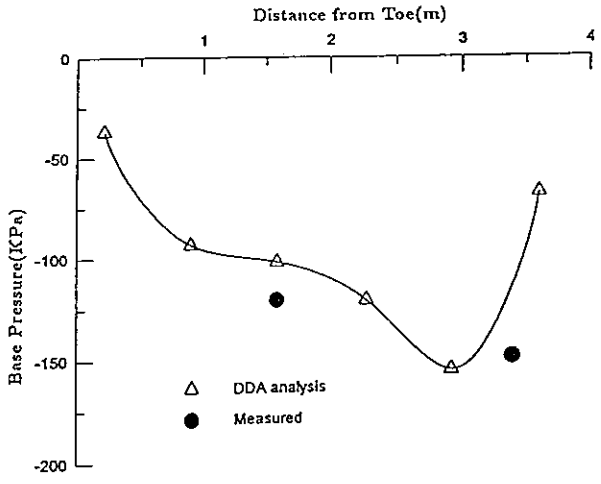

FIG. 23 Base Pressure Distribution of Field Test Wall

6. CONCLUSIONS

A new retaining wall is proposed in this paper. Advantages in using this type of retaining wall in engineering practice and design are discussed. The wall provides proper drainage system, is capable of sustaining differential settlement, develops a good stress transfer mechanism, and is cost effectiveness and ease of constructability. The DDA method is used to perform numerical studies in which three "H" block walls are investigated. Numerical results indicate that the proposed retaining wall has the features of providing good stability and earth pressure distribution. Through the field performance and verification, the "H" block wall is suitable for practical construction.

REFERENCES

1. Cundall, P. A., A computer model for simulating progressive, large-scale movements in blocky rock systems, *Proc. Int. Symp. on Rock Fracture*, Nancy, France, **II-8**, 11-18(1971).
2. Cundall, P. A., UDEC-A generalized discrete element program for modelling jointed rock masses, Final Technical Report to European Research Office, US Army, *Contract DAJA 37-79-C-0548*, NTIS order No. AD-A087 610/2(1980).
3. Cundall, P. A. and R. D. Hart, Development of generalized 2-D and 3-D discrete element programs for modeling jointed rock, Itasca Consulting Group, *Misc. Paper SL-85-1*, US Army Corps of Engineers(1985).
4. Lemos, J. V. and L. J. Lorig, Hydromechanical modeling of jointed rock masses using discrete element method, *Proc. of the 1st Conf. on the Mech. of it Jointed and Faulted Rock* Vienna, Austria, 605-612(1990).
5. Cundall, P. A. and R. D. Hart, Numerical modelling of discontinua, *Proc. of the* 1st Conf. on Discrete Element Method, Bolder, Colorado, 1-17(1989).
6. Shi, G-H, and R. E. Goodman, Two dimensional discontinuous deformation, *Int. J. Num. and Anal. Meth. in Geomech.*, 9(6), 541-556(1985).
7. Shi, G-H., Discontinuous deformation analysis : a new numerical model for the static and dynamics of block systems, Ph.D. Dissertation, Dept. of Civ. Engrg., Univ. of California at Berkeley(1988).
8. Shi, G-H., *Block System Modeling by Discontinuous Deformation Analysis*, Computational Mechanics Publication, Southhampton, UK(1993).
9. Chen, W. F., *Limit Analysis and Soil Plasticity*, Elsevier, Amsterdam(1975).
10. Chen, W. F. and A. P. Pan, Finite element and finite block methods in geomechanics, *Report No. CE-STR-90-20*, School of Civ. Engrg., Purdue Univ., West Lafayette, Ind.(1990).
11. Bowles, J. E., *Foundation Analysis and Design*, 4th edn., Singapore, McGraw-Hill(1988).

Discontinuous Deformation Analysis For Masonry Structures

Yaw-Jeng Chiou, Jyh-Cherng Tzeng and Ming-Jiunn Lin

Department of Civil Engineering, National Cheng-Kung University, Tainan, Taiwan, 701, R. O. C.

ABSTRACT: The structural behaviors of masonry structures are investigated by the method of discontinuous deformation analysis (DDA). The artificial joint is adopted to model the behavior of mortar, and its characteristics are specified by the Mohr-Coulomb failure criterion. The numerical results are compared with previous research and possess satisfactory agreement. In addition, the numerical results show that the behaviors of the masonry structures are highly influenced by the failure of mortar. The nonlinear behaviors become dominant when the mortar is fractured.

1. INTRODUCTION

Masonry structures are constructed with brittle materials and the failure of which is frequently initiated from the cracking of mortar and separation of brick. Structure failure induced by cracking and separation characterizes distinctive block elements and nonlinear behaviors.

Abrams and Paulson [1] studied the earthquake response of masonry built structures by the method of seismic testing. Similar studies were presented by Gulkan et al. [2] and Clough et al. [3]. Dhanasekr et al. [4] investigated the stress-strain relation for brick masonry and its deformation characteristics by the method of biaxial testing. Ali and Page [5] studied the stress distributions and failure behaviors of masonry structures by the finite element method. Similar numerical model was proposed by Lotfi and Shing [6]. Smith [7] examined the behavior of infilled frames by the finite difference method and proposed a simplified equivalent single strut model to replace the wall. Liauw [8] proposed an approximate equivalent frame method to analyze the infilled frames. Thiruvengadam [9] used the finite element method, the equivalent single strut model, and the equivalent multiple strut model to study the natural frequencies of infilled frames with opening and separation of wall. El Haddad [10] studied the cracking and stress redistribution of infilled frames by the finite element method.

The compatibility condition of finite element method is not valid for cracking and separation phenomena occurring in the masonry structures. This study applied the method of discontinuous deformation analysis (DDA) [11] to investigate the structure behaviors of masonry structures. The artificial joint [12] is adopted to model the behavior of mortar and to refine the stress distribution within a block. The Mohr-Coulomb failure criterion is used to analyze the cracking and separation phenomena. The proposed numerical method is verified by investigating the deflection of a

homogeneous beam. Then the discontinuous deformation behaviors of the masonry wall and reinforced concrete beam are fully studied.

2. PROBLEM FORMULATION

In the method of discontinuous deformation analysis (DDA) [11], the variables are displacements and the equilibrium equations are solved in the same way as finite element method does. However, DDA does not imply continuity at block boundaries. The blocks are independent and they only have connections while in contact with one another. These connections are performed by adding springs to the contacting positions. The compatibility conditions for the block systems are no-tension and no-penetration between any two blocks. These two constraints are inequalities in mathematical forms. However, the blocks are in contact only along the block boundaries so these inequalities can be transformed into a set of equalities upon which the equilibrium equations can be set up and solved. A complete first order polynomial is chosen as the displacement function for a two-dimensional block, and this displacement function restricts the block to constant stress.

Referring to Figure 1, the displacements (u, v) of any point (x, y) in a representative block *i* [11] are given as

$$\begin{Bmatrix} u \\ v \end{Bmatrix} = \begin{bmatrix} 1 & 0 & -(y-y_0) & (x-x_0) & 0 & (y-y_0)/2 \\ 0 & 1 & (x-x_0) & 0 & (y-y_0) & (x-x_0)/2 \end{bmatrix} \begin{Bmatrix} u_0 \\ v_0 \\ r_0 \\ \varepsilon_x \\ \varepsilon_y \\ \gamma_{xy} \end{Bmatrix} \tag{1a}$$

or

$$\begin{Bmatrix} u \\ v \end{Bmatrix} = [\mathbf{T}_i][\mathbf{D}_i] \tag{1b}$$

where (x_0, y_0) are the coordinates of block centroid, $[\mathbf{T}_i]$ is the first order displacement function, $[\mathbf{D}_i]^T = \left(u_0, v_0, r_0, \varepsilon_x, \varepsilon_y, \gamma_{xy}\right)$ is the displacement vector of block *i*, (u_0, v_0) are the rigid body translation, r_0 is the rigid body rotation, and $(\varepsilon_x, \varepsilon_y, \gamma_{xy})$ are the strain components in a two-dimensional geometry. By minimizing the total potential energy, the equilibrium equations for n blocks [11] are

$$\begin{bmatrix} \mathbf{K}_{11} & \mathbf{K}_{12} & \mathbf{K}_{13} & \cdots & \mathbf{K}_{1n} \\ \mathbf{K}_{21} & \mathbf{K}_{22} & \mathbf{K}_{23} & \cdots & \mathbf{K}_{2n} \\ \mathbf{K}_{31} & \mathbf{K}_{32} & \mathbf{K}_{33} & \cdots & \mathbf{K}_{3n} \\ \vdots & \vdots & \vdots & \ddots & \vdots \\ \mathbf{K}_{n1} & \mathbf{K}_{n2} & \mathbf{K}_{n3} & \cdots & \mathbf{K}_{nn} \end{bmatrix} \begin{Bmatrix} \mathbf{D}_1 \\ \mathbf{D}_2 \\ \mathbf{D}_3 \\ \vdots \\ \mathbf{D}_n \end{Bmatrix} = \begin{Bmatrix} \mathbf{F}_1 \\ \mathbf{F}_2 \\ \mathbf{F}_3 \\ \vdots \\ \mathbf{F}_n \end{Bmatrix} \tag{2}$$

where $\mathbf{K}_{ij}$ is the component of stiffness matrix, $\mathbf{K}_{ii}$ depends on the material modulus and inertia effect of block i, $\mathbf{K}_{ij}$ $(i \neq j)$ depends on the contacts or bolt connection between block i and block j; $\mathbf{D}_i$ is the displacement vector of block i, and $\mathbf{F}_i$ is the force vector of block i.

The artificial joint [12] is adopted to study the behavior of mortar and to refine the stress distribution within a block. The cracking and separation phenomena of the artificial joints are analyzed by the Mohr-Coulomb failure criterion.

$$\tau = c + \sigma_n \tan\phi \tag{3}$$

where τ is the shear strength, c is the cohesion, σ_n is the normal stress, and ϕ is the friction angle. In addition, on the investigation of the reinforced concrete structures, the steel is modeled as a bolt connection whereas the bond slip is neglected. The force vectors induced by the bolt with initial force f_0 are

$$\mathbf{F}_i = -f_0[\mathbf{E}_i] \tag{4}$$

$$\mathbf{F}_j = +f_0[\mathbf{G}_j] \tag{5}$$

where

$$[\mathbf{E}_i] = [\mathbf{T}_i]^T \begin{Bmatrix} l_x \\ l_y \end{Bmatrix} \tag{6}$$

$$[\mathbf{G}_j] = [\mathbf{T}_j]^T \begin{Bmatrix} l_x \\ l_y \end{Bmatrix} \tag{7}$$

$[\mathbf{T}_i]$ is the first order displacement function defined in equation (1), l_x and l_y are the direction cosines. The components of stiffness matrix induced by the bolt connection are the same as those given by Shi [11].

3. RESULTS AND DISCUSSION

The modified DDA method is verified first by investigating the static deflection of a homogeneous beam. Referring to Figure 2, a tip-loaded cantilever beam [12] subjected to a concentrated load $P = 1$ *ton* was analyzed by the currently modified DDA method. The length of the beam (L) is $8m$, the height (H) is $1m$, the thickness (B) is $1m$, the Young's modulus (E) is 10^5 *ton/m*^{2}, and the Poisson's ratio (v) is 0.2. Figures (3a)-(3d) show the element meshes divided by the artificial joints into rectangular and triangular blocks. Referring to Figure 4, it is found that the deflection calculated by the rectangular block of Figure (3a) is smaller than the exact analytical solution, while the deflection calculated by the triangular block of Figure (3b) agree well with the exact solution. However, the spring constant ($K_n = K_s = 1.65E$) used in Figure 4 sounds too

small, and this small spring constant might induce inter penetration between two adjacent blocks. The deflections calculated by the various triangular blocks (Figures (3b)-(3d)) with large spring constant ($K_n = K_s = 100E$) are shown in Figure 5. As expected, the deflection calculated by the finer mesh is closer to the exact solution. One can see that the deflection calculated by the mesh of 800 triangular blocks agrees satisfactorily with the exact solution.

Figure 6 shows a masonry wall constructed with 71 bricks [5]. The dimension of a brick is 4.5 *in* × 1.5 *in* × 2.1 *in* (or 11.43 *cm* × 3.81 *cm* × 5.33 *cm*). The tensile strength of the mortar is 42 *psi* (or 289.38 kN/m^2), and the shear strength depends on the status of the normal stress σ_n.

$$\tau = -0.66\sigma_n + 25.58 \qquad 42psi > \sigma_n \geq 0 \tag{8}$$

$$\tau = -0.87\sigma_n + 25.58 \qquad 0 > \sigma_n \geq -334\ psi \tag{9}$$

$$\tau = -0.11\sigma_n + 281.42 \qquad -334\ psi > \sigma_n \tag{10}$$

or

$$\tau = -0.66\sigma_n + 0.176 \qquad 0.289N/mm^2 > \sigma_n \geq 0 \tag{11}$$

$$\tau = -0.87\sigma_n + 0.176 \qquad 0 > \sigma_n \geq -2.3\ N/mm^2 \tag{12}$$

$$\tau = -0.11\sigma_n + 1.94 \qquad -2.3\ N/mm^2 > \sigma_n \tag{13}$$

Referring to Figure 7, the masonry wall is divided by the artificial joints into 134 blocks. The mortar is modeled by the artificial joint, and the whole brick is divided into two sub-blocks by the artificial joints. The failure of the mortar is determined by equations (8)-(10) (or equations (11)-(13)). The distribution of vertical normal stress is shown in Figures 8 and 9. It is found that when the load is small (P = 4.5 *kips* or 20 *kN*), the nonlinear phenomenon is less important, the stresses calculated by the currently modified DDA method approach those by the linear finite element method [5]. However, as the load increases, the nonlinear phenomenon becomes dominant and the stresses near the center region characterize high stress state. Referring to Figure 9, one can see that when the applied load is high (P = 18 *kips* or 80 *kN*), the stresses calculated by the currently modified DDA method are closer to the experimental measured values. The distribution of principal stress induced by P = 18 *kips* (80 *kN*) is shown in Figure 10. One observes that the principal stresses tend to arch shape distribution. Figure 11 shows the failure of the masonry wall subjected to P = 18 *kips* (80 *kN*). It is found that cracks occur in the mortar in which the fracture is in either shear failure mode or tensile failure mode.

The bolt connection is adopted to model the steel in the reinforced concrete. The steel and the concrete are assumed to be perfect bond, and the constitutive relation of the steel is accepted to be bi-linear.

$$\varepsilon_s = \frac{\sigma_s}{E_s}, \qquad \sigma_s \leq \sigma_y \tag{14}$$

$$\varepsilon_s = \frac{\sigma_y}{E_s} + \frac{1}{E_p}(\sigma_s - \sigma_y), \qquad \sigma_s > \sigma_y \tag{15}$$

where σ_y is the yield stress of steel. The moduli of the steel, E_s and E_p, are taken as

$$E_s = 29000000\ psi\ (\text{or } 2.04 \times 10^6\ kg/cm^2)$$

$$E_p = 0.02\ E_s$$

In addition, the shear strength of concrete is assumed to follow the model of the modified shear friction method [13, 14].

$$v_u = 400 + 0.8\,(\rho_v f_y + \sigma_n) \text{ but} \le 0.3 f_c^{'} \quad (psi) \tag{16}$$

or

$$v_u = 2.8 + 0.8(\rho_v f_y + \sigma_n) \text{ but} \le 0.3 f_c^{'} \quad (N/mm^2) \tag{17}$$

where ρ_v is the area ratio of shear friction (transfer) reinforcement, f_y is the specified yield strength of reinforcing steel, and $f_c^{'}$ is the cylinder compressive strength of concrete (6×12 *in*, or 152×305 *mm*).

Referring to Figure 12, a reinforced concrete beam was analyzed by the finite element method and the experimental method [15]. The length of the beam is 156 *in* (or 3962 *mm*), the height is 20 *in* (or 508 *mm*), and the thickness is 8 *in* (or 203 *mm*). The steel area is 1.58 in^2 (or 1019 mm^2), and the tensile strength of the concrete is 546 *psi* (or $3.76\,N/mm^2$). This reinforced concrete beam is analyzed by the currently modified DDA method, and its element mesh is shown in Figure 13. The concrete is divided by the artificial joints into 295 blocks, and the steel is modeled by 67 bolt connections. The Young's modulus of the concrete is taken as $E_c = 57000\sqrt{f_c^{'}}\ (psi)$ (or $5121\sqrt{f_c^{'}}\ (kg/cm^2)$). The load-deflection relation of this reinforced concrete beam is shown in Figure 14. It is found that the current result agrees well with the experimental result. The discrepancy between the current result and the experimental result increases for the reinforced concrete beam with yielding of steel. This discrepancy is induced by the rapid growth of depth of crack penetration and rapid change of stress after the yielding of steel. The constant stress element can not simulate the rapid stress change exactly, but it can be improved by refining the element mesh.

4. CONCLUSIONS

The modified DDA method is proposed to study the structural behaviors of the masonry structure and the reinforced concrete beam. The numerical method is verified first by investigating the deflection of a homogeneous beam, and the numerical solution agrees satisfactorily with the exact solution. Then the numerical modeling of the masonry wall and the reinforced concrete beam are investigated, and their solutions are compared with previous research. The proposed method is demonstrated to be appropriate for analyzing behaviors of masonry structure and reinforced concrete beam. The numerical results show that the behavior of the masonry structure is highly influenced by the failure of mortar. The nonlinear behaviors become dominant when the mortar is fractured.

5. ACKNOWLEDGMENTS

This study is supported by the National Science Council of Republic of China under grant No. NSC84-2621-P006-009B.

6. REFERENCES

1. Abrams, D. P. and Paulson, T. J., Modeling Earthquake Response of Masonry Building Structures, *ACI Structural Journal*, July-August, 475-485 (1991).
2. Gulkan, P., Clough, R. W., Mayes, R. L., and Manos, G. C., Seismic Testing of Single-Story Masonry House: Part 1, *Journal of Structural Engineering*, ASCE, **116**, 1, 235-256 (1990).
3. Clough, R. W., Gulkan, P., Mayes, R. L., and Manos, G. C., Seismic Testing of Single-Story Masonry House: Part 2, *Journal of Structural Engineering*, ASCE, **116**, 1, 257-274 (1990).
4. Dhanasekar, M., Kleeman, P. W., and Page, A. W., Biaxial Stress-Strain Relations for Brick Masonry, *Journal of Structural Engineering*, ASCE, **111**, 5, 1085-1100 (1985).
5. Ali, S. S. and Page, A. W., Finite Element Model for Masonry Subjected to Concentrated Loads, *Journal of Structural Engineering*, ASCE, **114**, 8, 1761-1784 (1988).
6. Lotfi, H. R. and Shing, P. B., An Appraisal of Smeared Crack Models for Masonry Shear Wall Analysis, *Computers & Structures*, **41**, 3, 413-425 (1991).
7. Smith, B. S., Behavior of Square Infilled Frames, *Journal of Structure Division*, ASCE, **92**, ST1, 381-403 (1966).
8. Liauw, T. C., An Approximate Method of Analysis for Infilled Frames with or without Opening, *Building Science*, **7**, 233-238 (1972).
9. Thiruvengadam, V., On the Natural Frequencies of Infilled Frames, *Earthquake Engineering and Structural Dynamics*, **13**, 401-419 (1985).
10. El Haddad, M. H., Finite Element Analysis of Infilled Frames Considering Cracking and Separation Phenomena, *Computers & Structures*, **41**, 3, 439-447 (1991).
11. Shi, G. H. *Discontinuous Deformation Analysis : A New Numerical Model for the Statics and Dynamics of Block Systems*, Ph. D. Dissertation, Department of Civil Engineering, University of California, Berkeley, USA (1988).
12. Ke, T. C., *Simulated Testing of Two Dimensional Heterogeneous and Discontinuous Rock Masses Using Discontinuous Deformation Analysis*, Ph. D. Dissertation, Department of Civil Engineering, University of California, Berkeley, USA (1993).
13. Mattock, A. H., Discussion of the paper "Modified Shear Friction Theory for Bracket Design," by B. R. Hermansen and J. Cowan, *ACI Journal*, **71**, 8, 421-423 (1974).
14. Walraven, J., J. Frénay, and A. Pruijssers, Influence of Concrete Strength and Load History on the Shear Friction Capacity of Concrete Members, *PCI Journal*, **32**, 1, 66-84 (1987).
15. Suidan, M. and Schnobrich, W. C., Finite Element Analysis of Reinforced Concrete, *Journal of Structural Division*, ASCE, **99**, ST10, 2109-2122 (1973).

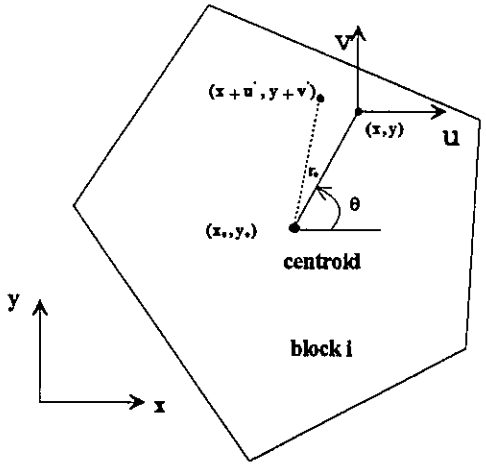

Figure1. Schematic configuration of block

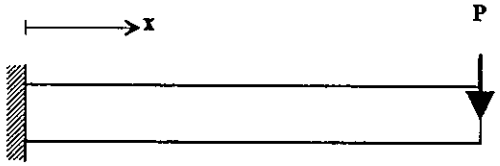

Length, L=8m ; Height, H=1m ; Thickness, B=1m

Young modulus $E = 10^3$ ton / m^2 ; Poisson's ratio, $\upsilon = 0.2$

Figure2. A tip-loaded cantilever beam[12]

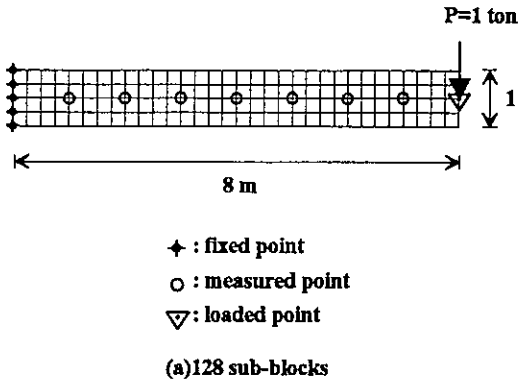

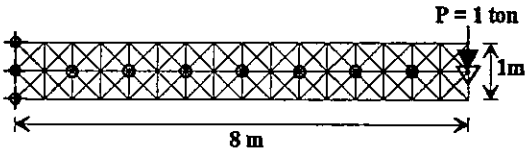

(b)128 sub-blocks

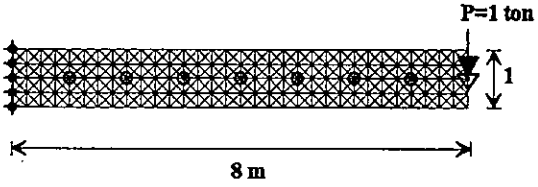

(c)512 sub-blocks

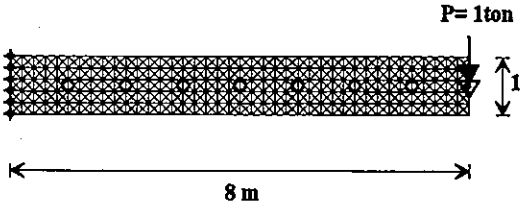

(d)800 sub-blocks

Figure3. A beam refined by artificial joints

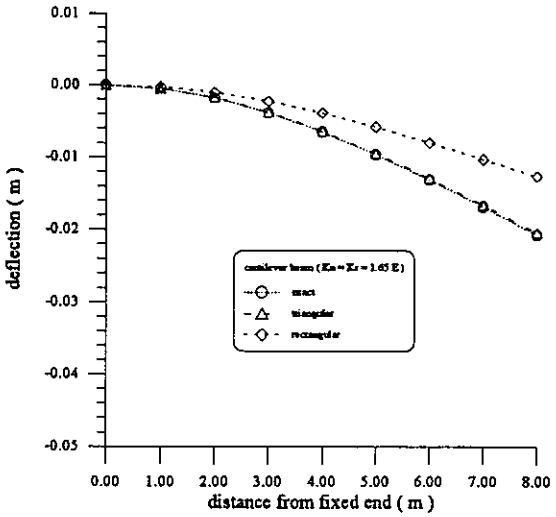

Figure4. Deflection of beam (128 rectangular and triangular blocks, and exact solution)

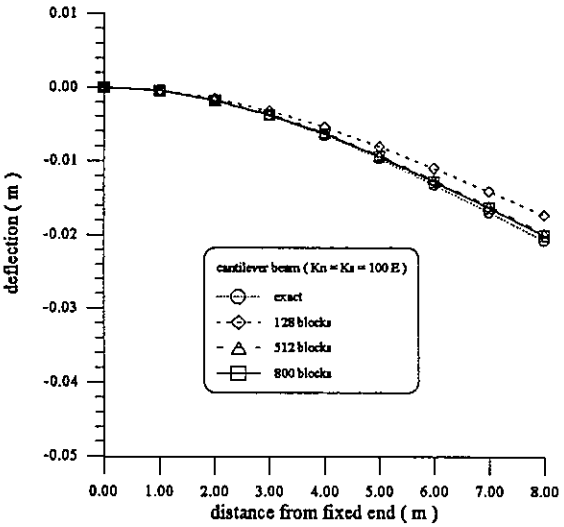

Figure5. Deflection of beam (128 ,512, 800 triangular blocks, and exact solution)

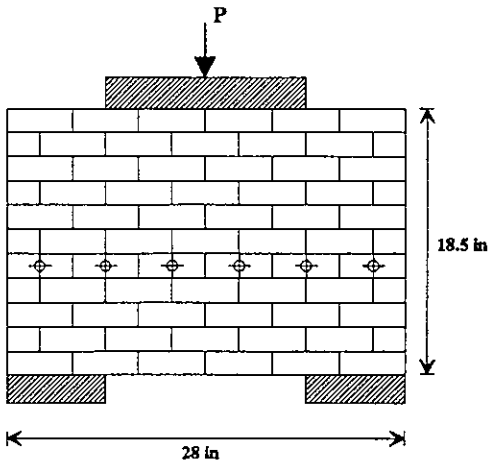

Figure6. Schematic configuration of a masonry wall [5]

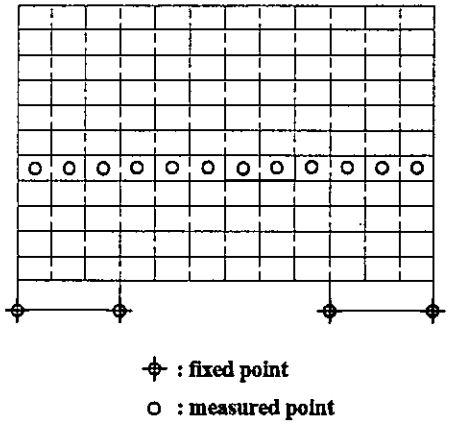

Figure7. A masonry wall refined by artifical joints

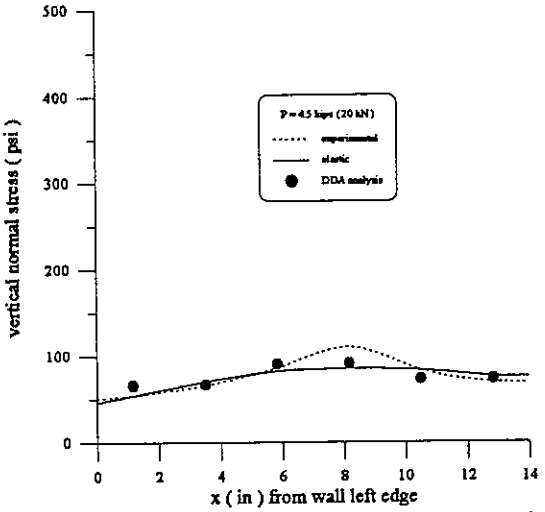

Figure8. Vertical normal dtress distribution of a masonry wall (P=4.5 *kips*)

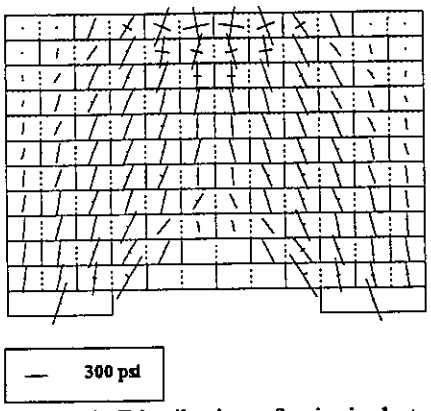

Figure10. Distribution of principal stresses (p=18 *kips*)

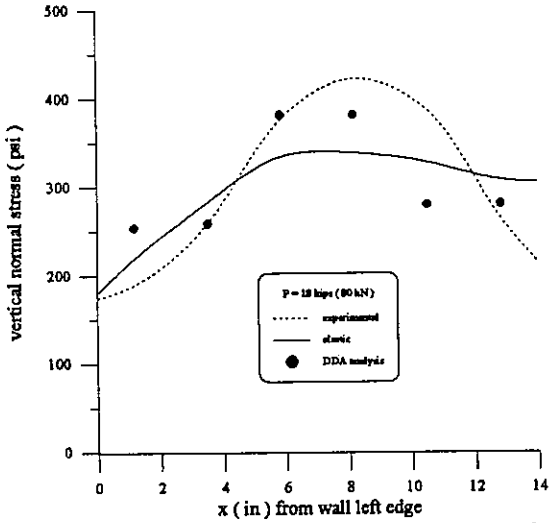

Figure9. Vertical normal dtress distribution of a masonry wall (P=18 *kips*)

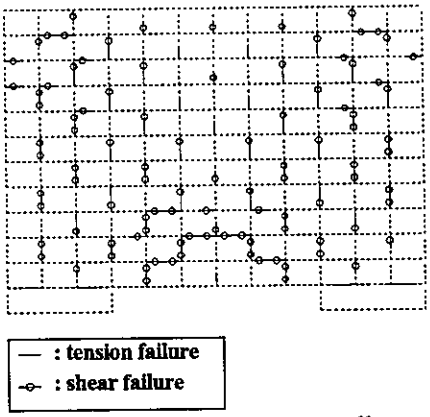

Figure11. failure of masonry wall

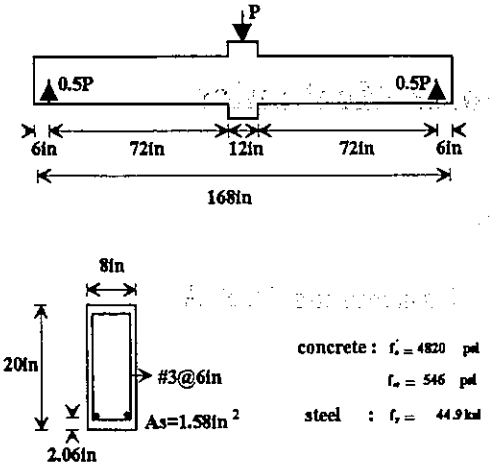

Figure12. Schematic configuration of a reinforced concrete beam

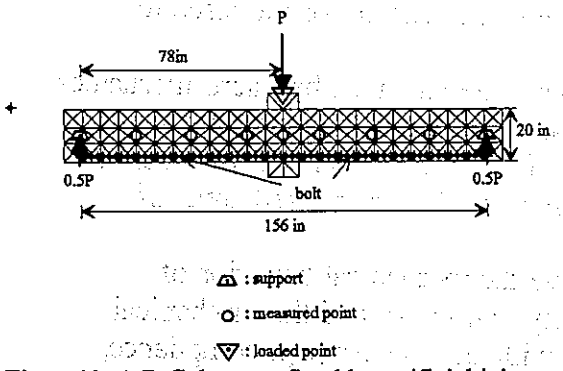

Figure13. A R.C. beam refined by artificial joints

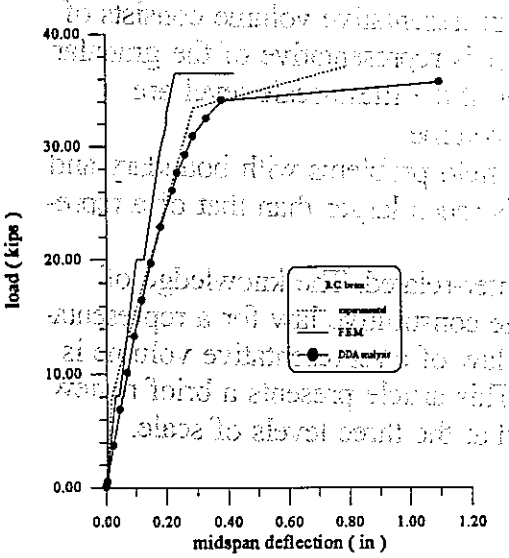

Figure14. The load-deflection relation of a R.C. beam

Recent Advances in Granular Mechanics

Ching S. Chang

University of Massachusetts, Amherst, Massachusetts, U. S. A.

1. INTRODUCTION

In granular mechanics, stress-strain behavior has been a study focus for last several decades. However, the conventional models have been confined to a phenomenological approach within the restrictive framework of classic continuum mechanics without considerations of either the microstructure or the discrete nature of granular materials.

A realistic mathematical model for granular materials must be micro-mechanics based which treats the material as a collection of individual particles and satisfies physical principles governing the interaction of particles. In general, micro-mechanics of granular media has the following three broadly categorized areas of study:

(1) At the micro-scale level, studies involve the mechanical behavior of individual particles (e.g. deformation, plasticity, crushing), and the mechanical behavior of two interacting particles with or without a binder (e.g. compliance, viscous, sliding), etc. The relationships that depict the behavior at the micro-scale level are termed as contact laws.

(2) At the meso-scale level, studies are devoted to the mechanical behavior of a representative volume of granular media. The representative volume consists of a large number of particles such that it's behavior is representative of the granular media. The relationships that depict the behavior at the meso-scale level are termed as constitutive laws for a representative volume.

(3) At the macro-scale level, studies concern field problems with boundary and initial conditions. The scale of a field problem is much larger than that of a representative volume.

The aforementioned three areas are closely inter-related. The knowledge of micro-scale behavior is the basis for deriving the constitutive law for a representative volume at the meso-scale. The constitutive law of a representative volume is a necessary input for the macro-scale analysis. This article presents a brief review of recent work on granular mechanics addressed at the three levels of scale.

2. CONTACT LAW

In order to deliberate the particulate nature of material, the behavior at micro-scale must be considered and adequately modelled. It is useful to have a plausible

and simple model that delineates the deformation of individual particles and the interaction between two particles. In the context of granular mechanics, very few attention has been given to the plasticity and crushing of individual particles . Existing contact laws have been developed mainly for the cases of elastic particles. The work on contact law is briefly reviewed in the following two categories, namely, the direct contact and the contact bonded by a binder.

2.1 Direct Contact

Theory for the contact stiffness of two elastic spheres of different sizes under compression has been described in the well known Hertz contact law. The tangential contact stiffness of two elastic spheres with a frictional contact can be found in the work by Mindlin and Deresiewicz [1] and Walton [2]. For two elastic spheres with a surface adhesion at the contact, contact laws have been investigated by Johnson [3] and Thornton [4]. The contact laws for two elastic spheres of different curvatures have been used to approximate the contact stiffness of two ellipsoids [5]. In the past decade, there has been very few research development in the contact laws for particles with direct contact. Most conventional types of problem have already been solved. The remaining problems are difficult ones such as contact laws for two arbitrary convexed surfaces including flat surface and angular surface.

2.2 Contact with a Binder

Recent development on contact laws has been mostly focused on the two-phase material. Other than a dry particle system, recent work [6] have considered a particle system partly saturated with immobile viscous liquid held at the contacts between particles. The contact forces in the partly saturated system include capillary tension and viscous resistance of the fluid. In a system saturated with fluid, the squirt flow mechanism has been investigated where the pore fluid is squeezed away from the contact due to the effect of hydrodynamics [7].

For the purpose of simulating cemented particulates, the contact law for two particles with an elastic binder has been studied by Dvorkin et al. [8, 9]. They formulated the governing equations and presented numerical solutions for both normal and tangential stiffness of the system. Zhu et al. [10] provided useful closed-form solutions for the stiffness of two elastic particles with an elastic binder. The solutions have also been extended for the time-dependent stiffness of two elastic particles with a visco-elastic binder. Contact laws of this type are useful in the study of particulate composite such as asphalt concrete or cemented sand.

3. Constitutive Law

There are two approaches for modelling the constitutive law of a representative volume for granular materials, namely, the discrete element method (DEM), and the microstructural continuum method (MCM). This review briefly identifies the difficulties encountered in the DEM approach. Many innovative methods in the

analysis of discontinuous deformation have been developed recently. However, the emphasis of the review is focused on the recent development in the area of microstructural continuum method.

3.1 DEM Approach

In the DEM approach, Newton's second law is accepted as the basic premise. Given a pertinent mechanism of two interacting particles, the movement of each particle in an assembly can be precisely calculated. This type of computer simulation is a direct method towards understanding the behavior of a meso-scale representative volume of granular material. A number of work have been addressed along this approach [12].

There are several difficulties involved in this approach:

(1) Granular material is a complex system, usually composed an enormous number of particles. The initial position of each particles and the boundary conditions are usually unknown.

(2) Even if the initial position of each particles and the boundary conditions are known so that the subsequent particle movements can be predicted. It is evident that the computational efforts are excessive if movements were to be followed through extended number of loading steps for millions of particles. The excessive computational effort makes it infeasible for the analysis of a large system.

(3) Results from the computer simulation supply a vast amount of information. It is desirable to interpret the behavior of a representative volume using continuum notions such as stress, strain and modulus. Thus constitutive laws of continuum type is needed which can provide insights to the nature of micro-scale process and meso-scale response.

3.2 MCM Approach

In a micro-structural continuum (MCM) approach, a set micro-systems are identified to statistically characterize the microstructure. Each micro-system has a different configuration/structure. A micro-system can be selected as a pair of particles or a group of particles. The material is an ensemble of the set of micro-systems.

In this approach, a continuum field is introduced in the beginning of the analysis. The continuum variables are linked to the discrete variables of each micro-system. The continuum variables can be used to retrieve and keep track the mean field movement of each discrete particles, at least in an approximate manner. Thus the influence of discontinuous deformation and microstructure are considered in the analysis.

From the behavior of each micro-system, predictions can then be made as to what may be expected on the average behavior for the entire system. On this basis, constitutive laws can be established for granular materials beyond the frame of conventional continuum mechanics.

This approach is useful in providing a conceptual link between the discontinuous deformation at micro-scale and the equivalent continuous deformation at meso-scale. This link cultivates fundamental understanding of the plasticity and

damage in continuum mechanics. Thus the approach is likely to manifest a physically realistic framework for the continuum modelling of granular materials. Several areas of development along this approach are briefly reviewed in the following sections.

3.2.1 Link between continuum and discrete variables

To treat the granular material as an equivalent continuum, it requires a relationship between the continuum variables and the discrete variables such that the continuum variables are capable of representing the discontinuous deformation behavior at the micro-scale level. There exists two types of hypothesis to provide the link: the kinematic hypothesis and the static hypothesis.

(1) Kinematic hypothesis

The commonly used relationship is a kinematic hypothesis providing a link between the strain and the mean field of displacements, given by

$$\delta_i = \epsilon_{ij} l_j \tag{1}$$

in which the displacements are related to the strain in a linear form, corresponding to a uniform strain assumption. According to Eq. (1) and the principle of energy conservation, the mean stress can be derived as a function of contact forces by

$$\sigma_{ij} = \sum f_j l_i \tag{2}$$

In a micromechanical approach for the constitutive modelling of granular material, the kinematic hypothesis of uniform strain has often been made to describe the displacement field of discrete particles [e.g. 2, 13, 14, 15].

The kinematic hypothesis furnishes a useful relationship for estimating the movement of particles. However, the approach leads to an upper bound solution due to the kinematic constraint of the system.

(2) Static hypothesis

Opposite to the kinematic hypothesis of uniform strain, a static hypothesis can be made providing the link between the stress and the mean field of contact forces. In the literature, very little attention has been paid to the formulation of a static hypothesis for granular systems. To this end, a static hypothesis has been recently proposed that delineates the distribution of forces at inter-particle contacts in a system of discrete particles [16, 17], given by

$$f_j = \sigma_{ij} A_{ik} l_k \tag{3}$$

where A_{ij} is the inverse of fabric tensor defined by

$$A_{ij}^{-1} = \frac{1}{V} \sum l_j l_k \tag{4}$$

in which the forces are related to the stress in a linear form, corresponding to a

uniform stress assumption. According to Eq. (3) and the principle of energy conservation, the mean strain can be derived as a function of the contact displacements

$$\epsilon_{ij} = \sum \delta_j A_{jk} l_k \tag{5}$$

The static hypothesis model utilizes the uniform stress assumption, consequently leads to a lower-bound stress-strain relationship due to the static constraint of the system.

Following the approach of a static hypothesis, stress-strain relationships of granular material can be derived. The elastic moduli have been derived in closed-form for assemblies of spheres with isotropic and anisotropic packing structures [18].

The stress-strain behavior derived based on the static hypothesis is quite different from that based on the kinematic hypothesis especially for particles with low tangential contact stiffness. In an elastic case, for particles with very low tangential contact stiffness, the static model predicts a very low value for the shear modulus and 0.5 for the Poisson's ratio. On the other hand, the kinematic model predicts a considerably high value for the shear modulus and 0.25 for the Poisson's ratio. In terms of inter-particle movement, under a given strain, the kinematic model over-predicts the normal compression between particles while the static model over-predicts the tangential displacements between particles.

In the formulation of static hypothesis, the derived stress-strain relationship is corresponding to a lower bound solution, in contrast to the upper bound solution from the kinematic hypothesis. The set of bounds is useful in estimating the exact solution. The bounds are particularly useful when the information on microstructure is limited so that an exact solution cannot be determined.

3.2.2 Small strain models

Studies have shown that the uniform strain assumption is reasonably good for estimating behavior of sands under certain loading conditions [19]. For example, the derived initial modulus of an assembly of sand under a confining pressure is given by [20]

$$G = \frac{2}{5}\left(\frac{5-4\nu_g}{2-\nu_g}\right)\left(\frac{\sqrt{3}\,\bar{n}(1-\phi)}{4\pi(1-\nu_g)}\,G_g\right)^{\frac{2}{3}}\sigma_c^{\frac{1}{3}} \tag{6}$$

where G_g and ν_g are respectively the shear modulus and Poisson's ratio for the sand grain. ϕ is the porosity, $\bar{n}$ is the coordination number, and σ_c is the confining stress of the assembly. Eq. (6) has been found in good agreement with the measured initial moduli from experiments [20].

The Poisson's ratio of the assembly of sand is given by

$$\nu = \frac{\nu_g}{2(5-3\nu_g)} \tag{7}$$

The uniform strain model has also been used for estimating secant modulus and

damping ratio under small amplitude cyclic loads [21]; and for estimating volume change under isotropic compression loading [22]. In all aforementioned loading conditions, particles may experience partial slip but very few sliding have occurred at inter-particle contacts.

3.2.3 Elastic-plastic models

Under a loading condition with high deviatoric stress, large shear deformation occurs accompanying with a significant amount of particle sliding. In this case, it has been found that the strain exhibits non-uniformity within the material sample and the overall behavior is no longer a straight volume average of the local behavior [23, 24]. Thus it is important to account for the non-uniformity of strain in the constitutive modelling of granular media under high deviatoric stress. To account for the strain heterogeneity, two models have been considered, namely, (1) branch model, and (2) cell model. An overview of these two models is given below.

(1) Branch model

Liao et al. [25] has developed an elastic-plastic model considering a set of particle pairs as the micro-systems for granular media. Thus the branch vectors connecting each pair of particles were used to characterize the microstructure. The plasticity model assumed the elastic strain is uniform. The plastic strain results from the sliding between particles when the contact shear force exceeds the frictional resistance. Thus the overall strain in the sample is not uniform. The model has been used in stress-strain predictions for steel and concrete. Physical phenomenon such as dilation, necking and effect of confinement can be predicted by the model.

(2) Cell model

To model the heterogeneity, material is divided into cells (i.e. micro-elements). Each cell represents a particle group and has its distinctive configuration. A statistical set of cells of different configurations is used to characterize the packing structure of the granular material. Under a deformation of the material, each cell is allowed to have a different value of strain depending on the stiffness of each cell. Thus the constraint of uniform strain assumption is relaxed in the cell model.

Self consistence method

The key issue of this model is a reliable method that correctly determine the strain for each cell under the application of a given meso-scale strain. Being conceptually viewed as a cell structure, the granular material in certain respects is analogous to the polycrystalline material. The self-consistent method used in polycrystalline was applied in the granular material to relate the strain of each cell and the meso-scale strain of the representative element. Consequently, stress-strain relationships were derived based on the self-consistent method for a two dimensional granular packing considering plastic sliding [26, 27]. The predicted stress-strain curves and the predicted volume change behavior show great improvement over the results predicted from uniform strain approach.

The self-consistent method can not be readily extended to a three-dimensional problem because it requires a Green's function for general anisotropic media which is not available for three-dimensional condition in the current literature. For this purpose, we recently developed an explicit series expression of a Green's function for a general three-dimensional anisotropic media [28].

Statistical method

Other than the self-consistent method, a canonical ensemble average technique used in statistical mechanics was adopted for developing the stress-strain relationship. A partition function was used to relate the strain of each cell and the meso-scale strain of the representative element. On this basis, a constitutive theory was derived considering the strain fluctuation and particle sliding [19, 23, 29]. The method was applied to the analysis of an idealized simple packing. The results have shown that the plastic yielding and the non-associated plastic flow behavior for this packing resemble those observed from experiments on sand.

The cell model allows the strain field to fluctuate within a representative volume of granular media under an applied meso-scale strain. The model greatly improves its performance over the model with uniform strain assumption [19, 29]. It is noted that, although the strains are different for all cells, the strain within each cell is still assumed to be uniform. Further investigation is needed to relax the constraint within a cell.

3.2.4 Micro-polar model

To treat granular media as equivalent continua, it requires a continuum representation for the discrete particulate system. Many processes can be utilized for the continuumization. A convenient one is to represent the deformation of granular materials by higher-order derivatives of displacement and rotation [30]. Using these continuum variables, a granular medium can be treated as a generalized continuum.

By selecting suitable continuum variables, a discrete granular system can be represented by an equivalent continuum of various type, for example, the micro-polar continuum, the high-gradient continuum, the non-local continuum, etc. These equivalent continua of different types model different aspects of granular media. A more complex continuum captures more features of the deformation behavior for the granular material.

For example, a micro-polar continuum captures the rotation mode of particles, thus models the consequence of asymmetric stress in granular material [31]. A high-gradient continuum, on the other hand, models the effects of heterogeneous strain field. Differed from the classic continua in solid mechanics, these continua display effects of internal characteristic length. When the particle size is relatively large compared to the sample size, the notion of classic continua is no longer adequate to represent the granular system.

For a granular media of micro-polar type, there are two sets of stresses: the usual Cauchy stress σ_{ij} and the polar stress μ_{ij}; and two sets of strains: the usual strain ϵ_{ij} and the polar strain γ_{ij}. For an isotropic medium of granular material, the constitutive law was derived to be [32]

$$\sigma_{ij} = \lambda \delta_{ij} \varepsilon_{kk} + \mu \varepsilon_{ij} + z u_{[i,j]}$$
$$M_{ij} = \lambda_r \delta_{ij} \gamma_{kk} + \mu_r \gamma_{ij} + z_r \omega_{[i,j]} \quad (8)$$

In Eq. (8a), the Cauchy stress and strain are related by the Lame constants λ and μ, and the spin modulus z. In Eq. (b), The material constants λ_r, μ_r and z_r govern the behavior of polar stress and polar strain. These material constants can be obtained from the normal and tangential inter-particle stiffness (k_n and k_t), and the rolling and twisting inter-particle stiffness (g_n and g_t), given by

$$\lambda = 4\alpha(k_n - k_t) \; ; \; \mu = 2\alpha(2k_n - 3k_t)$$
$$\lambda_r = 4\alpha(g_n - g_t) \; ; \; \mu_r = 2\alpha(2g_n - 3g_t) \quad (9)$$

$$z = 2(\mu - \lambda) \quad ; \quad z_r = 2(\mu_r - \lambda_r) \quad (10)$$

where $\alpha = Mr^2/30$; M is the number of contacts per unit volume and r is the radius of particle.

3.2.5 High-gradient model

For a granular media of high-gradient type, the constitutive law has been derived in which the stress is a function of not only strain but also the higher gradient of strain and rigid body rotation [33]. For media with isotropic microstructure, the constitutive law is expressed as follows:

$$\sigma_{ij} = \lambda \delta_{ij} \varepsilon_{kk} + 2\mu \varepsilon_{ij} + C_1 \delta_{ij} \nabla^2 \varepsilon_{kk} + C_2(\nabla^2 \varepsilon_{ij} + \varepsilon_{kk,ij}) + C_3 \nabla^2 u_{[i,j]} \quad (11)$$

where the constitutive constants λ and μ are the Lame constants which can be obtained from Eq. (9) using the normal and tangential inter-particle stiffness (k_n and k_t). The values of C_1 and C_2 can also be determined from the normal and tangential inter-particle stiffness, thus are dependent of the Lame constants and the internal length r of the material, given by

$$C_1 = \frac{2}{7} r^2 \lambda, \qquad C_2 = \frac{2}{35} r^2 (7\mu - 3\lambda) \quad (12)$$

The value of material constant C_3 represents the moment transfer ability of the material which can be determined from the rolling and twisting inter-particle stiffness (g_n and g_t), thus is independent of the Lame constants, given by

$$C_3 = 2\alpha(g_n - g_t) \quad (13)$$

There are two implications associated with the use of high-gradient strains: (1) the strain is not uniform within a representative volume; and (2) the stress of a representative volume depends not only on the strain of this representative volume but also on the strains of neighbouring volume. Thus the high-gradient model can be regarded as a non-local model in a differential form as oppose to the local-

model where stress of a representative volume depends solely on the strain of the same representative volume.

The high-gradient continuum is useful in representing phenomena associated with internal characteristic length of the granular material [34]. Material with same equivalent Lame constants behave differently depending on the size of particles. Thus the stress-strain relationship displays the effect of sample size. Although plastic behavior for such continua has not yet been studied, it is expected that the continua are useful in modelling localized deformation in plastic region due to microstructure effect.

4. BOUNDARY VALUE PROBLEM

Again, modelling of boundary value problems for granular material can be approached by the DEM approach or the microstructural continuum (MCM) approach . In the DEM approach, the same difficulties involved in the computer simulation at meso-scale are carried over to the macro-scale. Questions still exist on handling the enormous number of particles, the insurmountable effort of computation, and on interpreting the vast amount of data. Nevertheless, the computer simulation method is still attractive that can directly provide solutions to the behavior of macro-scale problems. A number of work have been addressed along this approach [12].

The MCM approach for constitutive law solves for the macro-scale problems using a continuum approach. For a macro-scale boundary value problem, the use of equivalent media leads to governing equations which are different from the classic governing equations. Therefore, the constitutive laws is not only useful in describing the meso-scale behavior of a representative volume but also show significant influence on the formulation of governing equation for macro-scale phenomena.

4.1 Micro-polar Model

The governing equation for a micro-polar media considers not only the force equilibrium

$$\sigma_{ij,i}=0 \tag{14}$$

but also the moment equilibrium,

$$\mu_{ij,i}-e_{ijk}\sigma_{ik}=0 \tag{15}$$

where e_{ijk} is the permutation tensor.

Based on these two governing equations and using the constitutive law that treats a granular medium as an equivalent continuum of micro-polar type, a finite element analysis was performed for a granular medium under a surface boundary pressure [32]. It has been found that particle rotations play an important role in the amount of deflection and pattern of stress distribution. The rolling and twisting inter-particle stiffness are responsible for the transmit of couple stress in

the media. The effects of particle rotation are not displayed in the usual classic continuum models.

4.2 High-gradient Model

Using the high-gradient constitutive law, the derived governing equation for the wave propagation in granular media is a fourth-order partial differential equation rather than the usual second-order partial differential equation in classic continuum mechanics. In a one dimensional case, the governing equation of wave propagation is in the following form

$$\rho\, \ddot{u}(x,t) = (\lambda+2\mu)(u''(x,t) + c\, u^{(4)}(x,t)) \tag{16}$$

where the variable c corresponding to the higher-order strain has the unit of length-square, given by $c = C_o r^2$ and $C_o = \frac{2}{7}\left(\frac{5k_n + 2k_t}{3k_n + 2k_t}\right)$.

When the influence of higher gradient behavior is neglected, i.e. c = 0, the wave equation in Eq. (16) is reduced to the usual second-order differential equation of wave propagation as that in the theory of elasto-dynamics. The high-gradient model has recently been used to analyze a boundary value problem of wave propagation in a bar of finite length fixed at one end and subjected to a dynamical traction at the other.

Solutions of the higher-order wave equation show several distinctive phenomena of waves in granular media that can not be obtained from solutions of the usual second-order wave equation [35]:

(1) granular material is a natural filter, in which short length waves and high frequency waves can not transmit through. The minimum admissible wave length for non-zero phase velocity is approximately two times of particle size for longitudinal wave, and 1.5 times of particle size for transverse wave. Inter-particle stiffness has a significant effect on the ranges of wave lengths and frequencies in which the wave can propagate.

(2) In the classic continuum theory, the wave excited by a dynamic impact is a simple compression wave propagating along the bar with a constant peak stress. In the high-gradient granular media, the solutions show a decay of the peak of stress wave propagating along the bar. This phenomenon is similar to the decay of peak contact force observed from experiments and from Discrete Element Analysis for a chain of disks [36, 37]. The decay of the peak stress and the dispersion of waves are influenced by the size of particles.

5. SUMMARY

This article presents a brief review of recent work on granular mechanics addressed at three different levels of scale: (1) contact laws at the micro-scale level, (2) constitutive laws at the meso-scale level, and (3) boundary value problems at the macro-scale level. Emphasis of the review is focused on the

recent development in the area of microstructural continuum method.

Granular media in nature is a discrete system in which discontinuous deformation occurs at inter-particle contacts. At the meso-scale level, the microstructural continuum method perceives the discontinuous system as an equivalent continuous system. The MCM approach aims to develop a meso-scale continuum theory that includes the effects of discontinuous deformation at the micro-scale of a granular medium.

This approach is useful in providing a conceptual link between discontinuous and continuous systems which is essential for a fundamental understanding of the plasticity and damage in continuum mechanics. This research area is a fruitful field with very little exploration. Cultivation of this field is in a great need from investigators with different disciplines and skills. The modest progress achieved in the recent years may be served as foundations for further development towards a physically realistic framework for the modelling of granular materials.

Acknowledgements

Results of this paper are derived from several research projects on which the author has worked in the past years under the support of the U.S. Air Force Office of Scientific Research and the U.S. National Science Foundation.

REFERENCES

1. Mindlin, R. D., and Deresiewicz, H. (1953), "Elastic Spheres in Contact under Varying Oblique Forces," *Journal of Applied Mechanics*, ASME, Vol. 20, No. 3, pp. 327-344.
2. Walon, K. (1987), "The Effective Elastic Moduli of a Random Packing of Spheres", *Journal of Mechanics and Physics of Solids*, Vol. 35, No. 3, pp. 213-22
3. Johson, K. L. (1985), "Adhesion at the Contact of Solids," *Theoretical and Applied Mechanics*, Ed. W. T. Koiter, pp. 133-143, Amsterdam: North Holland Publishing Company.
4. Thornton C. (1991), "Inter-particle sliding in the presence of adhesion," J phys. D: *Appl. Phys.*, Vol. 24, pp. 1942-1946.
5. Ng, T. T. (1994), "Numerical Simulations of Granular Soil Using Elliptical Particles," *Computer and Geotechniques*, Vol. 16, No. 2, pp 153-169.
6. Adams M.J. and Edmondson, B. (1987), "Forces between particles in continuous and discrete liquid media," *Tribology in Particulate Technology*, ed. by B. J. Briscoe and M.J. Adams, Adam Hilger.
7. Dvorkin, J., Nolen-Hoeksema, R., and Nur, A.(1994), "The Squirt-fow Mechanism: Macroscopic Describtion," *Geophysics*, Vol. 59, No. 3, pp. 428-438.
8. Dvorkin, J., Mavko, G. and Nur, A. (1991). The Effect of Cementation on the Elastic Properties of Granular Material. *Mechanics of Materials*, Vol. 12, pp. 207-217.

9. Dvorkin, J., Nur, A. and Yin, H. (1994). Contact Laws for Cemented Grains: Implications for Grain and Cement Failure. *Mechanics of Materials*, Vol. 18, pp. 351-366.
10. Zhu, H., Chang, C. S. and Rish, J. W. (1995), "Tangential and Normal Compliance for Conforming Binder Contact. I: Elastic Binder," *International Journal of Solids and Structures*, Pergamon Press (Accepted for publication).
11. Zhu, H., Chang, C. S. and Rish, J. W. (1995), "Tangential and Normal Compliance for Conforming Binder Contact. II: Visco-Elastic Binder," *International Journal of Solids and Structures*, Pergamon Press (Accepted for publication).
12. Williams J., and Musto, G. (1993), Editors of the *Proceedings of the Second International Conferences on Discrete Element Methods*, IESL press.
13. Digby, P.J. (1981), "The Effective Elastic Moduli of Porous Granular Rock", *Journal of Applied Mechanics*, ASME, Vol. 48, No. 4, pp. 803-808.
14. Jenkins, J.T. (1988), "Volume Change in Small Strain Axi-symmetric Deformations of a Granular Material", *Micromechanics of Granular Materials*, Eds. M. Satake, and J.T. Jenkins, Elsevier, Amsterdam, The Netherlands, pp. 143-152.
15. Chang, C.S. (1988), "Micromechanical Modelling of Constitutive Equation for Granular Material," *Micromechanics of Granular Materials*, Edited by J. T. Jenkins and M. Satake, Elsevier Science Publishers, pp. 271-278.
16. Chang, C. S., and Liao, C. L. (1994), "Estimates of elastic modulus for media of randomly packed granules," *Applied Mechanics Reviews*, ASME, Vol. 47, No. 1, Part 2, pp. 197-206.
17. Chang, C. S., and Gao, J. (1995), "Kinematic and Static Hypotheses for Constitutive Modelling of Granulates Considering Particle Rotation," *Acta Mechanica*, Springer-Verlag (in press).
18. Chang, C.S., Chao, S. C., and Chang, Y. (1995), "Estimates of Mechanical Properties of Granulates with Anisotropic Random Packing Structure," *International Journal of Solids and Structures*, Pergamon Press, Vol. 32, No. 14, pp. 1989-2008.
19. Chang, C. S., Kabir, M., and Chang, Y. (1992), "Micromechanics Modelling for the Stress-Strain Behavior of Granular Soil - II: Evaluation," *Journal of Geotechnical Engineering*, ASCE, Vol. 118, No. 12, 1975-1994.
20. Chang, C. S., Sundaram, S. S., and Misra, A., "Initial Moduli of Particulated Mass with Frictional Contacts," *International Journal for Numerical and Analytical Methods in Geomechanics*, John Wiley and Sons, Vol. 13, No. 6, 1989, pp. 626-641.
21. Chang, C. S., Misra, A., and Sundaram S. S., "Properties of Granular Packings under Low Amplitude Cyclic Loading," *International Journal of Soil Dynamics and Earthquake Engineering*, Vol. 10, No. 4, 1991, pp. 201-211.
22. Chang, C.S., "Inter-particle Properties and Elastic Moduli for Sand," *Mechanics of Granular Material*, Published by International Society of Soil Mechanics and Foundation Engineering, 1994, pp. 7-14.

23. Chang, C. S., Misra, A., and Acheampong, K. (1992), "Elastoplastic Deformation of Granulates with Frictional Contacts," *Journal of Engineering Mechanics*, ASCE, Vol. 118, No. 8, pp. 1692-1708.
24. Chang, C. S., Chang, Y., and Kabir, M. (1992), "Micromechanics Modelling for the Stress-Strain Behavior of Granular Soil - I: Theory," *Journal of Geotechnical Engineering*, ASCE, Vol. 118, No. 12, pp. 1959-1974.
25. Liao, C. L., Chang, T., and Young, D. (1995), "Elastic-plastic Constitutive Modelling of Granular Assembly," *International Journal of Solids and Structures*, Pergamon Press, Vol. 32, No. 8, pp. 1121-1133.
26. Chang, C. S., Misra, A., and Acheampon, K., "Elastoplastic Deformation of Granulates with Frictional Contacts," *Journal of Engineering Mechanics*, ASCE, Vol. 118, No. 8, 1992, pp. 1692-1708.
27. Misra, A. and Chang, C. S. (1993), "Effective Elastic Moduli of Heterogeneous Granular Solids," *International Journal of Solids and Structures*, Pergamon Press, Vol. 30, No. 18, pp. 2547-2566.
28. Chang, C. S., and Chang, Y. (1995), "Green's Function for Elastic Medium with General Anisotropy," *Journal of Applied Mechanics*, ASME, ASME, Vol. 62, No. 3, 1995, pp. 573-578.
29. Chang, C. S. (1993), "Micromechanics Modeling for Deformation and Failure of Granulates with Frictional Contacts," *Mechanics of Material*, Elsevier Science Publishers, Amsterdam, Vol. 16, No. 1-2, pp. 13-24.
30. Chang, C. S., and Liao, C.,"Constitutive Relations for Particulate Medium with the Effect of Particle Rotation," *International Journal of Solids and Structures*, Vol. 26, No. 4, 1990, pp. 437-453.
31. Chang, C. S. and Ma Lun., "Modelling of Discrete Granulates as Micropolar Continuum," *Journal of Engineering Mechanics*, ASCE. Vol. 116, No. 12, 1990, pp. 2703-2721.
32. Chang, C. S., and Ma, L. (1992), "Elastic Material Constants for Isotropic Granular Solids with Particle Rotation," *International Journal of Solids and Structures*, Pergamon Press, Vol. 29, No. 8, pp. 1001-1018.
33. Chang, C. S., and Gao, J. (1995), "Second-Gradient Constitutive Theory for Granular Material with Random Packing Structure," *International Journal of Solids and Structures*, Pergamon Press, Vol. 32, No. 16, pp. 2279-2293.
34. Chang, C. S. and Gao, J. (1995), "Non-linear Dispersion of Plane Wave in Granular Media," *International Journal of Non-linear Mechanics*, Pergamon Press, Vol. 30, No. 2, pp. 111-128.
35. Gao, J., and Chang, C. S., "Wave Propagation in Granular Material Using High Gradient Theory," *Micromechanics and Constitutive Modeling of Composite Materials*, ASME Applied Mechanics Division Publication, Vol. 202, pp. 35-47. (Edited by H. Zbib and I. Demir).
36. Shukla, A., and Sadd, M.H., and Mei, H. (1991), "Experimental and Computational Modelling of Wave Propagation in Granular Materials", *Exp. Mech.* Vol. 30, p. 377-381.
37. Sadd, M. H., Tai, Q. and Shukla, A. (1992), " Contact Law Effects on Wave Propagation in Particulate Materials Using Distinct Element Modelling", *Intern. J. of Nonlinear Mechanics*, Vol. 28, pp. 251-265.

A 3D Constitutive Model for Rock Joints and DEM Analysis

L. Jing

Royal Institute of Technology, Stockholm, Sweden

1. INTRODUCTION

Discontinuities in rocks play a dominant role in the performance of engineering structures of fractured rocks. Proper understanding of the mechanical behaviour of rock joints is often the key factor considered in the numerical analyses of rock engineering problems. Since closed-form solutions do not exist in general for problems of fractured rocks, numerical methods must be used to establish and solve the governing equations with properly defined initial and boundary conditions. The constitutive equations (or laws) for rock joints define the changes of contact stresses with changes of relative displacements of the two opposite surfaces of a rock joint, using a set of material properties and under certain assumptions. These constitutive equations are also often called models, or laws, of rock discontinuities and are important part of any numerical methods applied for fractured rocks, especially the Discrete Element Method (DEM).

Discrete Element Method (DEM) is a family of numerical tools which represent the fractured rocks as an assemblage of discrete rock blocks interfaced by joints. According to the principles used in formulating and solving the governing equations, the DEM can be divided into two groups: the explicit DEM and implicit DEM. The explicit DEM group, represented by the now widely applied computer codes UDEC and 3DEC [1, 2], uses a central finite difference scheme to solve the equations of motions of the blocks through a time marching process. Both the external forces and contact forces between blocks, which are determined by applying the proper constitutive models of rock joints, are calculated at each time step to determine the displacements and strain rates of blocks for the next time step. No matrix equation is needed for this approach and the integration of constitutive models of joints over the displacement paths is straightforward with no necessity to use iteration. The equilibrium of the system is, however, conditional to the choice of time step and damping terms used. The implicit group, represented by Discontinuous Deformation Analysis [3], uses the minimum potential energy principle to derive the equations of motion of blocks in matrix form, and solves this matrix equation by using an optimal storage algorithm of non-zero elements by graph theory. The equilibrium of the system by this approach is unconditional, but iteration must be used for integration of the constitutive models for rock joints over the displacement paths. In either case, the constitutive models for rock joints play a key role for determination of contact forces (or stresses) and displacement paths of blocks, are integral parts of the governing equations of the whole system, and must be properly defined and implemented.

In this paper, a three-dimensional constitutive model for rock joints are developed, based on the theory of plasticity and special characteristics of rock joints discovered in laboratory tests [4, 5, 6]. The model is then implemented in a 3D DEM code, verified against labotary test results and appkied to study the effects of fraction anisotropy of rock joints on the stability of a mine stope. The joint surface is assumed to be macroscopically planar and only the isothermal condition is considered. The convention of summation over repeated subindices is adopted unless stated otherwise. The tensile stress is taken as positive.

2. SPECIAL CHARACTERISTICS OF ROCK JOINTS IN THREE-DIMENSIONS

In general, problems with rock joints are three-dimensional problems. Two-dimensional idealization is rarely realistic for practical problems. One of the three-dimensional properties of a rock joint is the anisotropy in its shear strength and deformability. To characterize the three-dimensional effects, a local coordinate system is defined on the joint surface so that the x-axis is in plane and along the strike, z-axis is also in-plane but along the plunge (upward positive) and n-axis is along the outward normal direction of the surface (Fig. 1a). The experimental results reported in [4] and [7] show that the shear strength and shear stiffness of rough rock joints are both anisotropic in the nominal planes of the joints, and depend on the magnitude of normal stress (Fig. 1c). Assuming that the total friction angle of a rock joint equal to the sum of an isotropic residual friction angle, ϕ_r, and an asperity angle α_θ, in a particular direction angel θ, measured from x-axis, an elliptical approximation of asperity angle (Fig. 1b), written as [4]

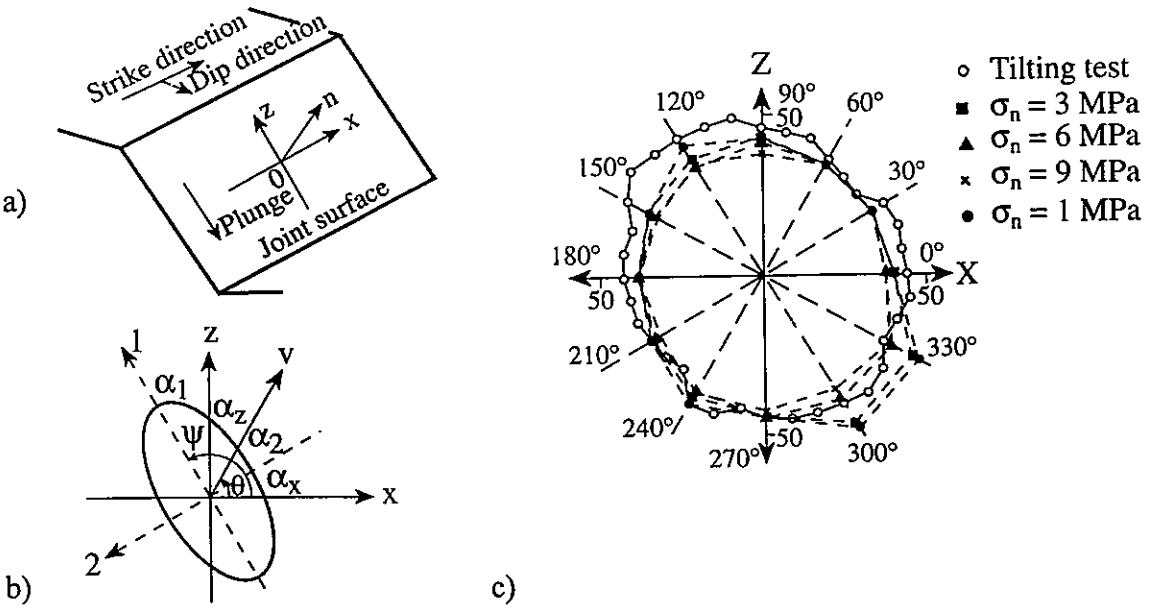

Fig. 1 a) Local coordinate system, b) polar diagrams of the friction angle (c) ellipse of the asperity angle [4].

$$\alpha_\theta = \sqrt{\left[C_1 \cos\psi - C_2 \sin\psi\right]^2 + \left[C_1 \sin\psi + C_2 \cos\psi\right]^2} \tag{1}$$

where $C_1 = \alpha_1 \cos(\theta - \psi)$, $C_2 = \alpha_2 \sin(\theta - \psi)$, and α_1 and α_2 are the asperity angles in the principal directions, respectively. Similar anisotropy was also observed for shear stiffness, k_θ, and an elliptical expression was proposed for shear stiffness,

$$k_\theta = \sqrt{\left[B_1 \cos\psi - B_2 \sin\psi\right]^2 + \left[B_1 \sin\psi + B_2 \cos\psi\right]^2} \tag{2}$$

where $B_1 = k_1 \cos(\theta - \psi)$, $B_2 = k_2 \sin(\theta - \psi)$,and k_1 and k_2 are the shear stiffness in the principal directions for shear stiffness ellipse, respectively. The shear stiffness was found to increase with the increase of the normal stress magnitude during shear tests and this effect was approximated as

$$k_i = k_i^m \left(2 - \frac{\sigma_n}{\sigma_c}\right)\frac{\sigma_n}{\sigma_c} \tag{3}$$

where k_i^m is the maximum value of shear stiffness, k_i, in the principal direction i (= 1, 2) and σ_c is the uniaxial compressive strength of the rock material and σ_n is the normal stress of the joint..

The roughness of the joint surface, represented by the asperity angle α_θ, will undergo a monotonic degradation due to damage accumulated on the asperities during the deformation process. This degradation is represented by an exponential law [8], given in the principal components of the asperity angles as [4, 6]

$$\begin{cases} \alpha_1 = \alpha_1^0 \exp[-d_m(\sigma_n/\sigma_c)W^p]\left|\cos(\theta - \psi)\right| \\ \alpha_2 = \alpha_2^0 \exp[-d_m(\sigma_n/\sigma_c)W^p]\left|\sin(\theta - \psi)\right| \end{cases} \tag{4}$$

where α_i^0 (i = 1,2) are the initial principal asperity angle, d_m is a material constant and W^p is the dissipated energy accumulated over the deformation paths.

The normal stiffness of the joint, k_n, is derived from a hyperbolic function between normal stress and normal displacement [9], given as

$$k_n = k_n^0 / (1 - u_n / u_n^m)^2 \tag{5}$$

where k_n^0 is the initial normal stiffness, u_n is the normal displacement of the joint, and u_n^m is the maximum closure.

The peak shear stress,σ_θ^p, of the joint, taking as the limiting constraint for the shear stress in the model formulation, is given as [4]

$$\sigma_\theta^p = \sigma_n \tan(\phi_r + \alpha_\theta) \tag{6}$$

where θ is the shear direction angle and is equal to 0 in positive x-direction and $\pi/2$ in positive z-direction.

The equations (1) - (6) forms the physical basis for the formulation of the constitutive model for rock joints developed in the next section.

3. MODEL FORMULATION AND VERIFICATION

The formulation of constitutive models for rock joints follows either an empirical approach or a theoretical approach. By the empirical approach, an model is defined by fitting the laboratory test results to mathematical functions, using usually the total stress and displacement components as the basic variables. The empirical models thus established usually have simpler functional forms, but have two major shortcomings: i) the models may not conform with some physical laws commonly accepted as axioms in physics, such as the second law of thermodynamics, and ii) the range of validity of material constants in the empirical models cannot be completely covered by laboratory tests. Extrapolation of the material constants often needs to be made and this may introduce unpredictable uncertainties. The theoretical approach, on the other hand, is based on the point of view that basic physical laws must be obeyed. The model is usually formulated within the framework of one branch of mechanics such as theory of plasticity, damage mechanics, theory of elastic contacts, etc. The fundamental laws in these branches of mechanics are then obeyed in the formulation. The increments of stress and displacements are usually used as the basic variables. However, models formulated in this approach may suffer from the limitation that no perfect theory exists today which can represent all aspects of the rock joint behaviour perfectly. Certain measures must be taken to ensure that the model behaviour is in agreement with test results when simulating laboratory test conditions. Therefore, a theoretical description with special considerations for characteristics of rough rock joints observed during experiments is a more reasonable approach. In this paper, the non-associative plasticity is used as a mathematical basis for developing a general solid interface model, and the mathematical functions representing special characteristics of three-dimensional rock joints are then introduced to yield a special model for three-dimensional rough rock joints. The second law of thermodynamics is used to limit the values of material constants used in the model to ensure that energy is dissipated through the deformation process.

A general model is developed, using a slip function F and a sliding potential Q, written

$$F = \left[(\sigma_x/\mu_x)^2 + (\sigma_z/\mu_z)^2\right]^{\frac{1}{2}} + \sigma_n - C \tag{7}$$

$$Q = \left[(\sigma_x/\mu_x)^2 + (\sigma_z/\mu_z)^2\right]^{\frac{1}{2}} + \sigma_n \sin\alpha_\theta \tag{8}$$

where σ_x and σ_z are the shear stress components in x and z-direction, respectively, and $\mu_x = \tan(\phi_r + \alpha_x)$, and $\mu_z = \tan(\phi_r + \alpha_z)$ represent the mobilized friction in the respective coordinate directions. The Functions F and Q play similar roles as the yielding function and plastic potential for a plastic solid.

The general model was developed based on an earlier work for two-dimensional problems without using the second law of thermodynamics [10]. The details for the derivation of this model can be seen in [4]. The resultant general model can be given in an incremental form as

$$d\sigma_i = \left(k_{ij} - \frac{k_{ir}\frac{\partial Q}{\partial \sigma_r}\frac{\partial F}{\partial \sigma_p}k_{pj}}{\frac{\partial F}{\partial \sigma_r}k_{rp}\frac{\partial Q}{\partial \sigma_p} + m\sigma_r\frac{\partial Q}{\partial \sigma_r}} \right) du_j \tag{9}$$

where i, j, r, and p have ranges (x, z, n) for three-dimensional model as defined above and (t, n) for two-dimensional model (representing the tangential and normal directions, respectively). k_{ij} is the stiffness tensor, and $d\sigma_i$ and du_i are the increments of stresses and displacements, respectively. The three diagonal elements of k_{ij} are $k_{xx} = k_x$, $k_{zz} = k_z$,, and $k_{nn} = k_n$, representing the normal stiffness and two shear stiffness in x and z-directions, respectively. The other off-diagonal elements are all zero. m is a modulus defining shear strengthening (m>0) and shear-weakening (m < 0), is analog to work-hardening and work-softening in the theory of plasticity and is assumed in this model as

$$m = h_c \sin\alpha_\theta (k_n / Q) \tag{10}$$

where h_c is a material constant. The dissipative energy during the sliding, dW^p, is given by

$$dW^p = \sigma_i du_i^p = \left(\frac{\frac{\partial F}{\partial \sigma_i}k_{ij}du_j}{\frac{\partial F}{\partial \sigma_r}k_{rp}\frac{\partial Q}{\partial \sigma_p} + m\sigma_r\frac{\partial Q}{\partial \sigma_r}} \right) \sigma_i \frac{\partial Q}{\partial \sigma_i} \tag{11}$$

The second law of thermodynamics requires that the entropy production of the sliding system, dE, be positive, i.e.

$$d\mathrm{E} = (d\mathrm{H} + dW^p)/\mathrm{T} \geq 0 \tag{12}$$

where H is the heat source and T is the absolute temperature, respectively. Due to the assumption of an isothermal condition (i.e. without considering the heat source and conversion between the mechanical energy and thermal energy), equation (12) is simplified into

$$dW^p \geq 0 \tag{13}$$

Values of material constants in the model should be restricted by the inequality (13).

After introducing the special functions (1) - (8) and (10), the resultant constitutive model can be written in an explicit, incremental form as

$$\begin{cases} d\sigma_x = \dfrac{1}{R}\left[\left(\xi_z{}^2 k_z + k_n \sin\alpha_\theta\right)k_x du_x - \xi_z\xi_x k_x k_z du_z - \xi_x k_x k_n du_n\right] \\ d\sigma_z = \dfrac{1}{R}\left[-\xi_z\xi_x k_x k_z du_x + \left(\xi_x{}^2 k_x + k_n \sin\alpha_\theta\right)k_z du_z - \xi_z k_z k_n du_n\right] \\ d\sigma_n = \dfrac{1}{R}\left[-\xi_x k_x k_n \sin\alpha_\theta du_x - \xi_z k_z k_n \sin\alpha_\theta du_z + \left(\xi_x{}^2 k_x + \xi_z{}^2 k_z\right)k_n du_n\right] \end{cases} \tag{14}$$

where $\xi_x = \dfrac{\sigma_x}{\mu_x{}^2}\left[\left(\sigma_x/\mu_x\right)^2 + \left(\sigma_z/\mu_z\right)^2\right]^{-\frac{1}{2}}$, $\xi_z = \dfrac{\sigma_z}{\mu_z{}^2}\left[\left(\sigma_x/\mu_x\right)^2 + \left(\sigma_z/\mu_z\right)^2\right]^{-\frac{1}{2}}$, and

$R = \xi_x{}^2 k_x + \xi_z{}^2 k_z + k_n \sin\alpha_\theta + hQ$

The second law of thermodynamics is obeyed when the inequality $h_c > -1$ holds. The joint models was developed for joints under normal stress constraint. To consider effects of deformability of surrounding rocks on the joint behaviour, additional increment of normal stress due to dilatancy and local stiffness of the surrounding rocks should be formulated properly in the criterion of the peak shear stress and the total increment of normal stress.

The three-dimensional model was implemented into a three-dimensional distinct element code 3DEC, and was verified against experimental results. Figures 2 and 3 show the model prediction against experiment results for a cyclic shear test under constant normal stress ($\sigma_n = 2$ MPa) in x and z -directions consecutively.

5. APPLICATION FOR STABILITY ANALYSIS OF A MINE STOPE

A site was selected in the Kiirunavaara Mine, Northern Sweden, to test the potential of the sublevel stoping method for reducing the ore losses and waste dilution, and increasing productivity. The test area is located in the central part of the orebody between level -598 m (drilling level) and -654 m (loading level) (Fig. 4). The three-dimensional Distinct Element Method code 3DEC [11], with the implementation of the developed joint model, was used to analyze the stability of one of the rib pillars of the

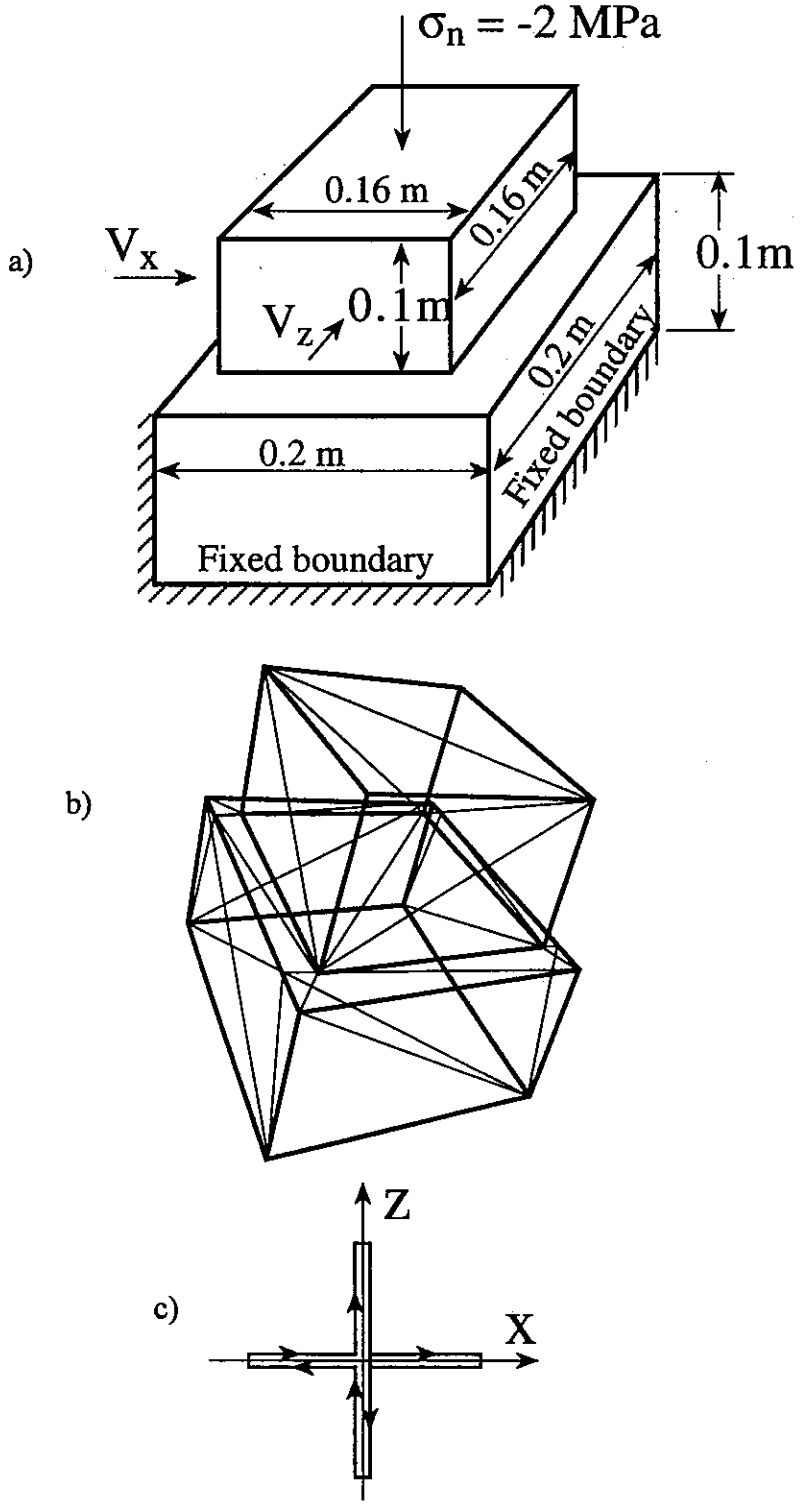

Fig. 2 Simulation of a laboratory shear test with the code 3DEC (Jing, 1990). a) sample size and test conditions; b) discretization of sample blocks; c) shear paths on the joint plane;

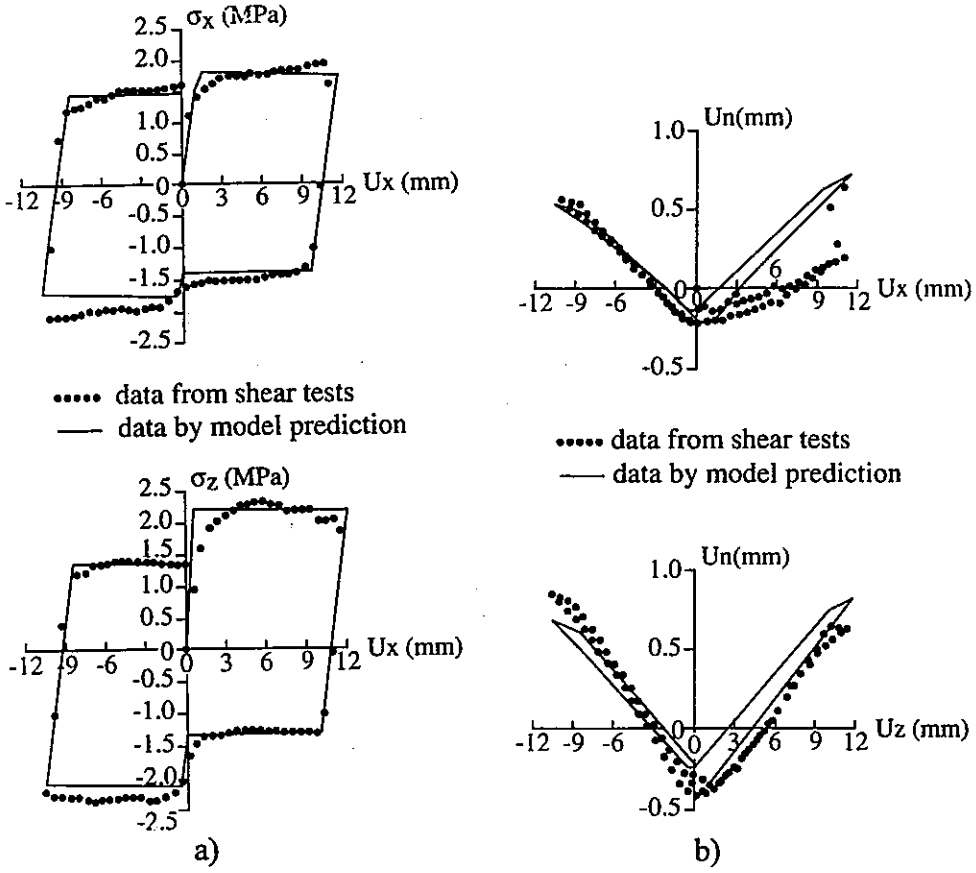

Fig. 3 Comparison of calculated and measured results. a) calculated and measured shear stress during shear in the x and z-directions; b) calculated and measured normal dilatancy during shear in the x and z-directions.

test stopes. Figure 5 shows the configuration of the computational model (called the regional model) used for the analysis, whose boundary stresses were calculated from simulation of a larger global model with in situ stress boundary conditions given by

$$\begin{cases} \sigma_x = 8.0 + 0.04H \\ \sigma_z = 8.9 + 0.036H \\ \sigma_y = -\rho h \end{cases} \tag{14}$$

where H is the mining level (e.g. -654 m), h is the thickness of the overburden and ρ is the unit weight of the rock mass. The coordinate system (see Fig. 4a) is defined that y is the vertical direction, z is horizontal along the strike and x is also horizontal but across the orebody. The test area was divided into four stopes (AD, B, C and E) which are further divided into rooms (AD1, B1, C1 and C1) and crown and rib pillars (AD2, B2, C2 and E2) (Fig. 5). Only primary room B1 is excavated in this simulation to test the stability of pillar B2 to the friction angle anisotropy.

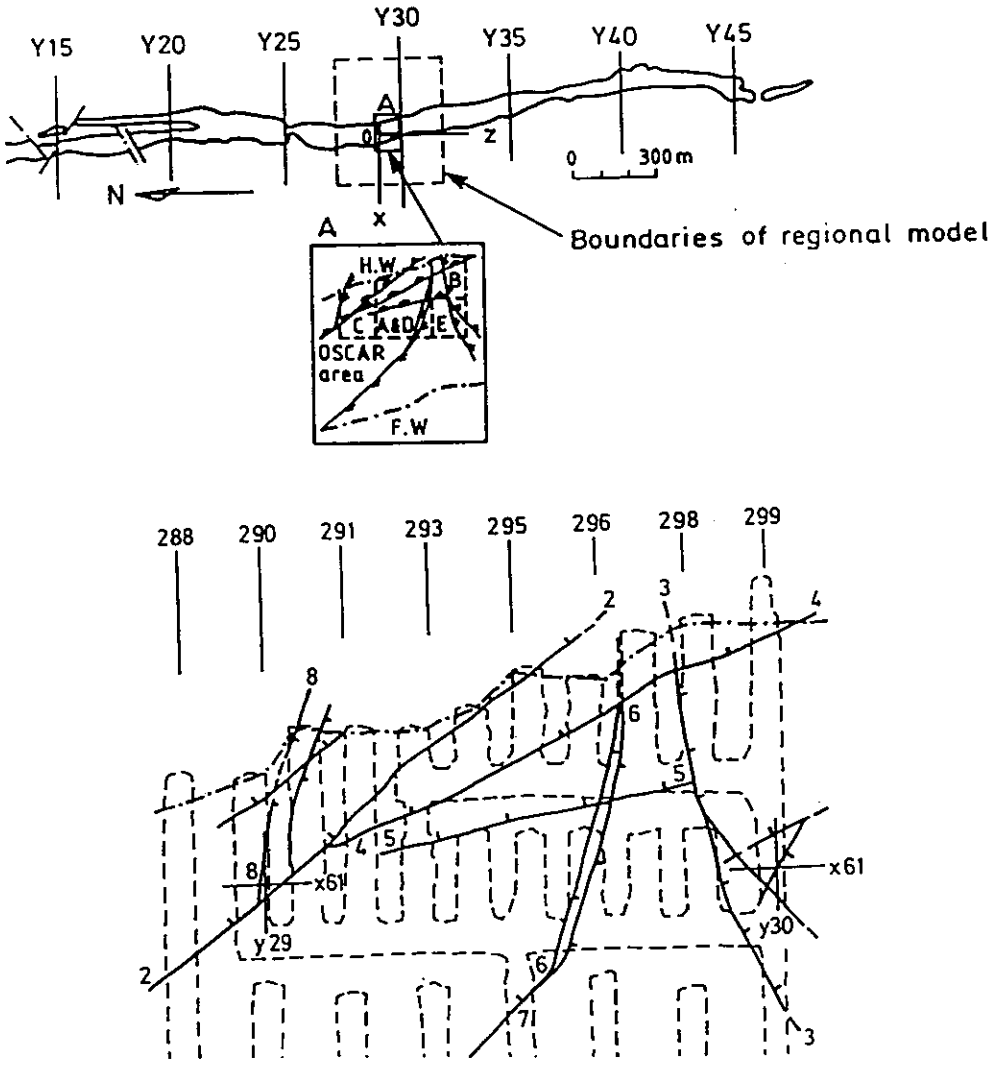

Fig. 4 Location of the test area in the Kiirunavaara orebody and rock structures. a) location of the test area; b) major faults in the test area.

The material properties are given in Table 1. The three values of inclination angle of the asperity ellipse, $\psi = 90^0, 45^o, 0^0$, are used for a sensitivity analysis of the test stopes on the anisotropy of the friction angle of rock faults. The computational model contains 265 blocks and 10048 finite difference elements.

The numerical results show that the magnitudes and patterns of deformations of rock block system of the test stopes are very sensitive to the friction angle anisotropy of the joints. Figure 6 shows the shear displacements in the crown pillar B2 when the calculation stops. The maximum shear displacement is 10.22 mm for $\psi = 90^o$ and 16.45 mm for $\psi = 45^o$, respectively, but 48.61 mm for $\psi = 0^o$ leading to a unstable crown pillar B1. Figure 7 shows the deformation paths of the mass center of a block 94812 in the rib pillar AD2 during mining of the primary room B1. The condition $\psi = 0^o$ again shows the largest deformation magnitude in this nearby stope.

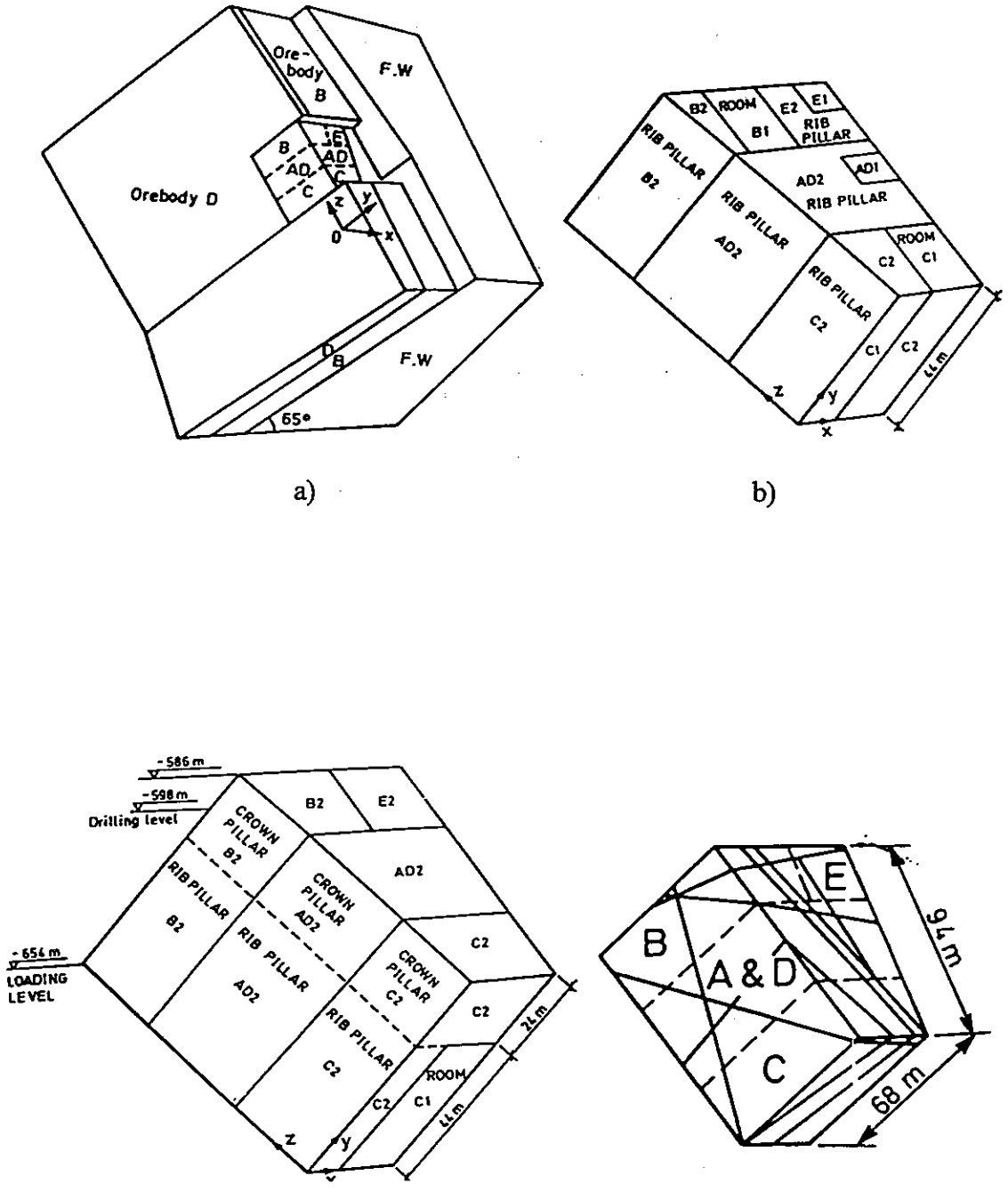

Fig. 5 Configurations of the computational model. a) locations of test stopes in the regional model (the hanging wall is hidden); c) division and dimensions of primary rooms and rib pillars; c) division and dimensions of rib and crown pillars d) discontinuities in the test stopes; [4].

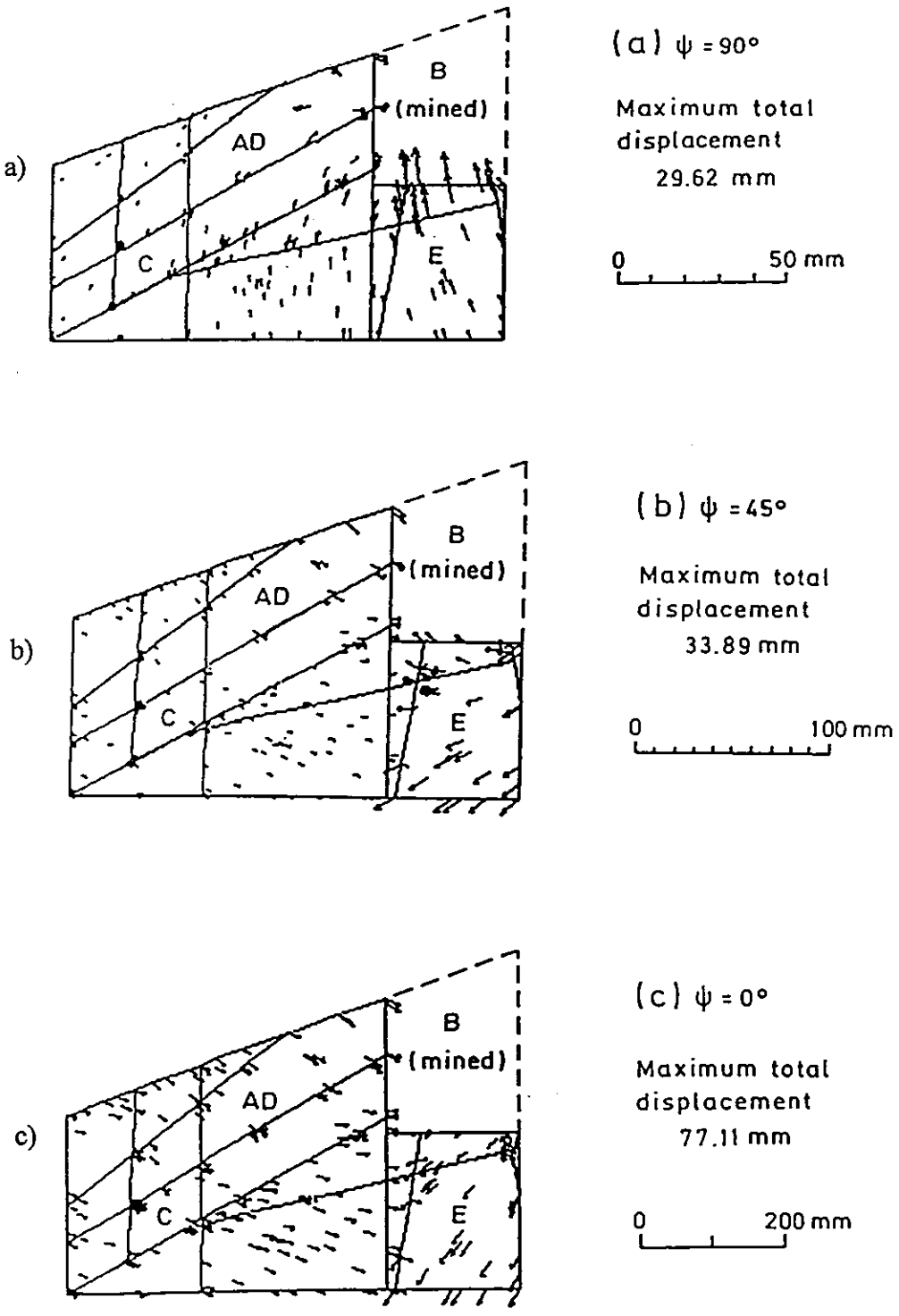

Fig. 6 Projections of total displacement vectors of test stopes after the mining of primary room B1 in the horizontal plane at the drilling level. a) $\psi = 90^{\circ}$; b) $\psi = 45^{\circ}$; c) $\psi = 0^{\circ}$.

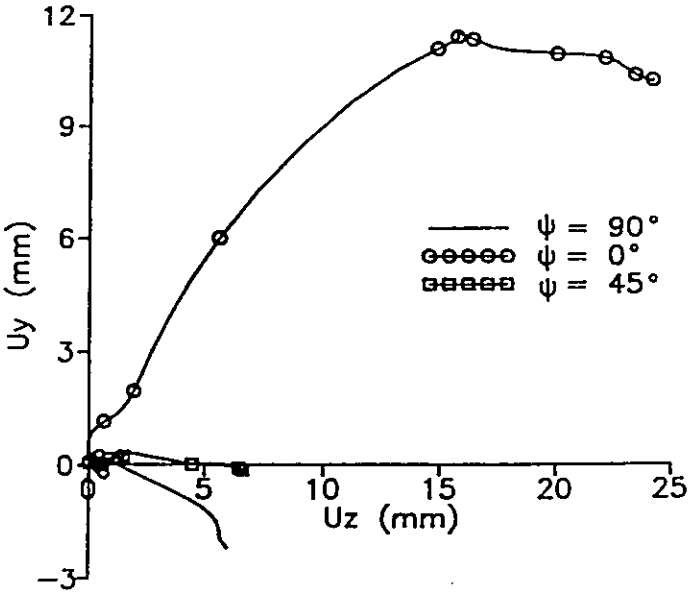

a)

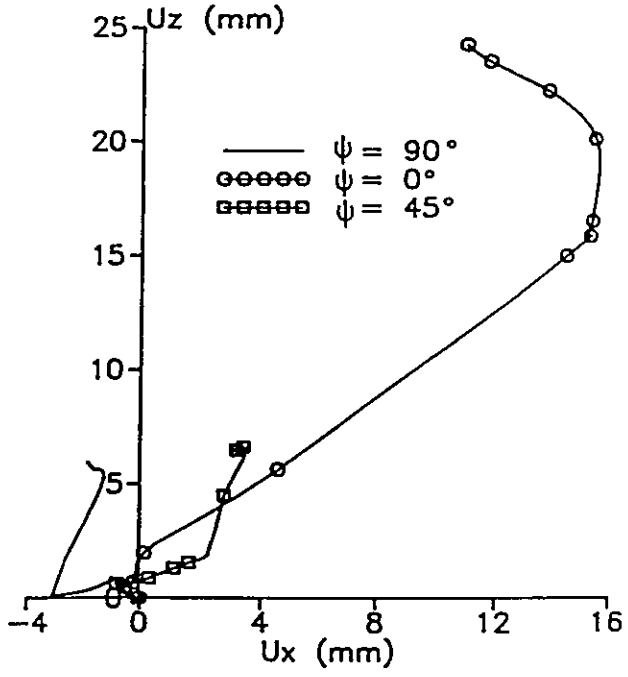

b)

Fig. 7 Displacement paths of the mass center of block 94812 in rib pillar of AD2 during mining of primary room B1. a) vertical displacement Uy versus horizontal displacement Uz; b) horizontal displacement Uz versus horizontal displacement Ux.

Table 1. Material properties

Intact rock properties				
	Orebody (B)	Orebody (C)	Hanging wall	Foot wall
ρ (kg/m^3) (Density)	4500	4500	2700	2700
K (GPa) (Bulk modulus)	32	40	40	40
G (GPa) (Shear modulus)	19	24	24	24
Rock faults properties				
$k_1^m = 0.41\ GPa/m$, $k_2^m = 0.21\ GPa/m$, $k_n \equiv k_n^0 = 0.26\ GPa/m$, $\sigma_c = -100\ MPa$, C (Cohesion) $= 0$, $h_c = 0$, $\phi_r = 20^o$, $\alpha_1 = 10^o$, $\alpha_2 = 3^o$, $\psi = 90^0, 45^o, 0^0$.				

6. CONCLUDING REMARKS

A three-dimensional constitutive model for rock joints is developed, using theory of plasticity as the mathematical framework. Some special characteristics of three-dimensional rock joints, found from laboratory tests, are represented by special mathematical functions in the 3-D joint model. The model was implemented in a three-dimensional Distinct Element code 3DEC, validated against laboratory test results and applied to a sensitivity analysis of the stope stability in the Kiirunavaara Mine, Sweden. The results show that friction anisotropy of joints does have significant impact on the stability of the examined test stopes, and should be considered in the rock mechanics experiments and design and analysis of mine works.

An important issue about the anisotropy in the shear properties of rock joints is that care should be taken when joint samples are taken *in situ*. The strikes and dip directions of the samples should be recorded and marked on the samples so that the samples are "oriented" according to the in situ conditions. The shear test then should be performed in the most probable shear direction if it can be estimated with confidence. Otherwise tilting tests in multiple directions should be performed first to determine the anisotropic characteristics of the shear properties. Shear tests under estimated magnitudes of in situ normal stresses then should be performed in the principal directions of the sample to determine true shear properties. Blind tests without considering probable shear directions may lead to incorrect estimation of shear properties.

Although much effort has been paid to develop constitutive models for rock joints, using either empirical or theoretical approach, the currently available models have still very limited capacities of predicting joint behaviour for complex deformation paths. The major difficulty is the lack of adequate understanding of a number of key factors which significantly affect the joint behaviour. These factors include the characterization of joint roughness, scale effect, dynamic properties, time effects (e.g. creeping properties) and effect of gouge materials. The dominant among them is the unique and quantitative characterization, and the damage evolution, of joint roughness in three-dimensions, which remains to be a still poorly understood aspect and a very challenging research subject. The other factors are closely related to this key uncertainty.

The coupled thermo-hydro-mechanical (T-H-M) behaviour of the rock joints is the most complex, least experimentally investigated, and not fairly understood, especially

under heated conditions. Understanding the coupled T-H-M processes in jointed rock masses is fundamental for many engineering problems, especially for underground radioactive waste repositories and geothermal energy extraction. More sophisticated tests on coupled behaviour of rock joints are needed to further our understanding of coupled T-H-M processes of rock joints, to establish physical laws governing the thermohydraulic phenomena of jointed rock masses, and to develop more reliable and general constitutive models for rock joints. A more detailed presentation and analysis of the experimental study of rock joints for both mechanical and coupled T-H-M processes can be seen in [12].

The Discrete Element Method (DEM) is now a well established research and simulation tool for rock engineering problems. The success of DEM applications depends on basically three conditions: i) proper understanding and adequate data for the geometry of rock joint network in the area under consideration; ii) proper understanding of the constitutive models for both rock joints and rock matrix and reliable data for mechanical properties of rock matrix and joints; and iii) adequate computing capacity (basically memory storage capacity and speed of computers and efficiency of the computer codes) for large scale in situ applications. The first condition is difficult to meet since data base for distributional properties of rock joint networks is usually very inadequate, especially at the beginning of a project. The difficulty may be partially and gradually overcome by accumulation of data volume and increasing of data quality with the progress of the project. Monte Carlo simulation using a large number of realizations of rock joint network, based on the same set of distributional properties of joint network geometry, may also be used to interpret the computational results in a stochastic, rather than only deterministic, sense. However, a complete knowledge of true geometry of joint systems is not possible even at the end of the project. Therefore, uncertainties always remain, although they may be reduced gradually with right steps.

The second condition represents our understanding of the physical behaviour of the fractured rocks today. As mentioned above, although progresses have been made, there is still a long way to go for obtaining reliable constitutive models for rock joints, which represent joint behaviour under any combination of truly three-dimensional loading paths, complex properties (e.g. roughness and scale effects) and environments(e.g. coupled T-H-M processes). There are many critical aspects of the joint behaviour to be investigated, both experimentally and theoretically. Especially important among them are the unique and quantitative characterization of joint roughness, its damage evolution in deformation processes, the gouge material production and effect, and the mathematical representations of these effects in the constitutive models for rock joints.

The constitutive models for rock joints determines the interactive forces and displacement of contacting blocks for DDA or any other DEM method. It is involved in each step of the DEM calculation and determine, to a great extent, the performance and reliability of the DEM codes. Great care should be taken in developing DEM codes to develop, implement and verify constitutive models for rock joints so that the codes can be applied to practical problems on a firm physical foundation.

ACKNOWLEDGMENT

The authors like to express their gratitude to Swedish Rock Engineering Research Foundation (SveBeFo), former Swedish Board for Technical Development (STU) and Swedish Natural Science research Council (NFR) for their financial support to the study reported in this paper.

REFERENCES

1. Cundall, P. A., A computer model for simulating progressive large scale movements in blocky rock systems, *Proc. Int. Symp. Rock Fractures, IRSM, Nancy, I, Paper II-8* (1971).
2. Cundall, P. A., Formulation of a three-dimensional distinct element model - Part I: a scheme to detect and present contacts in a system composed of many polyhedral blocks, *Int. J. Rock Mech. Min. Sic. & Geomech. Abstr. 25 (3), 107-116* (1988).
3. Shi, G., *Discontinuous deformation analysis - a new numerical model for the statics and dynamics of block systems,* Ph.D Thesis, University of California, Berkeley (1988).
4. Jing, L., *Numerical modelling of jointed rock masses by distinct element methods for two and three-dimensional problems,* Ph.D Thesis, 1990:90D, Luleå University of Technology, Luleå, Sweden (1990).
5. Jing, L., E. Nordlund and O. Stephansson, An experimental study on the anisotropy and stress-dependency of the strength and deformability of rock joints. *Int. J. Rock Mech. Min. Sci. & Geomech. Abstr. 29(6), 535-542* (1992).
6. Jing, L., O. Stephansson and E. Nordlund, A 3-D constitutive model for rock joints with anisotropic friction and stress dependency in shear stiffness. *Int. J. Rock Mech. Min. Sci. & Geomech. Abstr. 31 (2), 173-178* (1994).
7. Huang, T. H. and Y. S. Doong, Anisotropic shear strength of rock joints, *Proc. Int. Symp. on Rock Joints. Loen, Norway* (1990).
8. Hutson, R. W., *Preparation of duplicate rock joints and their changing dilatancy under cyclic shear,* Ph.D Thesis, Northwestern Univ., Evanston, Illinois (1987).
9. Bandis, S. C., A. C. Lumsden and Barton, N. R., Fundamentals of rock joint deformation, *Int. J. Rock Mech. Min. Sci. & Geomech. Abstr. 20 (6), 249-268* (1981).
10. Plesha, M. E., Constitutive models for rock discontinuities with dilatancy and surface degradation. *Int. J. Numer. Methods in Geomech. Vol. 11, 345-362* (1987).
11. ITASCA Consulting Group, Inc., *3DEC manual,* (1988).
12. Stephansson, O. and L. Jing, Mechanics of rock joints: experimental aspects. *In Mechanics of Geomaterial interfaces, Sevadurai and Boulon (eds.)*, Elsevier, Amsterdam (1995).

Nonlinear Upper Bound and Lower Bound Analysis Model for Granular Materials

Ching-Lung Liao and Dong-Hwa Yang

National Taiwan Institute of Technology, Taipei, Taiwan, R.O.C

ABSTRACT

This study investigated the failure mechanism between the contact interface and nonlinear stress-strain behavior of granular material from the microscopic viewpoint. Based on the assumptions of an equilibrium condition in the uniform stress field and a compatibility condition in the uniform strain field, two bounds of constitutive law , in terms of modules of elasticity, were found for granular materials.

The stiffness obtained from the static analysis for a real packing of granular materials falls between these two limiting values from both analytical models. In the nonlinear range, the peak stress and post-peak response from the upper bound solution model are always higher than those predicted by the Equilibrium. For example, the experimental data for uniaxial compressive strength of concrete are smaller than the values from the Kinematic model, but higher than those from the Equilibrium model. In conclusion, those two analytical models predict the range of stiffness of granular materials: the Kinematic model gives an upper bound solution, while the Equilibrium a lower bound.

1. INTRODUCTION

Elastic limit is used to check out whether the material yields or not. The yield criteria is based on the stress space or strain space from the macro point of view. But, from the micro point of view, the reason for plasticity is internal micro-cracking in the material , either separating or sliding increasing relative displacement ,stress release , and irreversible plastic deformation. Thus, the failure mechanism on the contact interface has major nonlinear effects for granular material. Concepts of the proposed constitutive

equations presented in this paper are based on the mechanism of slip and separation between particles. The concept of slip has been used by Taylor(1938) to model the stress-strain relationship of face-centered cubic(f.c.c) polycrystalline metals. There are 12 slip systems for f.c.c. crystals, of which only five slip systems are required to define the strain of aggregate produced by slips alone, while it is assumed that there is no volumetric change of strain. Bishop and Hill (1951)[1] found out the plastic strain from the maximum of external work which based on stress space. Chin and Mamnel(1969)[2] , Kallend and Davies (1972)[3] and Dillamore and Katoh (1971)[4] combined the above two methods to build up a plastic models for b.c.c , f.c.c and h.c.p in different types of metals. Bazant and Oh, (1985) [5] and Part, (1987) [6] proposed a microplane model from the particle displacement to find out particle shear strain.

Considering the variation of stress-strain distribution in granular materials, this paper proposes two analytical models: the first, based on the assumption of uniform distribution of strain field to derive the constitutive laws for granular materials, is termed the Kinematics model; the second, based on the uniform distribution of stress variation for the constitutive derivation is termed the Equilibrium model. From the microscopic point of view, the failure of interface between particles generally causes the slipping, spinning and separation of the particles. Including those failure mechanisms in the constitutive models, the proposed two material models can be properly extended from a linear to a nonlinear analysis. In other words, those two models analyze the elasto-plastic behavior of granular materials.

2. FAILURE MECHANISM ON CONTACT INTERFACE

Granular material, such as rock, concrete, ceramics is compressed by high temperature and compression or consists of cohesive material to make a bond force on particle interface. These particle interfaces contain a bond strength which can increase stiffness and strength of granular material. Microscopic observation shows that , when this interface separates or slips, irreversible plastic strain of material is caused. As a result, the failure mechanism on contact interface is due to material nonlinearity. Cundall(1987)[7] Proposed Phenomenological Modal classified three types of failure models : simple tension, rolling torsion and shearing torsion. This paper discussed the failure condition on interface and classifis the failures into two types of failure modes: separating failure mode and shearing failure mode. These two mechanism are shown as follows:

2.1 Separating failure mechanism

When interface separates , this releases tension force causing the particle to be unstable and particles have to move to a new location to reach a new balanced state. The separating displacement Δ^{dc} satisfies the equilibrium condition:

$$\left[K_{ij}^{a'}\right]\Delta_j^{dc} = -f_i^{dc} \tag{1}$$

Where $K_{ij}^{a'}$ is the particle's new stiffness tensor and f_i^{dc} is the force released by the separating bond. Then, release stress $\Delta\sigma^p$ can be:

$$\Delta\sigma^p = \frac{1}{v^a}\sum_{dc} f_i^{dc} x_j^c \tag{2}$$

2.2 Shearing-slip failure mechanism

When particle contact shear force f_s is larger than shear strength $F_{s,max}$ for bond material, slip failure occurs. Then, this residue force on the slip plane is the multiplication of normal contact force f_n and the interface friction factor μ :

$$F_{s,max} = |f_n| * \mu \tag{3}$$

when $f_s < F_{s,max}$ the shear spring k_s is constant. But, $f_s > F_{s,max}$, will cause a slipping failure and decrease the shear spring constant as.

$$k'_s = \frac{F_{s,max}}{\frac{1}{2}\left(\frac{f_s \cdot \Delta^e}{F_{s,max}} + \frac{F_{s,max} \cdot \Delta^e}{f_s}\right)} \tag{4}$$

This slip displacement Δ^{sc} can be shown as:

$$\Delta_i^{sc} = \Delta_i^{t} - \Delta_i^{e} = F_{s,max}\left(\frac{1}{k_s'} - \frac{1}{k_s}\right) \tag{5}$$

The release stress is

$$\delta\sigma_{ij}^p = \frac{1}{V^a}\sum_c \left| f_s^c - f_{s,max} \right| s_i^c x_j^c \tag{6}$$

2.3 Flow chart for the failure mechanism

The failure condition on cohesive inclusion of granular material correlats to the loading direction , such as ,tensile separating, and shearing sliding. If changing the loading condition, e.g. reloading and loading , the contact interface will contact again. But, contact bond strength is changed. Thus, the flow chart of particle contact strength is show as Fig 1.

2.4 Calculation of plastic strain

On micro-scope , this discontinue micro crack (shear crack Δ_i^{sc} or tension crack Δ_i^{cc}) is due to irrecoverable plastic deformation, which observation on macro scope. Defined u_i^p is plastic deformation :

$$\begin{aligned} u_i^p &= \frac{\partial u_i^p}{\partial x_j} x_j + \frac{\partial u_i^p}{\partial x_j x_k} x_j x_k + \cdots \\ &= \varepsilon_{ij}^p x_j + \varepsilon_{ijk} x_j x_k + \cdots \end{aligned} \tag{7}$$

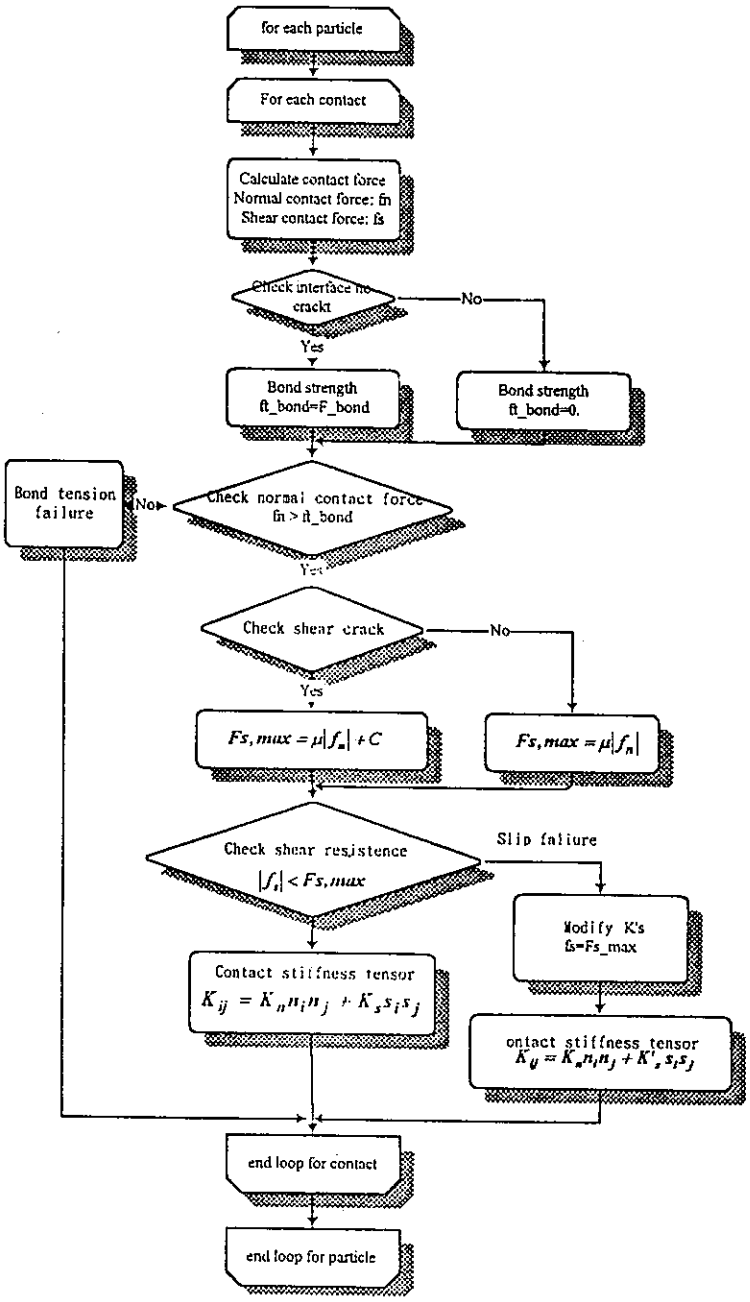

Fig 1.Flow chart for interface failure mechanism

Here, introducing sliding plastic strain tensor ε_{ij}^{sp} and cracking plastic tensor ε_{ij}^{cp}, and according to the least square method [8], the plastic strain tensor can be written as:

$$(\varepsilon_{ij}^{p})^{a} = (\varepsilon_{ij}^{sp})^{a} + (\varepsilon_{ij}^{cp})^{a}$$

$$= \frac{1}{V^{a}}\left(\sum_{c}\Delta_{i}^{sp}x_{n}^{c} + \sum_{c}\Delta_{i}^{cp}x_{n}^{c}\right)A_{jn}^{a} \qquad (8)$$

Then, average plastic strain tensor for the cracked material is :

$$\varepsilon_{ij}^{p} = \frac{1}{V}\sum_{a} V^{a}(\varepsilon_{ij}^{p})^{a} \tag{9}$$

3. NONLINEAR ANALYSIS

3.1 Nonlinear of kinematic model

In small strain conditions, particle strain approaches to micro-element strain and particle strain can be replaced by the average of micro-element strain. In large deformation , slipping or separating cracks on the particle interface make the strain distribution nonuniform and displacement field discontinuous. Hence, the strain distribution is uniform in the small strain condition. Whereas in particle contact interface failure, the displacement is discontinuous . This unrecoverable deformation causes plastic strain. As a result, the particle strain drives into elastic strain and plastic strain. This is the same as parallel arrangement of a spring. If one of the contact interface fails, the total spring will decays but remains stiff . Therefore, this solution of the nonlinear model is upper bound solution for granular materials.

The nonlinearity of granular material includes elastic strain and plastic strain. On microscope, the particle is an elastic body. Thus, the elastic part for granular materials can be written as [8]:

$$\bar{\sigma}_{ij} = \frac{1}{V}\{(\sum_{a} V^{a} A_{ijkl}^{a})\bar{\varepsilon}_{kl} + (\sum_{a} V^{a} C_{ijkl}^{a})\bar{\omega}_{kl}\} \tag{10}$$

and

$$\bar{\tau}_{ij} = \frac{1}{V}\{(\sum_{a} V^{a} D_{ijkl}^{a})\bar{\varepsilon}_{kl} + (\sum_{a} V^{a} F_{ijkl}^{a})\bar{\omega}_{kl}\} \tag{11}$$

This plastic strain of granular material can be calculated from Eq.(9),where Δ_i is plastic slip. Therefore, the calculation flow chart can be draw in Fig. 2.

During interface failure, contact force becomes a released force(δf_i^{cp}) and remains as a residual force (f_i^{ce}). Eq.(6) transforms this release force into release stress($\delta\sigma_{ij}^{p}$). Above all, the stress-strain nonlinear relationship can be drawn as Fig. 3.

3.2 Nonlinear equilibrium model

The equilibrium mode is based on the uniform stress distribution. The relation between particle mean stress and contact force is :

$$f_i^{c} = x_k^{c} A_{kj}^{a} \bar{\sigma}_{ij}^{a} \tag{12}$$

Where f_i^{c} is contact force, x_k^{c} is contact vector related to particle center, and A_{kj}^{a} is fabric tensor,was defined in Yang(1995)[8]. Assembling the flexibility of contact spring of each contact this spring model is similar to a series spring system . If failure at contact interface improves the flexibility of the series spring model and plastic deformation increases rapidly. This micro-structural is fails. As a result, the equilibrium model is a

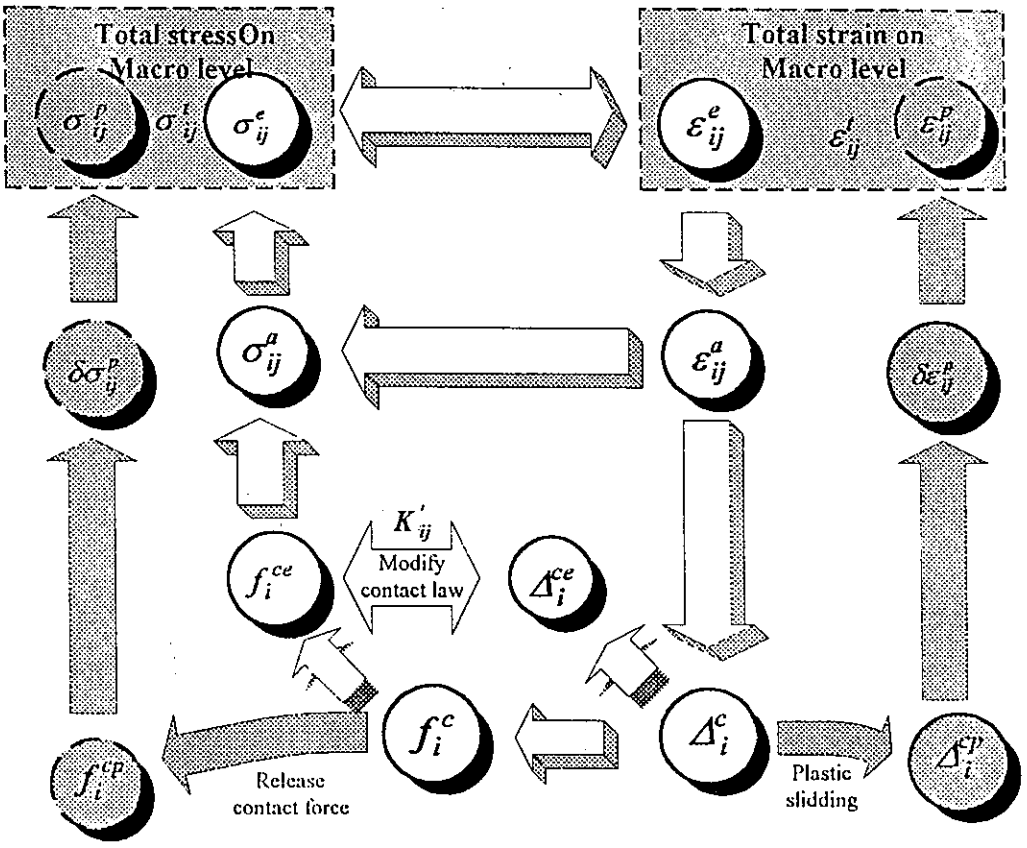

Fig. 2 Kinematic model calculation flow chart.

lower bound solution model. But, in real granular material, it combins like the parallel spring and serial spring models. If one of the contact interface fails, this failed spring is changed from one of a parallel spring into the other failure collecter. Then, micro-structural remains stable. This hybrid model seems huge and complicated. Hence, lower bound solution model combined with a bond of serial spring and parallel to a bond of failure spring, in order to keeps the stability of structure .

The lower bound solution model is based on the stress field is uniform distributionand assums each particle has the same effective stress , σ_{ij}^{e}. It can transform into contact force by fabric tensor.They based on failure criteria, check whether contact interface failed or not, and then, count plastic deformation Δ_i^{cp} and elastic deformation Δ_i^{ce}. Substitute the release contact force into Eq.(9) to count increment of release stress $\delta\sigma_{ij}^{p}$ and to find increment plastic strain $\delta\varepsilon_{ij}^{p}$. The overall nonlinear lower bound solution analysis flow chart is shown as in fig 4.

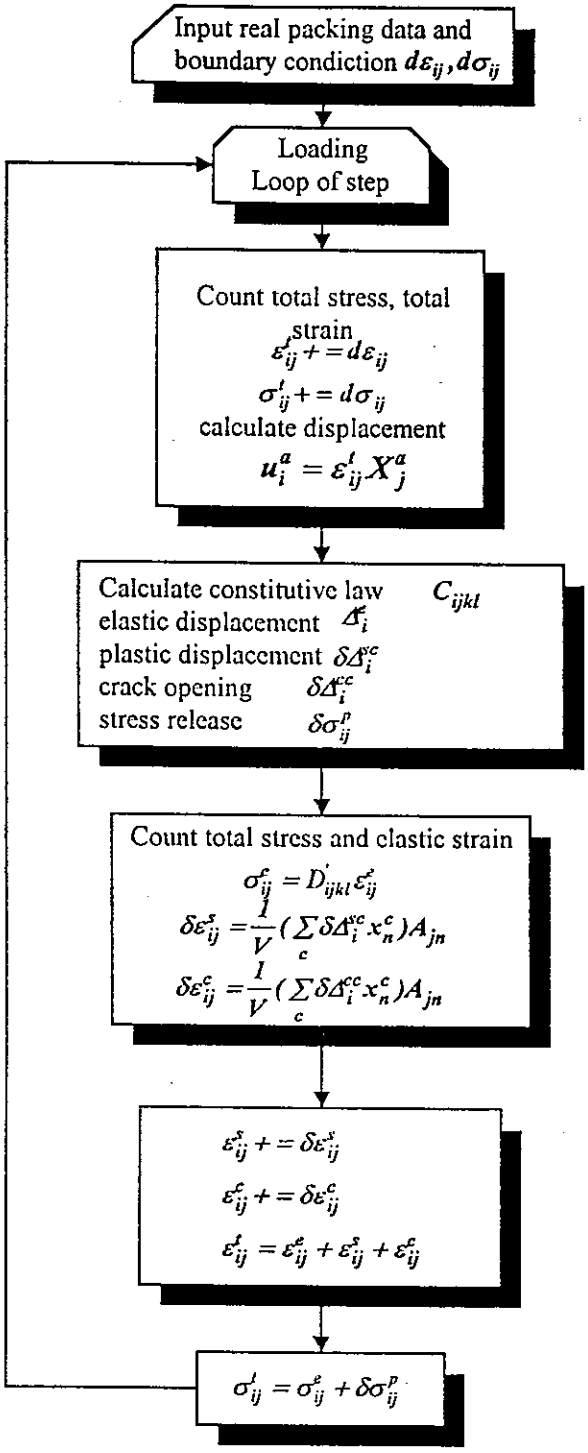

Fig. 3 The nonlinear stress -strain relationship.

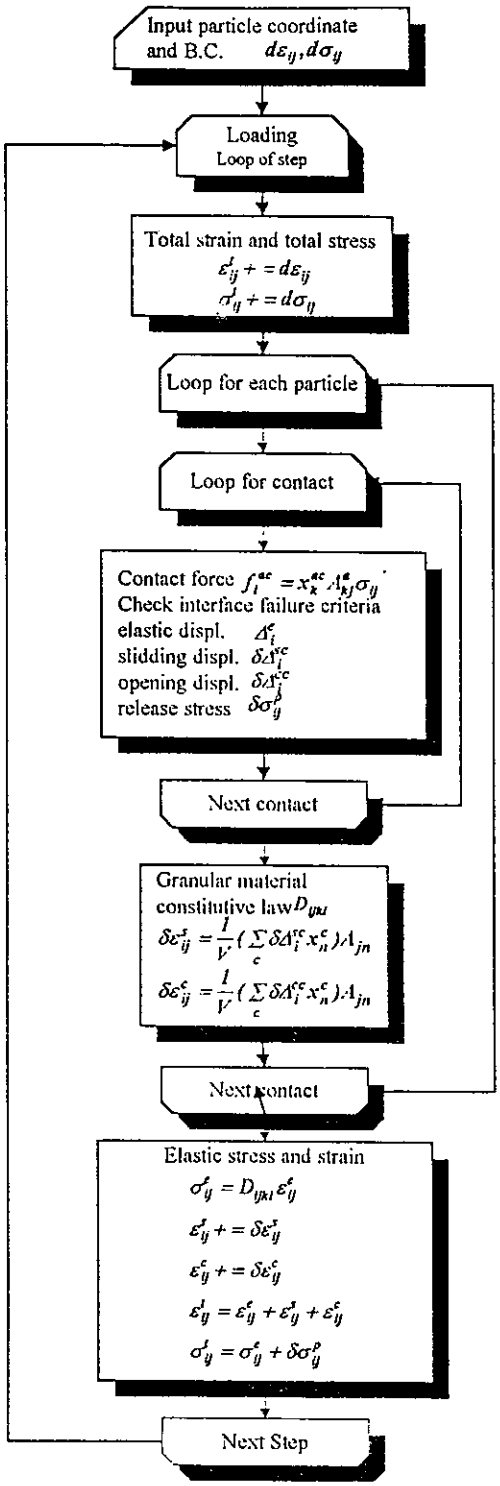

Fig. 4 Nonlinear equilibrium model analysis flow chart.

4. EXAMPLES

This paper shoes an exampleof a mortar sample in the size of 5cm×5cm. The mortar materials includs standard sand of the code ASTM C109 and 190, 1st portland cement, and the water/cement ratio of 0.47. The numerical data for this granular mortar material, uses a 5cm×5cm fill with 916 particles, which diameter average is 1.710mm and standard deviation is 0.365mm. From the isotropic materials relationship , assume the normal contact spring constant k_n equals to 478460kg/cm^2[8]. Fig. 5 .shows the tress-strain relation of the experiment data and upper and lower bound solution.

The other example uses the same mortar reinforced with 5×30mmϕ steel. Fig. 6 shows each stage of the sample during testing from initial conduction proceeding to failure stage. The stress-strain curve is shown in Fig. 7. Observatain shows the kinematic solution is near to experiment data, but the equilibrium solution seems relative soft.

5. CONCLUSION

This discussion of the nonlinear behavior of granular materials represented by kinematic model and equilibrium model we see a range of solution for random packing. The stiffness in the kinematic model based on uniform strain assumption is higher than those based on other models. However, the equilibrium model based on a uniform stress hypothesis is relatively lower than other known solutions. In conclusion , for granular material, regarding the contact properties of the particle, the proposed upper bound solution model and lower bound solution model can provide a bound any range of solutions respectively.

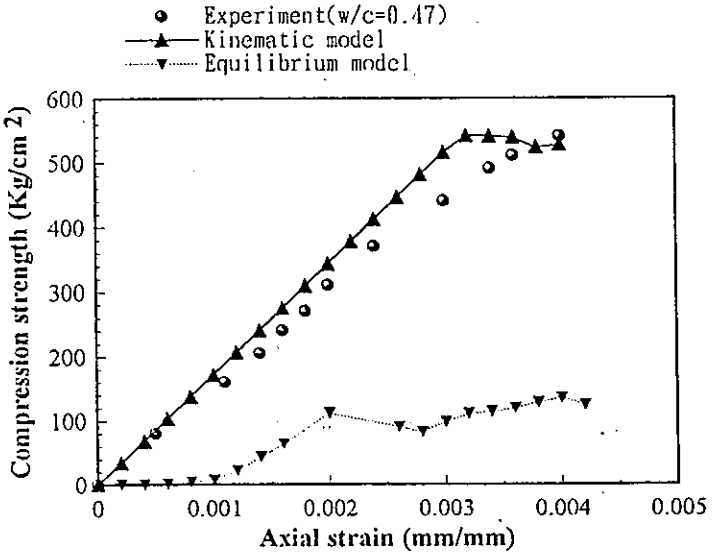

Fig. 5 Comparison of experiment data and simulation data for the stress-strain curve for mortar.

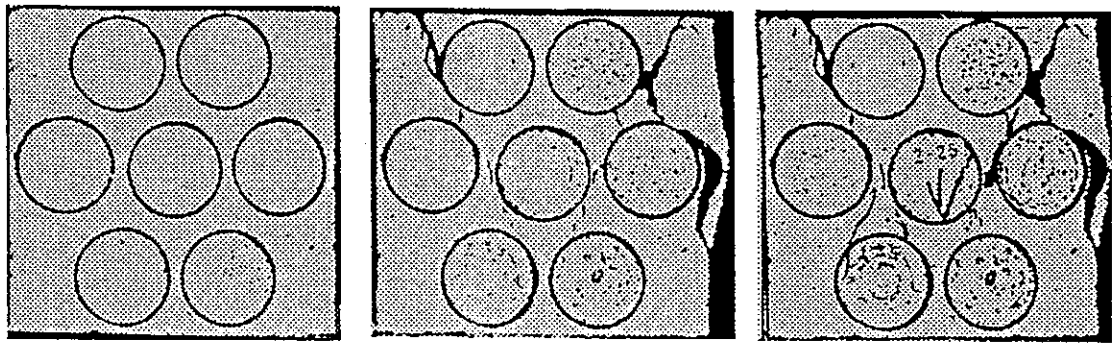

(a) Initial state (b) Yielding state (c) Faliure state

Fig. 6 Reinforced mortar sample.

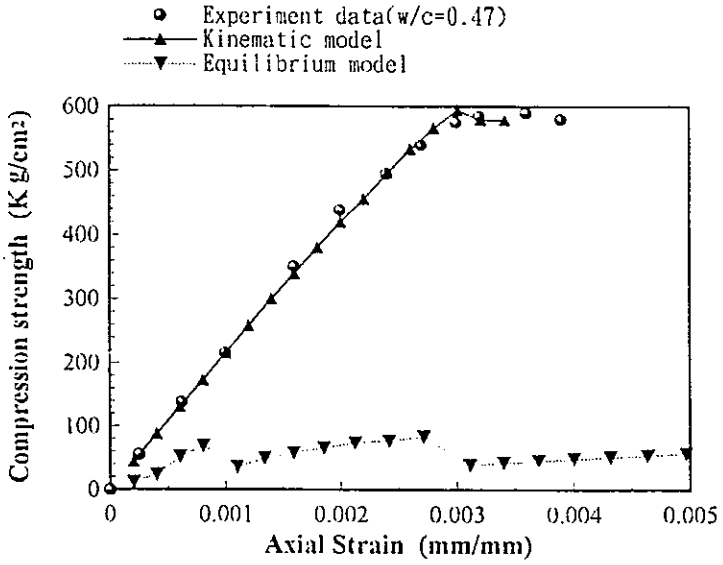

Fig. 7 Compared experiment data and simulation data stress-strain curve for reinforced mortar.

REFERENCE

1. Bishop, J, F. W. and Hill, R. *Phil. Mag.* 42,414,1298.(1951)
2. Chin, G. Y. and Mamnel, W. L. Trans. *AIME*, 245,1211,(1969)
3. Kallend, J. S. and Davies, G. J. ,*Phil, Mag.* ,25, 471 (1972)
4. Dillamore, I. L. and Katoh, H. ,BISRA Rept. No. MG/39#71; *Quantitative Analysis of Texttures* (Proc. of Int. Seminar, Cracow, pp. 315.(1971)

5. Bazant, Z. P. and Oh, B. H. , "Microplane model for Progressive fracture of Conrete and rock", *J. EM ASCE III*, pp.559-582, (1985)
6. Part, P. C.(1987), "Micromechanics modeling and fracture of concrete and geomaterials", *Ph. D. Disseration, Northeestern Universsity*, Evanston, IL.
7. Trent, B.C., Margolin, L.G. , Cundall, P.A. and Gaffeny, E.S.," The Micro-Mechanics of Cemented Granular Materoal, Constitutive Laws for Engineering Materials: Theory and Applicications" , *Elsevier Science* . (1987)
8. Yang, Dong Hwa, "An Investigation of Constitutive Law for Granular Material Based on Equilibrium and Compatibility Models", *Ph. D. thesis, National Taiwan Institute of Techanology, R.O.C.*(1995).
9. Liao, C. L. , Chang, T. P. and Yang, D. H., " Elasto-Plastic Constitutive Modelling of Granular Assembly", *Int. J. solids structures*, Vol. 32, No. 8/9, pp. 1121-1133 (1995).

Discrete Element Analysis for Limit Equilibrium Problems in Geotechnical Engineering

Sao-Jeng Chao[1] and Ching S. Chang[2]

[1] National I-Lan Institute of Agriculture and Technology, Taiwan, R. O. C.

[2] University of Massachusetts, Amherst, MA 01003, U. S. A.

ABSTRACT

Analysis based on Discrete Element Method (DEM) is presented for geotechnical problems within the class of limit equilibrium analysis, such as stability of slopes, earth pressure of retaining walls, and bearing capacity of shallow foundations. Soil mass in the present model is treated as comprising of blocks which are connected by elasto-plastic Winkler-springs. The solution of this method satisfies all equilibrium conditions and is admissible in accordance with the material strength. Formulation of the method is presented. Examples are shown to demonstrate the applicability of the proposed method to the analysis of those geotechnical problems. The advantages of this method over the conventional limit equilibrium analysis are also discussed.

1. INTRODUCTION

In the limit equilibrium analysis of the geotechnical problems, it is conjectured that a mass of soil mobilized along a failure surface. The objective is to obtain a set of stresses on the mobilized surface which satisfies equilibrium conditions and is admissible in accordance with the strength of the material. This set of stresses can be used for practical purposes to assess the instability of the system such as slopes, retaining walls, and shallow foundations.

In most limit equilibrium analyses, the soil mass is divided into a number of slices. The stress on the mobilized surface is estimated employing the conditions of static

equilibrium for each slice. However, the problem is indeterminate and the conditions of static equilibrium are not sufficient for determining the stresses on the mobilized surface. As a result, it is necessary to solve the problem by either neglecting part of the equilibrium conditions, or making assumptions on the location and inclination of inter-slice forces. The shortcoming, inherent with the limit equilibrium method, is unavoidable.

In view of the inept procedures for obtaining the stresses on the mobilized surface used in the conventional limit equilibrium method, more rigorous methods are desirable such as finite element techniques. With the advances in computer technology, extensive computational effort associated with finite element methods is no longer a major concern. However, finite element methods require information about the initial stress state existing in the soil mass, a correct constitutive model, and correct parameters for the constitutive model. This greatly increases the complexity of analysis and the uncertainty of its results.

The analytical model presented in this paper falls within the general class of discrete element model (Cundall [1], Shi [2], and Barbosa and Ghaboussi [3,4]). The specific aim of this paper is to employ a more direct and simple approach along the line of limit equilibrium method. At limit condition, the soil mass is viewed as discrete blocks sliding along the failure surface. The present approach treats the interfaces between blocks to be of elasto-plastic nature. This model, a slight extension of the conventional limit equilibrium analysis, permits a solution that satisfies all equilibrium and compatibility conditions. A discussion of the applicability of this model in the analyses of slope stability, earth pressure, and bearing capacity can be also found in the references by Chang [5] and Chang and Chao [6,7]. Compared with other discrete element methods, such as those used by Cundall and Shi in the analysis for movement of rock blocks, the present method is different in concept in that it is used in connection with the limit equilibrium analysis for soil mass.

In what follows, formulation of the present method is presented. Examples for slopes, retaining walls, and shallow foundations are shown to demonstrate the usefulness of this method. The advantages of this method over the conventional limit equilibrium analysis are also discussed.

2. DISCRETE ELEMENT METHOD FOR SOIL AT LIMIT CONDITIONS

2.1 Interface Between Blocks

To avoid the shortcoming of the conventional limit equilibrium method, the present method accounts for the compatibility between blocks so that sufficient equations can be provided for solving the problem. For this purpose, each block and its neighboring blocks are imagined to be linked together by Winkler-springs as shown in Fig. 1. One set of springs is in the normal direction to simulate the normal stiffness . The other set is in the shear direction to simulate the sliding resistance at the interface. Behavior of the normal and shear springs is elasto-plastic as shown in Fig. 2. The normal springs do not yield in compression but yield in tension with a tensile capacity (tension cut-off). The shear springs yield when the shear strength is reached.

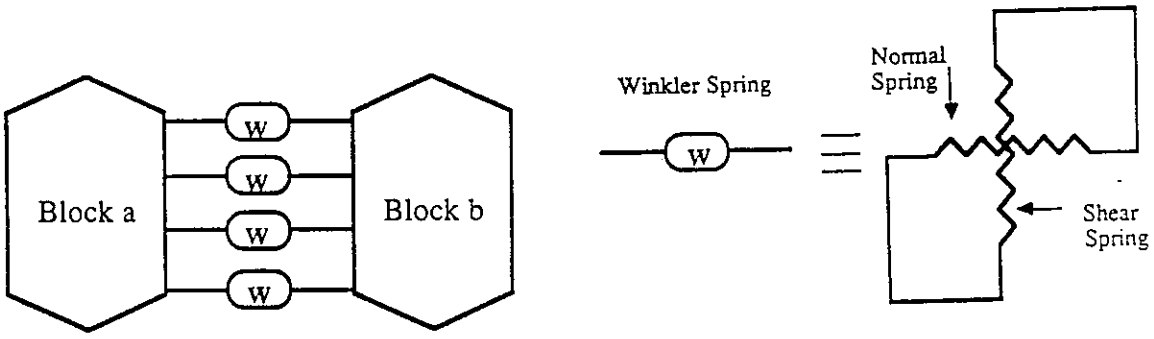

Figure 1. Schematic figure of Winkler-springs at interface between two blocks

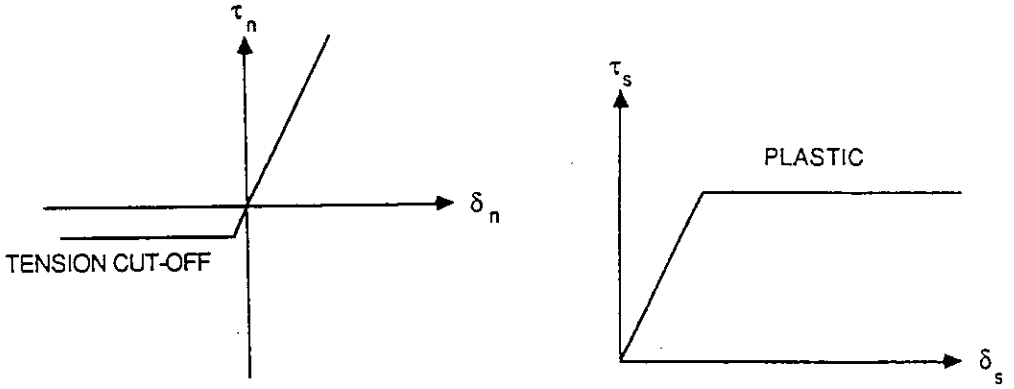

Figure 2. Behavior of normal and shear Winkler-springs

2.2 Method of Analysis

Formulation of the present method follows that of previous research (Chang and Misra [8]) on the mechanics of discrete particulates. Let u_i^a, u_i^b, and ω^a, ω^b represent the translations and rotations of block A and block B. Let point P be the middle point at

the interface between the blocks as shown in Fig. 3. The relative displacement vector representing displacements and rotation of block B relative to block A, at point P, is expressed as follows:

$$\begin{Bmatrix} \Delta_x^P \\ \Delta_y^P \\ \Delta_\omega^P \end{Bmatrix} = [R^b] \begin{Bmatrix} u_x^b \\ u_y^b \\ \omega^b \end{Bmatrix} - [R^a] \begin{Bmatrix} u_x^a \\ u_y^a \\ \omega^a \end{Bmatrix} \tag{1}$$

where

$$[R^b] = \begin{bmatrix} 1 & 0 & -r_y^{bp} \\ 0 & 1 & r_x^{bp} \\ 0 & 0 & 1 \end{bmatrix} \; ; \quad [R^a] = \begin{bmatrix} 1 & 0 & -r_y^{ap} \\ 0 & 1 & r_x^{ap} \\ 0 & 0 & 1 \end{bmatrix}$$

and r_i^{ap} is the vector joining the centroid of the block A to point P. If, however, the block B is immobile the values of u_x^b, u_y^b, and ω^b are taken to be zero.

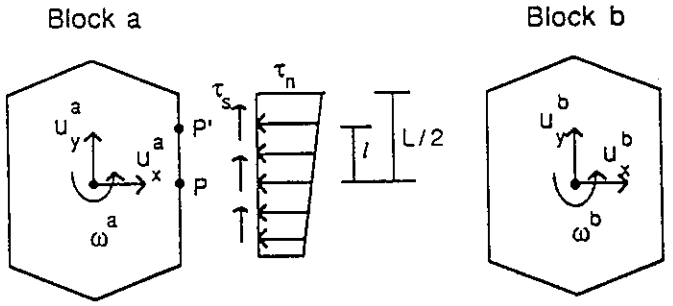

a. Shear and normal stresses between adjacent blocks due to their relative movement.

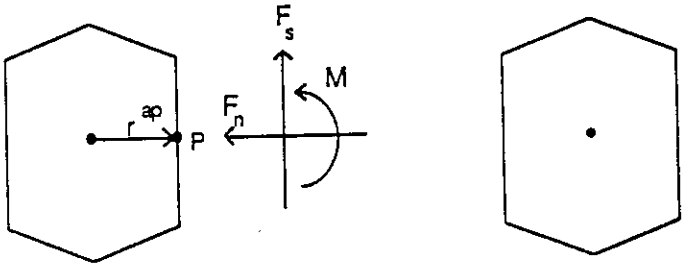

b. Equivalent forces and moments between adjacent blocks.

Figure 3. (a) Shear and normal stresses; (b) Equivalent forces and moment on the interface

Let n_i^p be an inward vector normal to the side face of block A at point P, defined as $n_i^p = (\cos\alpha, \sin\alpha)$ where α is the angle between the x axis and the vector n_i^p. The vector perpendicular to s_i^p is defined by $(-\sin\alpha, \cos\alpha)$. Thus the relative displacement vector on the left side of Eq. 1 can be transformed from the x-y coordinate to the local n-s coordinate as follows:

$$\begin{Bmatrix} \Delta_n^p \\ \Delta_s^p \\ \Delta_\omega^p \end{Bmatrix} = [T] \begin{Bmatrix} \Delta_x^p \\ \Delta_y^p \\ \Delta_\omega^p \end{Bmatrix} \tag{2}$$

where

$$[T] = \begin{bmatrix} \cos\alpha & \sin\alpha & 0 \\ -\sin\alpha & \cos\alpha & 0 \\ 0 & 0 & 1 \end{bmatrix}$$

Due to the relative movements of two neighboring blocks as shown in Fig. 3, at any point P' on the interface, the spring stretch in the normal direction δ_n and in the shear direction δ_s are given by

$$\begin{aligned} \delta_n &= \Delta_n + l\Delta_\omega \\ \delta_s &= \Delta_s \end{aligned} \tag{3}$$

where l = distance from the center point P to point P'.

As a result of spring stretch, the normal and shear stresses on the block interface are shown in Fig. 3. These stresses on the interface can be integrated to obtain the equivalent forces and moment as follows:

$$\begin{aligned} F_n &= \int_{-\frac{L}{2}}^{\frac{L}{2}} k_n \delta_n dl = \int_{-\frac{L}{2}}^{\frac{L}{2}} k_n \Delta_n dl + \int_{-\frac{L}{2}}^{\frac{L}{2}} k_n l \Delta_\omega dl \\ F_s &= \int_{-\frac{L}{2}}^{\frac{L}{2}} k_s \delta_s dl = \int_{-\frac{L}{2}}^{\frac{L}{2}} k_s \Delta_s dl \\ M &= \int_{-\frac{L}{2}}^{\frac{L}{2}} k_n l \delta_n dl = \int_{-\frac{L}{2}}^{\frac{L}{2}} k_n l \Delta_n dl + \int_{-\frac{L}{2}}^{\frac{L}{2}} k_n l^2 \Delta_\omega dl \end{aligned} \tag{4}$$

where

k_n = spring constant per unit length of the normal spring

k_s = spring constant per unit length of the shear spring

L = length of the interface

Note that the springs are elasto-plastic, thus the value of these spring constants should be obtained based on their stress-displacement relationship given in Fig. 2.

Since the terms on the right side of Eq. 4 involving first order of $k_n l$ are equal to zero, we have

$$\begin{Bmatrix} F_n^p \\ F_s^p \\ M^p \end{Bmatrix} = [K] \begin{Bmatrix} \Delta_n^p \\ \Delta_s^p \\ \Delta_\omega^p \end{Bmatrix} \tag{5}$$

where

$$[K] = \begin{bmatrix} K_n & 0 & 0 \\ 0 & K_s & 0 \\ 0 & 0 & K_\omega \end{bmatrix}$$

and

$$K_n = k_n L; \quad K_s = k_s L; \quad K_\omega = \frac{k_n L^3}{12}$$

For convenience, the interface forces F_n^p and F_s^p in the local coordinate system are transformed to F_x^p and F_y^p in the global coordinate system as follows:

$$\begin{Bmatrix} F_x^p \\ F_y^p \\ M^p \end{Bmatrix} = [T]^T \begin{Bmatrix} F_n^p \\ F_s^p \\ M^p \end{Bmatrix} \tag{6}$$

where

$$[T]^T = \begin{bmatrix} \cos\alpha & -\sin\alpha & 0 \\ \sin\alpha & \cos\alpha & 0 \\ 0 & 0 & 1 \end{bmatrix}$$

The forces acting on all sides of a block should satisfy the force and moment equilibrium requirement, given by

$$\begin{Bmatrix} f_x^a \\ f_y^a \\ m^a \end{Bmatrix} = -\sum_{P=1}^{N} [R^a]^T \begin{Bmatrix} F_x^p \\ F_y^p \\ M^p \end{Bmatrix} \tag{7}$$

where

$$[R^a]^T = \begin{bmatrix} 1 & 0 & 0 \\ 0 & 1 & 0 \\ -r_y^{ap} & r_x^{ap} & 1 \end{bmatrix}$$

and N is the total number of sides of the block. The variables f_x^a, f_y^a, and m^a are the body forces and moment of the block.

Combining equations 1, 2, 5, 6, and 7, a relationship is obtained between the forces and the movements of the block in the following form:

$$\begin{Bmatrix} f_x^a \\ f_y^a \\ m^a \end{Bmatrix} = -\sum_{P=1}^{N} [R^a]^T [T]^T [K][T]([R^b]\begin{Bmatrix} u_x^b \\ u_y^b \\ \omega^b \end{Bmatrix} - [R^a]\begin{Bmatrix} u_x^a \\ u_y^a \\ \omega^a \end{Bmatrix}) \tag{8}$$

Based on Eq. 8, three equations of force equilibrium can be set up for each block and $3N$ equations for a system of N blocks as follows:

$$\{f\} = [G]\{u\} \tag{9}$$

where

$\{f\}$ consists of f_x, f_y, and m for all blocks,

$\{u\}$ consists of u_x, u_y, and ω for all blocks, and

$[G]$ is the global stiffness matrix.

There are six variables for each block (i.e., body forces f_x^a, f_y^a, and moment m^a, and movements u_x^a, u_y^a, and ω^a) in which three of the variables are known. Therefore, the set of $3N$ simultaneous equations can be solved for the $3N$ unknown variables. The relative movement of two adjacent blocks can be determined by Eq. 1. The normal and shear forces between blocks can be obtained from the force-displacement relationships (Eqs. 2 and 5). The normal stress τ_n and shear stress τ_s of each interface between two

blocks can be determined by dividing the force by the length of the interface

$$\tau_n = \frac{F_n}{L}; \quad \tau_s = \frac{F_s}{L} \tag{10}$$

2.3 Iterative Procedure for Sliding and Separation of Blocks

In the analysis, incremental loading procedure is adopted. In each increment of load, the material is assumed to be linear. As a result, the stresses at the interface may exceed the admissible strength. To deal with the non-linearity of this problem, we employed a Newton-Raphson iteration scheme (Bathe [9]), which is similar to the initial stresses method in FEM (Naylor and Pande [10]). Figure 4 illustrates the procedure for the method of iteration. When the shear and normal stresses are in excess of the allowable strength: $\tau_{s(\max)}$ or $\tau_{n(\min)}$, the iteration process redistributes the excess amount of stress to neighboring blocks. The iterative procedure is carried out until the stresses at all interfaces of blocks are compatible with its deformation and completely satisfy the stress-displacement relationship.

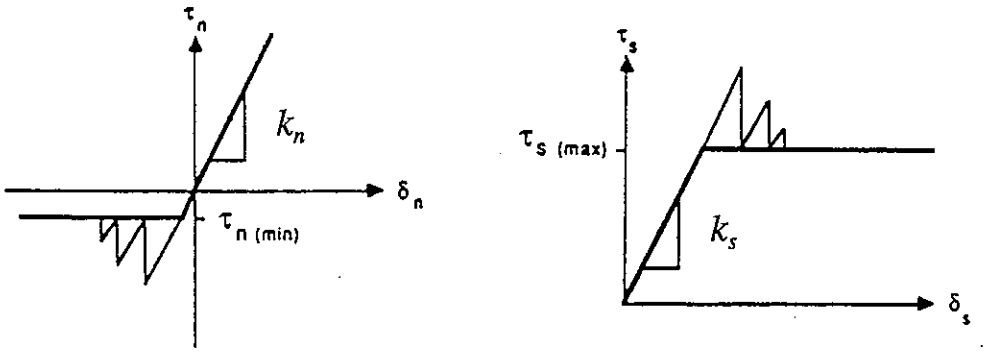

Figure 4. Newton-Raphson iteration scheme

2.4 Stiffness of Winkler-spring

The present method of analysis requires the values of stiffness k_n and k_s between the blocks. The ratio of stiffness in the normal and shear directions between blocks was estimated by taken analogous to the ratio of Young's modulus to the Shear modulus of the material. For isotropic elastic material, this ratio is given by $2(1+\nu)$. For the range of Poisson's ratio ν from 0 to 0.5, the ratio of k_n/k_s is suggested to be in the range from 2 to 3. It was found that the values of stiffness k_n and k_s, for a given ratio of k_n/k_s, have insignificant effect on the computed results.

3. APPLICATION ON LIMIT EQUILIBRIUM PROBLEMS

3.1 Stability of Slopes

In this section, the present method is illustrated by problems of slope stability. The results are discussed and compared with Bishop's simplified method [11]. The safety factor, F, of a homogeneous embankment depends on the following factors: the inclination β, the height H, the unit weight of soil γ, and the shear strength parameters, c and ϕ. Janbu [12] has shown that, by defining a dimensionless parameter λ as

$$\lambda = \frac{\gamma H}{c} \tan \phi \qquad (11)$$

The value of $F\gamma H/c$ is unique for a given set of values of λ and β.

Four cases with different values of λ and β were selected and analyzed. For these cases, the unit weight of soil is 123 lb/ft^3 and the height of the slope is 148 ft. The strength parameters, c and ϕ, shown in Table 1, were chosen so as to obtain F = 1.2 for all cases. Value of λ = 0 represents embankments with cohesive soils and λ = 20 represents embankments with predominantly cohesionless soils. For comparison purpose, the four cases are first analyzed using Bishop's simplified method. The failure surface obtained from Bishop's simplified method is used for the analysis with the present method. A schematic representation of the slope and the failure surfaces for the four cases is shown in Fig. 5.

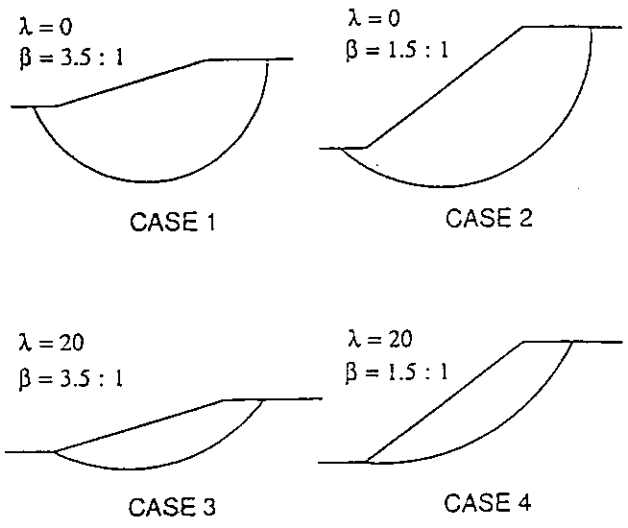

Figure 5. Four embankments and their mobilized surfaces used in example

Case (1)	ϕ (deg) (2)	c (psf) (3)	λ (4)	β (5)	F_{Bishop} (6)	F_{DEM} $k_n/k_s = 1$ (7)	F_{DEM} $k_n/k_s = 10$ (8)
1	0.0	3,319.0	0	3.5:1	1.2	1.19	1.22
2	0.0	3,600.0	0	1.5:1	1.2	1.19	1.24
3	14.8	240.6	20	3.5:1	1.2	1.16	1.17
4	26.3	448.6	20	1.5:1	1.2	1.13	1.16

Note: 1 psf = 47.9 Pa.

Table 1. Soil strength and computed factors of safety for four cases

Comparing the computed factors of safety in Table 1, when the ratio of k_n/k_s is within the range from 1 to 10, the variation of computed factors of safety is negligible. It is noted that, although the Bishop's simplified method does not satisfy the overall force equilibrium and make crude assumptions regarding the inter-slice forces, the overall factor of safety are in close agreement with that obtained from the present method. Although the differences in the factors of safety are insignificant, the computed stresses along the mobilized surface from the two methods differ significantly. As shown in Fig. 6, the shear stress calculated by the present method is generally lower than that determined by Bishop's simplified method in the central portion and higher at the toe or the heel of the mobilized surface. This shows that the toe or the heel of a slope are more susceptible to the initiation of failure, and the local failure propagates from these regions towards the central portion of the slope. It is worth noting that the distribution of normal stresses along the failure surface as determined by Bishop's simplified method and by the present method are in close agreement although the shear stresses deviate greatly. In conventional slope stability methods, it is assumed that the factor of safety is constant for all points on the shear surface. The present discrete element approach, however, is not limited by this assumption. Therefore, the stress computed from the present method is more realistic. Fig. 7 shows the variation of the factor of safety, along the mobilized surface, computed from the present method. The computed stress distribution is in agreement with results obtained from field studies and finite element analysis of embankment (Lo & Lee [13]).

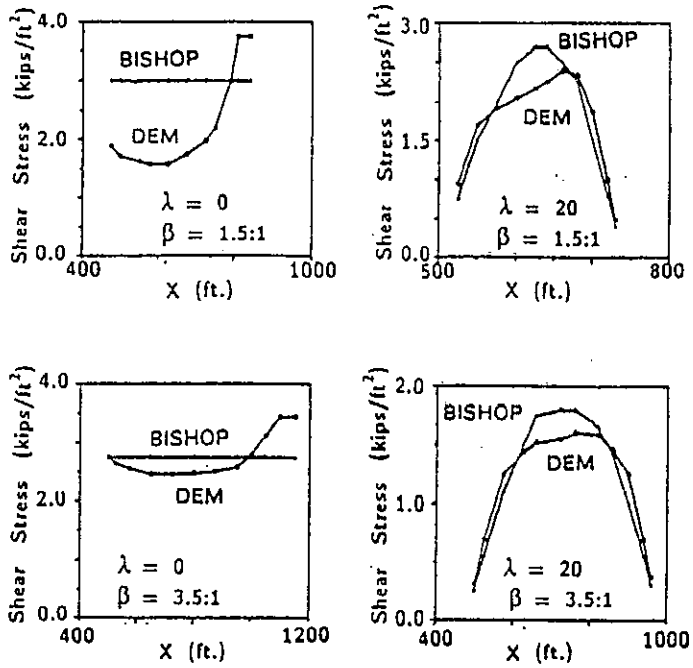

Figure 6. Shear stress distribution along mobilized surface obtained from Bishop's simplified method and the present method

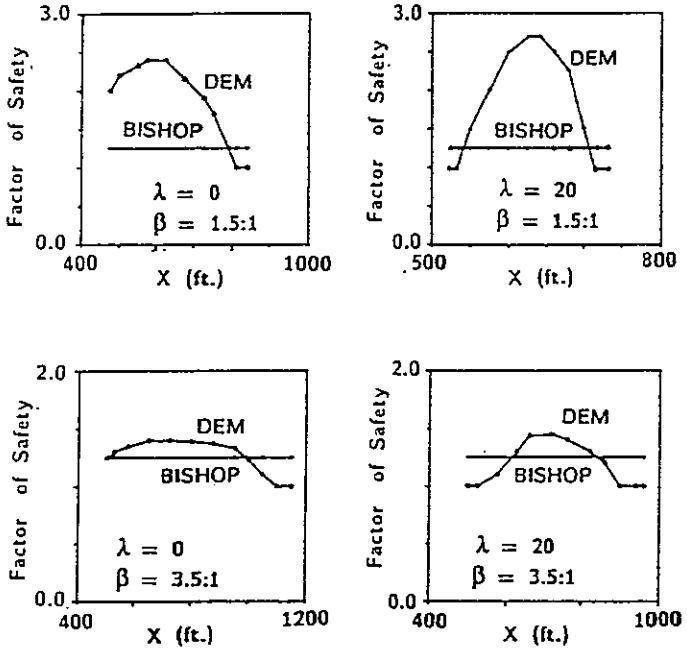

Figure 7. Factor of safety along mobilized surface obtained from Bishop's simplified method and the present method

3.2 Earth Pressure of Retaining Walls

The present method is then illustrated in the analysis of earth pressure problem for active condition. In an active condition, the wall moves away from soil to cause mobilizations along the failure surface in the soil mass and along the interface between the wall and soil. The soil-wall system is analyzed to obtain the force acting on the retaining wall. The body forces of the blocks are first applied and followed by moving the wall away from soil in incremental displacements until the active condition is reached. The unit weight of soil γ used for this example is 16.5 kN/m^3 and the height of the wall H is 4.6 m. The values of stiffness are assumed to be k_n = 10000 kN/m and k_s = 5000 kN/m.

To obtain the distribution of earth pressure on the wall, the failure wedge was divided into a number of blocks as in Fig. 8. Lateral earth pressure distribution against the retaining wall for three different modes of wall movement are analyzed. The computed distribution of the horizontal active earth pressure for the three modes of wall movement are shown in Fig. 9, in which the horizontal earth pressure is normalized by dividing γH. For comparison, the normalized Coulomb's active earth pressure [14] for $\phi = 30°$ and $\delta = 20°$ is plotted by the straight solid line in each case. Although the earth pressure of mode (a) and mode (b) are in agreement with the linear distribution, the pressure distribution of mode (c) deviates greatly from it. Similar trends have also been observed from finite element analysis (Chao [15]) as the comparison shown in Figure 9.

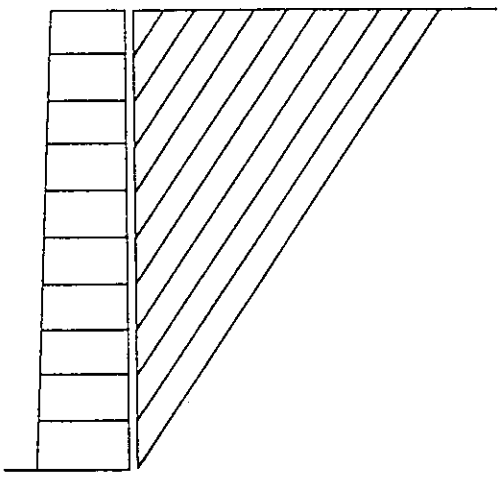

Figure 8. Discrete element mesh modelling relative sliding of backfill blocks under active condition

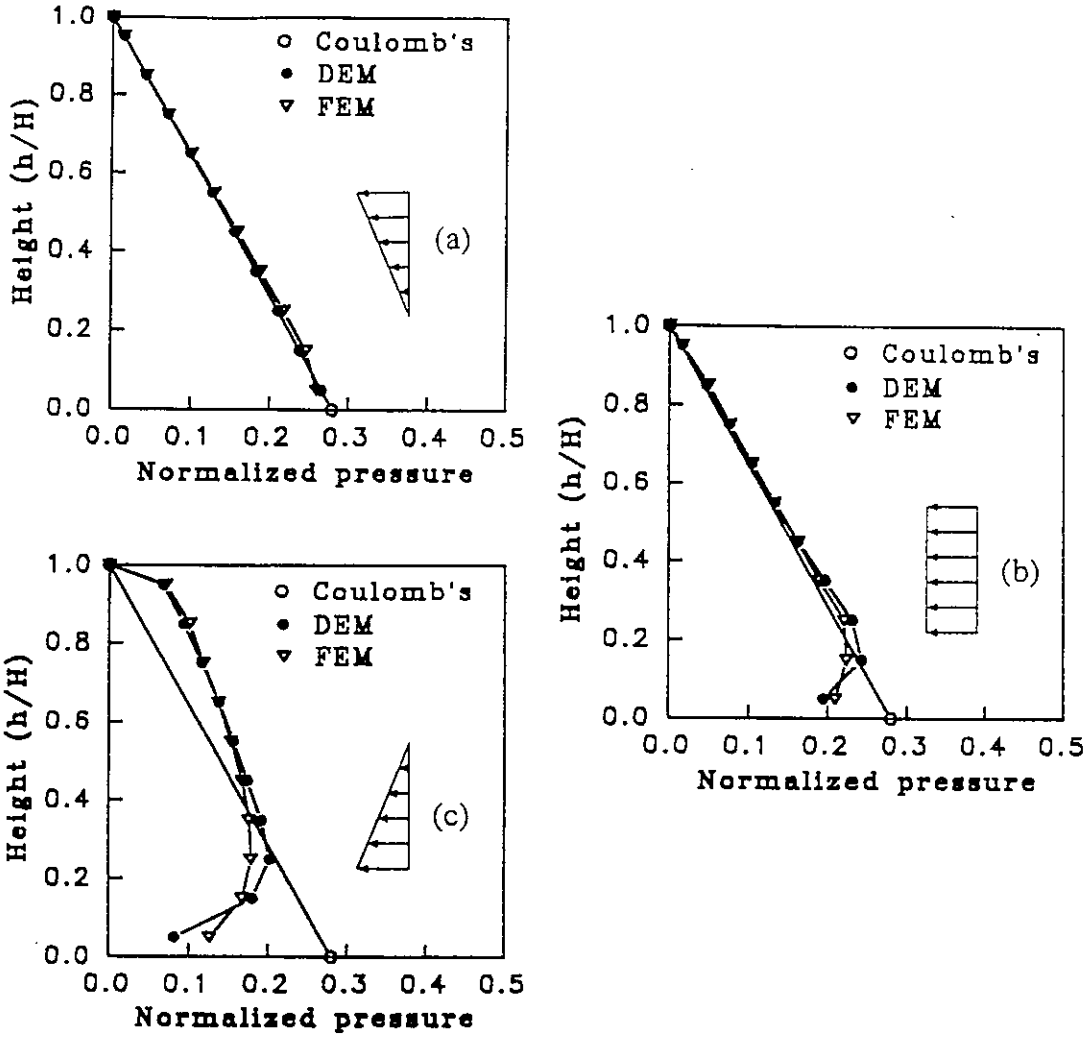

Figure 9. Normalized pressure for the three modes of wall movement under active condition

Although the results of Fig. 9 were obtained using k_n = 10000 kN/m and k_s = 5000 kN/m, it was found that the values of k_n and k_s, with the ratio of k_n/k_s ranging from 2 to 3, have insignificant effect on the computed active pressure against the wall.

The earth pressure distribution depends on the mode of wall movement as a result of soil arching. Mechanism of arching of the backfill soil can be characterized by both the pattern and the extent of sliding between backfill blocks. There are two types of sliding pattern between backfill blocks, namely, active sliding and passive sliding as shown in Fig. 10.

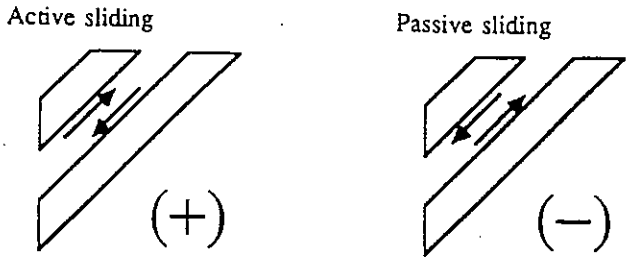

Figure 10. Active and passive sliding patterns

The extent of sliding is represented by the degree of the mobilized shear stress as compared to the shear strength between backfill blocks. Figure 11 shows the degree of mobilized shear stress between backfill blocks along the elevation of the wall. The positive ratios represent active sliding while negative ratios represent passive sliding. It can be found from Fig. 11 that all backfill blocks of modes (a) and (b) experience active sliding. The mode (c) of wall movement gives a pattern of mobilized shear stresses different from those of modes (a) and (b). In mode (c), at top of the all, the backfill blocks slide passively while blocks at the bottom part of the wall experience active sliding. This mechanism of mode (c) results to its unique distribution pattern of earth pressure.

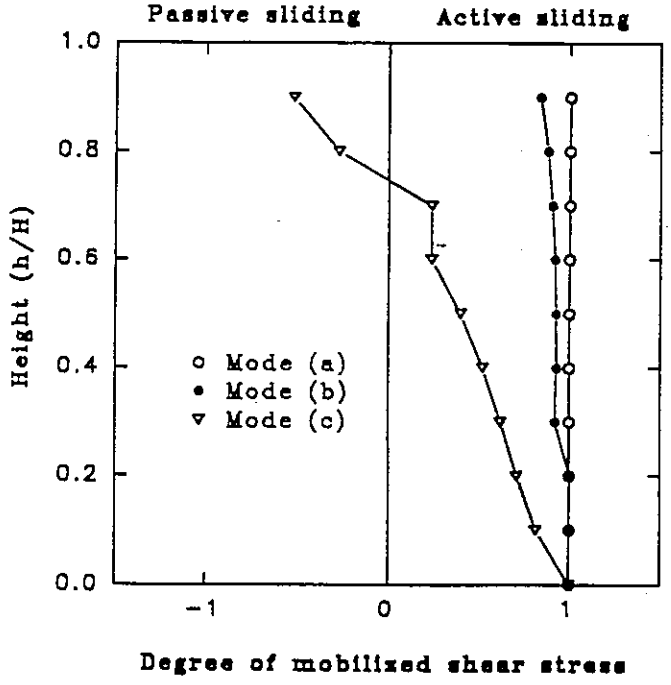

Figure 11. Sliding patterns for the three modes of wall movement under active condition

It is interesting to note that, in the active wall movement, part of the backfill may experience passive sliding which is opposite to the common concept that active wall movement must induce active sliding in the backfill as hypothesized by Dubrova [16].

The analysis is then performed to investigate the influence of soil friction angle ϕ, and wall friction angle δ, on the earth pressure. The influence of ϕ on pressure distribution is illustrated in Fig. 12 for values of soil friction angle ϕ = 10°, 30°, and 50°, while the wall friction δ is assumed to be $2/3\phi$. Figure 13 shows the earth pressure distribution for wall friction angle δ, equal to 0, $1/2\phi$, $2/3\phi$, and ϕ, while ϕ = 30°. It is observed that the magnitude of earth pressure is reduced with increasing values of wall friction angle and soil friction angle. The pressure distribution pattern for each movement mode is not affected by the values of soil and wall friction angles.

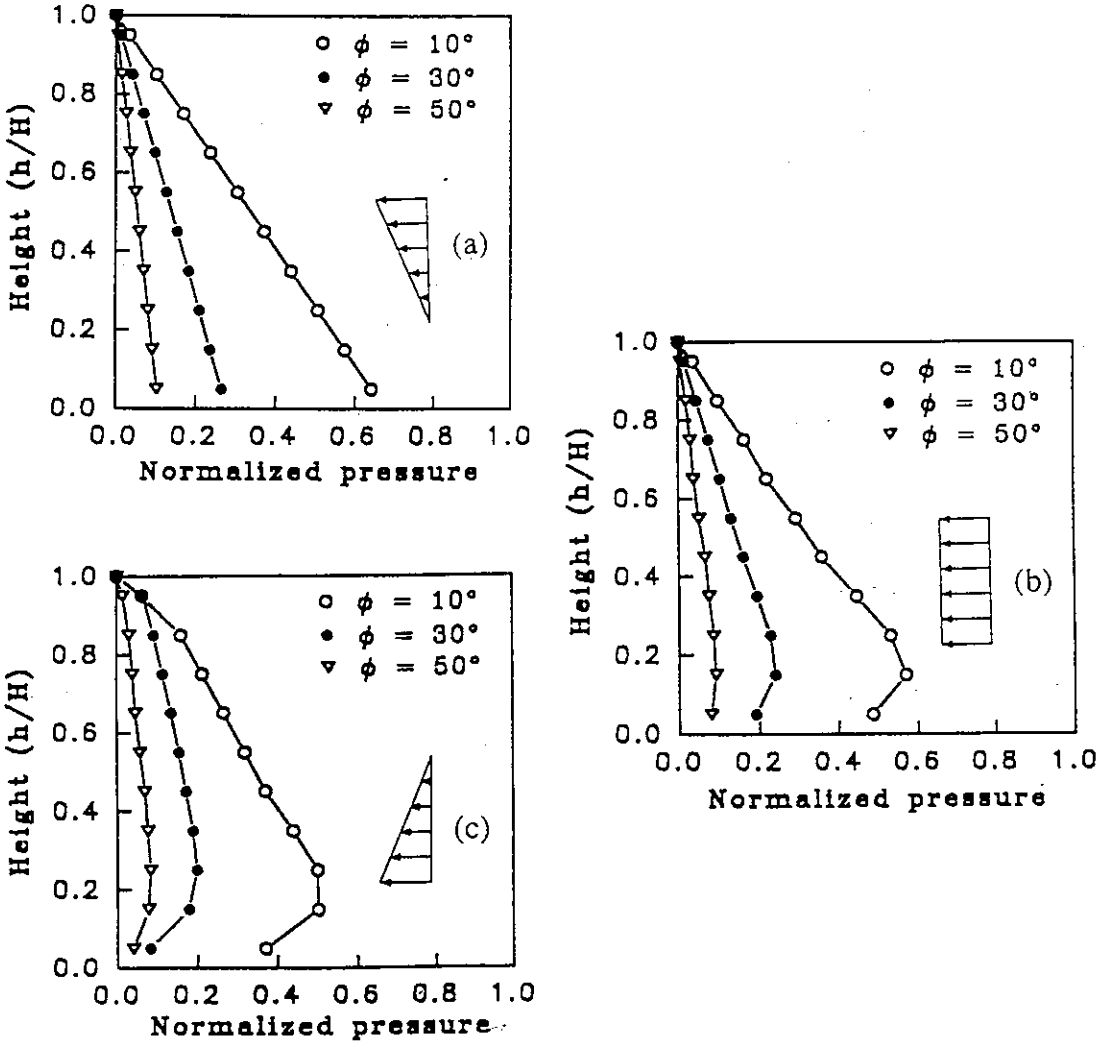

Figure 12. Influence of soil friction angle on earth pressure for the three modes of wall movement under active condition

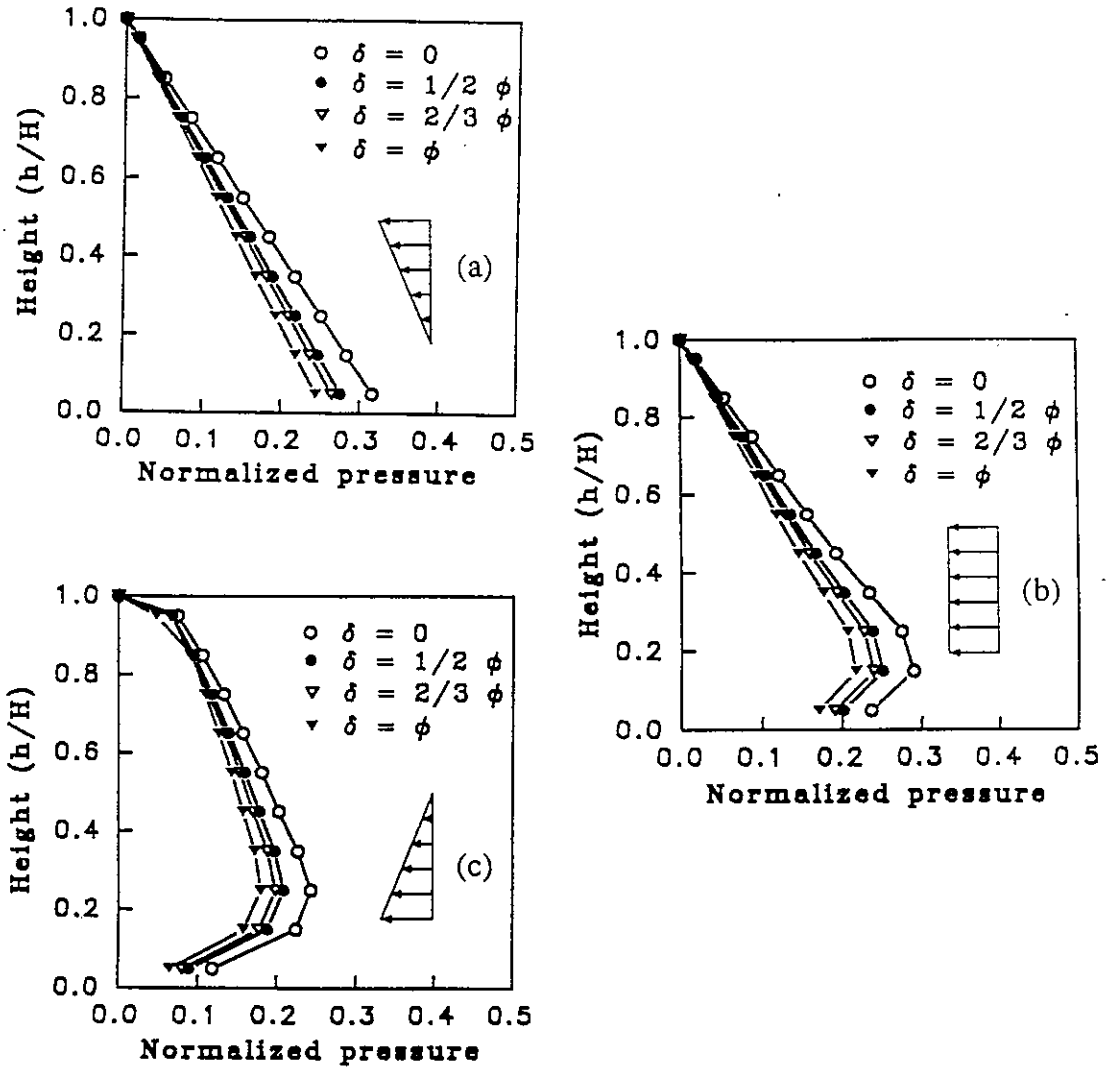

Figure 13. Influence of wall friction angle on earth pressure for the three modes of wall movement under active condition

3.3 Bearing Capacity of Shallow Foundations

The present method is also illustrated by the analysis of bearing capacity of shallow foundations. The failure zones of soil mass under a shallow foundation, as shown in Fig. 14, consist of a Rankine's active zone (zone I), a radial shear zone (zone II),and a Rankine's passive zone (zone III). The curve CD is an arc of a logarithmic spiral.

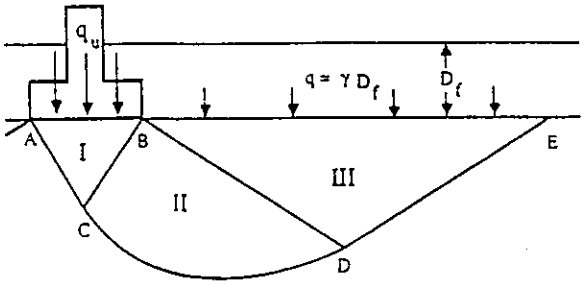

Figure 14. Bearing capacity for general shear failure

The first example is illustrated by considering the bearing capacity of a surcharged cohesive soil (i.e., angle of internal friction $\phi = 0°$). A discrete element mesh of the problem represented by seven blocks is shown in Fig. 15. In the mesh, the logarithmic spiral shear zone, which reduces to be a circular zone for cohesive soil, is modelled by three triangular blocks. The unit weight of soil γ used for this example is 120 lb/ft^3, the width of foundation B is 20 ft, and the surcharge q is 1800 lb/ft^2, corresponding to a depth D_f = 15 ft. The cohesion of soil c is 800 lb/ft^2. The body forces due to gravitation of the soil blocks (blocks 1 to 5 and block 7) are applied and followed by a subsequent loading of the foundation block (block 6) until the failure surface is fully mobilized.

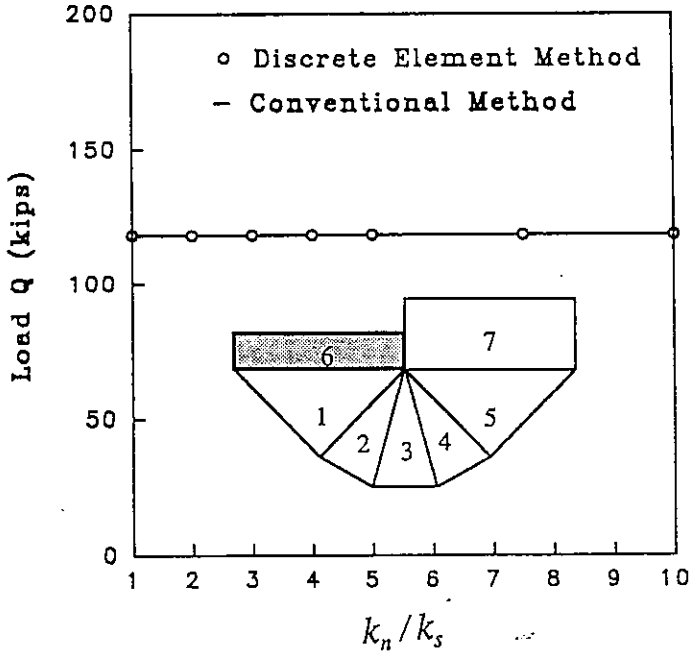

Figure 15. Discrete element mesh and computed results with various stiffness ratios ($\phi = 0°$)

Various values of stiffness were used in the analysis. The computed results of collapsing load with different k_n/k_s ratios ranging from 1 to 10 are also plotted in Fig. 15. As the results shown in Fig. 15, the computed collapsing loads are identical to that obtained from general bearing capacity equation (Meyerhof [17], Vesic [18]) regardless of the value of k_n/k_s ratio.

The second example is a case with soil cohesion c = 800 lb/ft^2 and internal friction angle ϕ = 15°. The configuration of failure surface is plotted as shown in Fig. 16 with log-spiral curve connecting the passive and active zones. It was also found that the values of k_n and k_s have insignificant effect on the computed results. The computed results with different k_n/k_s ratios are compared with the results from conventional method also in Fig. 16. The collapsing loads obtained from the present method are slightly higher than that obtained from the conventional method.

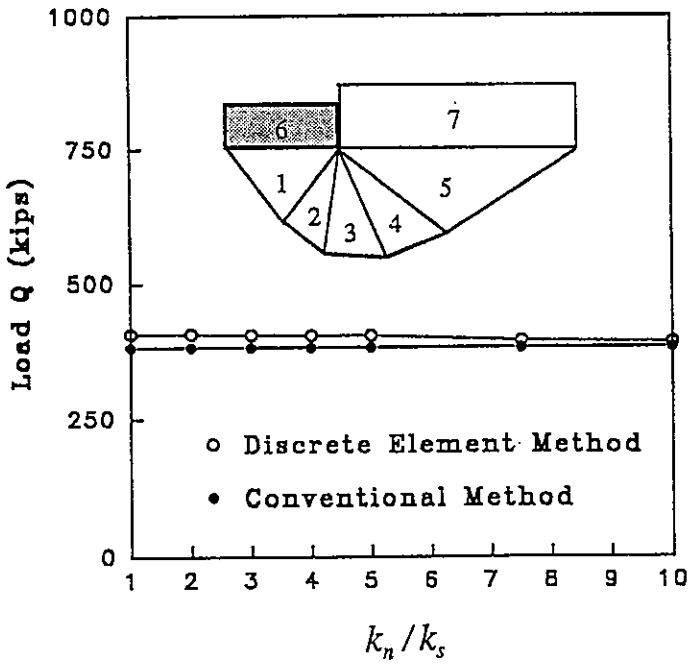

Figure 16. Discrete element mesh and computed results with various stiffness ratios (ϕ = 15°; c = 800 lb/ft^2)

The discrepancies are affected by the stiffness used in the present method. Although, by increasing the k_n/k_s ratio (i.e., reducing the k_s value), the result approaches to that obtained from the conventional method, it is believed that the computed collapsing loads are more realistic for the range of k_n/k_s ratio between 2 ~ 3. However, the difference are not significant for practical purposes.

It is obvious that the mesh with more blocks simulates better the shape of logarithmic spiral curve. Figure 17 shows the results ($k_n/k_s=2$) for meshes with different number of blocks in the shear zone BCD. It is interesting to note that a small number of blocks in shear zone appears to be enough for the analysis to reach a converged solution.

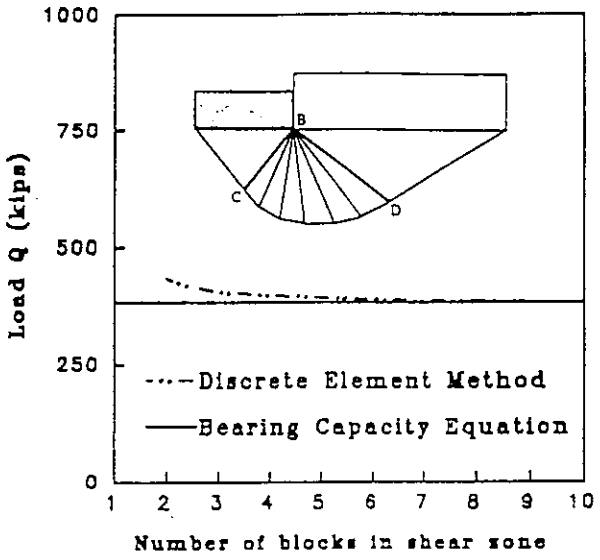

Figure 17. Effect of the number of blocks in shear zone

For the analysis of bearing capacity problems, the conventional limit equilibrium method with incorrect assumptions can be erroneous. For problems with complicated geometry and loading conditions, the knowledge of locations of failure surfaces are not readily available in literature. For example, in the cases (Fig. 18) such as: eccentric and inclined load, tilt footing base, footing adjacent to a slope, and footing on a slope, empirical reduction factors have been frequently used in determining bearing capacity. The present method is simple and straightforward, without ambiguous assumptions regarding inter-slice forces. The solution satisfies equilibrium conditions and is admissible in accordance with the material strength. The present method has the potential to be a useful tool in the class of collapsing load problems with complicated geometry and loading conditions where solutions are not readily available. These types of problem can be solved in a direct manner by the present method through the following steps:

1. Estimate a failure surface,
2. Discretize the soil mass into discrete elements,

3. Assign material properties, i.e., strength and stiffness for interface between blocks, and
4. Apply the gravitational body force and increase the foundation load to achieve the fully mobilized failure surface.

Repeat steps 1 to 4 for several trial failure surfaces until the critical collapsing load is determined.

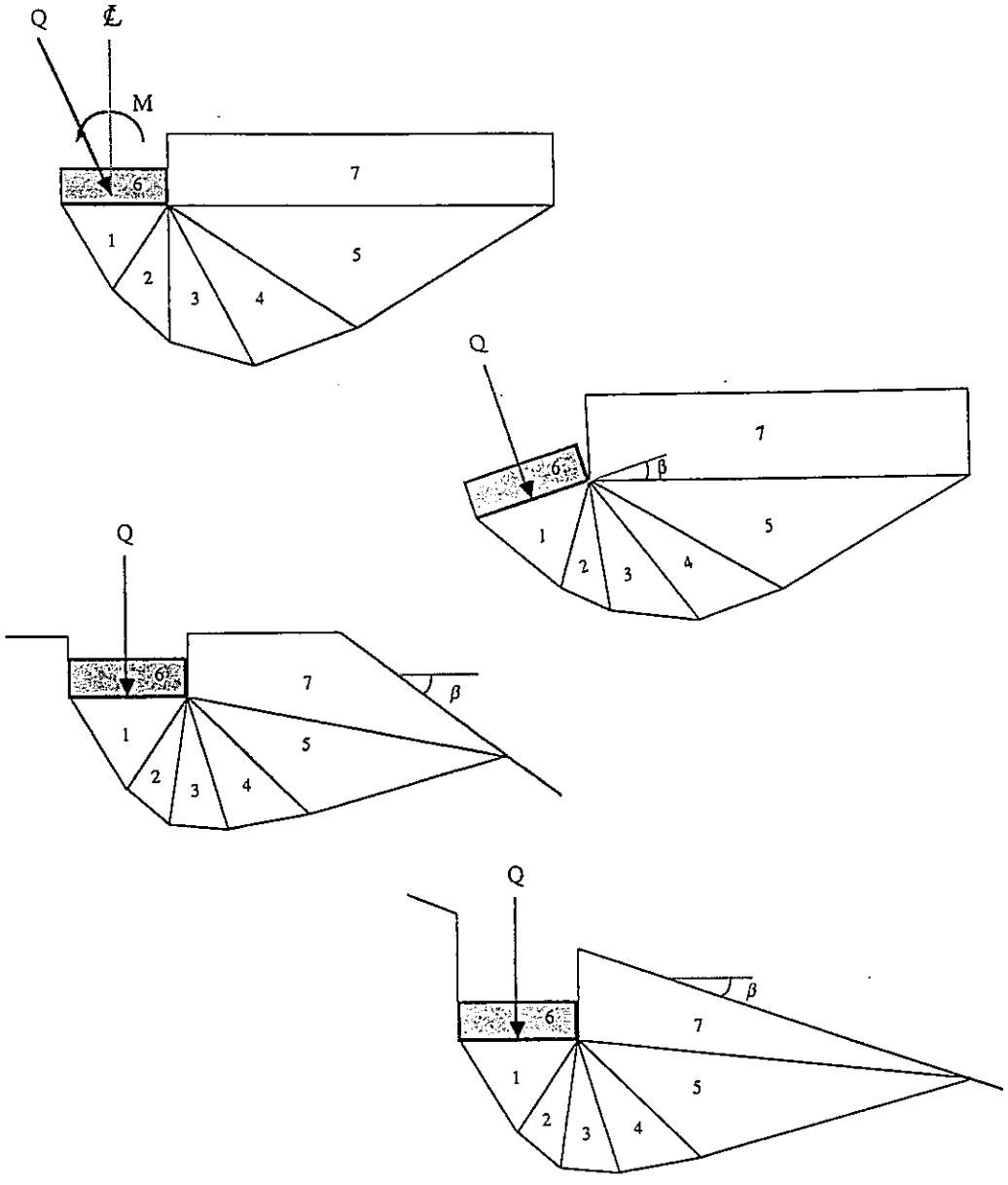

Figure 18. (a) Eccentric and inclined loads; (b) Tilt footing base; (c) Footing adjacent to a slope; (d) Footing on a slope.

4. CONCLUSION

A discrete element method is presented for the analysis of limit equilibrium problems in geotechnical engineering, such as stability of slopes, earth pressure on retaining walls, and bearing capacity of shallow foundations. Due to the nature of limit equilibrium analysis, all the conventional methods must make assumptions with regard to the inter-slice forces. The current approach, based on the discrete element method, provides a method of estimating the stresses on a mobilized surface that is both simpler and more direct. A soil mass, in the present method, is treated as comprising of blocks connected by elasto-plastic Winkler-springs. The stresses on the failure surface obtained by the present method satisfy all equilibrium conditions and are admissible in accordance with the material strength.

Compared with the conventional limit equilibrium methods, the present method requires material properties k_n and k_s in addition to the strength of soil. The range of stiffness ratio k_n/k_s for soil is suggested to be between $2 \sim 3$. Under this range of stiffness ratio, it is found that the values of k_n and k_s have negligible influence on the computed results.

The advantage of the present method over the conventional limit equilibrium methods are summarized as follows:

1. The present method is theoretically more rigorous. The consideration of elasto-plastic springs yields a statically deterministic system and facilitates the treatment of stress distribution along the mobilized surface.

2. The present method is simpler than the conventional limit equilibrium methods. The present model is simpler in the sense that no experience is required for making reasonable assumptions regarding the locations and inclinations of inter-slice forces.

3. In the conventional limit equilibrium methods for the problems of slope stability, it is assumed that the factors of safety are the same for all points on the mobilized surface. The present method, however, is not limited by this assumption. Therefore, The computed results can show the initiation of failure beginning at the toe and the heel, and the local failure propagating from these regions toward the central portion of the slope.

4. The present method is capable of predicting the earth pressure distribution behind the retaining wall. Earth pressure distribution is illustrated in the analyses under three different modes of wall movement. Different earth pressure distributions are caused by different patterns of relative sliding of backfill blocks.

The analysis of sliding patterns offers a better understanding of the arching mechanism of backfill that leads to different earth pressure distribution behind the wall.

5. Bearing capacity of shallow foundations computed using this method is found to be in good agreement with that obtained from the conventional limit equilibrium methods. The present method can be a useful tool for analyzing bearing capacity of shallow foundations with complicated geometry and loading conditions.

5. REFERENCES

1. Cundall, P. A. (1971). "A Computer Model for Simulating Progressive, Large-scale Movements in Block Rock Systems," Proceedings of the International Symposium on Rock Fracture, II-8, Nancy, France.
2. Shi, G. H. (1988). "Discontinuous Deformation Analysis: A New Numerical Model for the Static and Dynamics of Block Systems," Ph. D. Dissertation, Department of Civil Engineering, University of California at Berkeley.
3. Barbosa, R. and Ghaboussi, J. (1990). "Discrete Finite Element Method for Multiple Deformable Bodies," Journal of Finite Elements in Analysis and Design, Vol. 7, pp. 145-158.
4. Barbosa, R. and Ghaboussi, J. (1992). "Discrete Finite Element Method," Engineering Computations, Vol. 9, pp. 253-266.
5. Chang, C. S. (1992). "A Discrete Element Method for Slope Stability Analysis," Journal of Geotechnical Engineering, American Society of Civil Engineers, Vol. 118, No. 12, pp. 1889-1906.
6. Chang, C. S. and Chao, S. J. (1994). "Discrete Element Analysis for Active and Passive Pressure Distribution on Retaining Wall," Computers and Geotechnics, Vol. 16, pp. 273-288.
7. Chang, C. S. and Chao, S. J. (1991). "Discrete Element Method for Bearing Capacity Analysis," Computers and Geotechnics, Vol. 12, No. 4, pp. 273-288.
8. Chang, C. S. and Misra, A. (1990). "Computer Simulation and Modelling of Mechanical Properties of Particulates," Journal of Computer and Geotechniques, Elsevier Sciences Publishers, Vol. 7 , No. 4, pp. 269-287 .
9. Bathe, K. J. (1982). Finite Element Procedures in Engineering Analysis, Prentice-Hill, Englewood Cliffs, New Jersey.

10. Naylor, D. J. and Pande, G. N. (1981). Finite Element in Geotechnical Engineering, Pineridge Press, Swansea, U.K.
11. Bishop, A. W. (1955). "The Use of Slip Circle in the Stability Analysis of Slopes," Geotechnique, Vol. 5, No. 1, pp. 7-17.
12. Janbu, N. (1954). "Stability analysis of slopes with dimensionless parameters," Harvard Soil Mechanics Series ,Vol. 46, pp. 8-11.
13. Lo, K. Y., and Lee, C. F. (1973). "Stress analysis and slope stability in strain softening soils," Geotechnique, Vol. 23, No. 1, pp. 1-11.
14. Coulomb, C. A. (1776). "Essai sur une Application des Regles des Maximis et Minimum a quelques Problemes de Statique Relatifs a l'Architecture," Mem. Acad. Roy. des Sciences, Paris, Vol. 3, p. 38.
15. Chao, S. J. (1991). "Stability of Existing Granite Block Bridge Abutments," Massachusetts Department of Public Works, ISA No. 5516.
16. Dubrova, G. A. (1963). Interaction of Soil and Structures Izd. Rechnoy Transport Moscow.
17. Meyerhof, G. G. (1963). "Some Recent Research on the Bearing Capacity of Foundations," Canadian Geotechnical Journal, Vol. 1, No. 1, pp. 16-26.
18. Vesic, A. S. (1973). "Analysis of Ultimate Loads of Shallow Foundations," Journal of Soil Mechanics and Foundations Division, American Society of Civil Engineers, Vol. 99, No. SM1, pp. 45-73.

DDA Simulations of a Graded Particulate Assembly under Shear

An-Bin Huang, Ming-Chin Hsiao, and Yeh-Chian Lu

National Chiao Tung University, Hsin-Chu, Taiwan

ABSTRACT

Laboratory experiments have demonstrated that the fines content can affect the behavior of cohesionless soils. Earlier numerical simulations implicated that there is a possibility that the finer particles in a particulate assembly are subject to higher stress within the particle. Studies on cohesionless soil have mostly concentrated in uniformly graded, clean sand or commonly referred to as the "academic sand". However, the fines content in a natural sand could be significant. Little is known as to the mechanisms of fines interacting with lager particles in sand. A system of Discontinuous Deformation Analysis (DDA) simulation was developed to improve our understanding on the interaction between particles of different sizes in a graded assembly under shear. The simulated particulate assembly has a bimodal size distribution. The particulates were simulated as octagons. Computer codes were developed to create the particulate assembly and interpret the data. DDA was used to consolidate the assembly under K_0 conditions and perform simple shear tests on the assembly. The paper describes the numerical development of the DDA simulations and presents preliminary simulation data.

1. INTRODUCTION

In engineering practice, the strength parameter ϕ of a natural sand deposit is often determined using in situ testing methods, such as the cone penetration or standard penetration tests. The boundary conditions created by these in situ penetration tests are rather complicated. Interpretation of the test results relies heavily on experience and calibration tests in the laboratory. Available studies related to field penetration tests and their interpretation have been concentrated on clean, uniform sand. Natural sands, especially those along the west coast of Taiwan, have significant amounts of fines (particles passing #200 sieve) content. Experience indicates that fines can have significant effects on the behavior of a sand. Researchers [1,2] have recommended to increase the standard penetration test (SPT) blow count for silty sands when evaluating the liquefaction susceptibility. Tokimatsu and Yoshimi [2] suggested that sands with gravel are more

likely to liquefy. Been et al. [3] cited triaxial tests on Kogyuk sand with different fines content but under similar relative density and stress level. The results showed that the specimen with 2% fines was dilatant and that with 10% fines was contractive. Pitman et al. [4] reported that the amount of structural instability decreases with increasing fines content. The numerical simulations of cone penetration tests (CPT) in particulate assemblies using distinct element method (DEM) [5] showed that cone penetration seams to induce higher stress within smaller particles. While the physical evidence that demonstrates the effects of fines is ample, there is little knowledge as to how the fine and coarse particles interact with one another in sand under shear.

A numerical system was developed to simulate a particulate assembly with a bimodal size distribution. The particulates are simulated as octagonal blocks using DDA. The computations determine particle contact forces, contact orientations (direction of contacts in reference to the center of particles), and stresses within the particles are recorded. The results enable the assemblies be described from microscopic point of view as they relate to the size of particles. DDA is capable of calculating an average stress within each particle, herein after refer to as the internal stress. The internal stress provides an index as to the possibility of particle crushing. Previous numerical simulations have mostly concentrated in circular [6] or elliptical particulates [7]. Natural sands are more likely to have angularities. Thus to simulate particulates as polygons is believed to be more realistic. Except for the work by Issa and Nelson [8], studies on the micromechanical behavior of blocky or angular particulate assemblies have been limited.

Computer codes were developed to create the particulate assembly and interpret the data. A simple shear test was performed on the K_0 consolidated assembly. The main objective of the DDA simulations is to enable microscopic observation on these assemblies and describe interactions between the coarse and fine particles during shear. Three assemblies that represent uniform, low and high fines contents, respectively were used in the simulations. The paper describes the numerical development of the DDA simulations and presents preliminary results.

2. CREATION OF THE PARTICULATE ASSEMBLIES

The particulates are simulated as octagons. To provide a basis for comparison, three types of gradations were simulated. Table 1 shows the characteristics of these assemblies. Type I represents a uniform sand, Type II typifies a sand with bigger particles floating within the matrix of fines, Type III simulates sand with just enough fines to fill the voids between bigger particles. The nominal diameter of the coarse particles is 9 times that of the fines. According to author's experience, further increase of the diameter ratio would result in numerical instability in DDA computations. Since the DDA simulations do not consider surface tractions, the absolute dimensions of these particles have no physical meaning.

Table 1. Characteristics of the DDA simulated particulate assemblies.

Type	Nominal Particle Diameter, cm		Number of Particles	
	Small	Big	Small	Big
I	0.01	---	900	---
I I	0.01	0.09	624	4
I I I	0.01	0.09	124	16

Physical input parameters are listed below:

Unit mass of the particles:	300 kg/m^3
Young's modulus, E of the particles:	$6.6x10^4$ MPa
Poisson's ratio, υ of the particles:	0.15
Friction angle between particles:	20^o
Gravity:	3.33 $m/\sec^2$

The unit mass was set low to minimize inertia effects. A low gravity was used to reduce the downward acceleration of all the particles. The assembly is bounded by frictionless walls as shown in Figure 1. The top block is used to provide the vertical stress and confinement. The bottom block is allowed to slide horizontally. The side blocks are free to rotate and displace horizontally.

3. CONSOLIDATION AND SHEARING OF THE ASSEMBLY

The assemblies are normally consolidated with a vertical stress, σ_v of 15 MPa under K_o conditions prior to shearing. The vertical stress is applied through the three loading points on the Top Block 1 as shown in Figures 1. The coordinate system is depicted in Figure 1. The overall stress and strain of the assembly are monitored during computation. The assembly stress tensor, $\overline{\sigma}_{ij}$ is computed using the particulate contact forces according to Christoffersen et al. [9].

$$\overline{\sigma}_{ij} = \frac{1}{V}\sum_{\alpha=1}^{N}\frac{1}{2}\left(f_i^{\alpha} d_j^{\alpha} + f_j^{\alpha} d_i^{\alpha}\right) \tag{1}$$

where

f_i = contact force between particulates,

d_i = vector connecting the centers of particulates in contact,

V = total volume of the assembly,

N = number of particulates.

To compute the overall assembly strain ($\overline{\varepsilon}_{ij}$), the displacement of particulates are described by a set of linear equations first as

$$d_x = ax + bz \tag{2}$$

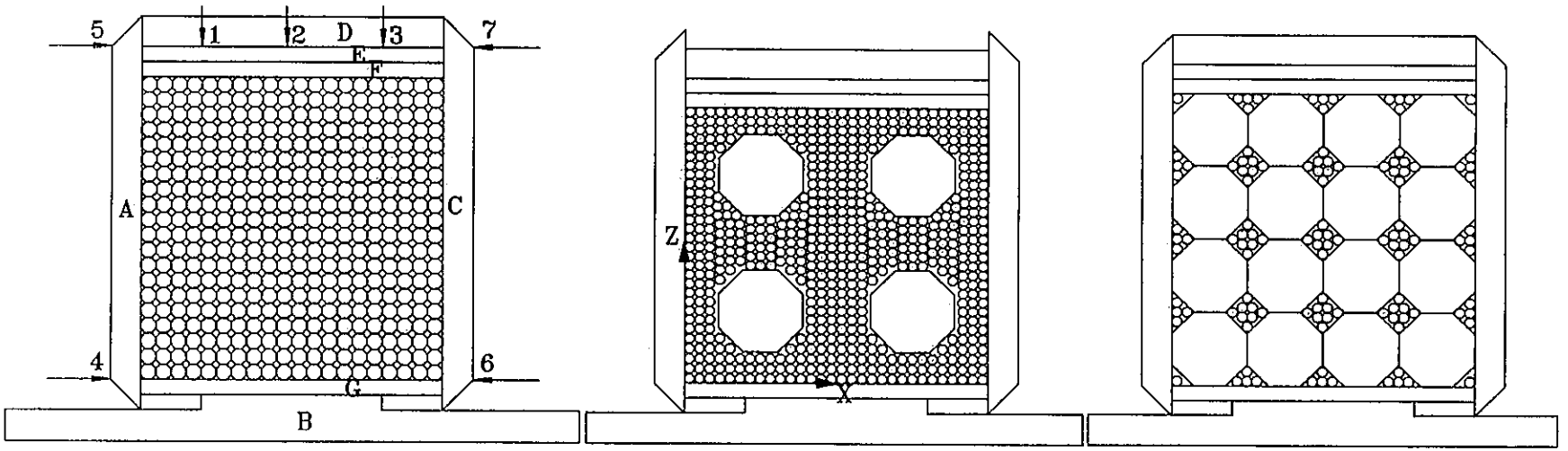

Type I Type II Type III

1~7	=	Loading Points	D	=	Top Block 1
A	=	Left Side Block	E	=	Top Block 2
B	=	Base Block	F	=	Top Block 3
C	=	Right Side Block	G	=	Bottom Block

Figure 1. Particulate assemblies at the end of K_o consolidation.

$$d_z = cx + dz \tag{3}$$

where

d_i = displacement in x and z direction,

The coefficients a,b,c and d are determined statistically using the least square method. The strain tensors are determined by taking derivatives of Equations 2 and 3. Thus $\bar{\varepsilon}_{xx} = a, \bar{\varepsilon}_{zz} = d$, and $\bar{\varepsilon}_{iz} = 0.5(b+c)$.

In presenting the data, all stresses are normalized with respect to the vertical consolidation stress σ_v. The initial K_o consolidation is necessary because there is no contact forces (hence no stress) between particulates in the beginning of computation. Shearing starts when $\bar{\sigma}_{zz}/\sigma_v$ exceeds 0.8.

A simple shear was applied to the assembly by rotating the side blocks (see Figures 1) while maintaining σ_v. The shearing ends when the relative horizontal movement between the Top Block 1 and the Bottom Block exceeds 15% of the assembly height. Figure 2 shows the assemblies after shearing.

4. MICROSCOPIC ANALYSIS OF THE RESULTS

Granular materials are assemblies of discrete cohesionless particles typically having arbitrary shape and a range of particle sizes. Cohesionless granular materials support the applied forces through particle contact forces. Therefore, the nature and distribution of the contacts are expected to have a significant influence on overall mechanical response of the granular mass. The term "fabric" has been used to characterize this kind of microstructure. According to Oda [10], the concept of fabric for a macroscopically homogeneous sample of granular material should include a measure of the orientation of individual particles (i.e., orientation fabric) and a measure that reflects the mutual relationship of individual particles (i.e., packing). Considering the large number of particles in a granular mass, the fabric must, out of necessity, be characterized statistically.

4.1 Fabric, Gradation, Particle Size and Angularity

Since the simulated particles reported in this paper are symmetric in shape, the orientation fabric has no meaning. Fabric is therefore, only related to packing of the particles. The concept of "contact vector" [11] is used to characterize packing. A contact vector is defined as a vector directed from the mass center to a point of contact with a neighbor. Fabric is graphically presented based on the statistics of the contact vectors. The full possible range (360°) of the direction of contact vectors is divided into 18 sections, each covering 20°. All the contact vectors from the DDA computations are grouped into these 18 sections according to their direction. The radial dimension of the fabric is a count of contact vectors normalized with respect to the total number of contacts in the assembly. Figure

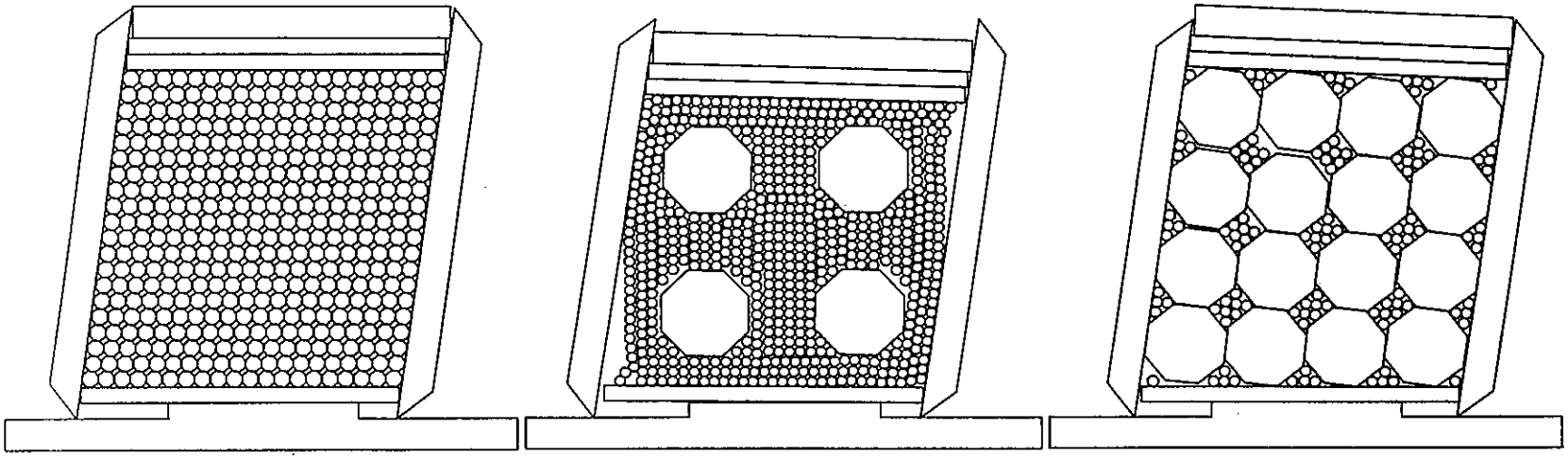

Figure 2. Particulate assemblies at the end of shearing.

3 depicts the fabrics of the assemblies at the end of K_0 consolidation and the end of shearing. To reveal the effects of particle sizes, the fabric of coarse and fine particles are shown separately when applicable. Previous studies have indicated that, at least during monotonic loading, the principle direction of fabric coincides with that of the principle stresses [e.g., 12 and 13]. In the DDA simulations, the K_0 is approximately 0.2 to 0.3 ($\overline{\sigma}_{xx}/\overline{\sigma}_{zz}$) at the end of consolidation for all the assemblies. Figure 3, however, does not indicate a clear coincidence between the principle directions of the fabric and stress, regardless of the particle sizes and gradation. This finding does not agree with the earlier studies [e.g., 12 and 13] on circular disk assemblies. The difference is believed to be related to the angularity of the particles and the uniformity of particle orientations in our simulations. Particle contacts are more likely to occur at the isotropically distributed vertexes of the octagons. Further study is required to verify if the same is true for angular particles with random orientations.

The effects of gradation on fabric are significant during shearing. For Type I assembly, shearing results in a clear principle direction of fabric as shown in Figure 3. This principle fabric direction rotates with shearing. The concurrent rotation agrees with earlier studies mentioned above. The graded assemblies (i.e., Type II and III) however, do not have a clear principle fabric direction after shearing. Macroscopically the assembly deforms according to the movements imposed on the boundaries. For uniformly graded assembly (Type I), the particle movements are rather uniform as depicted in Figure 2. However, for graded assemblies, the particle rotation/movement is influenced by its dimensions and relative position to particles of different dimensions. The shearing mode imposed by movements of neighboring particles with dramatically different dimensions may not coincide with that applied to the assembly boundaries. The mixed shearing modes experienced by particles of different sizes are believed to be the cause for the loss of a clear principle direction of the fabric.

4.2 Contact Force Distribution

According to their DEM simulations, Cundull and Strack [6] have indicated that in supporting a loading condition, the contact forces within a particulate assembly are not uniformly distributed. Rather, the contact forces are concentrated within a few branches. The distribution of contact forces from DDA simulations are presented graphically as shown in Figure 4. It is assumed that the contact forces experienced by a particle pass through the mass center. The contact force is depicted by a straight line connecting the contact point and the mass center. The line thickness is proportional to the magnitude of the contact force. The DDA computations agree with the findings by Cundull and Strack for assemblies at the end of K_0 consolidation. For Type II and III assemblies, the contact forces appear pass through coarse particles where the assembly matrixes are stiffer. DDA computations indicate that shearing disrupt the original concentra-

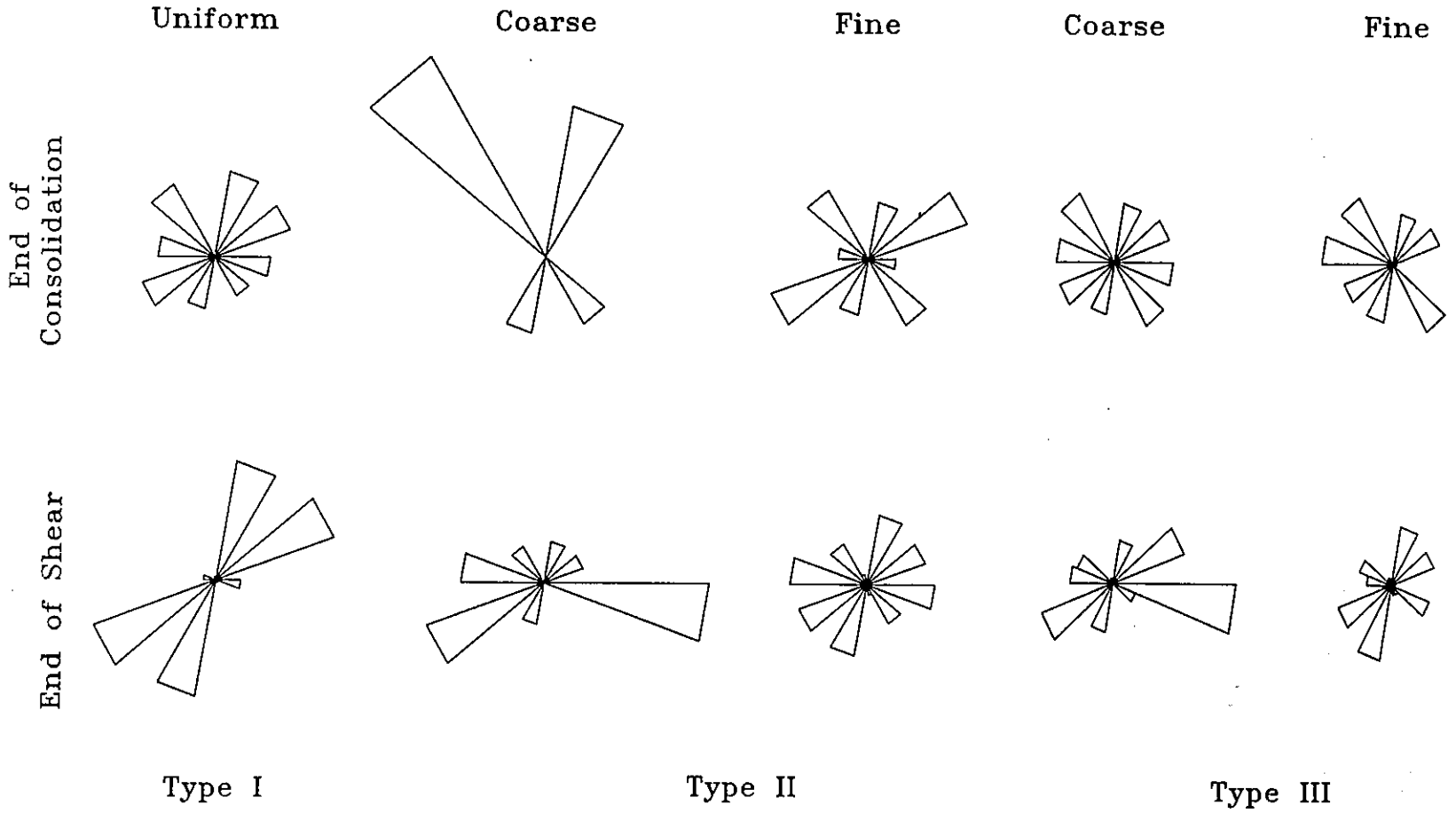

Figure 3. Fabrics of particle contacts.

Figure 4. Distribution of contact forces.

tion of contact force distributions. The contact force distributions become random at the end of shearing.

4.3 Internal Stress, Particle Size and Gradation

In laboratory tests, it is known that repeated usage of a sand specimen for shearing tests is likely to increase the fines content. Numerical simulations of CPT in graded granular material [5] indicated that the finer particles may experience higher stress induced by the cone penetration. Thus, there are reasons to expect that particles with different sizes may experience different levels of internal stress when the assembly is sheared. DDA assumes particles as linear elastic and the displacement within the particle as linearly distributed. Consequently, the result includes an average state of internal stress for each particle. The simulations took advantage of this capability and evaluate the possible discrepancies of internal stresses that might exist amongst particles of different sizes.

The values of σ_{zz} and σ_{xz} are the predominant components during consolidation and shearing, respectively. The results are presented as frequency distributions as depicted in Figures 5 and 6. The vertical coordinate shows the percentage of particles that experience a given stress value normalized with respect σ_v . For uniformly graded assembly (i.e., Type I), the stresses have a normal distribution in both cases as would be predicted by the central limit theorem. For graded assemblies, however, the internal stresses are closely related to the particle size. During K_o consolidation, the coarse particles appear to resist higher vertical stress in Types II and III assemblies. The simple shear causes higher σ_{xz} in coarse particles in Type II assembly. The reverse is true for the Type III assembly.

5. CONCLUDING REMARKS

The result from this DDA study, albeit preliminary, does point out that the gradation and particle dimensions could have significant effects on the behavior of a granular assembly during shear. The DDA simulations also indicate that the particle angularity may affect the fabric of the assembly. An important implication from this numerical study is that experience learned from tests on uniformly graded sand may not be valid if used directly for non-uniformly graded sands.

6. ACKNOWLEDGMENTS

The project was funded by the National Science Council of ROC under contract No. NSC 82-0115-E-009-373 and NSC 83-0410-E-009-026.

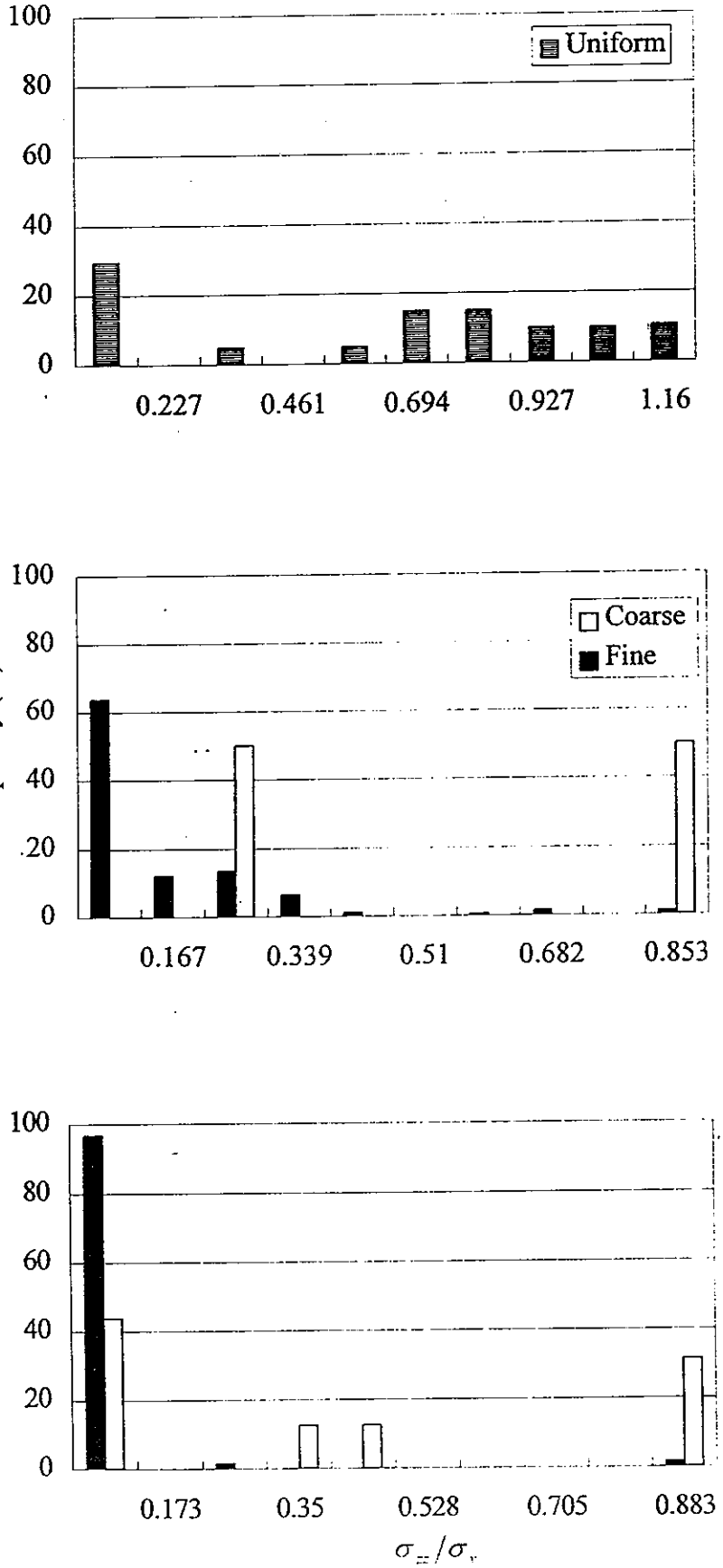

Figure 5. Frequency distribution of σ_{zz} at the end of K_0 consolidation.

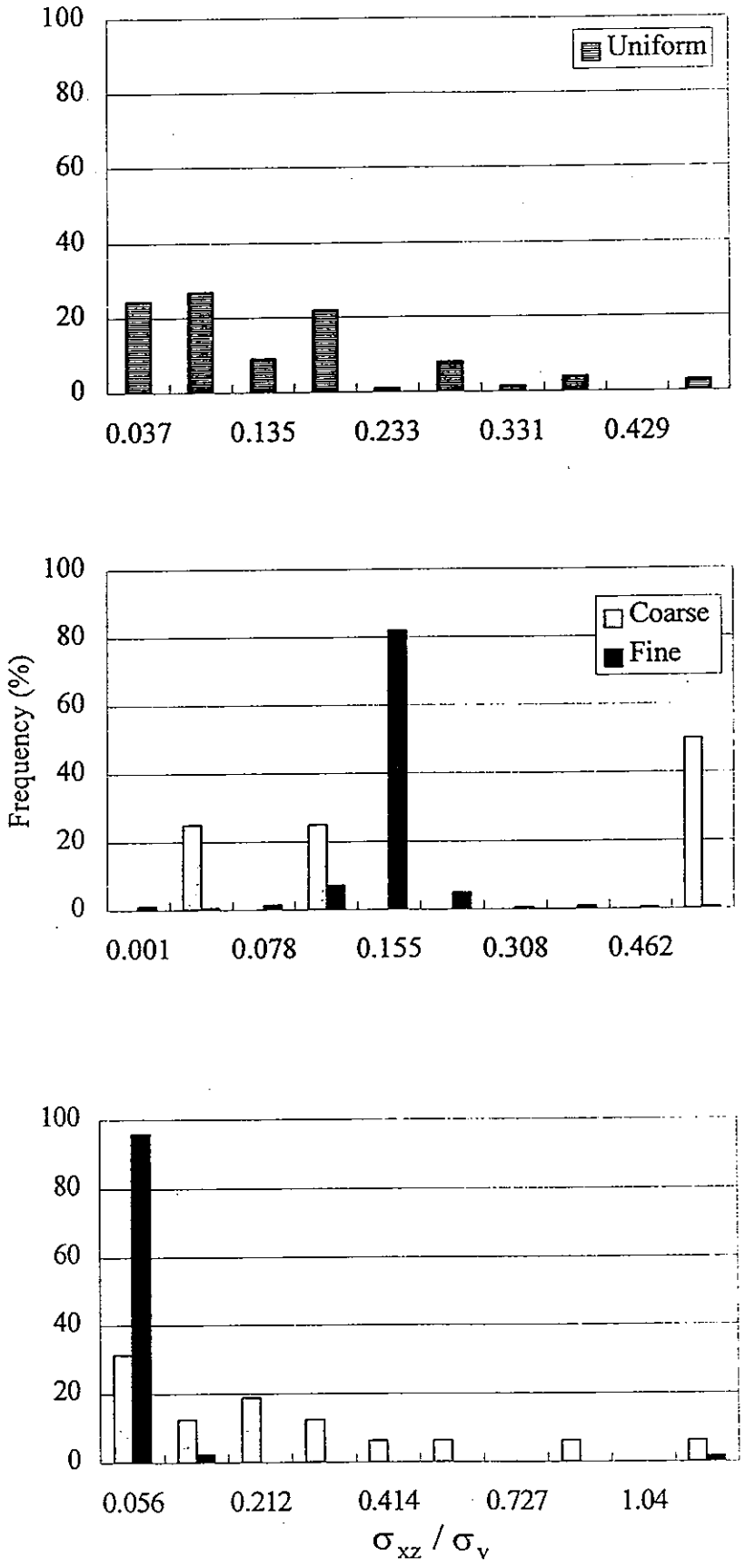

Figure 6. Frequency distribution of σ_{xz} at the end of shearing.

7. REFERENCES

1. Seed, H.B., and Idriss, I.M., (1981), "Evaluation of Liquefaction Potential of Sand Deposits Based on Observations of Performance in Previous Earthquakes." Preprint 81-544, In Situ Testing to Evaluate Liquefaction Susceptibility, ASCE National Convention, St. Louis, Missouri.
2. Tokimatsu, K., and Yoshimi, Y., (1983), "Empirical Correlation of Soil Liquefaction Based on SPT N-Value and Fines Content," Soils and Foundations, Vol.23, No.4, pp56-74.
3. Been, K., Crooks, J.H.A., and Rothenburg, L., (1988), "A Critical Appraisal of CPT Calibration Chamber Tests," Proceedings, 1st International Symposium on Penetration Testing, Orlando, Florida, pp.651-660.
4. Pitman, T.D., Robertson, P.K., and Sego, D.C., (1994), "Influence of Fines on the Collapse of Loose Sands," Canadian Geotechnical Journal, Vol.31, No.5, pp.728-739.
5. Huang, A.B., and Ma, M.Y., (1994) "An Analytical Study of Cone Penetration Tests in Granular Material," Canadian Geotechnical Journal, Vol.31, No.1, pp.91-103.
6. Cundall, P.A., and Strack, O.D.L., (1979), "A Discrete Numerical Model for Granular Assemblies," Geotechniques, Vol.29, No.1, pp47-65.
7. Rothenburg, L., and Bathurst, R.J., (1989), "Effects of Particle Shape on Micromechanical Behavior of Granular Materials, " Advances in Micromechanics of Granular Materials, Proceedings, 2nd US/Japan Seminar on Micromechanics of Granular Materials, Potsdam, New York, pp343-352.
8. Issa, J.A., and Nelson, R.B., (1989), "Numerical Analysis of Micromechanical Behavior of Granular Materials," Proceedings, 1st U.S. Conference on Discrete Element Methods, Denver, Colorado.
9. Christoffersen, J., Mehrabadi, M.M., and Nemat-Nasser, S., (1981), "A Micromechanical Description of Granular Material Behavior," Journal of Applied Mechanics, Vol.48, pp.339-344.
10. Oda, M., (1972), "Initial Fabrics and Their Relations to Mechanical Properties of Granular Material," Soils and Foundations, Vol. 12, No.1, pp.17-36.
11. Rothenburg, L., (1980), "Micromechanics of Idealized Granular Systems," Ph.D. Thesis, Civil Engineering Department, Carleton University, Ottawa, Canada.
12. Oda, M., (1972), "The Mechanism of Fabric Changes during Compression of Sand," Soils and Foundations, Vol. 12, No.2, pp.1-18.
13. Bathurst, R.J., (1985), "A Study of Stress and Anisotropy in Idealized Granular Assemblies," Ph.D. Thesis, Department of Civil Engineering, Queen's University at Kingston, Ontario, Canada, 219p.

Nodal-based Discontinuous Deformation Analysis with Four-node Isoparametric Finite Element Mesh

Kuokai Shyu and M. Reza Salami

North Carolina Agricultural and Technical State University, Greensboro, USA

ABSTRACT

This paper presents a numerical model that couples finite element mesh with each block of Gen-hua Shi's two-dimensional discontinuous deformation analysis. The main objectives of this research are to enhance block's deformation ability and to refine its stress distribution field. Computer programs were developed to model the combination of continuous and discontinuous analyses of large displacement, deformation and failure mode.

Numerical simulations are performed to show the improvement and flexibility achieved when finite element mesh is associated with discontinuous deformation analysis to handle contact problems. The first application is the stability analysis of blocky vaults built by the Mayan in Mexico. The second simulation is the failure analysis of Bartlett Dam, a multiple-arch type dam in central Arizona, USA. The last example is a simulation of the large displacement and vibration characteristics of an automobile's leaf spring-dashpot suspension system.

1. INTRODUCTION

For material analyses, the finite element method (FEM)[1,2] is the widely-used numerical tool. Conventional FEM was extensively used in the modeling of continuum. By the phenomenon of complicated boundaries and discontinuous interfaces in real world, people tried to develop contact finite elements by using different kinds of contact constraint formulations.

During the early years, Goodman *et al.*[3] developed the "joint element" for modeling discontinuous joint interfaces. The flexibility matrix method[4] and the transformation matrix method[5] have also been proposed for dealing the contact constraints of contact problems. Based on the formulations of variational principles, the methods of Lagrange multiplier[6,7] and penalty function[8,9] are the approaches commonly used to model constraint conditions for contact finite elements. However, using Lagrange multiplier method will increase the number of variables and will possibly produce zero diagonal terms. While for the penalty method, choosing of large penalty parameter may cause numerical instability. As improvements of these two methods, the perturbed Lagrangian method and the augmented Lagrangian method were introduced for contact finite element analyses. Wriggers and Simo[10]; Simo *et al.*[11]; Ju and Taylor[12], used the perturbed Lagrangian method to analyze frictional contact problems. The applications of the augmented Lagrangian

method can be seen in the works of Landers and Taylor[13]; Simo and Laursen[14]; Heegaard and Curnier[15].

Recently, Papadopoulos[16] and Zhong[17] proposed novel contact search algorithms with variational principles to model contact-impact problems for contact finite elements. These algorithms can be extended to multi-body contacts, however, the data preparations were designed for a small number of contacts. The difficulty still exists because we need a complete block kinematics to describe motions and contact behaviors of a multi-body block system. For modeling a multi-body contact system, Cundall[18,19] developed the "distinct element method," which has been used for numerical computations of jointed or blocky rocks in many engineering problems. Nevertheless, the distinct element method is an explicit method and it sometimes incorporates fictitious forces to reach the convergence criteria of block overlappings.

In 1988, Shi[20] proposed "discontinuous deformation analysis (DDA)," which includes a complete block kinematics to obtain large displacement and deformation solutions for discontinuous multi-body system. The contact constraint formulation of DDA is based on penalty method, and DDA is an implicit method because it solves equilibrium equations. The incorporation of diagonally-dominated inertia matrix for both static and dynamic calculations makes the global coefficient matrix well-conditioned. For a DDA system, the equilibrium condition, the no-tension, no-penetration constraint conditions, and the Coulomb's friction law are satisfied at all contacts.

DDA chooses the complete first order polynomial as displacement function for a two-dimensional block, no matter how irregular the shape of the block is. However, the stress field and the deformation ability of the DDA block are restricted. In order to refine stress field and to enhance deformation ability of the block, finite element meshes are incorporated into DDA blocks[21]. Some other improvements to the deformation ability of the blocks have also been done[22–25].

In this paper, the basic concepts of discontinuous computation of DDA are discussed in Section 2, and the implementation of finite element formulations into DDA is presented in Section 3. In Section 4, the Maya vaulted structure, the Bartlett multiple-arch Dam and the leaf spring-dashpot suspension system are simulated as numerical examples. And in the last Section, the conclusions of DDA's discontinuous computation and the proposed model are addressed.

2. BASIC CONCEPTS

The main subjects of DDA are: contact scheme, open-close iteration and the inertia matrix. The first two parts can be included in so-called "block kinematics."

2.1 Contact Scheme

The first part of block kinematics of DDA is the searching of possible contact pairs. DDA uses a value called "maximum displacement ratio" to define the possible contact pairs. Twice the ratio times maximum vertical size of the objects is the maximum displacement within which any vertex of the blocks could move relatively. The contact pair selection is first determined by the distance rule. The contact pair of an angle with an edge is deleted if the distance from the angle vertex to the edge is greater than the maximum displacement. And the contact pair of two angles is omitted if the distance between these two vertices

is greater than the maximum displacement. The rest of the contact pairs are further determined by the angle rule. Under the assumptions of small displacement and rotation, an angle and an edge are defined to be possibly in contact if there is no overlapping of the interior angles when the angle vertex is translated to the edge without rotation. And two angles are defined to be possibly in contact if there is no overlapping of the interior angles when these two angles are translated to same origin without rotation. Any contact will only occur among selected pairs after the elimination of overlapping ones. For detailed descriptions of defining contact pairs, see Shi[20].

The other important part of contact scheme is the "contact transfer." The contact states (e.g. contact forces, contact conditions) of all the contact pairs from previous time step have to be transferred to the current step, if it is possible, in order to preserve the correct contact status.

2.2 Open-close Iteration

Since the contact conditions are basically unknown and the contact positions are continuously changed, the system equations are solved iteratively. The convergence of iterations must satisfy the conditions of no-tension and no-penetration at any contact position.

Assuming that a penetration is detected between two blocks during contacting, then the contact condition is "close." A stiff spring (penalty) is added at the contact position to fulfill the no-penetration condition. On the other hand, if a tensile contact force is detected between two contacted blocks, then the condition is "open." The spring connecting the contact position is removed so these two blocks can separate independently. By adding or removing springs, the block kinematics allows each contact to open, slide, or lock. Each addition or removal of spring will significantly change the global equations and it may cause other contact positions to close or open. The global equations must be solved repeatedly until the no-tension and no-penetration conditions at all contact positions are satisfied. The procedure of adding or removing the springs is called "open-close iteration." During open-close iteration, DDA also applies the Coulomb's friction law at contact interface under nine combinations (e.g. open to lock, lock to slide) of open-close exchanging mode. After the convergence of open-close iteration, the correct contact conditions, positions, and forces of the block system are found.

2.3 Inertia Matrix

DDA chooses the complete first order polynomial as displacement function for a 2D block. The displacement field of the block can be written as

$$\begin{Bmatrix} u \\ v \end{Bmatrix} = \begin{bmatrix} 1 & 0 \\ 0 & 1 \\ -(y-y_0) & (x-x_0) \\ (x-x_0) & 0 \\ 0 & (y-y_0) \\ (y-y_0)/2 & (x-x_0)/2 \end{bmatrix}^T \begin{Bmatrix} u_0 \\ v_0 \\ r_0 \\ \epsilon_x \\ \epsilon_y \\ \gamma_{xy} \end{Bmatrix},$$

where (x_0, y_0) is the center of gravity of the block. u_0, v_0, r_0 are the rigid body translations and rotation of the center of gravity, and ϵ_x, ϵ_y, γ_{xy} are the normal and shear strains of the block.

The displacement of a point within the block is relative to its own center of gravity. The computation of DDA block system may be divergent if only the lumped mass matrix is used because the lumped mass matrix can not control the movement of every point in the block except the center of gravity. Therefore, DDA incorporated the accurately-integrated inertia matrix into system equations.

The inertia matrix is more important than the elastic stiffness matrix in large displacement and deformation computations because deformation strains are the first derivatives of displacements, and the integration part of inertia matrix is two order greater than that of elastic stiffness matrix. An accurate integration of inertia matrix can describe the complete wave-propagation equations and prevent the strain components from sudden accelerations in every direction. Under small time interval for time step, the perturbed waves from adding or removing springs could only disturb the block system locally around the contact positions. As a result, the open-close iterations could easily converge and the discontinuous computation is stabilized.

3. FORMULATIONS

The first order displacement function restricts the block to constant stresses and limits its deformation ability. Since blocks only contact along prescribed physical boundaries, it is practical to model blocks of flexible boundaries when the well-developed finite element meshes are incorporated into blocks and are coupled with algorithms of DDA's block kinematics, which is necessary for discontinuous system to obtain large displacement and deformation solutions.

The 2D four-node isoparametric element mesh is incorporated into DDA in this paper. The system variables become nodal displacements, and the equilibrium equations are derived by minimizing total potential energy of the system. These equations have the form: $[\mathbf{K}]\{\mathbf{D}\} = \{\mathbf{F}\}$, where $[\mathbf{K}]$ is the global coefficient matrix, and $\{\mathbf{D}\}, \{\mathbf{F}\}$ are the unknown and loading vectors.

Since the unknowns are nodal displacements, the submatrices and the equation solver are nodal-based. DDA's block kinematics remains unchanged. The derivations of submatrices follow classical finite element formulations[21]. Based on unique block kinematics of DDA, this numerical model combines both continuous and discontinuous computations for large displacement and deformation solutions.

3.1 Shape Functions

The displacement field $[\,u \quad v\,]^T$ of a four-node element i (Figure 1) can be described as

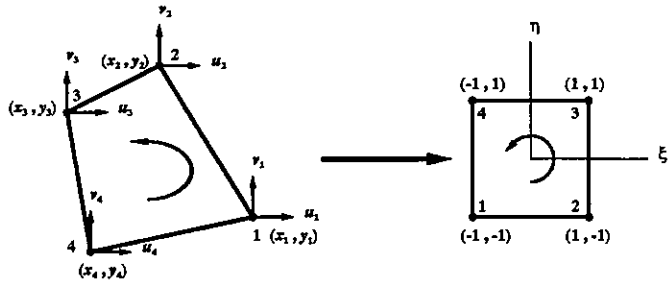

Figure 1. Four-node isoparametric element

$$\begin{Bmatrix} u \\ v \end{Bmatrix} = [\tilde{\mathbf{N}}_i(x,y)]\{\mathbf{d}_i\}, \tag{1}$$

where

$$[\tilde{\mathbf{N}}_i(x,y)] = \begin{bmatrix} \tilde{N}_1 & 0 & \tilde{N}_2 & 0 & \tilde{N}_3 & 0 & \tilde{N}_4 & 0 \\ 0 & \tilde{N}_1 & 0 & \tilde{N}_2 & 0 & \tilde{N}_3 & 0 & \tilde{N}_4 \end{bmatrix}$$

are the shape functions, and

$$\{\mathbf{d}_i\} = [\, u_1 \quad v_1 \quad u_2 \quad v_2 \quad u_3 \quad v_3 \quad u_4 \quad v_4 \,]^T$$

are the nodal displacements. However, $[\tilde{\mathbf{N}}_i(x,y)]$ are difficult to define for general four-node elements. By isoparametric transformation, the shape functions $[\mathbf{N}_i]$ are defined in natural coordinates system (ξ,η). The shape functions $[\mathbf{N}_i(\xi,\eta)]$ for the square element

$$N_{\mathrm{k}}(\xi,\eta) = \frac{1}{4}(1+\xi_{\mathrm{k}}\xi)(1+\eta_{\mathrm{k}}\eta), \quad \mathrm{k} = 1,2,3,4 \tag{2}$$

where $(\xi_{\mathrm{k}},\eta_{\mathrm{k}})$ are the nodal coordinates of square element in natural coordinates. And

$$x = \sum_{\mathrm{k}=1}^{4} N_{\mathrm{k}}(\xi,\eta)x_{\mathrm{k}}; \qquad y = \sum_{\mathrm{k}=1}^{4} N_{\mathrm{k}}(\xi,\eta)y_{\mathrm{k}}, \tag{3}$$

where $(x_{\mathrm{k}},y_{\mathrm{k}})$ are the nodal coordinates of general four-node element.

3.2 Elastic Stiffness Submatrix

For element i, strain field $\{\epsilon_i\} = [\mathbf{B}_i]\{\mathbf{d}_i\}$ and stress field $\{\sigma_i\} = [\mathbf{E}_i][\mathbf{B}_i]\{\mathbf{d}_i\}$, where

$$[\mathbf{B}_i] = \begin{bmatrix} \frac{\partial \tilde{N}_1}{\partial x} & 0 & \frac{\partial \tilde{N}_2}{\partial x} & 0 & \frac{\partial \tilde{N}_3}{\partial x} & 0 & \frac{\partial \tilde{N}_4}{\partial x} & 0 \\ 0 & \frac{\partial \tilde{N}_1}{\partial y} & 0 & \frac{\partial \tilde{N}_2}{\partial y} & 0 & \frac{\partial \tilde{N}_3}{\partial y} & 0 & \frac{\partial \tilde{N}_4}{\partial y} \\ \frac{\partial \tilde{N}_1}{\partial y} & \frac{\partial \tilde{N}_1}{\partial x} & \frac{\partial \tilde{N}_2}{\partial y} & \frac{\partial \tilde{N}_2}{\partial x} & \frac{\partial \tilde{N}_3}{\partial y} & \frac{\partial \tilde{N}_3}{\partial x} & \frac{\partial \tilde{N}_4}{\partial y} & \frac{\partial \tilde{N}_4}{\partial x} \end{bmatrix},$$

and

$$[\mathbf{E}_i] = \frac{E}{1-\nu^2}\begin{bmatrix} 1 & \nu & 0 \\ \nu & 1 & 0 \\ 0 & 0 & \frac{1-\nu}{2} \end{bmatrix}$$

for plane stress. E,ν are Young's modulus and Poisson's ratio. For plane strain, E,ν are replaced by $E/(1-\nu^2)$ and $\nu/(1-\nu)$.

The derivatives

$$\begin{Bmatrix} \frac{\partial \tilde{N}_{\mathrm{k}}}{\partial x} \\ \frac{\partial \tilde{N}_{\mathrm{k}}}{\partial y} \end{Bmatrix} = [\mathbf{J}_i]^{-1}\begin{Bmatrix} \frac{\partial N_{\mathrm{k}}}{\partial \xi} \\ \frac{\partial N_{\mathrm{k}}}{\partial \eta} \end{Bmatrix}, \quad \mathrm{k} = 1,2,3,4 \tag{4}$$

where

$$[\mathbf{J}_i] = \begin{bmatrix} \frac{\partial x}{\partial \xi} & \frac{\partial y}{\partial \xi} \\ \frac{\partial x}{\partial \eta} & \frac{\partial y}{\partial \eta} \end{bmatrix} \tag{5}$$

is the Jacobian matrix.

Then for element i, the local coefficient submatrix

$$\mathbf{t}\left(\sum_{\mathrm{m}=1}^{2}\sum_{\mathrm{n}=1}^{2}[\mathbf{B}_i(\xi_{\mathrm{m}},\eta_{\mathrm{n}})]^T[\mathbf{E}_i][\mathbf{B}_i(\xi_{\mathrm{m}},\eta_{\mathrm{n}})]|[\mathbf{J}_i]|W_{\mathrm{m}}W_{\mathrm{n}}\right) \tag{6}$$

is added to $[\mathbf{K}]$. $(\xi_{\mathrm{m}},\eta_{\mathrm{n}}) = (\pm 1/\sqrt{3},\pm 1/\sqrt{3}), \mathrm{m},\mathrm{n} = 1,2$ are the Gauss integration points, and $W_{\mathrm{m}}, W_{\mathrm{n}} = 1.0$ are the integration weights of Gaussian quadrature. $\mathbf{t}$ is the element thickness and $|[\mathbf{J}_i]|$ is the determinant of Jacobian matrix.

3.3 Inertia Submatrix

It is assumed that constant acceleration is over current time step and the initial element nodal displacements are zero (begins with updated configurations). Let M_i be the unit mass, Δ be the time interval of current step, and $\{\mathbf{v}_i^0\}$ be the initial nodal velocities of element i. Then the local coefficient submatrix (consistent mass submatrix)

$$\frac{2M_i}{\Delta^2}\mathbf{t}\left(\iint_R[\tilde{\mathbf{N}}_i(x,y)]^T[\tilde{\mathbf{N}}_i(x,y)]\,dx\,dy\right) \tag{7}$$

is added to $[\mathbf{K}]$, and the local force submatrix

$$\frac{2M_i}{\Delta}\mathbf{t}\left(\iint_R[\tilde{\mathbf{N}}_i(x,y)]^T[\tilde{\mathbf{N}}_i(x,y)]\,dx\,dy\right)\{\mathbf{v}_i^0\} \tag{8}$$

is added to $\{\mathbf{F}\}$. The analytical solutions of the integrations can be exactly evaluated[21]. For next time step, the initial nodal velocities will be the final velocities $\{\mathbf{v}_i\}$ at the end of current time step

$$\{\mathbf{v}_i\} = \frac{2}{\Delta}\{\mathbf{d}_i\} - \{\mathbf{v}_i^0\}. \tag{9}$$

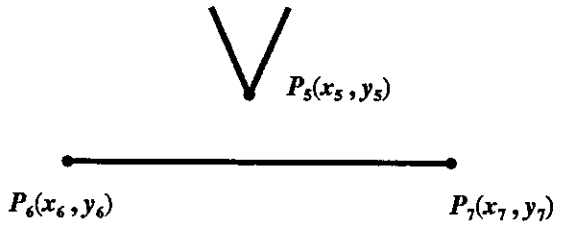

Figure 2. Normal contact of angle to edge

3.4 Normal Contact Submatrix

When a close contact is detected between two blocks, the no-penetration requirement has to be fulfilled. All the contact conditions can be finally converted into the case of an angle P_5 penetrating a contact edge $\overline{P_6P_7}$ (Figure 2). A spring (penalty) with stiffness p^n is introduced between the angle and the contact edge along normal direction of the edge. $P_5(x_5, y_5)$ is on element i and $P_6(x_6, y_6), P_7(x_7, y_7)$ are on element j. P_5, P_6 and P_7

are assigned counterclockwise. $(x_5, y_5), (x_6, y_6), (x_7, y_7)$ are mapped to $(\xi_5, \eta_5), (\xi_6, \eta_6)$ and (ξ_7, η_7). As spring is added, the distance from P_5 to $\overline{P_6 P_7}$ should be zero after the displacement increments are applied (the second order terms are discarded as infinitesimals). Denote

$$a^0 = \begin{vmatrix} 1 & x_5 & y_5 \\ 1 & x_6 & y_6 \\ 1 & x_7 & y_7 \end{vmatrix}$$

and

$$\{\mathbf{m}_i^n\}^T = \frac{1}{L} \begin{Bmatrix} y_6 - y_7 \\ x_7 - x_6 \end{Bmatrix}^T [\mathbf{N}_i(\xi_5, \eta_5)];$$

$$\{\mathbf{n}_j^n\}^T = \frac{1}{L} \begin{Bmatrix} y_7 - y_5 \\ x_5 - x_7 \end{Bmatrix}^T [\mathbf{N}_j(\xi_6, \eta_6)] + \frac{1}{L} \begin{Bmatrix} y_5 - y_6 \\ x_6 - x_5 \end{Bmatrix}^T [\mathbf{N}_j(\xi_7, \eta_7)],$$

where $L = \sqrt{(x_7 - x_6)^2 + (y_7 - y_6)^2}$ is the length of the contact edge. Then the local coefficient submatrices

$$p^n \{\mathbf{m}_i^n\} \{\mathbf{m}_i^n\}^T \tag{10}$$

$$p^n \{\mathbf{m}_i^n\} \{\mathbf{n}_j^n\}^T \tag{11}$$

$$p^n \{\mathbf{n}_j^n\} \{\mathbf{m}_i^n\}^T \tag{12}$$

$$p^n \{\mathbf{n}_j^n\} \{\mathbf{n}_j^n\}^T \tag{13}$$

are added to $[\mathbf{K}]$, and the local force submatrices

$$-p^n \left(\frac{a^0}{L}\right) \{\mathbf{m}_i^n\} \tag{14}$$

$$-p^n \left(\frac{a^0}{L}\right) \{\mathbf{n}_j^n\} \tag{15}$$

are added to $\{\mathbf{F}\}$.

4. NUMERICAL SIMULATIONS

Before the simulation begins, the block system configuration is prepared by a preprocessor. Two kinds of meshes are input: the prescribed physical block boundary mesh and the element mesh (Figures 3 and 4). These two meshes will form a discontinuous block system and a continuous element system respectively. Due to the discontinuity of block boundary, the nodes along block boundaries are further separately numbered. Then the blocks and the elements are mapped together to produce a complete discontinuous block system with continuous element meshes inside (Figure 5). Therefore, the block containing continuous element mesh can have a flexible boundary. The computer programs were written in ANSI C language and the computations were all performed on Silicon Graphics

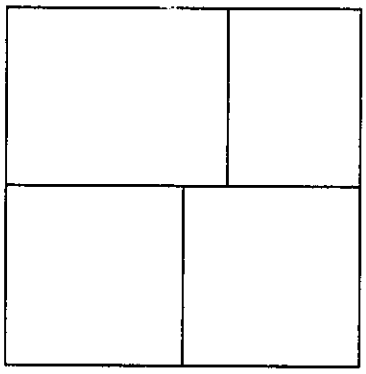

Figure 3. The block mesh

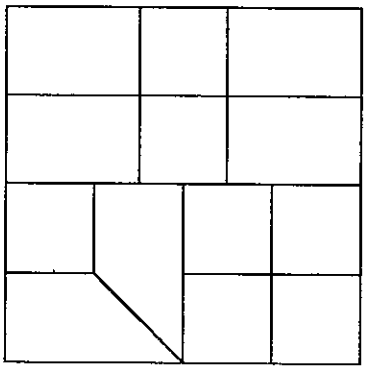

Figure 4. The element mesh

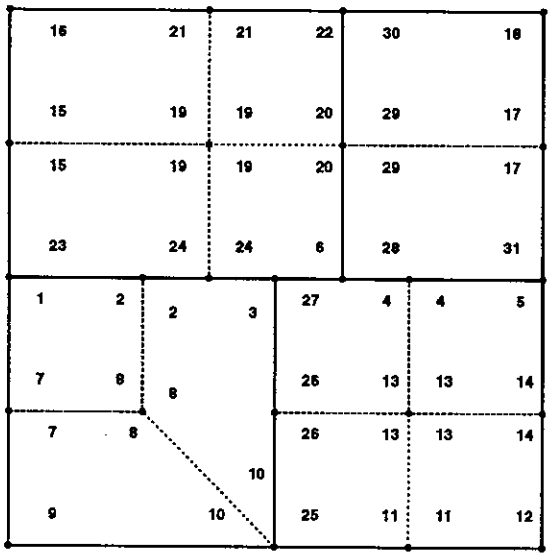

Figure 5. Block system with element meshes

workstation. This numerical model does not have the features of tensile strength nor cohesiveness, but friction between the joints. Numerical simulations are performed to show the improvement and flexibility achieved when finite element mesh is associated with block kinematics to handle discontinuous contact problems under large displacements and deformations.

4.1 Maya Architecture

The ancient architecture of the Maya was created over five hundred years and some of the constructions are even over one thousand years old. The vaulted roof was the highest engineering achievement of the Mayan. The building of an overhanging wall requires consideration of the stability problem. The Maya architect probably had certain knowledge of the principle of stability to construct such kind of structures.

The Maya vaulted chamber consisted of two sloping walls and row of capstones bridging the gap. The core (hearting) of the vault varied according to the evolution of develop-

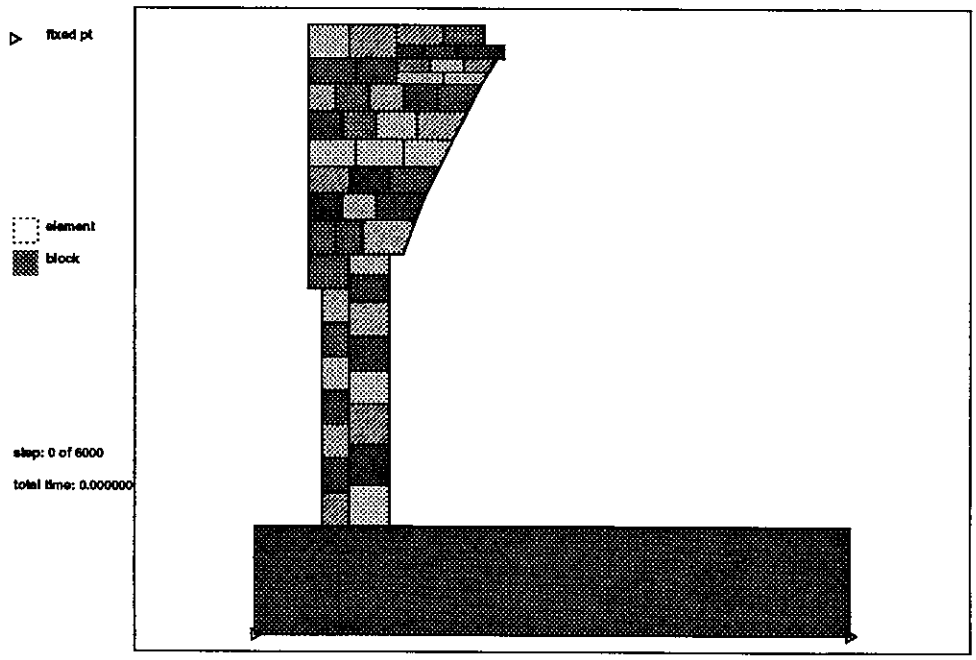

Figure 6. Single vaulted roof Maya structure

ment of the binding material—cement. Two extremely different types of construction were found in Maya vaulted roofs: from the Old Empire's flat stone work, where large flakes or slabs were roughly squared and laid in lime cement to form walls and vaults; to the New Empire's highest development of monolithic lime concrete, which was the composition of broken limestone and lime mortar. The Old Empire's flat stone work was studied in this simulation.

First, a single vaulted roof is modeled to examine the stability behavior of the overhang (Figure 6). The height of the vaulted structure is 3.70 m. The bottom of the ground base is fixed and the system is subjected to the gravity loading. The input data are the following:

static, plane strain condition,
time steps: 6000,
spring stiffness: 1000000 MN/m,
time interval: 0.002 s,
maximum displacement ratio: 0.002,
friction angle: 35°,
element thickness: 1.0 m,
unit mass: 0.0025 Mkg/m^3,
gravity: 9.81 m/s^2,
Young's modulus, Poisson's ratio: 25000 MPa, 0.20.

The stability of the early-built vaulted structures depended upon the binding material. It is supposed that the mortar was too weak during the period of aging for the purpose of supporting the weight of the overhanging vaulting. The weight of the overhang is not distributed over the entire thickness of the vertical wall, but is largely borne by the narrow

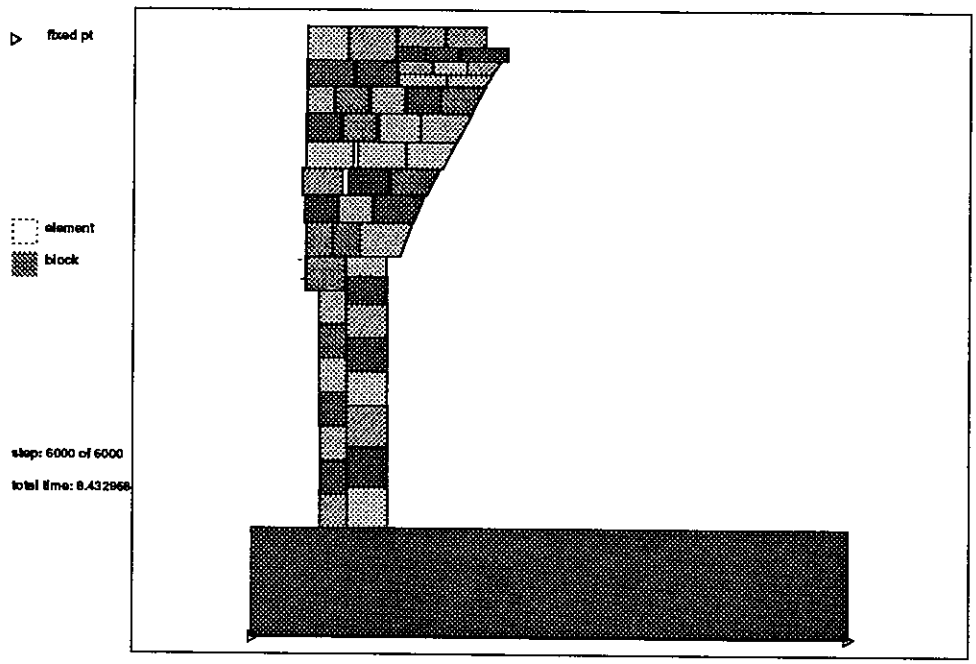

Figure 7. Single vaulted roof Maya structure under gravity, step 6000

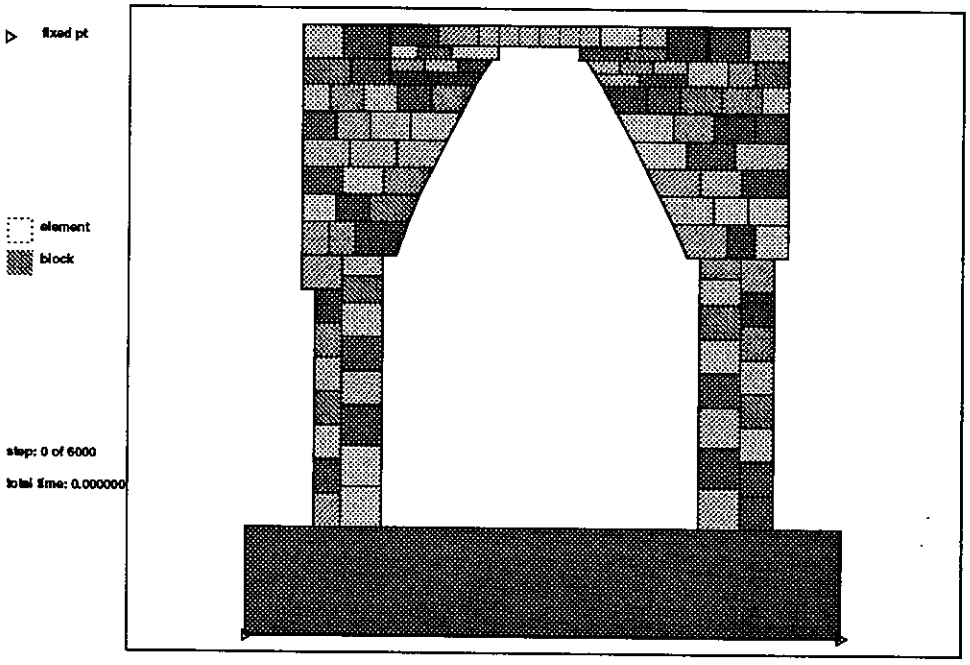

Figure 8. Two vaulted roofs Maya structure

zone of masonry close to the face of the vault. The weight of the upper stones was supported by the ones beneath them, and the upper vaulted structure tends to push the lower vertical wall to move outward. The instability causes the blocks to be separated and tensile strains are produced between the vertical joints due to large friction movements and complicated contact interactions. The result after time step 6000 is shown in Figure 7.

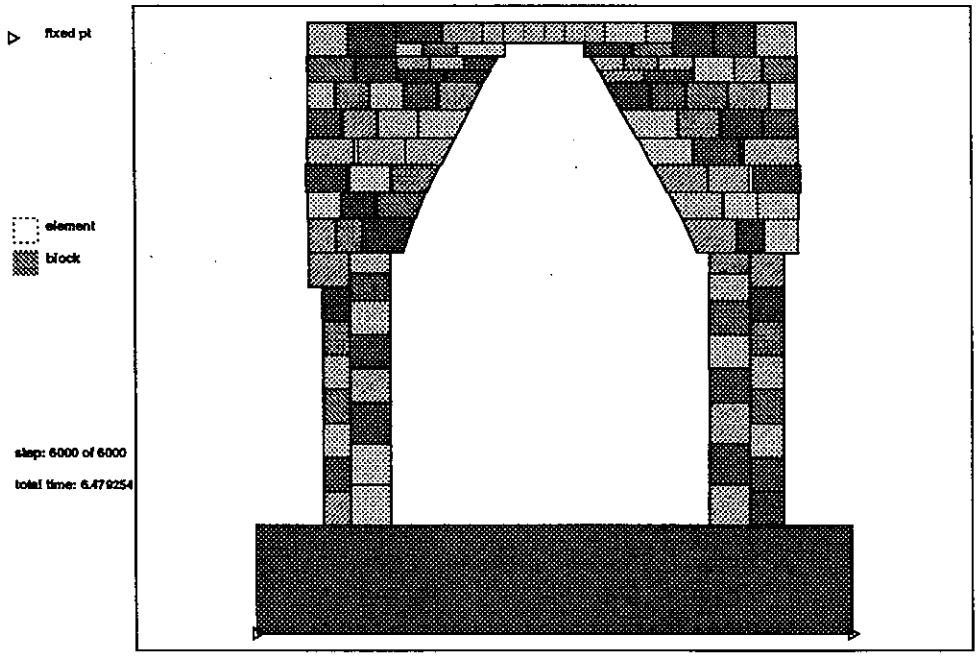

Figure 9. Two vaulted roofs Maya structure under gravity, step 6000

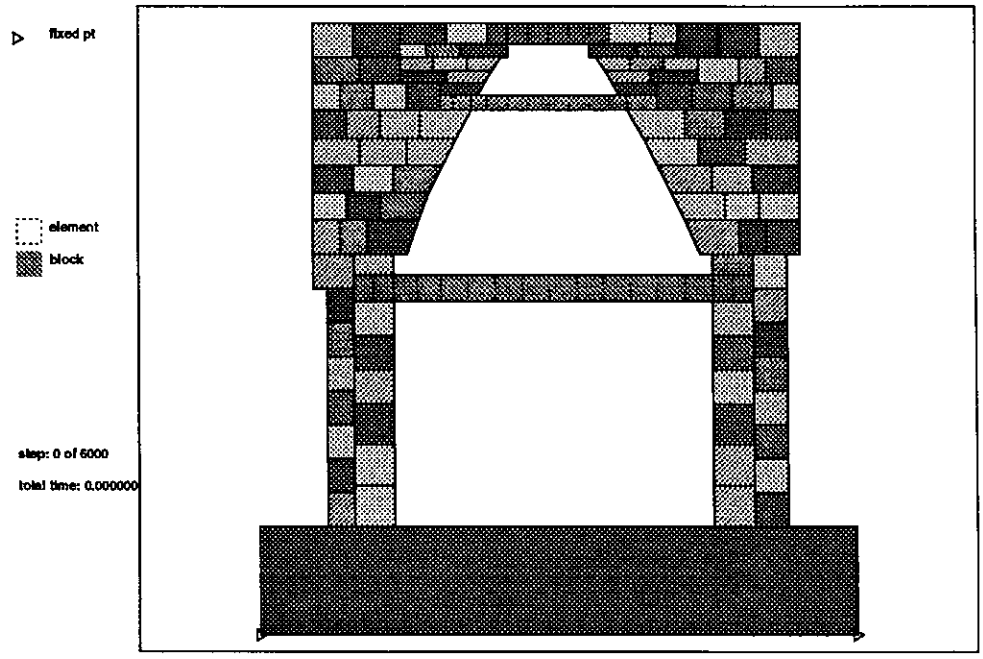

Figure 10. Maya structure with wooden beams

The structure of two vaults and capstones is further analyzed (Figure 8). The structure spanned about 3.60 m. The result after 6000 steps is shown in Figure 9. The numerical analysis of the two vaults structure display the similar instability shown from the computation of the single vault that the vertical walls tend to move outward and openings are generated between vertical joints.

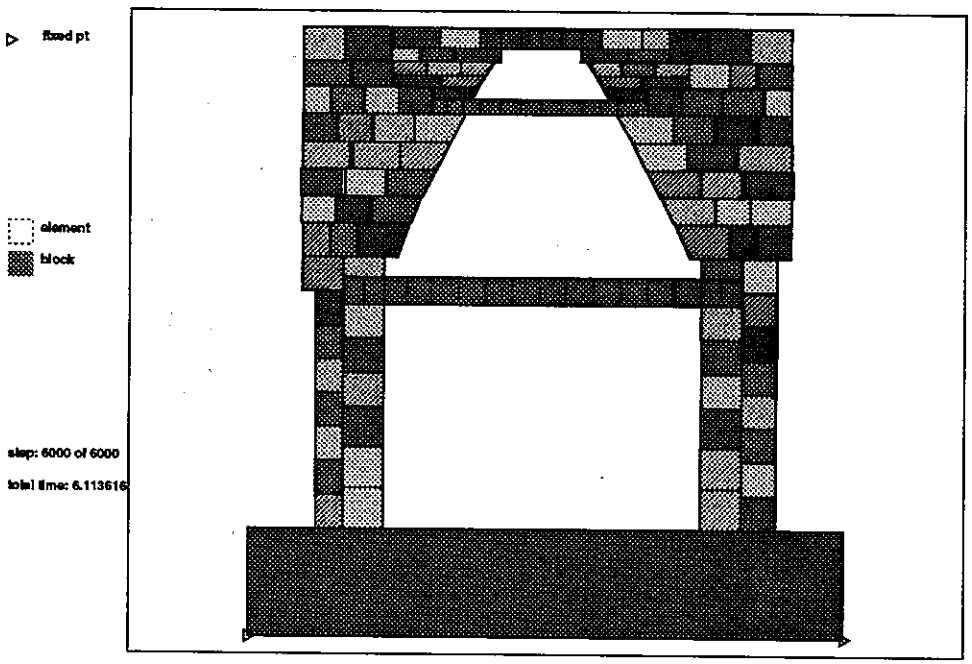

Figure 11. Maya structure with wooden beams under gravity, step 6000

The Maya architect was probably aware of the importance that the mechanical principle of stability and the engineering consideration of strength of the cement played in the construction of the buildings. It seems that the Maya architect has tried to solve the stability problem by inserting the wooden roof members into the vaults. The exact function of the beams has never been known, but may have been as the reinforcement in compensating for the weakness of the binding material used.

The vaulted block system with wooden beams is shown in Figure 10. The input data are the same, except for the unit mass (0.0006 Mkg/m^3), Young's modulus (12000 MPa) and Poisson's ratio (0.10) for the wooden beams. Figure 11 shows the result after time step 6000. The movements of the vaulted blocks are somehow less than those of the vaults without the wooden beams supporting. The computation shows that the wooden members just reinforce the regions near the sockets. The tensile strains as well as openings are produced between the joints because the weights of the vaulted blocks under the upper wooden beam are still borne by the blocks beneath them. The numerical simulation supports the facts that the beams undoubtedly reinforced the vault in the immediate neighborhood of the points where they were embedded. Around these local areas the vault face may have been guided and supported.

From the calculations shown, the instability problem exists in the Maya structures, and the factor that most influences the stability is the strength of the binding material. Without the development of the cement at the early stages of the Empire, the Mayan would not be able to build those unique vaults. The wooden beam members were used extensively to overcome the possible weakness of the mortar before it hardened. However, from the numerical senses, the wooden beams only reinforce the local areas where they were inserted. The instability still exists if the binding material is not strong enough to hold the vaulted stones at positions and to resist the overturning motion of the vaulted stones. With the well-developed cement and the aid of the wooden beams, the Mayan should have no problems in constructing the masonry vaults.

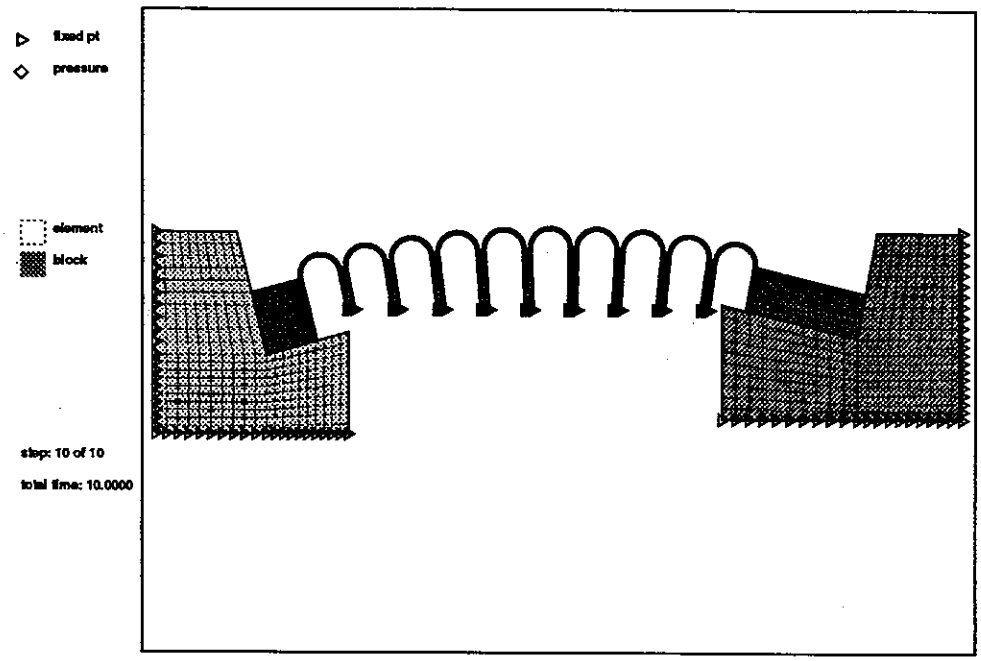

Figure 12. Bartlett Dam with barrels, buttresses, gravity blocks and abutments

4.2 Bartlett Multiple-arch Dam

Bartlett Dam, a multiple-arch dam, is located in central Arizona, USA about 35 miles northeast of Phoenix on the Verde River, the chief tributary of the Salt River. It was constructed for the Salt River Valley Water Users Association by the Bureau of Reclamation to serve as a regulative means for conserving seasonal run-off.

The dam has a maximum height of 286.5 ft, measured from the lowest point in the foundation to the top of the parapet, elevation 1803 ft. The dam is slightly curved in plane so as to most economically fit the topography, and the radius to the axis is 1379.7 ft. The crest length, including the ten arch-barrel sections, the gravity blocks at each end, and the spillway gate structure at the right abutment, is 970 ft. All arch elements of the inclined barrels are circular, and have a total central angle of 180°.

A 2D cross section of Bartlett Dam site is modeled for simulation. The configuration of this section consists of barrels, supporting buttresses, gravity blocks and abutments at each side (Figure 12). This section is assumed to be 60 ft below water level, and the radius to the inside or downstream face of each barrel is constant and equal to 24 ft. The thickness of the barrel at this section is 4 ft. The simulation is to study if the dam is still stable under the loadings of water pressure and earthquake excitation.

The dam is first modeled as a continuum and interacts with abutments at each side. Both sides of the abutments and bottoms of the buttresses are fixed. The dam is only subjected to the water pressure at the upstream face. The compressive water pressure is assumed to be always applied normally on upstream face. The input data are the following:

static, plane strain condition,
time steps: 10,
spring stiffness: 10000000 k/ft,
time interval: 1.0 s,
maximum displacement ratio: 0.0002,

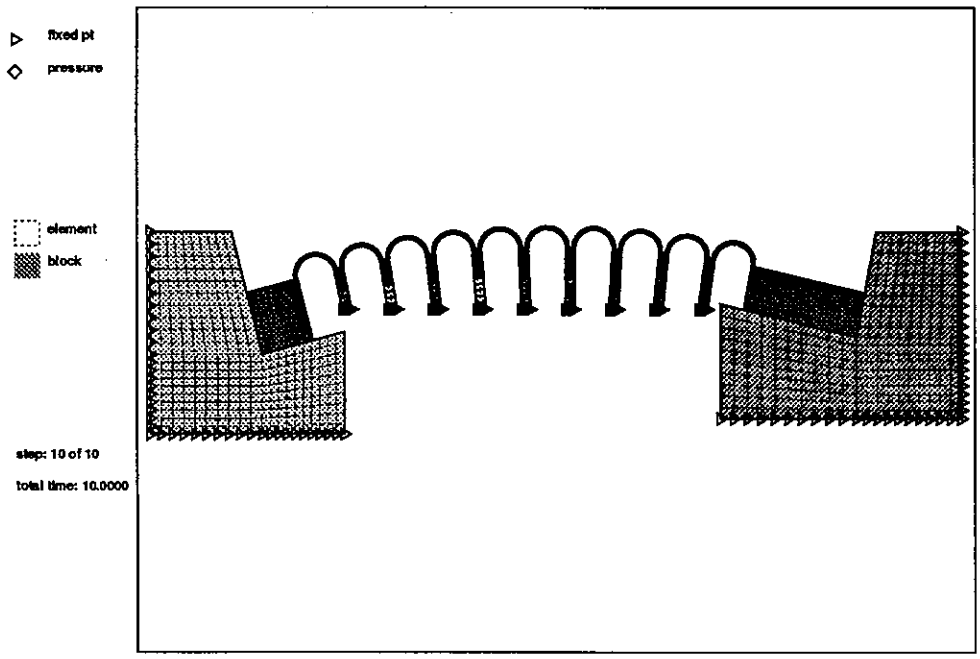

Figure 13. Bartlett Dam with cracks in barrels under water pressure

friction angle: 30°,
element thickness: 1.0 ft,
unit mass: 0.0047 kslugs/ft^3,
Young's modulus, Poisson's ratio: 633600 ksf, 0.20,
water pressure: –3.744 k/ft.

Under the loading of water pressure, the El Central ground motion record is also applied in plane horizontally at the abutments and buttresses (all use same shaking records). Time step of 2500 and time interval of 0.02 s are input for the dynamic calculation. The total shaking time is 50 s. When modeling the whole dam as a continuum, the dynamic earthquake excitation may produce tensile stress, which exceeds the designing strength, in the barrels. Due to this reason, each barrel is assumed to be damaged and break at the center section to form discontinuous blocks (Figure 13).

The same input data are used for the static water pressure loading. The dynamic calculation is performed for the earthquake excitation applied in plane horizontally and vertically. Total shaking time is close to 50 s. Figures 14 and 15 display the results after 2500 steps and they show some shearing effect at the barrels.

The Bartlett Dam is simulated from the continuous case to the discontinuous one. The dam should be stable under water pressure loading. The dynamic simulation for discontinuous case is not stable in 2D model. However, for true 3D structure, the dam is much stronger and the shaking record for each buttress could be different. The 2D computation is just to provide the qualitative information for the designing of a dam.

4.3 Leaf Spring-dashpot Suspension System

The analysis of leaf spring is a laminated beam problem. It has the characteristics of large displacements and deformations, as well as complicated contact geometry and slid

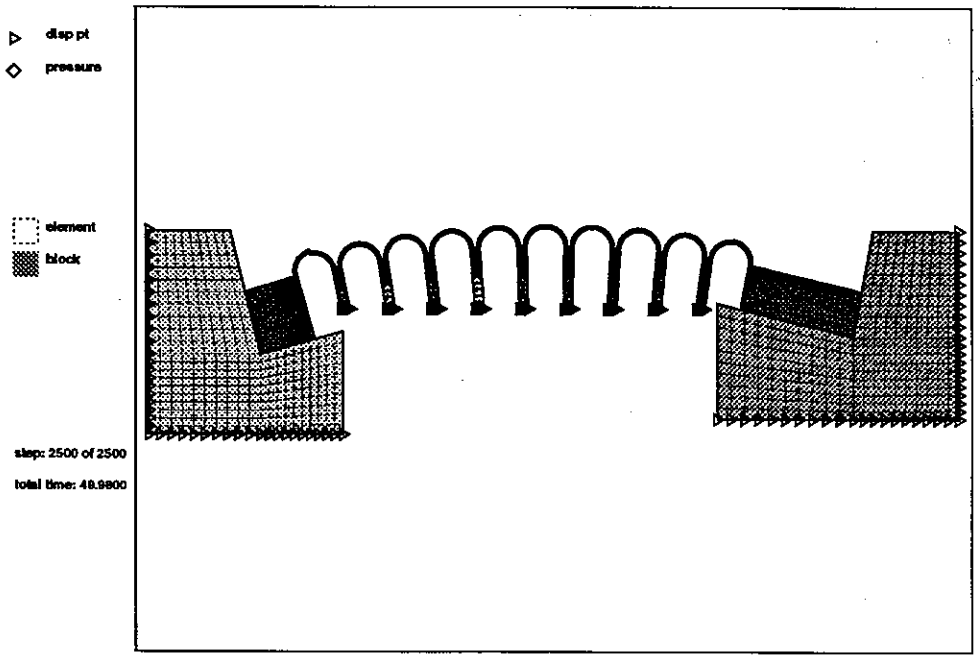

Figure 14. Bartlett Dam under in plane horizontal earthquake excitation

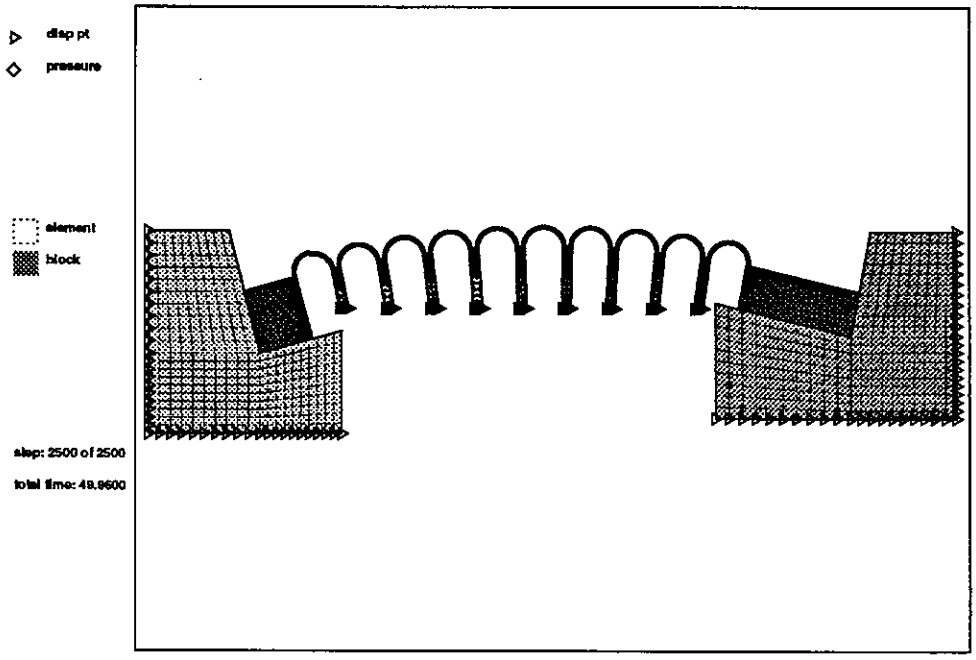

Figure 15. Bartlett Dam under in plane vertical earthquake excitation

ing conditions at discontinuous interfaces. The feature of flexible boundary of the block is suitable for modeling large displacements and deformations of the leaf spring system.

Four oblique beams are piled up to form a leaf spring system. The top beam is 1.4 m long, beam depth is 0.8 cm. On top of the leaf spring is a large mass body with depth of 7 cm. The top beam is connected with the large mass body and is fixed at one end, shackled

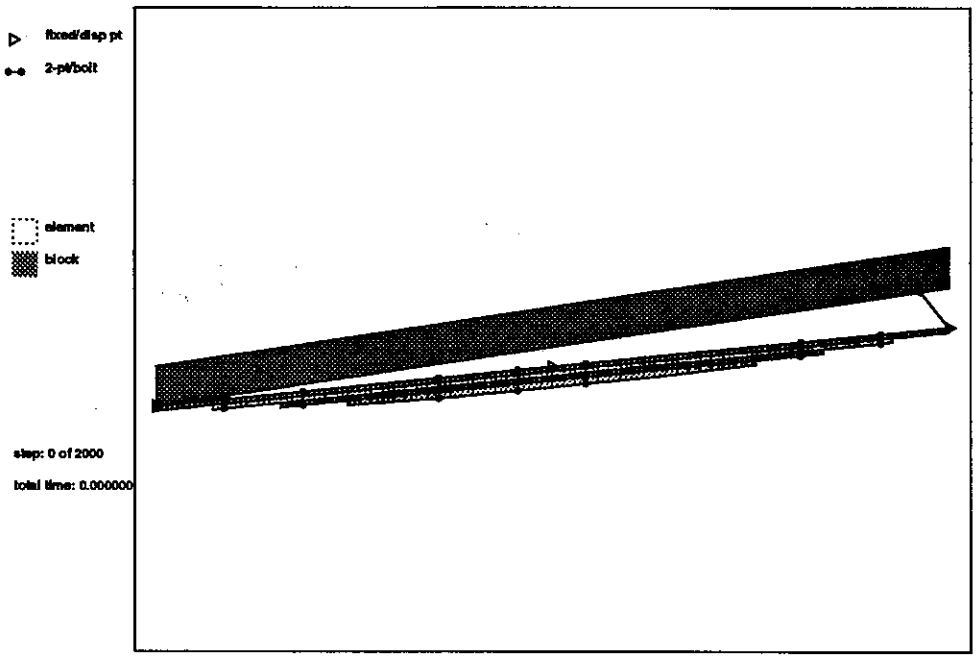

Figure 16. Leaf spring system, one end fixed; the other end shackled

at the other end (bolt with stiffness $EA = 200$ MN). Two bolts (stiffness $EA = 60$ MN) connect the top and third beams to simulate the hoop clamps often seen in automobile's leaf spring system. Some other bolts (stiffness $EA = 60, 200$ MN) are connected for the purpose of deforming the leaf spring system. The leaf spring (Figure 16) is forced 10.5 cm downward at the center within 1.5 s to deform to a shape of an arc since most of the leaf spring systems are arc-shaped. The input data are the following:

static, plane strain condition,
time steps: 2000,
spring stiffness: 1000000 MN/m,
time interval: 0.001 s,
maximum displacement ratio: 0.002,
friction angle: 20°,
element thickness: 0.1 m,
unit mass: 0.00785 Mkg/m^3,
gravity: 9.81 m/s^2,
Young's modulus, Poisson's ratio: 200000 MPa, 0.28.

The solution of large displacement is the accumulations of the small displacement in each time step. Figure 17 shows the result at the end of calculation. This simulation demonstrates features of the numerical model, which is capable of enhancing the deformation ability and refining the stress field of a block for discontinuous computation.

Suppose that the leaf spring will be mounted to a wheel to test the vibration behaviors of suspension system. The block system configuration from previous calculation is used and the stresses in beams as well as bolt forces are reset to zero. Six displacement-control points are assigned near the center region to simulate the mounting of leaf spring to a wheel. A dashpot is connected between the large mass body and the bottom beam.

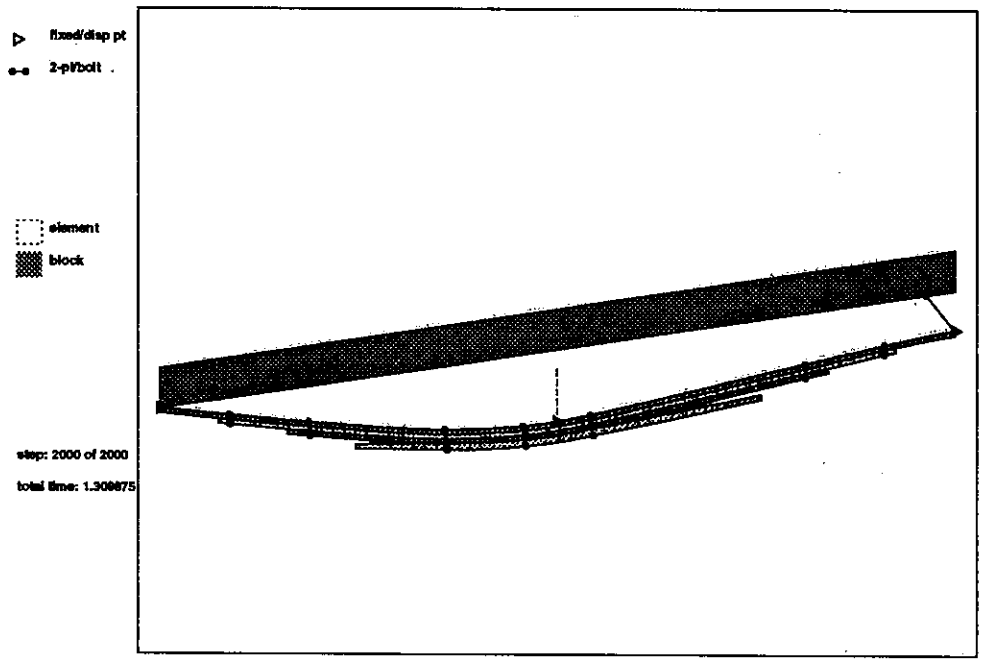

Figure 17. Deformed shape of the leaf spring

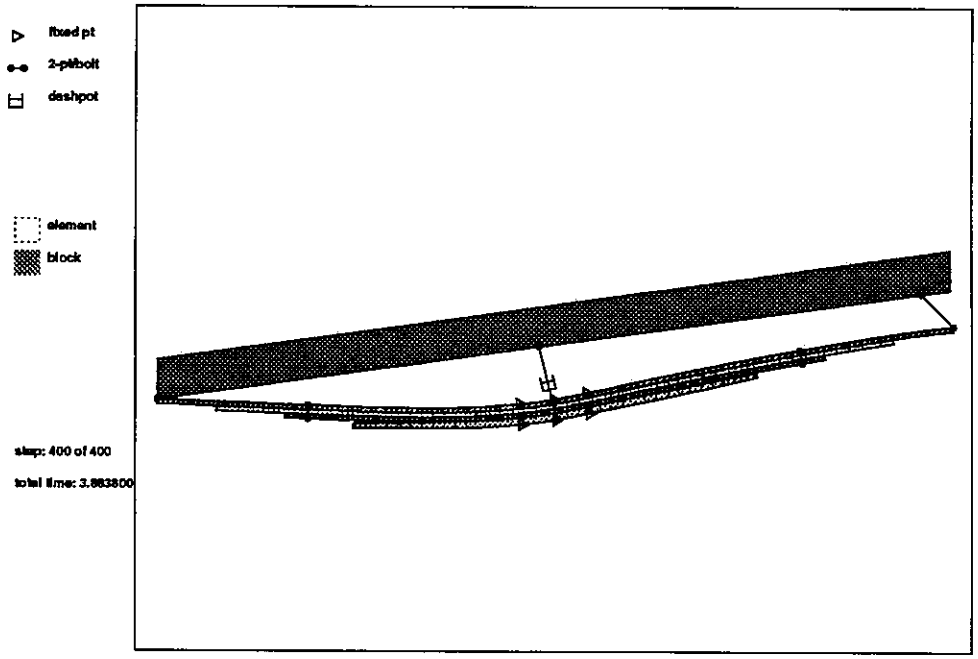

Figure 18. Equilibrium position of the leaf spring, car mass

The following computations intend to simulate the vibration response of an automobile under road excitation. The leaf spring carries two types of mass body: one is light mass (unit mass of 0.00785 Mkg/m^3), the other is car mass (unit mass of 0.05495 Mkg/m^3). The spring system is set to the equilibrium position under static loading of gravity force (Figure 18, car mass).

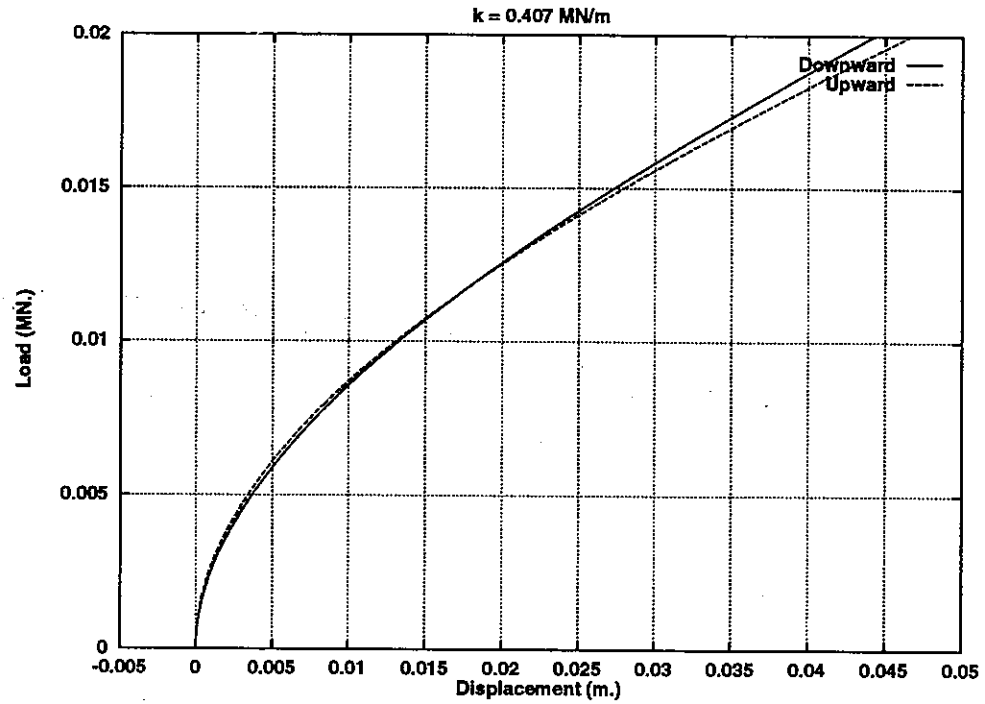

Figure 19. Load-displacement curves, light mass

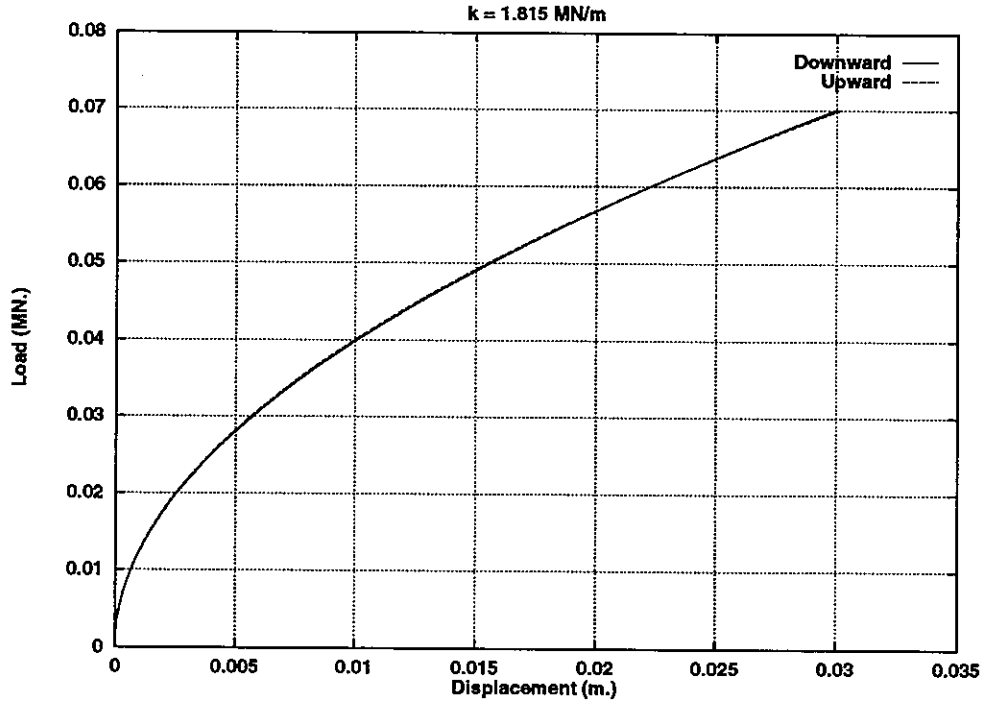

Figure 20. Load-displacement curves, car mass

The information of system stiffness of the leaf spring is required for dynamic computations. The loadings of $\pm$ 0.02 MN, $\pm$ 0.07 MN are separately applied on top of the light and car masses to obtain system stiffness. Using static calculations, the loadings are applied within 1.0 s and time interval is 1×10^{-3} s. Figures 19 and 20 show the load-displacement curves of static calculations for light and car masses. Therefore, the system stiffness is

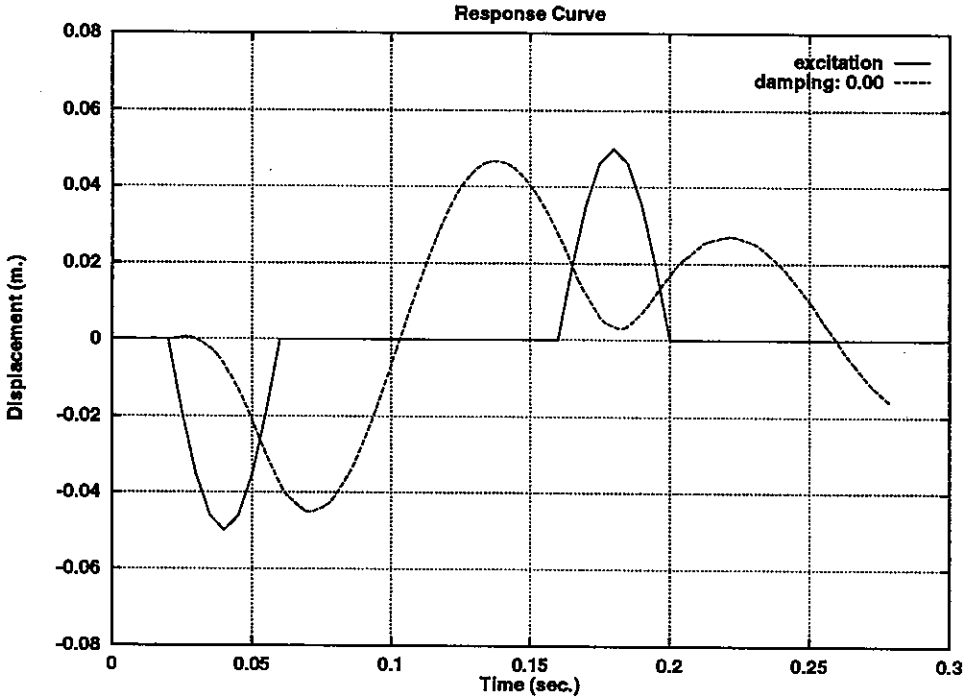

Figure 21. Response of the light mass

taken approximately as 0.407 MN/m for light mass case (1.815 MN/m for car mass) for the following dynamic vibration computations.

A road excitation record is applied at the positions of mounting area. Dynamic calculation is required for vibration simulation. The damping coefficient is defined by $\mu = 2\zeta\sqrt{mk}$, where ζ is damping ratio, m is total carrying mass, and k is system stiffness. Then the damping coefficient of dashpot is given by $\mu \approx 0.0112\zeta$ for light mass case ($\mu \approx 0.0625\zeta$ for car mass).

The response of the mass is recorded at the center on top of the mass body. The time step is 7500 and the time interval is 4×10^{-5} s. For light mass case, a damping ratio of zero is used for dashpot to record the response of free vibrations. Figure 21 shows the response of free vibrations of the light mass.

As for another simulation, the car mass is carried to simulate the real automobile's leaf spring-dashpot suspension system. For the consideration of comfortable ride for commercial automobiles, damping coefficient for the dashpot is normally set close to critical damping (damping ratio of 1.0). A damping coefficient of 0.05625 MNs/m (damping ratio of 0.9) is assigned for the computation. Figure 22 shows the response of the car mass. The result gives the right response that there is no oscillation in the free vibration region.

5. CONCLUSIONS

The objective of discontinuous deformation analysis is to find the solutions of large displacement and deformation for discontinuous contact analyses. The large displacements and deformations are the accumulations of the small increment from each time step. Based on the concept of integration from calculus that the result of a nonlinear integrating path

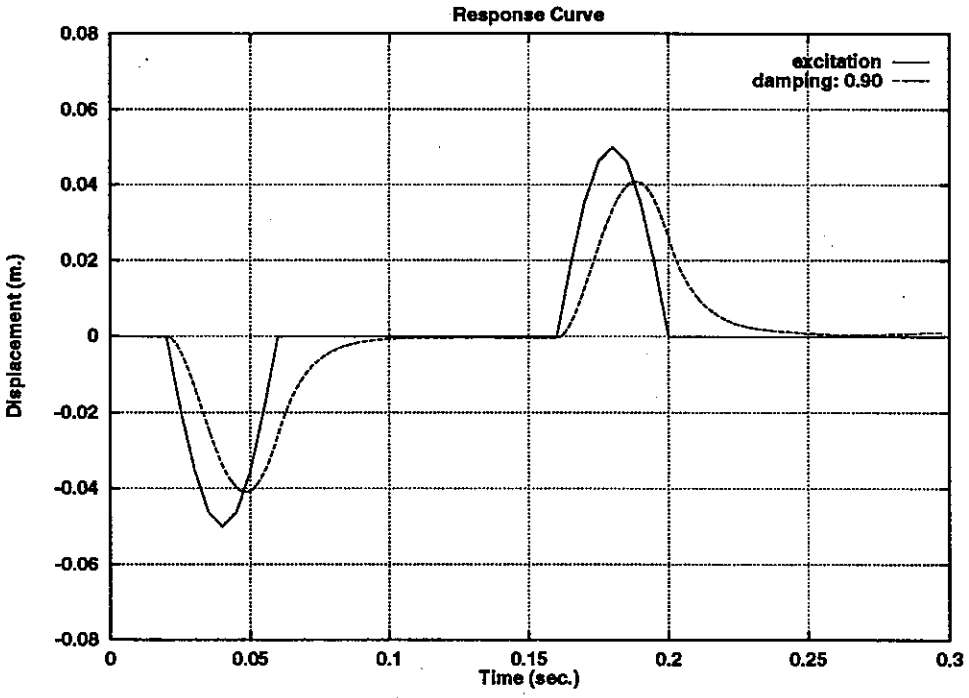

Figure 22. Response of the car mass

is the summation of linearly infinitesimal increments, discontinuous deformation analysis basically solves the problems of geometric nonlinearity by finding the result from linearly simultaneous equations for each time step and accumulating the increments for final solution.

At the end of each time step, the equilibrium condition, the no-tension, no-penetration constraint conditions, and the Coulomb's friction law are satisfied at all contacts. The unique block kinematics is necessary for computing the complicated contact geometry of multi-body block system and the accurately-integrated inertia matrix controls the convergence of open-close iterations for discontinuous system. Based on the formulations of penalty method, the incorporation of diagonally-dominated inertia matrix makes the global coefficient matrix well-conditioned, as long as the time interval is small enough.

For the considerations of flexible boundary and stress refinement of each block, the original constantly-stressed block is replaced by an element-meshed block. The unknowns are the nodal displacements, and the formulation is nodal-based. Numerical simulations demonstrate that the proposed numerical model satisfactorily gives the solutions for discontinuous contact problems.

ACKNOWLEDGEMENT

The authors are grateful to Dr. Gen-hua Shi for providing the source codes of DDA programs and for the guidance in the development of the computer programs.

REFERENCES

1. Zienkiewicz, O. C. and Taylor, R. L., *The Finite Element Method; Basic Formulation and Linear Problems,* **1**, 4th edn., McGraw-Hill, London (1989).
2. Zienkiewicz, O. C. and Taylor, R. L., *The Finite Element Method; Solid and Fluid Mechanics, Dynamics and Non-linearity,* **2**, 4th edn., McGraw-Hill, London (1991).
3. Goodman, R. E., Taylor, R. L. and Brekke, T. L., A model for the mechanics of jointed rock, *J. Soil Mech. Found. Div., ASCE,* **94**, 637–660 (1968).
4. Sachdeva, T. D. and Ramakrishnan, C. V., A finite element solution for the two-dimensional elastic contact problems with friction, *Int. J. Numer. Meth. Engng.,* **17**, 1257–1271 (1981).
5. Chen, W. H. and Yeh, J. T., Finite element analysis of finite deformation contact problems with friction, *Comput. Struct.,* **29**, 423–436 (1988).
6. Nour-Omid, B. and Wriggers, P., A two-level iteration method for solution of contact problems, *Comput. Meth. Appl. Mech. Engng.,* **54**, 131–144 (1986).
7. Carpenter, N. J., Taylor, R. L. and Katona, M. G., Lagrange constraints for transient finite element surface contact, *Int. J. Numer. Meth. Engng.,* **32**, 103–128 (1991).
8. Curnier, A. and Alart, P., A generalized Newton method for contact problems with friction, *J. Méch. Théo. Appl.,* **7**, 67–82 (1988).
9. Huněk, I., On a penalty formulation for contact-impact problems, *Comput. Struct.,* **48**, 193–203 (1993).
10. Wriggers, P. and Simo, J. C., A note on tangent stiffness for fully nonlinear contact problems, *Commun. Appl. Numer. Meth.,* **1**, 199–203 (1985).
11. Simo, J. C., Wriggers, P and Taylor, R. L., A perturbed Lagrangian formulation for the finite element solution of contact problems, *Comput. Meth. Appl. Mech. Engng.,* **50**, 163–180 (1985).
12. Ju, J.-W. and Taylor, R. L., A perturbed Lagrangian formulation for the finite element solution of nonlinear frictional contact problems, *J. Theor. Appl. Mech.,* Special issue, suppl. 1 to **7**, 1–14 (1988).
13. Landers, J. A. and Taylor, R. L., An augmented Lagrangian formulation for the finite element solution of contact problems, *Internal Report,* University of California at Berkeley (1985).
14. Simo, J. C. and Laursen, T. A., An augmented Lagrangian treatment of contact problems involving friction, *Comput. Struct.,* **42**, 97–116 (1992).
15. Heegaard, J.-H. and Curnier, A., An augmented Lagrangian method for discrete large-slip contact problems, *Int. J. Numer. Meth. Engng.,* **36**, 569–593 (1993).
16. Papadopoulos, P., On the finite element solution of general contact problems, *Ph.D. Thesis,* Department of Civil Engineering, University of California at Berkeley (1991).
17. Zhong, Z. H., *Finite Element Procedures for Contact-impact Problems,* Oxford University Press, Oxford (1993).
18. Cundall, P. A., A computer model for simulating progressive, large scale movements in blocky rock systems, *Symp. Int. Soc. Rock Mech.,* 11–18 (1971).
19. Cundall, P. A., Formulation of a three-dimensional distinct element model—part I. A scheme to detect and represent contacts in a system composed of many polyhedral blocks, *Int. J. Rock Mech. Min. Sci.,* **25**, 107–116 (1988).

20. Shi, G., Discontinuous deformation analysis—a new numerical model for the statics and dynamics of block systems, *Ph.D. Thesis,* Department of Civil Engineering, University of California at Berkeley (1988).
21. Shyu, K., Nodal-based discontinuous deformation analysis, *Ph.D. Thesis,* Department of Civil Engineering, University of California at Berkeley (1993).
22. Liang, G.-P. and He, H.-H., The non-conforming domain decomposition method for elliptical problems with Lagrange multipliers, *Chinese J. Numer. Meth. Appl.,* **15,** 8–19 (1993).
23. Ke, T., Simulated testing of two dimensional heterogeneous and discontinuous rock masses using discontinuous deformation analysis, *Ph.D. Thesis,* Department of Civil Engineering, University of California at Berkeley (1993).
24. Chang, C.-T., Nonlinear dynamic discontinuous deformation analysis with finite element meshed block system, *Ph.D. Thesis,* Department of Civil Engineering, University of California at Berkeley (1994).
25. Chern, J. C., Koo, C. Y. and Chen, S., Development of second order displacement function for DDA and manifold method, *Work. Forum Manifold Meth. Mater. Analy.,* **1,** 183–202 (1995).

Nonlinear Dynamic Discontinuous Deformation Analysis with Finite Element Mesh in Each Block

Chiao-Tung Chang

Lim and Nascimento Engineering Corporation
1971 E. Fourth St., Suite 200
Santa Ana, CA 92705, U.S.A.

ABSTRACT

A numerical model combining the Discontinuous Deformation Analysis (DDA) and the Finite Element Method (FEM) is developed to study the global stability and failure modes of the joints or interfaces in the discontinuous block (multibody) system, and the stress distribution analysis of each block. This model maintains the characteristics of DDA's *discontinuity*, FEM's *continuity*, and retains the DDA's *step-by-step linear kinematics* approach that has been successfully used in solving geometric nonlinearity problems. The new formulation improves the block's deformation ability by adding a finite element mesh in each DDA's block, and incorporates nonlinear inelastic material behavior in each element. Therefore, static and dynamic analyses can be performed to study the detailed mechanical response, and the global stability of the finite element meshed block system.

1. INTRODUCTION

Complex geometry is usually required in the modeling of realistic engineering problems. Using a piecewise smooth approach, the pioneers in the field of finite element method (FEM) were able to transform the differential equations into integral equations in order to solve the problems of continuous structures with general shapes. The stress (strain) distribution in the structure was used to successfully predict and detect weak zones. FEM is now a well-developed and powerful method for solving continuous deformation problems.

Practical geological discontinuity problems were taken into account after FEM development. Goodman et al[1] developed Jointed Element in 1968 and applied this method extensively in rock engineering. In 1971 Cundall[2] introduced the distinct element method (DEM), which is now widely used for jointed or blocky rock. These two methods are force methods that incorporate fictitious forces to reach the convergence criteria of block overlapping and equilibrium.

Adopting implicit algorithm and using minimization of total potential energy to reach equilibrium, Shi[3] developed discontinuous deformation analysis (DDA) in 1988. DDA can solve the stability and stress analysis of a system of blocks containing pre-existing cracks and joints, and it was primarily applied in rock mechanics with great success in the stability of tunnels and of rock slopes. DDA adopts the step-by-step linear approach to evaluate the failure modes and global stability of a discontinuous block system. The movement of the blocks is controlled by Coulomb's friction law, the contact modes (open, close, sliding) between blocks, and the kinematics restrictions of no-tension and no-penetration. With the addition of inertial force which controls the stability of open-close iteration of the block system, DDA is able to solve large displacement and deformation problems for numerous discontinuous blocks with moving boundaries under dynamic loads.

The original DDA approach uses a complete first order polynomial approximation of deformation in each block, therefore, making the stress or strain in each block constant. Since both FEM and DDA use the same implicit algorithm, it is natural to add a finite element mesh in each block to improve the deformation field in the block. The proposed numerical model developed the equations for the triangular elements. All the submatrices formulated to form the global stiffness matrix in the simultaneous governing equations were analytically derived and accurate. The task of detecting contacts between the element-meshed blocks is still carried by the DDA's algorithm of block kinematics. Since with the addition of a finite element discretization in the block, more nodes are scattered along the boundaries of the blocks, the search of reference lines for block contacts is changed from two consecutive vertices of the block in original DDA to two consecutive nodes of the element along the boundaries of the block in the present model. Therefore, the flexible boundaries of the blocks makes contact detection more complicated.

At each time step in the discontinuous deformation analysis, small displacements and deformations of the blocks are obtained in order to satisfy the infinitesimal displacement theory. Using the step-by-step linear approach, DDA solves large displacements and deformations of the blocks by accumulating small ones at each time step, thus, handling the nonlinear geometric problem. The proposed model also develops and implements nonlinear

material behavior in the element using step-by-step piecewise linear approximation. The deformation constants and the stiffness matrix are changeable at each time step. In addition to frictional energy lost, the change of deformability provided another source of energy consumption in the numerical model.

2. DDA WITH FINITE ELEMENT MESH

The main purpose of placing a finite element mesh in each block is to improve its deformation ability. Since the constant stress and strain in each block are not a realistic assumption for a big block in DDA, the addition of a finite element discretization in each block can eliminate this shortcoming. Not only the movement of the block system will be depicted by DDA, but stress distributions in the blocks can also be obtained.

2.1 Merging Finite Element Mesh into a Block

The finite element mesh of constant strain elements is chosen in the proposed model. The complete first order polynomial displacement function are used to describe the triangular element's behavior. The function of block shapes is used as the contact boundaries for the purpose of block kinematics in the block system. Thus, the block geometry doesn't need to be triangular. Consider a three-node element where the boundaries are drawn along the nodes in certain directions, forming a three-edge block with the same size as the element. This configuration is called a *three-node "element block"* — a block with nodal displacements as unknowns. If a three-node element is extended to an n-node element mesh, an *element-mesh block* with n nodes is obtained. In general, a block can be as small as an element or as large as an element mesh. Different meshes can also be put into different blocks if conditions permit.

The meshes of the elements and the boundaries of the blocks are input separately in the mesh generation program (Figure 1.a, 1.b). After tree cutting and forming process of element meshes and blocks, both are merged with same nodal numbers between the elements, but with different nodal numbers between the boundaries of the blocks (Figure 1.c). The basic element in this numerical model is a triangular element. For the convenience of putting the mesh in each block, four-node element meshes are generated first in the mesh program. Then, a condensed five-node element— a quadrilateral element with four nodes on its vertices and one additional node inside it that forms four triangular elements— is used for forward model computations.

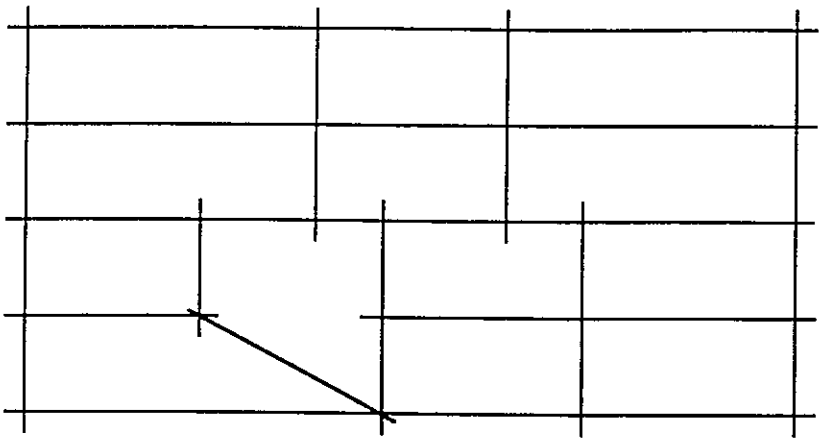

Figure 1.a. Input lines for elements

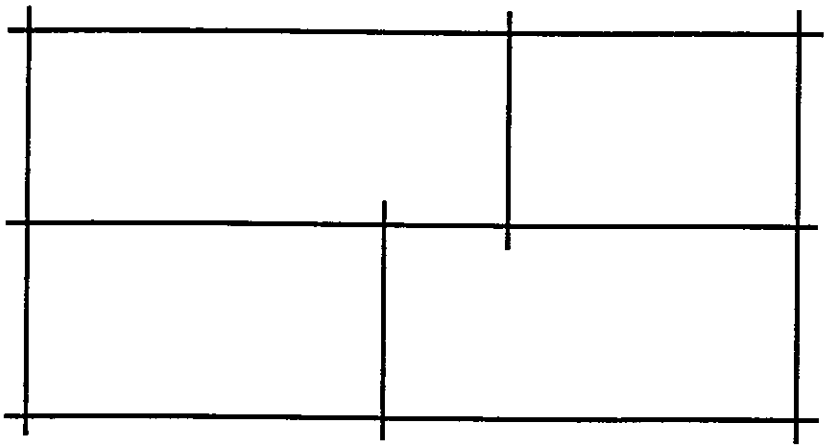

Figure 1.b. Input lines for blocks

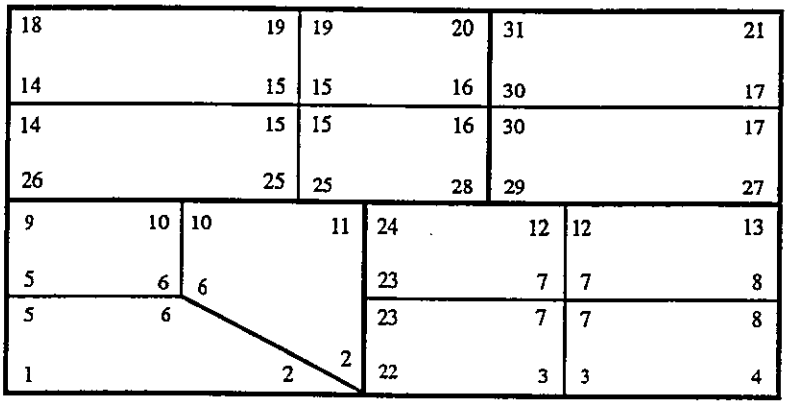

Figure 1.c. Mesh of elements and blocks
(same nodal numbers are shared between the elements, but different nodal numbers are used along the block boundaries)

Based on the idea of element-mesh blocks, the boundary of the mesh in standard FEM is just one block in DDA. By adding the finite element mesh into each block, it is possible to take advantage of the continuous properties in FEM and discontinuous characteristics of DDA, thereby simulating engineering problems more accurately. This significant contribution was first make by Shyu[4].

2.2 Simultaneous Equilibrium Equations

The simultaneous equilibrium equations derived by minimizing the total potential energy, Π, have the following form:

$$\begin{pmatrix} [K_{11}] & [K_{12}] & [K_{13}] & \cdots & [K_{1n}] \\ [K_{21}] & [K_{22}] & [K_{23}] & \cdots & [K_{2n}] \\ [K_{31}] & [K_{32}] & [K_{33}] & \cdots & [K_{3n}] \\ \vdots & \vdots & \vdots & \ddots & \vdots \\ [K_{n1}] & [K_{n2}] & [K_{n3}] & \cdots & [K_{nn}] \end{pmatrix} \begin{pmatrix} \{D_1\} \\ \{D_2\} \\ \{D_3\} \\ \vdots \\ \{D_n\} \end{pmatrix} = \begin{pmatrix} \{F_1\} \\ \{F_2\} \\ \{F_3\} \\ \vdots \\ \{F_n\} \end{pmatrix}$$

As in the FEM, the nodal displacements are chosen as unknown variables and each has two degree-of-freedom for the two-dimensional case. For the given i-th node, $[K_{ij}]$ is 2×2 submatrix representing the stiffness of displacement at the i-th node with respect to the load acting on the j-th node. $\{D_i\}$ and $\{F_i\}$ are 2×1 submatrices for the corresponding unknown nodal displacement and nodal loading matrices.

2.3 Displacement Functions

For a constant-strain triangular element (Figure 2), the displacement functions can be described by a complete first order polynomial so that

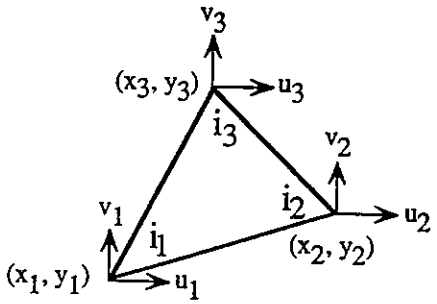

Figure 2. Triangular element

$$u = a_1 + b_1 x + c_1 y$$
$$v = a_2 + b_2 x + c_2 y$$

With (x_i, y_i) and (u_i, v_i) being the coordinates of nodes and related nodal displacements of the triangular element where $i = 1,2,3$,

$$\begin{pmatrix} a_1 \\ b_1 \\ c_1 \end{pmatrix} = \begin{pmatrix} 1 & x_1 & y_1 \\ 1 & x_2 & y_2 \\ 1 & x_3 & y_3 \end{pmatrix}^{-1} \begin{pmatrix} u_1 \\ u_2 \\ u_3 \end{pmatrix}, \qquad \begin{pmatrix} a_2 \\ b_2 \\ c_2 \end{pmatrix} = \begin{pmatrix} 1 & x_1 & y_1 \\ 1 & x_2 & y_2 \\ 1 & x_3 & y_3 \end{pmatrix}^{-1} \begin{pmatrix} v_1 \\ v_2 \\ v_3 \end{pmatrix}.$$

Set

$$\begin{pmatrix} f_{11} & f_{12} & f_{13} \\ f_{21} & f_{22} & f_{23} \\ f_{31} & f_{32} & f_{33} \end{pmatrix} = \begin{pmatrix} 1 & x_1 & y_1 \\ 1 & x_2 & y_2 \\ 1 & x_3 & y_3 \end{pmatrix}^{-1}, \qquad \begin{pmatrix} f_1 & f_2 & f_3 \end{pmatrix} = \begin{pmatrix} 1 & x & y \end{pmatrix} \begin{pmatrix} f_{11} & f_{12} & f_{13} \\ f_{21} & f_{22} & f_{23} \\ f_{31} & f_{32} & f_{33} \end{pmatrix},$$

then

$$\begin{pmatrix} u \\ v \end{pmatrix} = \begin{pmatrix} f_1 & 0 & f_2 & 0 & f_3 & 0 \\ 0 & f_1 & 0 & f_2 & 0 & f_3 \end{pmatrix} \begin{pmatrix} u_1 \\ v_1 \\ u_2 \\ v_2 \\ u_3 \\ v_3 \end{pmatrix} = [\mathbf{T}]\{\mathbf{d}\},$$

$$[\mathbf{T}] = \begin{pmatrix} \mathbf{T}_1 & \mathbf{T}_2 & \mathbf{T}_3 \end{pmatrix}; \qquad \{\mathbf{d}\} = \begin{pmatrix} \mathbf{d}_1 \\ \mathbf{d}_2 \\ \mathbf{d}_3 \end{pmatrix},$$

$$[\mathbf{T}_i] = \begin{pmatrix} f_i & 0 \\ 0 & f_i \end{pmatrix}; \qquad \{\mathbf{d}_i\} = \begin{pmatrix} u_i \\ v_i \end{pmatrix}, \quad i = 1,2,3.$$

$[\mathbf{T}_i]$ and $\{\mathbf{d}_i\}$ are the matrices of shape function and displacement variables per node.

2.4 Inertia Matrix

Because the inertia force plays a key role in rigid body motion, it is crucial to include it in dealing with the motions of a discontinuous block system. Assuming the acceleration in each time step is constant, the 2×2 nodal stiffness matrices and 2×1 force matrices of element i can be described as

$$[\mathbf{K}_{i(r)i(s)}] = \frac{2M}{\Delta^2}\left[\iint_A [T_{i(r)}]^T [T_{i(s)}] dxdy\right] \quad r,s = 1,2,3$$

$$[\mathbf{F}_{i(r)}] = \frac{2M}{\Delta}\left[\iint_A [T_{i(r)}]^T [T_{i(s)}] dxdy\right]\{V_{i(s)}(0)\} \quad \begin{cases} r = 1,2,3 \\ s = \text{tensor sum} \end{cases}$$

where

$$\{V_{i(s)}(0)\} = \frac{\partial}{\partial t}\begin{pmatrix} u_{i(s)}(0) \\ v_{i(s)}(0) \end{pmatrix} .$$

M is the mass per unit area, and Δ is time interval of current time step. The analytical solutions of the above integrations can be obtained[5].

2.5 Normal Contact Matrix

When two bodies are detected to be in contact, the requirement of no penetration must be satisfied in DDA's block kinematics. The contact problem reduces to the relationship of angle-to-edge (point-to-line) case. When interpenetration pushes the point P_4 through the reference line $\overline{P_5P_6}$ (Figure 3), the distance between them should be zero after the installation of spring with stiffness p at the contact position. The displacement of the spring is

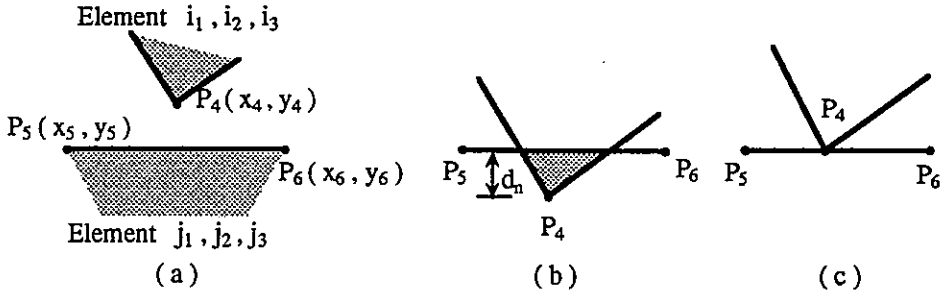

Figure 3. Angle-to-edge normal contact process

$$d_n = \frac{\Delta}{L} = \frac{1}{L}\begin{vmatrix} 1 & x_4+u_4 & y_4+v_4 \\ 1 & x_5+u_5 & y_5+v_5 \\ 1 & x_6+u_6 & y_6+v_6 \end{vmatrix} , \quad L = \sqrt{(x_5-x_6)^2+(y_5-y_6)^2}$$

Let

$$S_0 = \begin{vmatrix} 1 & x_4 & y_4 \\ 1 & x_5 & y_5 \\ 1 & x_6 & y_6 \end{vmatrix} , \quad \text{and} \quad \Delta = S_0 + \begin{vmatrix} 1 & u_4 & y_4 \\ 1 & u_5 & y_5 \\ 1 & u_6 & y_6 \end{vmatrix} + \begin{vmatrix} 1 & x_4 & v_4 \\ 1 & x_5 & v_5 \\ 1 & x_6 & v_6 \end{vmatrix} ,$$

where the determinant

$$\begin{vmatrix} 1 & u_4 & v_4 \\ 1 & u_5 & v_5 \\ 1 & u_6 & v_6 \end{vmatrix}$$

is second order term which can be neglected as an infinitesimal.

Then

$$\begin{aligned} \Delta = S_0 &+ \begin{pmatrix} (y_5 - y_6) & (x_6 - x_5) \end{pmatrix} \left[\mathbf{T}_i(x_4, y_4)\right] \left\{\mathbf{d}_i\right\} \\ &+ \begin{pmatrix} (y_6 - y_4) & (x_4 - x_6) \end{pmatrix} \left[\mathbf{T}_j(x_5, y_5)\right] \left\{\mathbf{d}_j\right\} \\ &+ \begin{pmatrix} (y_4 - y_5) & (x_5 - x_4) \end{pmatrix} \left[\mathbf{T}_j(x_6, y_6)\right] \left\{\mathbf{d}_j\right\} \end{aligned} .$$

Set

$$\{\mathbf{h}\} = \begin{Bmatrix} \{\mathbf{h}_1\} \\ \{\mathbf{h}_2\} \\ \{\mathbf{h}_3\} \end{Bmatrix} = \frac{1}{L}\left[\mathbf{T}_i(x_4, y_4)\right]^T \begin{pmatrix} y_5 - y_6 \\ x_6 - x_5 \end{pmatrix} ;$$

$$\{\mathbf{g}\} = \begin{Bmatrix} \{\mathbf{g}_1\} \\ \{\mathbf{g}_2\} \\ \{\mathbf{g}_3\} \end{Bmatrix} = \frac{1}{L}\left[\mathbf{T}_j(x_5, y_5)\right]^T \begin{pmatrix} y_6 - y_4 \\ x_4 - x_6 \end{pmatrix} + \frac{1}{L}\left[\mathbf{T}_j(x_6, y_6)\right]^T \begin{pmatrix} y_4 - y_5 \\ x_5 - x_4 \end{pmatrix} .$$

So

$$d_n = \{\mathbf{h}\}^T \left\{\mathbf{d}_i\right\} + \{\mathbf{g}\}^T \left\{\mathbf{d}_j\right\} + \frac{S_0}{L} .$$

The potential energy of the normal spring is $\Pi_n = p d_n^2 / 2$. After taking derivatives from the potential energy Π_n with respect to displacement variables, the nodal stiffness and force matrices of element i and j are described as

$$\begin{aligned} \left[\mathbf{k}_{i(r)i(s)}\right] &= p\left\{\mathbf{h}_r\right\}\left\{\mathbf{h}_s\right\}^T \qquad r,s = 1,2,3 \\ \left[\mathbf{k}_{i(r)j(s)}\right] &= p\left\{\mathbf{h}_r\right\}\left\{\mathbf{g}_s\right\}^T \qquad r,s = 1,2,3 \\ \left[\mathbf{k}_{j(r)i(s)}\right] &= p\left\{\mathbf{g}_r\right\}\left\{\mathbf{g}_s\right\}^T \qquad r,s = 1,2,3 \\ \left[\mathbf{k}_{j(r)j(s)}\right] &= p\left\{\mathbf{g}_r\right\}\left\{\mathbf{g}_s\right\}^T \qquad r,s = 1,2,3 \\ \left\{\mathbf{f}_{i(r)}\right\} &= -p\left(\frac{S_0}{L}\right)\left\{\mathbf{h}_r\right\} \qquad r = 1,2,3 \\ \left\{\mathbf{f}_{j(r)}\right\} &= -p\left(\frac{S_0}{L}\right)\left\{\mathbf{g}_r\right\} \qquad r = 1,2,3 \end{aligned}$$

where

for element i $\begin{cases} i(1) = i_1 \\ i(2) = i_2 \\ i(3) = i_3 \end{cases}$ for element j $\begin{cases} j(1) = j_1 \\ j(2) = j_2 \\ j(3) = j_3 \end{cases}$

The detailed derivation of internal stress, external loading, displacement constraint, and contact matrices are described in reference 4 and 5.

3. NONLINEAR MATERIAL BEHAVIOR

The main difference between continuous and discontinuous computation is the unrecoverable rigid body motion cause by the contact between the discontinuous blocks. Although permanent strain-induced displacement may have an unrecoverable effect on the body with inelastic material behavior, strain from the mathematical point of view is one order of magnitude less than rigid body displacement since it is obtained form the first derivative of the displacement function. Figure 4 shows the mechanical behavior of blocks with different material behavior after the release of the force in the continuous and discontinuous cases. The rigid body displacements, zero order terms in the displacement function, is dominant in discontinuous contact analysis. However, brittle and ductile materials show significantly different strain-induced effects upon loading, and the strain-induced deformation of the body may affect the contact behavior between the blocks, thus, both rigid body motion and strain-induced deformation should be considered in the numerical model. The present work develops material nonlinearity formulation and implementation for DDA.

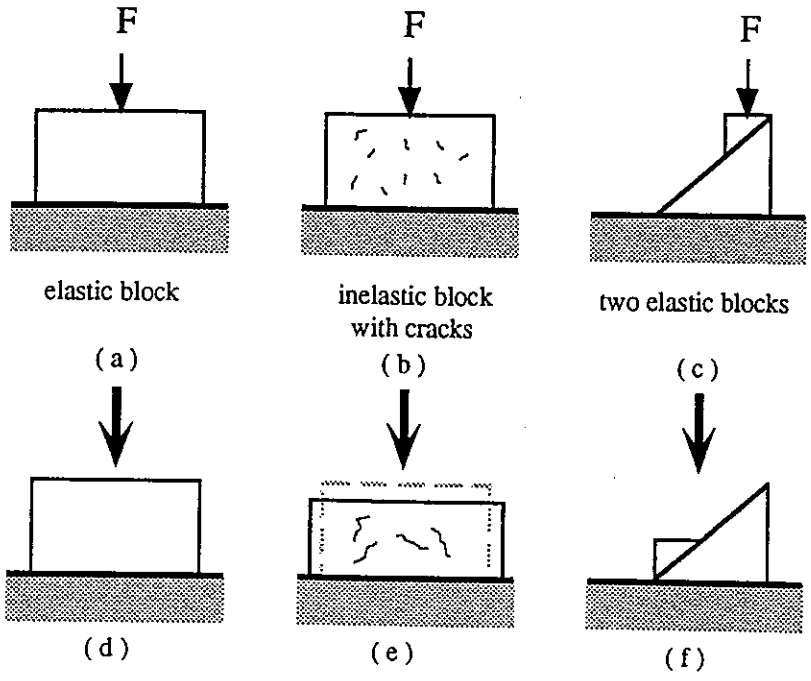

Figure 4. Mechanical behavior of continuous & discontinuous blocks after the removal of the force

Geometry nonlinearity is modeled in DDA uses a step-by-step approach in a discrete time system. Each step starts with the deformed shape and positions from previous step; the stresses from the previous step are considered as the initial stresses at the current step. After adopting the updated geometry, contact positions, velocities, and stresses from the previous time step, the computation for the current step is independent from the data of the previous step. All the deformability constants, loading, initial stresses, and boundary conditions can be changed at the current step. Since the time interval of each time step is very small, the displacement, deformations, and the changes of stresses are very small. With the addition of finite element mesh in each block, the tangent modulus of the stress-strain relationship at the current step is very close to the secant modulus of the stress-strain curve. Thus, the arc-length method (Figure 5) can be used to calculate the piecewise linear modulus based on the updated values of stresses and strains for nonlinear constitutive behavior of materials.

The use of piecewise linear line segments to depict the nonlinear material behavior shows that the linear step-by-step approach can solve both material and geometric nonlinearity problems. Trying to solve nonlinear material problems using only one step may violate the infinitesimal displacement theory. The present work develops equations for nonlinear isotropic materials using principal strain as the criterion for the change of Young's modulus E and Poisson's ratio v. The more line segments chosen to follow the stress-strain curve, the better approximation of nonlinear inelastic material behavior will be for each time step. Without the incorporation of fracture criterion, the element meshed block of the system always remains as intact material in the present model. The material is assumed to be strain hardening after yielding since the strain-softening behavior observed in the experimental stress-strain curve reflects the global specimen instead of the individual blocks. The true stress-strain curve is used in the model, plus the Bauschinger effect is considered in cyclic loading. The unloading and reloading paths after yielding are assumed to be the same in the stress-strain curve, as shown in Figure 6.

3.1 Stiffness Matrix

A linearly step-by-step approach to discretize the stress-strain curve can be used to simplify a material nonlinearity problem. For an isotropic inelastic material, the stress-strain relationship is assumed to be linear at each time step. After taking the derivatives of displacement variables from the elastic strain energy, three 2×2 nodal stiffness of element i are formed.

$$\left[\mathbf{k}_{i(r)i(s)}\right]=\left[\mathbf{B}_{i(r)}\right]^{T}\left[\mathbf{E}_{i}\right]\left[\mathbf{B}_{i(s)}\right];\qquad r,s=1,2,3$$

where

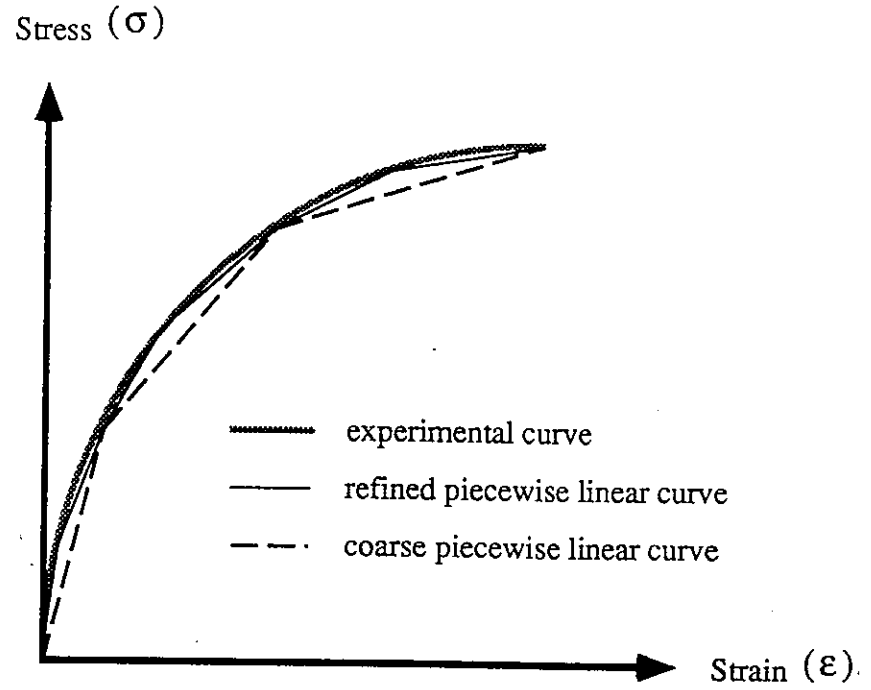

Figure 5. Arc-length method

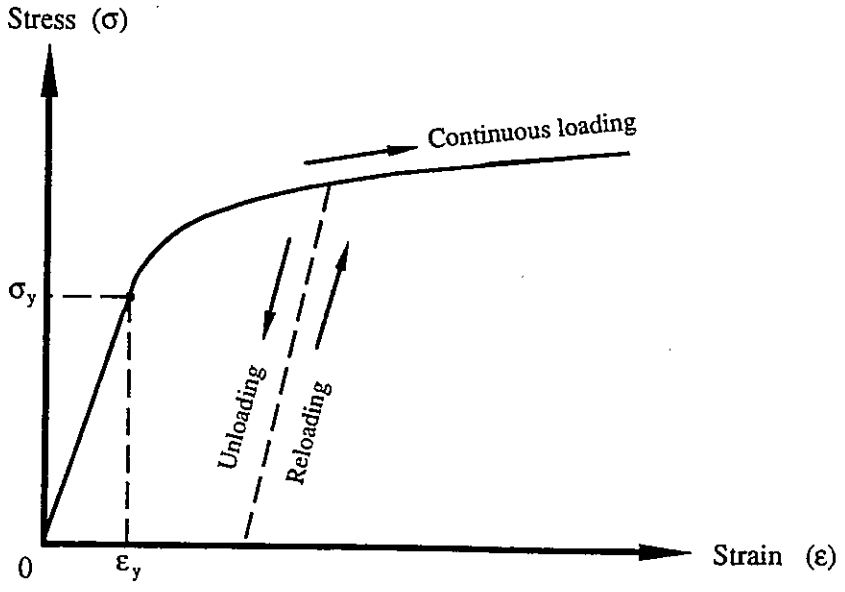

Figure 6. Nonlinear inelastic stress-strain modelling

$$[\mathbf{E}_i]=\frac{E}{1-\nu^2}\begin{pmatrix}1 & \nu & 0\\ \nu & 1 & 0\\ 0 & 0 & \dfrac{1-\nu}{2}\end{pmatrix}\ ;\quad [\mathbf{B}_l]=\begin{pmatrix}f_{2l} & 0\\ 0 & f_{3l}\\ f_{3l} & f_{2l}\end{pmatrix},\quad l=1,2,3;$$

$$i(l)=\begin{cases}i_1, & l=1; \quad \text{first node}\\ i_2, & l=2; \quad \text{second node}\\ i_3, & l=3; \quad \text{third node}\end{cases}$$

4. NUMERICAL SIMULATIONS

4.1 Elastic-Plastic Bending of a Cantilever Beam

A cantilever beam is 10 feet long, and 2 feet in depth with downward dynamic loading (12.5 kip/s) acting on the middle node at the end of the beam. This beam is meshed into 80 quadrilateral elements and 1 block. Figure 7 shows the original configurations of the beam. The following parameters were used:

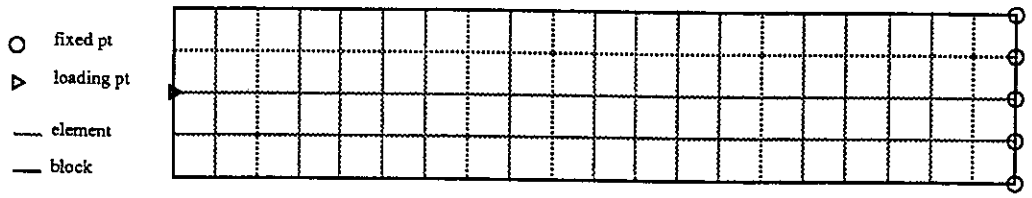

Figure 7. Original configuration of the beam

case: plane stress dynamics

time step: 400

stiffness of the contact spring (penalty): 1.0×10^7 kip/in

time interval : 0.02 s

unit mass : 5.26×10^{-3} kslugs/ft^3

gravity: 32.2 ft/s^2

initial stress $(\sigma_x,\sigma_y,\tau_{xy})$: (0, 0, 0) ksf

yielding strain $(\varepsilon_t,\varepsilon_c)$: (0.0007, -0.0007)

range of ε for (E,ν) in compression : (unit of E is ksf)

loading case:

range (1): $-0.0003<\varepsilon\le 0.0000$, $(E,\nu)=(5.760\times10^5,0.15)$

range (2): $-0.0005<\varepsilon\le -0.0003$, $(E,\nu)=(5.472\times10^5,0.17)$

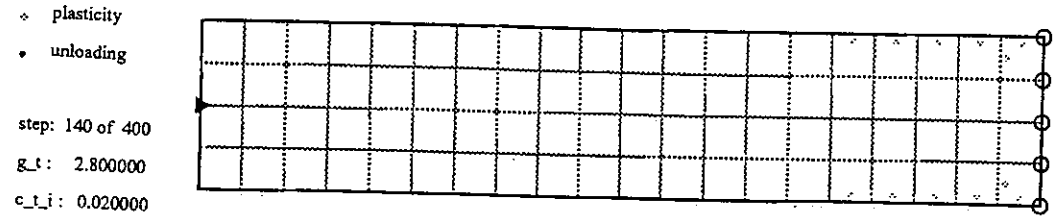

Figure 8.

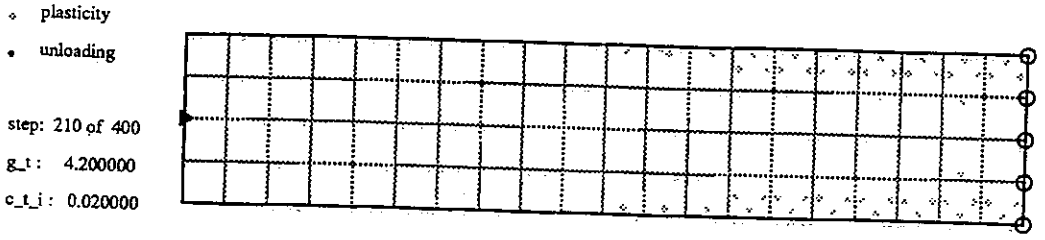

Figure 9.

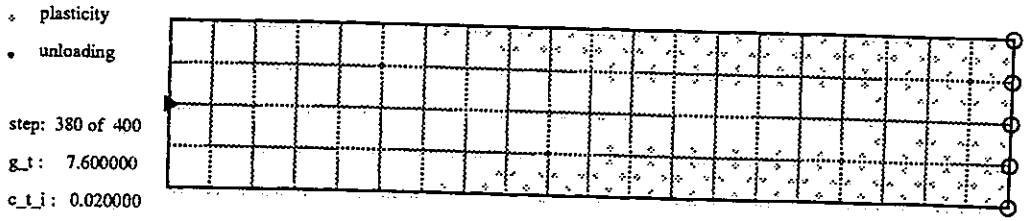

Figure 10.

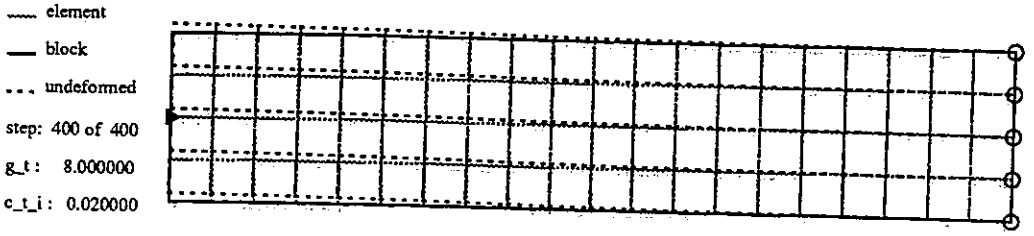

Figure 11.

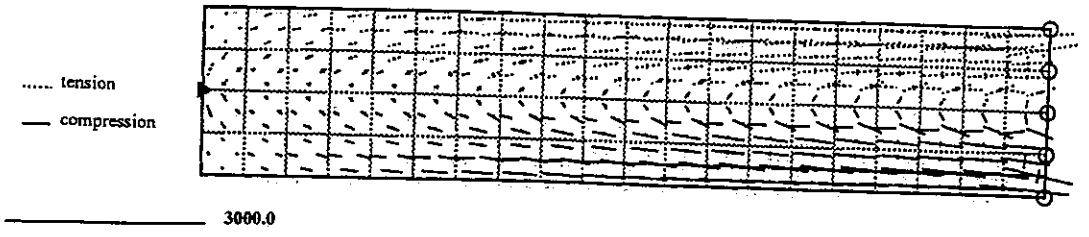

Figure 12.

range (3): $-0.0006 < \varepsilon \le -0.0005$, $(E,\nu) = (5.184\times10^5, 0.19)$

range (4): $-0.0007 < \varepsilon \le -0.0006$, $(E,\nu) = (4.896\times10^5, 0.21)$

range (5): $-0.0010 < \varepsilon \le -0.0007$, $(E,\nu) = (4.608\times10^5, 0.23)$

range (6): $-0.0016 < \varepsilon \le -0.0010$, $(E,\nu) = (4.176\times10^5, 0.25)$

range (7): $-0.0600 < \varepsilon \le -0.0016$, $(E,\nu) = (3.600\times10^5, 0.30)$

for unloading :

range (1): $-0.0600 < \varepsilon \le -0.0007$, $(E,\nu) = (5.760\times10^5, 0.19)$

Figure 8 to 10 show the results of deformed shape of the beam and propagation process of the plastic area after step 140, 210, 380, respectively. They seem to match the theoretical results in the process of forming the plastic zones[6]. The notation of g_t in the figures is the total time, and c_t_i stands for the current time interval used. Round tint marks indicate the area the structure reaches the inelastic range and stay in the continuous loading track, while the dark marks show the area also reach in plastic range but in unloading track. Finite or large deformation is step-by-step accumulation of small deformation. Figure 11 shows the comparison of deformed and undeformed shapes of the beam. Figure 12 shows the principal stresses and directions at the final step, where dash lines represent tension and solid lines represent compression.

4.2 Elastic Body into Convergent Walls

This kind of contact problem is common during metal forming process such as line or bar drawing. Because the preclusion of volumetric strain is neglected in the present model, the nonlinear elastic rubber-like material is assumed here. The element block system adopted from Papadopoulos[7] is comprised of 3 blocks and 152 elements. Displacement control (20 mm/s) is used as the pulling force in this case. Figure 13 shows the dimensions of the elastic body and the convergent wall. There is no friction assumed along the contact surfaces of convergent walls. The original configuration of the element block system is shown in Figure 14.

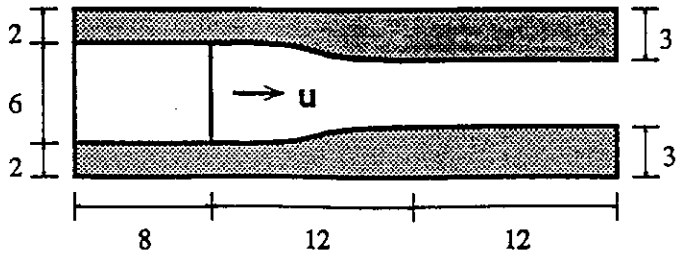

Figure 13. The dimensions of the elastic body and the convergent walls

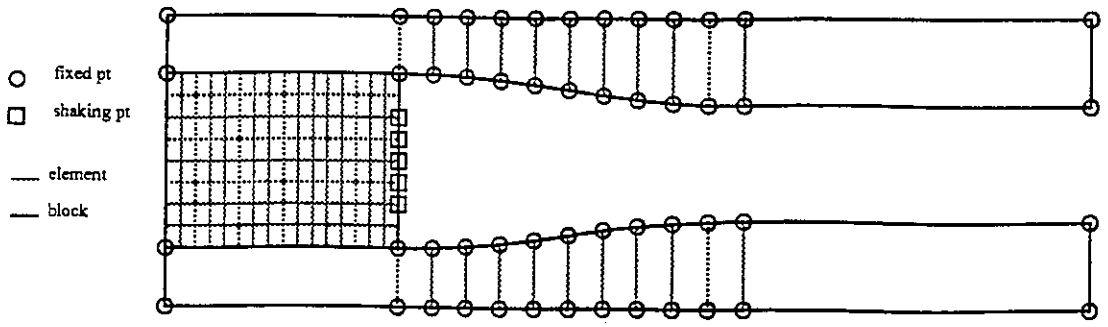

Figure 14. Original configuration of the elastic body and convergent walls

The following data are used:

case: plane strain dynamics

time step: 240

stiffness of the contact spring (penalty): 5.0×10^{8} 10^{-3}N/mm

time interval : 0.005 s

unit mass : 9.6×10^{-7} kg/mm^3

gravity: 9810 mm/s^2

initial stress $(\sigma_x,\sigma_y,\tau_{xy})$: (0, 0, 0) 10^{-3}N/mm

yielding strain $(\varepsilon_t,\varepsilon_c)$: (0.0007, -0.0007)

range of ε_1 for (E_1,ν_1) of the elastic body in compression :

(unit of E is 10^{-3}N/mm)

range (1): $-0.2000 < \varepsilon \le 0.0000$, $(E_1,\nu_1) = (1000,0.30)$

range (2): $-0.4200 < \varepsilon \le -0.2000$, $(E_1,\nu_1) = (910,0.32)$

range (3): $-0.5000 < \varepsilon \le -0.4200$, $(E_1,\nu_1) = (750,0.34)$

range (4): $-0.8000 < \varepsilon \le -0.5000$, $(E_1,\nu_1) = (466,0.36)$

range (5): $-1.5000 < \varepsilon \le -0.8000$, $(E_1,\nu_1) = (200,0.38)$

E_2,ν_2 of the convergent wall: 2.1875×10^{8} 10^{-3}N/mm^2, 0.2

Figures 15 to 19 show the results of deformation process of the elastic body into the convergent walls after step 50, 100, 150, 200, 240, respectively. This example performs the sliding contact between the blocks.

4.3 Post-failure Analyses of a Marble Specimen

This simulation analyzes the compressive post-failure behavior of a marble specimen with preexisting cracks. In order to determine the initiation, propagation and interaction of the stress-induced microcracks in complex materials such as marble, it is necessary to preserve the configuration of the microcracks under loads and to distinguish the cracks from the ones induced by unloading and artifacts produced during specimen preparation. "Wood's metal," a liquid metal alloy, can be used to fill the voids of microcracks of marble

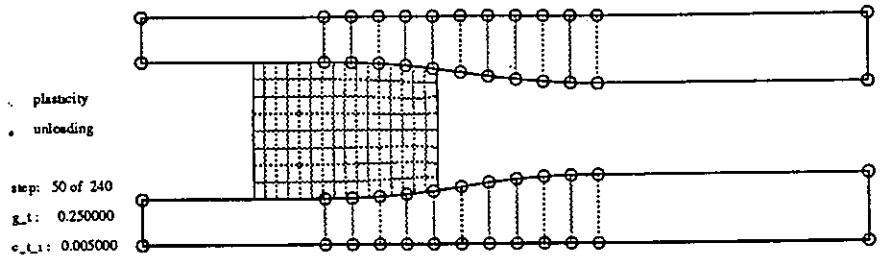

Figure 15.

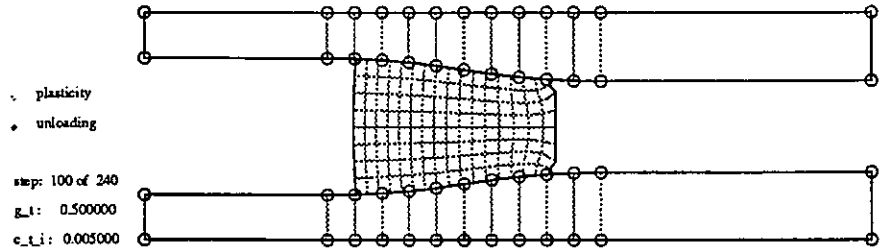

Figure 16.

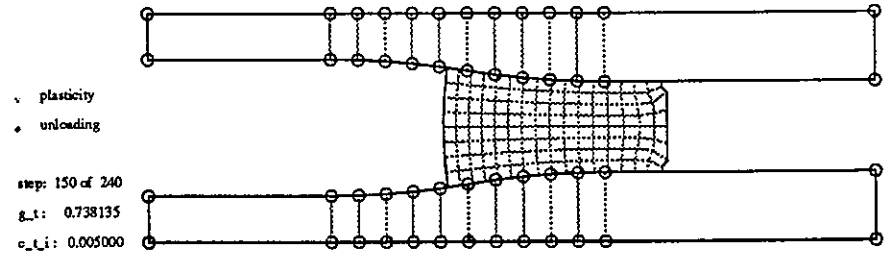

Figure 17.

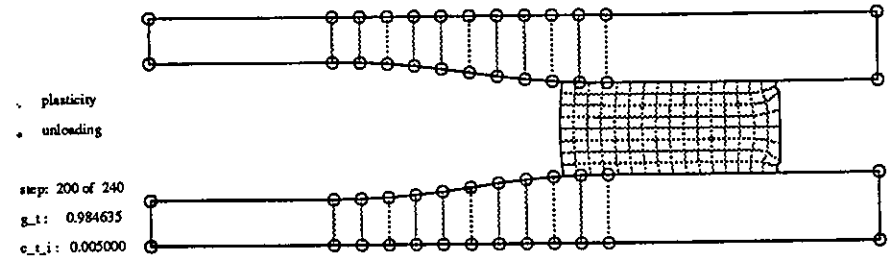

Figure 18.

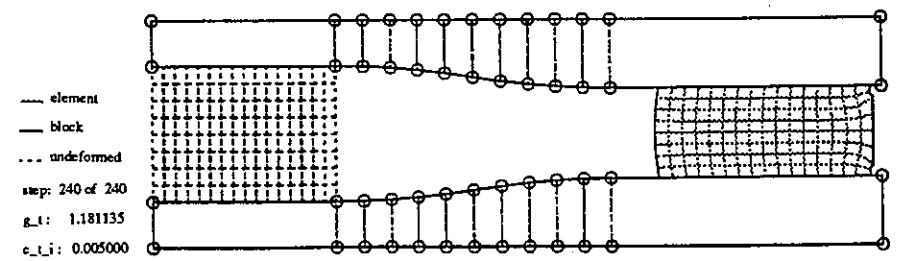

Figure 19.

specimens under loads. The alloy has a melting point of approximately 80°C and it is able to solidify at any stage of the experiment to preserve the geometry of microcracks as they exist under loads. With the surface tension of 400 mN/m, Wood's metal can penetrate into flat cracks. This technique not only allows one to observe the microcracks as they exist under load, but also facilitates observing the microcracks in three dimensions, once the specimen is leached away using a mild acid solution. Figure 20 shows the vertical cross section of the marble specimen that had been loaded up to failure[8]. The dark zones indicate the area the Wood's metal penetrated the cracks induced by the mechanical load. There is strain localization at the center of the specimen and four major lines of shear failure which started from the edges of the specimen. This image is used as a starting point for the post-failure analyses. The marble specimen is 1.436 inch long, 1.0625 inch wide and the mesh contains 28 elements and 8 blocks. Figure 21 shows the original configuration of the element block system. The upper and lower blocks are simulated as the loading and the base frames. The simulation is done under displacement control. To evaluate the effect of crack propagation or global stability of the element block system of marble specimen with respect to different friction angles and confined pressure with different loading rates, six cases are analyzed in the following:

(1) loading rate: 0.005 in/s, friction angle: 35°, without confined pressure;
(2) loading rate: 0.005 in/s, friction angle: 45°, without confined pressure;
(3) loading rate: 0.005 in/s, friction angle: 35°, confined pressure: 800 psi;
(4) loading rate: 0.0005 in/s, friction angle: 35°, without confined pressure;
(5) loading rate: 0.0005 in/s, friction angle: 45°, without confined pressure;
(6) loading rate: 0.0005 in/s, friction angle: 35°, confined pressure: 800 psi.

The following data were used:

case: plane strain dynamics
stiffness of the contact spring (penalty): 1.0×10^7 kip/ft
time interval: 0.001 s
unit mass: 5.2674×10^{-3} kslug/ft^3
maximum displacement ratio: 0.001
gravity: 32.2 ft/s^2
initial stress (σ_x, σ_y, τ_{xy}): (0,0,0) ksf
yielding strain (ε_t, ε_c): (0,001, -0,001)
range of ε_1 for (E_1, υ_1) of the marble specimen in compression: (unit of E is ksf)
for loading:
range (1): $-0.001 < \varepsilon < 0.000$, ($E_1$, υ_1) = (1.0728×10^6, 0.17)
range (2): $-0.900 < \varepsilon < -0.001$, ($E_1$, υ_1) = (4.32×10^5, 0.30)

Figure 20. Vertical cross section of the marble specimen loaded up to failure

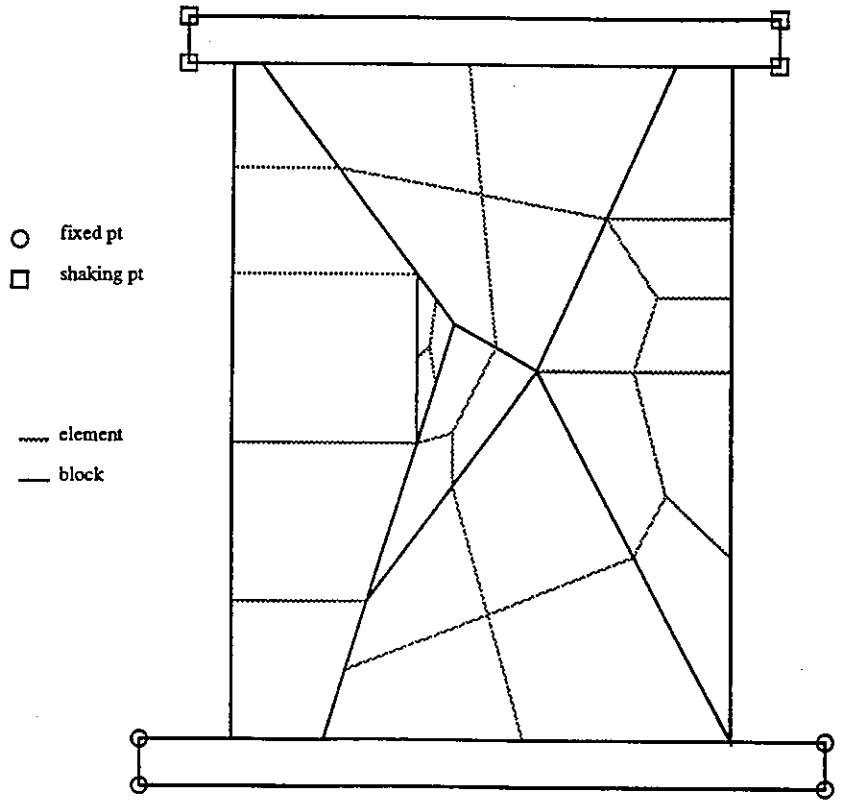

Figure 21. Original configuration of the marble specimen

for unloading:

range (1): $-0.900 < \varepsilon < -0.001$, $(E_1, \upsilon_1) = (1.0728 \times 10^6, 0.17)$

E_2, υ_2 of the loading and base blocks are 4.32×10^6 ksf, and 0.30, respectively

Case 1: fast loading rate, low friction, without confinement

7000 time steps (≈2.398 s) are used in the computation. Figure 22 and 23 show the results after time step 400 and 1000. These figures indicate the propagation of plastic regions. Figure 24 and 25 show the results after step 3461 (≈ 1.25s) and 7000. The figures show the failure mode and the progressive dilation of the marble sample.

Case 2: fast loading rate, high friction, without confinement

1000 time steps (≈ 1.25s) are used in the analysis. Figure 26 and 27 show the results after time step 4000 and 10000. The failure modes and distance of sliding and opening between the block seems to be the same with different friction angles.

Case 3: fast loading rate, low friction, with confinement

3070 time steps (≈ 2.398 s) are used in this case. Figure 28 and 29 show the results after time steps 1530 and 3070. Although the failure modes of the specimen compared to the above cases are the same, the amounts of sliding and opening between the blocks are less when the specimen is confined. With the same loading rate used in case 1 to 3, the confinement acts more significantly to maintain the global stability of the structure than higher friction between the blocks.

Case 4: low loading rate, low friction, without confinement

9000 time steps (≈ 3.483 s) are used here. Figure 30 and 31 show the results after time steps 600 and 1000. Because of the angle-to-angle contacts developed between the blocks, a different failure mode happened during slow loading rate. Being unable to push away the left large block, the wedged block in the middle moves back and forth, affecting the movements of other blocks in the system. Figure 32 and 33 show the results after step 8700 (≈ 3.373 s) and 9000.

Case 5: low loading rate, high friction, without confinement

10000 time steps (≈ 3.365 s) are performed in this case. Figure 34 shows the time step 10000. The sliding and opening distance between the blocks are less than those of case 4 with low friction, which is not the same as the results of case 1 and 2.

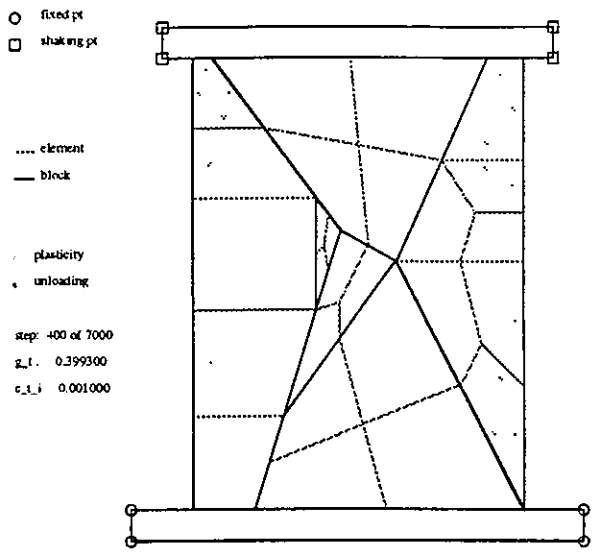

Figure 22.

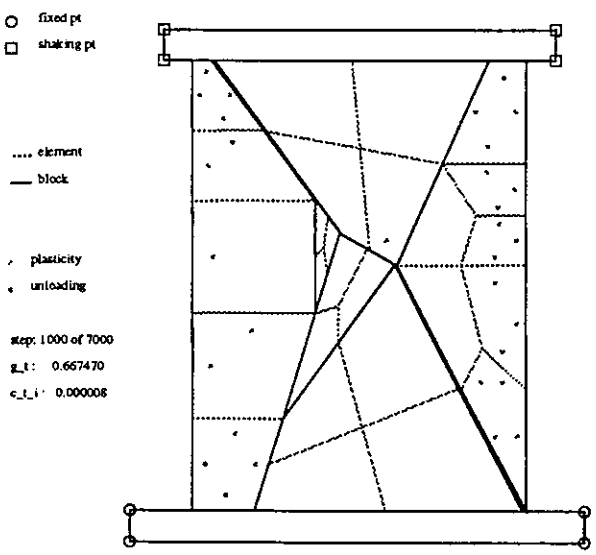

Figure 23.

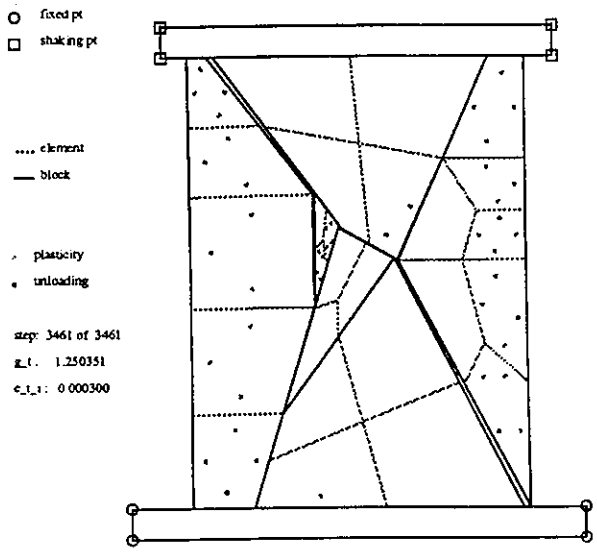

Figure 24.

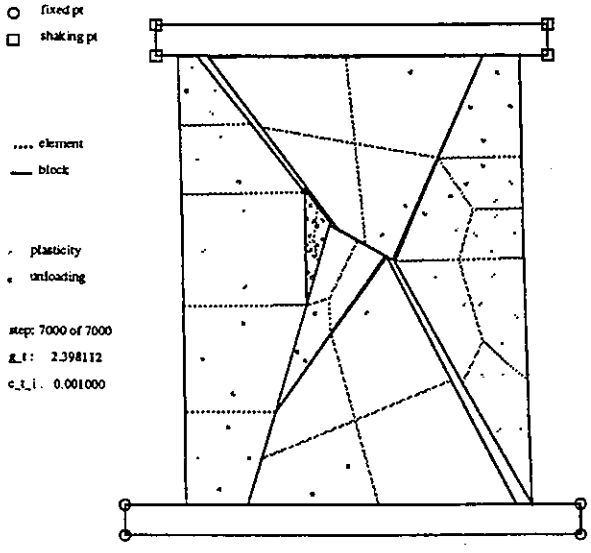

Figure 25.

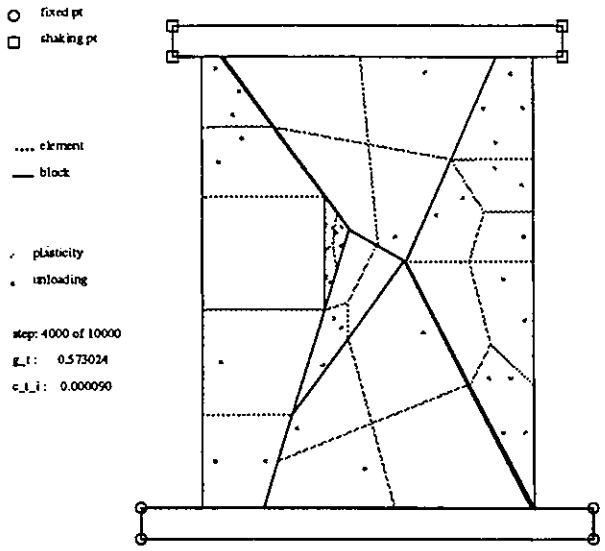

Figure 26.

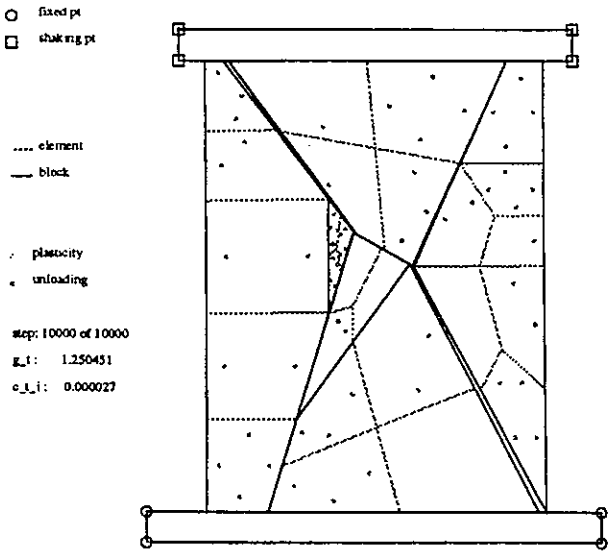

Figure 27.

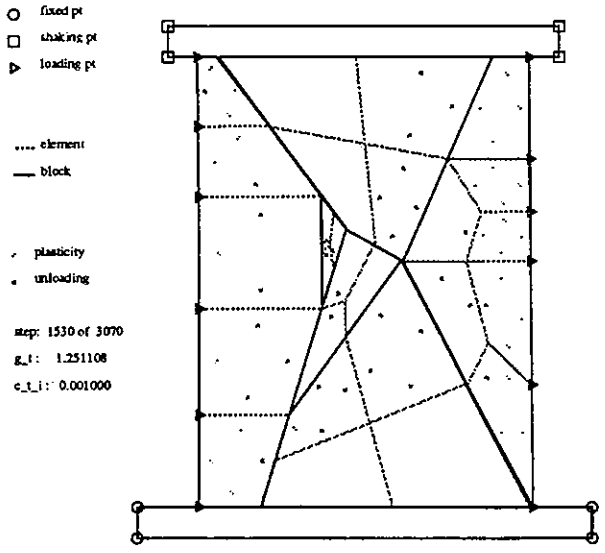

Figure 28.

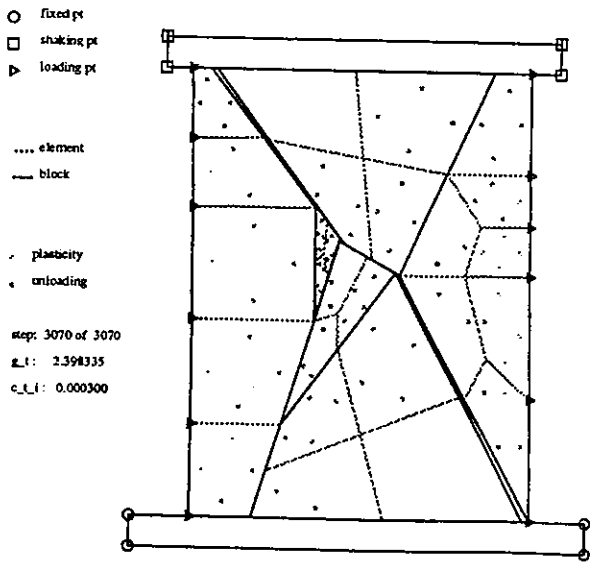

Figure 29.

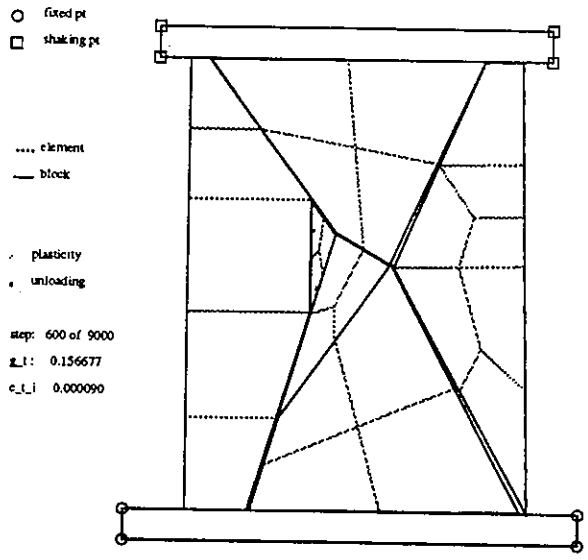

Figure 30.

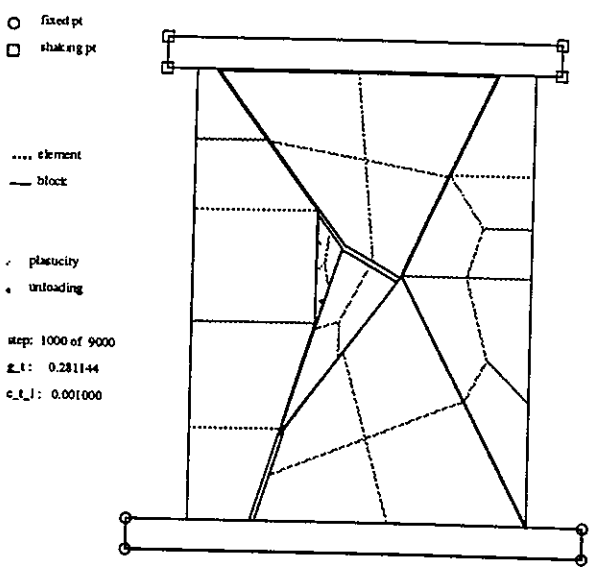

Figure 31.

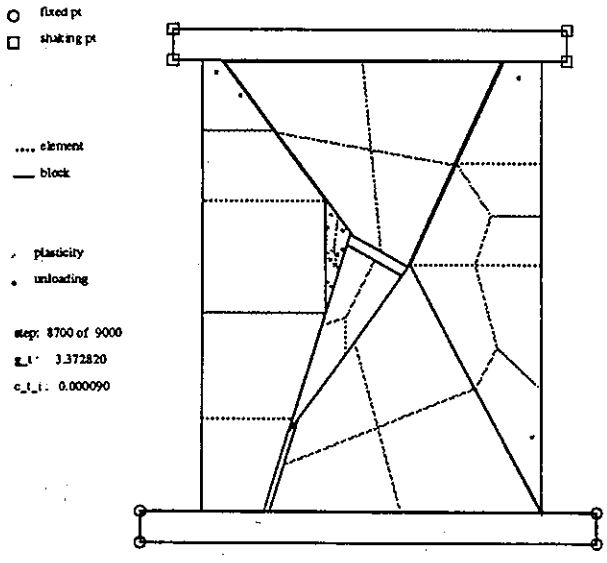

Figure 32.

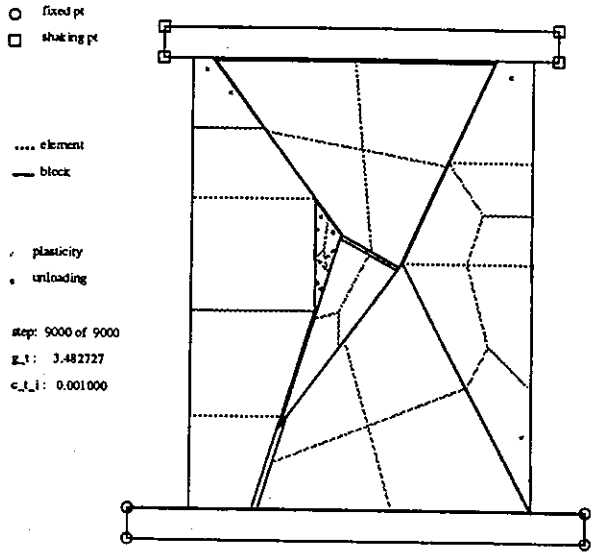

Figure 33.

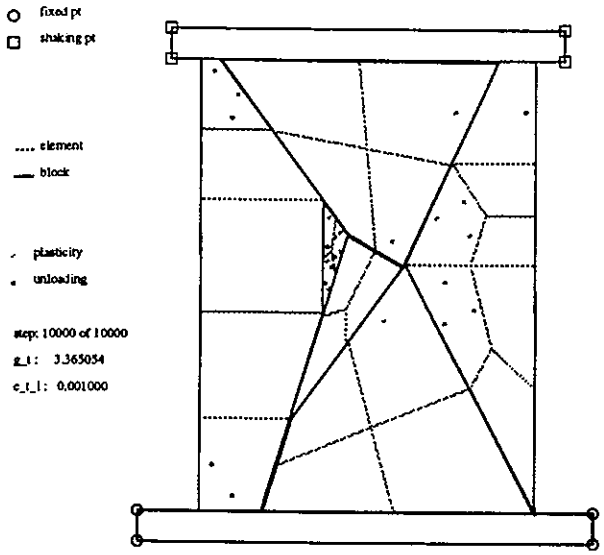

Figure 34.

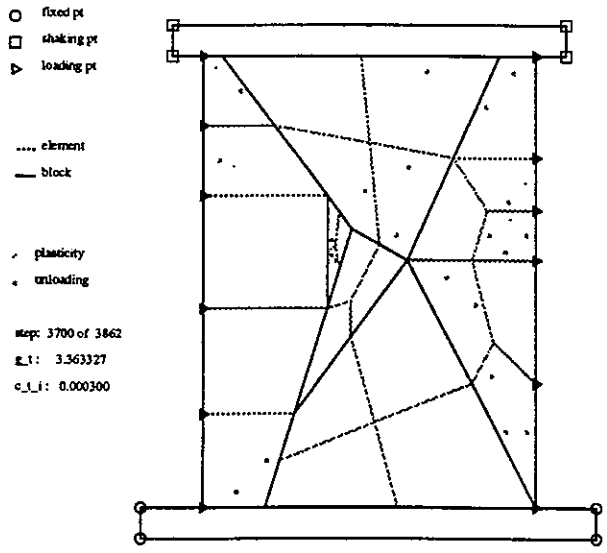

Figure 35.

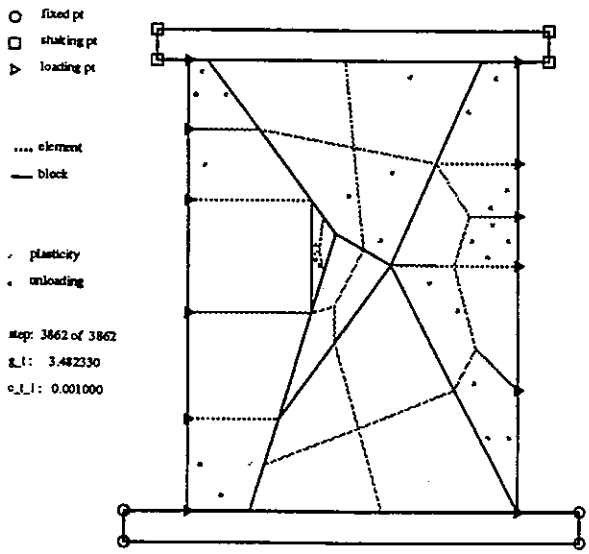

Figure 36.

Case 6: low loading rate, low friction, with confinement

3862 time steps (≈ 3.482 s) are used in the analysis. Figure 35 and 36 show the results after time steps 3700 (≈ 3.363 s) and 3862. No significant movements of the blocks are shown form the figures, the intact block stability demonstrates the effect of confinement. With the same loading rate used from case 4 to 6, the effect of confined pressure is still more significant to stabilize the structure system than that of higher friction between the blocks.

The results of above cases indicate that different loading rates may affect the failure modes of the stress-induced structure. Lateral confinement added to the structure has a significant effect in reducing the crack opening and sliding of the blocks in the system. The effect of higher friction to maintain the intact stability of the structure depends on the geometry, angle of contact plane between blocks, and failure mode in the system.

5. CONCLUSION

With the addition of a finite element discretization in each block, and the implementation of nonlinear inelastic material behavior, the proposed numerical model reaches the goal of providing a more realistic deformation ability in each block and consequently a more precise stress (strain) distribution field. The results of numerical simulations in material applications demonstrate that this enhanced version of DDA can solve large displacement and deformation problems in the discontinuous block system, and give a detailed mechanical description in the continuous element meshed block.

ACKNOWLEDGMENTS

The author would like to thank Dr. Gen-hua Shi for his guidance in the development of the computer program, and Prof. Paulo Monteiro for his valuable suggestions in the marble application.

REFERENCES

1. R. E. Goodman, R. Taylor and T.L. Brekke, A model for the mechanics of jointed rock." *Journal of the Soil Mechanics & Foundations Div.*, ASCE, **94**, pp. 37 (1968).

2. P. A. Cundall, A Computer model for simulating progressive, large-scale movements in blocky rock systems, *Symposium of International Society of Rock Mechanics*, Nancy, France. 11-18 (1971).
3. G.-H. Shi, Discontinuous Deformation Analysis—A New Numerical Model for the Statics and Dynamics of Block Systems, Ph.D. Dissertation, Department of Civil Eng., University of California at Berkeley (1988).
4. K. Shyu, Nodal Based Discontinuous Deformation Analysis, Ph.D. Dissertation, Department of Civil Eng., University of California at Berkeley (1993).
5. C.-T. Chang, "Nonlinear Dynamic Discontinuous Deformation Analysis with Finite Element Meshed Block System, Ph.D. Dissertation, Department of Civil Eng., University of California at Berkeley (1994).
6. J. Lubliner, *Plasticity Theory*, Macmillan, New York (1990).
7. P. Papadopoulos, On the Finite Element Solution of General Contact Problems, Ph.D. Dissertation, Department of Civil Eng., University of California at Berkeley (1994).
8. C.-T. Chang, P. J. M. Monteiro, K. Nemati, and K. Shyu, Behavior of marble under compression, *submitted to ASCE Material Journal.*
9. O. C. Zienkiewicz, and R. L. Taylor, *The Finite Element Method*, 4th ed. **1 & 2**, McGraw-Hill, London (1991).

Dynamic Responses of Sliding Structure subjected to Seismic Excitation

JiinSong Tsai[1] and WengChing Wang[2]
[1] Associate Professor of Civil Engineering
[2] Ph. D. Graduate Student
National Cheng Kung University, Tainan, Taiwan

ABSTRACT

The objective of this paper is to present the dynamic responses of structures which retain sliding base to limit the translation of external loads from ground excitation. Discontinuous deformation analysis method is adopted for this particular sliding boundary problem. The sliding interface which translates the friction forces from ground to superstructure is simulated by introducing pairs of fictitious contact-springs on and along the sliding base. Response of a simple idealized mass-spring structure subjected to harmonic ground excitation is first presented. The chosen analytical method is validated by the closed-form solutions for the same problem. Response of a three-story structure subjected to the 1940 El Centro earthquake is presented in a comparison of sliding and non-sliding cases. Results reveal that lowing the frictional coefficient of the sliding interface will reduce the peak responses. The present study shows that, for instance, the sliding base with frictional coefficient of 0.01 successfully cuts off the most severe excitation which may exert onto the structure and has the structure response under little deformation. Nevertheless, the structure displaces from its origin at the end of exercitation.

Key words: sliding boundary problem, contact-springs, sliding structure, discontinuous deformation analysis method

1. INTRODUCTION

In attempts to mitigate the feasible earthquake hazards on buildings, the concept of decoupling the structures, and/or its contents, from potentially damaging earthquake induced ground motion has been adopted in recent seismic resistance practices. Building retain a sliding joint underneath is probably the simplest type of these practices. The sliding joint offers a discontinuity to the ground motion propagation and dissipates energy through horizontal frictional force. In practices, teflon coated surface or a layer of sand used in the interface between the ground and the base of a building (Fig. 1) would essentially provide a pure-friction sliding base. This idea, although some experiments may have shown its attractive characteristics, has not been enough proven quantitatively and thus possibly merge into conventional and established design procedures. In fact, the responses of various sliding structure have not been thoroughly understood yet. Since the field of seismic design, as perhaps, befits a subject directly concerned with both life safety and uncertainty and is cautious to practice. Engineering application, such as structure with sliding base, must fulfill the concerns of liability and thus be undertaken exhaustive tests and intensive studies. This conceptually simple idea has obviously required much more research to make it feasible.

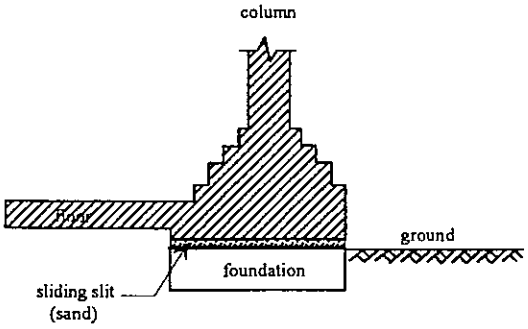

Fig.1 Frictional isolation base

Responses of sliding structures subjected to harmonic ground motion have been studied by Westermo and Udwadia[1] and Mostaghel et al[2]. Experiments of model on shaking table have been carried out by Li et al.[3] to study sliding structures subjected to sinusoidal excitation. The effectiveness of sliding supports in mitigating structures from damaging earthquakes has been investigated by Mostaghel and Tanbakuchi[4]. It should be mentioned that, in these early studies, a mathematical model with two degrees of freedom has frequently been adopted for the simulation of sliding structure. Either the superstructure and the sliding foundation is represented by single degree-of-freedom (SDOF). Yang et al.[5] has proposed a multi-degree-of-freedom (MDOF) model based on a similar formulation to represent multi-story shear resistant building.

The present paper is to study the dynamic responses of sliding structures with SDOF and MDOF by using discrete element method. The theoretical formulations are on the basis of the discontinuous deformation analysis method. The sliding joint is directly modeled by the separation feature of discrete elements. The friction along the sliding joint is assumed to be of the Coulomb type, which is independent of pressure and velocity, and thus no difference is expected between the coefficients of static and dynamic friction. The translation of friction forces is simulated by introducing contact-springs between elements. The equations of motion is solved in incremental, and virtually no restraint needs to be placed on the type of ground motion.

2. THEORETICAL FORMULATIONS

The analysis of the response of sliding structure involves a sliding boundary which is not usually for a common dynamic problem. In the present study, two types of models are used including the mass-spring model and the discrete element model. The mass-spring model is basically for shear resistant structure which is in the form of concentrated masses with springs. The discrete element model by using the discontinuous deformation analysis method represents a structure by directly meshing the configuration as the common used finite element model, but providing the simulation of discontinuous sliding interface between elements. Brief descriptions for both the mass-spring model and the discontinuous deformation analysis model are in the following. The simulation of the sliding interface for the dynamic contact interaction is also included.

2.1 Mass-spring model

The mass-spring model represents single or multi-degree-of-freedom by a few concentrated masses (m_N) and a sliding base (m_b) underneath (Fig.2). This model is for the shear resistant building subjected to a horizontal excitation. A fictitious spring is introduced along sliding interface to represent the frictional effect. Different constants for the spring are assigned for

either sliding or non-sliding phase. In early SDOF model, the spring with rigid-plastic behavior was first adopted[1,2], while a elasto-plastic spring was chosen lately for MDOF model[5]. This simply avoid the difficulty of solving the sliding boundary problem, and the number of equations remains the same in either the sliding or non-sliding phase. The equation of motion for a typical mass-spring model is

$$[M]\{\ddot{u}\}+[C]\{\dot{u}\}+[K]\{u\}=\{P\} \tag{1}$$

where [M] is the mass matrix, [C] is the damping matrix and [K] is the stiffness matrix, and {u} and {P} are displacement and external loading vectors, respectively.

The mass and the damping matrices are similar to those common in structural analyses, and the stiffness matrix with the fictitious spring is

$$[K]=\begin{bmatrix} k_1 & -k_1 & 0 & \cdots & 0 & 0 \\ & k_1+k_2 & -k_2 & & 0 & 0 \\ & & k_2+k_3 & & 0 & 0 \\ & & & \ddots & \vdots & \vdots \\ & symm. & & & -k_{N-1} & \vdots \\ & & & & k_{N-1}+k_N & -k_N \\ & & & & & k_N+k_f \end{bmatrix} \tag{2}$$

where k_f is the fictitious spring constant. This constant is a large number for the non-sliding phase and is assigned to be zero for the sliding phase. The horizontal seismic loading is prescribed as

$$P_i=\begin{cases} -m_N\ddot{u}_0 & i=N \\ -m_b\ddot{u}_0 & i=N+1 \end{cases} \tag{3}$$

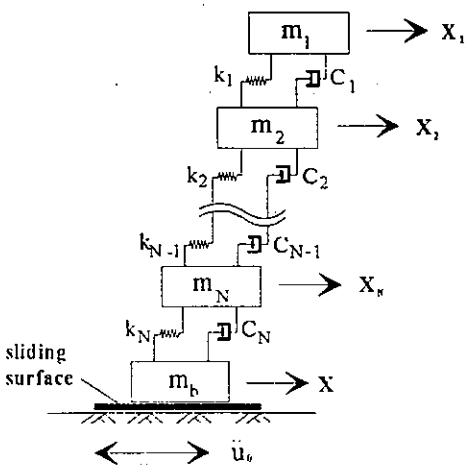

Fig.2 Mass-spring model

For finding the benchmark solution, a single-degree-of-freedom structure of mass m and stiffness k supported by a base raft M that can slide horizontally is shown in Fig.3. In this figure u_0, u_M and u_m are the displacements in an absolute frame for the ground, the base raft and the roof, respectively, u_s is the sliding displacement of the base raft relative to the ground, and u_r is the displacement of the roof relative to the base raft. The coefficient of sliding friction is ρ. If the structure slides under the ground excitation, in the Newton's second law, the equations of dynamic equilibrium are:

$$m\ddot{u}_m + ku_r = 0 \tag{4}$$

$$M\ddot{u}_M = F - m\ddot{u}_m \tag{5}$$

where F is the friction force mobilized in-between the base-raft and the ground. The maximum value of F during sliding is

$$F = \delta\rho(m+M)g \tag{6}$$

where δ is either +1 or -1 that is dependent on the coincidence between the direction of response inertia of the structure and the direction of the ground acceleration. As δ = +1, it means that they are in opposite direction.

Using the relationships of the displacements defined above, the equations (4) and (5) can be reformulated as

$$(\ddot{u}_r + \ddot{u}_s + \ddot{u}_0) + \omega^2 u_r = 0 \tag{7}$$

$$\ddot{u}_s = \delta\rho g - \alpha\ddot{u}_r - \ddot{u}_0 \tag{8}$$

where α is the mass ratio and is equal to m/(M+m). Substituting for u_s from equation (8) into the equilibrium equation (7), it can be shown that during the sliding phase

$$\ddot{u}_r + \omega^2 u_r = -\delta\rho g + \alpha\ddot{u}_r \tag{9}$$

$$(1-\alpha)\ddot{u}_r + \omega^2 u_r = -\delta\rho g \tag{10}$$

$$\ddot{u}_r + \omega_\alpha^2 u_r = \frac{-\delta\rho g}{1-\alpha} \tag{11}$$

where $\omega_\alpha = \dfrac{\omega}{\sqrt{1-\alpha}}$. The solution for the sliding phase is thus obtained by solving equation (11) when

$$\rho g - \left|\alpha\ddot{u}_r + \ddot{u}_0 + \ddot{u}_s\right| = 0 \tag{12}$$

On the other hand, in the non-sliding phase, u_s = 0 and the ground moves with an acceleration $u_o = a \sin \Omega t$, equation (7) thus becomes

$$\ddot{u}_r + \omega^2 u_r = -a\sin\Omega t \tag{13}$$

The solution for the non-sliding phase can be obtained by solving equation (13) when

$$\rho g - \left|\alpha\ddot{u} + \ddot{u}_0\right| > 0 \tag{14}$$

The incremental dynamic analysis for solving the above equations can be performed by following the algorithm of Mostaghel et al.[4]. It is assumed that the structure is in equilibrium at the time step for each increment. Transition of starting and end times of the sliding and non-sliding phases can be obtained as the solution process progresses.

2.2 Discontinuous deformation analysis model

For last two decades, many efforts have been spent on computational mechanics for the frictional contact problem. Cundall[6] has introduced distinct element method for the analyses of discrete materials. Goodman et al.[7] has proposed the joint element for solving rock discontinuity problems. These are basically the force method. Shi and Goodman[8] have presented a displacement method of discontinuous deformation analysis (DDA), and is mainly used for solving rock mechanics problems.

Using displacement method, the DDA can be treated as a generalization of the finite element method. The following will briefly describe some theoretical bases for solving the problem of sliding-base structure.

The discrete element (or block) used in the DDA is assumed to be constant stress and strain. Displacement (u, v) of any point (x, y) within an element is represented by six variables and formulated as a first order approximation form of

$$\begin{pmatrix} u \\ v \end{pmatrix} = \begin{pmatrix} 1 & 0 & -(y-y_0) & (x-x_0) & 0 & (y-y_0)/2 \\ 0 & 1 & (x-x_0) & 0 & (y-y_0) & (x-x_0)/2 \end{pmatrix} \begin{pmatrix} u_0 \\ v_0 \\ r_0 \\ \varepsilon_x \\ \varepsilon_y \\ \gamma_{xy} \end{pmatrix} \tag{15}$$

where (u_0, v_0) is the displacement of the center point (x_0, y_0) of an element; r_0 is the rotation angle and ε_x, ε_y, γ_{xy} are two axial and the shear strains.

Similar to the nodal point in a finite element mesh, the center (x_0, y_0) of each discrete element with six degrees of freedom is related to others and all the relations can then be summed up to form the global simultaneous equilibrium equations as

$$\begin{bmatrix} K_{11} & K_{12} & \cdot & \cdot & \cdot & K_{1n} \\ K_{21} & K_{22} & \cdot & \cdot & \cdot & \cdot \\ K_{31} & \cdot & \cdot & \cdot & \cdot & \cdot \\ \cdot & \cdot & \cdot & \cdot & \cdot & \cdot \\ \cdot & \cdot & \cdot & \cdot & \cdot & K_{n-1n} \\ K_{n1} & \cdot & \cdot & \cdot & K_{nn-1} & K_{nn} \end{bmatrix} \begin{Bmatrix} D_1 \\ D_2 \\ D_3 \\ D_4 \\ D_5 \\ D_6 \end{Bmatrix} = \begin{Bmatrix} F_1 \\ F_2 \\ F_3 \\ F_4 \\ F_5 \\ F_6 \end{Bmatrix} \tag{16}$$

Each K_{ij} is a 6×6 submatrix. Submatices D_i and F_i are both 6×1 and are the deformation variables and the loadings, respectively. Submatrix K_{ii} depends on the material properties of block i and K_{ij} is defined by the contact between block i and j.

The transition of the sliding and non-sliding phases in the DDA method is assumed to be governed by the Mohr-Coulomb criteria. The friction contact is represented by using pairs of stiff springs on and along the sliding interface. The static frictional force in the non-sliding phase is equal to the spring force, and the elongation of the stiff spring along the sliding interface remains negligible. The dynamic frictional force in sliding phase is equal to the product of the frictional coefficient and the normal contact force. The contact between two individual elements is decomposed as a normal component R_n and a shear component R_s. Once the R_s is greater than the friction defined by the Coulomb's law, sliding occurs.

$$R_s \geq R_n tan\theta \tag{17}$$

The right hand side of Eq.(17) is the resistance of Coulomb's friction. Kinematic energy of the sliding block element dissipates along the contact interface.

The seismic loading is introduced onto the block system through a large block underneath to represent the ground (Fig. 3). The ground excitation is treated in horizontal direction as an acceleration time history, and is in the form of the inertia force of the ground block. By solving the problem incrementally, the inertia force $f_x(t_i)$ of the ground block (m_g) at time step t_i is represented as

$$f_x(t_j) = m_g \ddot{u}_0(t_j) \tag{18}$$

where m_g is a chosen large mass to represent the ground and, $\ddot{u}_0(t_i)$ is constant acceleration within time step i. The vertical component of ground motion remains zero in the present study.

The connection between discontinuous elements to form a larger piece is accomplished by using bolt and connection elements. The bolt element is the simplest way to allow tension in-between discrete elements. If $P_i(u_i, v_i)$ and $Q_j(u_j, v_j)$ are displacements of the two ends of a bolt which connects two different elements i and j. Then the potential energy of the bolt is expressed as

$$\pi = \frac{1}{2} k \left\{ \left[(u_j - u_i) + u \right]^2 + \left[(v_j - v_i) + v \right]^2 \right\} \tag{19}$$

where k is the spring constant of the bolt, and u and v are the two relative displacement components of P_i and Q_j at previous time step as the Eq.(16) is solved incrementally. The stiffness matrix and the force vector of the bolt can be derived through minimization of total potential energy of the Eq.(19) and should be added into the global stiffness matrix and the global force vector in the Eq.(16).

The connection element is basically a constant strain triangle element which has nodal points located in two or three different discrete elements. Through the similar procedure of minimizing total potential strain energy as described above, the stiffness matrix and the force vector of the connection element are also added into the global stiffness matrix and the global force vector in the Eq.(16). In the current practices, two pairs of triangle elements are used for each connection in the numerical model. The strain energy for a single element is

$$\pi_e = \frac{1}{2}\int_0^{L_1}\int_0^{L_2} [\varepsilon_x\ \varepsilon_y\ \gamma_{xy}][E]\begin{Bmatrix}\varepsilon_x\\ \varepsilon_y\\ \gamma_{xy}\end{Bmatrix} J\, dL_1\, dL_2 \tag{20}$$

where L_1 and L_2 are the shape functions used in the constant strain element. J is defined as

$$J = \begin{vmatrix} J_{11} & J_{12} \\ J_{21} & J_{22} \end{vmatrix} \tag{21}$$

in which $J_{11}=x_1-x_3$, $J_{12}=y_1-y_3$, $J_{21}=x_2-x_3$, $J_{22}=y_2-y_3$ and (x_1, y_1), (x_2, y_2), (x_3, y_3) are the coordinates of the nodal points of the connection element.

3. NUMERICAL RESULTS

Numerical analyses presented to describe the dynamic responses of structures with sliding base include a simple two-element problems (Fig.3) and a three-story-structure problem (Fig.4). The analytical solutions the two-element problem obtained by using the mass-spring model are used as the benchmarks to assess the validity and accuracy of DDA results. The parameters chosen for these computations are

(1) natural frequency of the system ω_n= 1 Hz;

(2) frequency ratios for the harmonic ground excitation Ω/ω_n = 0.1 ~ 10.0;

(3) amplitude of the ground acceleration a_{max} = 0.3g;

(4) mass ratios of the two-element system α = m/(M+m) = 0.1, 0.5, 0.9;

(5) frictional coefficients ρ = 0.01, 0.05, 0.1, 0.25.

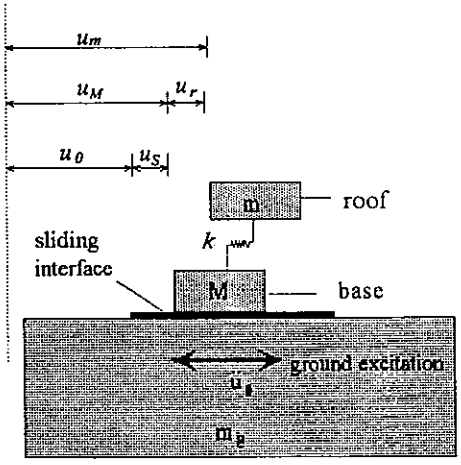

Fig.3 Sliding single-of-freedom model

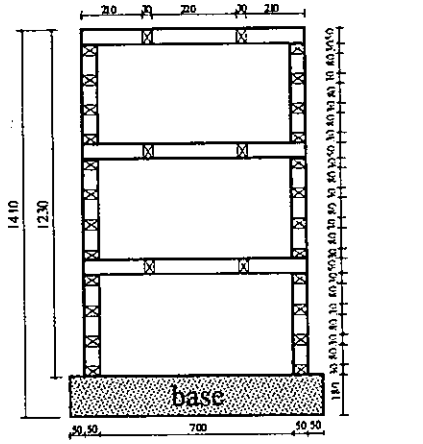

Fig.4 The three-story-building model

In the present study, material damping is not in the concern. Computed results of both the theoretical and the DDA solutions for the two-element system simulation are shown in Figs. 5 to 7. With different mass ratio α, each figure contains the comparisons of four different physical measurements: (a) the maximum relative displacement between the base and the ground $|u_s|_{max}/D$, (b) the maximum relative displacement between the roof and the base

$|u_r|_{max}/D$, (c) the maximum ratio of the base acceleration to the ground acceleration $|a_{base}/a_{ground}|_{max}$ and (d) the maximum ratio of the roof acceleration to the ground acceleration $|a_{roof}/a_{ground}|_{max}$. The first two measurements are normalized by a factor $D = a_{max}/\Omega^2$. All these results indicates that this numerical method can provide reliable solutions for simple model simulation when comparing to the theoretical solutions.

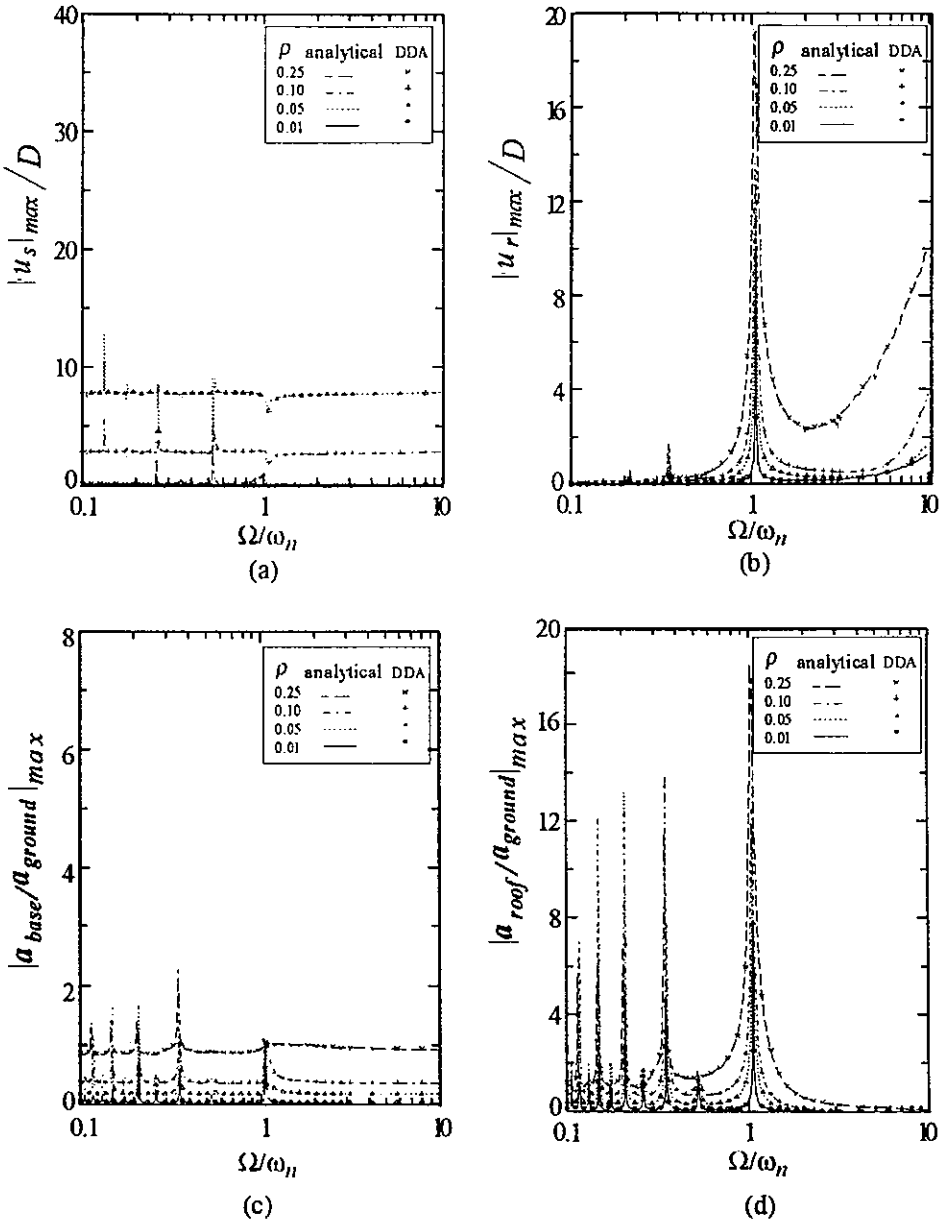

Fig.5 Comparisons of analytical and numerical solutions for α=0.1
(a) the maximum relative displacement between the base and the ground
(b) the maximum relative displacement between the roof and the base
(c) the maximum ratio of the base acceleration to the ground acceleration
(d) the maximum ratio of the roof acceleration to the ground acceleration

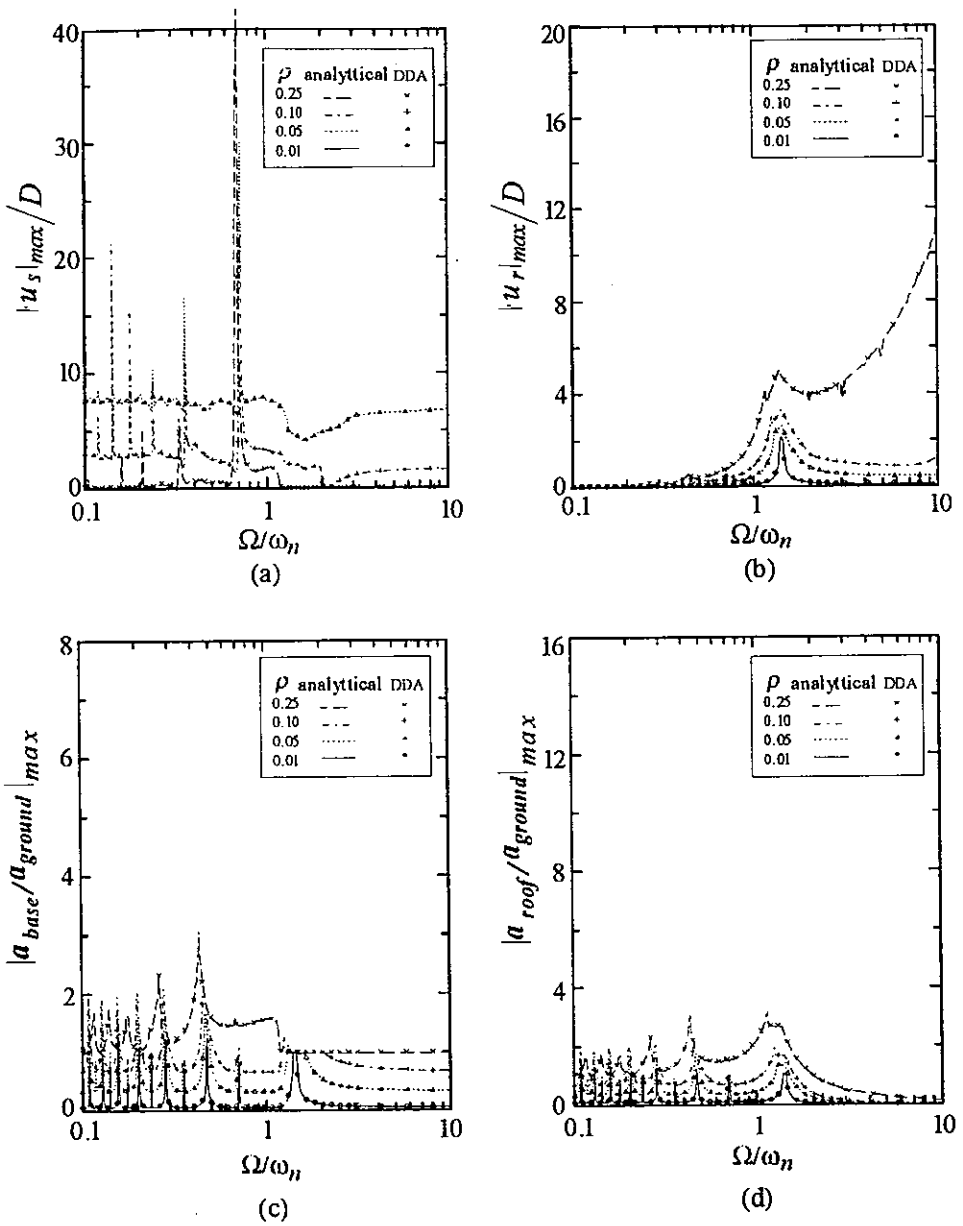

Fig.6 Comparisons of analytical and numerical solutions for α=0.5

(a) the maximum relative displacement between the base and the ground

(b) the maximum relative displacement between the roof and the base

(c) the maximum ratio of the base acceleration to the ground acceleration

(d) the maximum ratio of the roof acceleration to the ground acceleration

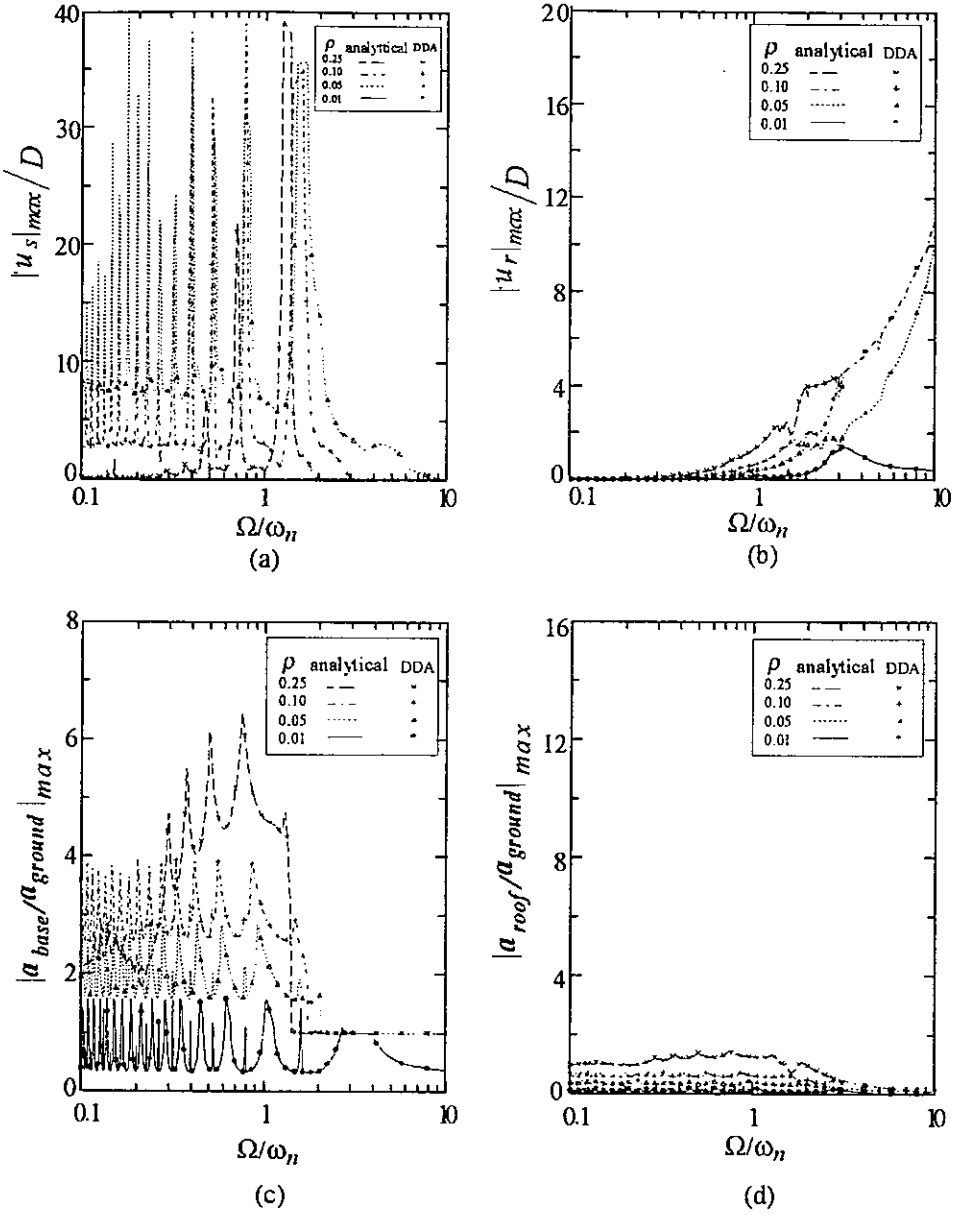

Fig.7 Comparisons of analytical and numerical solutions for α=0.9
(a) the maximum relative displacement between the base and the ground
(b) the maximum relative displacement between the roof and the base
(c) the maximum ratio of the base acceleration to the ground acceleration
(d) the maximum ratio of the roof acceleration to the ground acceleration

In the following, the DDA model is advanced to analyze a three-story structure subjected to a seismic loading. The configuration of the structure frame is directly meshed by discrete elements. The connection between any two discrete elements is accomplished by two pairs of triangle connection elements. The dimensions are shown in Fig.4. The Young's modulus and the Poisson's ratio of the material used are 2.0×10^7 kpa and 0.15, respectively. The frictional coefficient of 0.01 is chosen for the sliding interface for the sliding phase. The stiffness of the spring used to represent the contact of the sliding interface is chosen as 2.0×10^9 kN/m for the non-sliding phase. The natural frequencies for the first three modes of the structure are 0.638Hz, 1.788Hz and 2.583Hz. The acceleration time history of the 1940 El Centro earthquake with time increment of 0.001 second (Fig.8) is chosen as the seismic input. The

fourier spectrum of the chosen seismic input is shown as Fig.9, in which the predominant frequency is about 1.5Hz. Structural responses under two different conditions, fixed-base and sliding-base, are computed for the comparison. As can be seen in Fig.10, the computed sliding of the structure under the seismic ground excitation is presented in the form of the relative displacement of the base to the ground, in which the maximum slip during the excitation is about 0.3m. At the end of the excitation, the structure displaces about 0.18m from its origin. The seismic excitation which exerts to the sliding structure from the base through the sliding interface is actually very limit (Fig.11) if comparing to the chosen El Centro earthquake record (Fig.8). The fourier spectrum of the sliding base excitation is shown as Fig.12, and it needs to be mentioned that the predominant frequency is about 0.35Hz. Comparing to the frequency of 1.5Hz for the chosen El Centro earthquake record, the predominant frequency of input motion for the sliding structure has been significant reduced, and is below the nature frequencies for the structure itself. For the fixed-base condition, the responses of the structure at the roof are presented in Figs.13 and 14, in which the time history of the roof acceleration and the relative displacement of the roof to the base are shown, respectively. With the sliding-base of ρ=0.01, on the other hand, the acceleration of the vibration reduces to about one hundredth (Fig.15), and the amplitude of the vibration is also obviously decreased (Fig.16). The decrease of both the acceleration and the amplitude of the structural vibration indicates that the sliding-base successfully isolates the structure from the severe ground excitation. The effectiveness of using the sliding-base to avoid damaging earthquake is shown by not only the limit acceleration exerted onto the structure due to the sliding-base separation, but the similarity of accelerations for the base and the roof (Figs.11 and 15). This reveals that the structure behaviors with very little deformation (Fig.16).

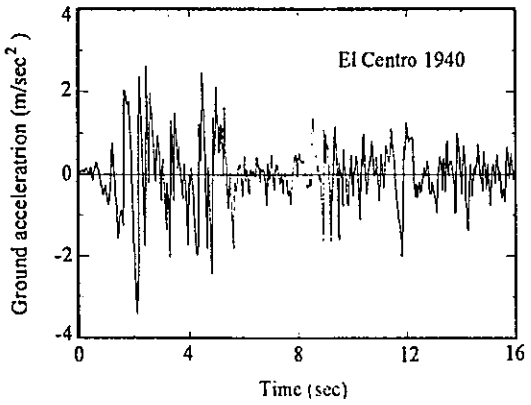

FIg.8 Acceleration time history of the El Centro earthquake motion

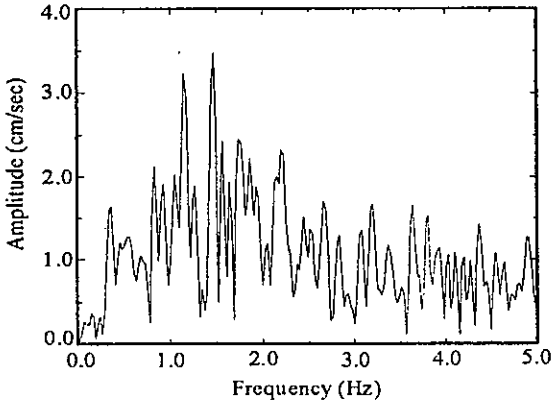

Fig.9 Fourier spectrum of the El Centro earthquake motion

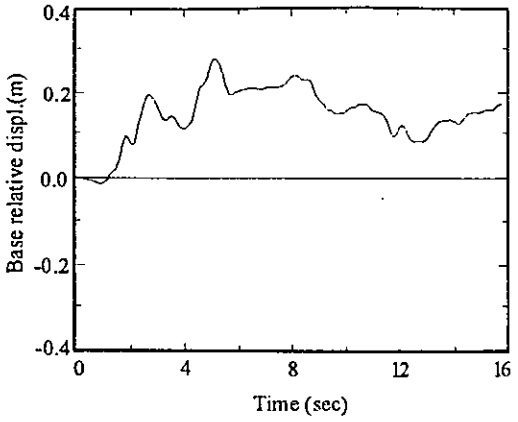

Fig.10 Relative displacement of the base to the ground (ρ=0.01)

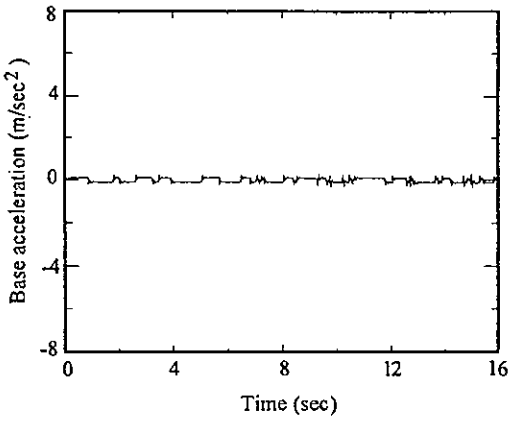

Fig.11 Base acceleration of the sliding structure (ρ=0.01)

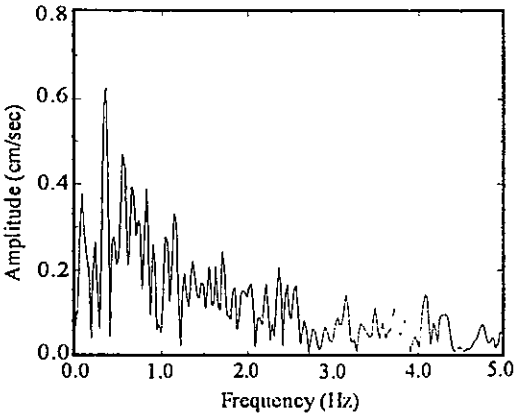

Fig.12 Fourier spectrum of the base excitation for the sliding structure

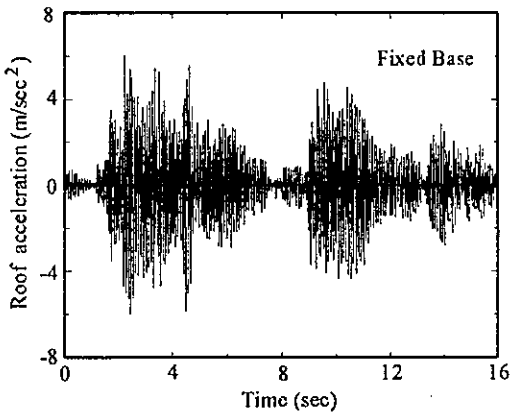

Fig. 13 Roof acceleration of the fixed-base structure

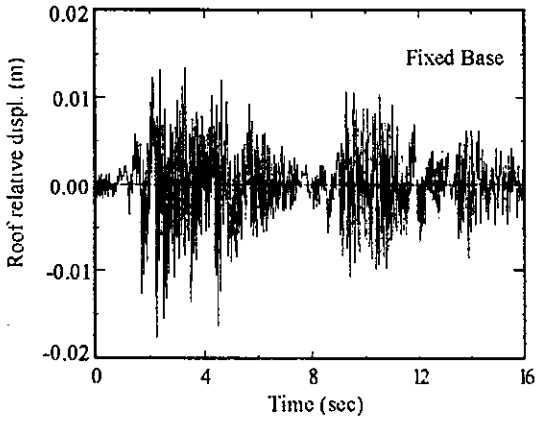

Fig.14 Relative displacement of the roof to the base for the fixed-base structure

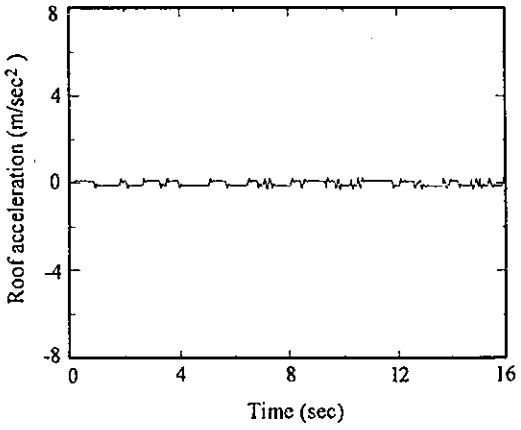

Fig.15 Roof acceleration of the sliding structure (ρ=0.01)

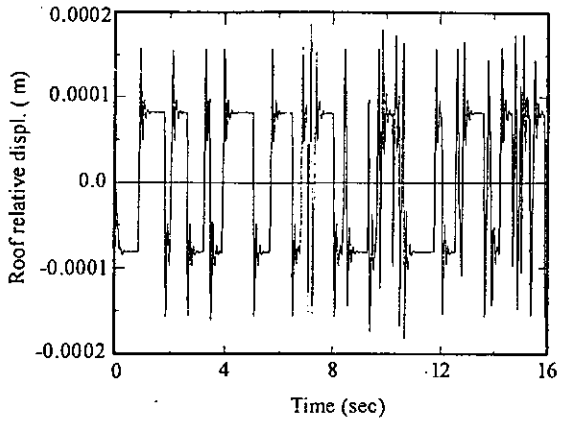

Fig.16 Relative displacement of the roof to the base for the sliding structure (ρ=0.01)

4. CONCLUSIONS

The effectiveness of applying sliding-base in reducing the peak responses of structures has been studied using the discontinuous deformation analysis method. This study shows that using this method can simulate the dynamic response of sliding structure with frictional cut-off in good accuracy.

Computations for a simple two-element mass-spring system indicate that the results obtained by using the DDA model have similar accuracy as those of the analytical solutions by using the idealized mass-apring model. Seismic response analysis for a three-story structure with sliding base reveals that the sliding interface can reduce the ground acceleration or the seismic loading exerting onto the structure. The sliding structure may therefore behave with very little deformation. Nevertheless, an irrecoverable displacement for the structure may also be existed after the seismic excitation.

REFERENCES

1. B. Westermo and F. Udwadia, Periodic response of a sliding oscillator system to harmonic excitation, *Earthquake Engineering and Structural Dynamics,* Vol. 11, 135-146 (1983).
2. N. Mostaghel, M. Hejazi and J. Tanbakuchi, Response of sliding structures to harmonic support motion, *Earthquake Engineering and Structural Dynamics,* Vol. 11, 355-366 (1983).
3. Z. Li, E.C. Rossow and S.P. Shah, Sinusoidal forced vibration of sliding substructure, *J. Struct. Engng. ASCE* Vol. 115, 1741-1755 (1989).
4. N. Mostaghel, and J. Tanbakuchi, Response of sliding structures to earthquake support motion, *Earthquake Engineering and Structural Dynamics,* Vol. 11, 729-748 (1983).
5. Y.-B. Yang, T.-Y. Lee, and I.-C. Tsai, Response of multi-degree-of- freedom structures with sliding supports, *Earthquake Engineering and Structural Dynamics,* Vol. 19, 739-752 (1990).
6. P.A. Cundall, A computer model for simulating progressive, large scale movements in blocky rock systems, *Symposium of International Society of Rock Mechanics,* Nancy, France, 11-18 (1971).
7. R.E. Goodman, R. Taylor, and T.L. Brekke, A model for the mechanics of jointed rock, *J. of Soil Mechanics & Foundations Div., ASCE,* Vol. 94, 637 (1968).
8. G.H. Shi and R.E. Goodman, Discontinuous Deformation Analysis, *Proc. 25th U. S. Symposium* on Rock Mechanics, 269-277 (1984)

Dynamic-Contact Analysis Scheme Applied in the DDA Method

Chung-Yue Wang, Jopan Sheng and Ming-Hong Chen

Department of Civil Engineering, National Central University Chungli, 32054, Taiwan, R. O. C.

ABSTRACT

In this paper, a quantitative analysis of the dynamic-contact scheme applied in DDA method was presented. An one dimensional model was degenerated from the original DDA theory to study the conservation of energy and accuracy of a simple dynamic problem with respect to the marching time step and strain increment. From stress wave propagation theory, a new criteria for DDA method user to determine the time step size and suitable value of contact penalty spring constant is proposed and verified by studying a stress wave propagation problem of a continuous medium. This criteria relates the acoustic impedance of materials in contact and can be applied in the dynamic analysis of any discrete element system.

1. INTRODUCTION

Finite element methods are well established in many branches of engineering and are now routinely used in the solution of large scale industrial problems. For some physical situations a finite element description is not, however, the most appropriate and a discontinuous approach is better suited to model the phenomenon concerned. Since the Discontinuous Deformation Analysis (DDA) method first developed by Gen-hua Shi [1] in 1988, a number of research works have been conducted by using this method to study the discontinuous behaviors of engineering system. Examples of such problems include the behavior of jointed rock, granular material flow in soils, missile/transport impact simulations and mining and rock blasting operations. Thus far, numerical simulations by DDA method can provide a fairly reasonable qualitative analysis of those interested problems. This DDA method is continuously improved by researchers and it is worth to mention that this DDA method together with the finite element method (FEM) can be grouped into a more general theory called Manifold Method which is also developed by Shi [2]. Therefore, the DDA method in nature is well compatible with the finite element method from a mathematical point of view. This feature enhance researchers confidence on adopting the existed methodologies and experience accumulated in FEM and continuously developing DDA method to accurately solve more challenging engineering problems.

Basically, the DDA method is an incremental dynamic formulation with contact detection algorithm among deformable bodies. During the application of this method, the time step size, Δt and the penalty spring constant K_p which is applied on the contact analysis between blocks have crucial effects on the analysis results. Since the

time that DDA method is proposed, rational analyses on the effect of time integration scheme and the determination of the penalty spring value in the DDA theory are lacking. In the present paper, the fundamental principles in classical mechanics were applied to evaluate the characters of the dynamic-contact scheme of DDA method. Through this quantitative study, it is desired to provide researchers some reference information about the dynamic features of DDA theory for further investigation.

2. ATTRIBUTES OF THE DDA METHOD

Most physical systems are discontinuous at some level. For attempting to model discontinuous systems, many numerical methods have been developed [3-9]. Methods for simulating the complete behavior of systems of discrete interacting bodies are collectively known as discrete element methods. There are three important aspects of every discrete element method:

(1) contact detection
(2) representation of contacts
(3) representation of solid material

According to Munjiza's [8] classification of discrete element methods, the DDA method has the following attributes:

(1) the contact is deformable and no penetration allowed.
(2) bodies can be deformable.
(3) large displacement and small strains are applied.
(4) the discrete system can consist of large number of bodies.
(5) the material properties of the bodies can be linear or nonlinear.
(6) fracture can be allowed.
(7) the packing of discrete bodies can be dense or loose.
(8) the problem considering discrete bodies can be static or dynamic.

Due to these attributes, the DDA approach is able to simulate large variety of problems in solid mechanics especially containing discontinuities compared with other computational methods.

For a discrete system under external excitation and constraints, the DDA method uses the generalized coordinates of each block as unknowns, by considering the inertia effect, constraint conditions, interaction behaviors among blocks and the work due to external load, the total potential of the system can be determined. Through variational method for minimizing the total potential energy, the simultaneous equilibrium equations of the discrete system can be obtained. The governing equations are solved in the same manner as the matrix analysis of discretized continuous media in the finite element method. The forces acting on each block, from external loading or contact with other blocks, satisfy the equilibrium equations in a variational sense. Equilibrium is also achieved between external forces and the block stresses. For each block, displacements, deformation and strains are permitted and for the entire block system, sliding, opening and closing of block interfaces are also permitted. Furthermore, the analysis fulfills constraints of no tension between blocks and no penetration of one block into another. To achieve equilibrium and satisfy these constraints, simultaneous equations are solved repeatedly with partial changes of the coefficients each time with respect to the chosen constraint conditions. There are two important features of DDA method that must be addressed in detail as following:

(i) Incremental Dynamic Formulation of DDA Method

The DDA method is an incremental dynamic formulation. As shown in Fig. 1, the DDA method uses the results of the previous time step as the new reference state to predict the behaviors of current state. The base function used to model the displacement and deformation of each block is keeping updated according to its reference configuration. For each time step , there are initial velocity components and initial stresses together with the contact forces existed in each block to form the updated governing equations. After solving the simultaneous large sparse matrix equations, the increments of the system are obtained. Accumulating all the increments of time steps the total displacements and deformation of the blocky system from the initial configuration can be traced.

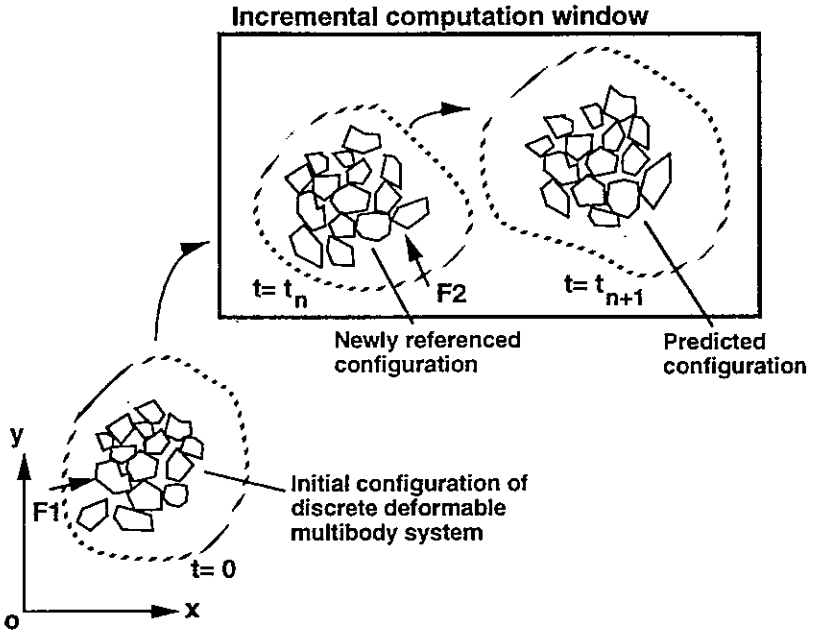

Fig. 1 Schematic diagram of the dynamic incremental analysis form of the DDA method.

(ii) Contact-Interaction Analysis in the DDA Method

Contact detection and interaction analysis among discrete bodies are the main features of any discontinuous analysis theorem. In the finite element method a special attention is paid to interaction itself, while contact detection is usually less important [8]. Various techniques for contact interaction in the finite element method have been developed and various interaction models including friction law were proposed [9-20]. A novel contact detection coupled interaction analysis algorithm called "Block System Kinematics" has been developed in the DDA method[1]. The direct mathematical descriptions of non-tension, non-penetration requirements among blocks are given by combination of inequalities. To minimize the total potential energy or the least square object function with inequality constraints is a nonlinear programing problem, which is extremly difficult. This is most likely the reason for tyhe absence of formal treatment of block system kinematics in classical mechanics up to the present time[1]. Nevertheless, there are some important physical factors that can be used to break

through the numerical impasse. When the block system moves or deforms, the blocks are in contact only along the boundary and the non-penetration inequalities can be transformed into equations when two blocks are in contact. The equation can be imposed on the global equations by adding very stiff springs or penalties to lock the movement in one or two directions. If two blocks have a tensile contact force between them, they will separate after the removal of the locks. Therefore, the non-tension constrainting ineqalities can be reduced to lock or unlock of the locks. The global governing equations have to be solved repeatedly while selecting the lock or constrainting position. Using this method, even a block system with tension and penetration can be corrected by the selection of lock positions a few times. There are three different kinds of contacts ibetween blocks identified in DDA theory: angle to angle, angle to edge and edge to edge (see Fig. 2). All of these contacts can be transformed to point-line crossing inequalities. In the case when inter-penetration occurs at a given position, a " lock" or penalty spring is applied, which starts from the point and lies along the direction normal to the reference line (see Fig. 3).

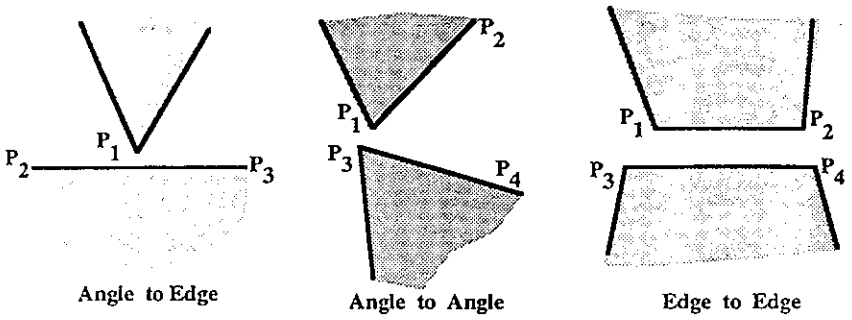

Fig.2 Three different kinds of contact identified in DDA theory.

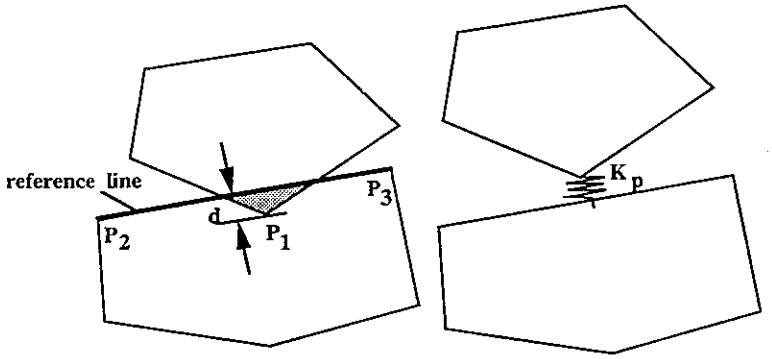

Fig. 3 Locking of penetration by penalty spring.

The physical meaning of applying penalty springs is " to push the invaded angle back along the shortest path". The value of penalty spring K_p is a very large value and is suggested by Shi [1] from 10 to 1000 times of the Young's modulus of the material, to guarantee the displacement of the spring is 10^{-3} to 10^{-4} times the total displacement. However, this emperical criteria has to be applied carefully in each particular case, otherwise large penetration may occur or extra energy will be introduced into the system and then causes the analysis inaccurate.

It can be seen from above discussion on DDA theory that time integration scheme and the contact penalty number have crucial effects on the accuracy of this analysis. In the following of this paper, some benchmark problems were studied to evaluate the accuracy and characters of the DDA method.

3. OSCILLATION OF A STEP LOADED SINGLE BLOCK

(i) Analytical Approach:

As shown in Fig. 4, a single elastic block with length L and of unit thickness and width subjected to a step loading F is designed to study the time integration scheme applied in the DDA method. This elastic block of Young's modulus E has zero Poisson's ratio. Due to the symetry of the loading and geometry, the block is oscillating harmonically about its static equilibrium position. This problem is equivalent to a problem shown in Fig. 5 with S equal to L/2. The governing equation of a single degree of freedom model of the bar can be derived and expressed in the following form[21]:

$$\left(\frac{\rho AS}{3}\right)\ddot{u} + \left(\frac{AE}{S}\right)u = P(t) \tag{1}$$

where A is the cross-sectional area, ρ is the mass density and u is the displacement at the end of the bar.

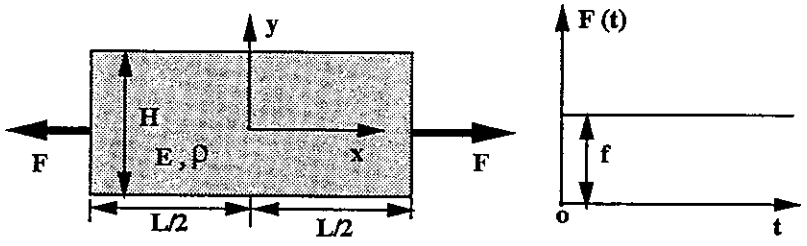

Fig. 4 A single block under step loading.

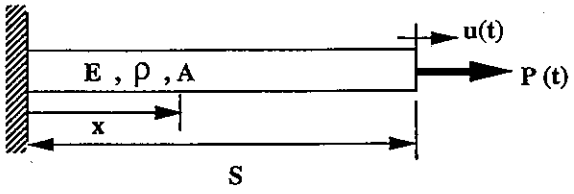

Fig. 5 An axial force P(t) is applied to the end of an uniform, linearly elastic bar.

If P(t) = f H(t), then the solution of Eq. (1) is

$$u(t) = \frac{fS}{AE} (1 - \cos (\omega_n t)) \tag{2}$$

where the natural frequency is

$$\omega_n = \sqrt{\frac{3E}{\rho S^2}} \tag{3}$$

and the natural period T_n is equal to

$$T_n = \frac{2\pi}{\omega_n} = 2\pi\sqrt{\frac{\rho S^2}{3E}} \tag{4}.$$

From Eq.(2), the time variation of the strain of the bar can be obtained as

$$\varepsilon(t) = \frac{u(t)}{S} = \frac{f}{AE} [1 - \cos (\omega_n t)] \tag{5}$$

(ii) DDA Approach:

According to the original DDA formulation [1], there are six general coordinates (or unknowns) for each block and can be expressed as

$$\{ \mathbf{d} \} = \{u, v, r, \varepsilon_x, \varepsilon_y, \gamma_{xy} \} \tag{6}.$$

These six to be solved unknowns are used to determine the displacement field of each block. The physical meaning of the first three variables u, v, r represent the rigid body translations and rotation of the block during motion. The remaining three variables,

ε_x, ε_y , γ_{xy} ,are the constant strains of the block. For the problem to be studied as shown by Fig. 4, due to the symetry of the loading and geometry condition coupled with the zero Poission's effect, the only remaining variable is the axial strain e. After formulating the problem according to the procedure of the DDA method, the displacement function, δ (x , t_n) of points inside the block at time step t_n can be modelled as

$$\delta\,(x\,,\,t\,) = (\,x - \frac{L_{n-1}}{2}\,)\,\Delta\varepsilon(t) \tag{7}$$

where L_{n-1} is the total length of the bar at time t_{n-1} and $\Delta\varepsilon$ represents the increment of the strain from prevrious time step. That is, the relationship between ε_n and ε_{n-1} is $\varepsilon_n = \varepsilon_{n-1} + \Delta\varepsilon$. The increment of the strain energy is expressed as:

$$\Delta\Pi_e = \frac{H}{2}\int_0^{L_{n-1}} (\,\varepsilon_n\, E\, \varepsilon_n - \varepsilon_{n-1}\, E\, \varepsilon_{n-1}\,)\, dx$$

$$= \frac{LHE}{2}\,(\varepsilon_{n-1}^2 + 2\,\Delta\varepsilon\,\varepsilon_{n-1} + \Delta\varepsilon^2\,) \tag{8}.$$

The change of the potential due to external load is

$$\Delta\Pi_f = -f \bullet \delta(L_{n-1}\,,\,t_n) - (-f) \bullet \delta(\,0,\,t_n\,)$$
$$= -\,f \bullet L_{n-1} \bullet \Delta\varepsilon \tag{9}.$$

The change of the total potential due to the inertial force can be written as

$$\Delta\Pi_i = \int_0^{L_{n-1}} m \bullet \delta(x,\,t_n\,) \bullet \ddot{\delta}\,(x,\,t_n\,)\, dx \tag{10}$$

where m is the mass density per unit length of the bar. It is noted that the central difference like time integration scheme were used in the DDA theory. Constant acceleration method is applied in its theory. Therefore, the acceleration at time t_n is approximated by the following formula

$$\frac{\partial^2\,\{\mathbf{d}\,(t_n)\}}{\partial t^2} \cong \frac{\partial^2\{\mathbf{d}\,(t_{n-1})\}}{\partial t^2} = \frac{2}{\Delta t^2}\,\{\mathbf{d}(t_n)\} - \frac{2}{\Delta t}\,\frac{\partial\{\mathbf{d}(t_{n-1})\}}{\partial t} \tag{11}$$

In Eq.(11), it can be found that the acceleration is expressed in term of displacement to be solved. Hence, we can say that the DDA is an implicit method. According to this time integration scheme, the Eq. (10) can be reformed as following

$$\Delta\Pi_i = \int_0^{L_{n-1}} m \bullet \delta(x\ ,\ t_n) \bullet \left[\frac{2\ \delta(x\ ,\ t_n)}{\Delta t^2} - \frac{2\delta(x\ ,\ t_{n-1})}{\Delta t} \right] dx$$

$$= \Delta\varepsilon \bullet m \bullet \left[\frac{2\Delta\varepsilon}{\Delta t^2} - \frac{2\dot{\varepsilon}_{n-1}}{\Delta t} \right] \bullet \int_0^{L_{n-1}} \left(x - \frac{L_{n-1}}{2} \right)^2 dx$$

$$= \frac{mL^3}{6\Delta t} \left[\frac{\Delta\varepsilon}{\Delta t} - \dot{\varepsilon}_{n-1} \right] \Delta\varepsilon \qquad (12).$$

The total change of the potential energy of the system is equal to

$$\Delta\Pi_T = \Delta\Pi_e + \Delta\Pi_f + \Delta\Pi_i$$

$$= \frac{ELH}{2}\Delta\varepsilon^2 + \left[ELH\varepsilon_{n-1} + \frac{mL^3}{6\Delta t^2}\Delta\varepsilon - \frac{mL^3}{6\Delta t}\dot{\varepsilon}^*_{n-1} - fL \right] \Delta\varepsilon \qquad (13).$$

From the minimum potential energy theory, the governing equation of the block motion is obtained as

$$\Delta\varepsilon = \frac{-ELH\ \varepsilon_{n-1} + \dfrac{mL^3\dot{\varepsilon}_{n-1}}{6\Delta t}}{ELH + \dfrac{mL^3}{6\Delta t^2}} \qquad (14)$$

where

$$\dot{\varepsilon}_n = \frac{2\Delta\varepsilon}{\Delta t} - \dot{\varepsilon}_{n-1} \qquad (15)$$

(iii) Numerical Simulation

Eqs. (14) and (15) were used to study a sigle block under step loading (see Fig. 4) with L = 1 m, H=1m, E= 10000 N/m^2 and f= 1N. Different time step sizes were applied into the recursive formula. All of these cases were also calculated by DDA code with zero Poisson's ratio value. Both the DDA simulation and the results obtained from Eq. (14) are exactly the same. Figures 6(a) to 6(d) show the behaviors of this suddenly loaded block at different time step size. It is interesting to find that there are some damping effect in the numerical scheme since the responses are similar to a damped spring-mass system in structural dynamics. The damping effect is reduced as the time step size decreases. At the case Δt equal to 10^{-6} second the amplitude, frequency and phase angle of simulation result are approaching to the ones of analytical solution expressed by Eq. (5) at the max. error around 0.1% (see Fig.

7(d)). Since there is no energy dissipation mechanism in the studied system, conservation of total potential energy should be satisfied. That means the total change of potential energy $\Delta\Pi_T$ expressed by Eq. (13) should be equal to zero.

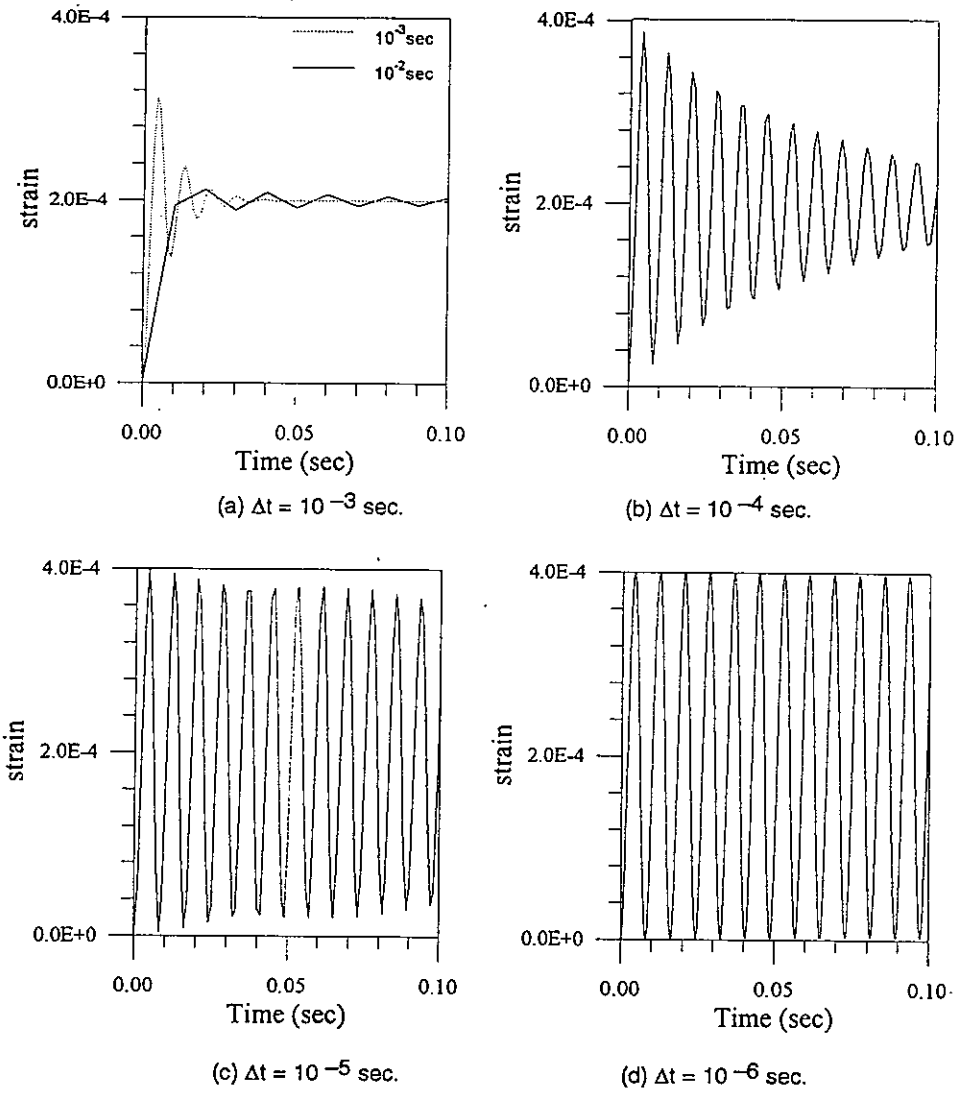

Fig. 6 Response of a single block under step loading simulated by DDA method using different time step sizes.

If one substitute the strain increment expressed by Eq.(14) into Eq.(13), the energy variation away from the conservation at each time step can be studied. Figures 7(a) to 7(d) show the traces of energy variation normalized by $\varepsilon_{max}^2 E/2$ vs. calculated strain increment at each time step for different time increment Δt. At large time increment (e.g. $\Delta t = 10^{-3}$ second) the energy error initially is around 55% and gradually reduced. The smaller the time increment used, the lower the energy

dissipation rate is generated. This can be a general guidance for DDA user in choosing the time step size. It is also revealed from Fig. 6(a) that large time step size can be used when using DDA code for static problems. Since the simulation result quiclly converges to the static equilibrium solution at large time step size.

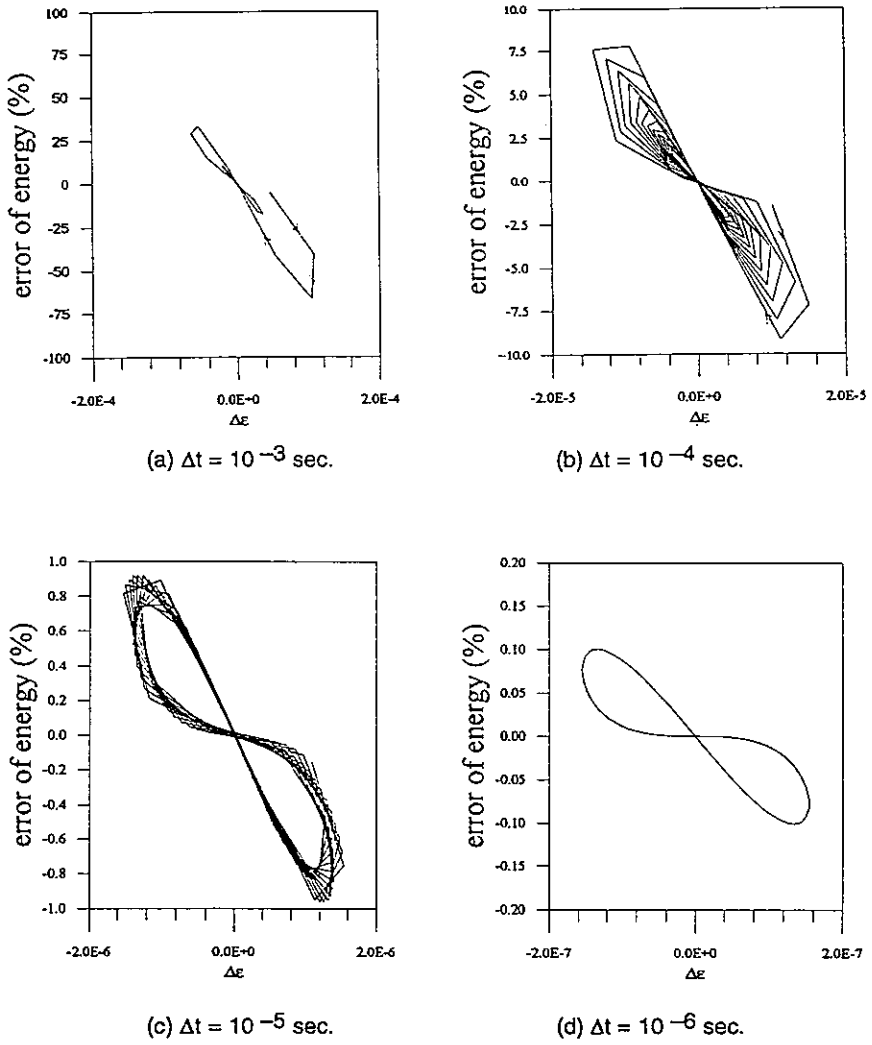

Fig. 7 Traces of normalized energy variation vs. strain increment during oscillation for different Δt..

4. DETERMINATION OF THE PENALTY NUMBER IN DYNAMIC-CONTACT ANALYSIS

As mentioned in the previous section, the determination of the penalty number for penetration locking in DDA so far is still using an empirical criteria. In this section, a rational analysis based on impact dynamics is presented and a criteria is proposed for DDA user in determining a suitable value of the penalty spring.

(i) Compatibility Condition at Shock Wave Front:

In one dimensional shock wave dynamics, a discontinuous shock front propagating in an elastic medium has to satisfy some dynamic compatibility conditions. As shown by Fig. 8, a shock front locating on position AB at time t propagates to position A'B' which is a distance "dx" from A'B' after a time interval "dt". Based on the principle in dynamics, the linear momentum of particles between ABA'B' has to be conservative. Thus, the following equation is obtained

$$(\sigma^+ - \sigma^-)\, A_0\, dt = \rho_0\, A_0\, dX\, (v^- - v^+) \tag{16}$$

where σ^- and v^- represent the stress and velocity of the particle behind the shock front, respectively while σ^+, v^+ represent the ones before the shock front. A_0 is the cross-sectional area and ρ_0 is the mass density.
Eq.(16) can be reformed as

$$[\,\sigma\,] = -\rho_0 \frac{dX}{dt} [\,v\,] = -\rho_0\, \alpha\, [\,v\,] \tag{17}$$

where a is the propagation speed of the shock front. This equation can be considered as the jump compatibility condition at the shock front.

(ii) Coaxial Impact of Two Elastic Rods:

Two elastic rods with same cross-sectional area and have acoustic impedance $(\rho_0 C_0)_1$ and $(\rho_0 C_0)_2$ respectively. As shown in Fig. 8, both rods initially stress free and rod B2 with a velocity v_2 impacts rod B1 with a velocity v_1 (where $v_2 > v_1$, see Fig. 9(a)). After the impact, there is a shock wave front propagating toward left in rod B2 and right in B1 rod (see Fig. 9(b)). Right at the contact interface two rods have a same particle velocity and impact stress.

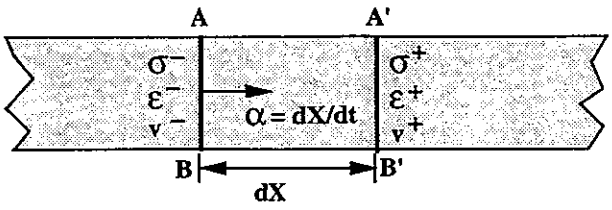

Fig. 8 Shock front propagation in an elastic medium.

According to the compatibility condition obtained from the conservation of linear momentum at the shock front as expressed in Eq. (17), one can has the following relations:

$$\sigma = -(\rho_0 C_0)_1 (v - v_1) = (\rho_0 C_0)_2 (v - v_2) \tag{18}$$

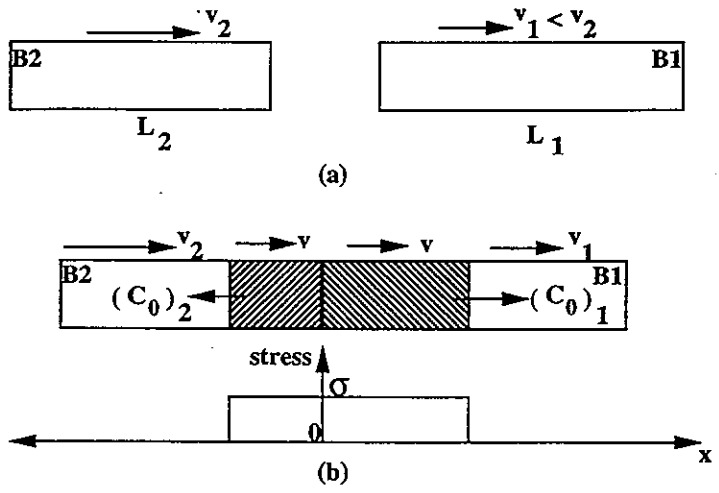

Fig. 9 (a) Coaxial impact of two elastic rods.
(b) Particle velocity and stress distributions of two rods after impact

From these equations the impact stress and particle velocity behind the shock wave front can be derived as

$$v = \frac{(\rho_0 C_0)_1 v_1 + (\rho_0 C_0)_2 v_2}{(\rho_0 C_0)_1 + (\rho_0 C_0)_2} \tag{19}$$

$$\sigma = -\frac{v_2 - v_1}{\frac{1}{(\rho_0 C_0)_1} + \frac{1}{(\rho_0 C_0)_2}} \tag{20}$$

where the wave speed C_0 in each rod is determined by its Young's modulus E and material density r_0 as

$$C_0 = \sqrt{\frac{E}{\rho_0}} \tag{21}.$$

The impact behaviors of these two coaxial impact rods can be examined by characteristic lines in the X-t plane and in the v– s plane. For example, an infinite long rod B1 initially at rest is impacted by rod B2 of finite length L_2 at velocity v_2. The behaviors depend on the impedance ratio $(\rho_0 C_0)_1 / (\rho_0 C_0)_2$ of these two rods and are

represented by the characteristic planes shown in Fig 10. From these plots the velocity and stress distribution inside each rod at any instant of time can be determined [22].

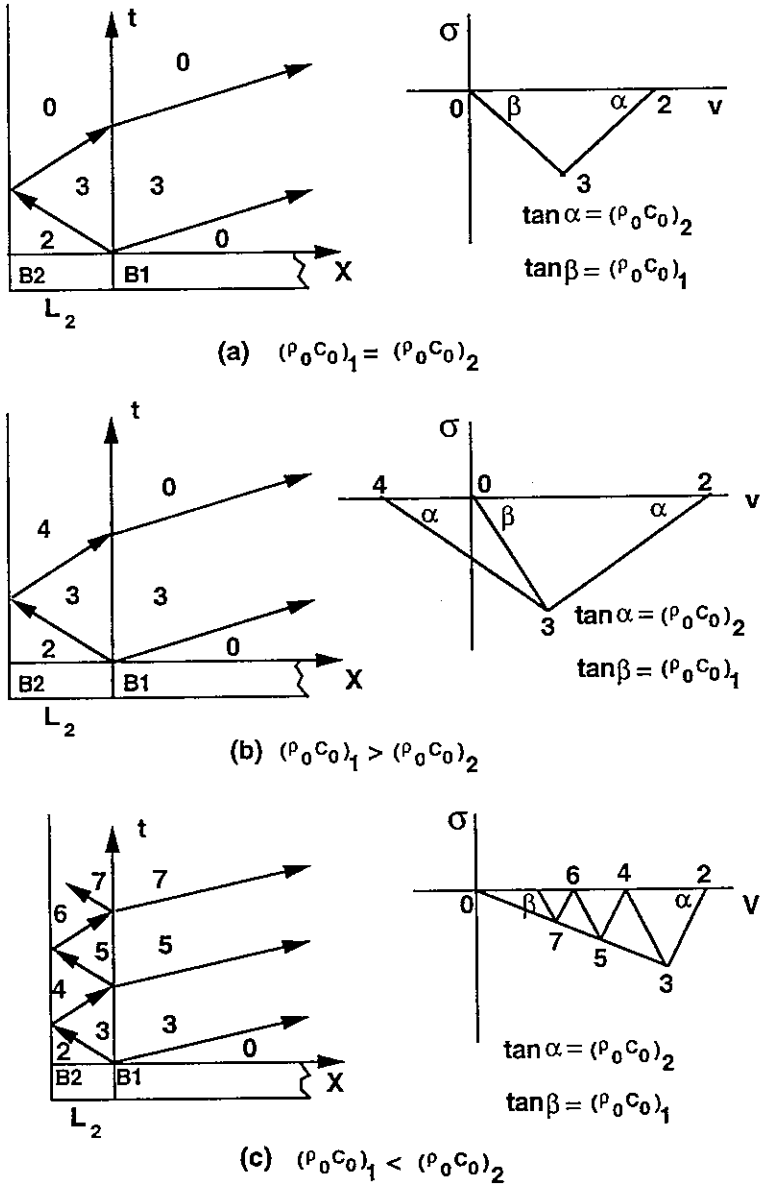

Fig. 10 Characteristics lines of coaxial impact of two rods in x-t and v-s planes.

(iii) Relationship Between the Penalty Spring and the Time Step Size in Dynamic – Contact Analysis:

In the dynamic contact analysis, the value of the penalty spring has a crucial effect on the analysis result. For the DDA method when two blocks in contact, a penalty spring has to be set to lock the penetration effect. This dynamic contact process just like the problem of two coaxial impacted rods which has been studied previously. The compatibility condition expressed by Eq. (17) at the impact site has to be satisfied. To determine a suitable value of penalty spring, the contact stress in Eq. (17) can be rewritten in term of the stiffness of penalty spring at contact interface as

$$\sigma = \frac{F}{A} = \frac{K_p \alpha}{A} = \frac{K_p(v_2 - v_1) \Delta t}{A} \tag{22}$$

where a represents the relative movement of two contact surfaces at speed v_1 and v_2 respectively.

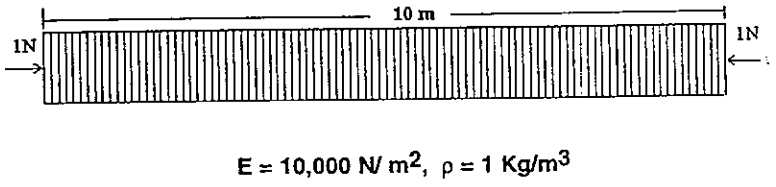

Fig. 11 Computation mesh of DDA method for a rod composed of 100 connected blocks under step loading.

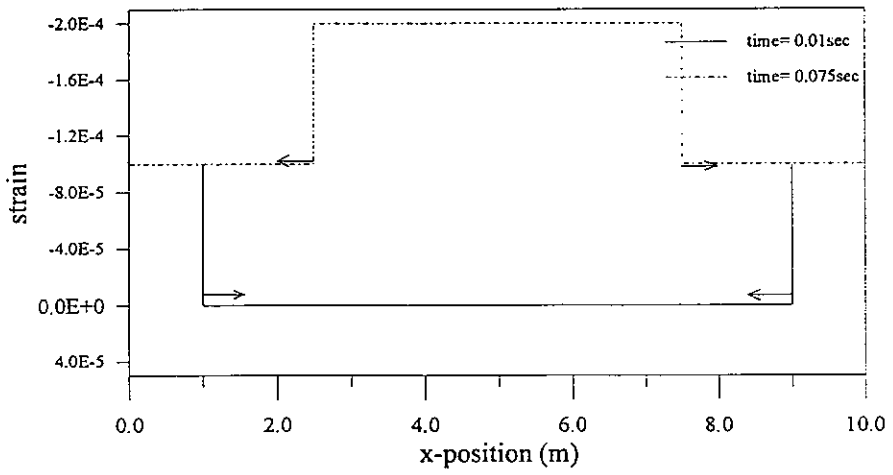

Fig. 12 Analytical solutions of stress states and locations of wave front at different time of a rod under step loading.

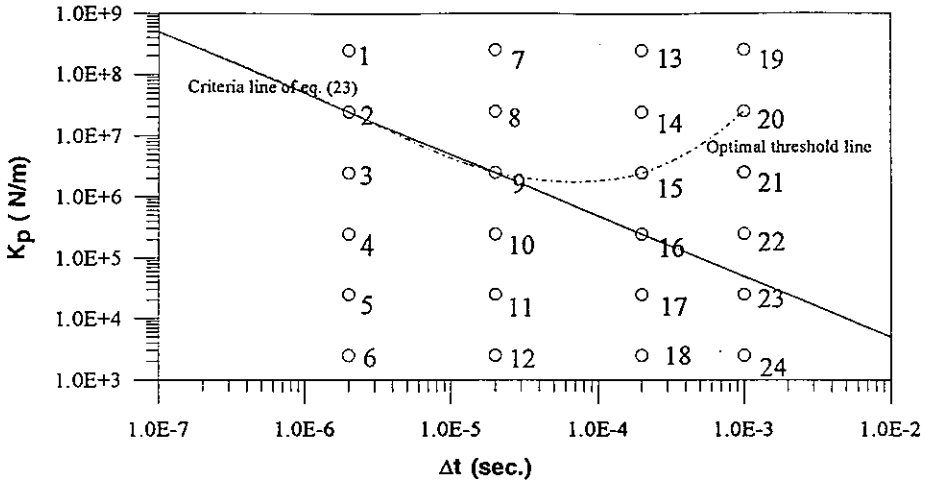

Fig. 13 Condition points for the verification of reference line and optimal threshold line used for the determination of penalty spring constant and time step size in DDA calculation.

Equate Eq.(20) and Eq.(22) and let A to be unit area, one can obtains

$$K_p \Delta t = \frac{1}{\frac{1}{(\rho_0 C_0)_1} + \frac{1}{(\rho_0 C_0)_2}} = \frac{1}{\frac{1}{\sqrt{(E\rho_0)_1}} + \frac{1}{\sqrt{(E\rho_0)_2}}} \qquad (23)$$

This equation relates the penalty number and time step size with the material properties of the two blocks in contact. To verify this newly proposed criteria, a problem shown in Fig. 11 was analyzed by DDA code and was compared with the exact solution. In the application of DDA code, the 10 meter long rod composed of 100 connected blocks is suddenly loaded by a 1 N constant force. Tension is allowed between these blocks to model a continuous medium. Those penalty springs located among interfaces of blocks start locking the penetration during the dynamic-contact process. Totally twenty-four conditions in $K_p - \Delta t$ plane (see Fig. 13) were applied into the DDA code to simulate the problem. The data of this problem are listed in Table 1. Figures 14 to 17 show the DDA results. Comparing these results with exact solutions (see Fig. 12) of the stress and location of wave front at different time level (t = 0.01 sec. and t = 0.075 sec.), one can leads to the following observations:

(1) In the $K_p - \Delta t$ plane, all the condition points for DDA code inputs below the criteria line of Eq. (23) can not provide accurate simulation results either the strain levels or locations of wave front. It shows that the Eq. (22) can be used

as a reference threshold line for DDA user to determine suitable penalty number and its associated time step size.

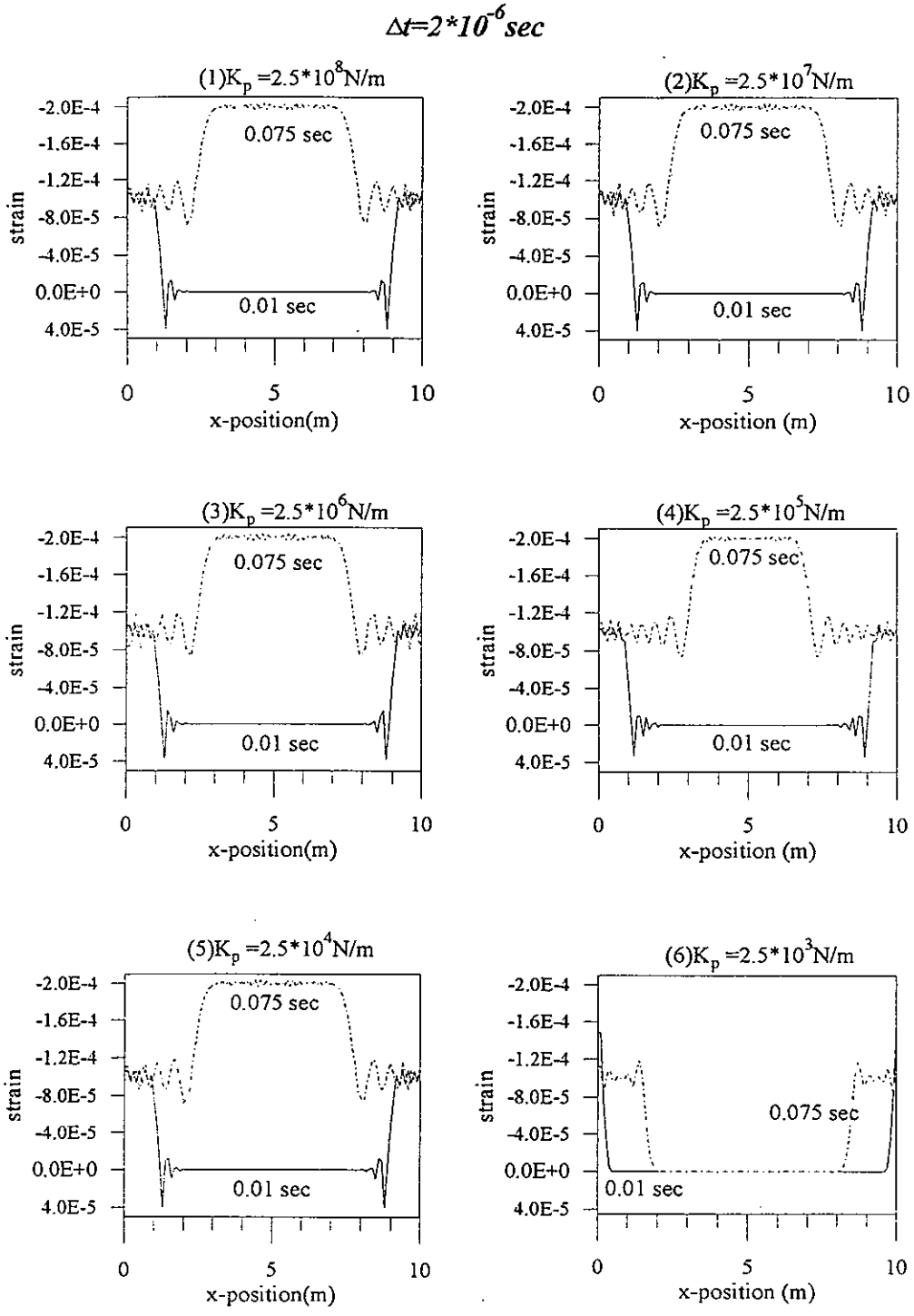

Fig. 14 DDA simulation for the condition points in $K_p - \Delta t$ plane with $\Delta t = 10^{-6}$ second.

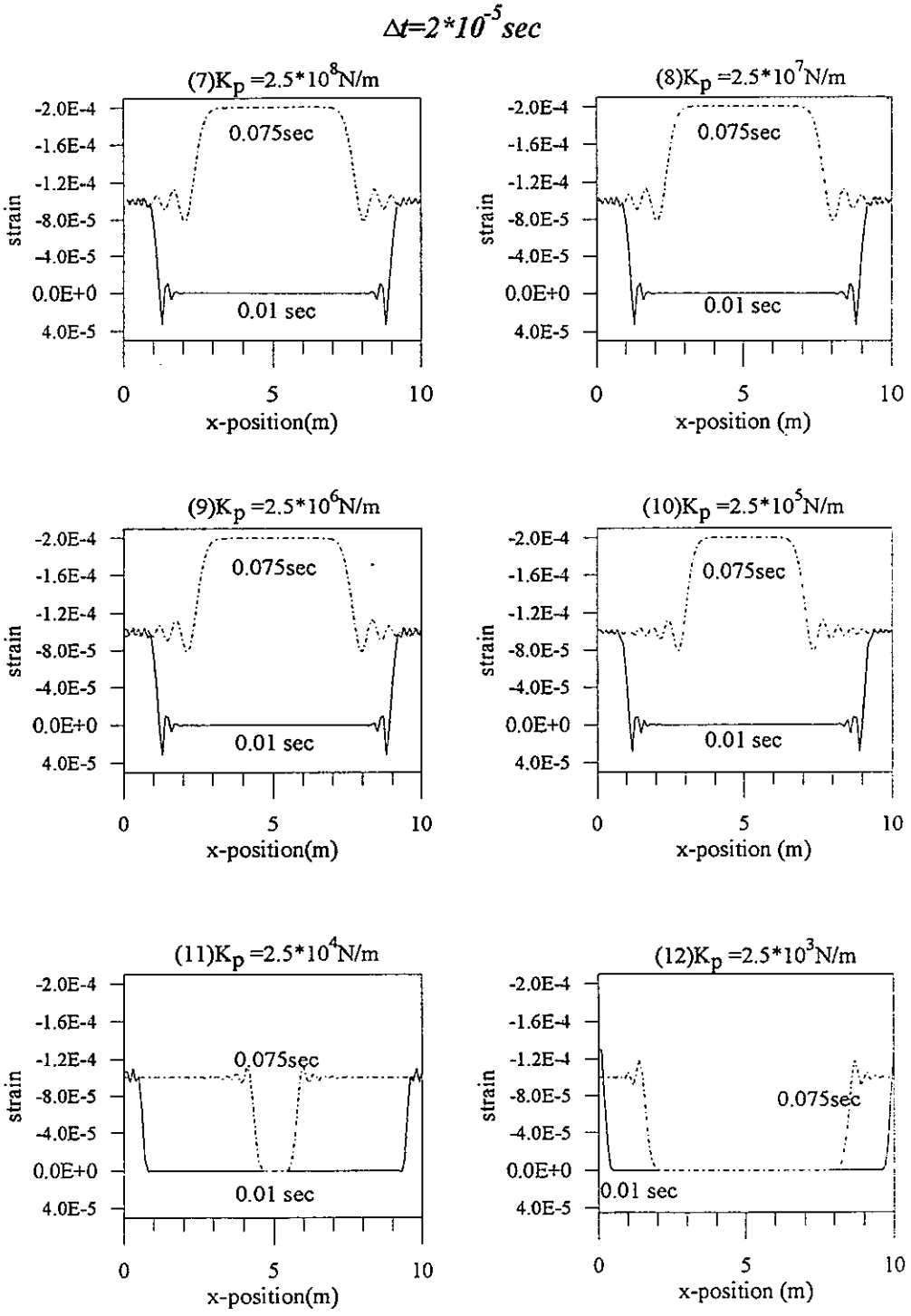

Fig. 15 DDA simulation for the condition points in $K_p - \Delta t$ plane with $\Delta t = 10^{-6}$ second.

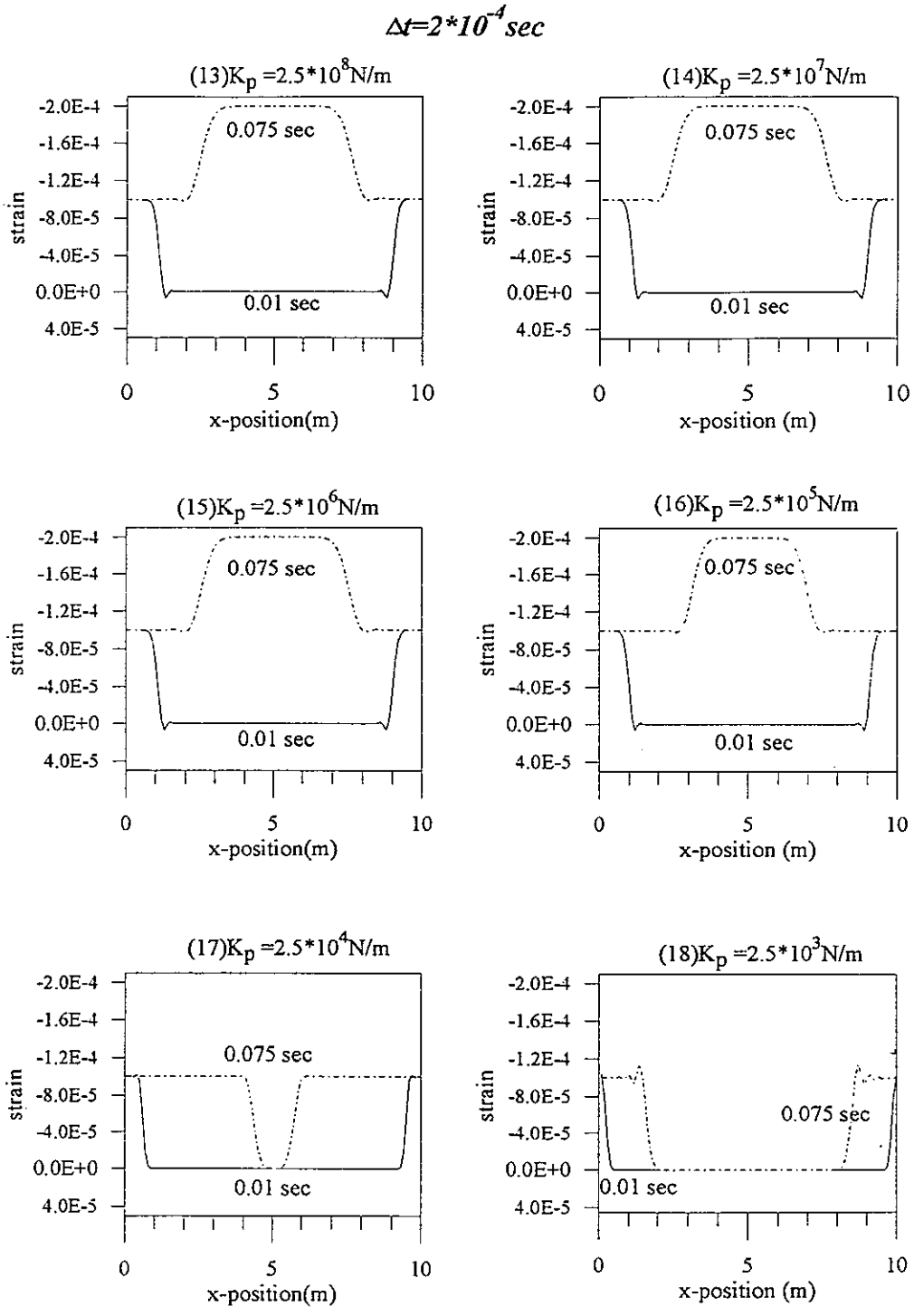

Fig. 16 DDA simulation for the condition points in $K_p - \Delta t$ plane with $\Delta t = 10^{-6}$ second.

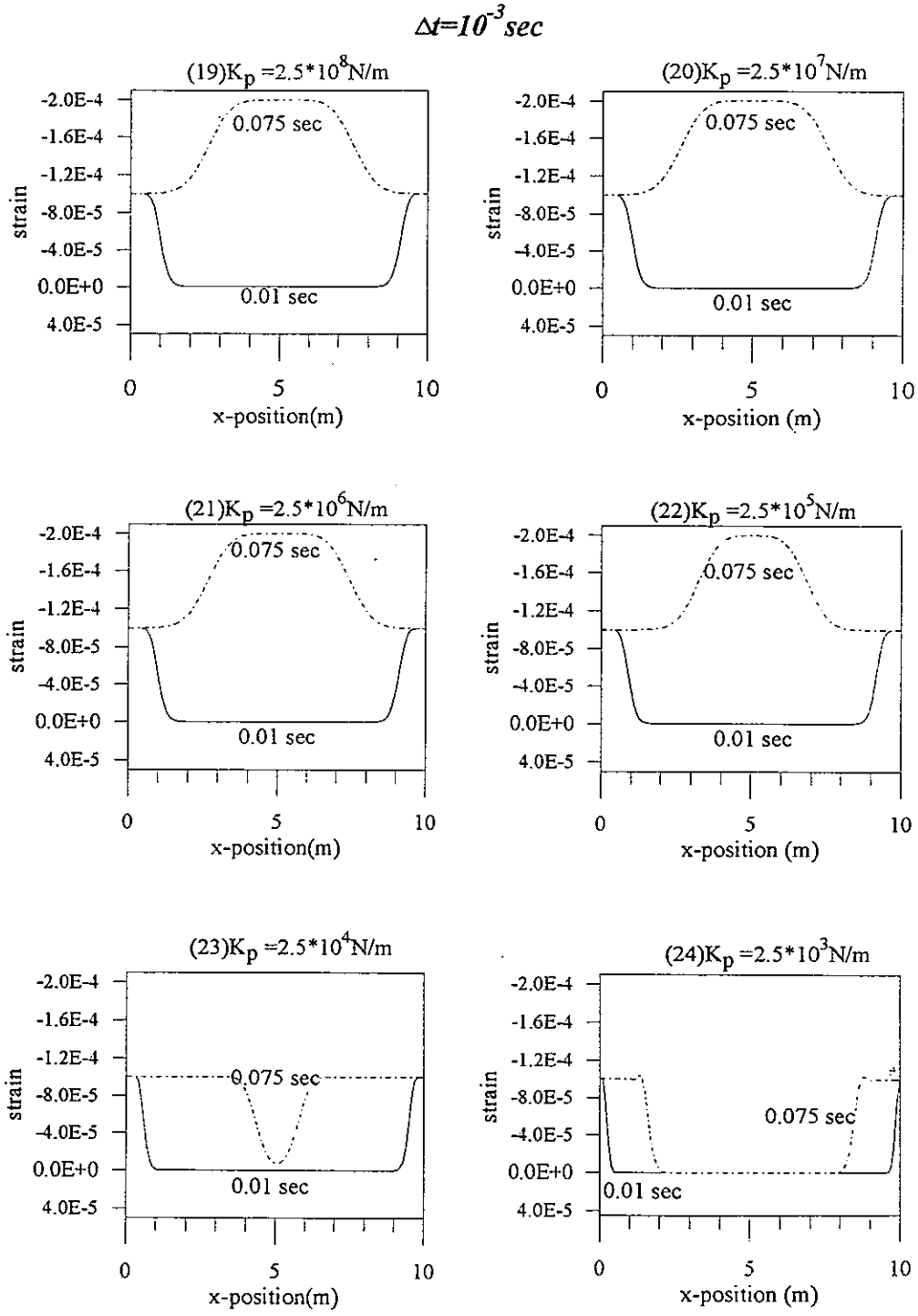

Fig. 17 DDA simulation for the condition points in $K_p - \Delta t$ plane with $\Delta t = 10^{-6}$ second.

TABLE 1 Input Data to the DDA Code For A Rod Under Step Loading

$E = 10{,}000\ N/m^2$, $\rho_0 = 1\ Kg/m^3$

Point No. in the $K_p - \Delta t$ plane	K_p (N/m)	Δt (sec.)
1	2.5×10^8	2×10^{-6}
2	2.5×10^7	2×10^{-6}
3	2.5×10^6	2×10^{-6}
4	2.5×10^5	2×10^{-6}
5	2.5×10^4	2×10^{-6}
6	2.5×10^3	2×10^{-6}
7	2.5×10^8	2×10^{-5}
8	2.5×10^7	2×10^{-5}
9	2.5×10^6	2×10^{-5}
10	2.5×10^5	2×10^{-5}
11	2.5×10^4	2×10^{-5}
12	2.5×10^3	2×10^{-5}
13	2.5×10^8	2×10^{-4}
14	2.5×10^7	2×10^{-4}
15	2.5×10^6	2×10^{-4}
16	2.5×10^5	2×10^{-4}
17	2.5×10^4	2×10^{-4}
18	2.5×10^3	2×10^{-4}
19	2.5×10^8	2×10^{-3}
20	2.5×10^7	2×10^{-3}
21	2.5×10^6	2×10^{-3}
22	2.5×10^5	2×10^{-3}
22	2.5×10^4	2×10^{-3}
22	2.5×10^3	2×10^{-3}

(2). The penalty spring serves as the dynamic loading transferring mechanism between the two contact bodies. Its stiffness affects the impulse transmissibility during the impact. As shown in Fig. 18 to Fig. 21, for the same time step size, larger penalty spring value compared with the one that Eq. (23) required provides more momentum into the neighboring medium. This effect causes larger influenced zone ahead of the major jump and let the wave front look moving faster. It is also noted for the same time step size the oscillation pattern in the zone around the wave front is fixed. For larger time step size the damping effect is stronger then the oscillation is smaller and the waveform look more clean.

(3) For the points on $K_p - \Delta t$ plane of same a $K_p \cdot \Delta t$ value, larger time step causes more energy dissipation from the system. This is due to the time integration scheme used in the DDA code and has been discussed in the previous section on the oscillation of step loaded single block.

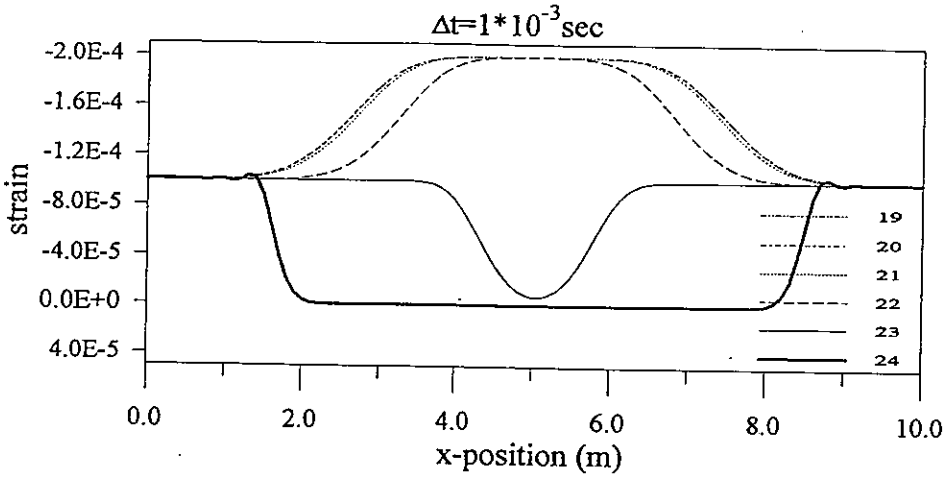

Fig. 18 Stress wave propagation simulated by DDA code at the condition points in $K_p - \Delta t$ plane with time step size $\Delta t = 10^{-3}$ second.

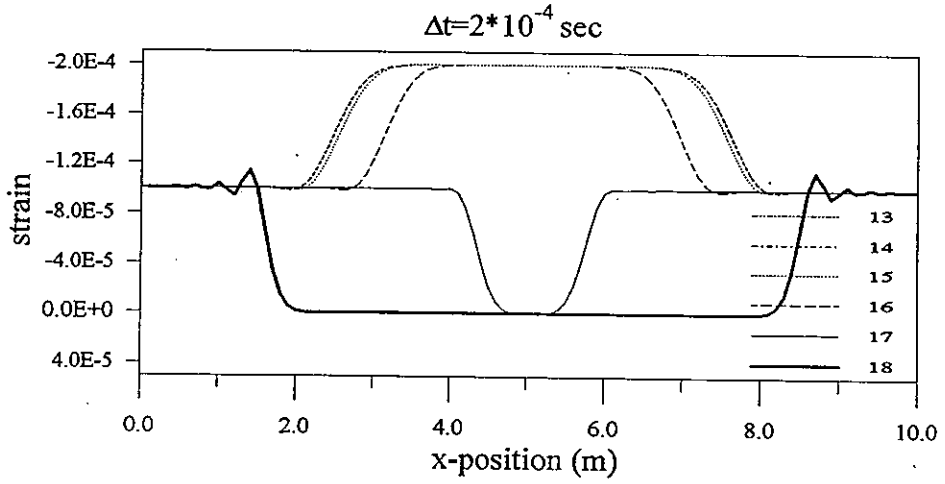

Fig. 19 Stress wave propagation simulated by DDA code at the condition points in $K_p - \Delta t$ plane with time step size $\Delta t = 2 \times 10^{-4}$ second.

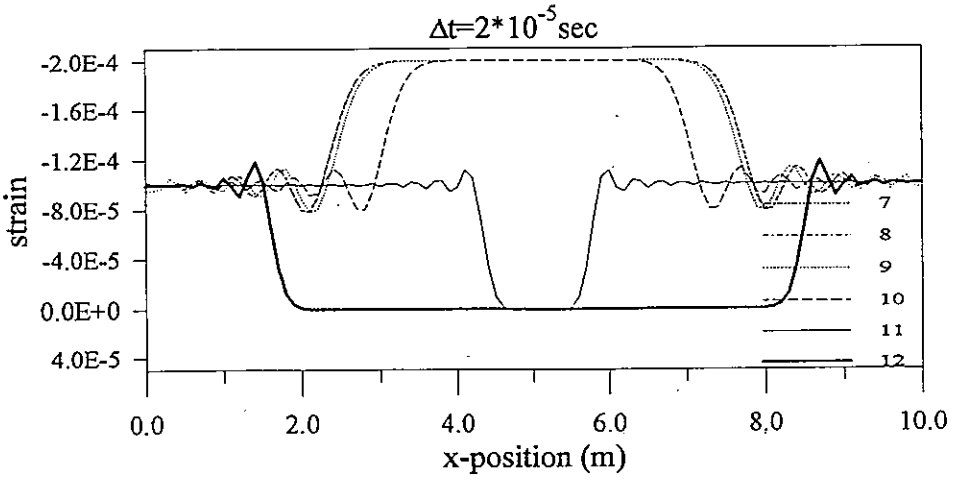

Fig. 20 Stress wave propagation simulated by DDA code at the condition points in $K_p - \Delta t$ plane with time step size $\Delta t = 2 \times 10^{-5}$ second.

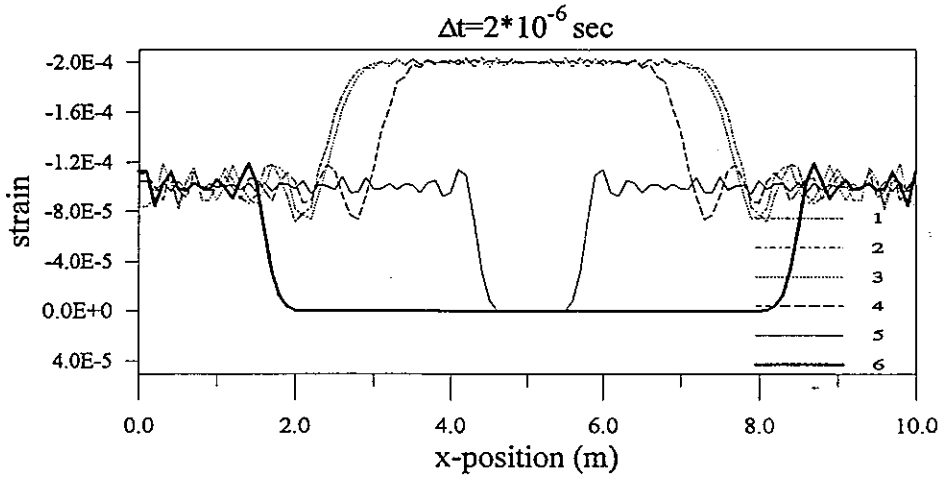

Fig. 21 Stress wave propagation simulated by DDA code at the condition points in $K_p - \Delta t$ plane with time step size $\Delta t = 2 \times 10^{-6}$ second.

Fig. 22 to Fig. 27 show the variation of the simulation results having the same penalty value but with different time step size. It is observed that the moving of the wave front is faster as the penalty value increased. This implies that the compensation mechanism between the damping effect due to the time integration scheme and the over-impulse transmission by stiffer penalty spring.

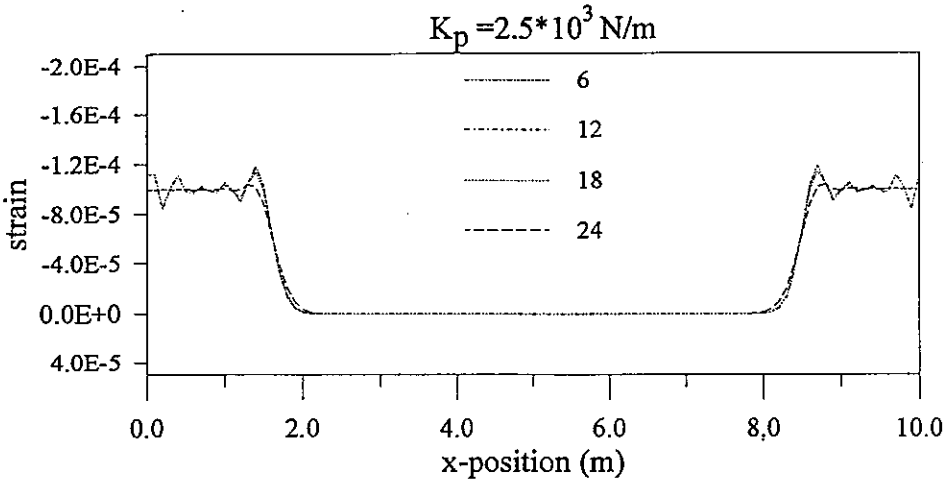

Fig. 22 Stress wave propagation simulated by DDA code at the condition points in $K_p - \Delta t$ plane with same penalty number $Kp = 2.5 \times 10^3$ N/m.

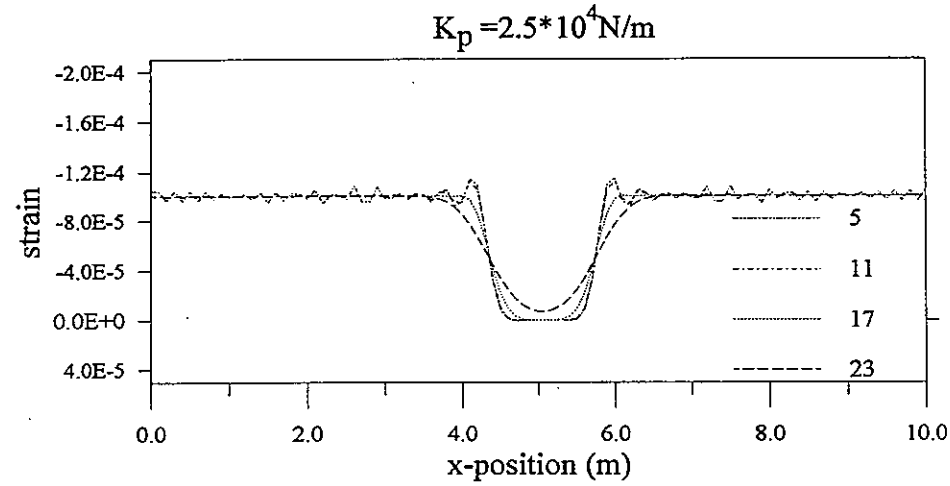

Fig. 23 Stress wave propagation simulated by DDA code at the condition points in $K_p - \Delta t$ plane with same penalty number $Kp = 2.5 \times 10^4$ N/m.

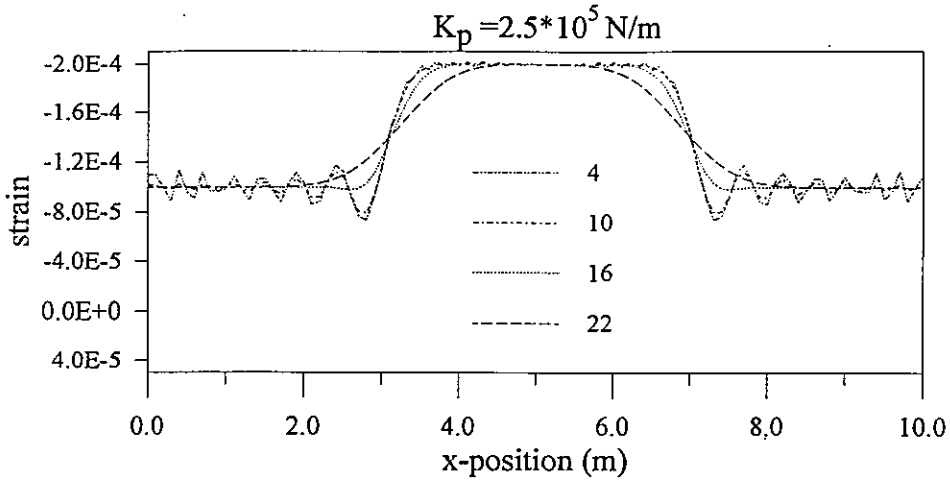

Fig. 24 Stress wave propagation simulated by DDA code at the condition points in $K_p - \Delta t$ plane with same penalty number Kp = 2.5 x 10 ^{5} N/m.

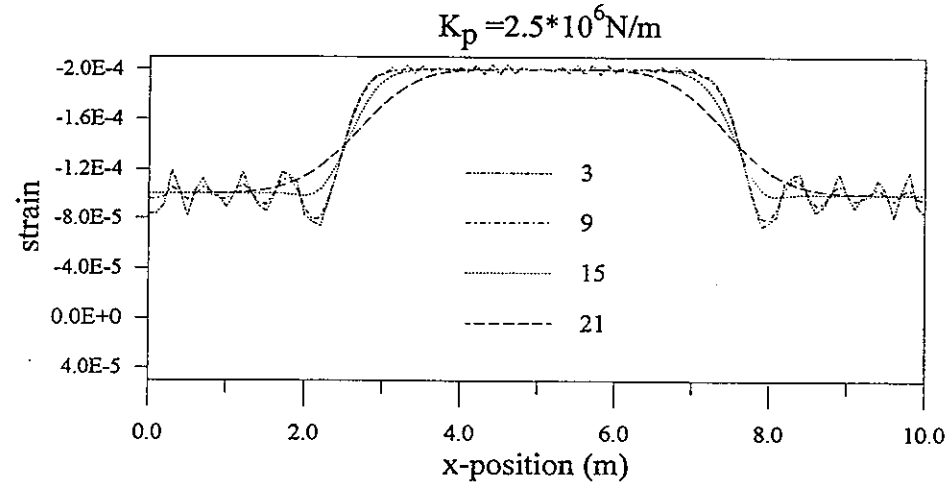

Fig. 25 Stress wave propagation simulated by DDA code at the condition points in $K_p - \Delta t$ plane with same penalty number Kp = 2.5 x 10 ^{6} N/m.

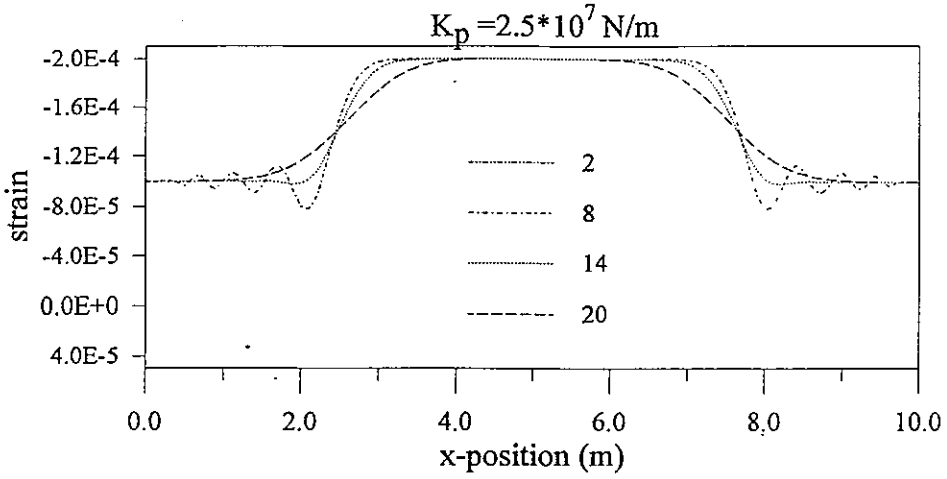

Fig. 26 Stress wave propagation simulated by DDA code at the condition points in $K_p - \Delta t$ plane with same penalty number Kp = 2.5 x 10 ^{7} N/m.

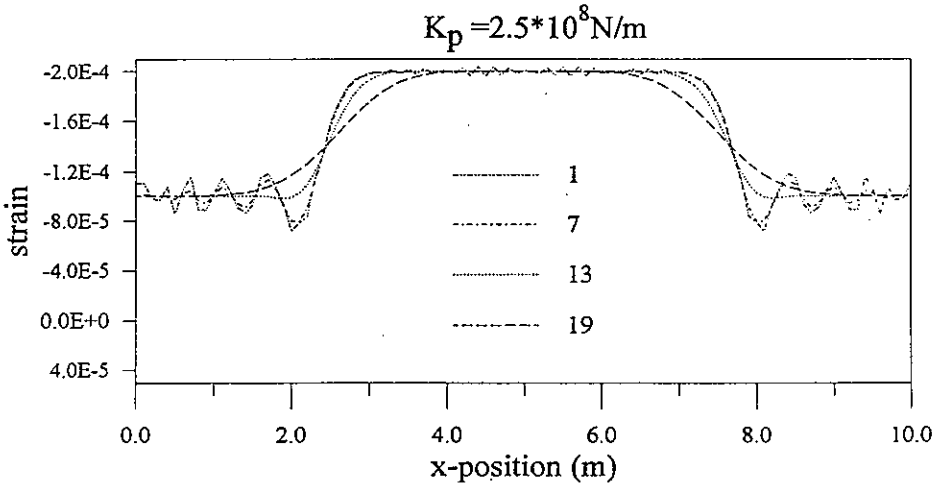

Fig. 27 Stress wave propagation simulated by DDA code at the condition points in $K_p - \Delta t$ plane with same penalty number Kp = 2.5 x 10 ^{8} N/m.

The optima criteria curve in the $K_p - \Delta t$ plane should be the equilibrium points of the above two mechanisms. For example of the studied problem shown in Fig12, an estimated threshold curve can be sketched as the dotted line shown in Fig. 13 according to the simulation results. If the time step size is adjusted in one's simulation procedure, the compatible penalty value Kp should be determined according to the Eq. (23). Nevertheless, the criteria proposed in Eq.(23) do generally provides a reasonable initial reference for analysts working on dynamic contact analysis.

5. CONCLUSIONS

In this paper the dynamic-contact scheme in the DDA method characterized by penalty spring value and time step size were studied in detail. It is believed that these two parameters are the most important factors which affect the simulation results of the DDA code. The central difference type time integration scheme used in DDA method has some energy dissipation effect especially at large time step size. For better analyses, the time integration scheme applied in the DDA method should be improved. An impedance matching type criteria based on the conservation of linear momentum principle in impact dynamics is proposed for analysts working on dynamic-contact problems to set a suitable penalty number at the contact interface. The adequateness of this criteria has been verified in the paper. This newly proposed criteria can be applied to any dynamic contact analysis method. In general, the DDA method has great potential and unique ability to help engineers and researchers solving the type of problems containing dynamic effect and contact interaction among multy deformable bodies. This DDA method needs more diverse application and quantitative analysis to gain the experience to reach its full potential.

REFERENCES

1. Shi, Gen-hua, 'Discontinuous Deformation Analysis, A New Numerical Model for the Statics and Dynamics of Block System', University of California, Berkeley, Ph. D. Thesis, August (1988).
2. Shi, Gen-hua, 'Manifold Method of Material Analysis', Proc. Ninth Army Conference on Applied Mathematics and Computing, 18-21 June 1991, Minneapolis, Minnesota.
3. Goodman, R. E.; R. Taylor; T. L. Brekke, 'A Model for the Mechanics of Jointed Rock', J. of Soil Mechanics & Foundation Division, Proc. ASCE Vol. 94, SM3, pp. 637 - 660 (1968).
4. Cundall, P. A., 'A Computer Model for Simulating Progressive, Large-scale Movements in Blocky Rock Systems', Proc. Int. Symp. on Rock Mechanics, Nacy, France, pp. II - 18, (1971).
5. Cundall, P. A. and O. D. L. Strack, 'A Discrete Numerical Model for Granular Assemblies', Geotechnique, 29,1, pp. 47-65 (1979).
6. Loring, L. J., B. H. G. Brady and P. A. Cundall, 'Hybrid Distinct Element-Boundary Element Analysis of Jointed Rock', Int. J. Rock Mech. Mining Sci., Vol. 23(4), pp. 303-312 (1986).
7. Williams, J. R. and G. G. W. Mustoe, 'Modal Methods for the Analysis of Discrete Systems', Computers and Geomechanics, 4, pp. 1 -19 (1987).

8. Munjiza, A., 'Discrete Elements in Transient Dynamics of Fractured Media', University of Wales, Swansea, Ph. D. Thesis, Sept. (1992).
9. Owen, D. R. J.; A. Munjiza; N. Bicanic, 'A finite element-Discrete Element Approach to the Simulation of Rock Blasting Problems', Proceedings FEMSA-92, 11th Symposium on Finite Element Methods in South Africa, Cape Town, pp. 39-59, January (1992).
10. Hughes, T. J. R.; R. L. Taylor; J. L. Sackman, 'Finite Element Formulation and Solution of Contact - Impact Problems in Continuum Mechanics', SESM Report No. 74-8, University of Calinifornia, Berkeley, May (1974).
11. Hallquist, J. O.; 'DYNA3D user's manual, rev. 3', University of California, Lawrence Livermore Laboratory, Livermore, July (1987).
12. Chaudhary, A. B.; K. J. Bathe, 'A Solution Method for Static and Dynamic Analysis of Three-Dimensional Contact Problems with Friction', Computer& Structures, Vol. 24, No. 6, pp. 855 - 873 (1986).
13. Hughes, T. J. R.; R. L. Taylor; J. L. Sackman, A. Curnier, W. Kanoknukulchai, 'A Finite Element Method for a Class of Contact - Impact Problems', Comp. Method Appl. Mech. Engng., 8, pp. 249 - 276 (1976).
14. Hallquist, J. O.; G. L. Goudreau; D. J. Benson, 'Sliding Interfaces With Contact - Impact in Large - Scale Lagrangian Computations', Comp. Meth. appl Mech. Engng., 51, pp. 107-137 (1985).
15. Oden, J. T.; E. B. Pires, 'Nonlocal and Nonlinear Friction Laws and Variational Principles for Contact Problems in Elasticity', J. Appl. Mech., Vol. 50, pp.67-76 (1983).
16. Pires, E. B.; J. T. Oden, 'Analysis of Contact Problems with Friction Under Oscilating Loads', Comp. Methods Appl. Mech., Vol. 39, pp. 337-362 (1983).
17. Oden, J. T.; J. A. C. Martins, 'Models and Computational Methods for Dynamic Friction Phenomena', Comp. Methods Appl. Mech., Vol. 52, pp. 527-634 (1985).
18. Zhong, Z. H.; L. Nilsson, 'A Contact Seraching Algorithm for General 3D Contact - Impact Problems', Computers & Structures, Vol. 34, pp. 327-335 (1990).
19. Huston, R. L.; C. Passarello, 'On Multi- Rigid-Body System Dynamics', Computers & Structures, Vol. 10, pp. 439-446 (1979).
20. Mahmoud, F. F.; Mahmoud, M. M. Hassan; N. J. Salamon, 'Dynamic Contact of Deformable Bodies', Computers & Structures, Vol. 36, No. 1, pp. 169-181 (1990).
21 Roy R. Craig, *Structural Dynamics - An Introduction to Computer Methods*, John Wiley & Sons, pp. 35-37 (1981).
22. M. Macaulary, *Introduction to Impact Engineering*, Chapman and Hall, (1987).